An experimental investigation of the contact behaviour of railway ballast

By

Aziz Urahman Hakimi

A thesis submitted in fulfilment of the requirements for the
degree of
Doctor of Philosophy

Department of Civil, Environmental & Geomatic Engineering

University College London

April 2025

Declaration

I, Aziz Urahman Hakimi, declare that the work presented in this PhD thesis is my own and has been carried out independently, except where otherwise acknowledged. This thesis has not been submitted, either in whole or in part, for any other degree or qualification at this or any other institution.

A portion of this work was previously submitted as part of the formal requirements for a PhD upgrade at University College London and has since been substantially developed and expanded for this final submission.

All information, ideas, and data drawn from other sources have been properly cited and acknowledged throughout. Any assistance received during the course of this research has also been clearly stated.

I take full responsibility for the content and integrity of this work.

Signed: ███

Date: 10/04/2025

Abstract

Accurate simulation of railway ballast behaviour in discrete element models (DEM) relies on precise contact-scale parameters, such as stiffness, friction, and damping. However, these micromechanical mechanisms are difficult to investigate experimentally and therefore remain poorly understood, especially under varying environmental and loading conditions. In most countries, railway ballast seems to be sourced from nearby locations but comparisons between properties of different ballasts and their performance are rare. This research addresses these gaps by investigating the contact-scale behaviour of ballast particles from multiple geological sources using unique experimental facilities and advanced experimental methods to enable more accurate characterisation of their mechanical and surface properties, allowing an informed comparison between the different types of ballast.

Railway ballasts of various origins and mineralogy (andesite from China, basalt from Australia, granites from the UK and China) were studied under varied loading conditions -- monotonic normal and tangential loading, normal cyclic loading and cyclic tangential loading, dry and wet contacts under different rates (slow and fast). The tests were carried out in a custom-built inter-particle apparatus—originally developed by Coop and Senetakis (2014) and later refined by Nardelli et al. (2016) and Wong et al. (2019), which was further modified by the author for the purpose of this study with help from Dr. Saurabh Singh. These modifications included increasing the size and number of vertical bearings and washers to enhance stiffness and control. Comprehensive calibration of load cells, displacement transducers, and the sliding mechanism ensured accurate force and displacement measurements. Particular attention was given to the methodology of carrying out the tests for more accurate results, and new procedures were developed. Among the outcomes are the new ways of applying load, with normal loading applied at a standardised rate of 150 mm/hr to avoid creep and asperity damage. Tangential shearing was also optimised and conducted at 0.1–0.5 mm/hr. High-frequency data from cyclic tests (recorded every 3–7 seconds) was processed using custom MATLAB scripts developed specifically for this research for cleaning, slope correction, and precise determination of tangential stiffness and friction. This new methodology provides a robust base for carrying out

particle-to-particle tests and obtaining more reliable results. A new procedure was also developed to quantify the roughness of the ballast surface at the contact and its evolution during loading. A systematic method using the ConfoMap software was developed, in the absence of industry standards. The method includes optimised Z-stack imaging (μm); a cut-off value selected through Power Spectral Density analysis in MATLAB, leading to a standardised 16 μm cut-off; form removal using a 9th-degree polynomial to exclude form from surface height data; optimal roughness extraction method, selecting a 0.2×0.2 mm area after form removal for filtering, ensuring consistent and representative measurements.

Mechanical testing involved monotonic and cyclic loading of ballast types including andesite (China), basalt (Australia), and granites (UK and China), under dry and wet conditions. Test results show that in monotonic normal loading, the load-displacement response of the contact is initially soft (0.01-0.5 N/μm) and with an increase in the load, the response gets stiffer (5-10 N/μm). The experimental response does not follow predicted responses from existing contact models such as Hertz (1882), and Modified Hertz (Yimsri and Soga, 2001).

The monotonic and cyclic shearing behaviour of ballast materials revealed distinct friction and stiffness characteristics. In monotonic tangential loading, the stiffness was found to be the highest at the start (1-3 N/μm, static friction) decreasing gradually to zero (kinetic friction, onset of sliding) at about a tangential displacement of 100-200 μm. The monotonic tangential stiffness increases with an increase in normal load. Post-sliding, the tangential force becomes constant with the coefficient of friction from 0.4-0.9. Andesite exhibited the highest friction (0.65-0.9) due to its rough texture, while Chinese granite showed the lowest (0.15-0.5) owing to its smooth surface. Basalt and fresh granite displayed moderate friction (0.4-0.7), with used granite performing similarly but more consistently. Washed-used granite achieved higher friction (0.7-0.8) and maintained the highest tangential stiffness across all conditions, reflecting improved stability after cleaning.

In the cyclic tangential loading, stiffness was found to increase with the number of cycles from (1 to 3 N/μm) as well as the coefficient of friction (0.6-0.8), because of changes in the surface roughness, however, the stiffness decreased as the tangential stiffness increased. Cyclic tests showed that basalt, Chinese granite and washed-used

iii

granite had the highest friction coefficients (0.65-0.8). Andesite and used granite exhibited moderate coefficients (0.6), reflecting balanced performance under shearing. Fresh granite, however, had the lowest coefficient (0.5-0.7), indicating reduced frictional properties. Interestingly, despite prior usage, used granite maintained a coefficient comparable to andesite, showcasing its durability and potential for reuse.

Chinese granite exhibited the least vertical displacement during cyclic shearing, while fresh granite showed the most, attributed to its angularity. Basalt and used granite resisted deformation well, while washed-used granite showed slightly higher displacement, potentially from washing-induced degradation.

The rate of abrasion during cyclic shearing identified Chinese granite and used granite as the most durable, with minimal wear under high loads, while fresh granite and andesite showed significant wear, raising concerns about their longevity. Basalt and washed-used granite consistently exhibited high tangential stiffness, though flooding reduced their performance.

Further, the cyclic stiffness and coefficient of friction decrease in the presence of water at contact, however, it was found that normal load level and rate of the cycles do not affect the coefficient of friction. Roughness was measured before and after the test for all types of ballasts, and it was found that the asperities deformed through plastic deformation.

This research identifies Chinese granite, basalt, and washed-used granite as the most reliable materials for demanding railway ballast applications due to their superior durability, stability, and frictional performance. Recommendations include prioritising these materials for high-performance applications, optimising washing treatments to enhance material reuse, and advancing modelling frameworks to simulate real-world conditions more accurately. Future work could focus on long-term performance testing, dynamic loading simulations, microstructural analyses, and the development of hybrid ballast materials to improve the sustainability and efficiency of railway infrastructure.

Impact Statement

his thesis provides critical insights into the micro-to-macro mechanical behaviour of railway ballast materials, delivering significant advancements in understanding their performance under varying mechanical and environmental conditions. By employing a combination of experimental methods and theoretical models, the research establishes a comprehensive framework for evaluating ballast materials of various geological origins. It identifies Chinese granite, basalt, and washed-used granite as optimal choices for high-performance railway infrastructure based on their superior durability, frictional performance, and deformation resistance.

Fresh granite, despite its initially high stiffness, exhibited substantial wear and angularity under loading, limiting its long-term structural stability. In contrast, used granite retained much of its integrity and frictional behaviour, indicating potential for sustainable reuse. Washed-used granite proved even more promising, outperforming both fresh and used variants in terms of friction and stiffness after cleaning. This highlights the practical value of post-use treatments, although it also underscores the need to optimise washing techniques to minimise structural degradation.

A major technical contribution of this thesis is the modification and enhancement of an existing custom-built inter-particle apparatus. Working alongside Dr. Saurabh Singh, I redesigned the loading system to improve its stiffness and control, allowing for more accurate force and displacement measurements. Extensive calibration was conducted, and new experimental protocols were introduced, including the standardisation of normal and tangential loading rates to prevent creep and ensure replicability. The test procedures were optimised further through the development of bespoke MATLAB scripts for high-frequency cyclic data processing, which improved noise filtering, slope correction, and stiffness evaluation.

The thesis also presents a novel methodology for measuring and tracking surface roughness at the contact interface during loading. A standardised process using Z-stack imaging and ConfoMap software was developed, incorporating power spectral density analysis and 9th-degree polynomial form removal, allowing consistent and meaningful roughness quantification in the absence of industry standards.

The findings have immediate practical implications for railway engineering. The data provides a robust basis for ballast selection and maintenance strategies that enhance track performance, longevity, and safety. Moreover, the demonstration of the durability and reusability of used and washed ballast supports more sustainable engineering practices aligned with global sustainability goals in infrastructure.

By providing experimental evidence on surface roughness evolution, plastic deformation of asperities, and inter-particle stiffness and friction under realistic loading scenarios, including wet and dry cyclic shearing. This research offers crucial input for validating and improving numerical models, particularly in the context of discrete element modelling (DEM). It also highlights the importance of environmental effects, such as water ingress and flooding, on ballast performance and emphasises the value of region-specific ballast assessment for infrastructure resilience.

In conclusion, this thesis contributes to the development of more resilient, sustainable, and efficient railway systems. Its recommendations for material selection, advanced laboratory testing, and numerical model calibration will inform engineers, researchers, and policymakers in improving the design, maintenance, and sustainability of global rail networks.

In the name of Allah, the Most Gracious, the Most Merciful.

Acknowledgements

I am sincerely thankful to my research supervisors, Dr. Beatrice Baudet and Professor Matthew Richard Coop, for their invaluable guidance, patience, and support throughout this project. A special, heartfelt thanks goes to Dr. Beatrice Baudet—your encouragement and belief in me have truly transformed my life. Your mentorship lifted me beyond the challenges of my homeland, Afghanistan, and allowed me to grow and thrive. For that, I will always be grateful.

To Dr. Fatin, thank you for your assistance in ensuring the safe execution of my experiments. To Dr. Pedro, I deeply appreciate your technical support and insightful contributions. I would also like to thank the lab technician, who is behind-the-scenes efforts, ensured the smooth functioning of the lab and played a vital role in my research.

A special and sincere thank you to Saurabh Singh for your constant help and encouragement throughout this journey. Your support has been truly invaluable, and I cannot thank you enough.

To my dear friends, thank you for walking alongside me through this chapter. Your companionship made this journey not only manageable but memorable. May Allah (SWT) preserve our bond and grant you all success in both this life and the next.

Many thanks to Prof. Glen McDowell, Dr. Mathias Tolomeo, Prof. Buddhima Indraratna, and Dr. Xiaoyan Zhang for kindly providing the materials used in this study. I also gratefully acknowledge the EPSRC for funding this project.

Finally, I humbly pray that Allah (SWT) accepts this work from me, forgives my shortcomings, and allows it to be a source of benefit. *Ameen.*

Contents

List of Figures

xiv

xvii

xviii

xix

xxi

xxix

xxxi

List of Tables

Nomenclature

a	Major radius of the equivalent area ellipse (Equation 2.47)
a*	Equivalent contact radius for a rough surface
a, a_0	Radius of the contact area
A, A_0	Projected area
AB	Andesite ballast (China)
A_e	Equivalent area ellipse
AR	Aspect ratio
b	Minor radius of the equivalent area ellipse
BB	Basalt ballast (Australia)
CB	Chines granite (China)
CDG	Completely decomposed granite
CR	Circularity
CS	Carbonate sand
d_f	Feret diameter
dF_{max}, dF_{min}	Maximum and minimum Feret diameter
di_{max}	Diameter of the largest inscribed circle
d_{max}, d_{int}, d_{min}	Maximum, intermediate and minimum diameters of the particle
dp	Distance between the platens at the start of the test
D_0	Initial displacement
DEM	Discrete Element Method
Df	Final displacement
Dk	Radius of curvature

E	Young's modulus
E*	Equivalent Young's modulus
E_{2D}	Ellipseness
f_c	Compressive strength
F_h	Horizontal force
F_N	Normal force
G	Shear modulus
GB	Fresh granite (UK)
G_s	Specific gravity of the particle
H	Hardness
H1	Horizontal 1 (along the moving direction)
H2	Horizontal 2 (orthogonal to the moving direction)
Hertz*	Hertz theory including surface roughness
HH	High humidity
H_{mic}	Effective microhardness
I_n	Intermediate dimension of the particle at rest position
K	Bulk modulus
K_{N*}	Normal contact stiffness
K_T	Tangential contact stiffness
K_{T*}	Tangential contact stiffness for rough surfaces
$K_{T,0}$	Initial elastic tangential contact stiffness
LBS	Leighton Buzzard quartz sand
LH	Low humidity
Lo	largest dimension of the particle at rest position

LS	Limestone
Lw	The longest diameter of a particle
LVDT	Linear Variable Differential Transformer
M	Critical state stress ratio (q'/p')
N	Normal force
P	Normal force
P_0	Particle's actual 2D projection perimeter
Pc	Perimeter
Pe	Perimeter of equivalent ellipse area
R	Equivalent radius
R_W	Roundness
RMS	Root mean square
S	Sphericity
S_a	Average deviation roughness
SA_{es}	Surface area of a sphere having the same volume as the particle
SA_{rp}	Actual surface area of the particle
SCC	Smallest circumscribable cuboid
SDU	Sample Dispersion Unit
SEES	Scalene ellipsoid equivalent sphericity
Sh	Smallest dimension of the particle at rest position
S_q	RMS roughness
S_{W2D}	2D sphericity
S_{W3D}	True sphericity
T	Effect of load (Equation 2.25)

T	Tangential contact force
UG	Used granite (UK)
W_m	Mass of the particle
WCDG	Washed completely decomposed granite
WUG	Washed used granite (UK)
α	Non-dimensional parameter (Equation 2.27)
β	Radius of the asperities of the rough surface (Equation 2.26)
δN	Normal displacement
δT	Tangential displacement
η	Energy loss factor
κ	Constraint factor (Equation 2.21)
μ	Inter-particle friction coefficient
ν	Poisson's ratio
ρ	Effective radius of curvature
ρ	Material's resistivity (ohm/m) (Equation 2.44)
ρ_r	Regularity
p_0	Maximum contact pressure
ρo	Flow pressure of the softer material
ρ_w	Density of water
σ	Combined RMS roughness
σ_f	Characteristic stress
φ'	Internal angle of shearing resistance (friction angle)
$\varphi \mu$	Inter-particle friction angle

1. Introduction

1.1 Background

Granular materials like railway ballast exhibit complex mechanical behaviour governed by the properties and interactions of individual particles. Unlike soils, ballast consists of angular, coarse rock fragments designed to provide exceptional interlocking and load-bearing capabilities, making it crucial for the stability and integrity of railway infrastructure. Despite its importance, much of the research in granular mechanics has historically focused on sands, leaving significant gaps in the understanding of the micromechanical behaviour of ballast under various loading conditions.

The Discrete Element Method (DEM), introduced by Cundall and Strack (1979), has emerged as a powerful tool for investigating granular materials, including railway ballast. DEM enables simulations of particle interactions under different loading scenarios, offering an alternative to continuum mechanics approaches like the Finite Element Method. However, for DEM simulations to yield accurate results, they require micro-scale input parameters such as inter-particle friction coefficients, normal and tangential contact stiffness, and particle shape. In most DEM studies, spherical particles are used, and input parameters are calibrated through curve fitting from macroscopic tests, such as triaxial or shear box tests. This reliance on spherical particles leads to inaccuracies, as they fail to replicate the angular geometry and surface roughness of real ballast particles. Moreover, rolling resistance parameters, often added to prevent particle spinning in DEM, do not correspond to physical mechanisms like interlocking that occur in angular ballast.

Recent advancements in DEM have allowed for more accurate modelling of particle shapes (e.g., Tolomeo & McDowell, 2022). However, incorporating realistic shapes demands equally realistic contact behaviour models. Experimental data on micromechanical properties of ballast, such as inter-particle friction coefficients, stiffness, and surface roughness, remain limited, with most prior studies focusing on sands (e.g., Skinner, 1969; Nardelli and Coop, 2019). For ballast materials, only a few studies, such as Cole and Peters (2007) and, more recently, Wong and Coop (2024),

have examined contact behaviour. While some studies, e.g. Cole and Peters (2007), largely relied on artificially prepared surfaces rather than natural ones, recent studies have started to explore the micro-mechanical behaviour of railway ballast under various loading conditions.

 For example, Wong (2022) used advanced experimental setups to measure the inter-particle friction of granite ballast and investigate deformation. Other studies (Altuhafi et al., 2024; Suhar et al., 2020) have shown the critical role of surface roughness and particle geometry in defining mechanical behaviours such as tangential stiffness and abrasion resistance. However, much of this work remains focused on one specific type of ballast, but there are not sufficient data to be also able to extrapolate to other types e.g. of other mineralogy.

This research builds on recent advancements by examining railway ballast particles with distinct mineralogical compositions, including, basalt ballast (BB) from Australia, fresh granite (GB) used granite (UG) and washed-used granite (WUG), from the UK, and Chinese granite (CB) and andesite ballast (AB) from China. Using the inter-particle apparatus initially developed by Coop and Senetakis (2014) and modified by Wong and Coop (2019), this study investigates deformation, contact areas, and surface roughness under monotonic and cyclic loading conditions.

The findings aim to contribute to the development of a framework of behaviour application to all railway ballast. In doing so, this research supports the development of more robust and reliable models for predicting ballast behaviour, thereby contributing to the design and maintenance of railway infrastructure.

1.2 Aim and Objectives

The research aims to develop a comprehensive understanding of inter-particle behaviour in a range of railway ballasts by testing and measuring critical parameters under normal and tangential conditions, with or without water, enabling more sustainable choices of ballasts based on performance instead of single geographical proximity.

In the following are the main objectives to achieve the main aim:

1. To investigate the nature of contact in soil and ballasts, e.g., whether it is elastic or plastic or both, and changes in surface roughness, during normal loading of different ballasts.

2. To investigate the efficiency of already existing simple contact models for normal loading of a variety of railway ballasts, including used and washed re-used ballasts.

3. To investigate the load-deflection behaviour of different types of ballasts under monotonic loading, including stiffness, normal and tangential, and coefficient of friction.

4. To measure the coefficients of friction, vertical displacement, and rate of abrasion of different railway ballasts under cyclic loading.

5. To investigate the effect of rate and flooding on the coefficient of friction of the different ballasts.

6. To make a comparison of the performances of the different types of ballasts.

1.3 The Outline of the Thesis

Chapter 2: Literature review

This chapter provides an overview of the existing research relevant to this study. It begins by summarising the morphological properties of soil particles and describes in detail the methods used for measuring and quantifying surface roughness. Additionally, the chapter reviews the historical development of studies related to friction and its progression over the years. Major contact mechanics models for normal and tangential loading, which are pertinent to the current study, are explained in detail. Finally, the chapter concludes by presenting an overview of the main experimental works related to the study of railway ballasts, highlighting their relevance and limitations in the context of this research.

Chapter 3: Materials and experimental equipment

This chapter discusses the materials and equipment used throughout this research project. A significant focus is placed on the three-dimensional version of the Inter-Particle Loading Apparatus, Wong et al. (2019) detailing the improvements made to

the apparatus for the purpose of this experimental research. In addition, the chapter includes a brief review of other experimental equipment, such as the Zeiss optical microscope and the Zeiss ConfoMap and Keyence systems (laser confocal), which were utilised for image analysis and surface metrology. The methodology adapted to measure the surface roughness of soil grains is described along with the preparation processes for the samples. The experimental procedures and preliminary test results from the early stages of this PhD study are also presented. The chapter concludes with a detailed explanation of the apparatus calibration procedures undertaken to ensure the reliability of the experimental results.

Chapter 4: Monotonic normal loading behaviour of railway ballasts

In this chapter, the behaviour of railway ballast particles of various origins under normal loading conditions is presented. It is divided into three parts. The first part focuses on the measurement of the surface roughness of different ballast particles, presenting detailed findings from surface metrology techniques. The second part discusses the results of single-particle testing, introducing the primary outcomes from inter-particle testing using the three-dimensional Inter-Particle (IP) loading apparatus. The normal stiffness at contact is determined. The final section compares the experimental results with theoretical models, including Hertzian and modified Hertzian models, the latter including roughness. This chapter forms the foundation for the subsequent analysis of ballast behaviour under shearing conditions.

Chapter 5: Monotonic shearing behaviour of railway ballasts

Following the exploration of ballast behaviour under normal loading, this chapter presents the results of monotonic shearing tests conducted on the various ballast particles. The response of these materials under different normal load conditions during monotonic shearing is examined. The chapter also includes data from local shearing tests, which provide additional insights into particle interaction under shear loading. Furthermore, the effects of normal cyclic loading behaviour are briefly discussed. The tangential stiffness and mobilised coefficient of friction are determined.

Chapter 6: Cyclic shearing behaviour of railway ballasts

Railway ballasts are routinely subjected to cyclic loading, making the understanding of their behaviour under these conditions critical. This chapter investigates the cyclic shearing behaviour of ballast particles through a series of tests conducted using the IP apparatus. Surface quantification before and after testing is performed to evaluate changes in surface texture and roughness. Tangential stiffness and mobilised inter-particle friction (μ) values are determined, and their evolution during cyclic loading is thoroughly analysed.

The chapter examines the influence of various factors on cyclic shearing behaviour, including the number of cycles, loading interface conditions, normal load levels, and shearing rates. Limited attention is given to the effects of water immersion, the presence or absence of powder generated at the contact, and the role of pre-sheared surfaces in frictional behaviour.

A summary of the loading parameters is presented in tabulated form. Due to the extensive amount of data collected, the chapter is organised to first present individual test results for each ballast type, followed by combined data analyses for each material. Finally, a comparative analysis of the cyclic shearing behaviour of the different ballast types is provided, highlighting their relative strengths and weaknesses.

Chapter 7: Comparative analysis of ballast mechanical behaviour

This chapter synthesises the findings from the previous chapters, offering a comprehensive comparison of the mechanical behaviour of the ballast materials studied. The analysis is divided into three main sections. The first section focuses on monotonic normal loading behaviour, comparing stiffness, deformation, and stability across low, medium, and high normal load ranges for all ballast types.

The second section examines monotonic shearing behaviour, with a focus on the coefficient of friction and tangential stiffness exhibited by the different ballast materials under varying monotonic shearing conditions.

The final section explores the cyclic shearing behaviour of all ballast types under different normal loading conditions. The analysis considers key parameters such as mobilised inter-particle friction (μ), vertical displacement, rate of abrasion, and

tangential stiffness, while also exploring the impact of factors such as surface conditions and environmental influences.

This chapter integrates the results from monotonic and cyclic tests to provide a detailed comparative assessment of the materials studied, offering insights into their suitability and performance in railway engineering applications.

Chapter 8: Conclusion and Future Work

This chapter summarises the key findings of this PhD research, which investigated the micro-to-macro mechanical contact behaviour of various railway ballast materials. The research combined experimental methods and theoretical models to examine the performance of these materials under different loading conditions.

The chapter concludes by recommending further studies to refine experimental methodologies, explore additional ballast materials, and extend investigations to real-world ballast beds. The findings provide valuable guidance for improving the design, maintenance, and longevity of railway track structures.

All references cited in the thesis are provided at the end, along with appendices containing supplementary material. Tables and figures are shown at the end of each relevant chapter.

2. Literature review

A review of the most necessary references related to the current work is given here. They include existing data available on the properties of granular materials and the parameters derived from them, their mechanical characterisation at the microscale and their theoretical representation in terms of responses. In addition to understanding experimental results from tests conducted on granular materials and the different phenomena which influence their mechanical behaviour, a basic understanding of the numerical methods used to simulate the response of granular materials is essential because it can inform the interpretation of the experimental findings and provide insights into the mechanisms governing their behaviour under various conditions.

The morphological properties of soil particles, including their shape, form and size, sphericity, roundness and surface texture, and properties of the soil that influence its behaviour, are discussed in Section 2.1. In Section 2.1.4, methods for measuring and quantifying surface roughness (texture) are reviewed in detail. Section 2.2 presents an overview of previous studies about friction, not only in soil, the development of friction through the years, and the contact behaviour of some minerals. Section 2.3 presents the major contact mechanics models (theoretical and experimental) which have been developed for normal and tangential loading. Several aspects of soil behaviour that are affected by the soil particles are also presented, for example, how surface roughness affects the behaviour of rough surfaces in contact.

In the literature, normal and tangential forces are often referred to respectively by FN and FT, but sometimes as N and T or P and T. Section 2.5 provides details of the main experimental works relevant to the current work. As this thesis focuses on the contact behaviour of particles, one of the main objectives is to study their main features systematically and comprehensively, for example, finding the real T/N of railway ballasts. Many aspects of the mechanical behaviour of granular materials have been studied, but few studies have focused on this aspect.

2.1 Characterisation of soil grains

Soil is described by three main characteristic parameters: particle size, particle size distribution, and particle shape (Altuhafi et al., 2013). Sand sizes are commonly measured with sieve analysis, whereas particle shapes are typically assessed qualitatively in geotechnical engineering research and industry practice. A morphological description of soil particles includes their shape and surface texture (Blott & Pye, 2008). Particle shape is a fundamental property of natural sand, which is based on three aspects: form (sphericity), roundness (reflects the sharpness or angularity of corners) and surface texture (Barrett, 1980). Because of its discrete nature, soil behaviour is affected by size, shape, and strength (Cavarretta, 2009).

It has been established whether there is a link between size and shape, where the shape is more affecting the behaviours of sands, and size is usually related to the dimensions of the particles in different directions (Cavarretta et al., 2010).

2.1.1 Shape

Research on particle shape has existed, even though the definition of shape is not universally accepted. In some explanations, shape refers to external morphology and is synonymous with form (Shorter Oxford English Dictionary, 1955; Gary, McAfee & Wolf, 1972). In contrast, Sneed & Folk (1958) used the term form to refer to the shape of the particle as determined by taking measurements along three orthogonal axes and plotting them on a form triangle. This means the term 'form' excludes other shapes, such as roundness which exists at a shallow scale. However, Whalley (1972) regarded shape as only one of several properties giving rise to external morphology, while form referred to the process of forming the shape.

Sand's mechanical response is influenced by its particle's shape, and the variations in void ratios and density also depend on the shape (Mitchell & Soga, 2005). Stiffness is also affected by the shape (Cho et al. 2006; Pestana and Salvati 2006). Furthermore, it was demonstrated by Cho et al. (2006) that shape is related to critical state soil mechanics parameters. According to Clayton et al. (2006), shape affects how much degradation occurs during cyclic loading. Studies in the literature document the impact of particle geometry on sand response, so a robust approach to quantifying sand

particle shapes has been necessary. Several approaches are given by Clark (1981) to quantify particle shape in geomechanics and geology. For shape classification, it is thought by some researchers ideal to use descriptors that can express particle form, surface texture, or roundness separately (Barrett 1980; ISO 2008; Cavarretta 2009). i.e. the affected scales of particle shape. The descriptors also need to be compatible with creating realistic shapes in DEM.

Barrett (1980) proposed that all the external characteristics of particle morphology should be parts of the shape, as three independent aspects: the surface texture, the form, and the roundness (Fig. 2.1). In his work, Barrett summarised the various definitions of form and roundness proposed by the literature, where each parameter can be varied irrespectively of the other two parameters. His definition of the three aspects of particle shape and concept was adapted by the ISO (2006) and considered a 2D feature projection of particle shape, which may be a limitation since particles are 3D.

Blott & Pye (2008) used a morphological description of sediment soil particles that includes their shape, surface texture and form, while roundness, irregularity, and sphericity were identified as characteristics of the shape. They used similar definitions of shape and roundness to the ones of Barrett (1980). According to them, particle irregularities are not determined by form. Instead, they are determined by indentations (concavities) and projections (convexities). Sphericity is defined as the degree of shape a particle approximates to a proper sphere. It has been recognised to play a crucial role in the macroscale behaviour of soil (e.g., Cho et al., 2006).

The form is generally defined as the first scale property describing the geometric proportions and represents the relationship between the particle's three dimensions, such as particle sphericity. Roundness is the second scale property, and the shape of the particle at the scale of its asperities is reflected by its roundness. The third scale is roughness, which refers to the surface texture, and it can be superimposed on the particle on both corners and edges between the corners. The influence of the roughness on the overall shape has long been thought of as being minimal, and it can be

challenging to measure by traditional methods, so it has often gone unmeasured in previous studies. Recent work has shown, however, that roughness influences soil behaviour, for example, its stiffness (Otsubo et al., 2015).

Generally, these three parameters are thought to be independent of each other, which means, the change in one of these parameters will not change the other (Wadell, 1932; Barret, 1980). This has not really been proven.

Among the criteria ISO (2006) proposed for evaluating shape description, memory and processing time are taken into consideration. The shape property (e.g., roundness) must be described. The link between the shape and descriptor must be unique (one-to-one mapping). The quality of the description is based on small changes in form.

The ISO 26824:2022 was issued to provide a standard method of characterising particulate systems. ISO (2006) criteria for defining shape descriptors are as follows. Rotation and reflection invariance: consistency with changes of shape orientation.

➢ Scale invariance: invariability for identical shapes of different sizes.
➢ Independence: discarding one descriptor, the others do not need to be recalculated.
➢ Parsimony: thriftiness in the number of terms used to describe a shape.

Research results have usually shown that not all ISO requirements for shape quantification can be fulfilled for soils, e.g., scale invariance, rotation, and independence (Cavarretta, 2009).

2.1.2 Size and form

1) Size

Particle size is an essential property of soil, and the particle size varies depending on the materials. The definition of representative sizes helps describe the 3D geometry of particles (Endoh, 2006). The soil type is typically determined by particle size, and soil characteristics are influenced by particle size distribution. For instance, the angle of shearing resistance (Holtz and Kovacs 1981), compressibility (Yang, 2006), as well as internal erosion susceptibility (Kenney and Lau 1985). Even though the size is not a

feature of shape, it is a helpful starting point for considering morphological descriptions of particles.

Soil grains are irregular, and therefore determining their size is not straightforward. Generally, if soil particles drop into a horizontal plane, the smallest dimensions will lie perpendicularly to it. It was called the plane of greatest stability by Feda (1982) because it corresponds to the particle's maximum potential energy. Since sands are complex in morphology, making it challenging to measure particle size in three dimensions, the size is commonly expressed as three parameters L, I, and S representing the dimensions in three orthogonal directions. Krumbein (1941) described L as the longest dimension, I as the intermediate dimension perpendicular to L, and S as the shortest dimension perpendicular to I and L. Blott and Pye (2008) made a different proposal defining the small circumscribing cuboids that could contain particles (SCCs) as a measurement unit to reduce the measurement error caused by the irregularity of the particles. Cavarretta's (2009) study suggested measuring the three dimensions on the plane of greatest stability, and his concept and description of the smallest circumscribed cuboid SCC are shown in Fig. 2.2.

ISO (No. 26824: 2022) introduces a parameter called the Feret diameter dFeret to simultaneously calculate L, I, and S values. It represents the distance between parallel tangents to the outline of the particle. It is also called the calliper diameter since it uses the calliper to measure the size of particles. For a given shape, dFmax and dFmin, are measured as the maximum and minimum values of dFeret, respectively, as given in Fig. 2.3. The values of dFeret are commonly determined in software used in particle sizers such as Qicpic (Ting, 2018).

Measuring these three dimensions requires more specific equipment than sieves. The particle size distribution can be found with some available methods, such as laser diffraction or single-particle optical sizing. A calliper can be directly used to measure gravel size and coarse sand particles; however, for fine sand and silt-size particles, the three dimensions can only be determined by a microscope or digital image analysis

Particle size significantly influences aggregate and single-particle strength. The compression strength of rock particles decreases with increasing particle size, although tests have found that the size of particles has a negligible effect on the shear strength of rock particles (Becker et al., 1972). The study of Griffith (1921) showed that the cracks occurring in a particle under compression start from the tips of the internal surface defects. As a result, the larger the rock specimen, the more likely the rock specimen will contain defects and fail under compression. A relationship between particle size and single-particle strength of sand particles is illustrated in Fig. 2.4, and there is a linear relationship between quartz particle strength and particle size (Nakata et al. 1999). In this thesis, however, particle behaviour will only be examined before failure.

2) Form

The form constitutes the first scale property of the geometric proportions, representing the relationship between the three dimensions. One way it can be quantified is by measuring the similarity between a particle and a sphere, for example, particle sphericity, measures how similar a particle is to a sphere. For the description of the form, various parameters have been suggested in previous studies. Most of the particle's descriptors are related to L, I, and S, but none of the methods is universally accepted and acknowledged.

Among the proposed classifications those of Zingg (1935) are straightforward based on Fig. 2.5. However, the resulting diagram becomes crowded in sectors I, II, and IV for S/I (thickness to breadth ratio) and I /L (ratio between breadth and length) value higher than 2/3. Limitations to Zingg's diagram were highlighted by Sneed & Folk (1958), who pointed out Zingg's diagram might not be comprehensive as it includes only four form classes. In his studies, Krumbein (1941) also suggested classifying the form into four different classes of the shaped particle such as 'disc', 'spherical', 'bladed' and 'roller' as shown in Fig. 2.5.

In Fig. 2.6, the ratios of S/L and (L-I)/(L-S) are considered (Sneed & Folk, 1958). allowing a disc-rod index to be determined by the ratio S/L, which represents the flatness, while (L-S)/(L-I) indicates the disc-rod index. In total, ten form classes are

classified in this diagram, including compact, compact-party, compact-bladed, compact-elongate, platy, bladed, elongated, very platy, bladed, and elongated. A new method of classifying particle forms was later proposed by Blott & Pye (2008) by equating elongation (I/L) and flatness (S/L) with an equant, and they adopted this method to describe particle form. A list of descriptive terms of the form indicating the degree of elongation and flatness is presented in Table 2.1. Additional methods include every aspect of the three form dimensions, from simple expressions to indices presented in Table 2.2. Blott & Pye (2008) investigated the comparison of 23 gravel-sized particles with 13 daily objects using the form factors shown in Table 2.2. Most shape parameters are, however, based on two-dimensional images, where it is widely used to calculate the aspect ratio (A.R.). The aspect ratio can be connected to dFeret, and in that case, it could be defined as the following:

$$\text{Aspect Ratio (A.R.)} = \frac{dFmin}{dFmax} \tag{2.1}$$

In Yang and Luo's (2015) work, particle shape was found to significantly affect the macro-mechanical behaviour of sand. The result was that A.R. was directly responsible for influencing the intercept and gradient of the critical state line (CSL), as shown in Figure 2.7. for uniform and binary sand.

2.1.3 Sphericity and Roundness

1) Sphericity

Sphericity informs about the first such shape of a particle while roundness informs its ingredients in the 2nd scale. The first research into the sphericity and roundness of particles was carried out by Wadell in the early 1930s. Wadell (1932) presented a new systematic approach to shape analysis, applied to sedimentation problems and erosion of gravel particles. He proposed that the two factors (sphericity and roundness) must first be separated to understand shape. Wadell (1932) used the fact that spheres have the highest volume ratio to the surface area and defined sphericity as a property related to form with sensitivity to particle elongation. Roundness relates to angularity, which refers to particle protrusions or corners (Wadell 1932). According to his definition, a spherical particle is characterised by the maximum ratio between the volume and the surface area. It has the highest settling velocity of any shape with the same volume and

density when in suspension. Hence, he proposed the concept of true sphericity SW3D, which is usually expressed as the ratio of the surface area of a sphere with a similar volume as the particle (SAes) to the actual surface area of the particle (SArp):

The degree of true sphericity $S_{W3D} = \dfrac{SAes}{SArp}$ (2.2)

Different theories describe particle shape in different ways regarding sphericity, and there are two attitudes towards the roles of sphericity. While some researchers (such as Cho et al., 2006) consider that sphericity is one part of the form of particles, others (such as Barrett, 1980) believe that it is the only parameter representing shape. The true sphericity of Wadell, however, is difficult to measure as the real surface area of the particle cannot be determined easily. As a result, the maximum sphericity of the projection, proposed by Sneed & Folk (1958), has often been approximated to the real sphericity.

For regular shapes, true sphericity can be calculated, e.g., sphere sphericity, regular dodecahedron sphericity, and cube sphericity are 1.0, 0.91, and 0.81, respectively. Nevertheless, Wadell (1932) stated that sphericity is highly dependent on roundness, so cannot be considered as an independent variable. For example, when the edges of a cube become rounder, its sphericity will change. Considering that natural sand particles have irregular shapes, it is not easy to measure their surface area. Several alternatives to quantifying sphericity based on particle projections in two dimensions have been proposed.

For example, another concept known as a degree of circularity was introduced by Wadell (1933) as the maximum diameter of a circle that has a similar area to the particle's projection divided by the actual perimeter of that projection. The parameter C_{W2D} is described here and in the following text:

Degree of circularity $C_{W2D} = \dfrac{C}{P} = \dfrac{\sqrt[2]{\pi A}}{P}$ (2.3)

In this formula, A represent the actual and convex areas of the hull, and P represents the outline's perimeter. This definition has the advantage that those quantities can be determined from the projected particle, but it has the bias of the plane of repose. Fig. 2.8 shows examples of aspect ratio, sphericity, and convexity measuring for Leighton Buzzard sand particles along with elongation (Altuhafi & Coop, 2011).

After Wadell, a new 2D sphericity method was developed by Riley (1941), which is very simple and defined as projection sphericity. In soil mechanics, this has led to the development of a more straightforward SC (sphere circularity) formula based on Riley's sphericity that ignores square root, which has been used in recent studies by, e.g., Santamarina & Cho (2004); Cho et al. (2006) or Cox & Budhu (2008).

Krumbein (1941), also proposed a simplified calculation of sphericity, where the sphere diameter was compared with the diameter of the smallest circumscribed sphere and called the SKS (the sphericities used in the chart of Krumbein and Sloss).

All the definitions to calculate sphericity directly that are presented above are time-consuming. However, it is still possible to estimate sphericity by visual comparison with reference charts (Folk, 1955; Barret, 1980). In some cases, a silhouette of particles with a specific shape is used in these visual comparators, while others use images of soils and adopt them as the comparator (Schneider et al., 2012). As a result, Krumbein & Sloss (1963) introduced a new reference chart that had an enormous impact on the subsequent work on the shape of particles. He used intervals of 0.2 in his chart, and the values of spheres and rounds were separated by columns and rows, which can be seen in Fig 2.9. The sphericity of these projections is derived from their proportional lengths and widths and their roundness as defined by their convex profiles.

More recently, the study of Zheng & Hryciw (2015) compared five existing sphericity descriptors with SKS to clarify their differences and figure out whether they could effectively describe sphericity, as shown in Fig. 2.10. According to their study, the area sphericity S.A., measured by comparing a particle's projected area with the radius of the minimum circumscribed circle, agrees best with SKS. The simplicity and efficiency of the Krumbein & Sloss (1963) reference chart make it a quick tool for the description of particle shape today, but it has several shortcomings, including inadequate shape descriptors and single-particle image intervals that cannot be ignored. Thanks to the development of technology digital image analysis with computational methods can now be applied, such as the estimation of Fourier descriptors and fractal analysis, which enable the measurement of particle shape and

reconstruction in three dimensions (Hyslip & Vallejo, 1997; Bowman et al., 2001; Fonseca et al., 2012; Mollon & Zhao, 2012 & 2013).

2) Roundness

Before Wadell (1932), the shape of the particle with roundness was described for the first time by Wentworth in 1919 when he was studying the abrasion of cobbles. In his proposed theory, roundness was determined by the sharpness of the corners rather than by the overall shape of a particle, and the definition has been widely acknowledged and accepted by many researchers. The following is the equation of Wentworh (1919) that defines the roundness of particle shape:

$$\text{Roundness} = \text{Rw} = \frac{\text{Dk}}{\frac{\text{Lw}}{2}} \qquad\qquad (2.4)$$

The radius of curvature (Dk) is the radius at the sharpest corner, and the diameter (Lw) is NGTNp. Based on this equation, the roundness calculation of a particle can be significantly affected by its form, so it can be noted that an elongated particle with sharp corners will have a lower roundness than another with the same sharp corners. In a later revision, Wenworth (1922) showed that roundness is the ratio between the radius of the sharpest corner and the average radius obtained from the particle, which is equivalent to the average of L and I. It is because measuring roundness is scale-dependent that particle diameters are typically used to normalise roundness.

Donkins & Folk (1970) later proposed to use the ratio of the radius of a particle's largest inscribed circle to the Dk formula. Particles may have more than one sharp corner that contributes to the roundness; however, these definitions of roundness only examine the sharpest corner.

According to Wadell (1932), roundness can be estimated from the ratio between the radius of the maximum circle inscribed and the radius of the average radius of the surface, as represented in Fig. 2.11. Wadell (1932) also illustrated the three stages of particle roundness occurring during erosion, as shown in Fig. 2.12. The sharpness of

the particle corners decreases firstly because of erosion and then increases by weathering.

Realistically, when the image magnification is increased in the irregular outline, more corners appear, but the radius of curvature decreases. In other words, a particle appearing smooth to the naked eye may not appear round under a magnifying lens. Consequently, Wadell's roundness is a scale-dependent parameter, unlike sphericity. Wadell (1932) overcame this challenge by adopting a nominal, but not precisely defined, particle size of 70 mm while adjusting the dimensions of particles for the screen projection, illustrated in Fig. 2.13. The roundness definition provided here is widely accepted and used worldwide by many researchers. However, Cavarretta's (2009) experimental studies show that the parameter is still found to have scale-dependent properties, which can be due to the inability to consider all corners.

Researchers have defined roundness by reference charts, such as Krumbein & Sloss's (1963) chart, for its ease of use. It is one example of a reference chart that describes roundness in traditional ways, where the roundness of the particles is found to be related to the particles' surface texture (Mackey, 1956). Roundness is usually quantified by the roundness descriptors rather than by specific values.

Russell and Taylor (1937) classified particle roundness into five different categories, based on comparing photos of the particle with the chart. The five classifications are named based on the particle's angularity and roundness, and they are: a) angular, b) sub-angular, c) sub-rounded, d) rounded, and e) well-rounded. However, the classification of roundness by Russell and Taylor (1937) shows some weakness when distinguishing very angular particles. A very angular term was added to Russell & Taylor's chart by Powers (1953) to place lower classes in a different division (Fig. 2.14). According to this chart, the concept of roundness is like that of Wadell (1932). Although the chart is demonstrated as subjective, it can still be used to estimate particle roundness.

Digital images of particles can now be used to figure out roundness more accurately and objectively. To obtain three-dimensional and two-dimensional images of the

particles, a computer can now make high-resolution images of particles using advanced devices such as the laser scanner, scanning electron microscope (Bowman et al., 2001), and computed tomography (Zhou et al., 2015).

Ehrlich & Weinberg (1970) developed the first Fourier descriptors analysis applied to roundness. The lower-order of Fourier descriptors indicate the shape of an object, including its roundness, and higher-order descriptors indicate the surface. The sand grains in Fig. 2.15 presented here were generated by Mollon and Zhao (2012) using Fourier descriptors. A sand particle with high sphericity can have sharp corners. Wadell (1932) thought that roundness and sphericity should be independent. However, new research by Zhao & Wang (2016) found a possible correlation between these two properties, examining both crushed Leighton Buzzard and intact sand by X-ray (using the computed tomography method). Zhao & Wang (2016) suggested that particle shape might be affected by aspect ratio and roundness. This is illustrated in Fig.2.16, and it can be noted that the roundness calculated from the mean curvature of LBS particles is linked to their sphericity. Links to both particle sphericity and roundness for the minimum and maximum void ratio were found by Cho & Santamaria (2006) as illustrated in Fig.2.17. This results in more angular, than spherical particles having higher compressibility and lower packing density than spherical particles (Miura et al., 1998; Cho et al., 2006). It follows, according to Rothenburg & Kruyt (2004), that spherical and round particles have a higher packing density and a lower coordinate number (which measures how many contacts a particle has on average), which can affect small-strain stiffness. Payan et al. (2016a, 2016b) applied this finding by proposing a model of small-strain stiffness that was highly influenced by particle sphericity and roundness.

2.1.4 Roughness

Roughness is the third, small-scale parameter of soil particle morphology after form and roundness. If sand particles are inspected at high resolution, the surface is not perfectly smooth. To study the influence of roughness on the mechanical behaviours of sand particles, more work is needed. In practice, it is complicated to measure the surface roughness, and it is usually ignored in the quantification of particle

morphology because of the small size and shape irregularity of natural sand, which make it difficult to measure. Sand surface roughness has often been described qualitatively based on microscope scanning images, such as Fig. 2.18 (Santamarina & Cascante, 1998). The surface texture of sand grains is illustrated mainly by the micro-features present on the surface. There may be a relationship between the degree of surface roughness and the properties of the micro-features.

In the geological literature, a glossary of sub-micrographic surface textures of quartz sand particles was presented by Kimmel & Donahue (1968) through their analysis of quartz sand particles by scanning electron microscope (SEM). In their analysis, more than 400 samples and 4000 surfaces were tested for eight years, presenting four different surface textures. These surface textures included littoral, aeolian, glacial and diagenetic, and these were usually V-shaped patterns, as Tanner (1960) revealed that V-shaped patterns usually follow well-oriented paths. Brown (1973) investigated the surface textures of Pleistocene quartz grains from SEM images as illustrated in Fig.2.19, with the four different types of surface texture. This study investigated the criteria for interpolating the depositional history of sand grains proposed by Krinsley & Donahue's (1968). The micrograph shown in Fig. 2.19 illustrates a freshly weathered granite grain of quartz collected from a Northumberland stream. Krinsley & Donahue (1968) claimed that the texture indicates glacial activity because of the high angle and relief and semi-paralleled fracture, indicating the mechanical abrasion of these grains in an environment with a high energy level, such as a pebble beach with a surf zone, upper stretches of rivers, and upper reaches of streams.

Bowden & Tabor (1939) proposed that, as a consequence of surface roughness, the real contact area should be a very small part of the nominal area, even between two flat metal surfaces. Therefore, the theories of contact mechanics developed for perfectly smooth surfaces may not be valid for rough surfaces. Roughness parameters have been developing, often linked to the development of computing devices, and this means there is the possibility that parameters could change with future developments. One of the most often used approaches is based on dividing roughness into two categories as defined by Thomas (1999): average values and extreme value parameters, which are

relevant to the profile and surface. Based on the topography, these parameters can be used in both two-dimensional profiles and three-dimensional surfaces.

In early experiments, the roughness was initially only measurable by a light-section microscope; then, later electrical filters were developed, yielding more robust results. There are three main filters applied to surface measurements, such as shape effect, sound effect, and wavelength effect, which can all affect the grain roughness value if not applied. These are applied to calculate the ultimate roughness depth (St) in the filtered profile. Generally, St is divided into two for more values giving information about the profile: Sp represents the distance from the highest peak to the mean line in the profile, and Sm represents the depth of the lowest position from the mean line, as shown in Fig. 2.20 (Sander, 1991).

Bhushan (2001) suggested that surfaces are composed of numerous length scales of roughness that are superimposed, and therefore, the definition and value of roughness are dependent on the measuring device. This means that the roughness parameters are not universally defined and depend mainly on how well they are measured. As a result, in order to describe roughness, one should either show all the scales that are of interest or at least explain the range of scales that were taken into consideration; For example, Fig.2.21 shows that the roughness of a profile at different scales that is self-similar and fractal.

An elegant technique for describing self-similar surfaces is the fractal framework, developed by Richardson (1961) and Mandelbrot (1982). However, truly self-similar surfaces are rare in nature, and when they are observed, they are usually limited to a fixed range of scales. The surface of soil grains is often described as self-affine (Persson, 2001) with different vertical and horizontal scales. The fractal dimension $D_F = D_{F1D}$ is considered by ISO (2006) as a good descriptor of particle roughness, although it is defined in 1D from the particle outline. The ISO (2006) also suggested in D_{F1D}; roughness might be represented as a small parent outline, while angularity or roundness indicates a large one. Vallejo (1996) used fractal analysis to determine sand particles and angularity.

A more common way to describe the topography is by the statistical average parameters, of which the centre-line average roughness is the most straightforward, usually called Sa:

$$Sa = \frac{1}{L}\int_0^L |z|dx \qquad (2.5)$$

Where L represent a certain length and z is the difference between an elevation above the mean height and a point on the profile. In terms of average parameters, the mean height's root-mean-square deviation of z(x) can be more informative. In literature, this parameter is commonly known as RMS or Sq, which is:

$$RMS = Sq = \sqrt{\frac{1}{L}\int_0^L z^2 dx} \qquad (2.6)$$

According to Thomas (1999), when considering a sinusoidal profile, the ratio Sa/Sq≈ 0.9 is observed. When examining a Gaussian function with a height distribution, the ratio is approximately 0.8 and is affected by peaks or valleys. The diagram in Fig.2.22 demonstrates how Mate (2008) illustrated the limitations of Sq, despite its self-proclaimed superiority to Sa, as it is evident that Sq cannot separate the simple profiles with asperities of different shapes and frequencies. One main problem is that neither Sa nor Sq can provide a measure of variation in texture or any specific amplitude about the textural difference at any specific point of the profile or surface. By analysing a filter, as Senetakis et al. (2013) did, Sq can be measured from the flattened particle surface while avoiding shape effects. One limitation, however, as highlighted by Otsubo et al. (2015), is that filters typically available are scale-dependent and affect the value of roughness.

Yang et al. (2016) suggested that the surface roughness of sand can be measured by the method of power spectrum density (PSD) using white light optical interferometry, from which the fractal dimension and RMS roughness can be attained for the 3D surface without the need for filtering. Recent experimental research and DEM modelling by Nardelli & Coop (2018) and Sandeep et al. (2018) indicate that the surface roughness of sand particles affects small-strain stiffness at the macroscale and contact behaviour and inter-particle friction angles at the microscale, in the sense that

measuring techniques greatly influence the results. Moreover, surface roughness could affect both the contact behaviour and the interparticle friction coefficient of sand particles (Nardelli & Coop, 2018).

With the development of new instruments, surface roughness measuring techniques are continuing to develop. The most widely used methods for measuring the surface roughness of particles are listed below:

- ➤ Comb profilometer
- ➤ Stylus
- ➤ Optical techniques such as an interferometer, z-stack, etc.
- ➤ Atomic force microscope
- ➤ Ultramicroscopic measurements of surface roughness, known as scanning tunnelling microscopy (STM)

Optical techniques that do not require contact have an advantage over other measuring techniques, and optical techniques would require less time than microscopy (Whitehouse & Reason, 1965; Greenwood & Williamson, 1966). For this research, the roughness of ballasts was determined using an optical microscope, as will be described in Chapter 3.

Summary on morphology:

Soil is naturally made from discrete particles, and the behaviour of soil is highly affected by its size, shape, and strength. Micro-mechanical behaviours of soils and broken rock (e.g. ballast) are greatly influenced by particle morphology, and a morphological description of soil and rock particles includes their shape (form, roundness) and surface texture. Particle morphology might have been affected by transportation and deposition in the case of natural sands, or formation and wear in the case of ballast. While size is usually related to the dimensions of the particles in different directions and can be measured relatively easily, shape parameters were first visually characterised by comparing them to reference tables. Recent developments allow us to define and quantify particles' form, sphericity, and roundness in 2D and

3D; however, there is to date no universally recognised definition of sphericity or form, and surface roughness is usually ignored as the third scale of particle shape. That is difficult to quantify, although experimental and DEM studies suggest that the surface roughness of sand particles affects strain stiffness at the macroscale and contact behaviour and inter-particle friction angles at the microscale. Quantifying surface roughness is still challenging, as highlighted in the literature, and in this research, new methods to analyse the surface roughness of ballast, and its role in the mechanics of contact will be examined.

2.2 A background to contact mechanics: Studies on Friction and adhesion

Friction plays a significant role in the stability of soil masses and tribology problems. Several phenomena are affected by the frictional properties of materials, studied and analysed by scientists and engineers in different engineering fields such as Civil Engineering and Mechanical Engineering. It has been established that different frictional phenomenon theories share an everyday basis. However, some of their details and mechanical features are still unknown and interpreted in various ways. Even though the laws of friction are stated, Hahner and Spencer (1998) wrote that "the friction laws summarise a vast display of microscopic and nanoscopic phenomena and their interpretation in applied physics has become one of the fascinating studies". According to the American Society of Mechanics (ASM) Handbook report in 1992, there is no universal agreement on what causes friction, and a comprehensive picture will not be formed until much more work is done.

There have been four phases of research on friction between solid surfaces:

1- The establishment of traditional laws of friction by Leonardo da Vinci during the 16th century until Coulomb in the 18th century.
2- Tomlinson's theory of friction as well as the lubrication theory (1850-1930).
3- The emergence of tribology, wear theories and Bowden and Tabor's synthesis (1930-1980).
4- The study of nanotribology, friction at the atomic scale, and the most recent research work (since 1980).

During the years 1452 - 1519, Leonardo da Vinci studied a wide range of topics, including friction, wear, bearing materials, and lubrication systems. A significant contribution made by him was the study concerning the principles that control friction on solid surfaces. His landmark contributions demonstrate that friction between sliding surfaces is directly proportional to the normal force, regardless of the number of contacts between surfaces. He also found out that most of the clean and smooth surfaces have a coefficient of friction of 0.25. He added that the friction resulting from a body with more apexes (with uniform flexible asperities) is greater than from those with fewer apexes.

The scientific community rediscovered and accepted these laws when Amontons (1699) proposed them almost three centuries later. According to the first two classic laws he introduced, the friction force is proportional to the load. It is independent of the contact area since it relies on the height of asperities, which play a significant role. Amontons' laws were reconsidered by Coulomb (1736-1806), who studied the friction generated by sliding and rolling for application to the design of engines and vehicles. In his study, the influence of four primary variables was examined: the type of surface, the amount of contact area, the load supported by the surfaces, and the contact duration. He examined the impact of the first three factors on the next and their relationship to speed.

According to Coulomb, the force of friction (here called FT) and the load (here called FN) are relatively proportional, and cohesion would only have a small impact (since it will act according to the contact surface area or the contact points). It can be noted that Coulomb was always using the FN/FT ratio instead of the more common FT/FN ratio.

Hence, the well-known Amontons-Coulomb friction law was established, which is represented by the equation below.

$$FT = \mu FN \qquad\qquad\qquad (2.7)$$

A sliding friction coefficient μ is used in the above equation to explain the direct proportionality between the tangential force FT and the normal force FN. Amontons added the direction of load in his relationship and the concept of friction coefficient.

Over the nineteenth century, much experimental and theoretical work was conducted on lubricating fluids, where the first Reynolds (1886) theory was found and used. He demonstrated that fluid could separate two sliding surfaces. The frictional resistance develops in relationship to the fluid viscosity even though it was discovered by Kingbury (1903) that some fluid lubricants could reduce friction apparently independently of viscosity.

Hardy & Bircumshaw's (1925) study found that static friction between two lubricated surfaces is directly proportional to the normal force when a curved surface is involved. In the same year, it was proposed by Terzaghi (1925) that the friction force built between two unlubricated surfaces depends on a molecular bond formed between them. He explained that friction is determined by the product of the actual contact area by the unit shear strength of the bonds and surfaces.

Tomlinson (1929) developed another, more unusual approach based on dry solid friction in the interactions between molecules of the two bodies in contact and deduced a formula for the coefficient of sliding friction μ based on the properties and interactions of molecules. Cavaquot (1934) demonstrated a relationship between the shearing resistance and inter-particle friction angle of granular assemblies $\phi\mu = \arctan (FT/FN)$.

When studying the concepts of friction resistance between metal surfaces, Bowden & Tabor (1958) suggested a new theory similar to Terzaghi's. They introduced the concept of the real contact area which depends on the deformation (plastic or elastic), in (Fig. 2.23), and that the development of the frictional force depends on the real contact area between the two sliding surfaces. Their adhesive theory of friction is based on the following: a) when two bodies are in contact, the asperities on their surfaces are deformed by plastic deformation, b) the interfacial stress component describes the materials' shear strength where it is expressed as s and friction is expressed by the force FT in the equation below:

$$FT = s * Ar \qquad\qquad (2.8)$$

Ar gives the total real contact area.

Bowden & Tabor (1958) also proposed that the real area of contact is proportional to load. An increase in contact area Ar is caused by increasing the load FN (load will continue to crush the asperities) if the contact pressure reaches fully plastic flow of the material. With:

$$FN = \rho o * Ar \qquad (2.9)$$

Where, in the zones closest to the actual contact area, ρo represents the flow pressure of the softer material.

The friction force is given by.

$$FT = sFN/ \rho o \qquad (2.10)$$

The coefficient of friction is computed from (2.8) and (2.5) in coherence with Amontons' law.

$$\mu = s/\rho o = FT/FN \qquad (2.11)$$

In their work, Bowden & Tabor (1950) showed that the ratio of the plastic properties of both the contacting and the adjacent materials is accurately represented by the equation (2.9).

There was another mechanism of dynamic friction proposed by Bowden and Tabor, where the friction force $\propto$ can be decomposed into:

$$FT = Fadhesion + Fploughing \qquad (2.12)$$

Although Bowden and Tabor estimated that the second term due to ploughing is smaller than the other (adhesion) in many cases.

In the case of smooth Perspex cylinders, Archard (1957) determined that:

$$FT \propto FN^{0.76} \qquad (2.13)$$

In the case of rough Perspex cylinders, when tested under the load of 80 N, it was found that:

$$FT \propto FN \qquad\qquad\qquad (2.14)$$

In thin polymeric film shearing mechanisms, Briscoe et al. (1973) and Briscoe and Tabor (1978) found a dependence between contact pressure and coefficient of friction. Briscoe & Tabor (1978) introduced a term to describe the interfacial shear resistance between contacting surfaces into the Amontons-Coulomb friction law:

$$\mu = \frac{FT}{FN} = \frac{\tau}{\rho}(\tau 0 + \alpha\rho) = \frac{\tau 0}{\rho} + \alpha \qquad\qquad (2.15)$$

Where τ represent the frictional force per unit contact area, ρ defines the average contact pressure, and both $\tau 0$ and α are constants in the expression.

As a summary, this section contains the following points:

➢ The force of friction, FT and the load FN are relatively proportional, and cohesion would only have a small impact.

➢ Fluid lubricants can reduce friction without considering viscosity, and the coefficient of friction can be affected by humidity.

2.3 Contact Mechanics: Theory

Contact mechanics studies bodies stress and strain states when they are in contact and plays a crucial role in several fields, including tribology, lubrication, and sealing (Yastrebov et al., 2015). A pioneer was Hertz (1882), who focused on the deformation of solids, including soils, minerals, metals, and rubbers that touch each other at one or more points. Classical contact mechanics assumes that deformed materials are isotropic and homogeneous; in principle, its findings can be applied to global contacts and those with interacting asperities.

According to Johnson (1985), there are two types of contacts, conforming and non-conforming. A conforming contact (e.g., a flat slider bearing) corresponds exactly to the surface of two bodies without deformation on initial contact. On the other hand, non-conforming contacts occur with initial deformation since the two contacts have remarkably different profiles and cannot fit exactly.

In non-confirming contacts, the initial deformations can be purely elastic or involve additional plastic, and permanent changes in shape and texture. Such changes in the surface profile of the components can be seen on two different scales. For instance,

when studying the contact between a heavily loaded roller and the inside and outside races within a rolling element bearing, the degree of flattening of the rollers may be stated as a proportion of their radii, i.e., on a macro-scale. If the roller or the race is not smooth, they will touch initially at a discrete number of points as asperities are pushed into contact. Some material deformation occurs on a small scale at, or close to, these areas of actual contact. The stresses that result from these regions ensure that the applied load is balanced.

In non-conforming surfaces, the stress is concentrated near the contact and not much affected by body shapes elsewhere. When two bodies are in contact, and a force is transmitted between them, their mechanical response is therefore greatly affected by their contact. Even a light force can cause concentrated strains because of the intensity of stress and the nonconformity of the surfaces. In the case of two hard particles that are not in conformity, these particles would undergo plastic displacement and maintain a small apparent stiffness. When their surfaces conform to each other in the contact area, they start experiencing elastic deformations with a high level of stiffness.

2.3.1 Contact of smooth non-conforming surfaces

For non-conforming smooth surfaces under normal load, Hertz's analysis of elastic response is the most widely used method, although progress over the past century in contact mechanics can be seen as a gradual easing of the restrictions imposed by the original Hertzian theory (Johnson, 1985). Johnson (1985) wrote a comprehensive review of this theory and presented various means of implementing it. When any two smooth bodies of revolution of different radii of curvature are brought into contact, they will initially touch at either a point or along a line. With the most negligible load application, deformation expands these into contact areas through which the loads are distributed as pressures. Hertz's analysis of this situation is based on the following assumptions:

1. The surfaces are continuous, smooth, and non-conforming,
2. The size of the contact area is small compared to the size of the bodies, i.e., the strains associated with the deformities are minor,
3. Each solid may be considered to behave like an elastic half-space in the vicinity of the contact area,

4. The surface is frictionless.

The Hertzian analysis is mostly used to examine the contact of spheres, ellipsoids, and cylinders. There are several types of Hertzian and non-Hertzian contacts, as shown in Table 2.3; however, this study will focus on the contact of particles that can be approximated as spheres or as flat, at least at the contact.

Hertz (1882) predicted how the shape of the contact area changed, how the size increases with increasing load and the magnitude of normal stress transmission across the interface. This is illustrated in Fig. 2.24, where a contact pressure is applied between two lenses, and the surface deformation of the lenses is measured as the intensity of the surface normal stresses.

Hertz's theory can be summarised as when two solids of revolution are in contact, and their radii are R1 & R2, the contact area between them is defined as circular by equation (2.18), where the elastic properties can be expressed as E1, and E2 (young's modulus), and V1 and V_2 (Poisson's ratio) of the solids.

$$\frac{1}{R} = \frac{1}{R1} + \frac{1}{R2} \tag{2. 16}$$

Two quantities are defined: a combined Radius R, and a relative Young's modulus, E*,

$$\frac{1}{E*} = \frac{1-V_1{}^2}{E1} + \frac{1-V^2}{E2} \tag{2.17}$$

Equation (2.18) can be used to express the radius of the contact area a, which has a circular shape, with respect to the properties of the solids in contact and the load level.

$$a = \left(\frac{3PR}{4E*}\right)^{1/3} \tag{2.18}$$

When P is the normal load. The relative displacement between two solids (spheres) subjected to normal loading is:

$$\delta = a^2/R = \left(\frac{9P^2}{16RE*^2}\right)^{\frac{1}{3}} \tag{2.19}$$

and the maximum pressure on the contact area is:

$$p_0 = \frac{3P}{2\pi a^2} = \left(\frac{6PE_*^2}{\pi^3 R^2}\right)^{1/3} \qquad (2.20)$$

In summary, Hertz's theory applies exclusively to homogeneous, isotropic, and linear elastic materials, with smooth contact.

The fundamentals of Hertz's model are:

➢ As the load increases, the area of contact increases but at a slower rate.
➢ With increasing loads, the stiffness increases.
➢ Stresses generated between two contacts depend on the surface's geometries and elastic parameters.

2.3.2 Contact of non-conforming rough surfaces

Most surfaces are not perfectly smooth, and for those, the contact between two (rough) surfaces occurs first at the asperities,

The onset of plastic deformation of metals was studied by Tabor (1951) through indentation experiments. According to Tabor's (1951) experimental evidence, when the area could support the load applied, the asperities on that surface deformed plastically, and when the maximum Hertz pressure was reached, then the smooth surfaces began to yield. He referred to the data of Moor (1948) who observed the deformation of a grooved copper surface in contact with a hard cylinder (Fig. 2.25) where it was concluded that the asperities flow plastically until their area is enough to support the load. Moor (1948) found out that when heavy loads are applied, the bulk flow increases but it is constrained by the surrounding elastic material. A direct relationship between the maximum contact pressure p_0, and the indentation hardness H, was proposed. Furthermore, it was noticed that under full bulk plastic flow also there is residual roughness, and the contact area does not exceed about 50% of the

gross area. Based on his findings, he concluded that surface roughness does not significantly influence hardness measurements.

$$p_0 = KH \tag{2.21}$$

Based on indentation tests between a spherical indenter and a metal specimen, Tabor (1951) proposed that the value of K should be 0.6.

By extending Hertz's theory to rough surfaces in contact with smooth planes, Archard (1957) superimposed over a smooth surface (Radius R1), spherical protuberances of radius R2 $\ll$ R1, with an equal number of m, per unit area, is evenly distributed over the radius R1 of the Hertz model. According to Archard (1957), the area of contact (A_1) between a smooth surface of radius (a) and a plane can be obtained by squaring equation (2.18) and then multiplying by π, as shown in the formula below:

$$A_1 = \pi a^2 = \pi \left(\frac{3R}{4E}\right)^{2/3} N^{2/3} = K_1 N^{2/3} \tag{2.22}$$

The following new relation, derived from the rough surface being generated on the smooth surface, was proposed:

$$A_2 = K_2 N^{e_2} \tag{2.23}$$

In this equation, A_2 is the real contact area at the contact with the rough surface S2, where $e_2 = 8/9$ ($< 2/3$) and $K_2 \propto (k_2, K_1, m)$, where k_2 corresponds to the Hertzian ratio and N is the pressure or load at the contact. The same method was repeated five times and Archard (1957) found that there was a direct relationship between the total area of contact Ac and the load N. Thus, when rough surfaces approach the condition of flat surfaces after n protuberances the total contact area is equal:

$$A_c = K_n N \tag{2.24}$$

Later on, Greenwood & Williamson (GW) (1966) conducted several studies on rough contacts between nominally flat surfaces. Their work suggested that asperities are hemispherical and that their height distribution could be described by a Gaussian

function. Deformations at the contacting asperities are purely elastic in the GW model with deformations occurring only at the asperities, without considering bulk displacement.

Much later Greenwood and Wu (2001) analysed Archard's (1957) work and stated that he considered fractal surfaces two decades before the term was introduced to describe their surfaces.

Following on the work by Greenwood and Williamson, the contact behaviour of a smooth sphere of radius R and a rough plane was considered in Greenwood and Tripp's GT model (1967) who suggested that the deformations at the contacting asperities are purely elastic and do not consider any bulk displacement. According to Figure 2.26, the distance between the rough surface's mean plane and the smooth surface is called 'u' for an asperity of height z. As a result, a given distance u determines the probability of touching one asperity at a given height z. Greenwood & Tripp (1967) demonstrated that the deformations of asperities are purely plastic when contact between a smooth sphere and a rough plane takes place. Greenwood & Tripp (1967) expanded the GW model to include two rough surfaces in their 1970 paper, where two variables were proposed non-dimensionally to describe the contact.

$$T = \frac{2P}{S_q E_* (2RS_q)^{1/2}} \tag{2.25}$$

Where the effect of load is represented by T and Sq is the root-mean-square roughness of the rough surface.

$$\mu = \frac{8}{3} S_q \eta (2R\beta)^{1/2} \tag{2.26}$$

Where μ is governed by the geometry of the surfaces and the density of asperities within per unit area is η and β is the radius of the asperities.

A simpler method was used to extend the Hertz theory to rough surfaces by Greenwood et al. (1984) and Johnson (1985), suggesting a new term for the non-dimensional roughness parameter α as described below:

$$\alpha = \frac{S_q^* R}{a^2} \tag{2.27}$$

Where S_q^* represents the equivalent roughness, defined in the following manner:

$$\frac{1}{S_q^*} = \frac{1}{S_{q1}} + \frac{1}{S_q} \tag{2.28}$$

With the two surface roughnesses represented by, S_{q1} and S_{q2}. The roughness parameter α has a direct relation with T:

$$T = \frac{4 \times 2^{1/2}}{3} \alpha^{-2/3} \tag{2.29}$$

As shown in Figures 2.27 b & c, two different values of α were used in the GT model to determine the pressure distributions, and can be seen to resemble that of Hertz theory when α is small, since the asperity deformation is small relative to the bulk deformation. The pressure distribution becomes much wider when the asperities deformations become more pronounced, as α increases. Clearly in Fig. 2.28, the parameter α has a greater effect on the radius of the contact area than parameter μ. Figure 2.29 shows the result of Yimsiri and Soga (2000), which determined a best-fit curve to the data. They proposed a relationship between the radius of the rough contact area a^{rough} and the smooth contact area radius a^{smooth} :

$$a^{rough} = \left(\frac{-2.8}{\alpha + 2} + 2.4 \right) a^{smooth} \tag{2.30}$$

By combining the Eqs. (2.18) and (2.30), a rough contact's normal displacement can be calculated as below:

$$\delta_N = \frac{2 (a^{rough})^2}{R} \tag{2.31}$$

Greenwood and Tripp (1967) noticed that rough hard materials behaved more like Hertzian materials, and the Hertz theory was applicable when the normal load $N \geq N_{T2}$, while the force-displacement relation is dominated by asperity deformation when $N < N_{T1}$, with:

$$N_{T1} = S_q E \sqrt{2RS_q} \tag{2.32}$$

$$NT_2 = 100N_{T1} = 100S_q E \sqrt{2RS_q} \tag{2.33}$$

Using Hertz contact theory, Cavarretta et al. (2010, 2012) attempted to simulate the relationship between normal loading (N) and displacement (δ) of a single particle of

sand, as seen in Fig 2.30. they defined three stages of N-δ: asperity domain, transitional phase, and Hertz phase, respectively:

$$N = N_{T1} \left(\frac{\delta}{\delta_{T1}}\right)^c \qquad\qquad \delta < \delta_{T1} \qquad\qquad (2.34)$$

$$N = N_{T2} \left(\frac{\delta - \delta_1}{\delta_{T2} - \delta_1}\right)^b \qquad\qquad \delta_{T1} \leq \delta \leq \delta_{T2} \qquad\qquad (2.35)$$

$$N = 3/4 \, ER^2 \, (\delta - \delta_{T1} - \delta_{T2})^{2/3} \qquad\qquad \delta \leq \delta_{T2} \qquad\qquad (2.36)$$

Where b and c are constants, and assuming that δ_{T1} and δ_{T2} are the threshold contact displacements at $N = N_{T1}$ and N_{T2}; Cavarretta's contact model expressed the δ_2 as a function of surface hardness, as shown below.

$$\delta_{T2} = R\left(\frac{3\pi H}{4 E}\right)^2 \qquad\qquad (2.37)$$

Where the radius R is related to the shape of the particle. According to Otsubo's et al. (2016), it is, however, difficult to determine whether roughness affects the contact behaviour of sand particles when using Cavarretta's model or not. Consequently, Otsubo's et al. (2016) proposed a new model where the threshold displacement is given by the following:

$$\delta_{T2} = \left(\frac{3}{4} \frac{N_{T2}}{ER^{1/2}}\right)^{2/3} + \delta_1 + \delta_2 \qquad\qquad (2.38)$$

$$\delta_{T1} = \left(\frac{N_{T1}}{N_{T2}}\right)^{1/b} (\delta_{T2} - \delta_1) + \delta_2 \qquad\qquad (2.39)$$

By fitting a smooth load-displacement curve, the constants in the Eqs. 2.35, 2.36, and 2.39 can be obtained. However, the yielding of asperities was not considered in either Cavarretta's or Otsubo's model. Although roughness has been shown to generate non-Hertzian behaviour, Hertz theory is still one of the 50 most popular contact models.

Tangential Loading

It was proposed by Mindlin (1949) that the tangential stiffness at the interface of smooth spheres under a constant normal load (P) can be applied to elastic-frictional

contacts for two identical spheres under various normal and tangential loadings. The concept was further developed by Mindlin and Deresiewicz (1953) to account for elastic-frictional contacts. An illustration of normal and tangential loading on two spheres in contact is shown in Fig. 2.31.

Under the initial condition of Hertzian theory, the incremental equation between the tangential contact force (T) and the change of tangential displacement ($\Delta\delta_T$) is given by:

$$T' = T + K_T\Delta\delta_T \tag{2.40}$$

Equations 2.41a to 2.41d can be used to calculate the tangential contact stiffness (K_T), specified by the loading history (Fig. 2.32). It is noted that there is a non-linear relationship between displacement (δ_T) and tangential force (T). Local microslips on the contact surfaces cause it to be non-elastic, which means energy is dissipated.

$$K_T = K_{T,0} \left(1 - \frac{T-T^*}{2\mu P}\right)^{\frac{1}{3}} \tag{2.41a}$$

$$K_T = K_{T,0} \left(1 - \frac{T}{\mu P}\right)^{\frac{1}{3}} \tag{2.41b}$$

$$K_T = K_{T,0} \left(1 - \frac{T^*-T}{2\mu P}\right)^{\frac{1}{3}} \tag{2.41c}$$

$$K_T = K_{T,0} \left(1 + \frac{T}{\mu P}\right)^{\frac{1}{3}} \tag{2.41d}$$

Where T^* is the maximum previous tangential force, μ represents the sliding friction coefficient, $K_{T,0}$ is the initial elastic tangential contact stiffness which is expressed as:

$$K_{T,0} = 8a \left(\frac{2-V_1}{G_1} + \frac{2-V_2}{G_2}\right)^{-1} \tag{2.42}$$

where G_1 and G_2 are the shear moduli of the two spheres, and a is the radius of the contact area, which is defined in Equation (2.18).

Based on Johnson's (1985) theory, Yimsiri and Soga (2000) and Otsubo et al. (2015) developed the following equation to represent the tangential contact stiffness for rough surfaces (K_T^*):

$$K_T^* = \frac{2(1-V)}{(2-V)} K_N^* \left(1 - \frac{T}{\mu P}\right)^{\frac{1}{3}} \tag{2.43}$$

Where K_N^* is the stiffness for rough contacts. This implies that the ratio $K_T / K_N = K_{T^*} / K_{N^*}$ i.e. it is not affected by roughness. This assumption was made by Otsubo and O'Sullivan (2016) in their model.

2.4. Contact mechanics: Experimental studies

There have been relatively few experimental studies on inter-particle interactions in soils, mostly over the past twenty to fifty years. The use of real soil parameters in DEM has led to a resurgence of this field in recent years. Despite this, most experimental studies used artificial materials like glass beads and steel balls with well-defined shapes, and studies describing the surface roughness of natural sand particles are limited.

Horn and Deere (1962) studied soil friction using a custom-made apparatus to test soil minerals (Fig. 2.33). They investigated how sliding velocity, surface moisture, and roughness affected the frictional behaviour of minerals. They found that water lubricates lattice-structure minerals (e.g., iron, chromium) but increases friction in massive-structure minerals (e.g., diamond, gold). This anti-lubricating effect disappeared when the quartz surface roughness was increased through etching. Humidity reduced the static friction coefficient (Fig. 2.34), but stick-slip behaviour, likely from apparatus defects, may have influenced results on saturated surfaces. As humidity increased, the static friction coefficient decreased, as seen in Fig. 2.35.

Skinner (1969) tested several materials with spherical shapes, including glass ballotini, lead shot, and steel balls. He measured the interparticle sliding friction using a custom-built apparatus (Fig. 2.36). A shearing test was also performed on glass ballotini over plate glass, and when dry samples were flooded, Skinner (1969) found an increase in the interparticle friction coefficient as shown in Table 2.4. He analysed glass ballotini of 1mm diameter, in dry and flooded samples in shear box tests, obtaining similar results.

Rowe and his team at Manchester University developed a custom apparatus used in Barton's (1972) experiment (Figs. 2.37 and 2.38), testing both artificial (glass spheres, steel, bronze) and natural (quartz, feldspar) materials. Surface contamination (oil) from improper cleaning affected results, with inter-particle friction increasing from 6-8° (dry samples) to 15° (flooded samples) due to water's anti-lubricant effects on glass ballotini. Differences from Skinner's (1969) results were attributed to sample preparation and experimental methods.

Procter & Barton (1974) conducted tests on glass ballotini and sand particles using the same device as developed by Rowe. The device could apply confining forces as low as 0.1N to 0.6N on average. Load cells for forces were installed on the device as well as LVDTs for measuring displacements. They also investigated the use of acetone to clean particles, stating that stronger cleaning methods would have resulted in higher scatter. Results were obtained under both saturated and dry conditions, where a small scatter of inter-particle friction was observed, as demonstrated in Table 2.5. The authors also proposed that water increases friction coefficients inversely to surface roughness when minerals have a crystalline structure.

An attempt was made to link the micro-behaviour of soil to the macro-behaviour. Thornton (2000) simulated axisymmetric tests with DEM code, suggesting that shear force is mobilised by inter-particle friction. Earlier, Horne (1969) had predicted the theoretical values and performed numerical analyses as illustrated in Fig. 2.39, and Skinner (1969) determined them experimentally. Horne's results do not agree with those of Skinner, who did not observe a correlation between the values of the critical state and the inter-particle friction coefficient. In addition, Horne's (1969) theoretical

model cannot accommodate particle rotation, resulting in differences between calculated and theoretical data points.

Mullier et al. (1991) tested cellulose acetate spheres and acrylic beads using a custom-made apparatus in a series of experiments. The apparatus could investigate the normal and tangential contact behaviours between two spherical particles loaded under different conditions. A comparison of the experimental results and theoretical values predicted by Hertz and Mindlin & Deresiewicz's theories are shown in Table 2.6. The experimentally measured shearing displacements do not agree with the theoretically predicted displacements at the gross sliding limit. According to Mullier et al (1991), these differences could be due to contact surface topography and interface deformation.

Two different experimental techniques for glass beads of different diameters (1.6-5mm) were tried by Ishibashi et al. (1994), of pulling or sliding glass beads against clear or smoked glass. In their experiments, three glass beads were tested each time, applying a normal load to confine the materials as dead weights. Based on the Hertz contact theory, normal forces were applied to reproduce pressures between $34.5kN/m^2$ and $207kN/m^2$. When normal loading is applied to the pulling method, the static coefficient of friction tends to decrease (Fig. 2.40), while this effect is less evident when applied to the sliding method. In addition, the authors noticed that static friction coefficients are higher when using a clear plate instead of a smooth one and when water is present on the surface versus a dry surface, as seen in Table 2.7.

 Under normal haversine loading (one-way sinusoidal function), a load-deflection response was investigated by Cole and Peters (2007) using pairs of crushed gneiss weathered and fresh aggregate (unweathered). Later, Cole et al. (2010) used a specially designed apparatus (Fig. 2.41) for normal and sliding laboratory conditions when conducting tests on gneiss. The samples were loaded with normal force at the contact point, and the loading rate or compressive haversine loading was imposed with a defined frequency and peak load. To study the non-monotonic loading's effect on energy dissipation, their research focused on rocks' non-monotonic or cyclic

behaviour. Sphere-sphere contact was studied in their experiments, as well as the sphere-flat contact. The spherical samples tested were large, with a 15 mm diameter, and the rock mineralogy was mixed. The study may, therefore, be better suited to understanding rock behaviour rather than soil minerals. According to Fig. 2.42, the Hertzian curve can be fitted with a much smaller stiffness (53GPa) than measured for the spherical grains of gneiss. As the loading cycle number increases, the stiffness decreases on the same pair of spherical gneiss grains. The behaviour converges by the time of cycle run 38, as illustrated in Fig. 2.43. An optical microscope was also used to measure the radius of curvature of grains, and a contact profilometer was used to determine the surface roughness of test materials. It was found that surface roughness and curvature play an important role in load deformation analysis.

A study performed by Cavarretta et al. (2010) considered the micromechanical behaviour of soil particles and both glass and crushed ballotini. A particle compression apparatus was used for normal loading, and a custom-designed inter-particle friction apparatus was used for shearing tests, as shown in Fig. 2.44. In both vertical and horizontal directions, displacement was measured with two LVDTs. The apparatus was built in two versions, one capable of applying 2.3N and the other 0.9N, with 140-200m/h displacement rates. In each test, recordings of the temperature and humidity were taken. Leighton Buzzard sand type A was subjected to normal loading. The observed soil behaviour differed from the theoretical one (based on Hertz theory) due to the plastic deformation of asperities on the soil surface. In Fig. 2.45, the load needed to satisfy the Hertzian curve is indicated. The necessary displacement is given to meet the Hertzian curve and represents the displacement offset for starting the Hertz curve.

In a later study, Cavarretta et al. (2011) found that particles submerged in water have lower sliding friction than particles in dry air (Fig. 2.46), which was a significant move from previous findings of Horn & Deere (1962).

Senetakis et al. (2013a & 2013b) used a specially designed inter-particle loading apparatus (IP Apparatus) to test sand particles. The apparatus can apply both a normal and shear load. The apparatus was used to test 26 Leighton Buzzard quartz sand particles, dry or submerged in water. The calculated friction coefficient between

particles was similar in dry and saturated conditions: for dry particles, they ranged from 0.093 to 0.231, and for particles immersed in water, they ranged from 0.114 to 0.193, (Table 2.8). The authors also demonstrated that tangential loads and stiffness degradation are affected by the normal load at contacts of dry quartz particles. An increase in normal load will increase the elastic tangential stiffness, as seen in Fig. 2.47, as would be predicted by models for example Mindlin and Deresiewicz (1953). Furthermore, for the same dry quartz particle pair contacts, load-deformation curves for cyclic unloading and unloading series show good agreement with monotonic loading, and the subsequent behaviour is not affected by unloading, as illustrated in Fig. 2.48. It appeared that some particles were damaged during loading, but there was little evidence that breakage had occurred at the contact.

Senetakis and Coop (2015), with their IP Apparatus, compared the maximum tangential stiffness for pairs of Leighton Buzzard sand (LBS) particles under normal force with that under a confining load as shown in Fig 2.49. Using confining forces between 0.25 and 5N, force-controlled type tests were performed. The authors demonstrated that the tangential stiffness increases with an increase in normal confinement at the particle contact. As the first device designed for experimental micromechanics purposes capable of measuring the evolution of contact tangential stiffness of the particles tested, this device determined the stiffness evolution of the particles tested.

Wang and Michalowski (2015) used a custom-made apparatus (Fig. 2.50) to investigate the creep behaviour of individual Ottawa sand particles. The particle was glued on a holder and loaded onto a plate by rotating a micrometre. The particle was then displaced and subsequently loaded. Measurements were made using three potentiometers to check for convergence and measure displacement. Based on three experiments on single grains of sand, Fig. 2.51 illustrates that displacement caused by creep is greater for higher confinement forces. As the confinement forces increase, these displacements tend to converge more slowly towards constant values.

In an experimental study, Otsubo et al. (2015) examined the effect of surface roughness on the stiffness of an assembly of borosilicate ballotini. Both smooth and

rough ballotini were used in this experiment. Afterwards, S-waves were applied on assemblies of particles using bender elements and applying different isotropic pressures to the assemblies, as seen in Fig. 2.52. They observed the rough ballotini to have lower shear stiffnesses for increasing confining pressure than the smooth ballotini. By using the optical interferometer, the authors measured both smooth and rough ballotini's average roughness. A comparison of the measured roughness and the theoretical stiffness was plotted using the calculated roughness values. These results show good agreement between models considering roughness and experimental measurements, as shown in Fig. 2.53.

Nardelli & Coop (2018) examined several soils under normal cyclic loading, suggesting that Limestone (LS) is the softest, followed by carbonate sand (CS), while Leighton Buzzard sand (LBS) has the highest stiffness, as shown in Fig.2.54. Nardelli and Coop's (2018) results also show that weathering has an effect, as shown by data on LBS, completely decomposed granite (CDG), and washed CDG (WCDG) behaviour as shown in Fig. 2.55. A thin layer of clay is created on CDG during weathering, which leads to increased initial particle deformation. That is similar to what Cole et al. (2007) found, but with much smaller particles. Even after the clay coating had been removed, the washed completely decomposed granite (WCDG) was still found to be softer than the LBS.

However, both washed and unwashed particles were found to have a very similar slope of force-displacement curves. In addition, a comparison was also made with the theoretical analysis of the original Hertz theory and Hertz theory with roughness (Greenwood et al., 1984). LBS and CS were found to follow the Hertz model with Young's moduli ranging from 94-98GPa, (Mavko et al., 2009; Jaeger et al., 2009). Young's modulus is typically lower for low loads than average values when fitting the Hertz curve, and Hertz's roughness can be fitted by a reasonable Young's modulus (Fig. 2.56). The Hertz equation without roughness fits the data better for a reasonable E value at higher loads, since the load may have squashed the contact roughness.

Nardelli and Coop (2018) investigated the shear behaviour of different soils in the same paper. An example of the effect of shearing rate on the contact behaviour of LBS

particles is illustrated in Fig. 2.57. It shows that particle contact properties are unaffected by the rate of shearing. During "friction" tests, the normal load was changed during shearing while tracing the failure envelopes to see how it affected the failure envelopes. Fig. 2.58 represents the simple tangential loading and friction tests performed on LBS particles by the authors. It was found that the coefficient of friction values varied within this range of loading, but that there were clearly defined failure envelopes in the friction experiments. However, based on Fig. 2.59, the coefficient of friction appears to change according to the normal load ranges. The failure envelope of chrome steel balls (ST) and different types of sands, including Eglin sand (ES), is shown in Fig. 2.60. In all cases, the coefficients of friction of the sands are higher than those of the chrome steel balls, limestone sand (LS), carbonate sand (CS), crushed limestone (LS), and completely decomposed granite (CDG). Furthermore, the authors also tested different colours of the Eglin sand, and they also looked at its mineral content, which is shown in Fig. 2.61 together with other sands, chrome steel balls, and ceramic balls (CB). With increasing particle roughness, the friction coefficients increased for all materials. Results of the cyclic tangential loading test carried out on LBS under 1N constant normal load are shown in Fig. 2.62 with different cycles.

According to Mindlin & Deresiewicz (1953), the predicted shear stiffness for small and large particles is much larger than what appears in reality, as seen in Fig. 2.63. Furthermore, Mindlin & Deresiewicz (1953) calculated the initial stiffness with an error claimed by different researchers. Who suggested that using initial experimental stiffness would improve the predictions.

2.4.1 Experimental methods for determining the contact area

In contact mechanics, experimental work to determine the real contact area has been less developed than analytical and numerical work. This is due to the rough surface of materials since it is not accessible for direct visual observation and engineering materials are usually non-transparent.

In metals, the detected properties of the materials in contact are used:

$$R = \rho \sum_{i=1}^{n} a_i \qquad\qquad (2.44)$$

Experimentally, these parameters can be determined in several ways, where ρ is the material's resistivity (ohm/m). There is no way to determine the real contact area directly since the resistance R depends on the contact spot radius (not the spot area). However, it can be measured if assumptions are made about the number or size of the individual contact spots. The techniques for determining this contact area can be categorised into electrical, optical, acoustic, and surface coating methods:

Ø Electrical and Thermal Resistance

Ø Optical Methods

Ø Ultrasonic Reflection and Transmission

Ø Thin Surface Coatings (method preparing samples SEM)

As part of this project, optical methods will be used to measure the surface roughness and if possible contact area of sand particles and ballasts. Optical microscopy has been used to determine the roughness of ballast particles, as described in Chapter 3. The advantage of optical measurement techniques over other measuring techniques lies in the need for no contact, and optical methods often take less time than microscopy (Whitehouse & Reason, 1965; Greenwood & Williamson, 1966). Different techniques will be tried to measure the real contact area.

2.4.2. Factors affecting the contact area

According to Yoshida et al., (1988), some of the factors that increase the real contact area include:

Ø Stress: The true contact area is increased by stresses, due to the greater potential for deformation.

Ø Higher temperature: can result in a greater real contact area because the material strength decreases, causing the contact area to deform.

Ø Time: the rate of flow increases with time. The contact area increases at high temperatures due to the creep deformation of the contact area over a longer period.

Another factor that increases the real contact area is surface roughness changes, which may occur when surface textures are altered by salt corrosion, the formation of

composite oxides, particularly when sodium is present, or the formation of composite oxides.

Summary on contact mechanics:

Several models were introduced for normal and tangential loadings, including Hertz (1882) and Mindlin-Deresiewicz (1953). By using computational methods, these models can be used to model contact behaviour among particles. In the past, they were developed for different problems in engineering than those in soil mechanics. Despite their simplicity and clarity, these are popular for these applications, even though they are based on hypotheses and assumptions that differ from those which govern particle interactions.

In the application of normal load N, a contact's mechanical response depends on its geometry. If the contact is non-conforming, the stress will be high even if N is low. Using Hertz's model, one can predict how non-conforming contacts behave when subjected to various loads. It has been proposed that an increase in N can result in an increase in the Hertzian nominal pressure up to the hardness H. When N is low, the apparent area of contact between two rough surfaces is underestimated by Hertz's model compared to models for rough surfaces.

Several models were developed recently that incorporate the effect of surface roughness on particle behaviour (Greenwood et al., 1984; Yimsiri and Soga, 2000; Bahrami et al., 2005). These models can provide a more realistic representation of the contact behaviour of bodies. In the past, mineral frictional properties have been investigated. Researchers have analysed the behaviour of idealised materials, such as glass ballotini (Ishibashi et al., 1994; Cavarretta et al., 2010), in order to gain new insights about particle micromechanics, other researchers focused on soil particles (Nardelli & Coop, 2018, Yang et al. 2016). With the development of computing power and the popularity of DEM models to simulate soil behaviour, the prevalence of DEM models has increased. Recent research including this work has focused on understanding the contact behaviour of real particles, which has not been extensively studied before, as reported by Cole et al. (2010), Cavarretta et al. (2011), Senetakis et al. (2013), Michalowski (2015), Wong (2022) and Altuhafi et al., 2024.

2.5 Previous research on railway ballasts

2.5.1 Geological origin & shape

There has been a steady increase in freight tonnage, traffic speeds, and train frequency over time throughout the world. All track components in the superstructure and substructure have suffered from increased wear and shorter lifetimes due to these changes in traffic characteristics. Settlement in the ballast layer contributes most to track deterioration due to degradation of the track geometry (Selig 1998).

There are many different types of track systems in railways, but ballasted tracks are the most commonly used around the world. Ballasts are the materials that distribute the traffic load from the sleepers to the formations by being laid and packed below, between, and around the sleepers. It is necessary to drain water from the railway track longitudinally and transversely as well as maintain its alignment. Ballast plays an important role in moving forces (both vertically and horizontally) between the wheel and rail contact. The distribution of these forces within the ballast varies depending on the operating conditions (e.g. speed, axle load, tangent versus curved track) but it has not been completely understood and is still being investigated. It is therefore essential to understand the role of ballast in the conventional track structure and in this experimental research work different types of ballasts will be investigated under different conditions (dry and wet) and different speed rates (slow and fast) for normal and tangential loading.

Materials and sizes

The importance of ballast has increased with the increase in axle loads and train speeds. Preliminary work has shown that new ballast should contain a narrow range of particle sizes and be open-pored and permeable. In the UK, aggregates for railway ballast must meet the requirements of BS EN 13450:2013 with the UK guidance PD 6682-8:2004. Where it is required, railway ballasts have to be clean, strong, angular, and abrasion-resistant.

According to the Geological Society (2001), dense, tough, siliceous rocks tend to work well as ballast, such as basalts and dolerites, as well as metamorphic rocks, but limestones are not recommended because they are not resistant to abrasion. Although limestone is recommended for use as ballast by the United Kingdom Ministry of Defence (MOD) (2009), the document also stated that crushed granite is the best material. A very detailed report on the United Kingdom minerals industry has been published by Idoine et al. (2016) in the United Kingdom Minerals Yearbook 2015. Great Britain used approximately 3 million tonnes of crushed rock for railway ballast in 2014, which is 8% of the total production of crushed rock. Between 2002 and 2014, Great Britain produced a wide range of crushed rock types for railway ballast, but igneous rock was the most common type as shown in Table 2.9. As per BS EN 13450:2013, ballast sizes range from 31.5mm to 50mm, which is a grading category A specification given in Table 2.10. A Category A product can contain a maximum of 0.6% fine particles that pass through a 0.5mm sieve. In Table 2.11, different types of rock and particle sizes are listed by country and author. Traditionally, latite basalt is used in Australia, while granite is used more commonly in the UK. Particle sizes range from 2.36mm to 73mm, depending on the different tests conducted.

Shape analysis

Le Pen et al. (2013) identified railway ballast particles that can be identified by shape analysis by using pseudo-3D measures of 2D digital images. The intermediate dimensions (I_n) and largest dimensions (L_O) of the particle were captured as the particle reached the lowest potential energy position on the plane in both methods. In a few cases, the first image gave L_O and S_h instead of L_O and I_n. Similarly, some of the ballast particles had similar S_h and I_n dimensions. A second image was taken after rotating the particle orthogonally in order to obtain the shortest dimension (S_h). Using Clayton et al. (2009)'s scalene ellipsoid equivalent sphericity (SEES) methodology, the value of S which represents the shape, was calculated by.

$$S = \frac{W_m}{\rho_w G_s} \times \frac{6}{\pi L_o I_n} \qquad (2.45)$$

Where W_m is the mass of the particle, ρ_w is the density of water, and G_s is the specific gravity of the particle material.

Most tested particle sizes were underestimated by the SEES methodology compared to using two orthogonal views. Overestimations of the S_h / L_O ratio was found for particles with sizes between 30 mm and 50 mm. Fig. 2.64 illustrates a cumulative distribution curve of the S_h / L_O the ratio in each sieve interval. Except for particles from the 9.5mm sieve, the curves of particles of larger sizes tend to group together on the left and the curves of particles of smaller sizes tend to group together on the right. A reasonable agreement was claimed between the SEES approach and the two orthogonal views approach by the authors.

Pen et al. (2013) also quantified roundness by determining the perimeter and area from the images. This was done with a definition of Ellipseness (E_{2D}) as follows:

$$E_{2D} = \frac{P_e}{P_0} \tag{2.46}$$

P_0 represents the particle's actual 2D projection perimeter, while P_e represents its equivalent ellipse area, which can be calculated as below:

$$Pe \approx \pi(a + b)\left(1 + \frac{3\left(\frac{a-b}{a+b}\right)^2}{10 + \sqrt{4 - 3\left(\frac{a-b}{a+b}\right)^2}}\right) F_h \tag{2.47}$$

Here, a and b represent the major and minor radii of the equivalent area ellipse, respectively, as shown below:

$$a = \frac{L_o}{2} \tag{2.48}$$

$$b = \frac{A_o}{\pi a} \tag{2.49}$$

With Ao the 2D projection area of the particle, a sample of cumulative distribution curves for Ellipseness in each sieve interval is shown in Figure 2.65, where greater particle size results in greater angularity.

2.5.2 Element tests

Research on railway ballast has primarily focused on element tests. Most standard apparatus cannot be used to test ballast particles due to their large size, so large-scale apparatus or scaled-down ballast was used to fit in standard apparatus. The majority of research has used a triaxial apparatus to test the compression behaviour of ballast while some authors (e.g. Indraratna et al., 1997) also used one-dimensional loading apparatus.

A large-scale triaxial apparatus was used to study the shear behaviour of latite basalt ballast by Indraratna et al. (1998). Test specimens had a diameter of 300mm and were enclosed by a rubber membrane four millimetres thick, with ballast stacked 50-60 millimetres thick. Compared to the standard membrane, which is around 0.4mm thick, the thick membrane used in their research could have applied extra confining pressure to the sample, and its strength and stiffness may have affected the results.

As a result, for the low cell pressure tests, the authors introduced a correction for membrane stiffness. According to Fig. 2.66, particle breakage occurred in smaller sizes of particles, while the larger sizes of particles remained unchanged. The stress-strain behaviour for drained triaxial tests at varying confining pressure values for ballast is shown for the latite in Figure 2.67. In the graph, it is clear that the tests had not yet reached the critical state correctly as the volume changes were not constant.

As with normal sands, triaxial testing on dense basalt produces an envelope where the peak increases as the effective confining pressure decreases (Fig. 2.68). Furthermore, a large-scale triaxial apparatus was also used by Indraratna et al. (2015) for monotonic loading tests on Latite basalt ballast. It was concluded by the author that, as the confining pressure increases, the critical state stress ratio (M) decreases, resulting in a curving critical state line for the latite basalt ballast. The volume did not reach a true critical state in any of the tests.

2.5.3 Single particle load tests

There are few studies focusing on the behaviour of ballast under single particle loads, such as Lim et al. (2004) platen loading experiment, and Koohmishi and Palassi's (2016) point loading experiment. In both figures 2.69 and 2.70, they concluded that ballast with a smaller particle size will be stronger. Koohmishi and Palassi (2016) also concluded that the shape of ballast particles (Fig. 2.71) does not affect their strength.

2.5.4 DEM modelling of ballast

When the DEM studies started to simulate real soil particles, many DEM analyses used spherical particles as the basis for simulation. Spherical particles spin, while real particles cannot spin because of their shapes. An artificial parameter called the "rolling resistance" parameter was introduced by Ai et al. (2011), as during analysis this artificial parameter stops particles from spinning in the DEM.

In order to create DEM particles of realistic shape, or able to break, a number of studies have used non-overlapping clumps or clusters when modelling sands (e.g. Cheng et al., 2003). Similarly, the same principle has been applied to ballast (e.g., Indraratna et al., 2010; Thakur et al., 2010). When the inter-ball bond strength is exceeded, the particle can break into one or more pieces. As there are cavities between the balls, the particles will break and create new voids when they break. These new voids will be the main disadvantage of this approach because as the particle is broken, the sample's void ratio changes. Additionally, in order to model shape better, many balls are required. As an alternative, replacing a larger particle with two or smaller daughter particles when it breaks is a simpler way to model breakage. There is then typically only one type of particle per parent, which can be a simple sphere (Indraratna et al., 2010; Thakur et al., 2010).

The presence of non-overlapping clumps is often replaced by overlapping ones in DEMs in order to obtain more accurate shapes in Fig. 2.72 (Lu and McDowell, 2006; Ferellec and McDowell, 2010). However, Lu and McDowell (2006), discovered that, unlike rockfill, large-scale breakage is not common in ballast (Tapias et al., 2015). The

overlapping clumps can't break between the spheres, but large-scale breakage can occur at the edges of the clumps. Despite the fact that rockfill is frequently subject to high stress levels, ballast placed near the surface today is under low stress levels, so even if the rail sleepers underlying are under greater stress, the stress will still be lower than that experienced by rockfill. Rather than creating bulk fractures in the particles, Lu and McDowell simulated asperities within the particles by using overlapping clumps with small balls around the perimeters, allowing abrasion to knock off the asperities.

Using Houlsby's (2009) model of potential particles, Ahmed et al. (2016) modelled railway ballast using the potential particle model technique. Despite the fact that the real particle may have a concave shape, the potential particles can only have convex shapes with this technique, and every particle surface has curvatures, so small-scale shape (i.e. roughness) cannot be modelled (Fig. 2.73). For modelling, however, this method is efficient in terms of computation. In order to perform sensitivity analyses, different parameters were changed in the simulation of a DEM triaxial test on a potential particle specimen. There were very different behaviours observed during the tests when the interparticle friction or contact stiffness values were changed, as shown in Fig. 2.74. According to the data in the subsequent chapters, these high inter-particle friction values can also be measured for ballast, which is higher than that of Nardelli and Coop (2018) for sands. Figure 2.75 displays a contrast between the DEM analysis and actual test data. The contribution of input parameters was determined by means of curve fitting in the absence of experimental data, which is full of uncertainty because the behaviour would differ for slightly different input parameters and the same set of parameters cannot accurately model tests under a range of varied pressures.

It was suggested by Harkness et al. (2016) that during tangential loading, simple Hertzian contact models featuring elastic-perfectly plastic behaviour cannot accurately replicate the behaviour under various confining pressures using the same input parameters. This problem can be more effectively addressed with the use of a conical damage model (Fig. 2.76). In this model, a spherically capped cone is flattened as load increases, to represent the stiffer loading behaviour after reloading. Cole et al. (2010), however, found that stiffness decreased as reloading progressed. It was also possible to reduce the friction coefficient of ballast under load. In a similar study, Nardelli and

Coop (2019) found slightly lower friction coefficient values on sand, but at a much smaller magnitude than Harkness suggested. This large reduction in friction coefficient did not appear to be supported by any evidence.

A study by Gupta et al. (2023) investigated the shape and surface characteristics of fresh and used railway ballast and found that used ballast is generally more spherical and smoother than fresh ballast. The angularity of fresh ballast ranges from 10-40%, while the angularity of used ballast is lower. The surface roughness of fresh ballast is higher than the surface roughness of used ballast. The study also found that fresh ballast can be made to resemble used ballast in terms of its surface roughness after 90 minutes of abrasion in a Micro-Deval apparatus shown in Fig. 2.77. The findings of this study suggest that the shape and surface characteristics of railway ballast can change over time due to traffic and tamping. This can have a significant impact on the performance of the ballast, such as its ability to resist deformation and provide support for the track.

Tolomeo & McDowell (2022) have carried out DEM analysis on railway ballast, where various features of the influence of particle form on a granular assembly's mechanical response were investigated. The two most popular modelling techniques were applied to the modelling of triaxial tests on ballast; a) clumps (Fig. 2.78), which is the collections of overlapping spheres with no internal contacts, and b) polyhedral that may be used to represent an irregular shape in a DEM and are easily accessible in some of the better liked DEM codes. It was demonstrated that as they do not recreate concavity, which is discovered to play a critical role in the mechanics of irregularly shaped granular materials, the latter when restricted to be convex, may systematically underestimate the shear strength.

In addition, it also investigated how interparticle friction affects the mechanical response of an assembly of real-shaped angular particles combined with shape. A monotonic increase in peak strength was observed with interparticle friction, while a gradual decrease in ultimate strength was observed for higher values (Fig.2.79), which is consistent with classic results for basic granular assemblies (disk/sphere, polygon, ellipsoid).

Suhr et al. (2022) investigated the use of the Conical Damage Model (CDM) as illustrated in Fig. 2.80 for DEM modelling of railway ballasts (Calcite and Kieselkalk). They found that the CDM was able to reproduce the experimental results more accurately than the Hertz-Mindlin contact law particularly comparison and direct shear tests. They also investigated the influence of the CDM parameters on the simulation results (Fig. 2.81). They found that the parameters had a significant influence on the simulation results and that the choice of parameters was important for obtaining accurate results. They concluded that the CDM is a promising contact law for DEM modelling of railway ballast. However, they also noted that more research is needed to better understand the influence of the CDM parameters on the simulation results.

Guo et al., (2020) provided a comprehensive overview of the different methods that can be used to model ballast particles, breakage, abrasion, and contact. For particle modelling, the authors recommended clump and image-based methods (Fig. 2.82). The bonded-particle model and fragment replacement method are commonly used, depending on the desired level of accuracy and computational cost. To module particle abrasion (Fig. 2.83), releasing small spheres or discs from the main particle, or increasing the radius of spheres at edges or corners, are common methods.

According to Guo et al., (2020), the Hertzian contact model is more promising than the linear contact model due to its ability to capture the effects of particle size on contact forces (Fig. 2.84). Therefore, in this experimental research thesis, experimental data will predominately be compared with the Hertzian contact models (with surface roughness and without).

The DEM models previously mentioned however suffer from the same problem: no particle loading tests were conducted to estimate input parameters. In fact, KN increases become stiffer behaviour as the load increases and KT decrease softer behaviours as the load increases, but the input parameters for normal loading stiffness (KN) and tangential contact stiffness (KT) are often assumed to vary linearly, in direct proportion of each other.

2.5.5   Experimental work on ballast

A series of simple experimental tests were conducted by Tapias et al. (2015) to determine the parameters that would be used to model oedometer tests and triaxial tests on rockfill in DEM. Fig. 2.85 shows the test setup of pyramidal shapes of limestone load against flat surfaces of limestone to determine the normal contact stiffness. The test data obtained agree reasonably well with the theoretical curve derived from the original Hertz theory (Fig. 2.86). A rough contact might have caused the scatter of data, according to the authors. Using limestone samples with varying roughnesses, both direct shear box and tilting table tests were carried out to determine sliding friction angles. The higher the sliding friction angle, the rougher the surface. By comparing the DEM analysis based on measured input parameters to experimental test data from Ortega (2008), a good agreement was found between the simulation and the experimental results. However, the deviatoric strength in the DEM was overestimated in comparison to the actual test results (Fig. 2.87).

 Sandeep and Senetakis, (2019) carried out an experimental work on friction, tangential stiffness, and normal contact response of crushed granitic materials. During shearing tests, the natural grains of crushed granite displayed highly nonlinear and hysteretic behaviour; Hertzian fitting revealed apparent Young's modulus values ranging from 7 to 11 GPa. The shearing test results showed that the inter-particle coefficient of friction ranges from 0.22 to 0.43 (Table 2.12), although a steady state cannot be observed for larger displacements. In contrast, the author mentioned that granitic granules showed fluctuations in tangential force and there is a possibility that the asperities are deformed through plastic deformation due to their microslip behaviour, which changed their surface roughness and friction properties.

 Suhr et.al (2020) conducted a comparison of calcite and kieselkalk stones used as railway ballast. Additionally, 3D scans were performed to determine the roughness, contact area, contact pressure, and wear resistance of the investigated ballast stones. The following conclusions were drawn from these investigations: the authors suggested that the contact area increases as the normal load increases. The inter-particle coefficient friction was to be found much higher (0.8-1.2) than that used in DEM (0.4-0.8) shown in Fig. 2.88. There are some indications that the coefficient of friction depends on the contact pressure, but the relationship is not conclusive.

Therefore, more sophisticated friction models are required for DEM simulations, both cyclic and noncyclic shearing. According to Suhr et al., these contradictions may result from multiple mechanisms, for instance, the stress caused by roughness changes and the contamination of the contact by wear debris.

When comparing the two types of ballast particles, the coefficient of friction measurements showed no obvious differences. However, both types of ballast displayed significant scatter in measured values, which was not solely a result of surface roughness. A problem with controlling the vertical load may have contributed to the observed scatter as it was observed during the lower vertical loads, that there was a higher relative error in controlling the vertical load. The author also found a much lower coefficient of friction at the start of the test which stabilised after a few cycles (Fig. 2.89). In terms of contact area and wear volume (wear resistance), both ballasts showed similar patterns. The wear volume, along with the contact area, are both influenced by cycles and cumulative dissipated contact energy in a non-linear manner.

Wong (2022) designed and built an inter-particle loading apparatus, and various modifications were made throughout to test railway ballast (granite). The apparatus is capable of measuring the coefficient of interparticle friction (μ), contact stiffness, and loop size with high accuracy. Wong performed cyclic loading experiments to measure the coefficient of interparticle friction (μ) of granite ballast, which typically stabilised at about 0.6-0.85 after 100 cycles (Fig. 2.90). The powder generated during the test was weighed and its particle size and the size of the powder were determined to be about 25 microns. It was, however, unexpected to find that the roughness of the interface had decreased and that the linear shearing values had been lower (about 0.25-0.75) than those after cyclic loading. This could imply that the repeated loading and movement of the particles had a smoothing effect on the contact surfaces. Despite the fact that water immersion affects the coefficient of interparticle friction values clearly, it was not affected by the level of the load. Also, no differences were found between loading fresh contacts and loading old contacts, and sliding rates did not affect the values. The loop size increased with the load both for normal and tangential load

cycling and the energy loss factor η reduces with cycles. It was also found that the T/N values for the monotonic shearing and tangential stiffnesses are increased with increasing the normal load as illustrated in Fig. 2.91.

 In normal loading, as the load increased the responses became increasingly steep, and the normal stiffness increased. New contacts are very much softer than the simple Hertz model predicts, because of the roughness of the particles (Fig. 2.92). When compared to Hertz-Mindlin elastic solutions, normal and tangential contact stiffnesses determined experimentally are highly nonlinear (Fig. 2.93). If the whole particle size was used instead of the measured contact radius as an input parameter, a Hertz model could account for surface roughness in normal loading.

Altuhafi et al. (2024), examined the validity of contact models on natural and artificially shaped granite ballast and found that with increasing surface roughness, deviations from the Hertz model increase (Fig. 2.94). In order to estimate the radius of surface curvature at the tip, the authors used three different methods: (a) digital camera, (b) profile images obtained by a microscope, and (c) Z-stack data obtained by optical microscope. Models that take into account both surface roughness and fractality were found to give a more accurate representation of the data (Fig. 2.95). These models seem to have validity up to the point of excessive plastic deformation, after which the contact seems to deform, despite constant stiffness. When using the modified Hertz model (RMS) to determine the normal contact area of rough surfaces, the deformation at lower loading levels is generally overestimated. Surface morphology features like peaks and asperities have a great impact, which the RMS model does not consider. It was found that surface roughness has a very significant effect on contact stiffness, and the effect is very large at lower load levels.

The focus on the investigation of real particles, exemplified by the research conducted by Tapias et al. (2015), Nardelli and Coop (2018), Sandeep and Senetakis (2019), Cole et al. (2010), Cavarretta et al. (2011), Tolomeo & McDowell (2022), Suhr et al. (2022), (Wong, 2022), and Altuhafi et al. (2022), signifies a significant shift in the domain of contact mechanics research. Nonetheless, a notable gap remains in the comparative analysis of different railway ballasts and their respective contact behaviours. The research presented here will address this gap, contributing to a more

comprehensive understanding of contact mechanics and its practical implications in the context of railway ballast materials.

In addition, despite the extensive use of railway ballast in track infrastructure, significant gaps remain in understanding its micromechanical behaviour under various mechanical and environmental conditions. Current models, including those based on Hertzian contact theory, often fail to capture the complexity of real ballast interactions, especially when accounting for surface roughness, particle shape, and moisture effects. Discrete Element Method (DEM) simulations offer a powerful tool for evaluating ballast performance, but their reliability is highly dependent on accurate input parameters, particularly contact-scale properties such as stiffness, friction, and damping. However, experimental data to inform these parameters remains limited used inconsistent, especially for recycled and treated materials.

To address these gaps, this thesis is structured around the following research questions:

1. What are the micromechanical behaviours of different ballast types (natural, used, and washed) under monotonic and cyclic loading conditions, in both dry and wet states?
2. How do inter-particle properties such as friction, stiffness, and surface roughness vary across ballast materials of different geological origins and conditions?
3. Can experimental procedures be optimised to provide reliable, reproducible parameters suitable for use in DEM simulations of ballast performance?
4. How do environmental factors, particularly moisture and loading rate, influence inter-particle behaviour and surface degradation?
5. What implications do these micro-scale behaviours have for the long-term stability and sustainability of ballast materials in railway infrastructure?

This research is of particular relevance to DEM modellers, offering a detailed and experimentally validated dataset of contact-scale mechanical and surface parameters across a range of ballast materials. The findings enable more accurate calibration of DEM input variables, enhancing the predictive capacity of numerical simulations used

in track design and maintenance planning. In particular, the thesis introduces a novel surface quantification methodology and a rigorous testing protocol for determining stiffness and friction under representative loading conditions—providing a foundation for more realistic and granular simulation models.

By bridging the gap between laboratory-scale experimentation and macro-scale simulation, this work supports the development of more sustainable, cost-effective, and resilient railway systems. The experimental insights on particle behaviour, degradation, and performance under flooding further contribute to region-specific assessments, essential for practical engineering applications and environmental risk planning.

2.5.6   Summary on railway ballasts:

It is difficult to obtain a lot of information on ballast contact behaviour. A critical state is not reached when triaxial tests are not performed on ballast at large enough displacements. As load levels increase in triaxial tests, critical state line M values tend to decrease, but incomplete tests may also contribute to this. A significant amount of particle breakage was observed in triaxial tests.

Similar to sand, load-deformation of particle-to-particle testing is highly nonlinear under normal and shear loads. At low load levels, normal stiffnesses of ballasts were lower than Hertz stiffnesses. During cyclic loading, the hysteresis loops grew with load level, whether normal or shear. The coefficient of interparticle friction (μ), which typically stabilised at about 0.6-0.85 after 100 cycles and the size of powder was about 25 microns, however, the linear shearing values had been lower (about 0.25-0.75) than those after cyclic loading. Despite the fact that water immersion affects the coefficient of interparticle friction values clearly, they were not affected by the level of the load. These results were obtained on granite ballast by Wong and Coop (2024).

Models that take into account both surface roughness and fractality give a more accurate representation of the data. These models seem to have validity up to the point of excessive plastic deformation, after which the contact seems to deform, despite constant stiffness. Surface morphology features like peaks and asperities, however, are not considered by models such as the RMS model. Surface roughness has a very significant effect on contact stiffness, and the effect is very large at lower load levels. The Hertzian contact model is more promising than the linear contact model due to its ability to capture the effects of particle size on contact forces. Therefore, in this experimental research work, experimental data will be compared with the Hertzian contact models

The next chapter explains the testing apparatuses and procedures used in this research. In the experiments carried out, different particles (ballast of various origins) were analysed under normal loads and tangential loading, but particle strength has not been considered since breaking is not a concern in this research. The surface roughness evolution with loading has also been examined.

Chapter 2 Tables and Figures

Table 2.1 The definition of degree of elongation and flatness that classifies particles in terms of shape (Blott & Pye, 2008)

Elongation			Flatness		
I/L	Class	Term	S/I	Class	Term
0-0.2	5	Extremely elongate	0.2-0	5	Extremely flat
0.2-0.4	4	Very elongate	0.4-0.2	4	Very flat
0.4-0.6	3	Moderate elongate	0.6-0.4	3	Moderate flat
0.6-0.8	2	Slightly elongate	0.8-0.6	2	Slightly flat
0.8-1.0	1	Not elongate	1-0.8	1	Not flat

Table 2.2 Parameters for estimating the shape of forms from three dimensions, L = largest diameter, I = intermediate diameter, shortest diameter, Krumbein (1941)

Index	Formula	Range	Author
Flatness index	$\dfrac{L+I}{2S}$	$1\sim\infty$	Wentworth, 1922
Corey shape factor	$\dfrac{S}{\sqrt{LI}}$	$0\sim1$	Corey (1949)
Maximum projection sphericity	$\sqrt[3]{\dfrac{S^2}{LI}}$	$0\sim1$	Sneed & Folk (1958)
Aschenbrenner shape factor	$\dfrac{L\times S}{I^2}$	$0\sim\infty$	Aschenbrenner (1956)
Janke form factor	$\dfrac{S}{\sqrt{\dfrac{L^2+I^2+S^2}{3}}}$	$0\sim1$	Janke (1966)

Table 2.3 Typical types of contacts studied

Hertzian Contacts	Non-Hertzian Contacts
- Contact of Spheres. - Contact of Two Cylinders with Axes Parallel - Contact of Two Cylinders with Inclined Axes - Contact of Bodies of Arbitrary Shape - Surface and Subsurface Stresses (Nominal Point Contacts, Elliptical Contacts - Surface Tractions and Sliding Contact (Rolling, Sliding, and Spin) - Cylinder Sliding Perpendicular to its Axis and Sliding Spheres (Gross Sliding, Incipient Sliding — Microslip, Free and Tractive Rolling, Tractive Rolling)	- Flat Rigid Planar Punch - Flat Rigid Axisymmetric Punch - Indentation by an Angular Wedge - Indentation by a Cone

Table 2.4 Inter-particle friction apparatus results (Skinner, 1969)

Material	Test condition	Contact load, gm	Coefficient of friction
1 mm dia. glass ballotini	dry	5·7 11·5 23·1 52·0	0·03—0·05 0·05—0·07 0·07—0·09 0·06—0·08
	flooded	5·7 11·5 23·1 52·0	0·50—0·58 0·64—0·72 0·76—0·79 0·78—0·80
3 mm dia. glass ballotini	dry	5·7 11·5 23·1 52·0 109·7	0·03—0·06 0·03—0·07 0·05—0·07 0·07—0·12 0·07—0·08
	flooded	5·7 11·5 23·1 52·0 109·7	0·79—0·89 0·83—0·93 0·87—0·89 0·85—0·86 0·80—0·82
⅛ in. dia. steel balls	dry	5·7 11·5 23·1 52·0 109·7	0·29—0·48 0·46—0·62 0·52—0·66 0·63—0·66 0·60—0·62
3 mm dia. lead shot	dry	5·7 11·5 23·1 52·0 109·7	0·07—0·08 0·06—0·08 0·08—0·09 0·10—0·11 0·10—0·12
3 mm dia. glass ball sliding on plate glass	dry	10·0 20·0 40·0 90·0 190·0	0·02—0·07 0·02—0·08 0·06—0·11 0·11—0·13 0·11—0·14
	flooded	10·0 20·0 40·0 90·0 190·0	0·61—0·90 0·85—0·88 0·85—0·88 0·89—0·91 0·80—0·90

Table 2.5 An overview of the Procter and Barton (1974) results.

Saturated or dry	Material	Particle–particle		Particle–plane	
		Mean $\phi\mu$, degrees	Standard deviation, degrees	Mean $\phi\mu$, degrees	Standard deviation, degrees
Saturated	Glass ballotini	17·9	±2·8	15·5	±5·1
	Stainless steel ballotini	8·1	±2·1	8·6	±1·7
	Quartz	26	*	22·2	±2·3
	Feldspar	†	†	28·9	±1·1
Dry	Glass ballotini	5–10	*	5–10	*
	Quartz	†	†	17·4	±0·6

* Insufficient data to give meaningful values.
† No tests performed.

Table 2.6 For cellulose acetate spheres, a comparison of experimental and theoretical values of the maximum contact displacement prior to gross sliding (Mullier et al., 1991)

Applied normal load W (N)	Hertz contact area a (μm)	Tangential force F_c (N)	Experimental displacement δ_{max} (μm)	Theoretical displacement[a] δ_{max} (μm)
0.5	72.4	0.15	10.0	0.69–1.55
0.8	84.7	0.38	16.0	1.50–3.36
1.5	104.4	0.33	30.0	1.05–2.37

[a]The lower values correspond to the Poisson ratio $v = 0.4$, the higher values $v = 0.8$.

Table 2.7 Average coefficients of sliding friction (Ishibashi et al., 1994).

Test Method	Particle Diameter	Dry Surface on Clear Plate	Dry Surface on Smoked Plate	Water Flooded on Clear Plate	Water Flooded on Smoked Plate	Oil Flooded on Smoked Plate
Pulling	1.6 mm	0.178	—	0.262	—	—
	3.0 mm	0.151	0.095	0.291	0.204	0.083
	5.0 mm	—	0.076	—	0.099	0.034
Sliding	0.6–5.0 mm	0.156	—	—	—	—
Average		0.162	0.086	0.277	0.152	0.059

Table 2.8 Inter-particle shearing test results on Leighton Buzzard sand particles (Senetakis et al., 2013b).

Code of test	Particle size (mm)	State	Sliding velocity (μm/h)	F_v (N)	$\mu^{(3)}$	$\varphi^{(3)}$ (deg)	Frame
LBS01A	2.36-5.00	Dry[1]	200	1.97	0.128	7.3	1
LBS01B	2.36-5.00	Dry	200	1.97	0.106	6.1	1
LBS02	2.36-5.00	Dry	200	1.98	0.150	8.5	1
LBS03	2.36-5.00	Dry	200	1.98	0.156	8.9	1
LBS04	2.36-5.00	Dry	300	4.97	0.145	8.3	1
LBS05A	2.36-5.00	Dry	300	4.98	0.179	10.2	1
LBS05B	2.36-5.00	Dry	300	4.98	0.170	9.7	1
LBS06	2.36-5.00	Dry	600	7.97	0.123	7.0	2
LBS07	2.36-5.00	Dry	600	15.98	0.231	13.0	2
LBS08	1.18-2.36	Dry	600	2.97	0.115	6.6	2
LBS09	2.36-5.00	Dry	600	0.86	0.216	12.2	2
LBS10	1.18-2.36	Dry	1000	9.99	0.195	11.0	2
LBS11	2.36-5.00	Dry	600	11.98	0.171	9.7	1
LBS12A	2.36-5.00	Dry	600	2.99	0.162	9.2	1
LBS12B	2.36-5.00	Dry	600	2.99	0.150	8.5	1
LBS13A	1.18-2.36	Saturated[2]	600	4.98	0.136	7.8	1
LBS13B	1.18-2.36	Saturated	600	4.99	0.114	6.5	1
LBS14	2.36-5.00	Saturated	600	7.98	0.193	10.9	1
LBS15	2.36-5.00	Saturated	600	7.99	0.171	9.7	1
LBS16	2.36-5.00	Saturated	600	7.98	0.191	10.8	1
LBS17	2.36-5.00	Saturated	900	4.98	0.135	7.7	1
LBS18	2.36-5.00	Dry	600	7.99	0.138	7.9	2
LBS19	1.18-2.36	Dry	600	0.94	0.093	5.3	1
LBS20	2.36-5.00	Saturated	900	4.98	0.154	8.8	1
LBS21	2.36-5.00	Saturated	900	4.98	0.128	7.3	1
LBS22	2.36-5.00	Saturated	900	4.98	0.163	9.3	1

[1] Dry state: Particles tested at a relative humidity of about 93%-97%
[2] Saturated state: Particles immerged in distilled water
[3] Mean values along the shearing track

Table 2.9 An overview of Great Britain's crushed rock production for railway ballast during 2002–2014 (modified from Idoine et al., 2016).

Year	Sandstone	Igneous rock	Limestone and dolomite	Total
		Thousand tonnes		
2002	190	3324	—	3514
2003	…	2669	…	(a)2895
2004	…	3074	…	3832
2005	…	3072	…	3403
2006	…	3102	…	3543
2007	…	3372	…	3904
2008	157	…	…	3408
2009	—	…	…	2556
2010	…	2154	…	2158
2011	…	1417	…	1421
2012	—	2312	142	2454
2013	39	2561	0	2600
2014	—	2989	…	2989
(a) British Geological Survey estimate Source: Office for National Statistics				
… Figures not available — Nil				

Table 2.10 Ballast equivalent to 31.5/50 BS EN 13450 in grading category A (modified from BS EN 13450:2013).

Sieve size (mm)	Percentage passing by mass
63	100
50	70-99
40	30-65
31.5	1-25
22.4	0-3
31.5-50	≥50

Table 2.11 A summary of the type of rock and particle size used in different countries and by different authors.

Authors	Country	Types of rock	Sizes of particles
Indraratna et al. (1997)	Australia	Latite basalt	13-73mm
Indraratna et al. (1998)	Australia	Latite basalt	13-73mm
Lim et al. (2004)	United Kingdom	Granite, granodiorite, felsite and mixture of metasediments, pyroclastics and granodiorite	10-50mm
Lackenby et al. (2007)	Australia	Latite basalt	2.36-63mm
Le Pen et al. (2013)	United Kingdom	Granite	9.5-62.5mm
Sun et al. (2014)	Australia	Latite basalt	13.2-53mm
Indraratna et al. (2015)	Australia	Latite basalt	2.36-53mm
Koohmishi and Palassi (2016)	Iran	Basalt, marl, dolomite and trachyte	19-62.5mm

Table 2.12 Inter-particle sliding tests on natural granite granules.

No. of test	Code of test	Material type	Apparatus	Normal force, F_N (N)	Tangential force, F_T (N)	Inter-particle coefficient of friction, μ
1	LA-G-1	Crushed granite	Large-size	10	2.20	0.22
2	LA-G-2	Crushed granite	Large-size	10	3.77	0.38
3	LA-G-3	Crushed granite	Large-size	10	3.23	0.32
4	LA-G-4	Crushed granite	Large-size	20	5.32	0.27
5	LA-G-5	Crushed granite	Large-size	30	8.26	0.28
6	LA-G-6	Crushed granite	Large-size	20	6.45	0.32
7	LA-G-7	Crushed granite	Large-size	30	12.82	0.43

Note: Each code represents a different pair of grains.
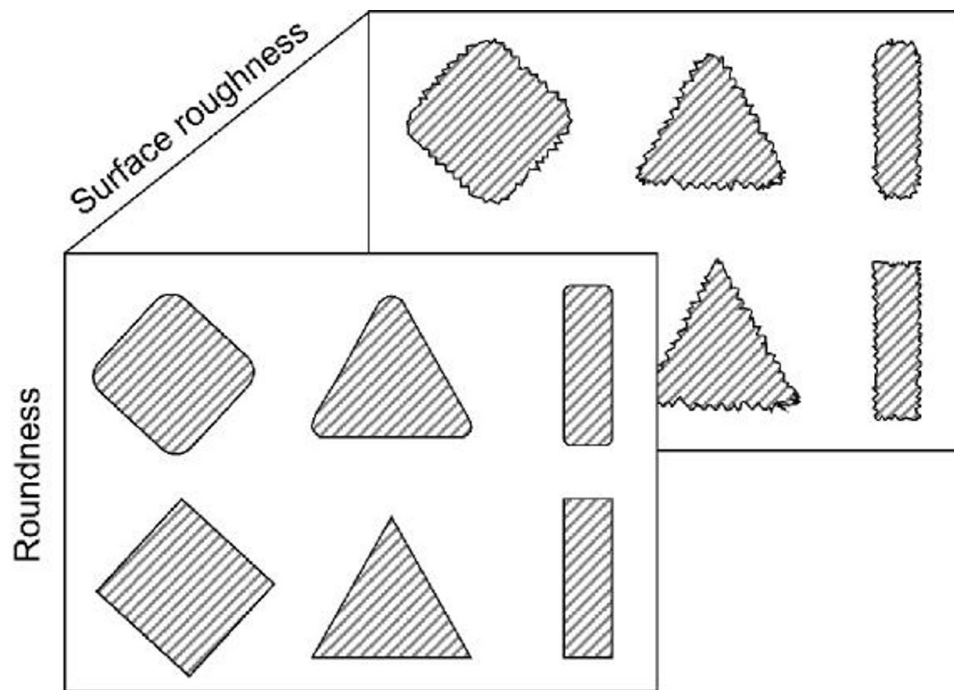
Figure 2.1 Illustration of three scales of particle shape (Barret, 1980).
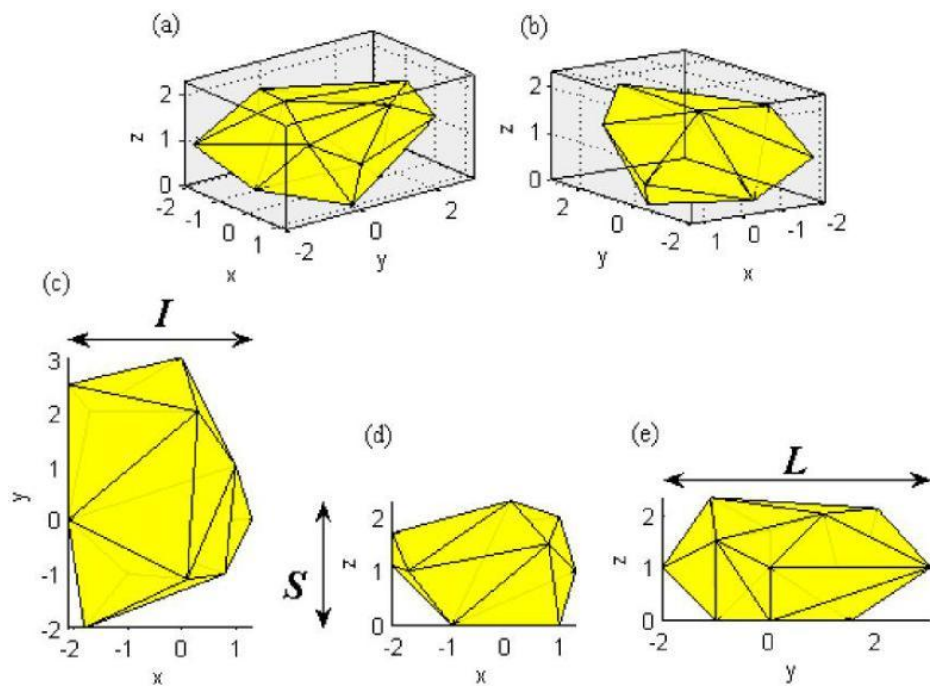
Figure 2.2 Concept and description of the smallest circumscribed cuboid SCC
(Cavarretta, 2009)
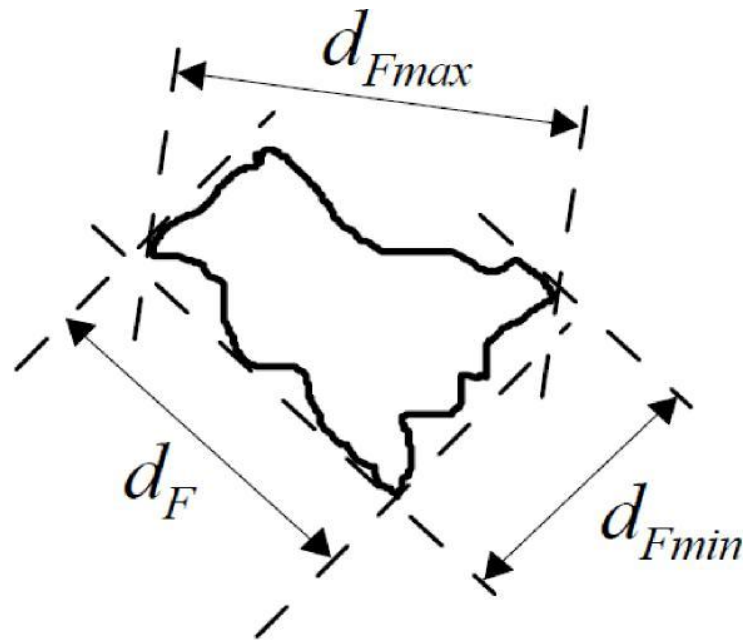
Figure 2.3 Definition of Feret diameters (after Cavarretta, 2009)
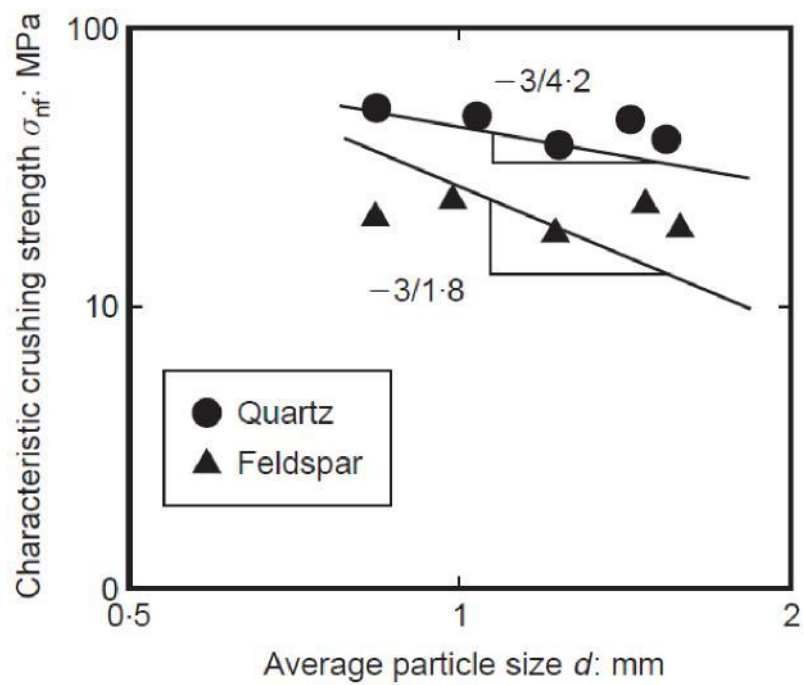
Figure 2.4 Effect of particle size on the single particle strength of sand particles

(Nakata et al., 1999)
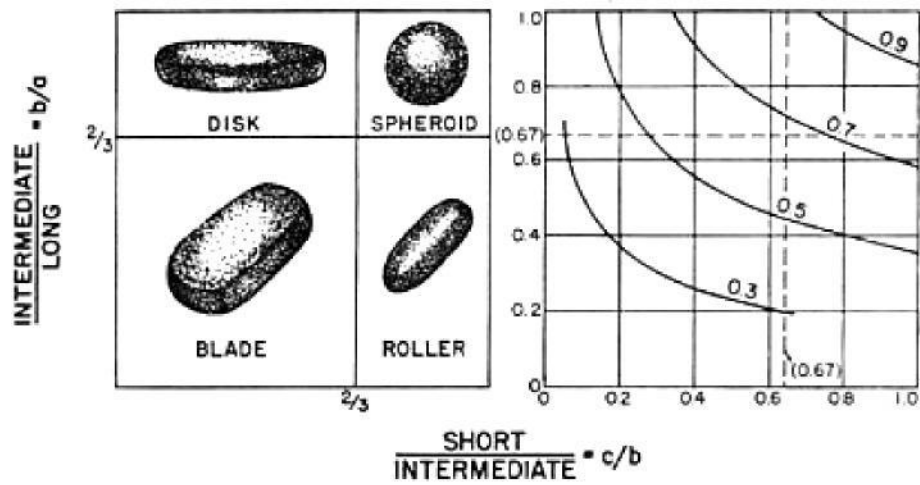
Figure 2.5 Zingg's classification of particle shape (Zingg, 1935)
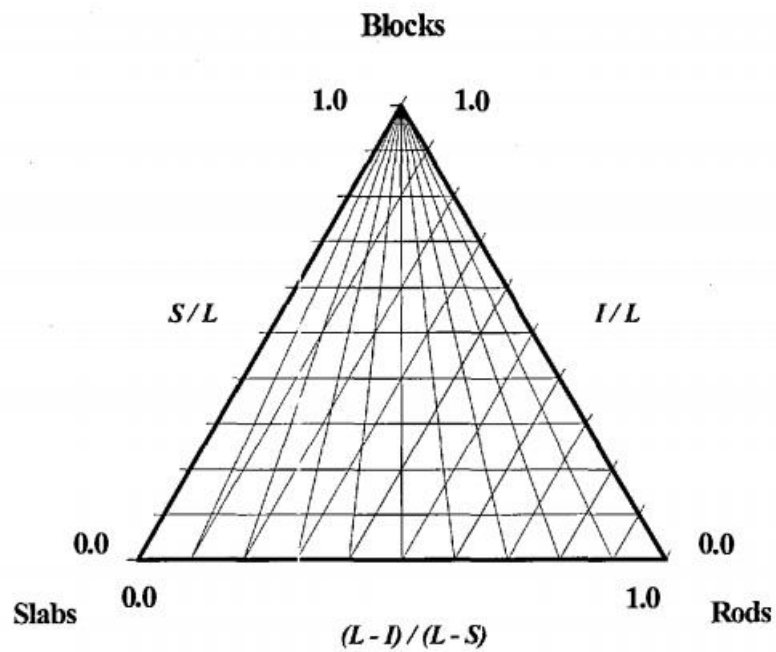
Figure 2.6 Redrawn by (Cavarretta-I-2010-PhD-Thesis): triangular plot for form classification (Sneed and Folk, 1958)
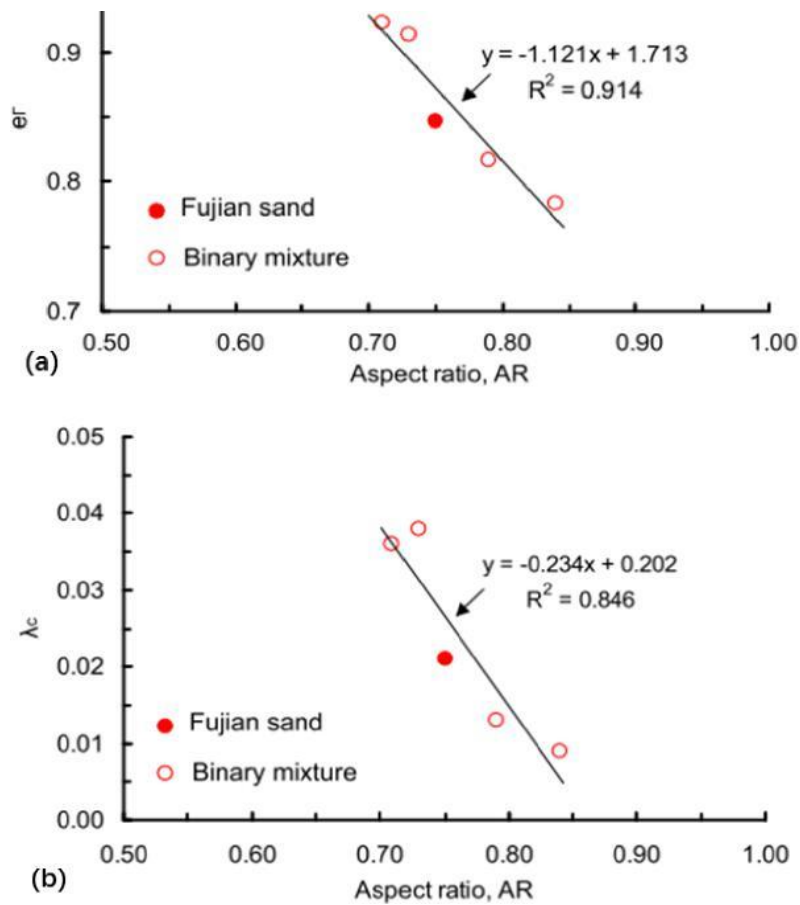
Figure 2.7 Effect of aspect ratio on the critical state parameters: (a) eΓ; (b) λc (Yang & Luo, 2015)
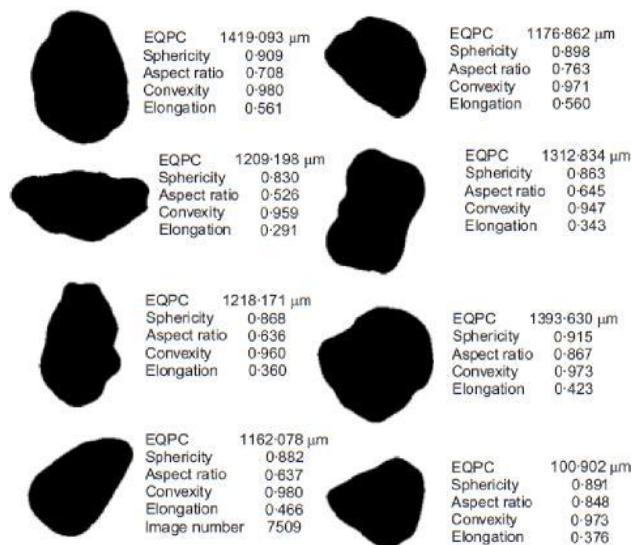
Figure 2.8 Examples of aspect ratio, sphericity, and convexity of Leighton buzzard sand particles along with elongation (Altuhafi and Coop, 2011)
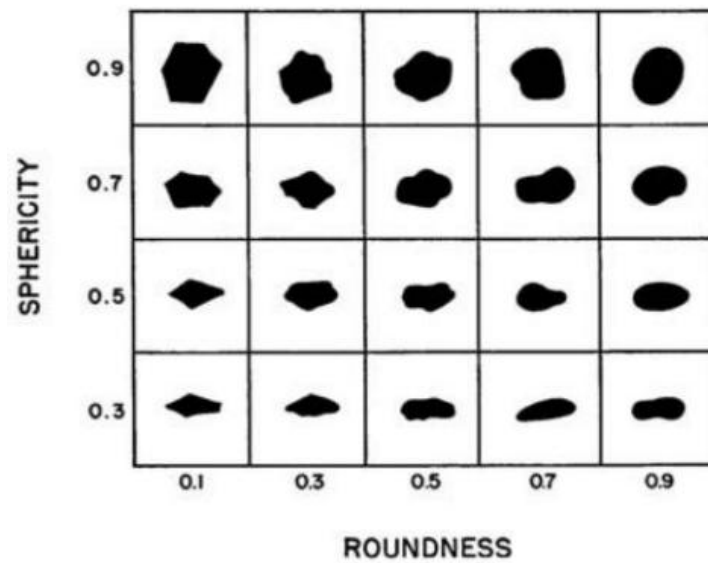
Figure 2.9 Sphericity and roundness of sand particles determined from the reference chart (Krumbein & Sloss, 1963)
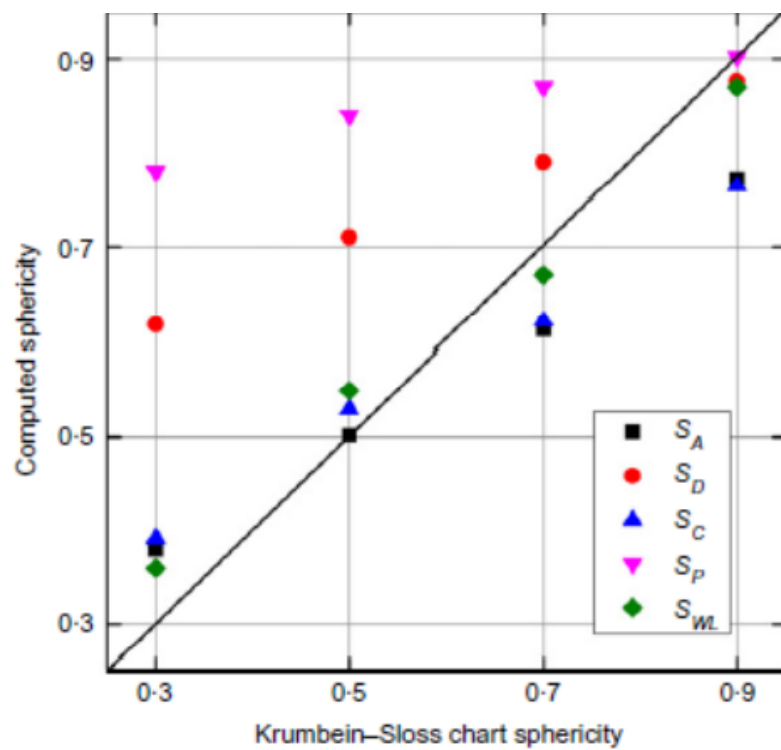
Figure 2.10 Comparison of the Krumbein & Sloss (1963) chart values to sphericity by various definitions (Zheng & Hryciw, 2015)
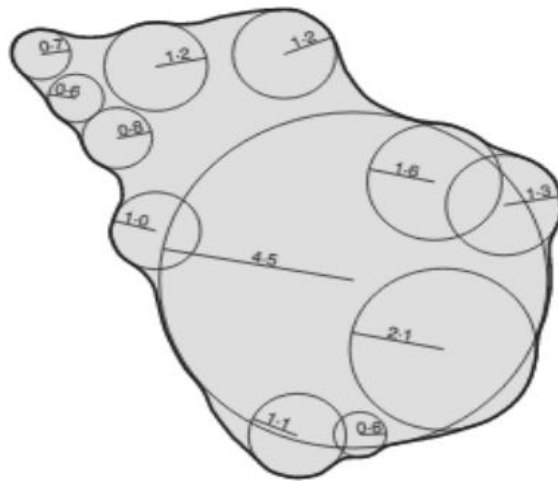
Figure 2.11 A diagram illustrating Wadell's roundness (Wadell, 1932)
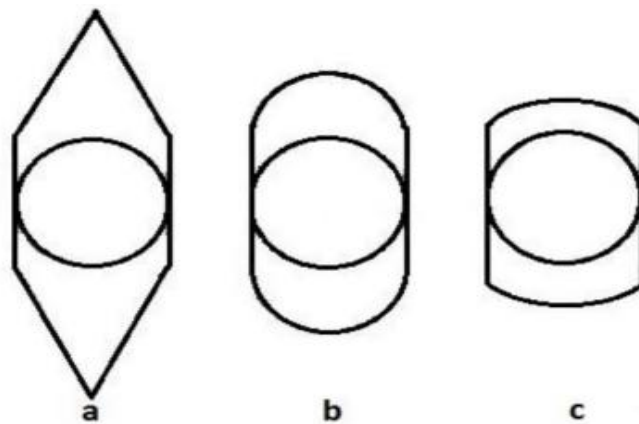
Figure 2.12 An illustration of the three stages of particle roundness during erosion
(Wadell, 1932)
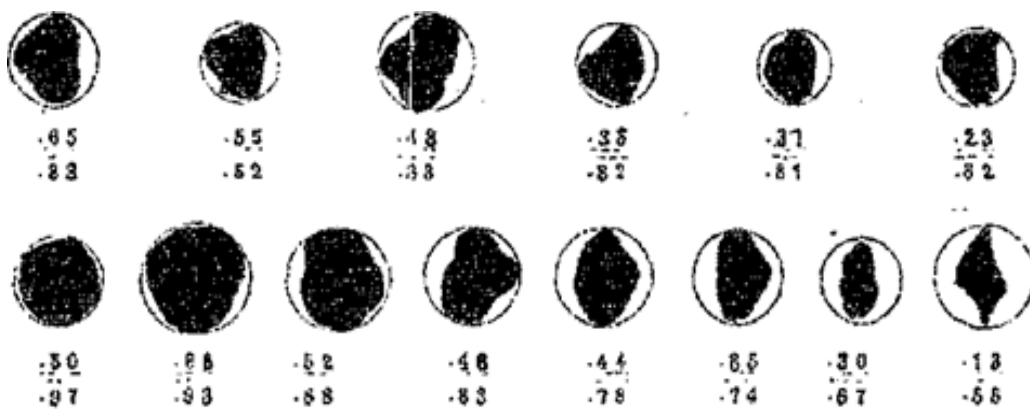
Figure 2.13 Reference shape descriptors of sand grain outlines (For each geometry the
values given are Roundness/ Sphericity), (Wadell, 1932)
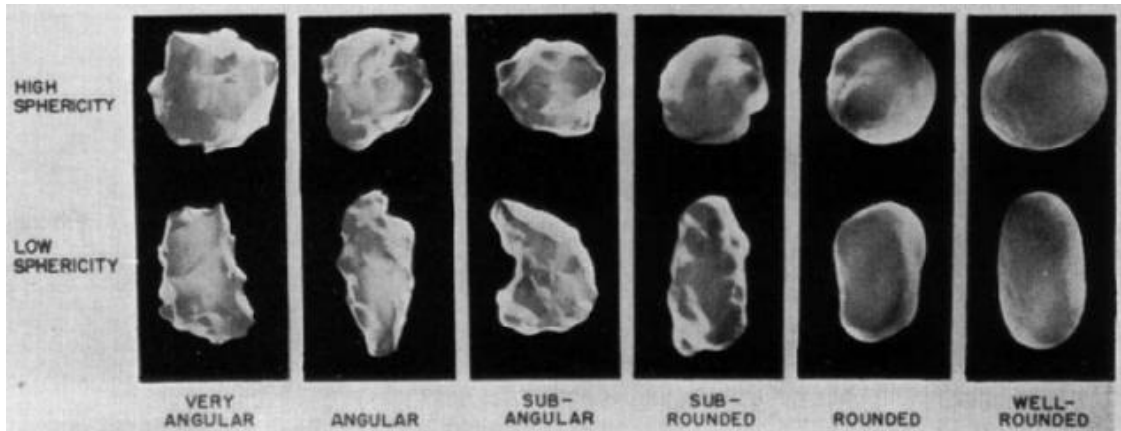
Figure 2.14 A visual comparison of particle roundness and sphericity using photographs of sand particles (Powers, 1953)
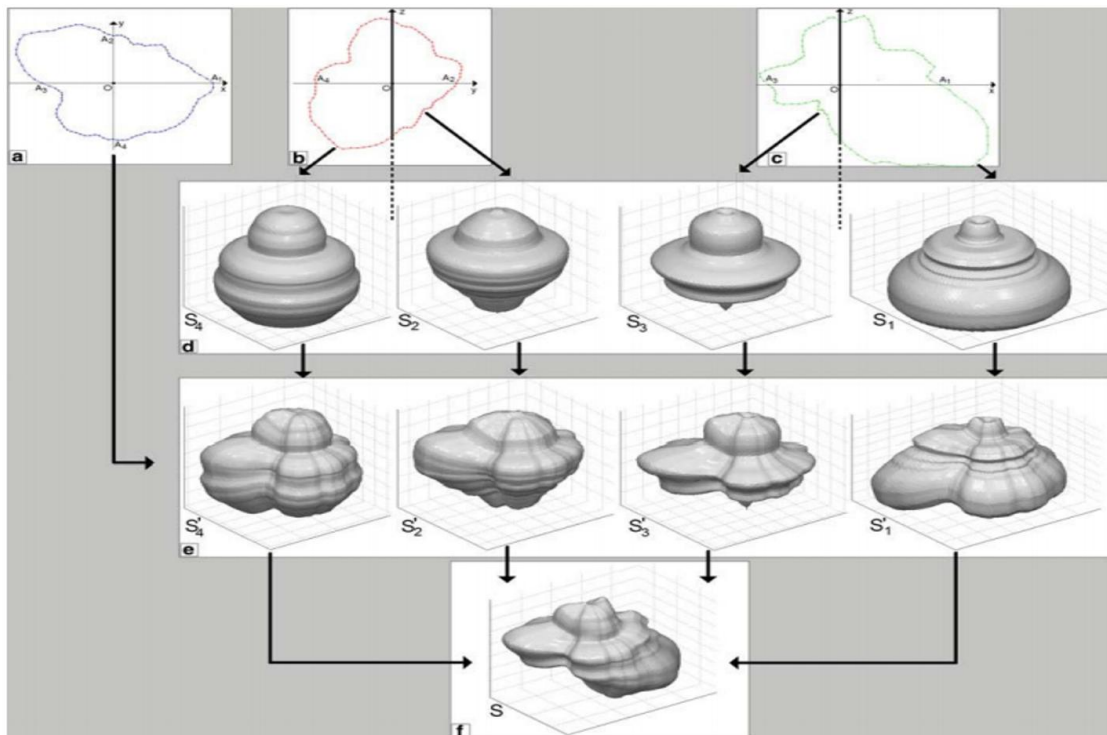
Figure 2.15 Principle of the 3D generation method. a) (x, y) cross-section; b) (y, z) cross-section; c) (x, z) cross-section; d) solids S1 to S4 obtained by revolution of half-cross-sections; e) solids S1 to S4 obtained by horizontal stretching of S1 to S4; f) final solid S (Mollon & Zhao, 2013)
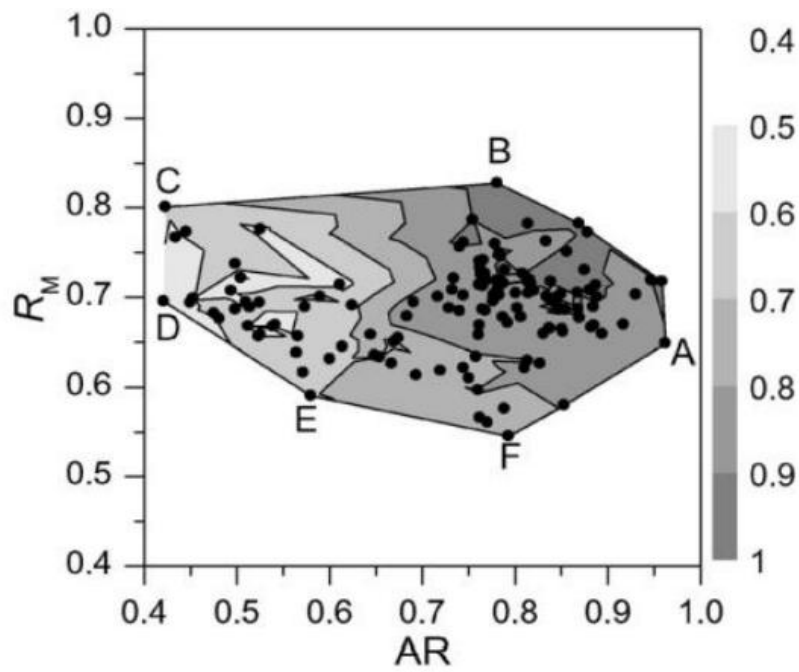
Figure 2.16 Relationship between sphericity and aspect ratio (AR), and roundness and mean curvature (RM) (Zhao & Wang, 2016)
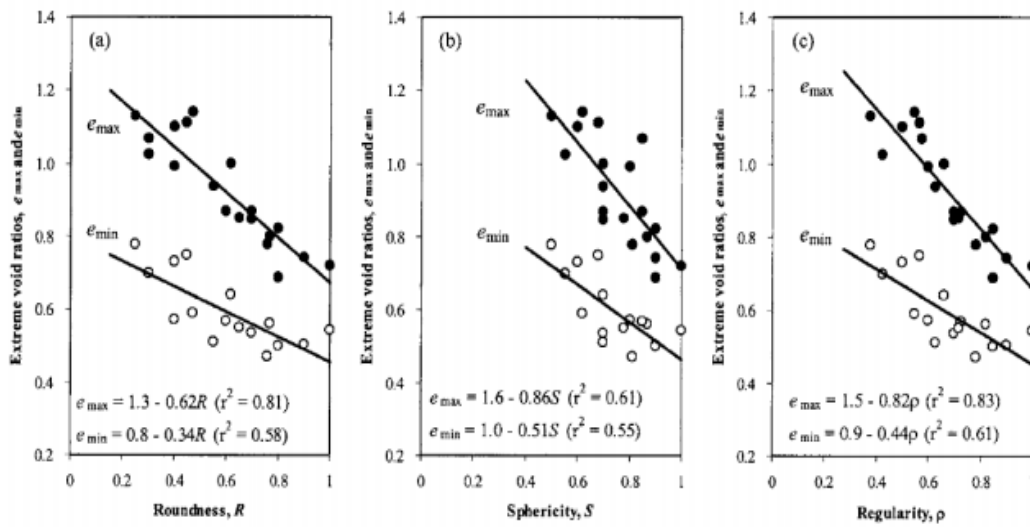
Figure 2.17 An analysis of the effects of roundness and sphericity on packing density (Cho & Santamaria, 2006)
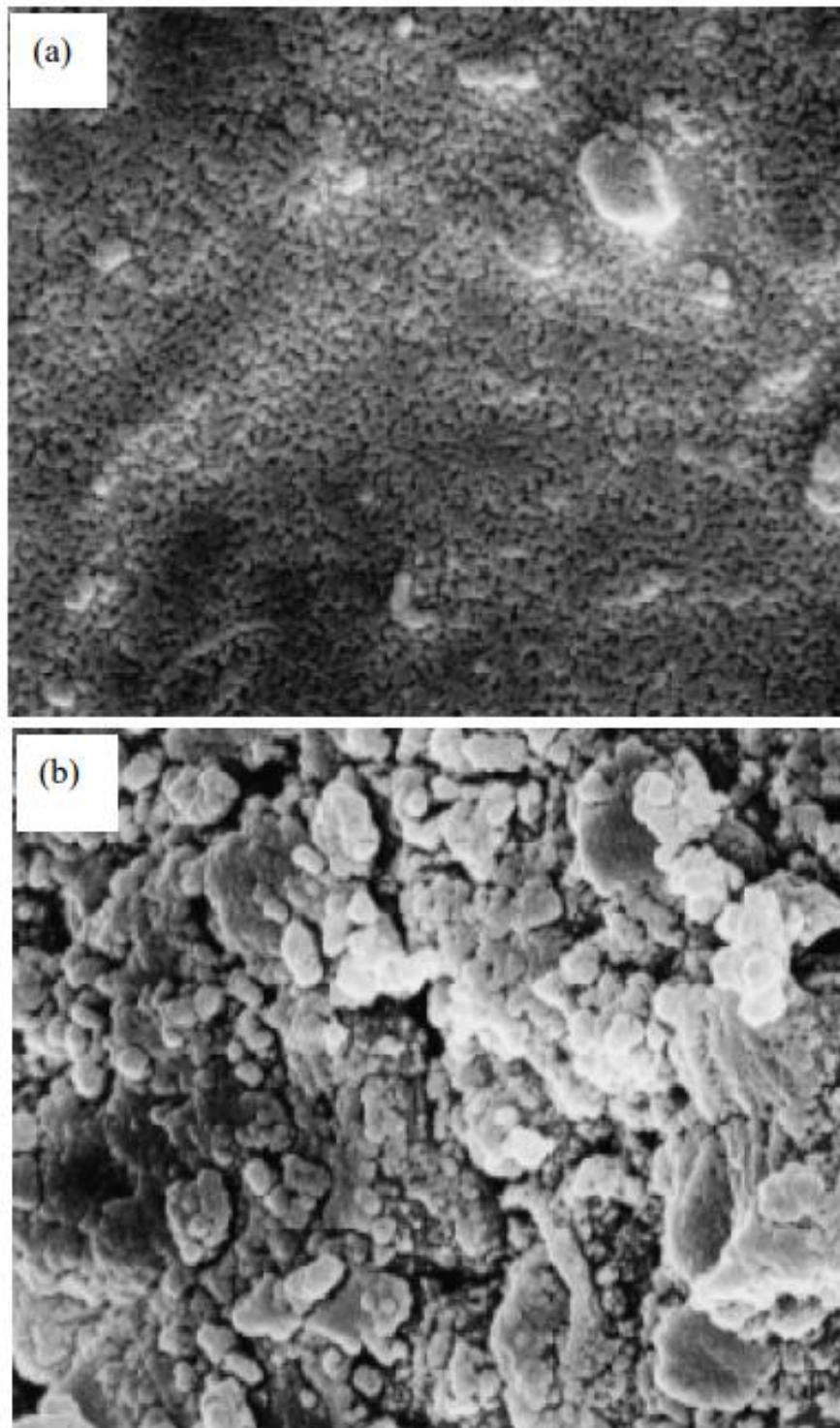
Figure 2.18 Images of steel balls scanned by SEM: (a) mild rust; (b) rusted
(Santamarina & Cascante, 1998)
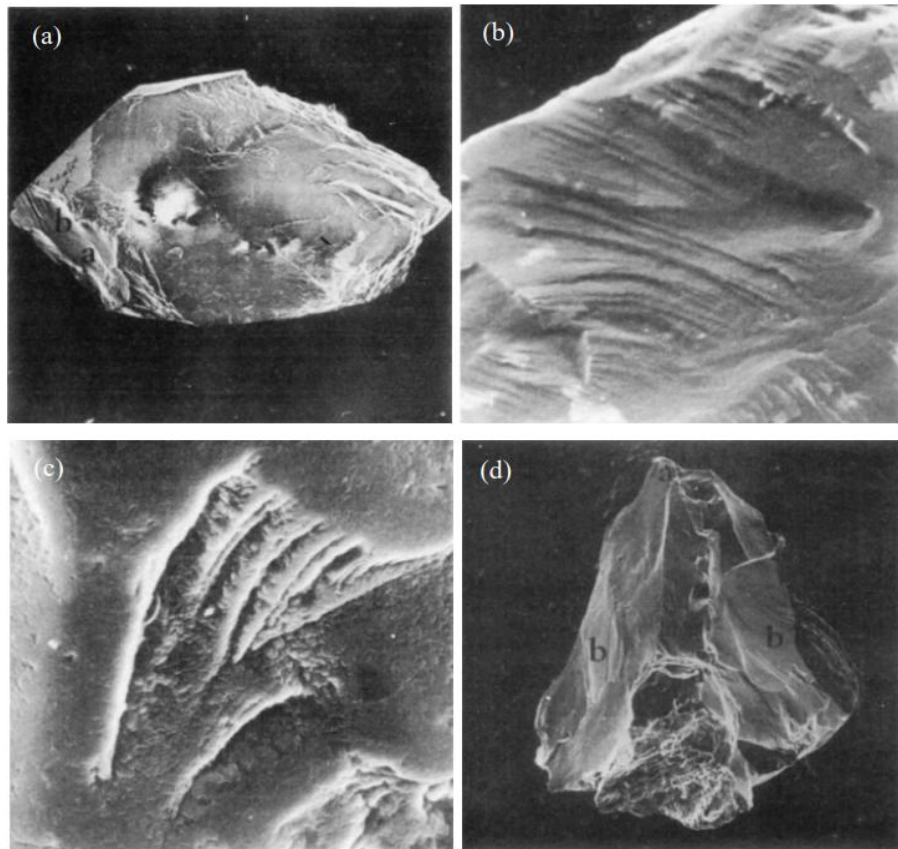
Figure 2.19 Graphs of the surfaces of quartz grains from different environments, including (a) freshly weathered granite from Cheviot, Northumberland (×56); (b) a portion of a freshly weathered Millstone Grit (×440): c) a quartz grain found at Studland Heath, Dorset (×920); An occurrence of quartz grain from Pleistocene Middle Sands of NE Cheshire (Brown, 1973).
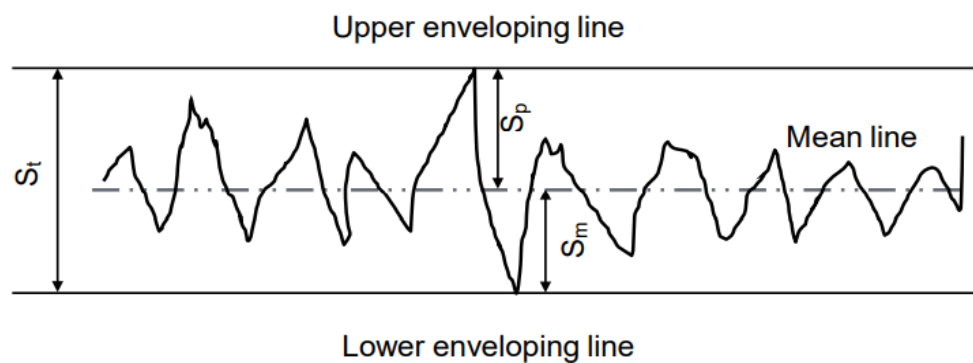
Figure 2.20 The parameters St, Sp, and Sm of the profile are Illustrated above, (Sander, 1991).
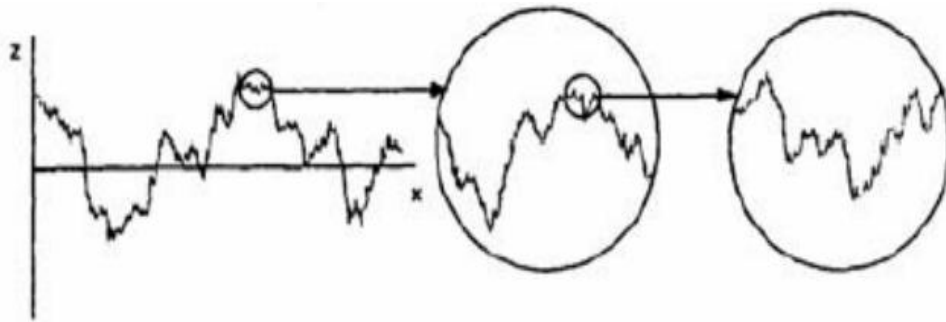
Figure 2.21 Surface profile with self-similarity (Bhushan, 2001).
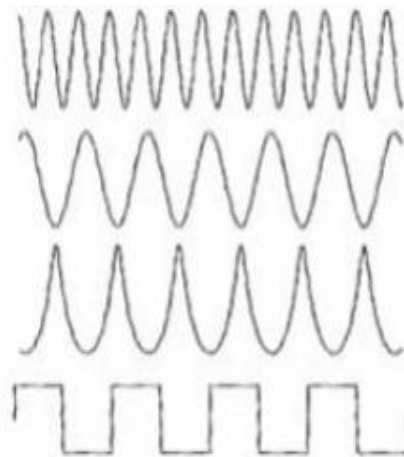
Figure 2.22 Identical profiles with the same Sq values (Mate, 2008).
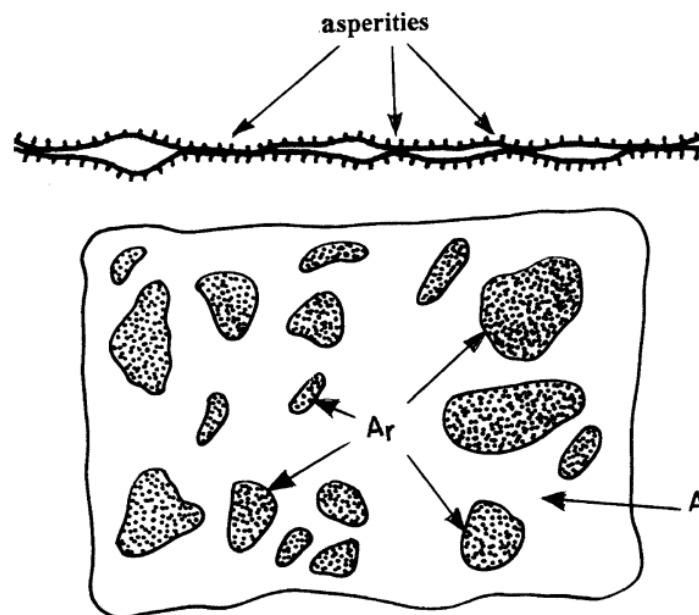
Figure 2.23 Two surfaces, their apparent contact area(A) and Ar real contact areas (Bowden & Tabor, 1950).
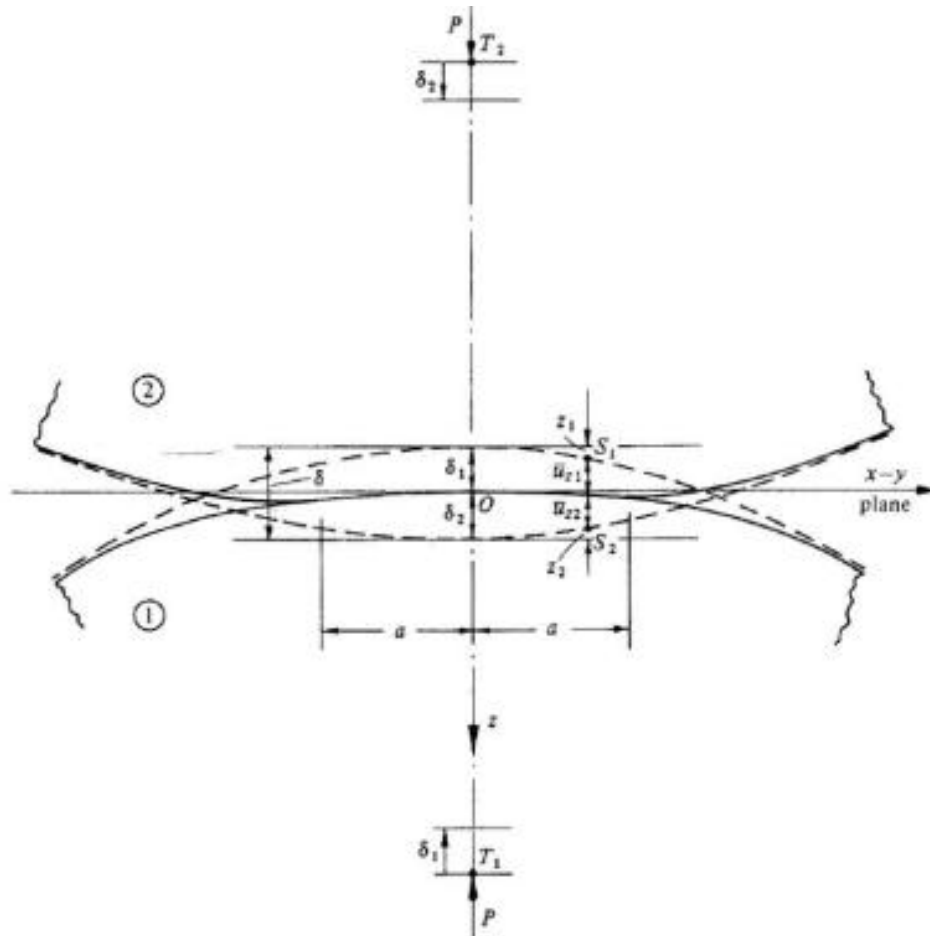
Figure 2.24 Contact problem by Hertz (Johnson, 1985).
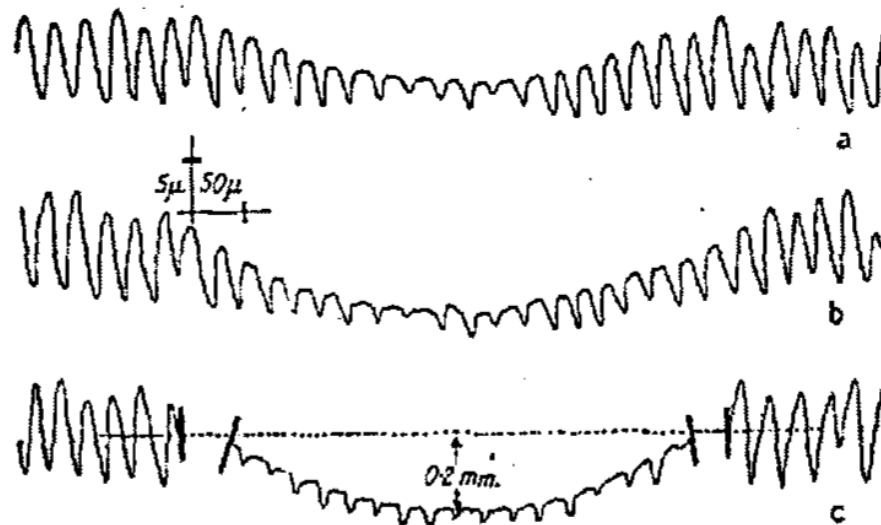
Figure 2.25 Record of the deformed surface of a grooved metal under (a) light, (b) heavier, and (c) very heavy loads (Moore, 1948).
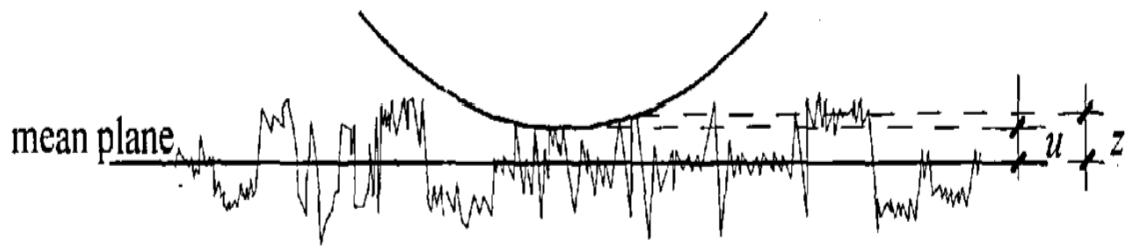
Figure 2.26 In GT model, surface asperity height z and separation u of the surface (Greenwood & Tripp, 1966).
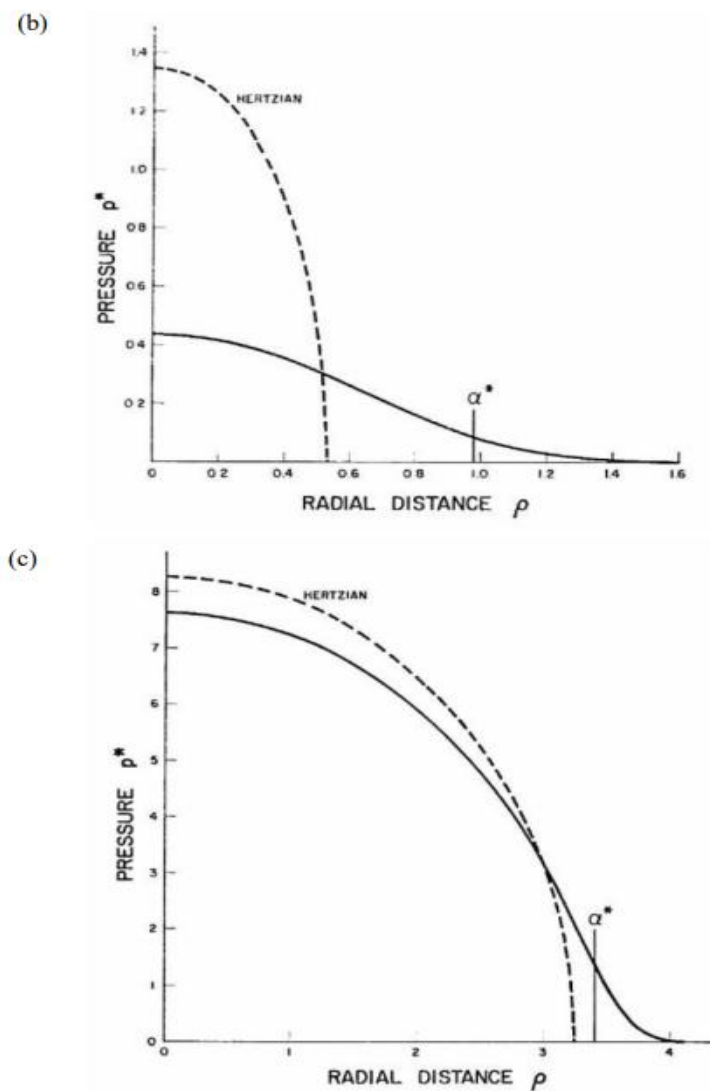
Figure 2.27 An elastic sphere in contact with a flat rough plate surface (b) at low loads and (c) at high loads (Greenwood & Tripp, 1966)
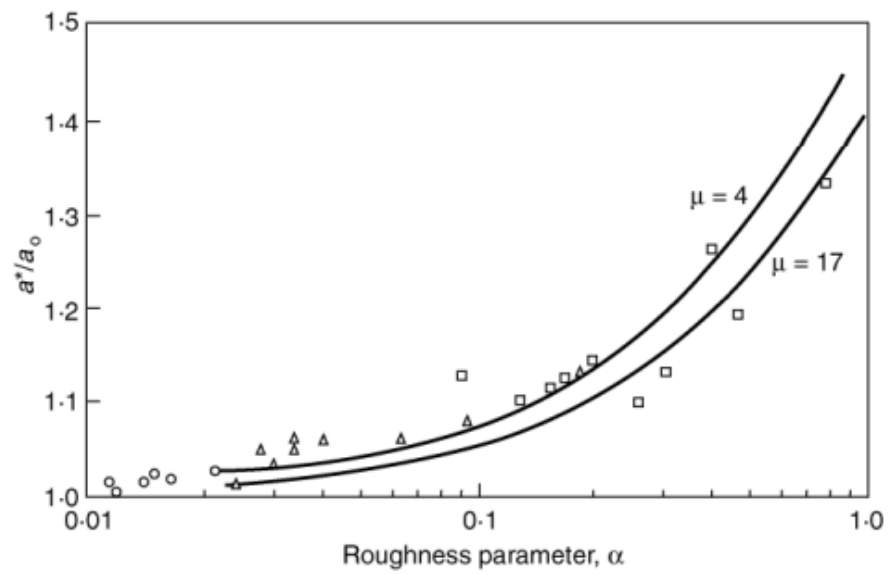
Figure 2.28 Fig. 2. 28 Influence of the surface roughness parameter α on the contact radius (Johnson, 1985).
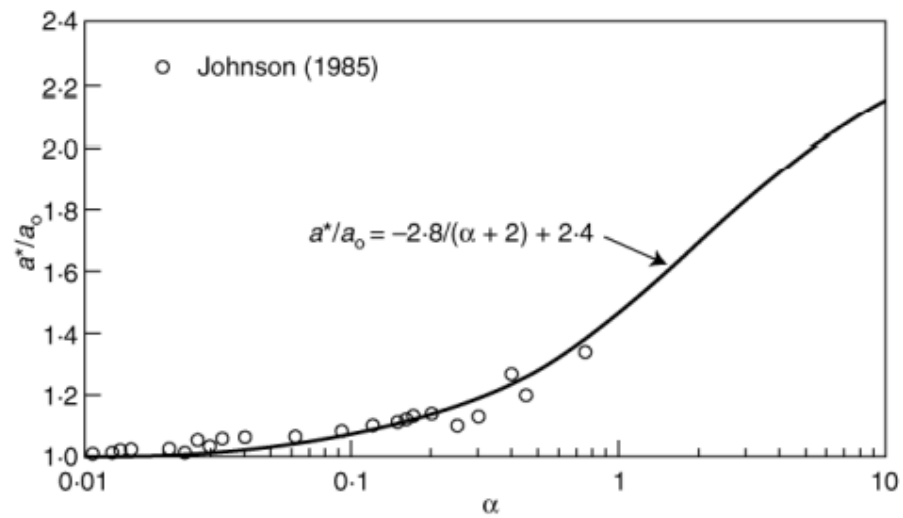
Figure 2.29 Fitting results based on the data of Johnson (Yimsiri & Soga, 2000).
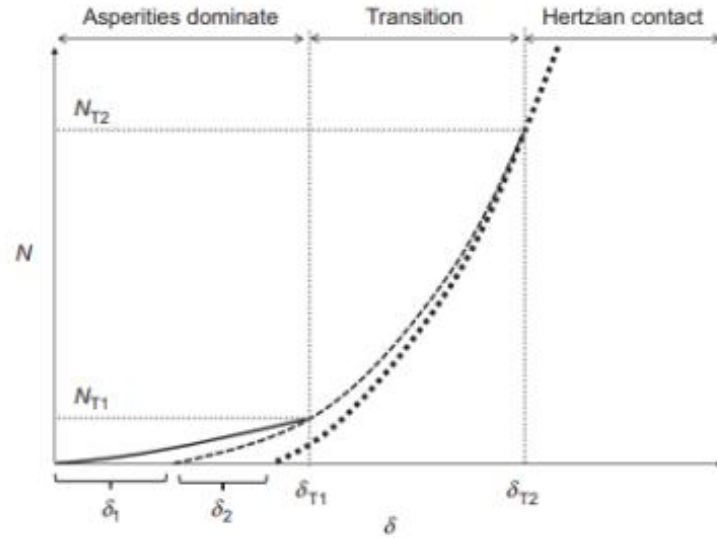
Figure 2.30 Illustration of the normal contact model proposed by Otsubo et al. (2016).
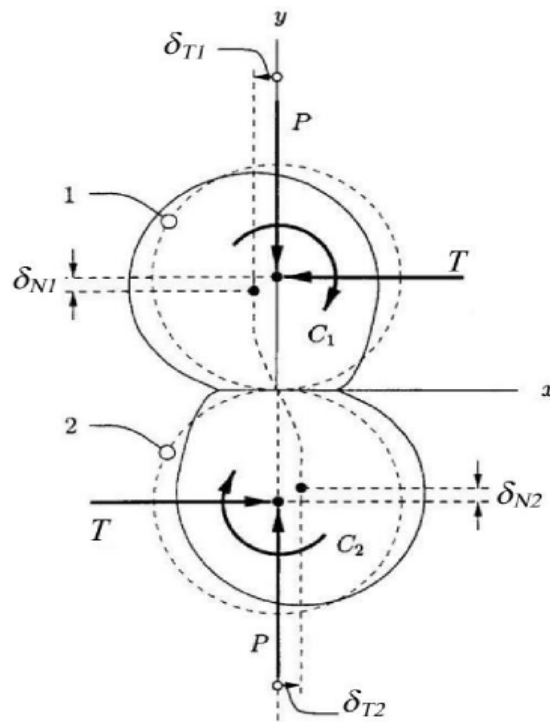
Figure 2.31 A simple-loading history of two spheres in contact and subjected to normal and tangential loadings (Vu-Quoc and Zhang, 1999, modified by Nardelli, 2017).
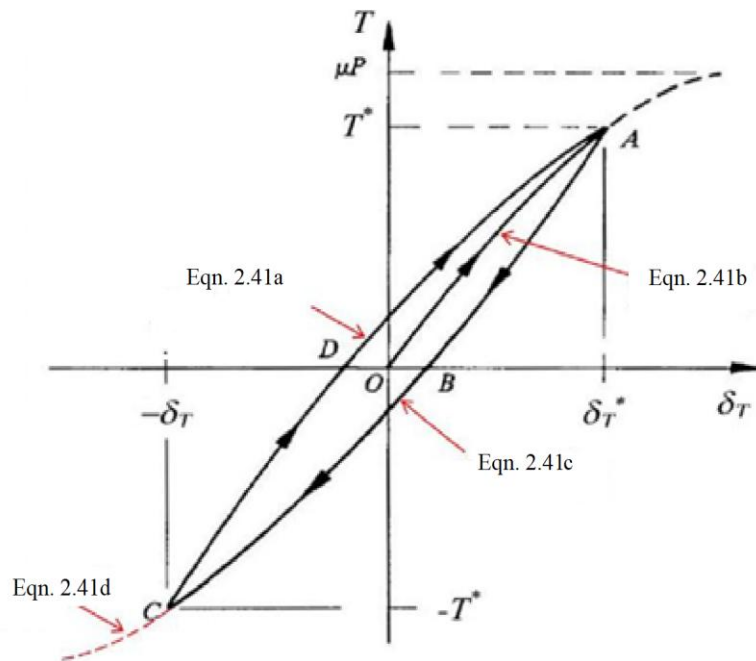
Figure 2.32 Tangential load-displacement relationship for the Mindlin and Deresiewicz (1953) contact model (Johnson, 1985, modified by Nardelli, 2017).
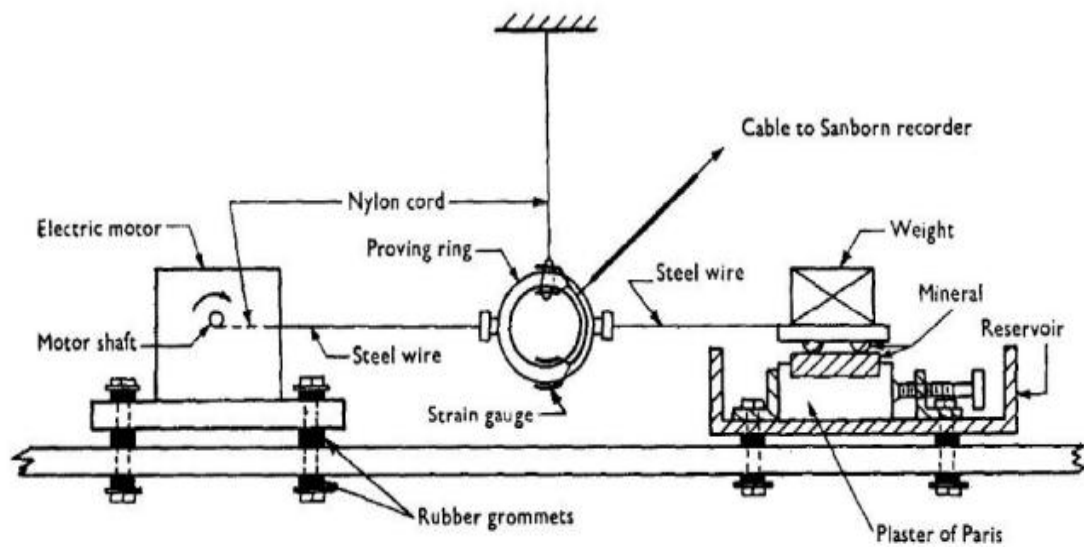
Figure 2.33 First designed and built custom apparatus the investigate inter-particle friction (Horn & Deere, 1962).
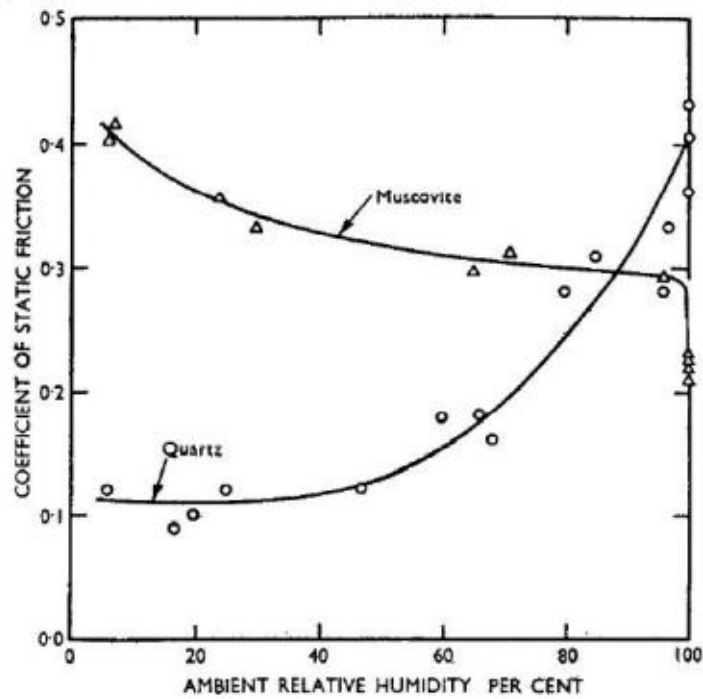
Figure 2.34 Calculation of the coefficient of static friction for muscovite and clear quartz with respect to the ambient relative humidity (Horn and Deere, 1962).
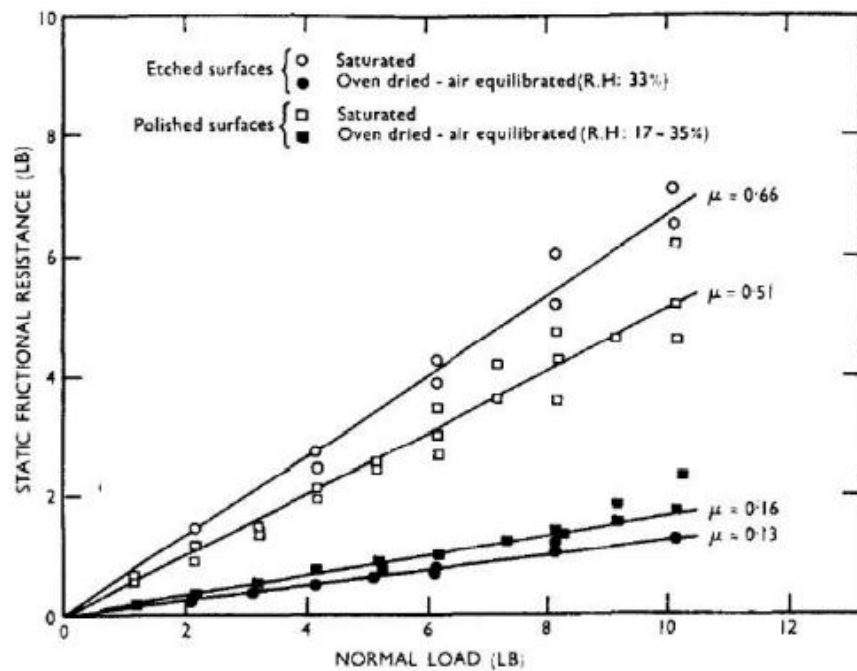
Figure 2.35 A study of the static frictional characteristics of polished quartz and the surfaces after they are etched (Horn and Deere, 1962).
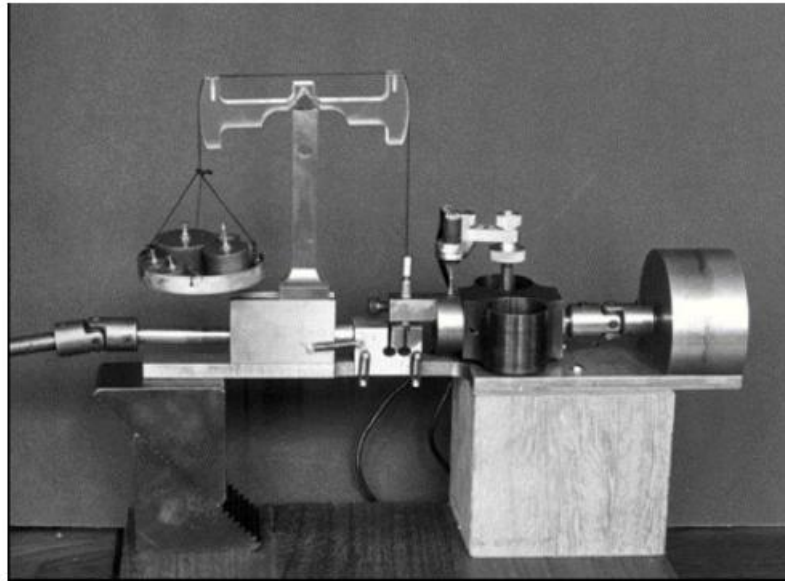
Figure 2.36 An apparatus for measuring inter-particle friction (Skinner, 1975).

1. Vertical load cell
2. Horizontal load cell
3. Vertical LVDT
4. Horizontal LVDT
5. Upper particle podium
6. Upper mounting assembly
7. Lower particle podium
8. Lower mounting assembly
9. Bath, made of thin aluminium alloy
10. Leverarm
11. Vertical position adjustment screws for horizontal LVDT coil

12. Horizontal position adjustment screws for horizontal LVDT coil
13. Tico anti-vibration pad
14. Pivot adjustment screw
15. Bearing—two synchro bearings
16. Counterweight
17. Horizontal load cell retaining nuts
18. LVDT core
19. LVDT coil
20. Worm gear housing

Figure 2.37 The Rowe device (inter-particle friction) developed at the University of Manchester (Procter and Barton, 1974).
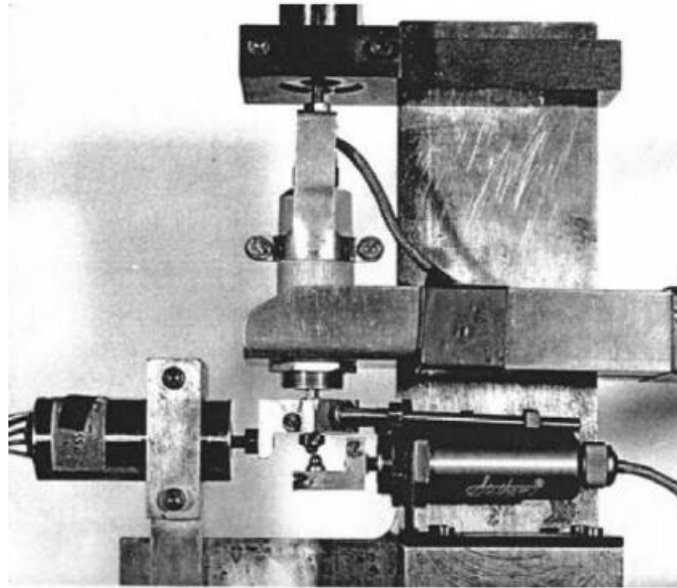
Figure 2.38 Device for interparticle friction (Procter and Barton, 1974).
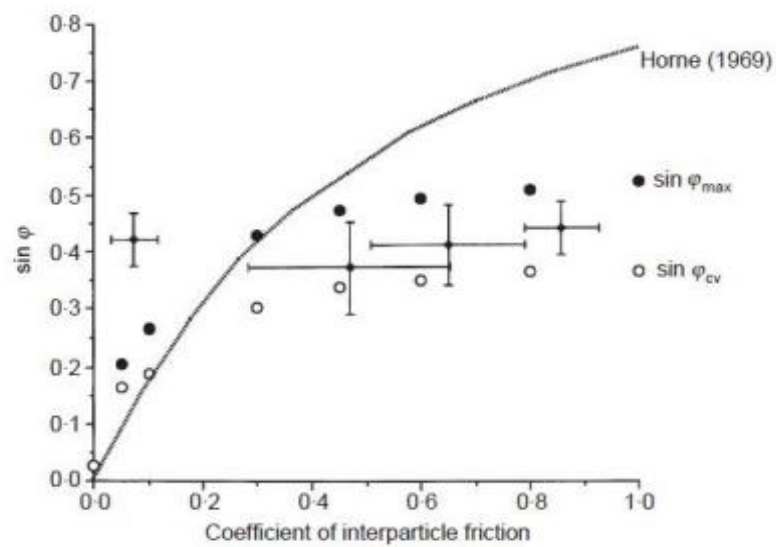
Figure 2.39 Mobilisation of internal friction angle by interparticle friction. Taking Horne's (1969) theoretical solution to sin φcv and comparing it to Skinner's (1969) experimental results (including error bars), we see an overlay.
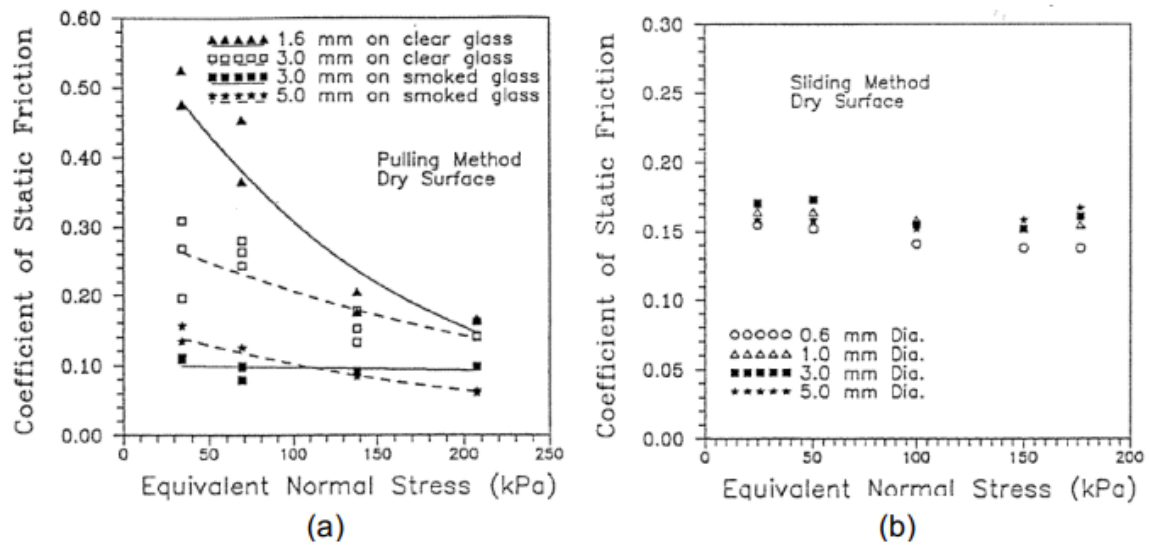
Figure 2.40 Calculating static friction coefficients for dry surfaces: a) pulling method; b) sliding method (Ishibashi et al., 1994).
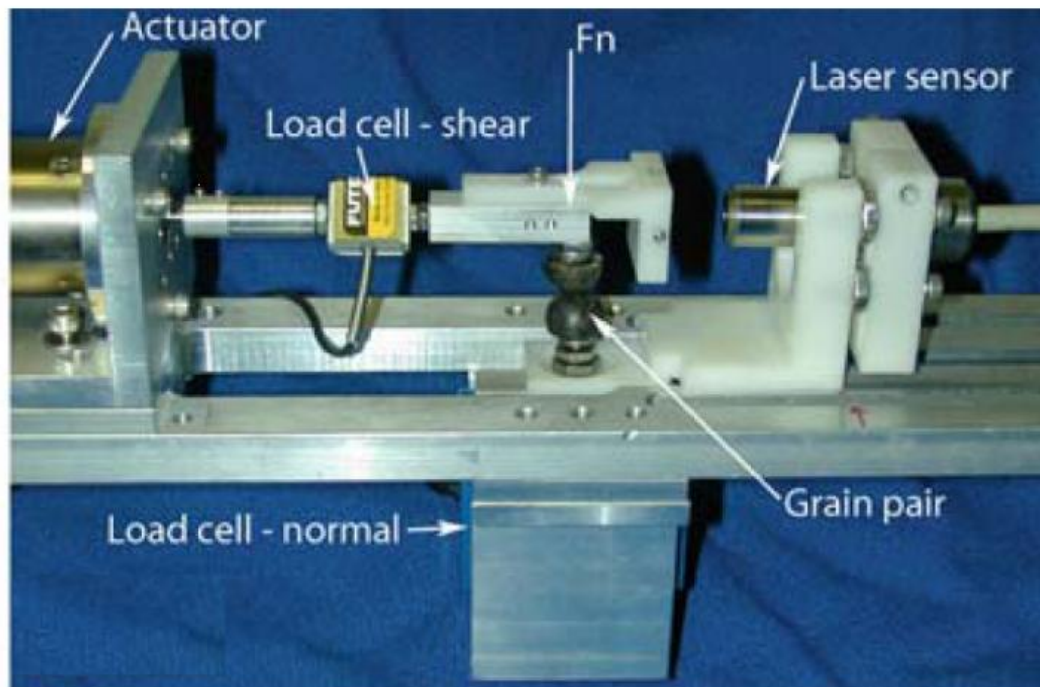
Figure 2.41 Experimental device built for different loading (Cole et al., 2010).
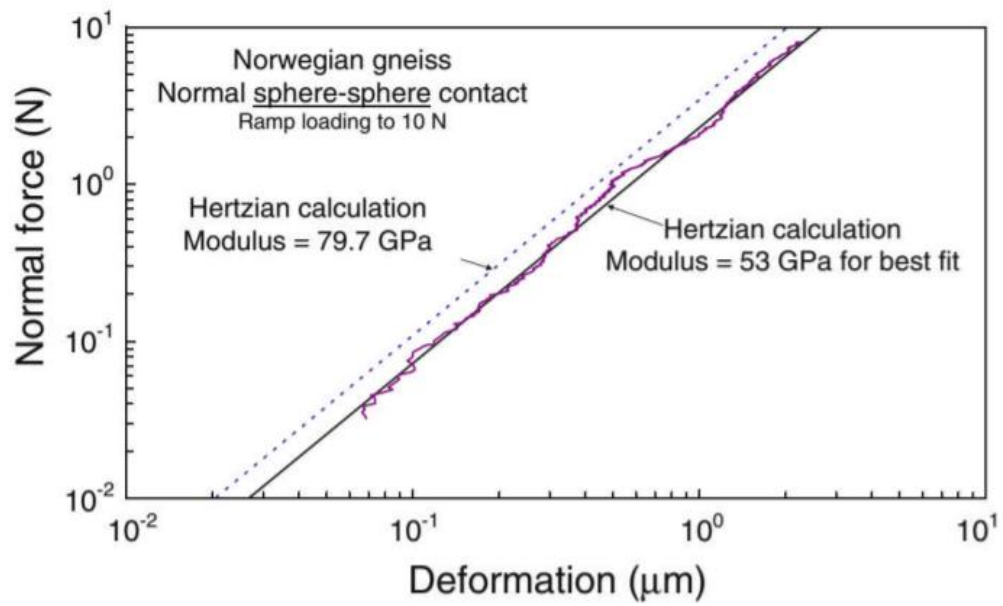
Figure 2.42 Spherical gneiss grains (irregular curve) under normal loading (Cole et al., 2010).
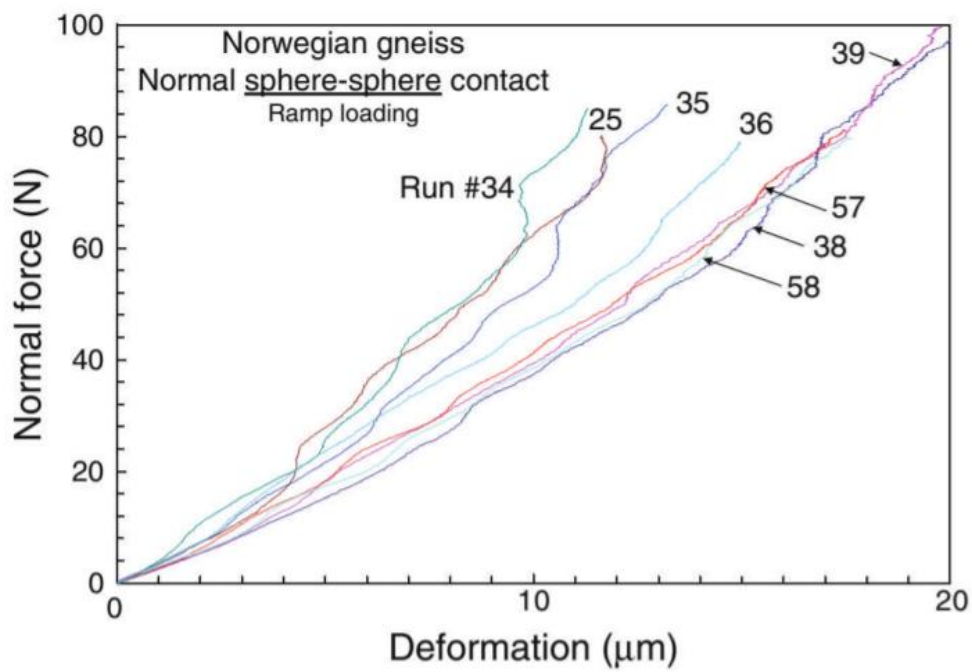
Figure 2.43 The deformation of the same pair of gneiss (spherical grains) after run #38 showed convergence (Cole et al., 2010).
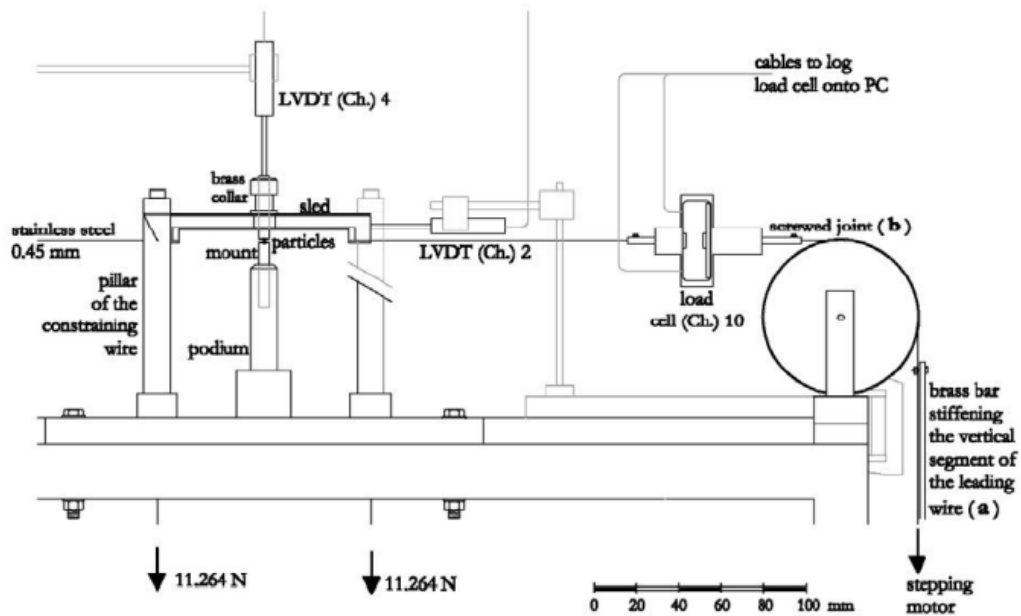
Figure 2.44 This apparatus was custom-made for analysing the inter-particle friction of small particles including soils (Cavarretta et al., 2011).
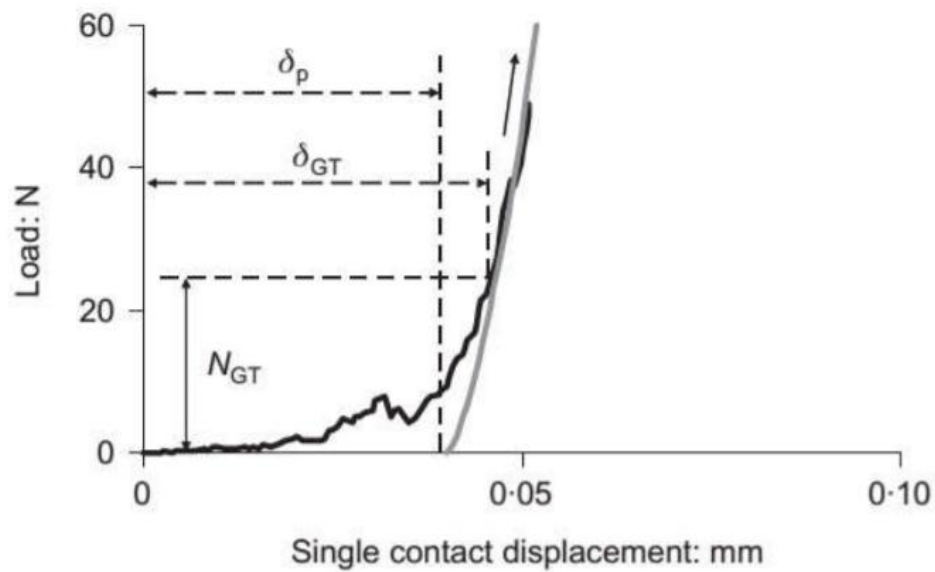
Figure 2.45 At small displacements, typical compression test results for Leighton Buzzard sand (Cavarretta et al., 2010).
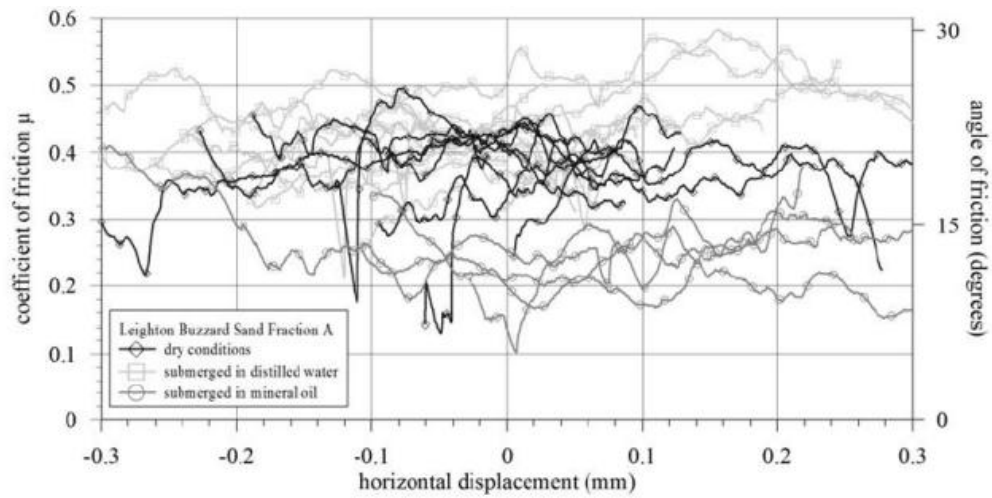
Figure 2.46 Environmental influences on Leighton Buzzard sand's inter-particle friction (Cavarretta et al., 2011).
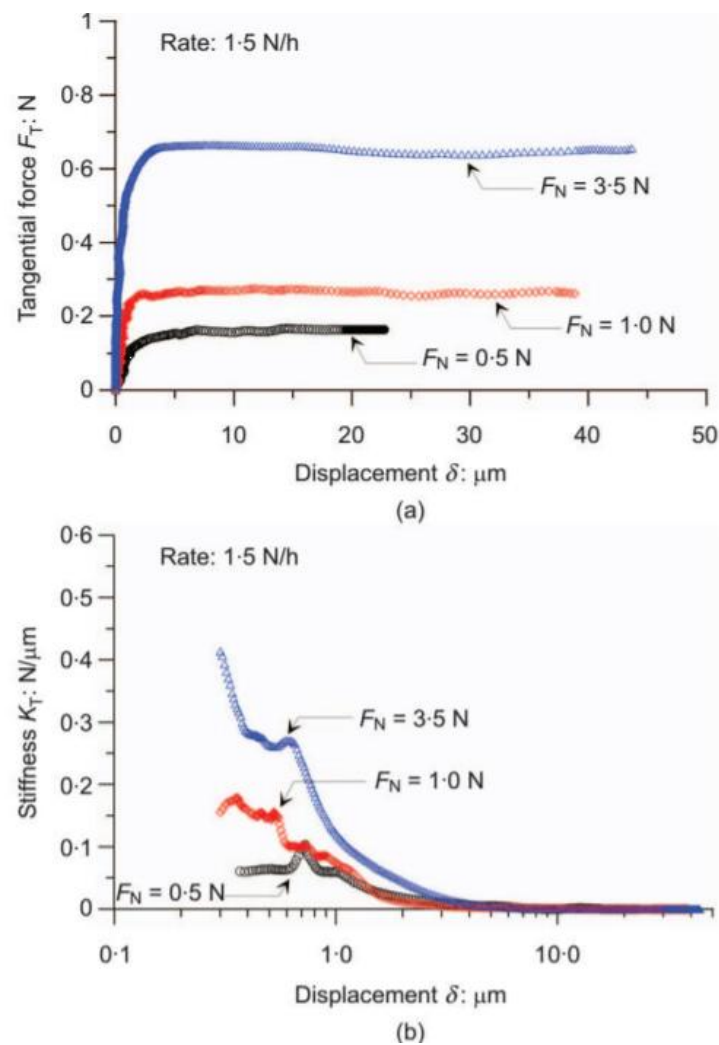
Figure 2.47 A comparison of the effect of tangential load and displacement at the contacts of dry quartz particles under normal load (Senetakis et al., 2013).
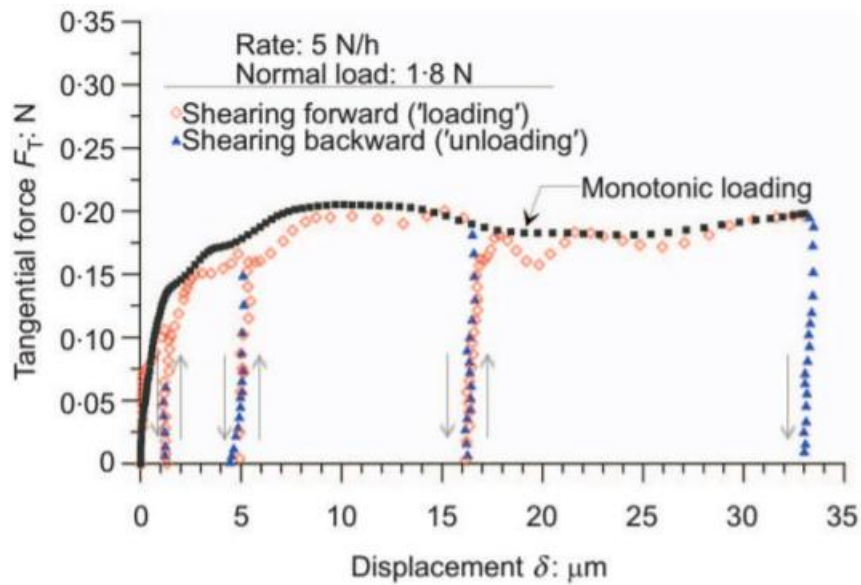
Figure 2.48 Comparing the contact response for dry quartz particles under monotonic loading and shear unloading during a series of shear loading and unloading cycles (Senetakis et al., 2013).
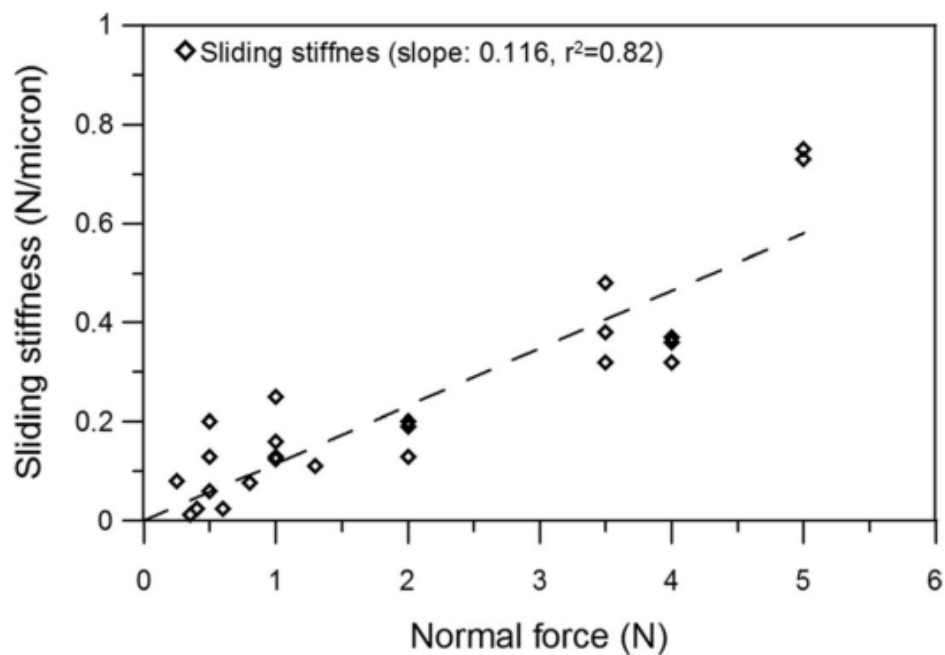
Figure 2.49 Leighton Buzzard sand (LBS) particles have a maximum sliding stiffness against normal forces (Senetakis and Coop, 2015).
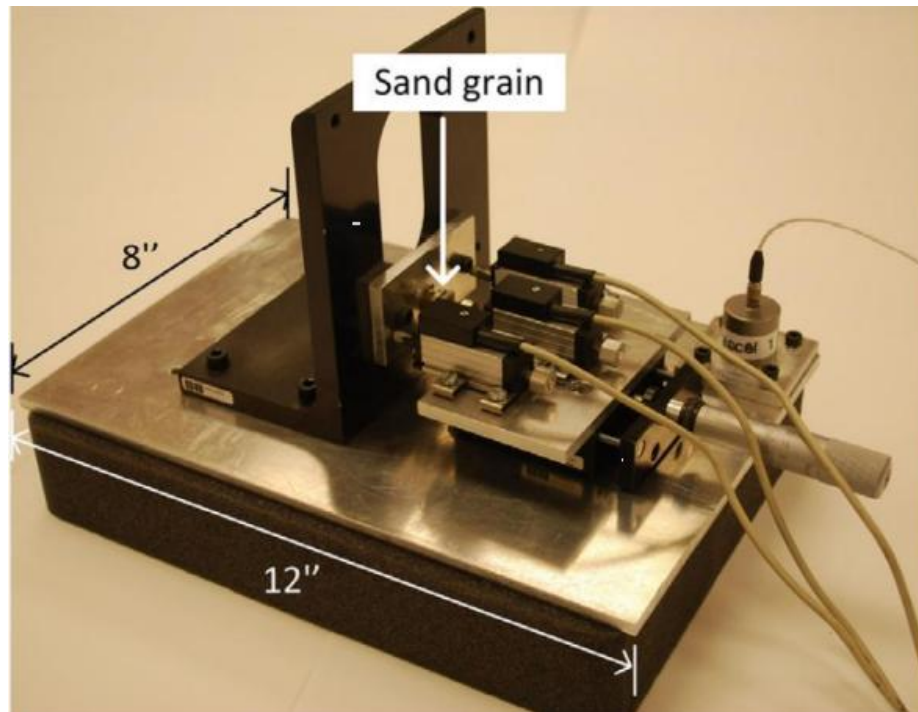
Figure 2.50 The experimental device of Wang & Michalowski (2015).
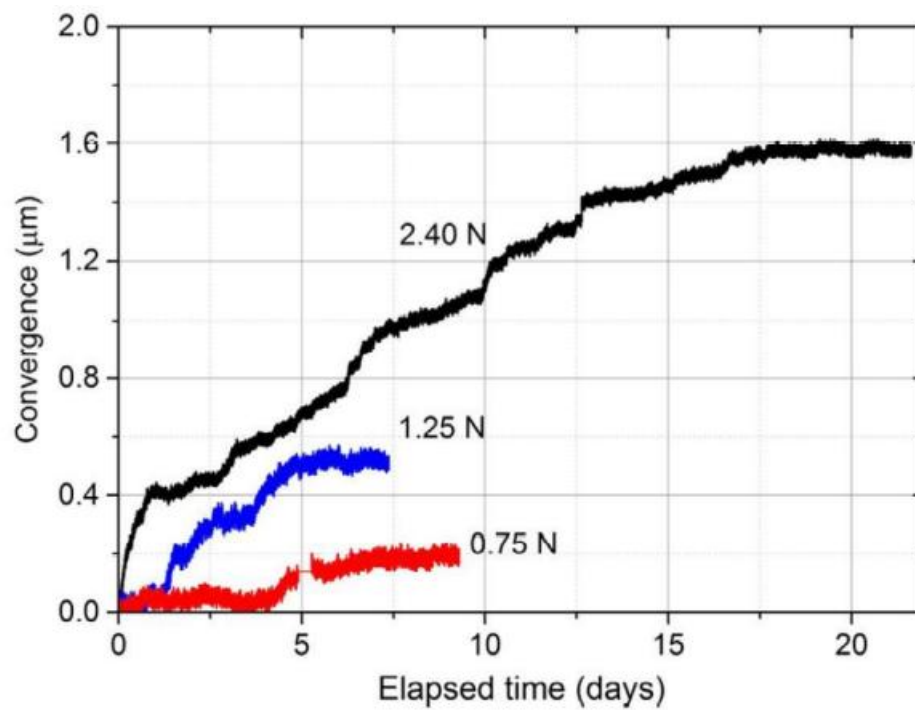
Figure 2.51 Creep test results for Ottawa sand based on displacement (convergence) (Wang and Michalowski, 2015).
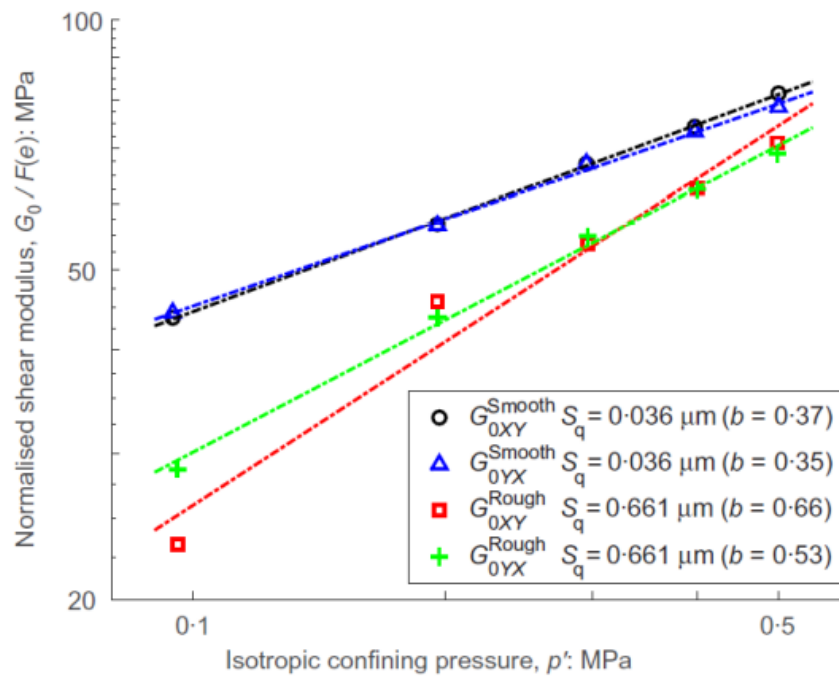
Figure 2.52 Measurements of shear wave velocity for smooth and rough ballotini samples showing pressure dependence of the shear stiffness during isotropic loading (Otsubo et al., 2015).
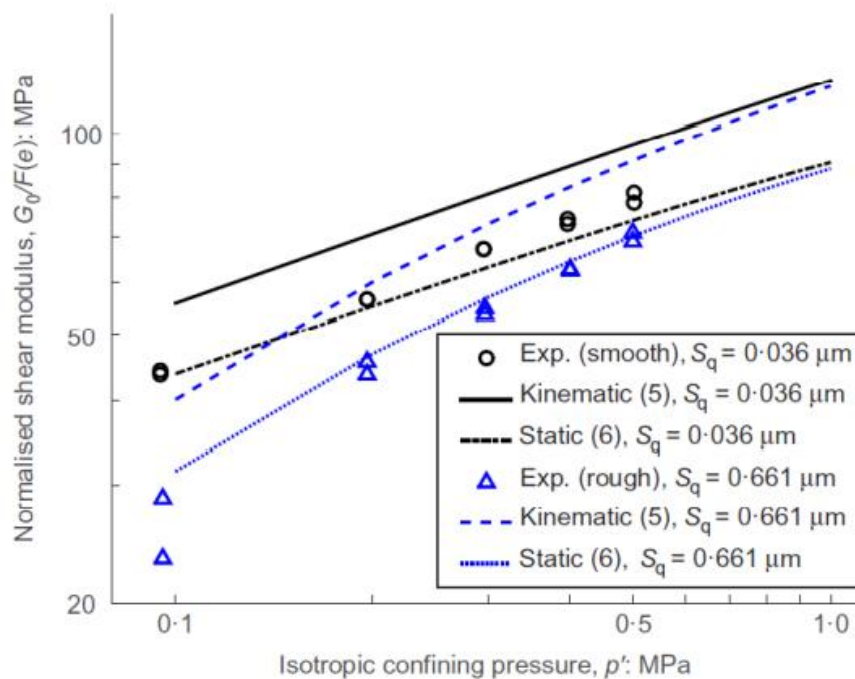
Figure 2.53 Analysis of the difference between analytically predicted and experimentally measured shear moduli under isotropic confining pressures (Otsubo et al., 2015).
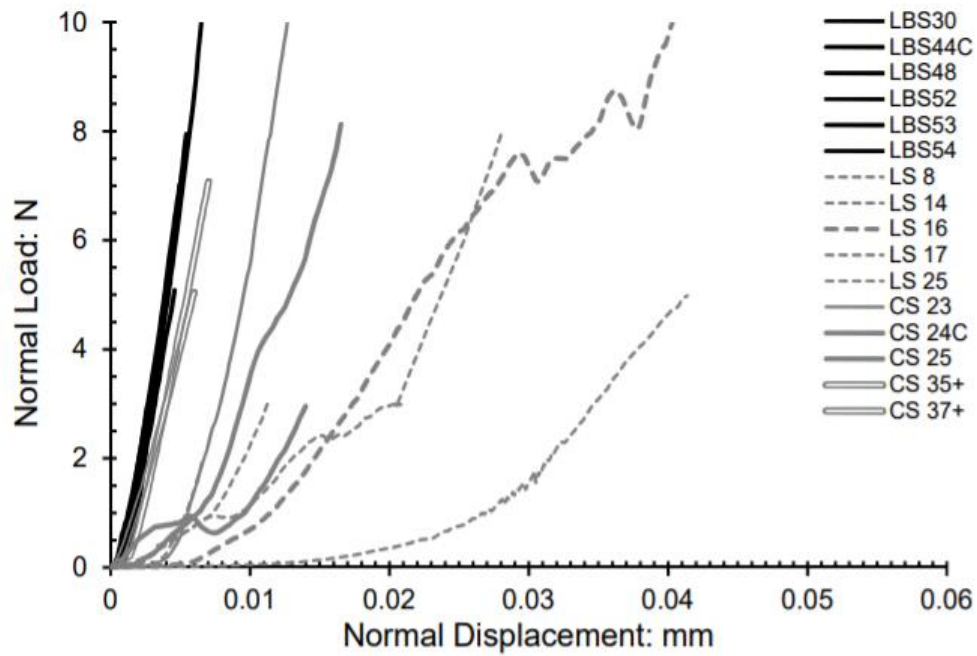
Figure 2.54 Results of normal loading tests for limestone (LS), carbonate sand (CS), and Leighton Buzzard quartz sand (LBS) (Nardelli and Coop, 2018).
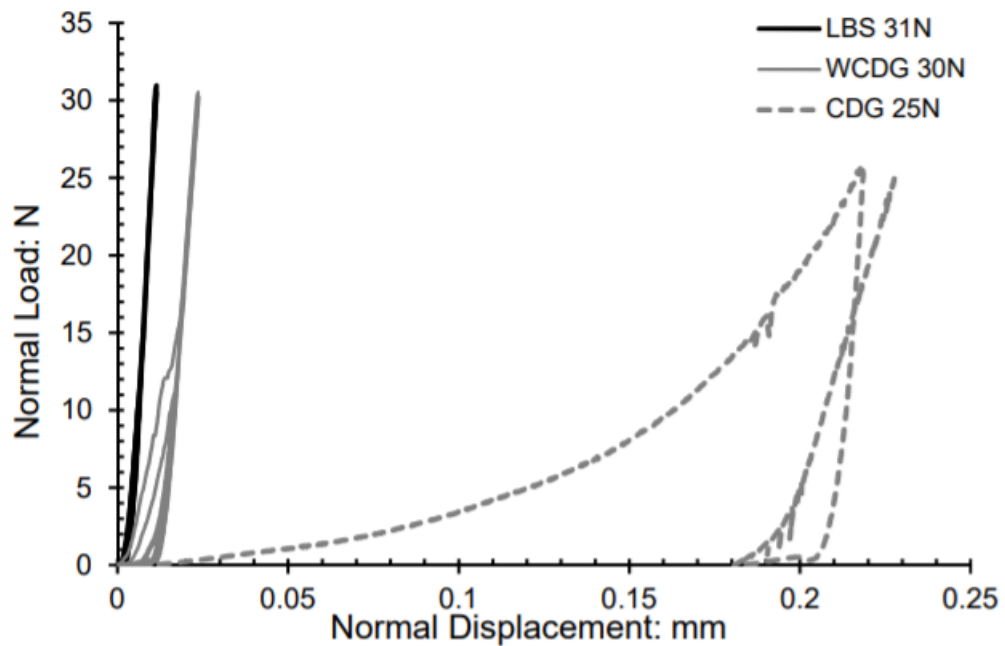
Figure 2.55 Results of cyclic normal loading test on the Leighton Buzzard sand (LBS), completely decomposed granite (CDG), and washed completely decomposed granite (WCDG) by Nardelli and Coop (2018).
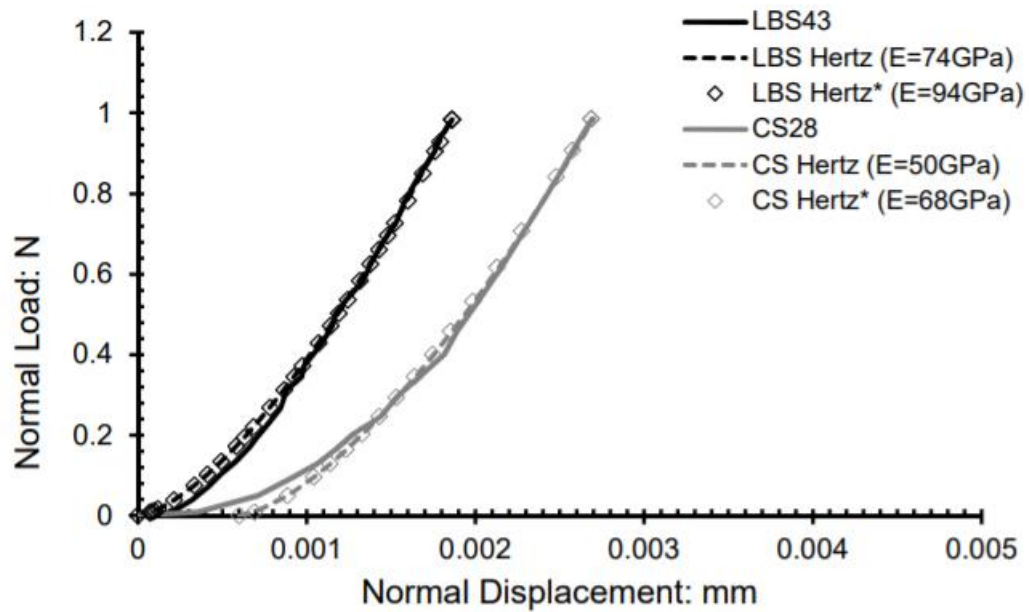
Figure 2.56 Experimental and theoretical comparisons of Leighton Buzzard sand (LBS) and carbonate sand normal loading test data up to 1N based on the original Hertz theory and including surface roughness (Hertz*) (Nardelli and Coop, 2018).
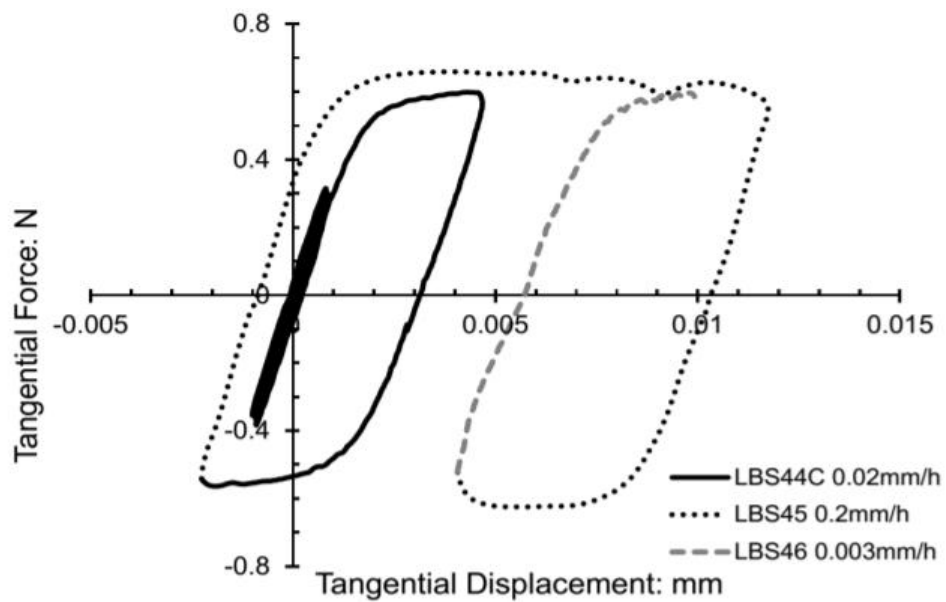
Figure 2.57 Analysis of the tangential loading tests performed on Leighton Buzzard sand (LBS) particles under a constant normal load of 3N (Nardelli and Coop, 2018).
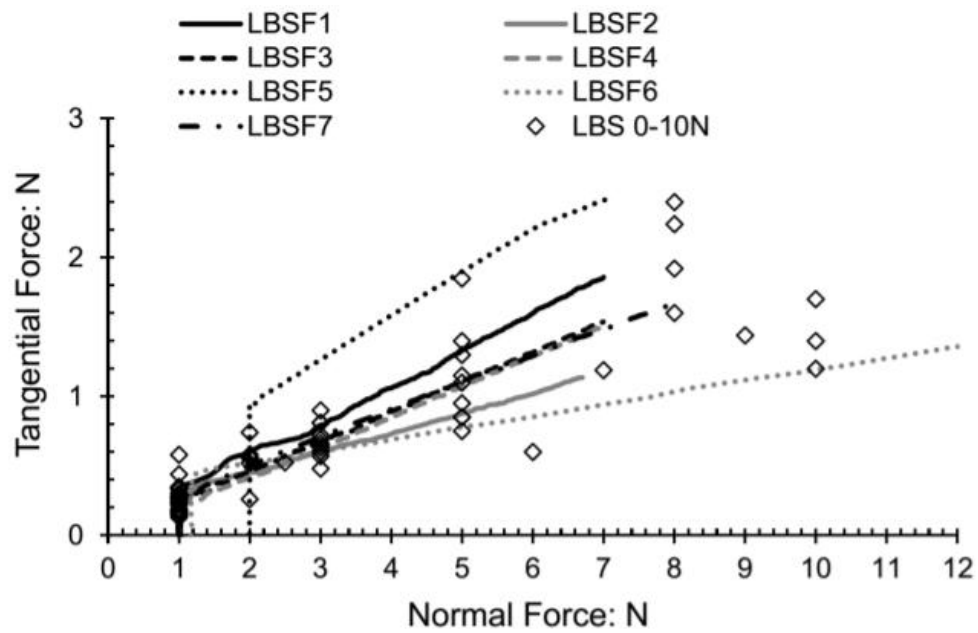
Figure 2.58 Summary of the friction and tangential loading for LBS particles
(Nardelli and Coop, 2018).
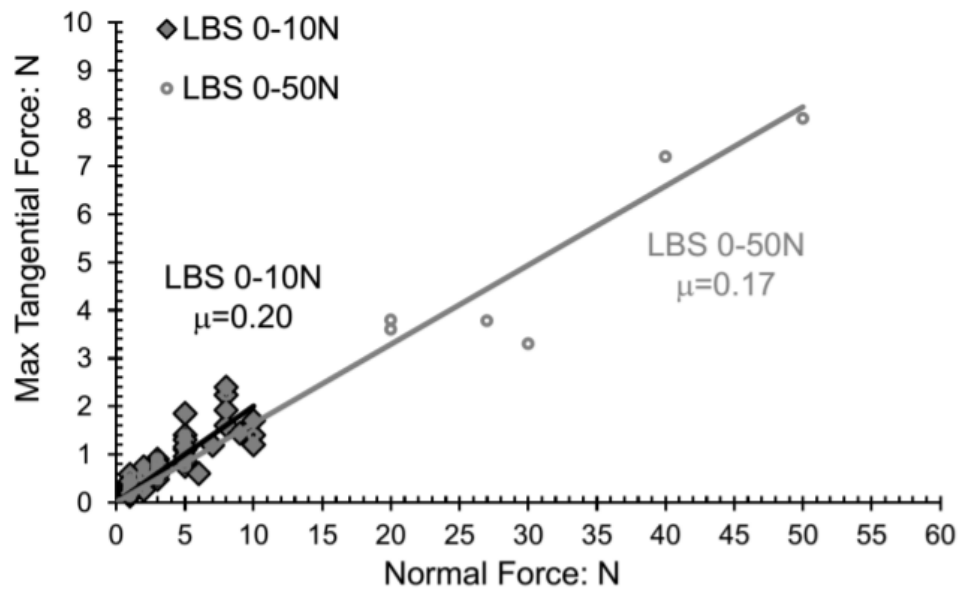
Figure 2.59 An envelope of failure for LBS particles for different normal loads
(Nardelli and Coop, 2018)
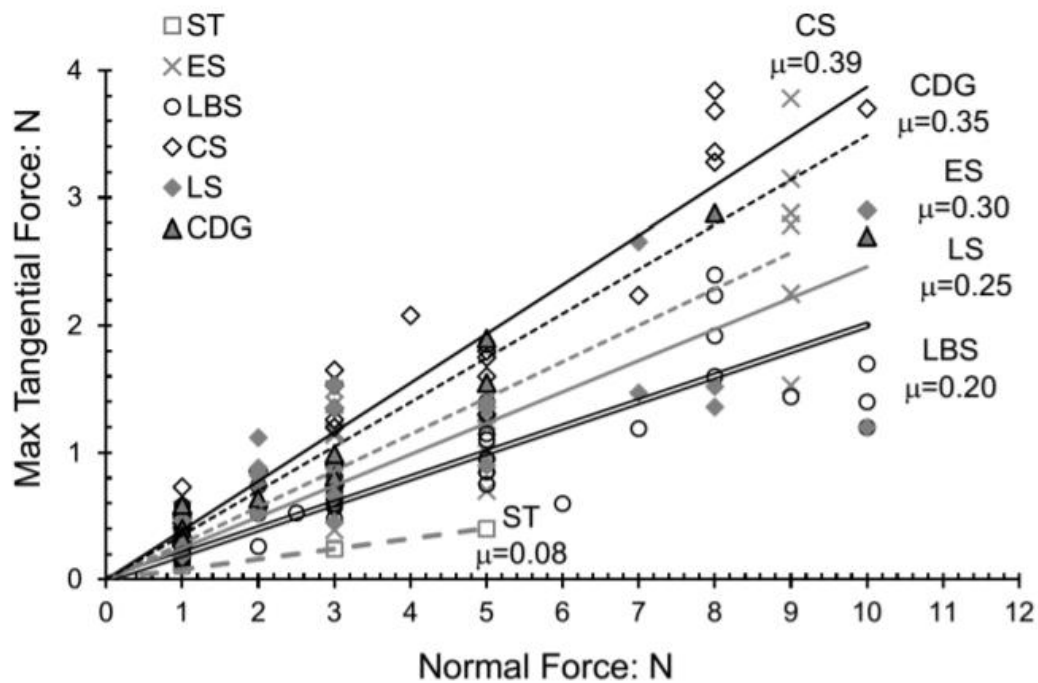
Figure 2.60 Data summary for chrome steel balls (ST), Eglin sand (ES, data from Nardelli et al., 2017), limestone, sand carbonate, crushed limestone, and completely decomposed granite (Nardelli and Coop, 2018).
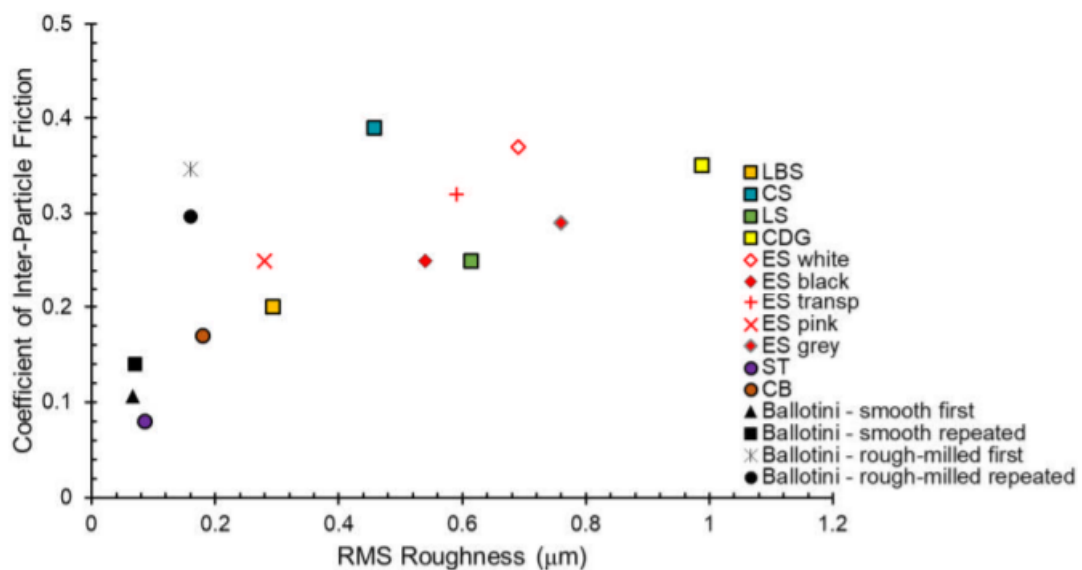
Figure 2.61 The effect of the average roughness of different materials on the friction coefficients of (CS) carbonate sand, (LS): crushed limestone, (CDG): completely decomposed granite, (ES): Eglin sand, (ST): chrome steel balls, (CB): ceramic balls from Nardelli and Coop (2018); results of ballotini from Cavarretta et al. (2010).
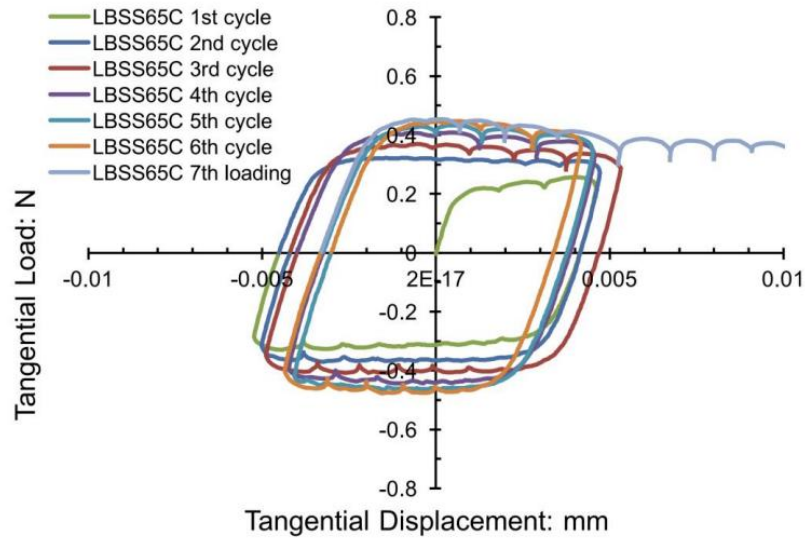
Figure 2.62 Results of the cyclic tangential loading test carried out on LBS under 1N constant normal load with different cycles (Nardelli, 2017).
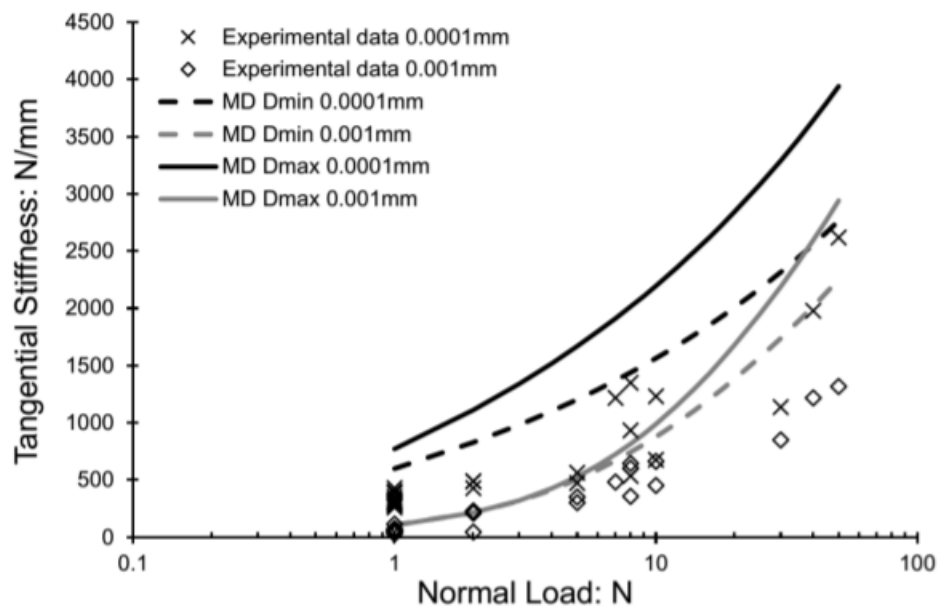
Figure 2.63 Stiffness of LBS calculated using Mindlin & Deresiewicz's equation (1953) for small and large particles (Dmin = 1.18mm; Dmax = 3.5mm) (after Nardelli and Coop, 2018).
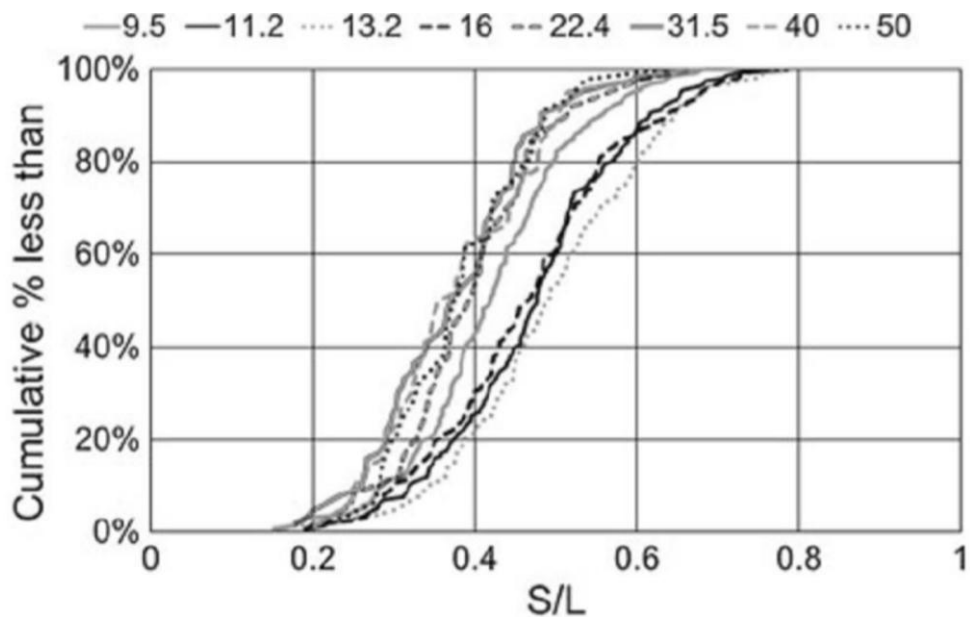
Figure 2.64 Example of the cumulative distribution curves for the S/L ratio in each sieve interval for ballast (Le Pen et al., 2013).
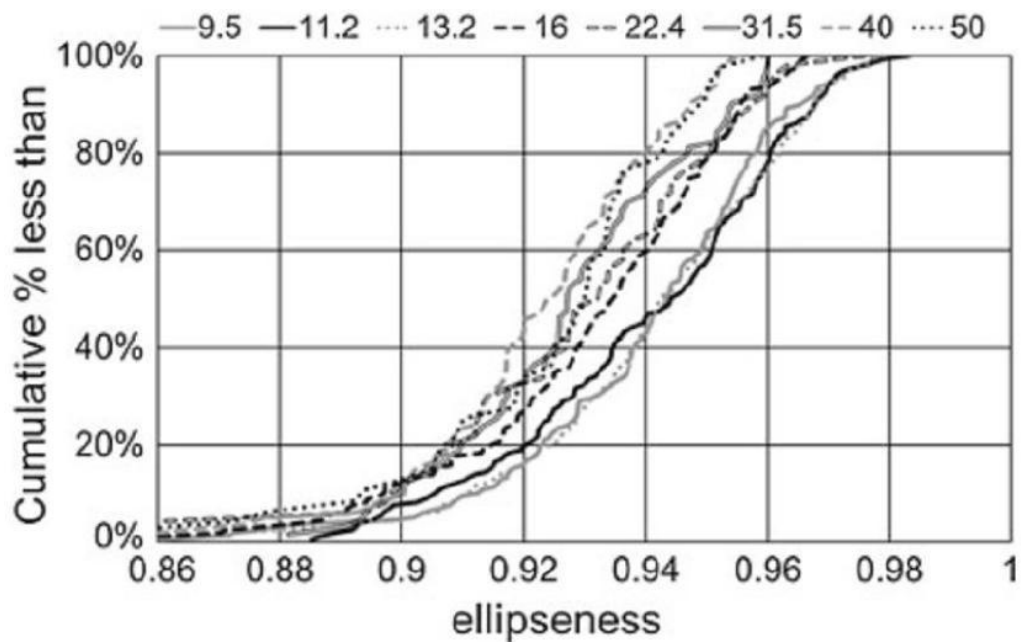
Figure 2.65 Example of the cumulative distribution curves for Ellipseness in each sieve interval for ballast (Le Pen et al., 2013).
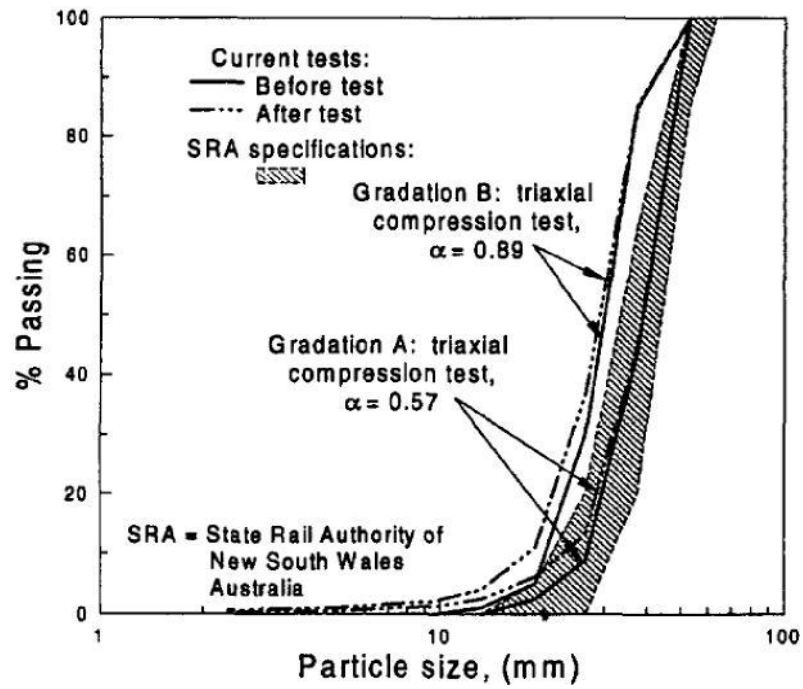
Figure 2.66 Particle size distribution of Latite basalt ballast before and after testing (Indraratna et al., 1998).
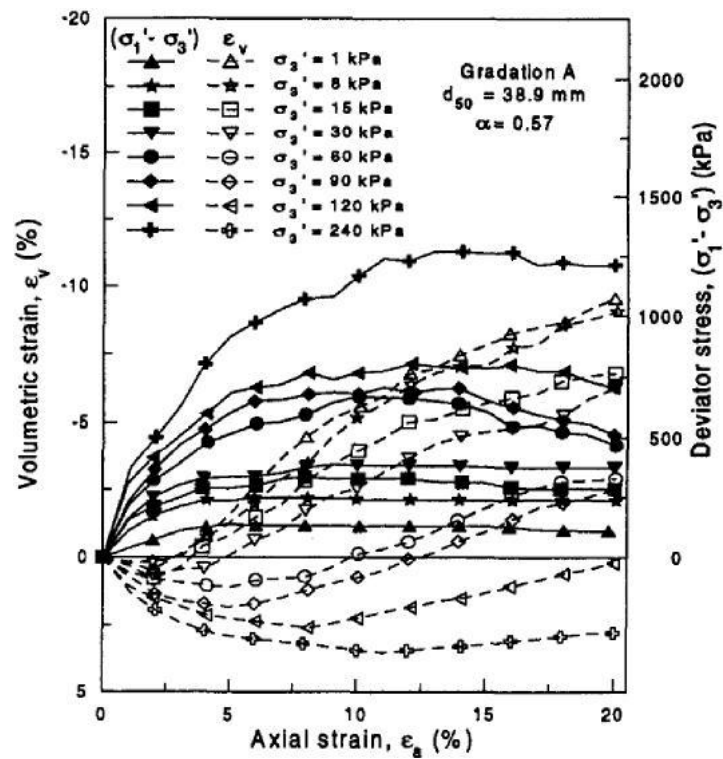
Figure 2.67 Example of a typical stress-strain behaviour of drained triaxial tests at different confining pressures on Latite basalt ballast (Indraratna et al., 1998).
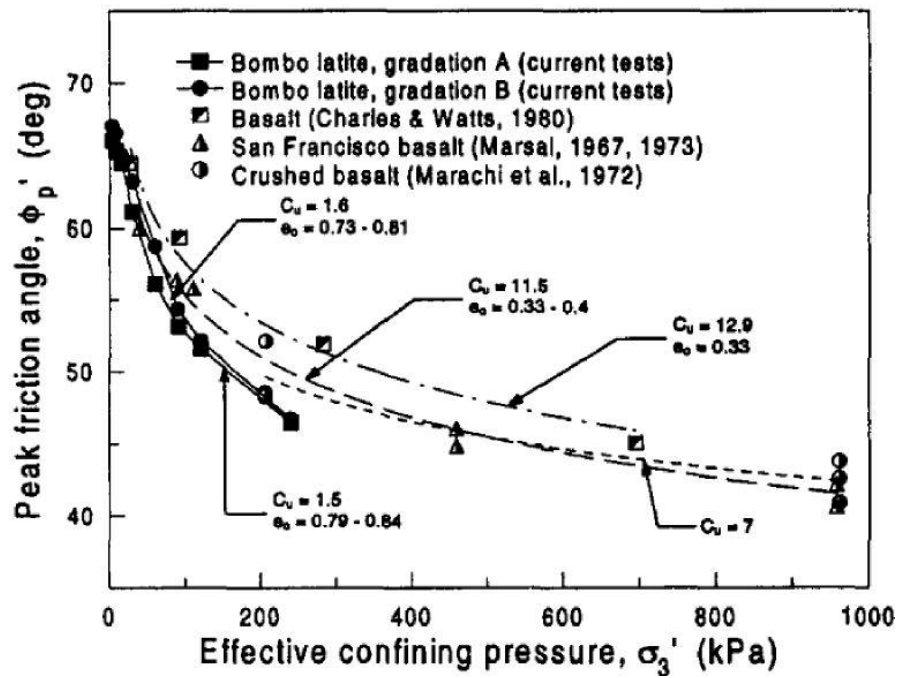
Figure 2.68 Peak envelopes of basalt of different shape descriptors (Indraratna et al., 1998).
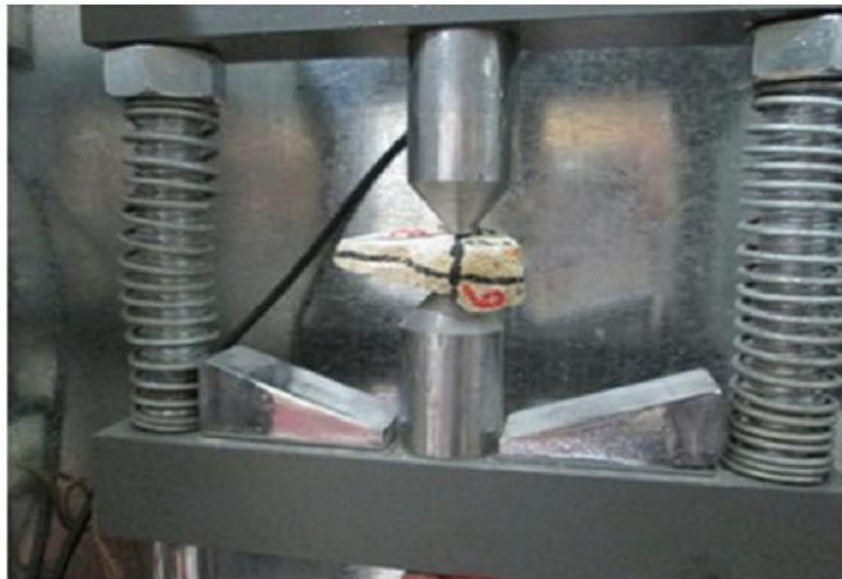
Figure 2.69 Set up of single particle point load test of Koohmishi and Palassi (2016).

Ballast	b
A	-0.41
B	-0.42
C	-0.40
D	-0.56
E	-0.69
F	-0.40
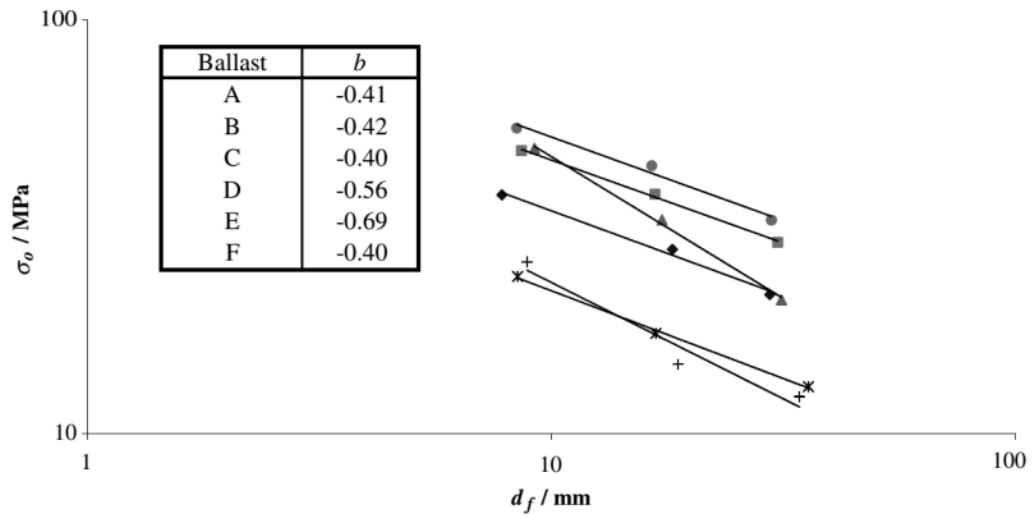
Figure 2.70 Effect of average particle sizes on 37% tensile strength of the particles (Lim et al., 2004).

(a) Hexahedron (H)   **(b)** Pentahedron (P)   **(c)** Tetrahedron (T)
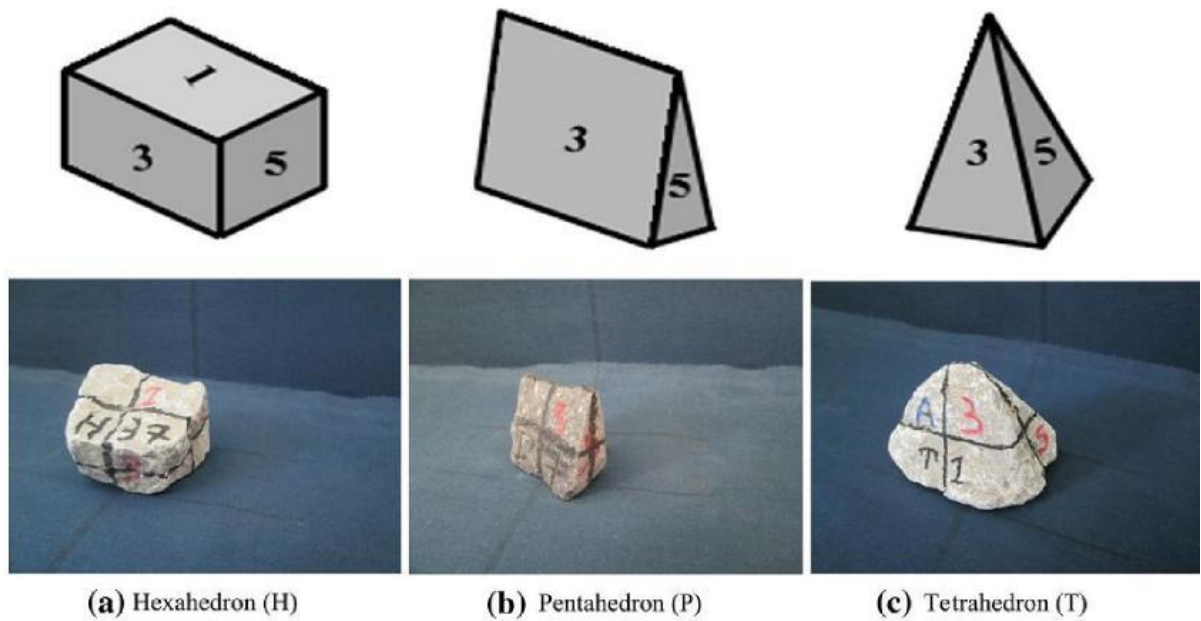
Figure 2.71 Particle shapes of ballast tested by Koohmishi and Palassi (2016).
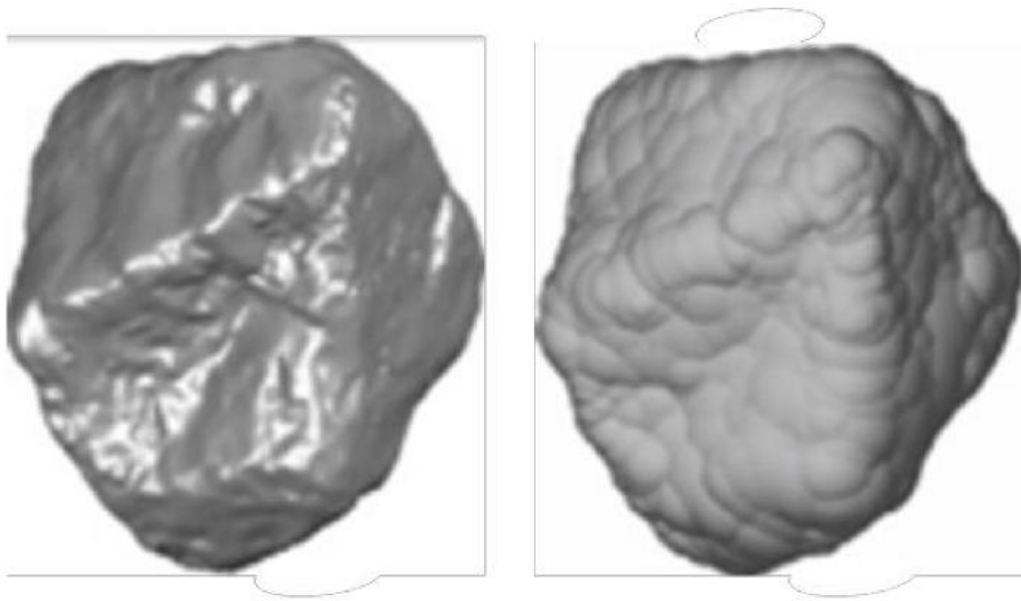
Figure 2.72 Example of modelling a real ballast particle with overlapping spheres
(Ferellec and McDowell, 2010).

Figure 2.72 Example of potential particles and their corresponding real ballast
particles (Ahmed et al., 2016).
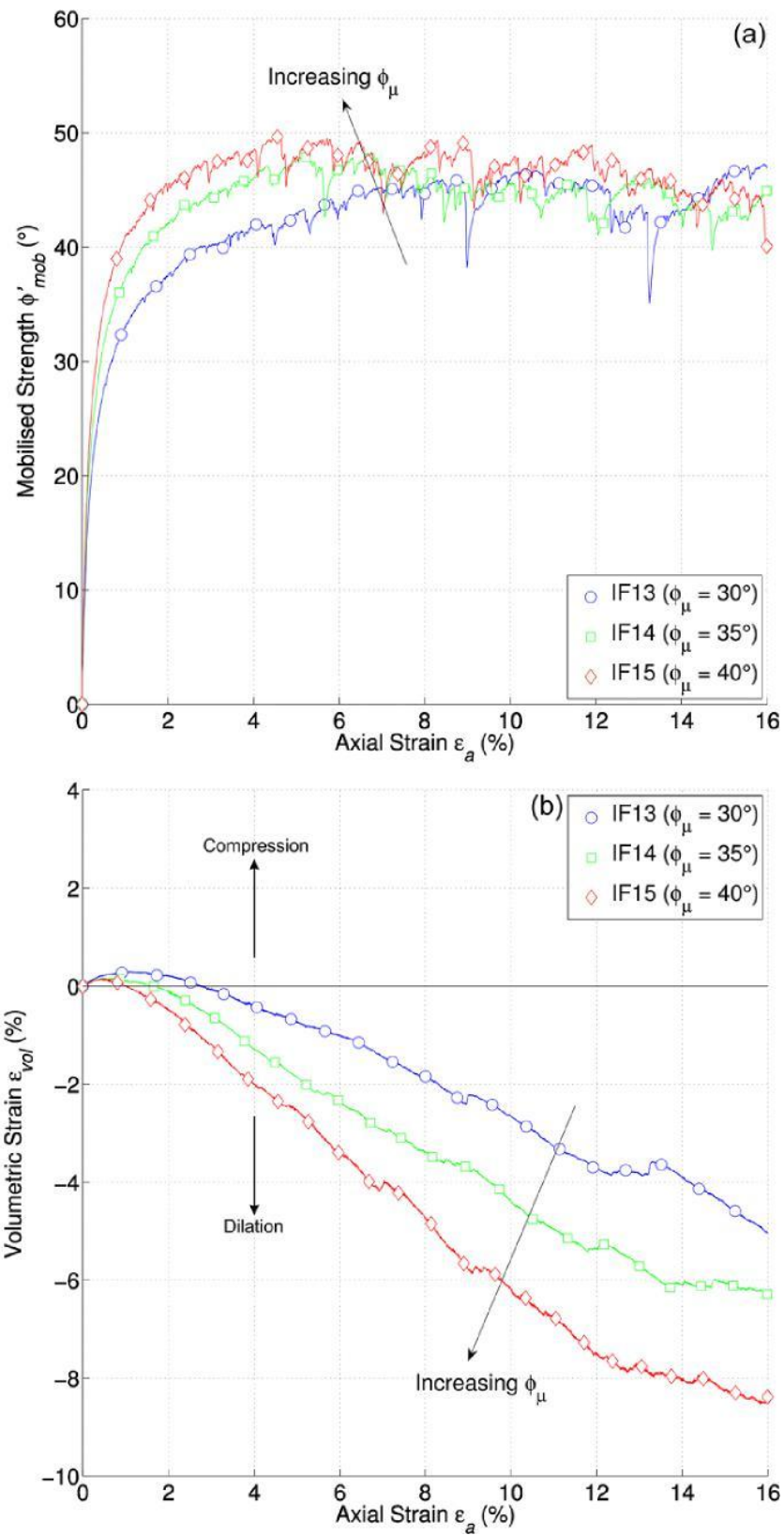
Figure 2.74 Effect of inter-particle friction on mobilised shear strength and volumetric strain (Ahmed et al., 2016).
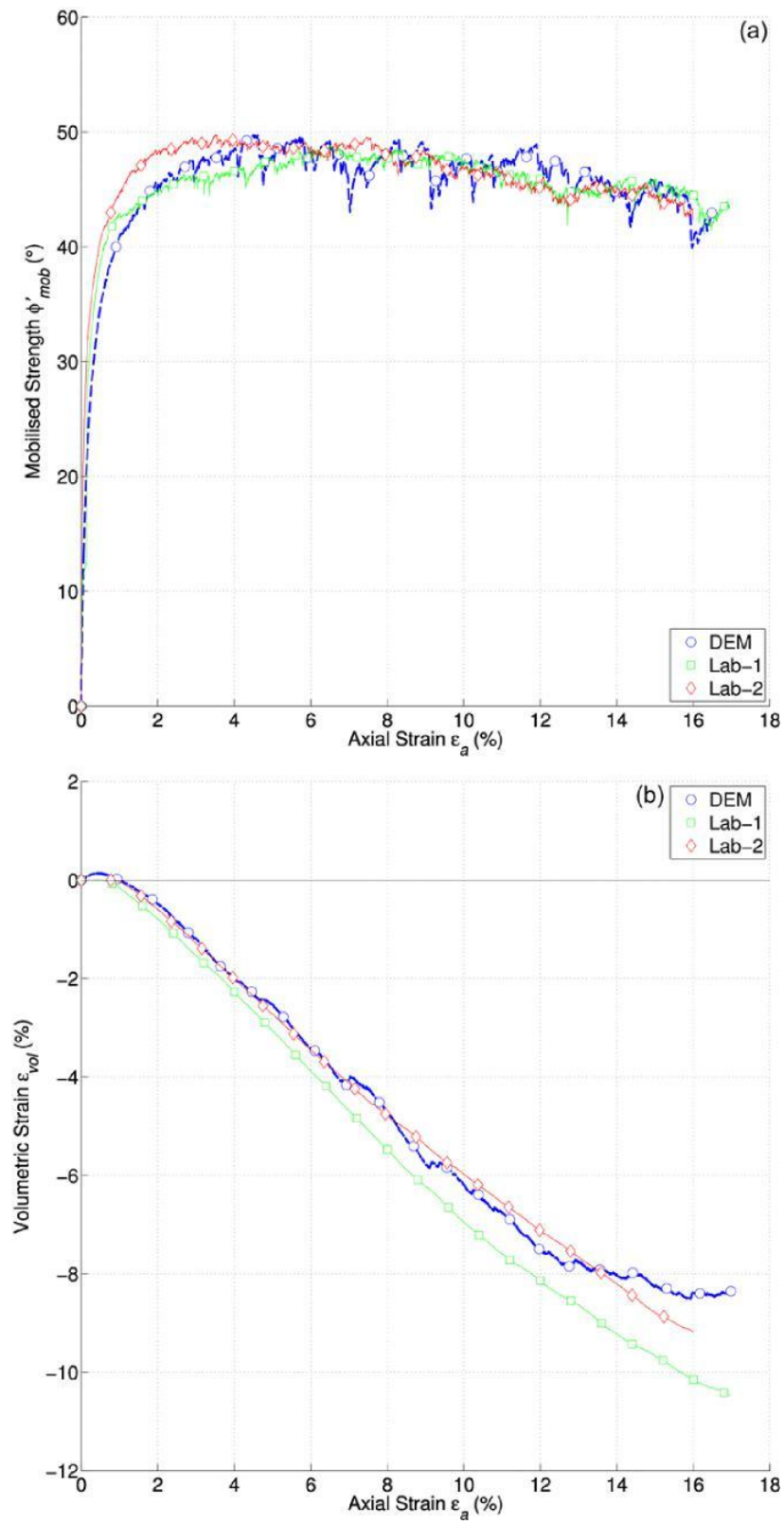
Figure 2.73 Comparison of the DEM analysis with data for actual tests (Ahmed et al., 2016).
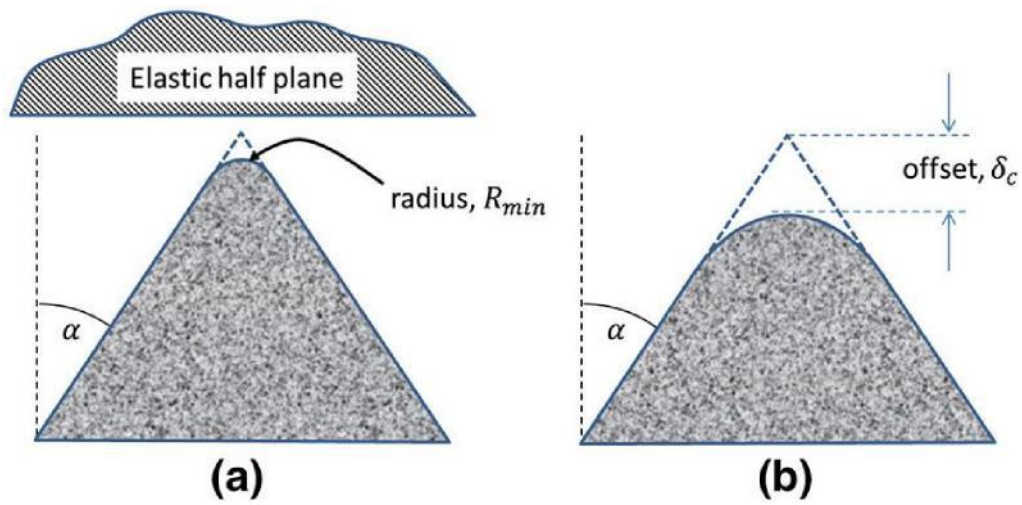
Figure 2.74 Conical damage model (Harkness et al., 2016).
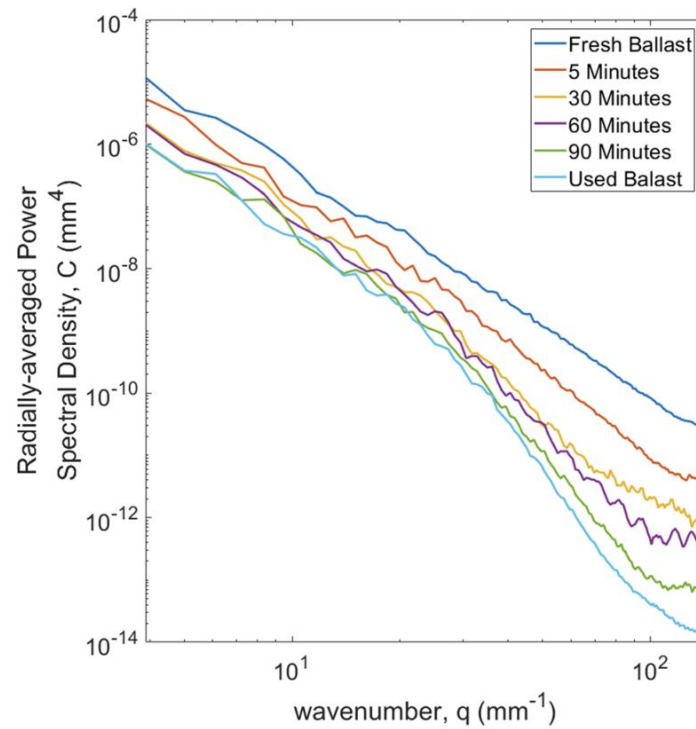
Figure 2.75 Evolution of damage and comparison of roughness for the same location of the same grain for increasing periods of abrasion in the Micro-Deval (Gupta et al., 2023)
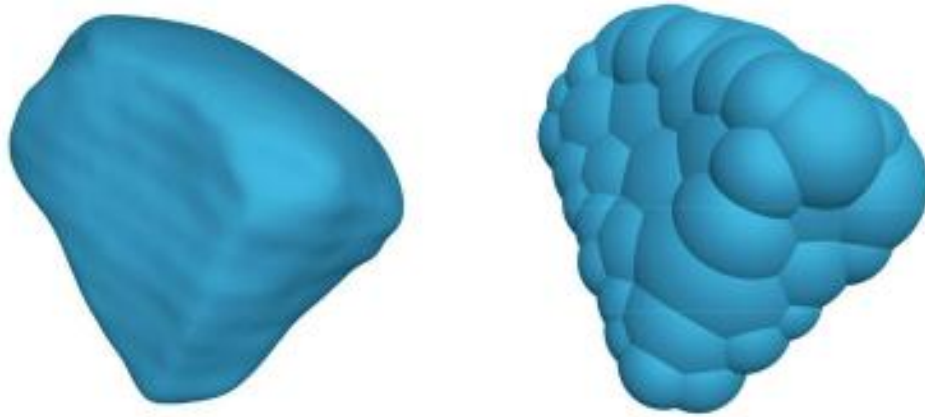
Figure 2.76 Left: a triangular mesh made of 76000 faces from a 3D laser scan of a granite ballast grain. Right: a clump made of 56 spheres, obtained from the mesh on the left (Tolomeo & McDowell, 2022).
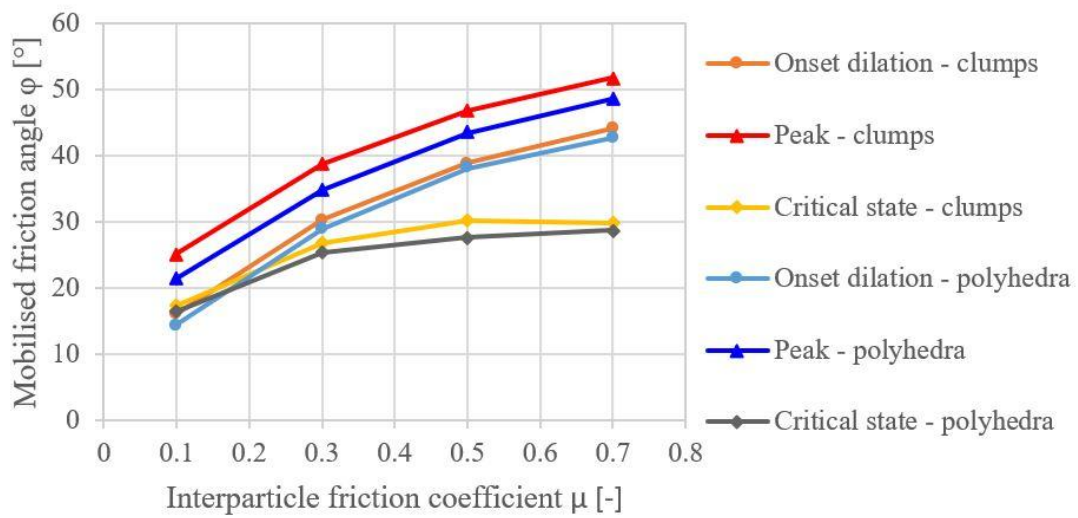
Figure 2.77 Mobilised friction angle φ for clumps and polyhedra at different stages (onset of dilation, peak, critical state) and for different values of interparticle friction coefficient μ (Tolomeo & McDowell, 2022).

(a) purely elastic case: real contact configuration (left) and imagined equivalent sphere-plane contact (right)

(b) damage / plastic yielding: real contact configuration (left) and imagined equivalent sphere-plane contact (right)
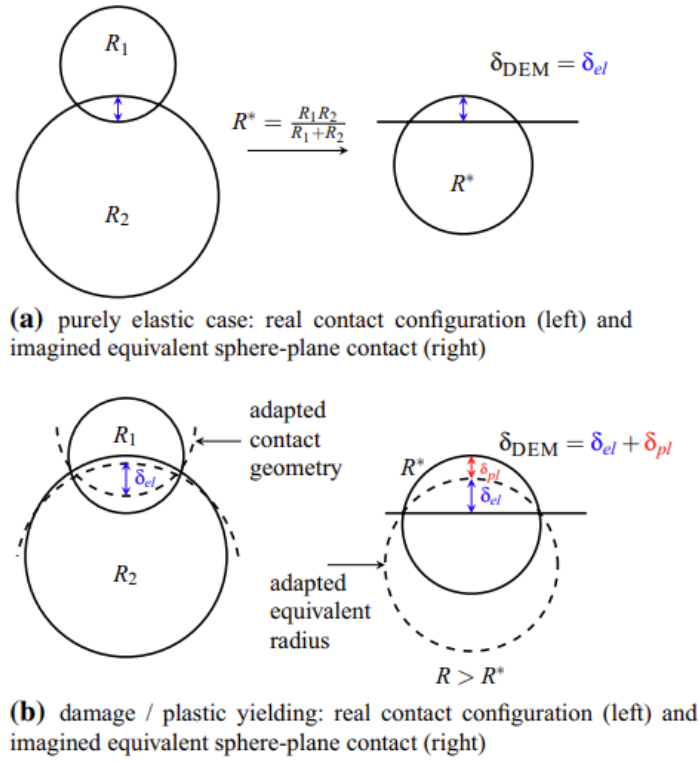
Figure 2.78 Conical damage model for a sphere-sphere contact (Suhr et al. 2022).
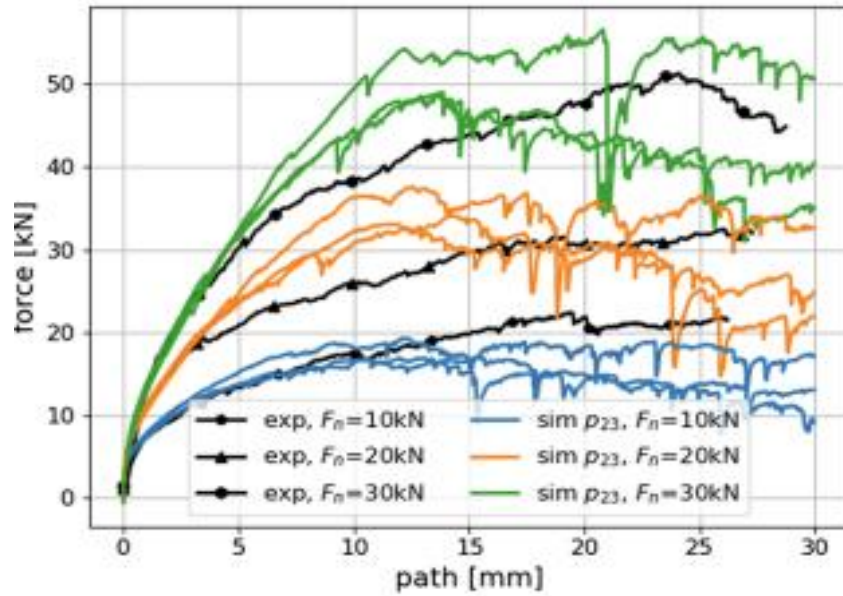
Figure 2.79 Experimental results of shear force path in direct shear test (Suhr et.al, 2020).
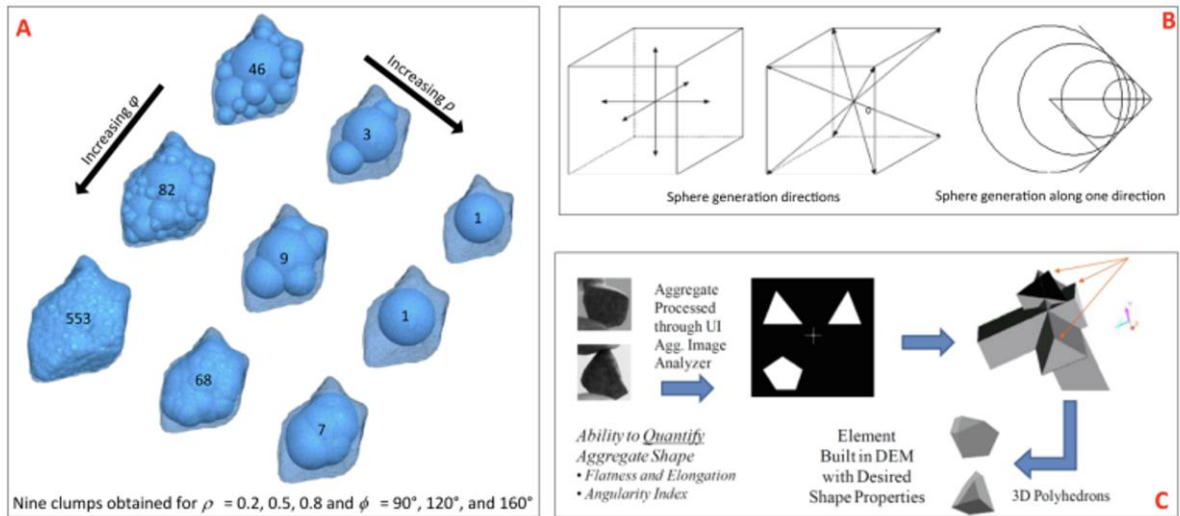
Figure 2.80 (A) clump generation method example; (B) Particle generation method;
(C) Particle shape determination method based on imaging (Guo et al., 2020).
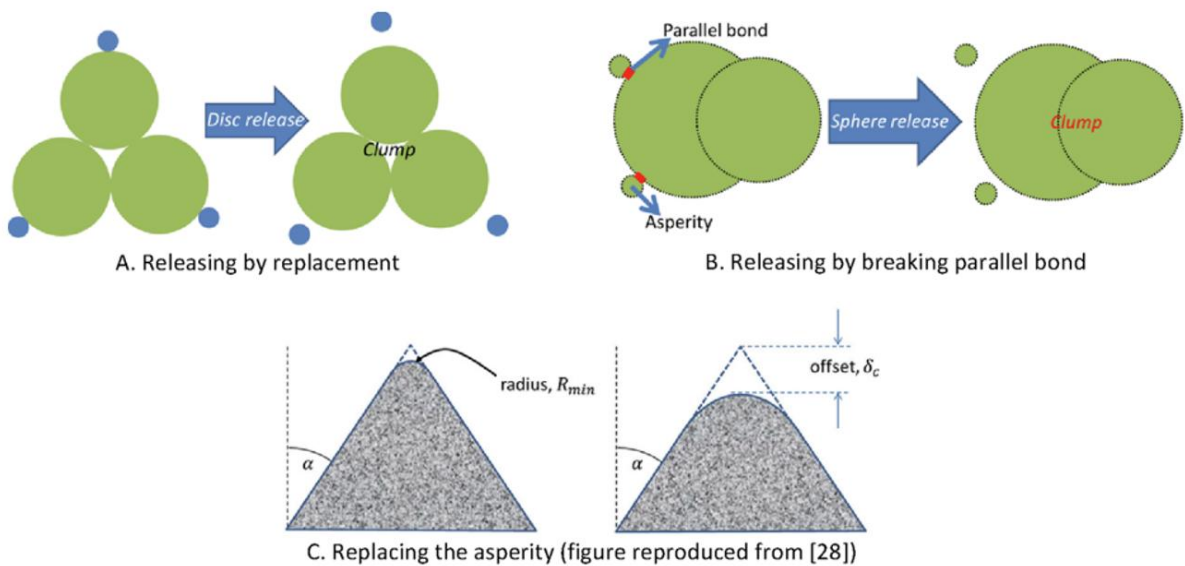
Figure 2.81 Two general means for presenting abrasion (Guo et al., 2020).
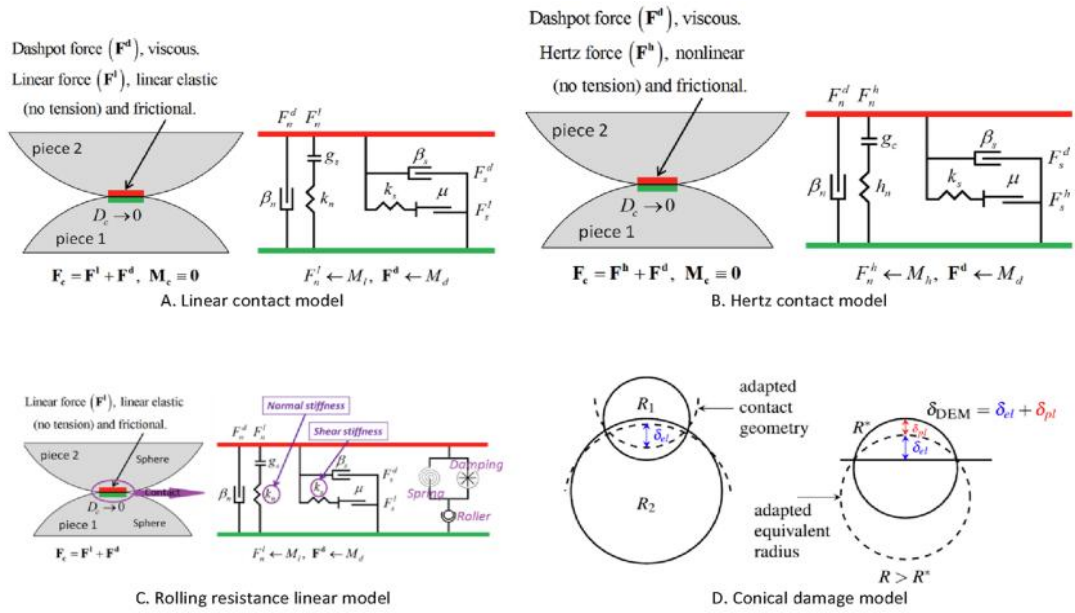
Figure 2.824 Contact models for particle interaction (Guo et al., 2020).
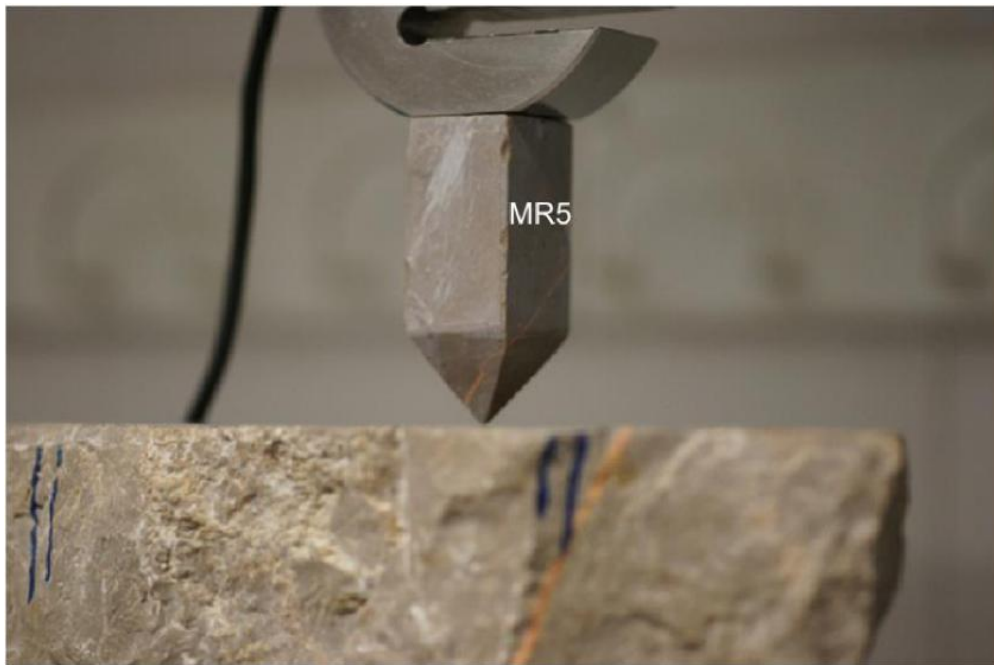
Figure 2.83 Arrangement of contact stiffness tests on limestone sample (Tapias et al., 2015).
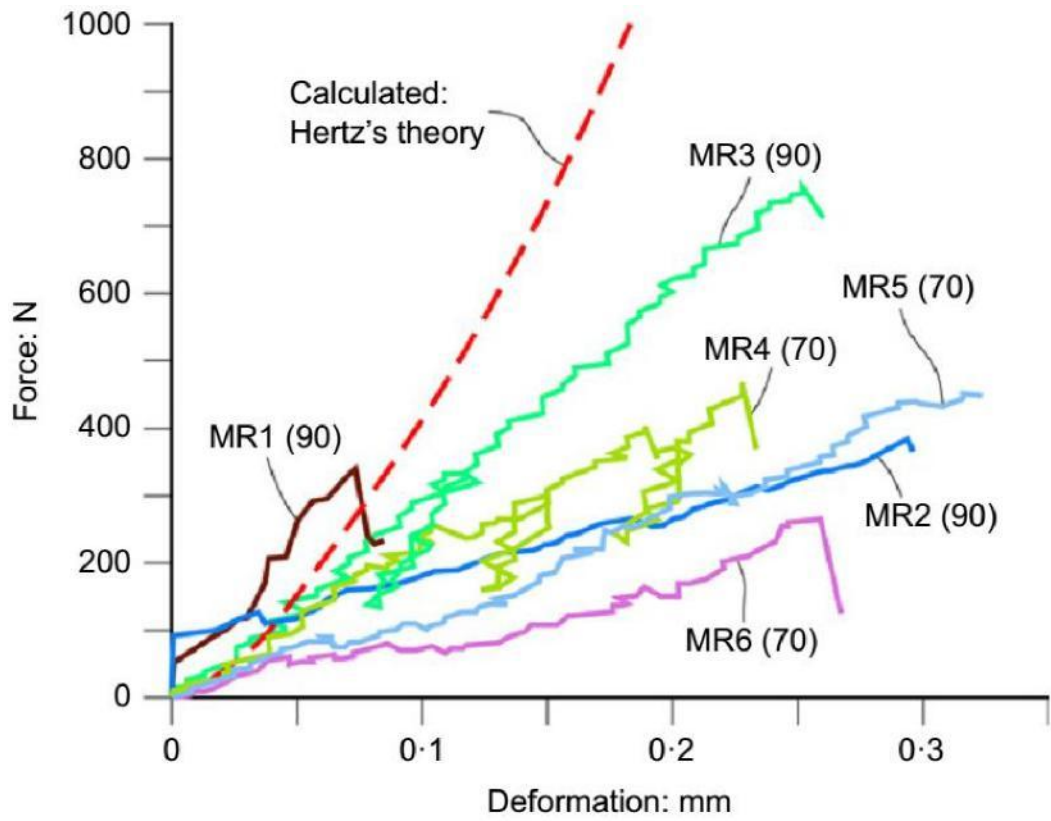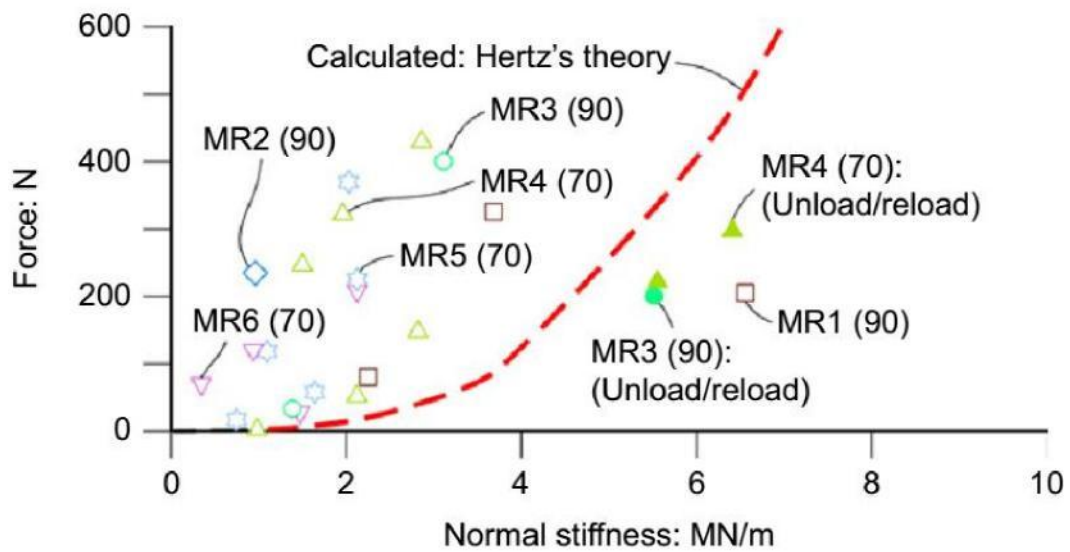
Figure 2.84 Comparison of experimental data for normal loading test data of limestone pyramidal samples to the theoretical curve obtained from the original Hertz theory (Tapias et al., 2015).
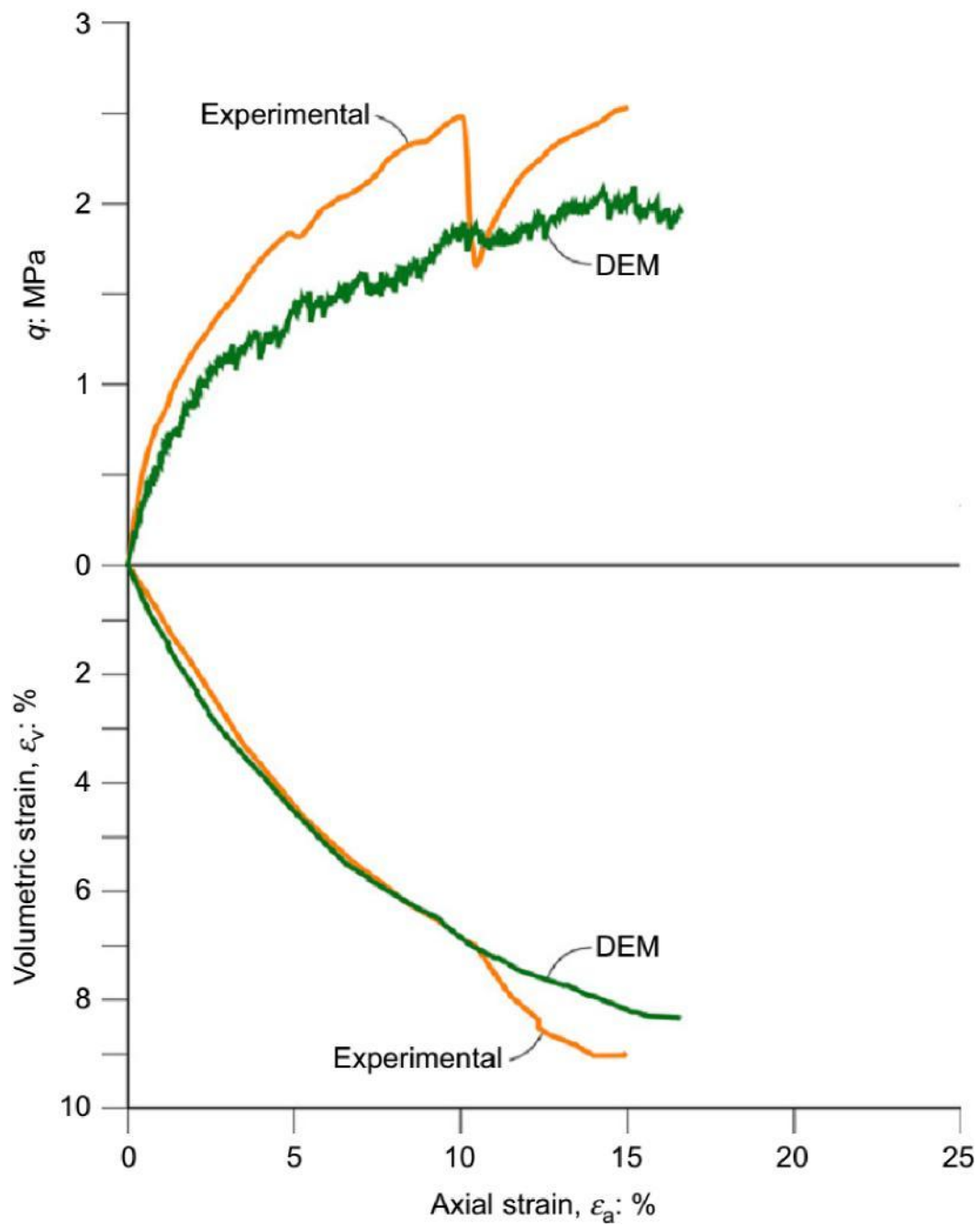
Figure 2.85 Comparison of the DEM analysis using measured input parameters with experimental tests data from Ortega (2008) (Tapias et al., 2015).
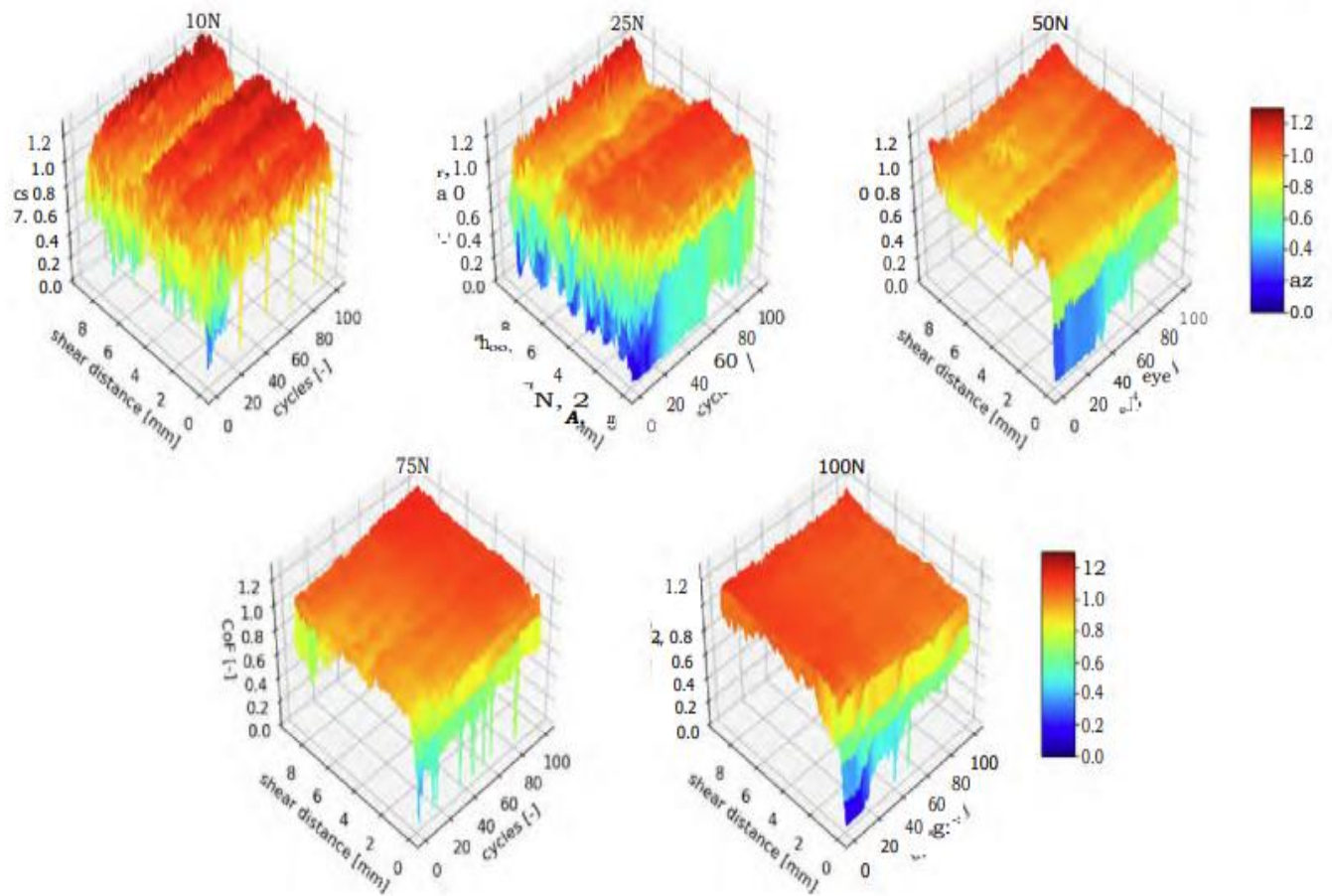
Figure 2.86 Coefficient of friction dependent on number of cycles and shear distance. Results are shown for Calcite test for all vertical loads (Suhr et.al, 2020)
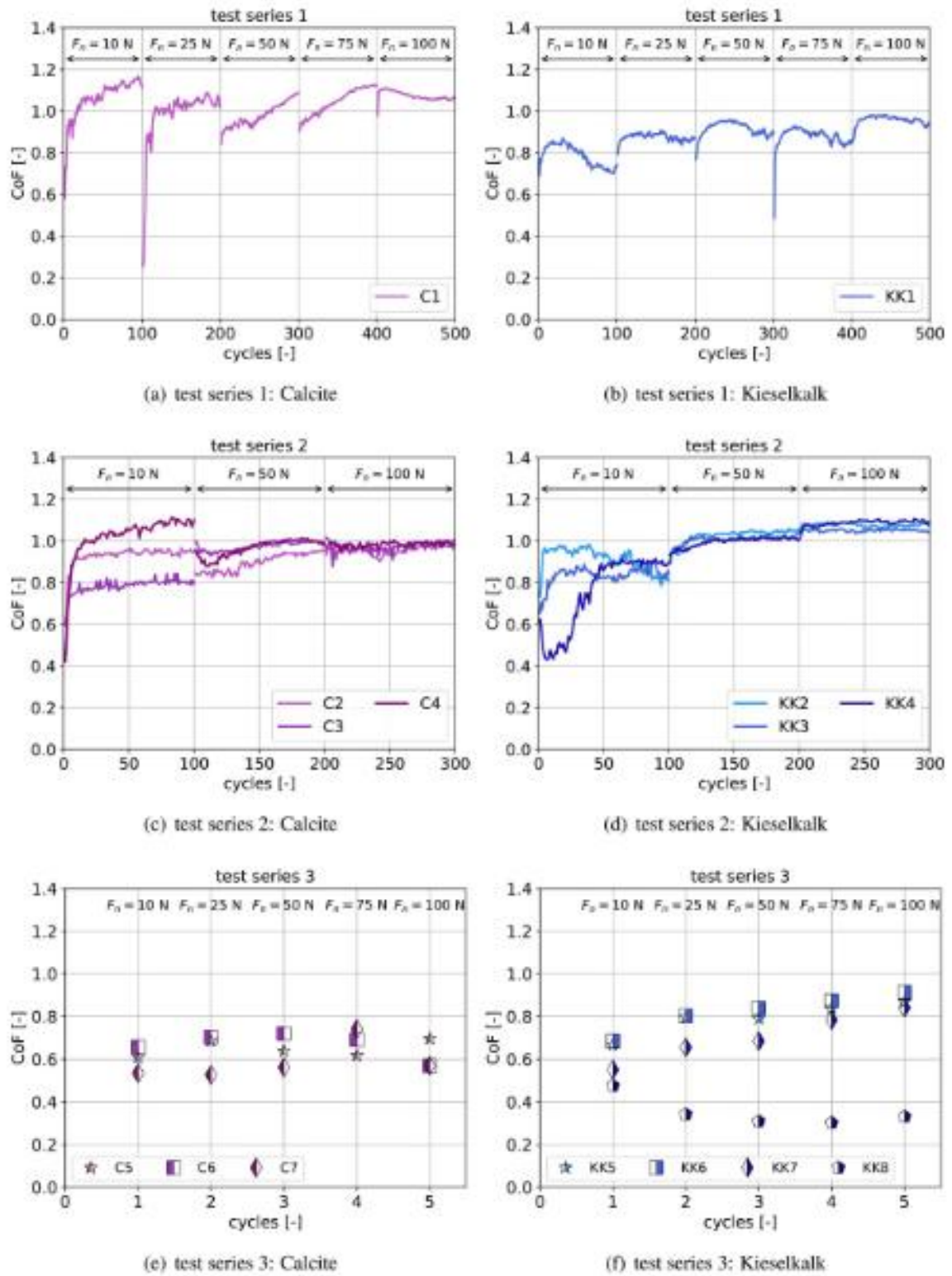
Figure 2.87 Coefficient of friction plotted over cycles for both Calcite and Kieselkalk for test series 1, 2 and 3 (Suhr et.al, 2020)
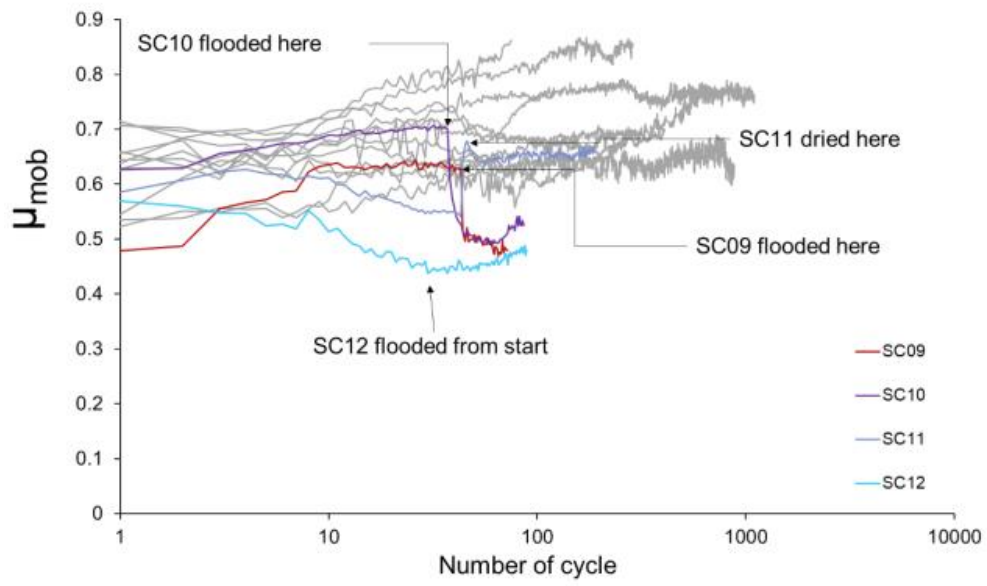
Figure 2.88 Change of the mobilised inter-particle friction (μmob) for flooded tests (Wong, 2022).
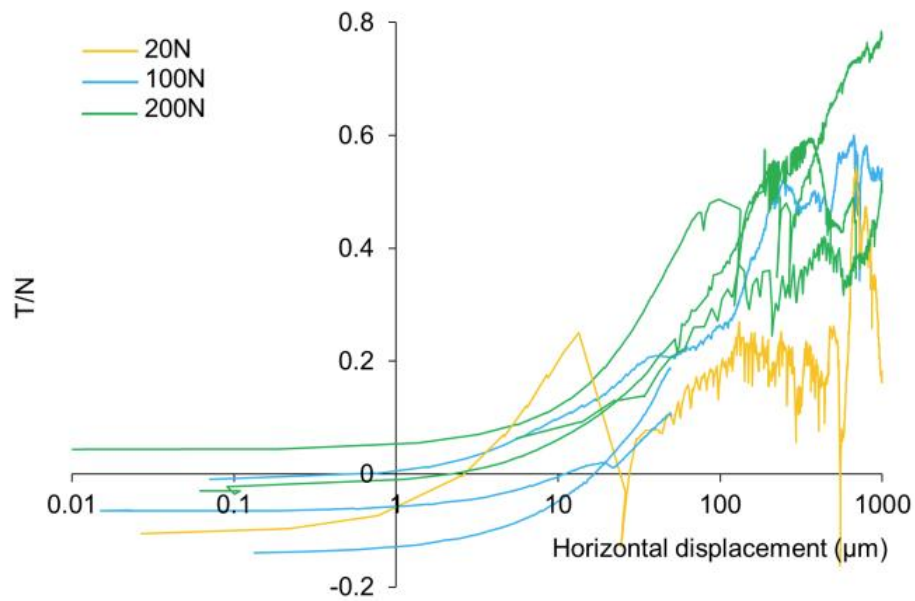
(a)
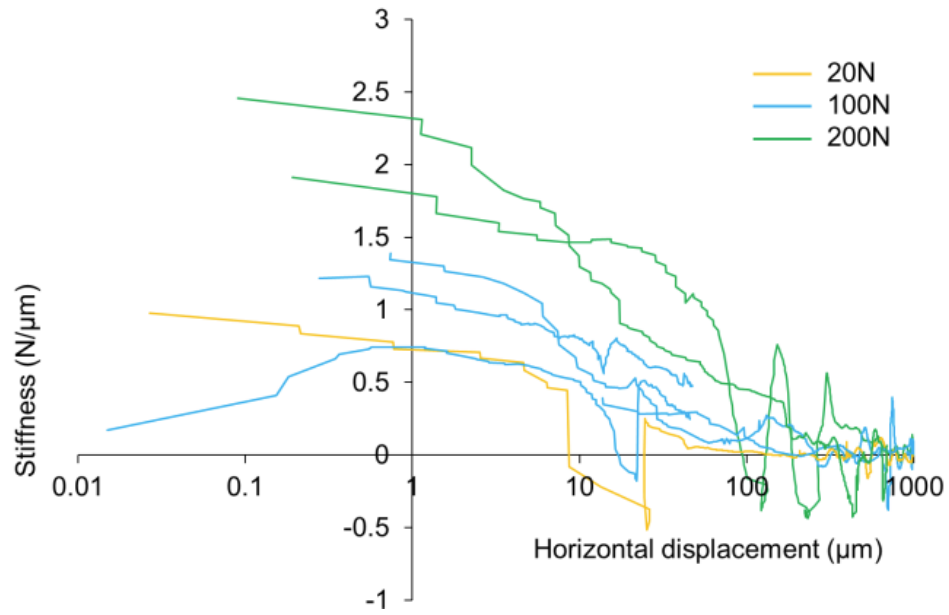
Figure 2.89 Change of T/N values for the monotonic shearing and tangential stiffnesses for different normal load levels (Wong, 2022).
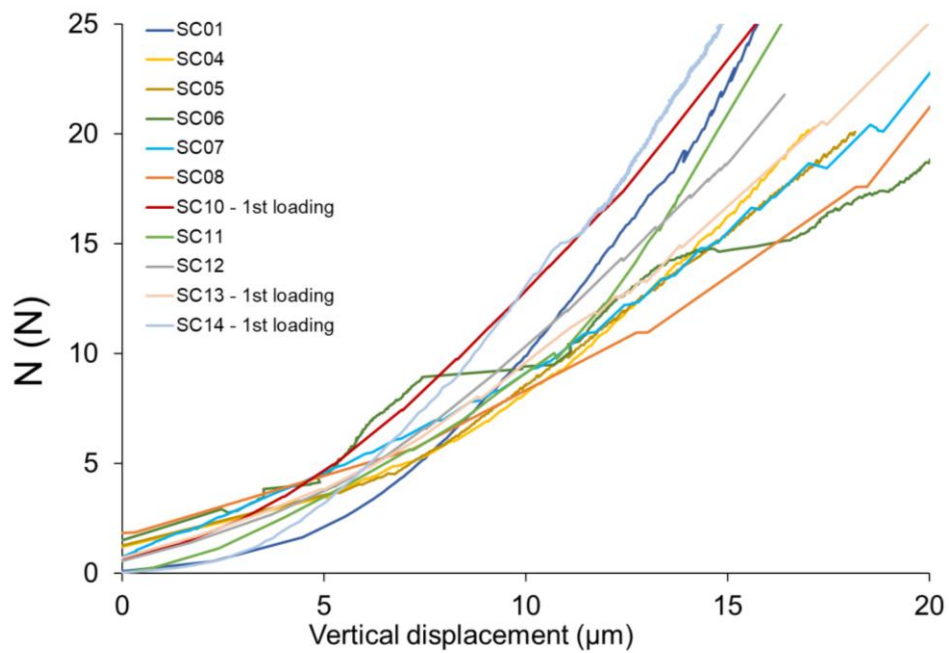
Figure 2.90 Normal load-deformation responses at small displacements (Wong, 2022).
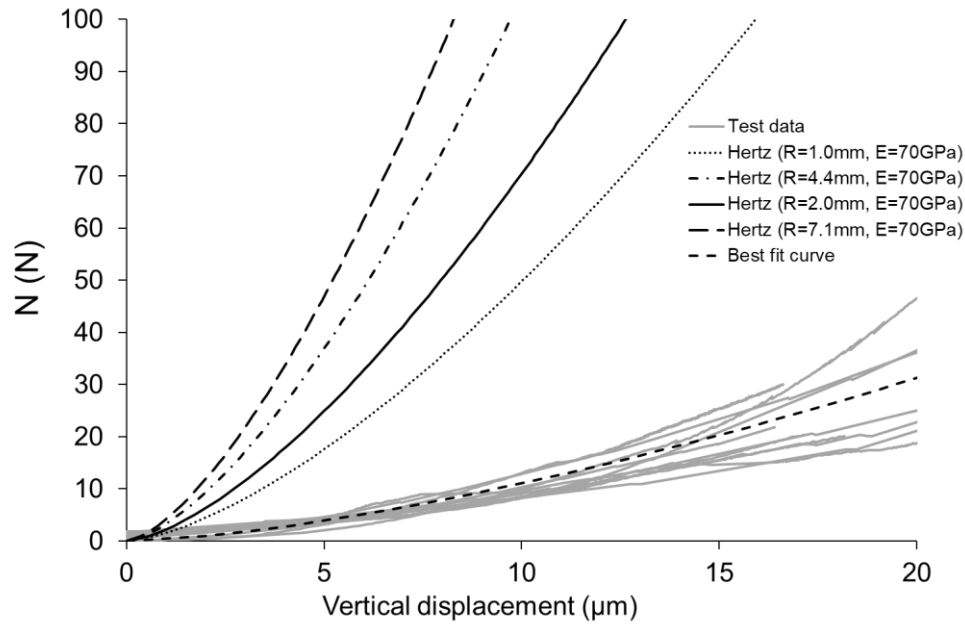
(a)
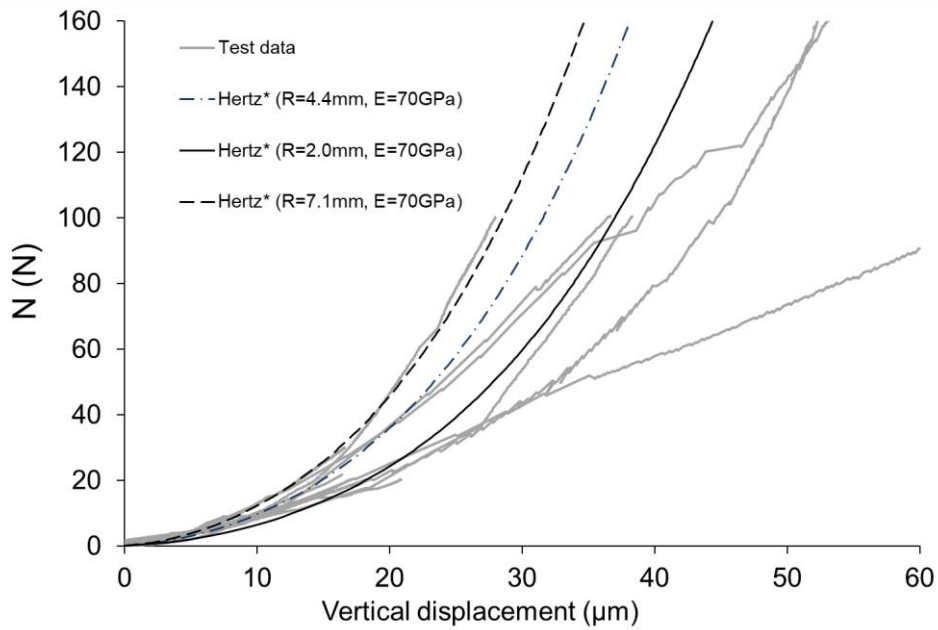
(b)

Figure 2.91 Comparison between test data and (a) Hertz (1882) for different contact radii, (b) Hertz modified for roughness (Hertz*, Greenwood et al., 1984), (Wong, 2022).
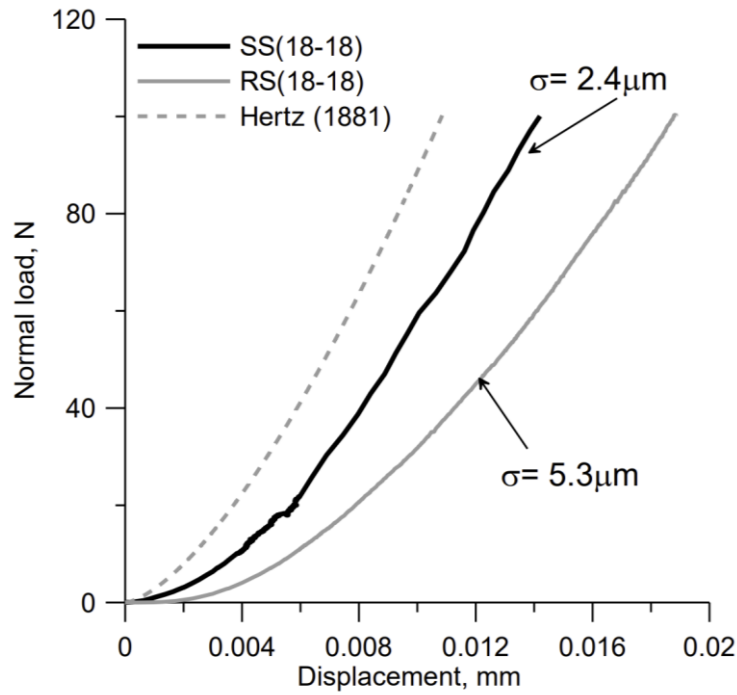
Figure 2.92 Force- displacement response of two tests of sphere-sphere with similar equivalent radius but with two different combined roughness values (after Altuhafi et al., 2024).
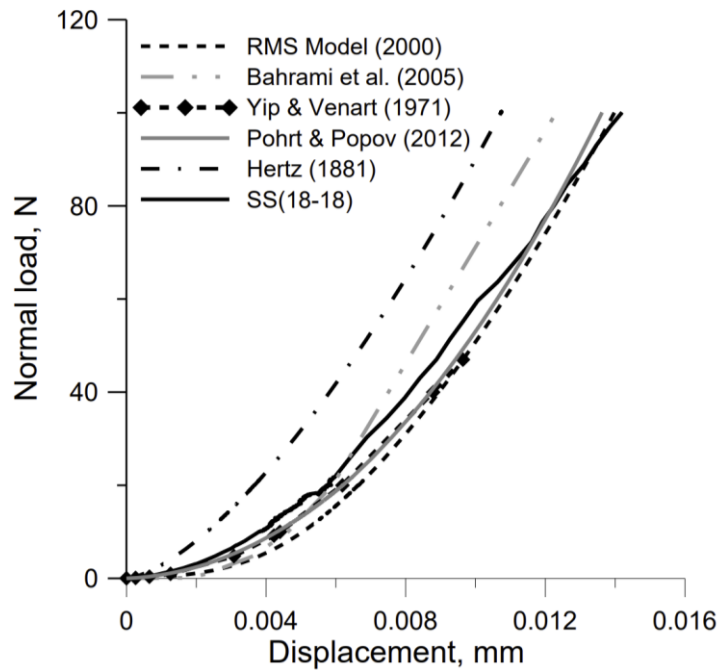
Figure 2.93 Data for monotonic normal loading compared with various models (after Altuhafi et al., 2024).

3. Experimental Procedures and Materials

This chapter describes the apparatus, then the materials used in the experimental research. In the recent past, discrete element simulations have gained popularity for numerical analysis of ballast-like materials. These simulations require parameters for contact behaviour such as normal stiffness, tangential stiffness, coefficient of friction, damping coefficient, etc. To extract parameters at the contact scale, an inter-particle apparatus was initially designed by Coop and Senetakis (2014), which has been modified several times, and was recently modified by Nardelli et al. (2016) and Wong et al. (2019). The current work used mainly the I.P. apparatus modified by Wong et al. (2019). A later modification, undertaken by the author and Dr. Saurabh Singh, involved changing the vertical arm washers and the bearings of the apparatus were changed to a bigger size and the number of bearings were increased. Before testing, comprehensive calibration was performed on the load cells, displacement transducers, and the sliding mechanism. Throughout this process, loads, displacements, and frictions were meticulously checked and corrected as necessary. The general design of the I.P. apparatus is outlined in Section 3.1.1. For comprehensive details, readers are directed to the relevant references. In Section 3.1.2, the methodology for measuring soil grain and ballast surface roughness using optical microscopy and various software tools is reviewed. Section 3.2 describes the materials (introduction to different types of ballasts, including calcite particles) examined in this study. Section 3.3 provides insight into the preliminary tests conducted and the procedures for sample preparation, including a method for surface quantification with some examples. Section 3.4 covers the calibration of transducers, load cells, linear actuators, and the sled on the 3-point bearing system, ensuring accuracy and minimal drift. These calibrations are crucial for obtaining reliable experimental data. Modifications of the apparatus will be covered in section 3.5. and at the end of the chapter, a summary will be provided.

3.1 Apparatus and Techniques

3.1.1 Inter-Particle (I.P.) apparatus

The I.P. apparatus used in this experimental work was originally designed by Senetakis & Coop (2014) to test the mechanics of granular soils at the contact and was upgraded to a three-dimensional (3D) configuration by Nardelli et al. (2016). It was conceptually

redesigned and modified (Fig. 3.1) by Wong et al. (2019) for large particles such as ballast, using the guidance of Professor Matthew Coop (supervisor). To test the micromechanical properties of ballast, a larger and more robust apparatus was required with the same functions as the previous one, since ballast particles are much coarser than sand. The design and manufacturing of it (including machining of the metal components) were carried out largely by Mr Ben Boorman (soil laboratory technician at UCL) with the recommendation from Professor Matthew Coop. With the assistance of supervisors, Wong selected and calibrated each component (e.g., transducers, data loggers, and motors). Professor Matthew Coop and Dr Wong contributed to the development of the computer program. The apparatus is described below.

A three-axis control is used, as shown in Fig. 3.2. Each of the three loading arms is equipped with linear actuators, load cells, and displacement transducers that can be moved in any of the three directions. Figure 3.3 illustrates the three linear actuators; the vertical actuator is positioned on stainless-steel frames, whereas horizontal means positioned on horizontal arms attached to the frame (Fig. 3.4). Between the linear actuator and the particles, load cells were positioned. The following section describes the different components.

The linear actuators control the force or displacement in any of the three directions using stepper motor controllers in all three directions. The loads are measured using miniature stud load cells with high accuracy, with a capacity of 1000N vertically and 500N horizontally. Non-contact capacitive displacement transducers are used to measure displacement. Custom holders were used to mount the vertical transducer and steel targets for the horizontal transducers on the top platen. The same custom-made holders are used to mount the horizontal transducers and the vertical target on the bottom platen. The frame must be stable and stiff so that it does not deflect under the applied load, resulting in inaccurate measurements. A vertical load cell is attached to the top platen, and a 3-point bearing system is used for the bottom platen. Fig. 3.5 shows two 100x100mm plates between which hardened steel ball bearings were placed, and this will harden the plates to prevent indentation when the bearings roll over them.

The linear actuators and the loading arms are guided by stainless steel miniature linear bearings (model Hepco Motion MLG5CZ0) incorporating guide rails of 5x35mm (model Hepco Motion MLG5). Fig. 3.6 shows linear bearings with guide rails installed on the

horizontal arms to facilitate perpendicular movement of the sledge. Linear bearings were also used in the vertical loading system, and details of the modifications will be discussed later.

Several digital microscope cameras (model Dino-Lite AM2111) with digital zooming from 10x to 200x are used to check the alignment of the particles before testing. In Fig. 3.1, the cameras were located next to the frame on adjustable microscope stands (model DP-M14 3D). Cameras used in testing can take single pictures and videos at 0.3MPix.

The apparatus is controlled using a QBASIC program adapted from a program used by Nardelli (2017), which was written by Professor Matthew Coop. Data are recorded from a data logger using an RS232 serial port that uses the QBASIC computer program that provides input commands. The load cells were all connected to amplifiers (models RDP S7DC). The readings were subsequently more stable and precise. A modification was carried out to the I.P. apparatus for this doctoral study and will be covered in section 3.5.

3.1.2 Optical Microscopy techniques

Surface roughness is important in contact mechanics from adhesion to friction, wear, and lubrication (Bowden & Tabor, 1958). Despite the considerable amount of research already conducted, the contact behaviour of realistic roughness surfaces remains largely unknown. Optical microscopy has been used to determine the roughness of ballast and natural sand particles, as discussed in Chapter 2. The advantage of optical measurement techniques over other measuring techniques lies in the need for no contact, and optical methods often take less time than other techniques (Whitehouse & Reason, 1965; Greenwood & Williamson, 1966).

Zeiss optical microscope

The experiments were conducted with different magnifications using a Zeiss's Stereo-Discovery V8 optical microscope (Fig. 3.7a) in reflected light mode (10-80 magnification). The size of the surface profile measurement depends on the magnification of the optical lens, with a maximum viewable area of 1.62mm x 1.34mm. With the newer versions, it is also possible to view images in 3D after a reliable calibration. The microscope available at UCL is equipped with a special software program called Axioscope (Carl Zeiss Micromanaging, 2021), which can process the data. Additionally, the images can be viewed in ConfoMap using z-stack to analyse them further to find the surface roughness. With the z-stack

function, images can be captured across different planes and can be used as a powerful tool in microscopy to reveal conditions not seen with standard wide-field imaging. As an additional feature, the z-stack focus feature collects a series of images in the z-axis, identifies the brightest pixel in each image layer, and returns a single image with the extended focus for 3D analysis. Z-stack is used in this approach to take a set of images at 0.006mm or 0.012mm steps to select the most in-focus pixels from each image and create a unified image. When the z-stack is selected, the image is moved to one side until it becomes unclear, and nothing can be seen. Set First is selected, and then the image moves in the opposite direction until it is again unclear. Finally, Set Last is selected to get a compacted image, which uncovers the changes in the surface of the particle automatically. The detailed procedure is given in Appendix A. As the research advanced into its later stages, several minor modifications were implemented. Notably, the thickness of the slices was initially reduced to 0.003mm (from 0.006mm and 0.012mm), therefore achieving better resolution. Subsequent discussions and thorough consideration within the research team led to a unanimous agreement that a more substantial reduction to 0.001mm would likely result in enhanced research outcomes, as it was reduced with the aim of achieving superior results when measuring particle surface roughness.

Keyence Microscope

Used for limited tests and bought at the end of the of this PhD research, the microscope had the advantage of focus variation and the laser confocal combined in one. Here's how each method works:

Focus Variation: This technique takes multiple images of the same object at different focal points and then combines them to create a detailed 3D surface model. It's really useful for looking at rough or uneven surfaces and measuring their height and shape accurately.

Laser Confocal Microscopy: This method uses a laser to scan the sample, focusing on one tiny point at a time. It filters out blurry, out-of-focus light, giving super sharp, high-quality images. This allows you to examine both the surface and the inner structures of the sample in great detail.

By combining these two methods, the Keyence microscope allowed for detailed 3D images of both the surface and internal features of samples, which was crucial for this research.

Zeiss ConfoMap

ConfoMap is a software platform that provides image analysis and surface metrology, and the surface imaging provided by ConfoMap is of the highest quality. The software allows to view a surface in 3D, zoom in and rotate in real-time, apply different renderings, adjust the heights and switch between lighting types. The software is designed to work with profilometers, 3D light microscopes ("MountainsMap"), scanning electron microscopes ("MountainsSEM") and scanning probe microscopes ("MountainsSPIP"). The ConfoMap advanced profile features metrological filters (roughness and waviness) assigned by ISO 16610, which help measure particle roughness using the Zeiss optical microscope images by removing the shape effect. Several other features are also available, such as form removal, 2D spectral analysis, fractal analysis, statistical analysis of series of profiles, peak count distribution, subsurface extraction, and profile extraction. All of them allow quantifying the roughness of the particle surface, e.g., Sq or fractal dimension. A more detailed procedure is given later in section 3.3.2.

3.2. Materials

The aim of the study is to widen the database on the micro-behaviour of railway ballast. To this end, different ballast particles with distinct mineralogical compositions were sourced from various locations. The materials examined include calcite particles (CS), used granite (UG), fresh granite (GB) from the United Kingdom, basalt ballast (BB) from Australia, Chinese granite (CB) and andesite ballast (AB) from China. All the particles tested had different sizes and tended to have different curvatures at the contact. Typically, the tests were programmed on a naturally angular ballast particle in contact with a flat surface of another particle of the same ballast.

The selection of materials in this study, was designed to expand the current understanding of the micro-behaviour of railway ballast by incorporating a wider variety of mineralogical compositions, particle textures, and mechanical properties. These materials represent commonly used ballast types from different geographical regions including the United Kingdom, Australia, and China. While individual materials such as granite and basalt have been the subject of previous research due to their widespread use in railway track systems, this study introduces several novel aspects:

Inclusion of less common ballast types: Materials like calcite (CS) and andesite (AB) have not been extensively studied at the micro-mechanical level in the context of railway ballast, providing new data on their behaviour under contact loading.

Used vs. fresh material comparison: By including both used granite (UG) and fresh granite (GB), the study sheds light on the effect of material degradation, an area that has received limited attention in the literature.

Geographical and mineralogical diversity: The inclusion of ballast materials from different continents brings broader geological variation to the analysis, which has been largely absent in earlier studies that typically focus on single-source materials.

Focus on micro-contact behaviour: Most previous studies have concentrated on the bulk mechanical behaviour of ballast aggregates, with limited investigation into micro-scale contact mechanics, including the role of particle curvature and surface characteristics.

Lack of comparative studies: Critically, there has been no comprehensive study in the existing literature that directly compares the micro-mechanical behaviour of these diverse ballast materials under identical testing conditions. This study fills that gap by offering a systematic comparison that was previously missing.

Therefore, while some of the individual materials may have been examined in isolation in past research, the combination of materials, the comparative framework, and the focus on micro-scale behaviour make this study a new and valuable contribution to the field.

3.2.1 Calcite

Calcite is a natural mineral and one of the most prevalent minerals in geothermal fields. Calcite is found in sedimentary, metamorphic, and igneous rocks, formed through the replacement of primary minerals with calcium-bearing carbonate via fluid-rock interaction, and by precipitation through CO_2 loss from fluids due to boiling (Arnórsson, 1989). According to the literature, calcite exhibits a Young's modulus ranging from 73 to 84 GPa and a shear modulus of 28 to 32 GPa (Mavko et al., 1998; Jaeger et al., 2007). The Poisson's ratio for calcium carbonate varies between 0.3 and 0.33 (Kristalle, 2022; Ekprasert et al., 2020). An example of a pair of calcite sand particles before testing is shown in Fig. 3.8. In this research calcite was used in preliminary tests to optimise testing procedures.

3.2.2　Basalt ballast (BB)

Natural basalt is found in volcanic rocks formed from sublimating lava. Basalt ballast (BB) from Australia, in various sizes, was washed and dried before testing (Fig. 3.9). The deformability of intact basalt within the elastic range is constrained by Poisson's ratio and Young's (elastic) modulus. The parameters from selected basaltic rocks at room temperature, summarised by Birch (1966), are listed in Table 1. It has been shown that Young's modulus, when measured at 50% peak stress (e.g., Kulhawy, 1975), ranges between 20 GPa and 100 GPa, with an average value of 73 GPa at ambient temperature (20°C). Ryan (1987) demonstrated that the Young's modulus of Hawaiian olivine tholeiite decreases linearly with temperature.

According to Nafe and Drake (1968), a Young's modulus of 60 GPa at 20°C is consistent with experimentally derived values for other basalts. Poisson's ratio for intact basalt, which is relatively insensitive to temperature changes, is approximately 0.25 and may increase slightly with pressure. The material was provided by Professor Buddhima Indraranta from Australia.

3.2.3　Andesite ballast (AB)

Andesite is a type of volcanic rock that typically comprises plagioclase feldspar, pyroxene, and amphibole (Fig. 3.10). It has a density of approximately 2.6 g/cm³ and a compressive strength of about 100 MPa (Jones et al., 2018). The Poisson's ratio of andesite ballast typically falls within the range of 0.2 to 0.3 (ASTM International, 2022). The Young's modulus of andesite generally ranges between 5 and 10 GPa (Smith and Houston, 2020; Brown and Green, 2015). The Young's modulus of a material can vary depending on several factors, including its composition, microstructure, and temperature. For instance, the Young's modulus of andesite will be higher if it contains more plagioclase feldspar and less pyroxene and amphibole (Doe and Roe, 2017). The Young's modulus of andesite is also influenced by its porosity. Porous materials exhibit a lower Young's modulus compared to non-porous materials because the pores act as stress concentrators, reducing the material's overall strength and stiffness (Miller et al., 2019).

3.2.4 Fresh granite (GB)

Mountsorrel granite ballast is a type of rock that is mined in Leicestershire, UK (Fig. 3.11). It is very strong and durable and can withstand a lot of wear and tear. It is also resistant to weathering, so it can be used outdoors for many years. Mountsorrel granite ballast as an assembly of grains has a high porosity (Network Rail, 2023), which means that it allows water to drain through it easily. This is important for railway track beds, as it helps to prevent water from pooling and causing problems (Lafarge Tarmac, 2023; Network Rail, 2023).

It is the same type of granite ballast that was tested by Wong and Coop (2024), which has an elastic modulus of 30-60 GPa and a Poisson ratio of 0.2-0.3. This means that it is a relatively stiff and incompressible material. This makes it well-suited for use in applications where high load-bearing capacity and resistance to deformation are required. Mountsorrel granite ballast is a popular choice for use in railway track beds because of its many advantages. It is strong, durable, resistant to wear and tear, resistant to weathering, and has a high elastic modulus (Lafarge Tarmac, 2023; Network Rail, 2023; Chen et al., 2021). This material was provided by Professor Glenn McDowell from Nottingham.

3.2.5 Chinese granite (CB)

Chinese granite ballast is quarried in China (Fig. 3.12). It is a strong, durable, and hard-wearing material that is commonly used in railway track beds, roads, and other construction applications (Chinese Railway Society, 2021; Ministry of Transport of China, 2023).

Chinese granite ballast has a high compressive strength, typically over 200 MPa. This makes it resistant to crushing and deformation. It is also resistant to weathering, abrasion, impact, and frost damage. Chinese granite ballast is also resilient to dynamic loads, such as those imposed by passing trains (Chen et al., 2021; Liu et al., 2022; Li et al., 2023).

The porosity of Chinese granite ballast as an assembly of grains is typically around 20%. This allows water to drain through it easily, which is important for preventing waterlogging and frost heave. The particles of Chinese granite ballast are typically angular in shape, which helps to interlock and create a stable ballast bed. Chinese granite ballast also produces very little dust, which is important for environmental protection and worker safety (Chen et al., 2021; Liu et al., 2022; Li et al., 2023).

The elastic modulus of Chinese granite ballast is typically between 30 and 60 GPa, and the Poisson ratio is typically between 0.2 and 0.3. This means that Chinese granite ballast is a relatively stiff and incompressible material. This makes it well-suited for use in applications where high load-bearing capacity and resistance to deformation are required. Chinese granite ballast is available in a variety of colours, including grey, pink, and red owing to its varied mineralogy. This makes it a popular choice for use in landscaping and other decorative applications (Chen et al., 2021; Liu et al., 2022; Li et al., 2023). Chinese granite and andesite were provided by Dr Xiaoyan Zhang from China.

3.2.6   Used granite ballast (UG)

Used granite ballast (UG) is referred to as granite ballast that was recovered from existing tracks, and it was collected by the author and Dr Saurabh Singh from Nottingham network rail depot (Fig. 3.13). It is a useful and durable material, characterised by its high strength, durability, resilience, porosity, and elastic modulus (Chen et al., 2021, 2022; Liu et al., 2023; Zhu et al., 2022). It is commonly re-used and employed in railway track beds, construction, and land reclamation.

UG possesses an elastic modulus ranging from 30 to 60 GPa and a Poisson's ratio of 0.2 to 0.3, indicating that it is relatively stiff and incompressible (Chen et al., 2021; Liu et al., 2023). These properties render it well-suited for applications requiring high load-bearing capacity and resistance to deformation. The properties of UG can vary depending on several factors, such as the source of the granite, the age and condition of the ballast, and the type of treatment it has undergone (Chen et al., 2021, 2022; Liu et al., 2023). When selecting used granite (UG) for testing, it was crucial to ensure that it was also tested in its intact state without any washing or cleaning (Fig. 3.13). Used granite was provided by network rail.

3.2.7   Washed used granite Ballast (WUG)

Washed granite ballast (WUG) refers to granite ballast recovered from existing tracks, then cleaned to remove debris, dust, and fines. Sourced from the Nottingham Network Rail Depot (Fig. 3.13), WUG is a durable material known for its high strength, resilience, porosity, and elastic modulus (Chen et al., 2021, 2022; Liu et al., 2023; Zhu et al., 2022). With an elastic modulus of 30–60 GPa and a Poisson's ratio of 0.2–0.3, WUG demonstrates high stiffness

and low compressibility (Chen et al., 2021; Liu et al., 2023). Its mechanical behaviour depends on factors such as the granite source and its condition prior to treatment. For testing, WUG samples were cleaned to accurately evaluate their performance, ensuring no residual dust or fines remained (Fig. 3.14). The properties of all railway ballasts tested in this research are given in table 3.1. and regular shaped ballast particles selected for testing from the samples available are illustrated in Fig. 3.15. The WUG are the used granite in 3.2.6 these were washed in the environmental laboratory.

3.3 The Preliminary tests

Preliminary normal loading tests were conducted on three different types of particles including sand, gravels (limestones) and ballast (basalt); in addition, basalt and limestone particles were tested under both normal and tangential load. Surface quantification has been carried out on all particles before and after the tests. These preliminary tests were used to determine the procedures for the other tests on railway ballasts.

3.3.1 Sample preparation initial procedures

The particles were first washed apart from used granite, allowed to dry, and then stored for testing or used immediately. A consistent process was followed in selecting and mounting them before testing. To facilitate the testing procedures and interpretation of test results, particles with a more regular shape were selected from the samples available (Fig. 3.15). For this purpose, visual observations were made to select particles with the highest sphericity and roundness. Furthermore, it was crucial to ensure that the particles (ballast) were the appropriate size (under 40 mm) for the I.P. apparatus; otherwise, they had to be cut accordingly. It was also important to verify that the particle surfaces had not been altered or treated and that the particles were chosen in their natural form and had not been previously used or cut.

Particle selection typically involves two particles for most specimen preparation tests, with one or two extra particles as backups in case one breaks. Ballast and sand (preliminary tests) particles are usually selected for point-to-flats and edge-to-flats combinations to avoid having more than one nominal contact at the start of the test. To ensure the particles adhere properly to the platens (Fig. 3.16 & Fig. 3.17), they must be cut with flat surfaces and then glued to the mounts, ensuring they fit within the 40 mm height of the apparatus. To minimise the effect of the contact geometry, the cut surface of the particle with the flat surface must be parallel to

the contact surface. Cavarretta et al. (2010) found that a non-flat contact led to less stable control during cyclic shearing tests, regardless of the forces parallel and normal to the contact surface. A plastic brush was used to rinse the particles under running water to remove dust and grease from the cutting process, and a cloth towel was used to dry them. This was done on all particles, excluding used granite, where samples were selected in their natural state without any washing or cleaning. To prevent contamination of the contact surfaces, gloves were worn while handling the particles.

<u>Glue procedures</u>

 Placing the particles near the centre of the loading system ensures that the contact point is easily accessible before preparing the glue, for glueing the chosen adhesive, a blend of equal parts Araldite glue A and B, is thoroughly mixed for at least 2 minutes. This adhesive is selected for its resistance to oil, chemicals, impact, and high temperatures. Precise quantities of both components are measured using a precision scale, typically around 3-5g depending on the size of the particles. The two-part glue is mixed thoroughly and then evenly applied to the cut surface of the top particle.

Following this, the top particle is carefully positioned on the top platen, and the base particle on the base platen. Pressure is applied for a few minutes to initially set the glue. A custom-made protective cap (Fig. 3.18 & Fig. 3.19) is then placed atop the glued particle, and dead weights are added to reduce glue thickness. Subsequently, the glued particles are left to gain full strength overnight, as it is recommended to allow a 24-hour curing period before conducting any tests (Fig. 3.20). The design of the glue protector cap aims to prevent load application to the particle contacts during the setting of the glue.

After removing the dead load, the particle positions are reassessed to ensure their correct placement (Fig. 3.21). The same procedure, including glue application and curing, is repeated the following day for the bottom particle. Finally, the particle sizes are determined using a calliper with a precision of 0.001 mm, and the Krumbein and Sloss (1963) characterisation chart is referenced for the shape of sand and basalt particles.

<u>Setting up the particles</u>

The surface of the sled was cleaned to make sure there is nothing on the sled, including dust, as it will create extra movement during the test and might affect the overall result. The bottom platen with the glued particle was put inside the apparatus after cleaning it, then the standard tests were conducted.

The vertical system was positioned as close to its home as possible (moving it upward by 3mm at least). As a result, the particles could be placed without touching, allowing more space for fitting. After removing the dead weights and the protective cap, the particles and the glued surfaces were examined. The top platen with the glued particle was tightened with a custom-made spanner to have the same tightness throughout the tests. The top platen was attached to a custom-made holder with a vertical transducer and two horizontal targets.

Afterwards, the bottom platen was placed onto the sled and screwed down using the custom transducer holders. Once the bottom platen and target were connected, an image was taken to see if they were right. Each of the transducers was aligned perpendicularly towards its target. Their distance was centred around the middle of the measuring range to allow enough movement in both directions and ensure that the transducer was not touching the targets.

Two digital cameras were placed next to the apparatus in orthogonal directions to take photos and videos of the particles during the test. The bottom particle could be approached without touching. The loads and displacements between the particles were zero before contact was made. During the test, the transducer was checked regularly to ensure that it was not touching the targets, and a distance of at least 2.5 to 3.50 mm was maintained. An illustration of typical testing procedures is shown in Fig. 3.22. The next section covers the procedure for surface texture quantification.

3.3.2 Surface Quantification (Roughness)

As reviewed in Chapter 2, sand and ballast particle surfaces are not perfectly smooth, and their roughness significantly influences mechanical behaviour, yet remains under-researched. Measuring roughness is challenging due to the small, irregular shapes of particles, leading to its frequent omission in morphological studies. While early measurements used light-section microscopes and later electrical filters, modern approaches like fractal analysis (Richardson, 1961; Mandelbrot, 1982) and power spectrum density methods (Yang et al., 2016) provide

improved descriptors. Roughness affects macroscale strain stiffness, microscale contact behaviour, and inter-particle friction angles. This study uses advanced 3D methods and ConfoMap7 software for comprehensive surface roughness analysis of soil and railway ballast particles, advancing understanding of their mechanical interactions. In the later stages of this PhD research the Keyence Microscope was used for limited tests and the results were compared with ConfoMap7.

Examples of measuring surface quantification

The original z-stack compacted image (Fig. 3.23a) is opened in 3D software ConfoMap7. The surface texture images are shown (Fig. 3.23b) in various colours. White and red represent the upper part of the particle's asperities, and black and blue represent the lower part of the particle asperities or apex. The surface can be made more readable and clearer by applying different filters, including the noise effect, waviness effect, and shape effect. After applying these filters, a change in the surface can be seen and it is used for surface analysis, where Sq, Sa and Df are obtained.

Using ConfoMap7, Altuhafi (2022) has emphasised the considerable changes in roughness associated with the dimensions of the field of view. This observation aligns with the findings in this thesis, which revealed a noteworthy fluctuation in the Sq value based on the size of the field of view. To address this inherent variability, a series of trials were conducted on identical particles: The initial assessment of roughness encompassed various total areas in view, ranging from 1.62 mm x 1.34 mm (Fig. 3.23b) down to 0.1 mm x 0.1 mm. Finaly, a field of view measuring 0.2 mm x 0.2 mm was selected (Fig. 3.24), guided by a Hertz prediction of the contact area.

Given the absence of definitive guidance for utilising the ConfoMap software in railway ballast analysis, three connective stages were employed to establish the appropriate Sq, Sa, and Df values, both before and after testing:

Z-stack Imaging

The Z-stack approach involved capturing images at incremental intervals of 1 μm, 3 μm, 5 μm, 6 μm, and 12 μm. This facilitated the selection of the sharpest pixels from each image to form a consolidated image. Notably, finer slices yielded a more densely packed image and

higher surface roughness, leading to a collective decision to standardise slice thickness to 1 μm for subsequent tests.

Cut-off Selection

The purpose of using a cut-off in measuring surface roughness is to filter out specific wavelengths or spatial frequencies in the surface texture data. This helps to focus on and quantify the relevant features of the surface, such as removing long-wavelength components related to overall shape or form and filtering out short-wavelength noise or fine details that do not contribute to the surface's functional properties. Cut-offs also aid in standardising roughness measurements and ensuring consistency in comparing results across different studies and applications. A range of cut-off values (from 2 μm to 80 μm) were trialled on multiple particles, with outcomes compared via power spectrum density (PSD) analysis in MATLAB in collaboration with Dr. Saurabh Singh. Following extensive experimentation, a consensus was reached on a 16 μm cut-off, which effectively minimised noise while preserving surface texture.

Form Removal

Height measurements of the surface are affected by the local shape (form). A feature of the ConfoMap software is form removal, where the local shape is fitted by a polynomial function. A conclusive trial was conducted to address uncertainties surrounding the software's form removal functionality. This involved testing form removal using polynomial degrees ranging from 5 to 12, with various graphs and profiles generated to discern differences. The higher degree above 10 were found to fit in details that may belong to surface roughness. Subsequently, a 9th-degree polynomial was collectively agreed upon for form removal. Adjustments were planned in cases where the resulting fit was deemed inadequate.

These methodologies were pivotal in addressing concerns regarding the variability of Sq values and ensuring the accuracy and reliability of roughness measurements within the railway ballast analysis context.

Extracting areas of measurement

Another challenge lies in determining the optimal sequence to extract the approximate contact area for more precise roughness measurements, given the absence of clear

instructions within the software. Altuhafi (2022) proposed that filters should be applied to the entire field of view, followed by roughness assessment, before extracting the 0.2 x 0.2 mm area. To address this, four trials were undertaken:

1- Extraction of a 0.2 x 0.2 mm area before filter application, followed by filter application for roughness assessment.
2- Extraction of a 0.2 x 0.2 mm area post-filter application, then roughness measurement.
3- Extraction of a 0.2 x 0.2 mm area after form removal, followed by filter application for enhanced accuracy.
4- Extraction of areas measuring 0.2 x 0.2 mm, 0.3 x 0.3 mm, and 0.5 x 0.5 mm after filter application, subsequently measuring roughness.

It was collectively agreed to extract a 0.2 x 0.2 mm area post-form removal and then apply filters for more precise measurements (method 3 above). This approach was uniformly implemented across all tests. The following gives an example of the procedure applied to pairs of calcite particles and railways ballasts. When the pair of particles were subjected to normal loading and the roughness of the surface at the contact was measured before and after the test. Two pairs were selected: with irregular shapes and with regular shapes and almost with the same size (2-5 mm).

Examples of calcite pairs with irregular shapes

Sand and ballast particles have irregular shapes and rough surfaces. As size increases, surface curvature also increases, requiring separation methods to calculate surface roughness. Roughness was measured as root-mean-square height (RMS), with Sq values of 0.00318 mm for base particles (0.5 mm x 0.5 mm area) and 0.0125 mm for top particles (0.3 mm x 0.3 mm area). Irregular particles showed higher Sq values due to apexes and asperities, while fractal dimension (Df) analysis was not applied for the calcite.

Calcite pairs with regular shapes

Two spherical particles were tested, with surface roughness analysed before and after the test. Significant surface changes and varied mineralogy were observed. RMS analysis showed Sq roughness values of 0.00911 mm for the base particle (0.5 mm x 0.5 mm) and 0.00411 mm for the top particle (0.3 mm x 0.3 mm).

Basalt ballast pairs test

ConfoMap7 software was used to analyse particle surface topography, including fractal and peak analysis, and calculate the fractal dimension (Df) using the boxing method. Surface roughness, measured as root-mean-square height (Sq), varied with the measurement area, ranging from 5.68 μm (top) to 3.89 μm (base) on spherical and flat surfaces, respectively. Smaller extracted areas (e.g., 0.2 mm x 0.2 mm) revealed reductions in RMS values, peak counts, and Df (from 2.10 to 2.08).

Results showed RMS roughness increases with surface irregularity and field of view, but particle size had minimal effect on RMS. This study measured three specific areas (0.1 x 0.1 mm, 0.2 x 0.2 mm, and 0.5 x 0.5 mm), highlighting that surface roughness depends on the measurement area, particle shape, and mineralogy.

3.3.3 Normal loading

Hertz's theory (1882) underpins elastic contact mechanics but assumes smooth surfaces, which doesn't apply to soils and ballast that also deform plastically. A modified Hertz model incorporating RMS roughness better captures deformation in materials like calcite sand and basalt ballast. Tests using a 3D IP-apparatus examined calcite sand (UK) and basalt ballast (Australia) under normal loads, revealing significant roughness changes due to plastic deformation, aligning with findings by Wong & Coop (2022) and Altuhafi et al. (2022). Basalt ballast served as a baseline for further analyses. The properties given earlier and roughness measurement (also shown in Table 2) were used for data analysis and comparison with theoretical models.

1-Calcite pairs with irregular shapes

Three normal load tests were conducted on irregular calcite particle pairs up to 100N. Before reaching 100N, the top particle broke (Fig. 3.27), likely due to apex failure around 40N or a soft mineral (Fig. 3.28). Between 40N–80N, the behaviour appeared zigzagged. Initial tests (10N & 20N) showed linear loading. Stiffness increased with load, aligning with Hertz's

theory, while stiffness matched Hertz's model at some points (Fig.3.29). Test under normal load of 10N diverge from Hertz and RMS (Fig. 3.30), but stiffness closely followed Hertz and RMS models (Fig. 3.31).

2-Calcite pairs with regular shapes

Six tests were conducted on calcite particle pairs with regular spherical shapes, compressed under normal loads up to 200N (Fig. 3.32). The findings confirm that normal stiffness starts near zero at zero force, aligning with Hertz's predictions (Fig. 3.33). Initial data for normal load 100N closely align with Hertz and RMS models (Figs. 3.34). Stiffness results also match with these models, consistent with Hertz's (1882) theory for spherical contacts, stiffness increases with normal load, as demonstrated in Fig. 3.35.

3-Basalt pairs

The first test used the I.P. loading apparatus to evaluate the normal and tangential loading properties of natural basalt ballast particles. Pre-cut basalt particles were selected for their regular shapes (flattened and spherical) and glued for stability. Fig. 3.36 shows the load-displacement response, with a steepening curve as the load increases and the data deviate from Hertz's model and RMS model but align more closely with the RMS model than the Hertz model. Basalt particles showed no apex breakage during loading, unlike earlier calcite tests. Wong (2022) and Cole and Peters (2008) observed gradients much lower than 2/3 of Hertz's values after 5N, which aligns with this study. Log-log plots (Fig. 3.37) indicate a power stiffness-displacement relationship, with stiffness increasing with load, consistent with Hertz and RMS models.

3.4 Calibration

This section details the calibration and stability of the transducers, including the capacitive non-contact displacement transducers, load cells, and linear actuators. Prior to calibration, the apparatus was disassembled (Fig. 3.38) and cleaned, to ensure proper functionality. The bearings on the sled's 3-point bearing system were replaced due to loss of grip. Calibration was then performed to reduce drift and ensure accuracy. These calibrations are essential for obtaining reliable experimental data.

3.4.1 Load Cells

The calibration procedures for load cells are meticulously detailed here. By applying dead weights directly onto the load cells, calibration constants were derived on all three load cells to ensure accurate force measurements in all three directions. The calibration of all three load cells involved the direct application of dead weights onto each cell, as illustrated in Figure 3.39. Specifically, the vertical load cell underwent meticulous fastening to a metal block, followed by the proper securing of a top platen to prevent any potential movement during the application of load. Graduated dead loads ranging from 5N (Fig. 3.39) to 200N (Fig. 3.40) were systematically applied and recorded, with the vertical load cell consistently exhibiting readings closely aligned with the applied loads and the difference was less than 1% (Fig. 3.41). Consequently, no correction was thought necessary for the normal loads.

Similar procedures were employed for the horizontal load cells, H1 and H2, to ensure the accuracy and reliability of the experimental data. Minor discrepancies were identified in the H1 load cell (Fig. 2.42), necessitating a detailed recalibration process followed by verification under supervised conditions. To assess the stability and performance of the H1 load cell, a static dead load of 10 kg (approximately 100 N) was applied. The load cell was monitored continuously for 15 hours. While the load exhibited minor fluctuations initially, it stabilised after approximately 14 hours. Post-stabilisation data indicated minimal deviations, as illustrated in Fig. 3.43. Despite the minor differences, it was jointly concluded that corrective measures would be applied to experimental data involving the H1 load cell to ensure precision and consistency. The remaining tangential tests were carried out in the H2 direction (using an H2 load cell).

In contrast, the H2 load cell demonstrated stable and reliable behaviour throughout the verification process, with no significant discrepancies observed. Consequently, no adjustments were considered necessary for H2, as illustrated in Fig. 3.44.

These findings emphasise the importance of individualised calibration and verification for each load cell. While both sensors were subjected to identical procedures, the variability observed highlights the need for rigorous testing to account for potential deviations. The recalibration and subsequent corrections for H1 further underscore the commitment to maintaining the highest standards of experimental accuracy.

Previously, Wong, (2022) assessed noise and drift for all three load cells. As the vertical load cell's capacity was double that of the horizontal ones, so measurements for channel 1 were double those of channel 2. Noise levels for channel 1 were about 0.02N, and for channel 2, they were less than 0.01N. Covering the load cells with a box did not affect noise levels but significantly reduced drift. The observed cyclical pattern in the data was minimal compared to the measured loads.

3.4.2   Capacitive Non-Contact Displacement Transducers

The calibration of the capacitive non-contact displacement transducers was conducted using a custom-made calibrator (Fig. 3.45). This setup included a micrometre with a spindle, on which the target was mounted. The transducer was positioned within a cylindrical tube facing the micrometre. The study examined the effects of the target's size and material, revealing no significant impact of the target size after repeating a few times with different lengths (distance between the target). Calibration curves for circular steel targets with diameters of 15 mm and 20 mm exhibited perfect linearity within the manufacturer's specified measuring range of up to 4 mm and slightly beyond. The smaller target was recently constructed to replace the original one used by Wong (2022), which was missing. The apparatus measured only relative displacements via the vertical displacement transducer (Fig. 3.46), utilising gradients in the program. A new zero reading was taken at the start of each test, eliminating the need for intercept values.

During the testing process, a slight discrepancy was observed in the H1 displacement transducer, necessitating its replacement and recalibration. The recalibrated results are shown in Fig. 3.47. Minimal variation was noted in the H2 displacement transducer (Fig. 3.48), which was utilised while waiting for the H1 transducer to be fixed.

3.4.3   Friction of the Sled

Originally Wong et al. (2019) had designed the sled on the 3-point bearing system to measure friction, but this was later modified by the author and Dr Saurabh Singh as shown in Fig. 3.49. This was investigated by putting dead weights (from 1kg to 20kg) directly on the sled and not using the vertical loading system. The sled was pushed and pulled in the horizontal (H1) direction and a very small amount of friction was measured. At first attempt it was found that friction was quite higher than it was expected due some errors during assembling the apparatus. The problem then almost no loads were measured in the orthogonal direction

was also found. However, the unusual feature of the data was that the friction force was not found to be proportional to the dead load. This friction was tiny and represented only about 1% of the lowest load levels used in this research. Nevertheless, all μ values were corrected for the average value of the friction.

3.5 Modification

The modifications were primarily carried out on the I.P. apparatus, which had been previously designed and modified by Wong et al. (2019). Recognising the limitations in the stability of the vertical arm, the author, in collaboration with Dr Saurabh Singh, undertook additional modifications to rectify this issue.

These modifications included increasing both the size and the number of bearings supporting the sled, thereby enhancing the accuracy of the inter-particle coefficient of friction measurements. The augmentation of the bearing system ensured smoother and more controlled sled movements, which are crucial for precise data acquisition.

Furthermore, washers were added to the vertical arm. This enhancement resulted in a more robust design for the vertical arm, enabling it to withstand greater loads without generating noise. The increased structural integrity provided by the washers ensured that the applied loads during testing remained consistent, eliminating potential variability in the experimental results.

The addition of extra bearings was another significant modification. This adjustment facilitated a more even distribution of the load across three contact points, markedly improving the stability of the sled during operation. By preventing tilting and uneven wear, this modification contributed to the accuracy and reliability of the measurements.

In conclusion, the collaborative modifications to the I.P. apparatus involved several key changes: increasing the size and number of bearings, adding washers to the vertical arm, and incorporating additional bearings to ensure even load distribution. These enhancements significantly improved the stability and robustness of the apparatus, thereby ensuring the accuracy and reliability of the inter-particle friction coefficient data obtained from the experiments. Such modifications are essential for producing reliable experimental data and advancing the understanding of material behaviour under various conditions.

3.6 Summary

This chapter detailed the principal attributes of the 3D interparticle apparatus, initially developed by Coop and Senetakis (2014) and subsequently refined by various researchers, including the author and Dr. Saurabh Singh. The apparatus includes three-axis control, linear actuators, load cells, and displacement transducers, enabling precise measurement of force and displacement during experiments. Additionally, optical microscopy techniques, such as the Zeiss optical microscope and ConfoMap software, were employed to analyse particle surface roughness.

Materials tested include calcite, granite, basalt ballast, and andesite ballast. Preliminary tests on sand, gravel, and ballast particles ensured consistent testing conditions, with detailed sample preparation procedures. Guidelines were provided for adhering particles onto platens using glue and arranging them for testing.

Surface quantification procedures utilised advanced 3D methodologies to analyse particle surface roughness, focusing on railway ballast particles. Techniques like Z-stack imaging, cut-off selection, and form removal were used for precise roughness measurements.

Calibration and stability evaluations of key experimental transducers are detailed in Section 3.4. Capacitive non-contact displacement transducers were calibrated using a custom device, emphasising the importance of grounding to reduce noise. Load cells were calibrated with dead weights, and protective enclosures significantly reduced noise and drift. Linear actuators were adjusted for speed and distance to ensure accuracy. The friction of the sled on the 3-point bearing system was minimal, ensuring precise measurements. These calibrations are essential for obtaining reliable experimental data.

Basalt ballast and calcite sand, as granular materials, have bulk properties like load-bearing capacity determined by inter-particle contact force distribution. Roughness measurements verified particle deformation after testing, with initial contact areas chosen at the apex of spherical shapes. The square root height (Sq) value varied with the measurement area size. Mineralogy and particle shape also influenced surface roughness.

Sand particle deformation under compression has traditionally been considered purely elastic, modelled using Hertz's classical theory. However, this study found, aligning with findings by Nardelli (2017), Altuhafi (2021), and Wong (2022). Then when using Hertz theory to model

displacement curves, some results were unrealistic if elastic moduli were applied, due to plastic deformation of asperities affecting surface roughness.

In the following chapters, systematic testing carried out in normal and tangential directions, monotonic and cyclic, on the different railway ballasts, is described the results used to bring more understanding to contact behaviour.

Chapter 3 Figures and Tables

Table 3.1 shows the properties of the different railway ballasts from

Material	Colour	Texture	Strength	Durability	Young's Modulus (GPa)	Poisson's Ratio	References
Andesite	Dark gray to black	Fine-grained	Moderate to high	Moderate	30-50	0.2-0.3	Marek & Török, (2020)
Basalt	Dark gray to black	Fine-grained	High	High	40-60	0.25-0.35	González-Pimentel & Pérez-López, (2011)
Granite	Light to dark gray	Coarse-grained	Very high	High	50-70	0.25-0.35	Hernández-Cruz & Gómez-Cervantes, (2010)
Used Granite	Varies	Rounded, weathered	Similar to fresh granite	May have reduced durability	40-60	0.25-0.35	Chen et al., 2021, 2022; Liu et al., 2023; Zhu et al., 2022

Chinese Granite	Varies	Coarse-grained	Generally high	High	40-60	0.25-0.35	Gao et al., 2021

Table 3.2 Parameters used in DEM Modelling

Materials	Base particle (Sq) (µm)	Top particle (Sq) (µm)	DF
Calcite (irregular shapes)	3.18	12.5	
Calcite (regular shapes)	9.11	4.11	
Basalt ballast pairs test	3.89	5.68	2.17
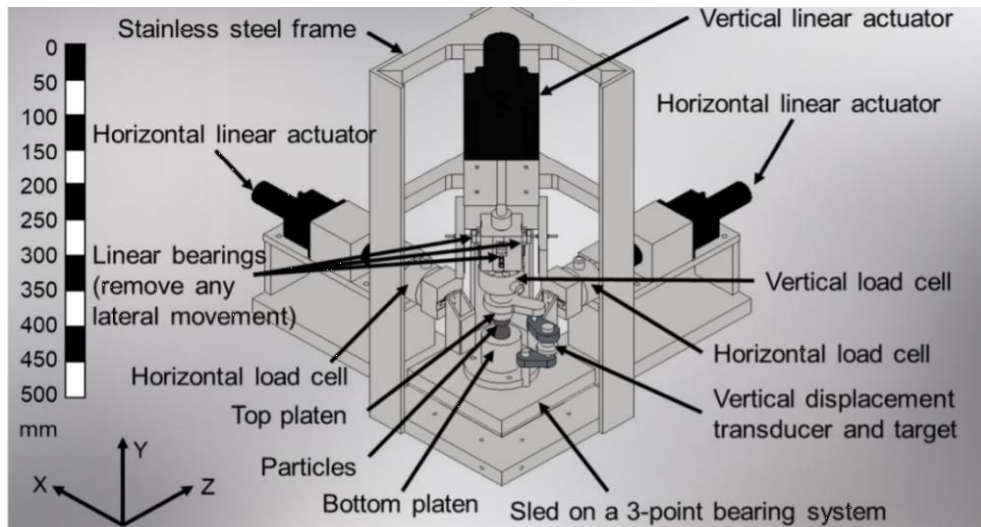
Figure 3.1 Isometric view of the initial design of the inter-particle loading apparatus (modified from an original diagram by Ben Boorman) (Wong, 2022).
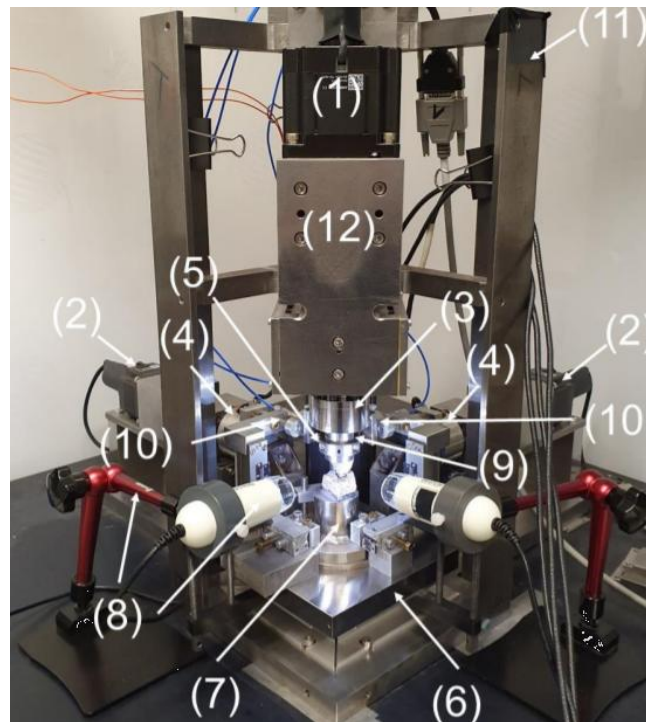
Figure 3.2 The interparticle loading apparatus appears in the following photo: (1) vertical linear actuator, (2) horizontal linear actuator (3) vertical load cell, (4) horizontal load cells, (5) vertical displacement transducer, (6) sledge, (7) bottom platen, (8) digital microscope camera and stand, (9) top platen, (10) horizontal displacement transducer, (11) stainless steel frame (12) front plate (Wong, 2022).
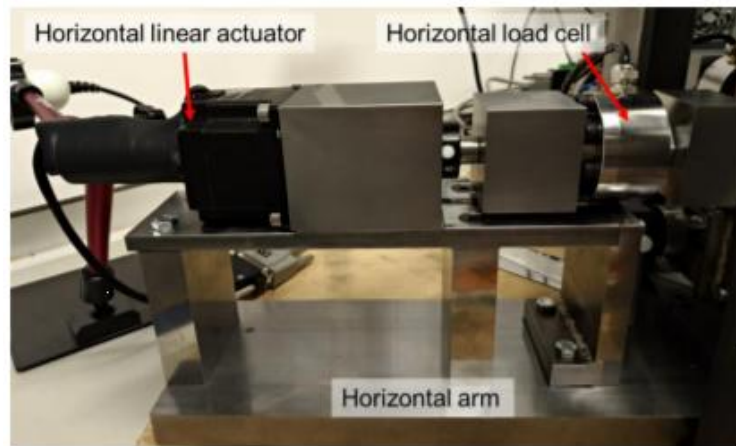
Figure 3.3 Horizontal loading system (Wong, 2020).
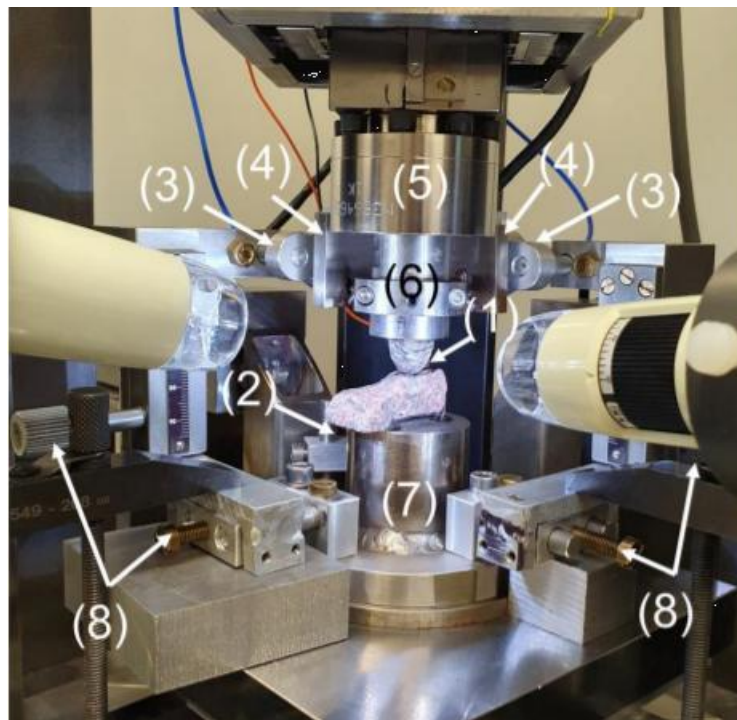
Figure 3.4 Arrangement of the capacitive non-contact displacement transducers: (1) vertical transducer (behind the particles), (2) vertical target, (3) horizontal displacement transducers (4) transducers targets (5) vertical load cell, (6) top platen, (7) bottom platen (Wong, 2020).
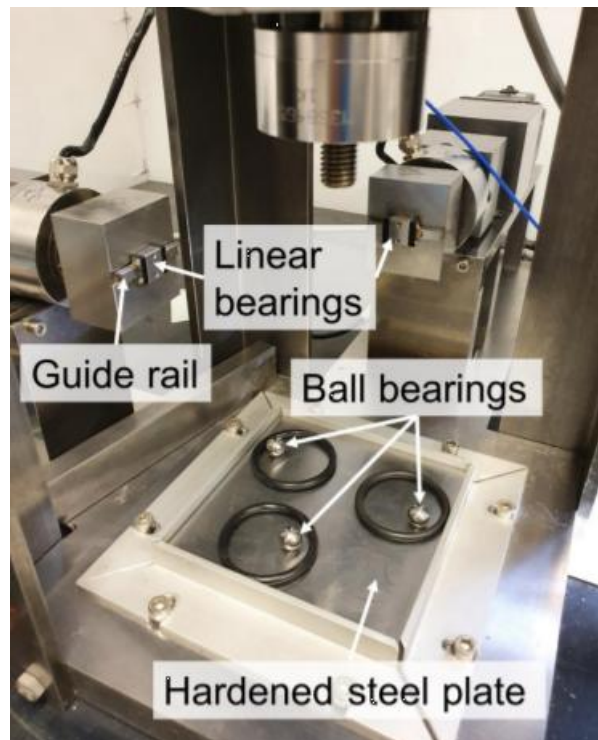
Figure 3.5 Arrangement of the 3-point bearing system and the linear bearings at the end of the horizontal arms (Wong, 2020).
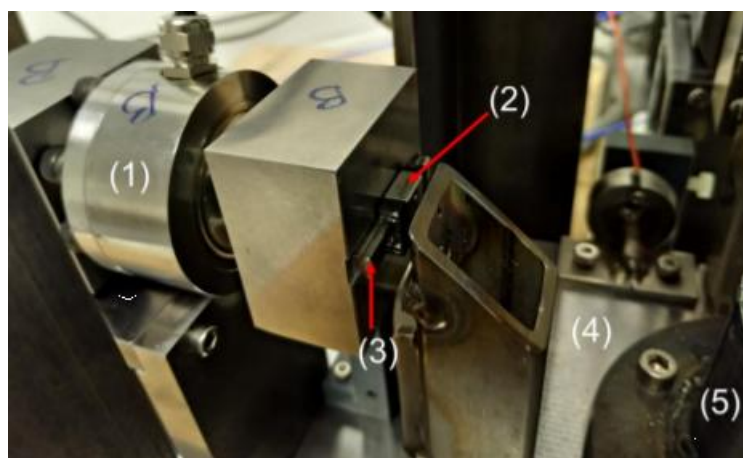
Figure 3.6 Arrangement of the linear bearing at the end of the horizontal arm: (1) horizontal load cell, (2) linear bearing, (3) guide rail, (4) sledge, (5) bottom platen (Wong, 2020).
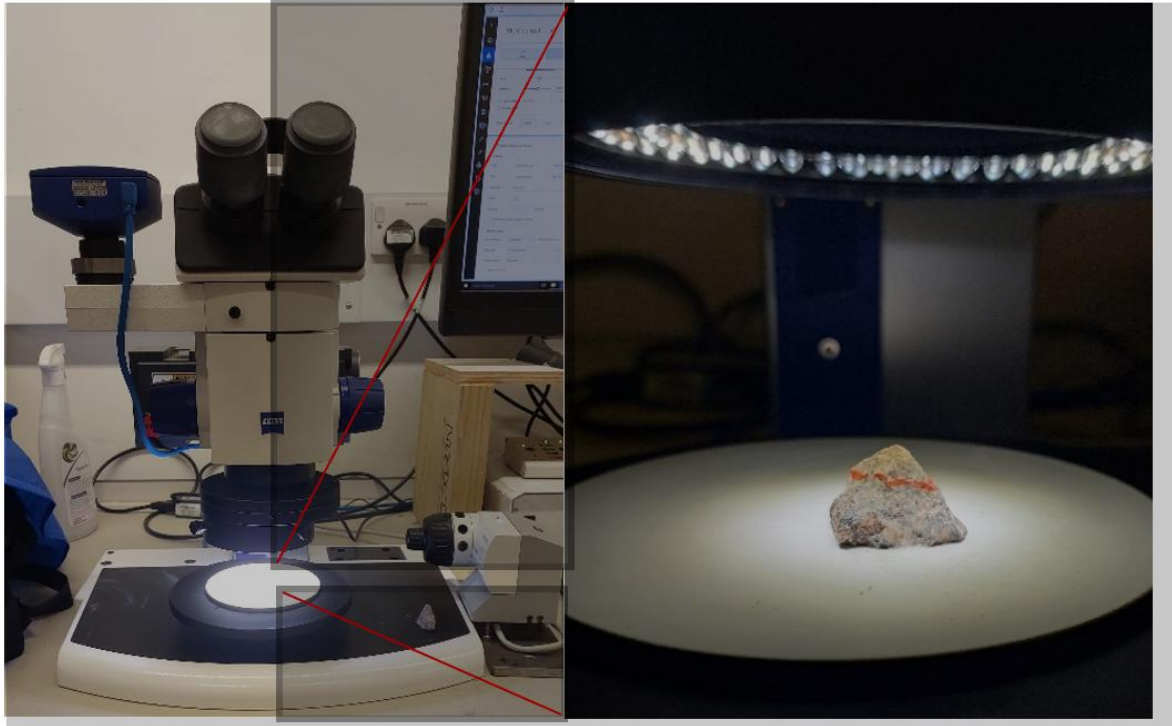
Figure 3.7 Zeiss optical microscope used for topography.
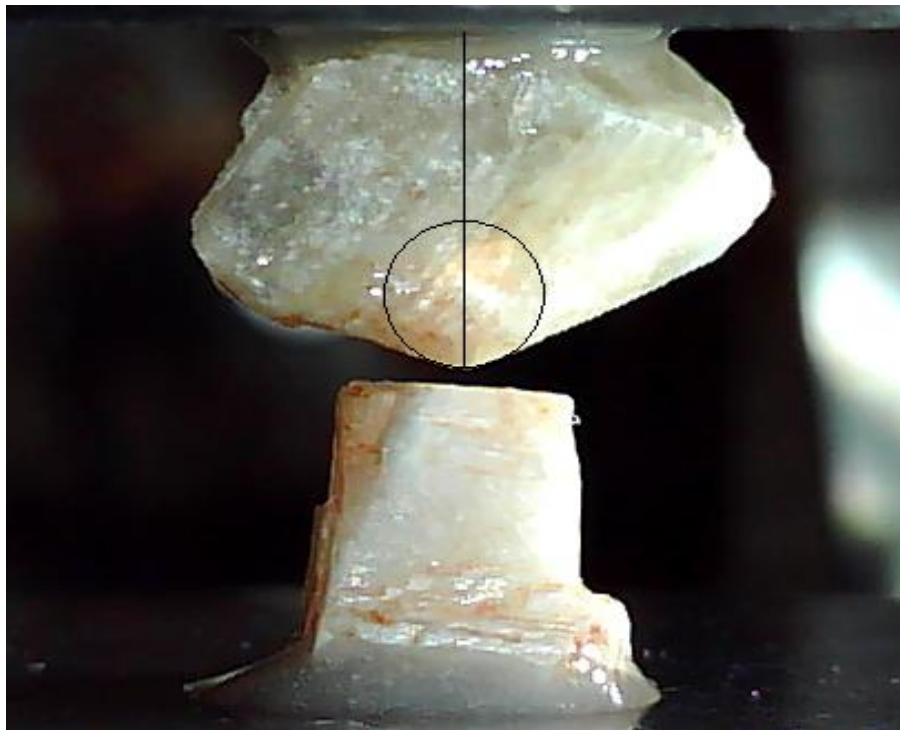
Figure 3.8 A pair of calcite particles before being tested by the I.P. loading apparatus for normal loading and a contact radius is measured digital cameras (from UK).

Figure 3.9 Australian basalt ballast particles are washed and dried before testing
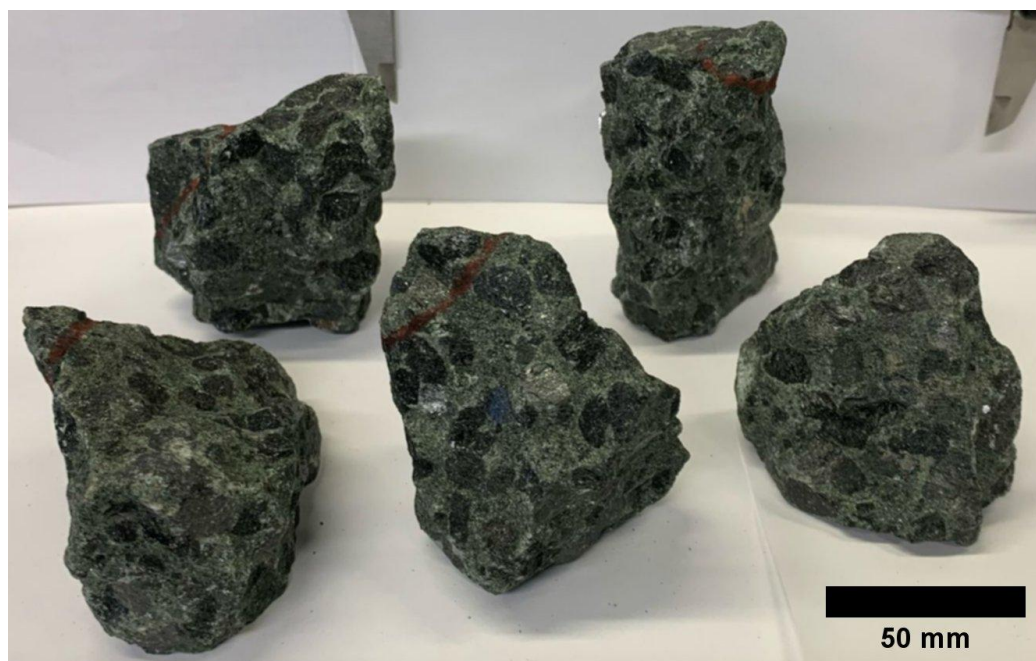
Figure 3.10 Andesite ballast particles from China before testing
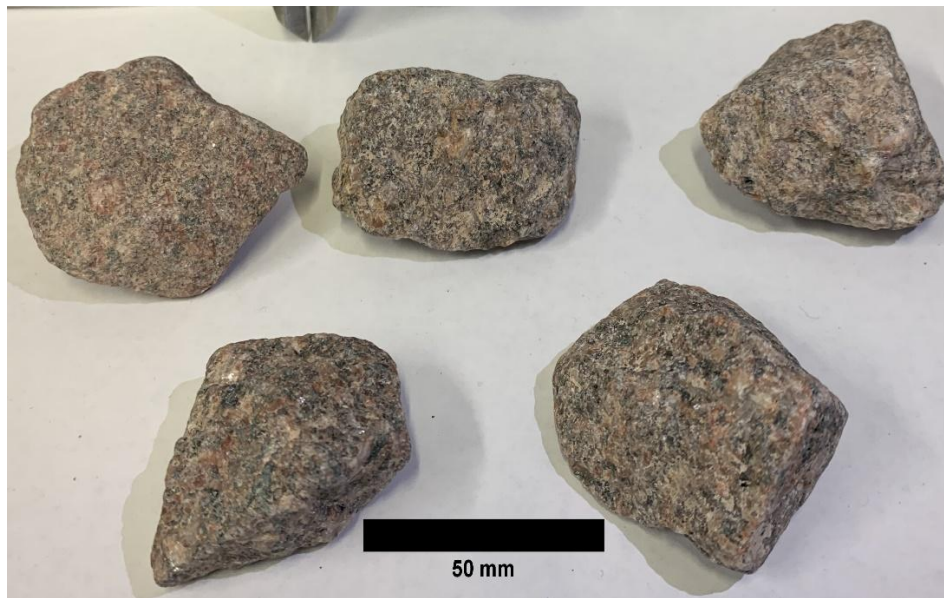
Figure 3.11 Fresh granite from U.K. before testing

Figure 3.12 Chinese granite ballast particles before testing

Figure 3.13 Used granite samples (from UK) selected for testing, shown in their natural state without any washing or cleaning.

Figure 3.14 Washed used granite samples (from the UK) after cutting to the right size and after washing and cleaning.
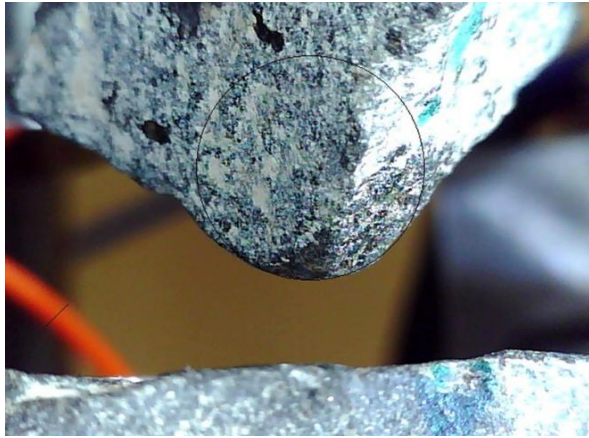
(a) Basalt (Australia)
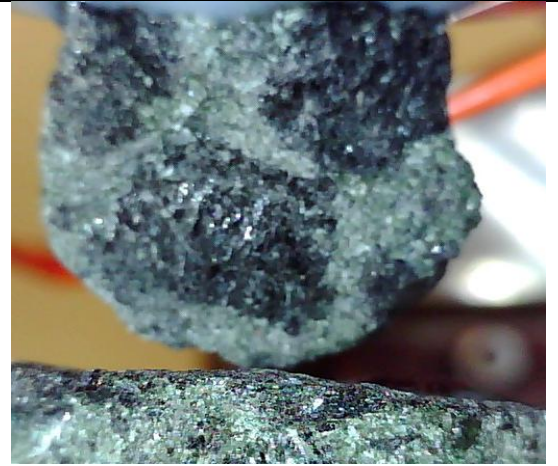
(b) Andesite (China)

(c) Fresh granite (UK)
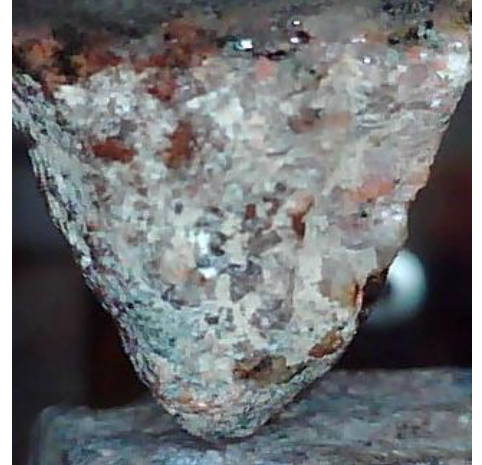
(d) Used granite (UK)

(e) Chines granite
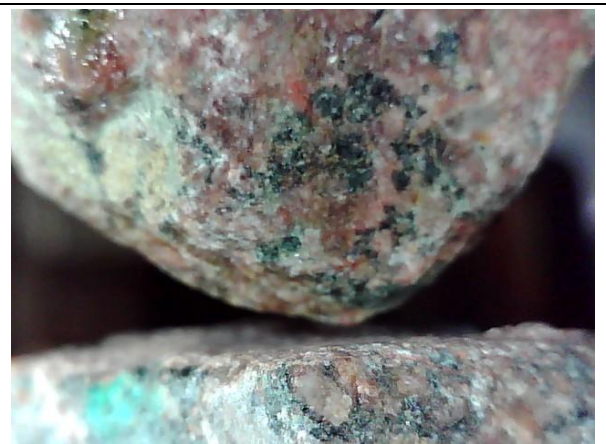
(f) Washed used granite (UK)

Figure 3.15 Regular shaped ballast particles selected for testing from the samples available.

Figure 3.16 The base platen.

Figure 3.17 The top platen.

Figure 3.18 Custom-made protective caps for big particles (ballast).
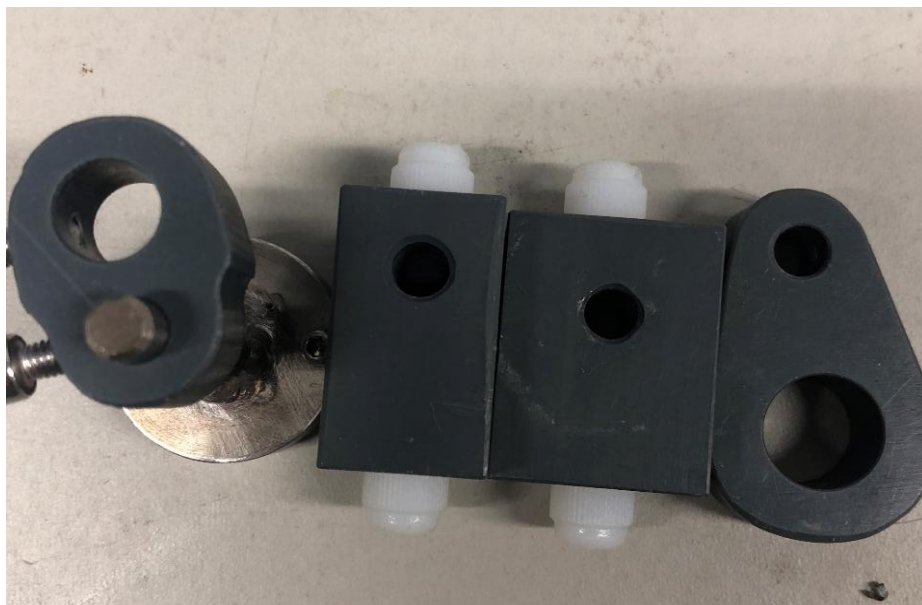
Figure 3.19 Custom-made protective caps for big particles (sand).
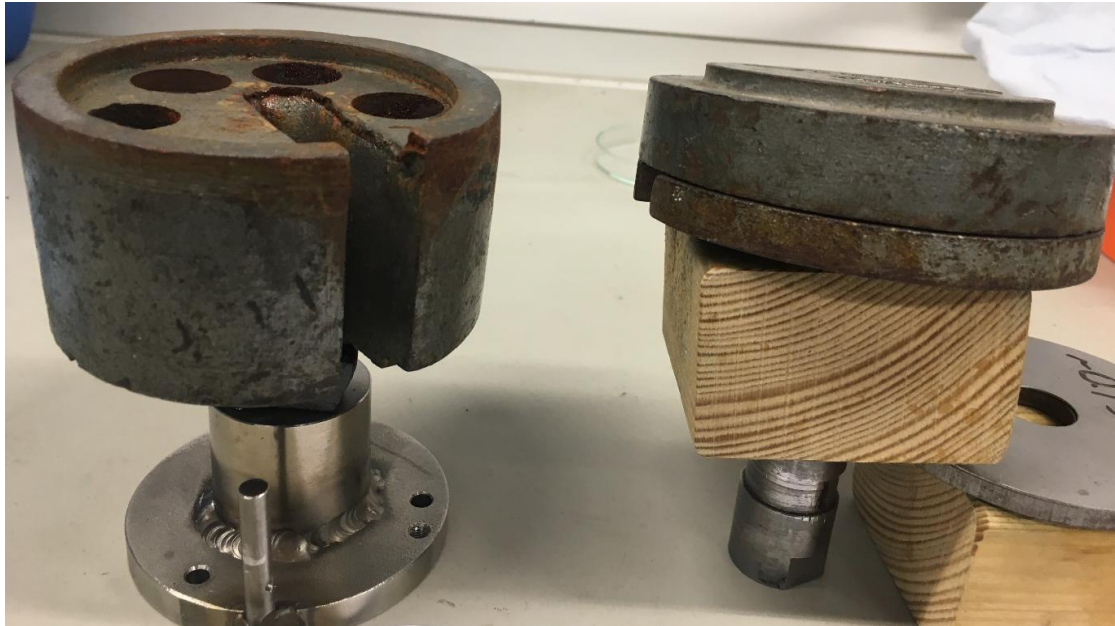
Figure 3.20 Setup of dead reduce glue thickness and stick them properly

Figure 3.21 After the dead load is removed, the particle position is checked
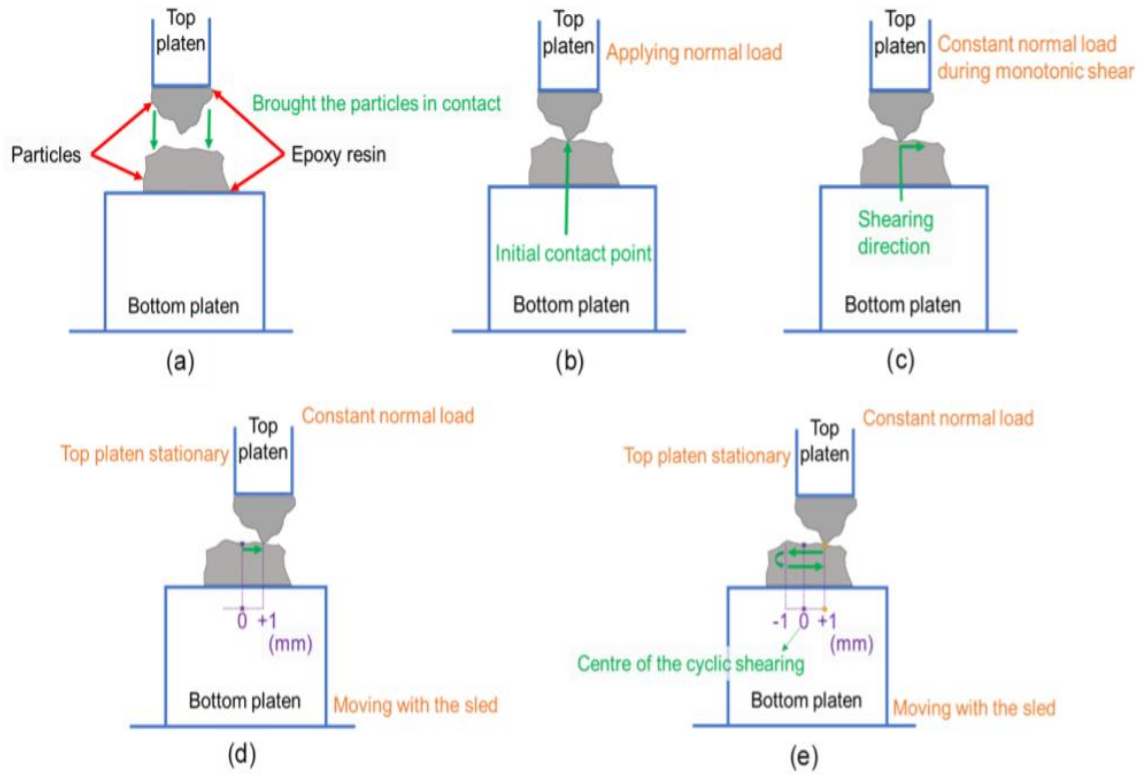
Figure 3.22 An illustration of a typical test procedure (Wong, 2022)
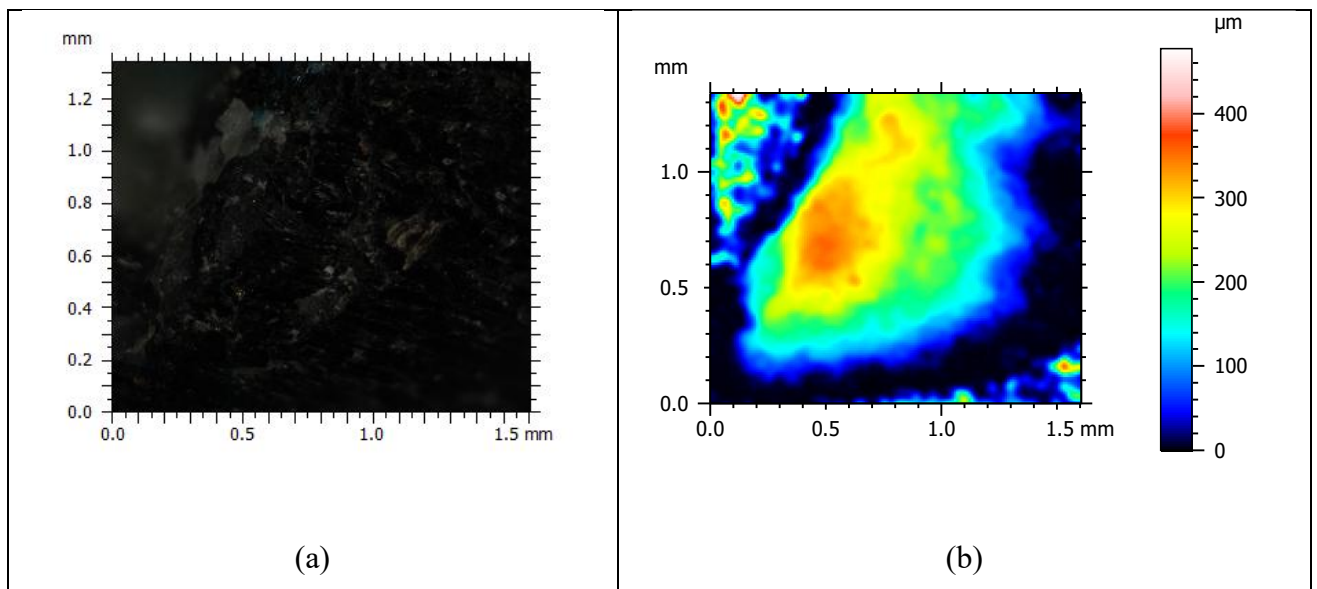
Figure 3.23 Z-stack under microscope (a) and heightmap in ConfoMap7 before apply filters (b)
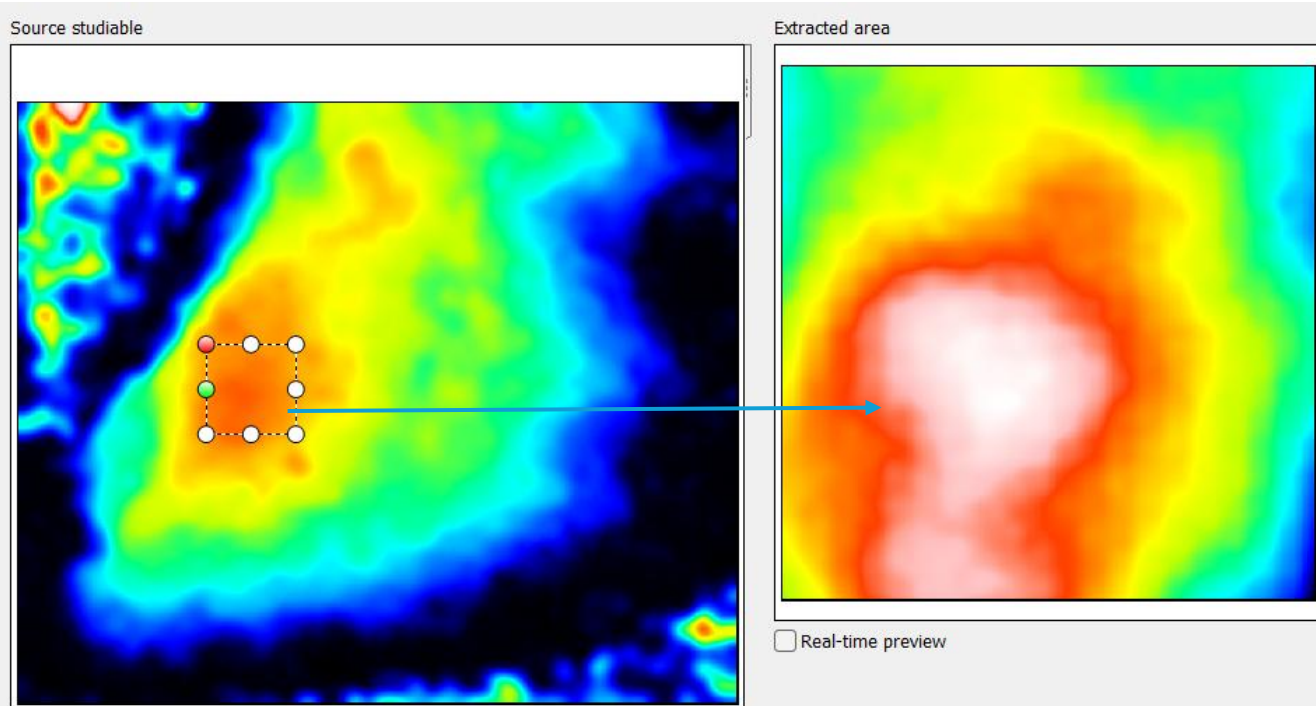
Figure 3.24 Extracted area by 200x200 after applying noise filter (after noise removal)

Parameters	Value	Unit
Length	200	µm
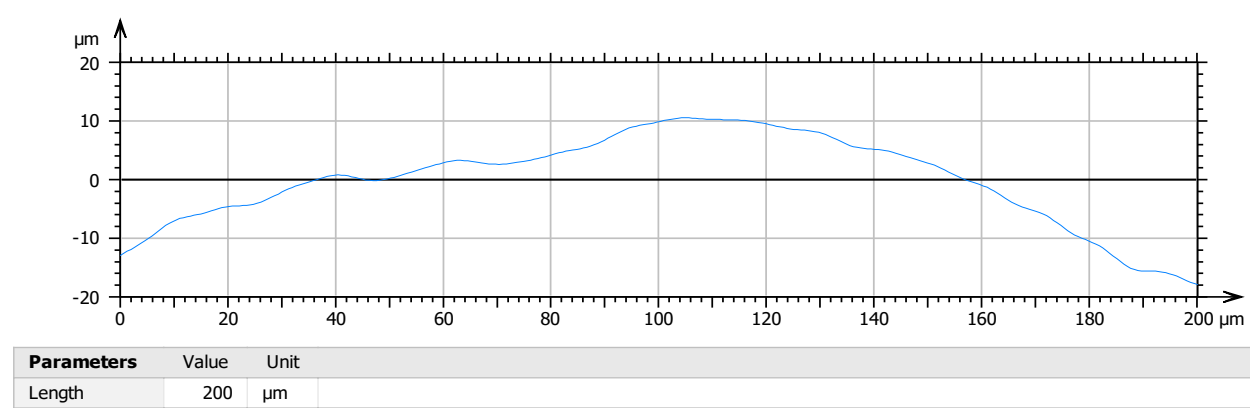
Figure 3.25 Profile of the extracted area by 200x200 after noise removal

Parameters	Value	Unit
Length	200	µm
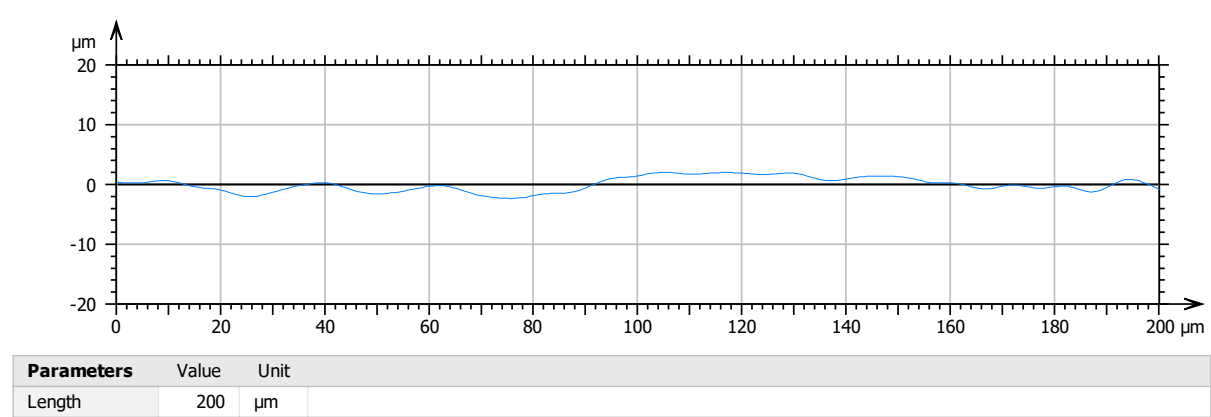
Figure 3.26 Surface profile after removing form with polynomial of degree 9

152

Figure 3.27 Calcite particle after test
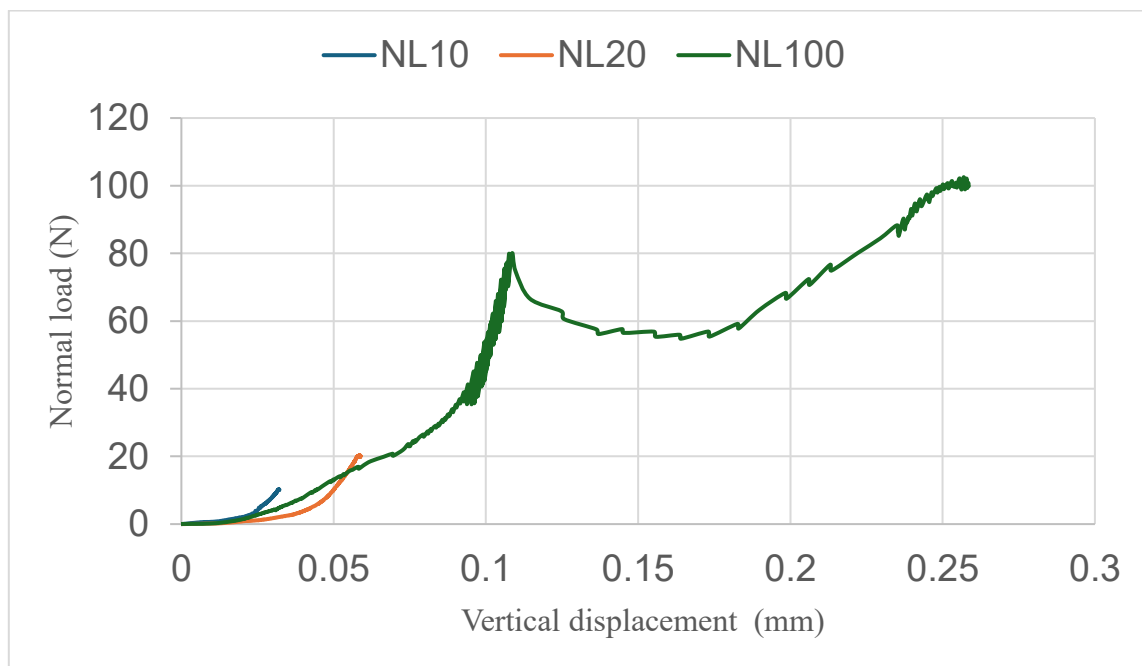
Figure 3.28 Calcite particles force-displacement response of initial tests
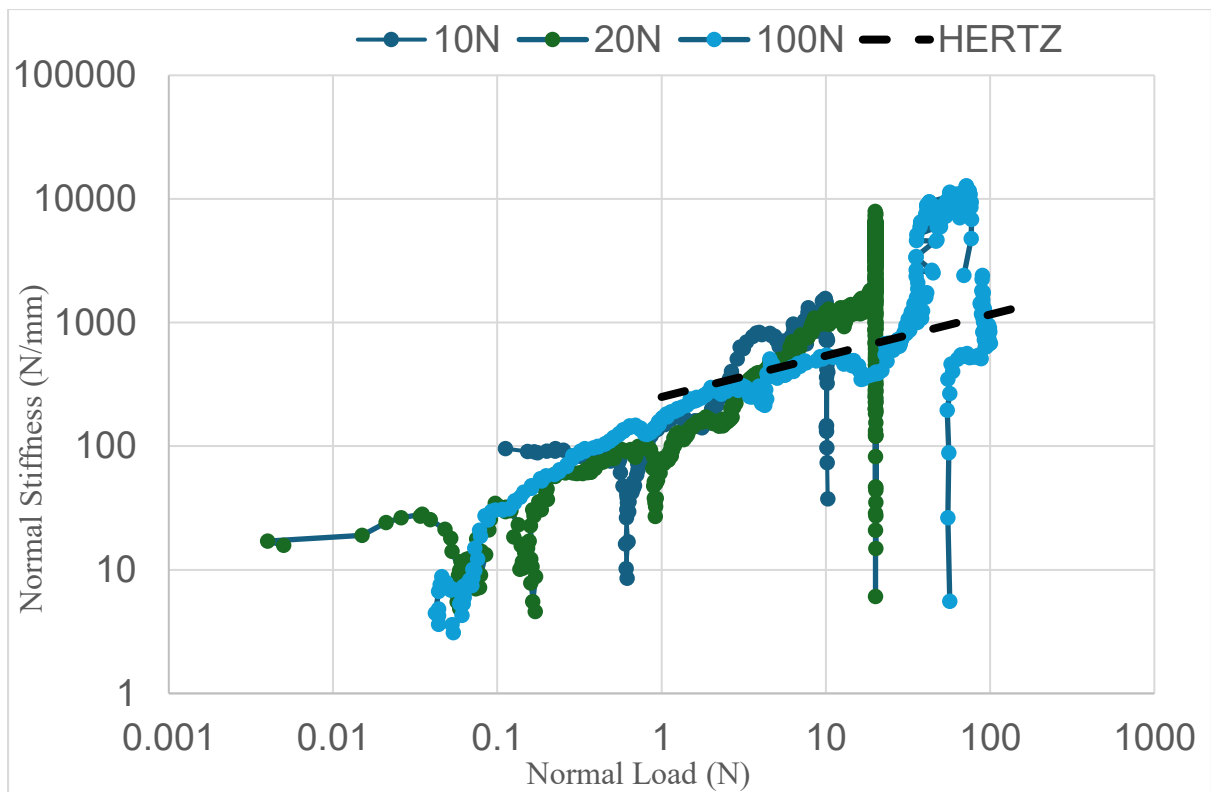
Figure 3.29 Normal stiffness of all loads in comparison to Hertz.
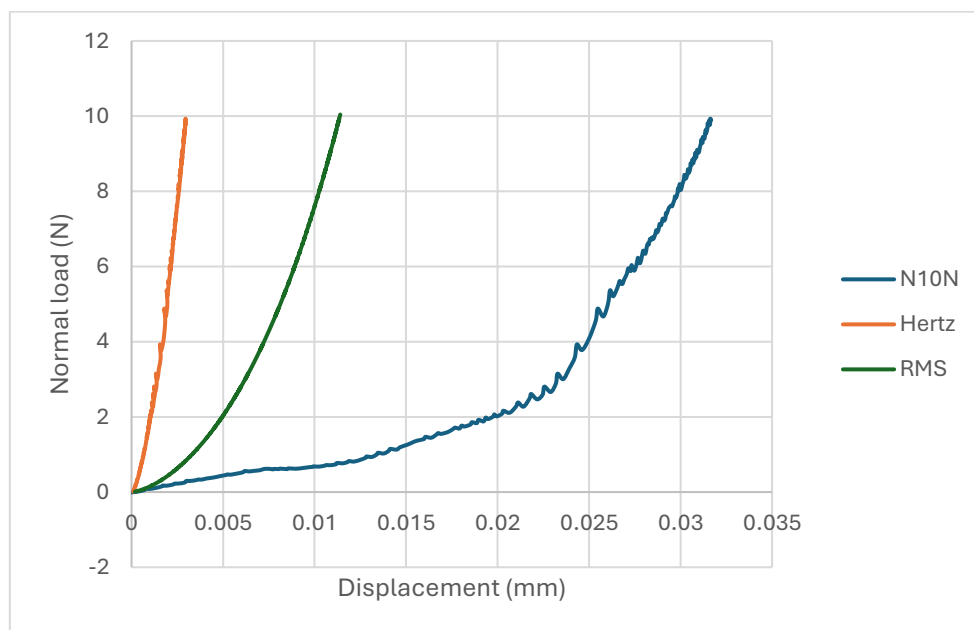
Figure 3.30 Normal loading of 10N data in comparison to Hertz and RMS
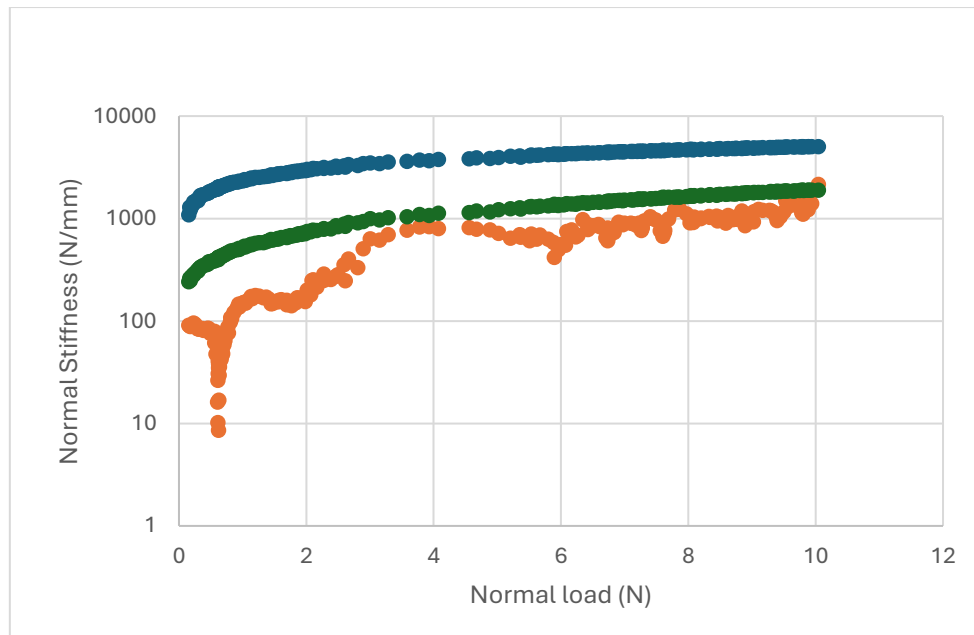
Figure 3.31 Development of normal stiffness in comparison to Hertz and RMS under 10N normal loading
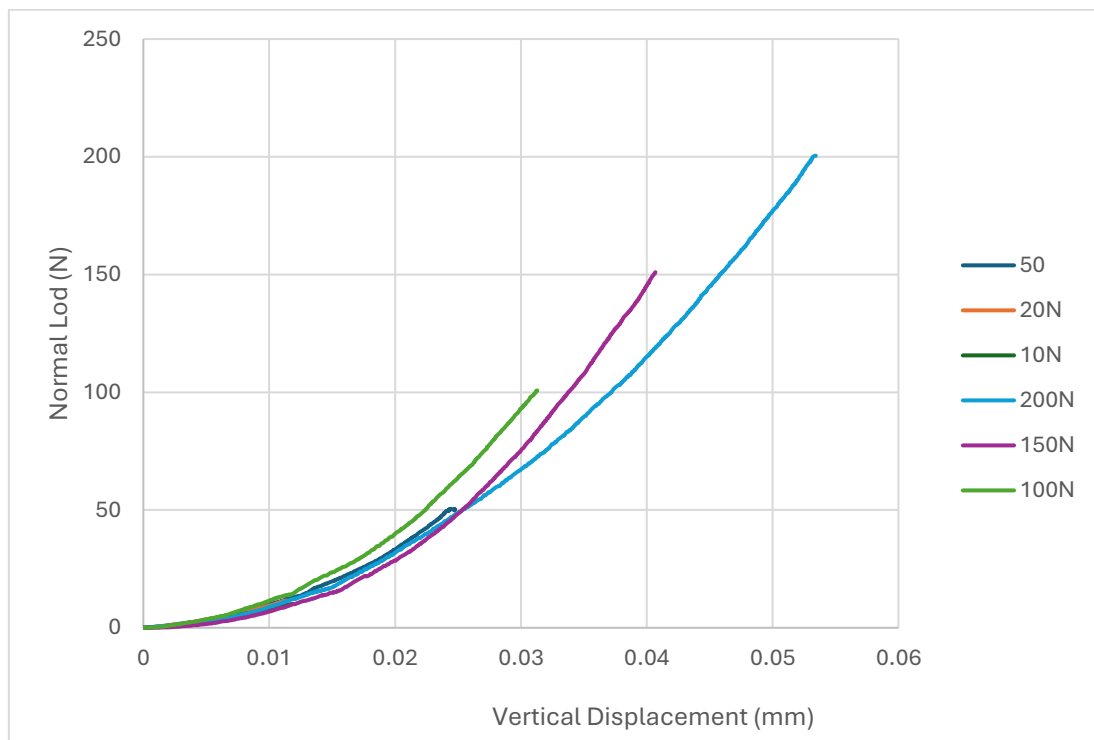
Figure 3.32 Six different normal loads were applied to calcite particles to evaluate their mechanical behaviours
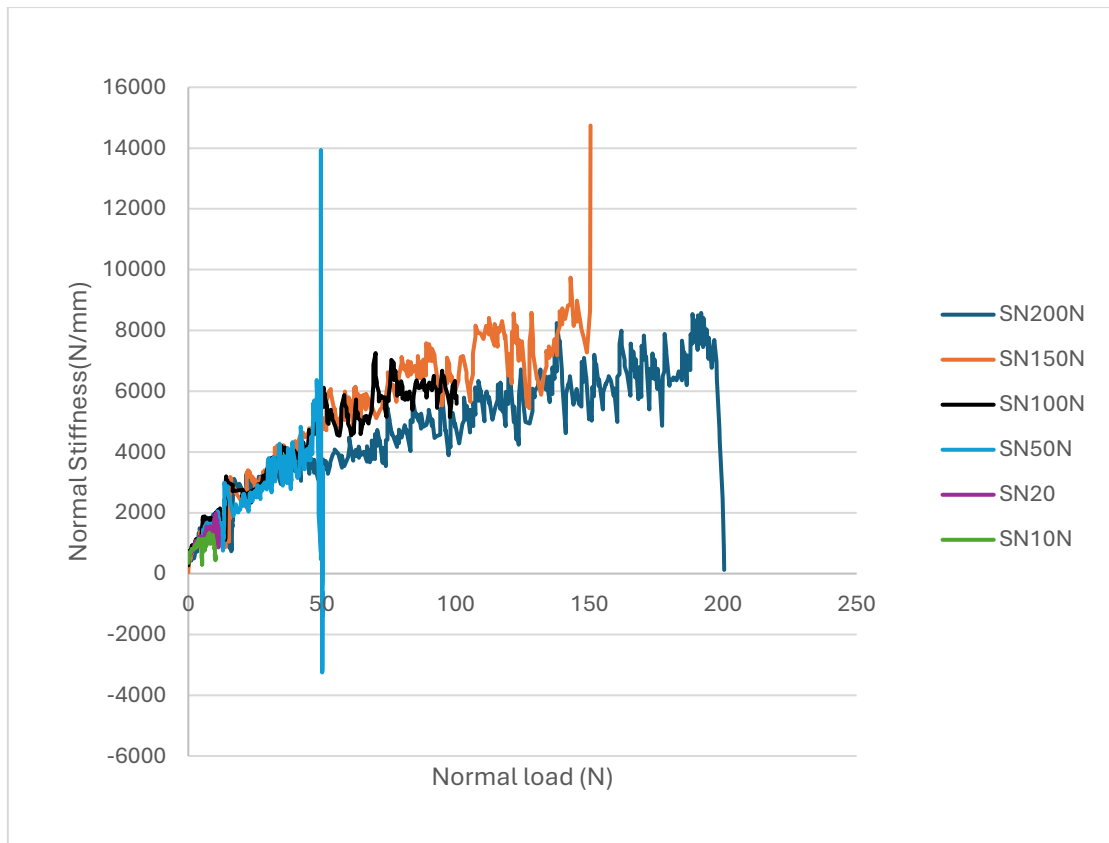
Figure 3.33 Normal stiffness of six different normal loadings on calcite particles
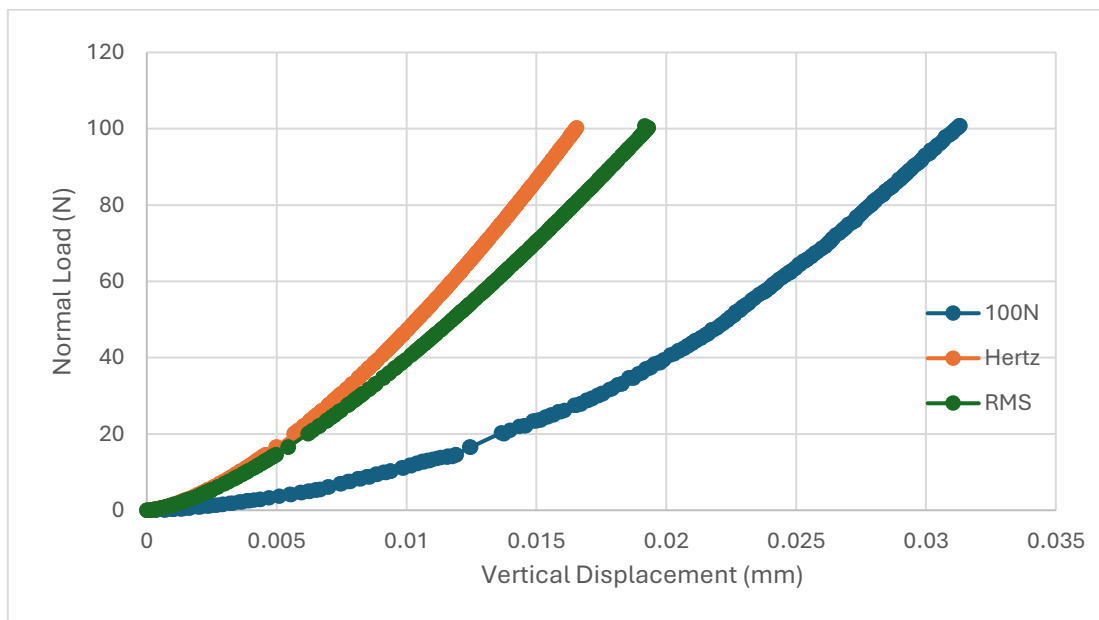
Figure 3.34 Data of normal loading 100N in comparison to Hertz and RMS

156
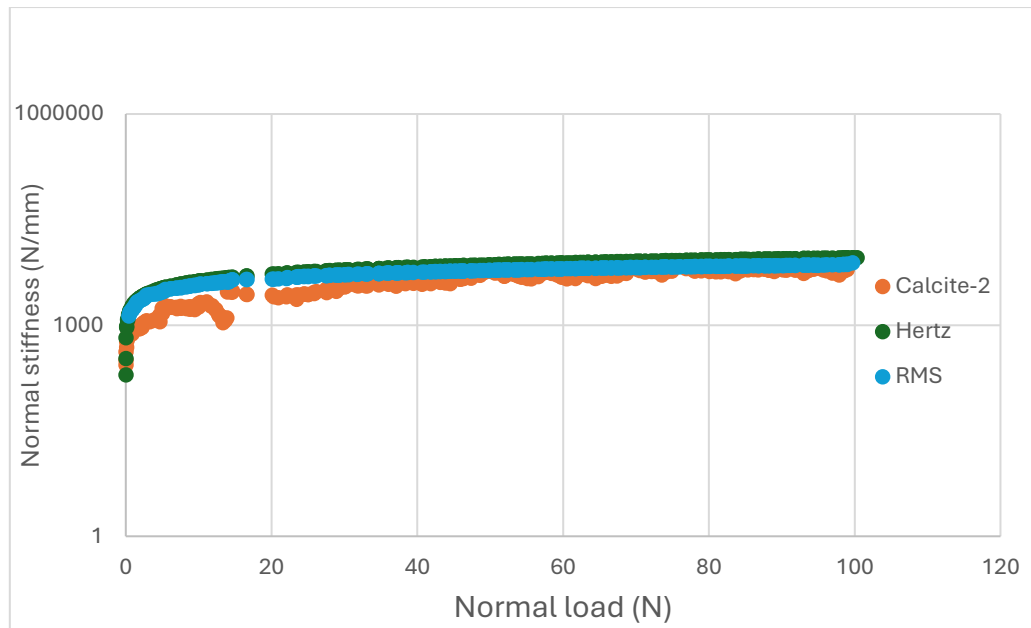
Figure 3.35 Calcite particles stiffness under normal load of 100N in comparison to Hertz and RMS.
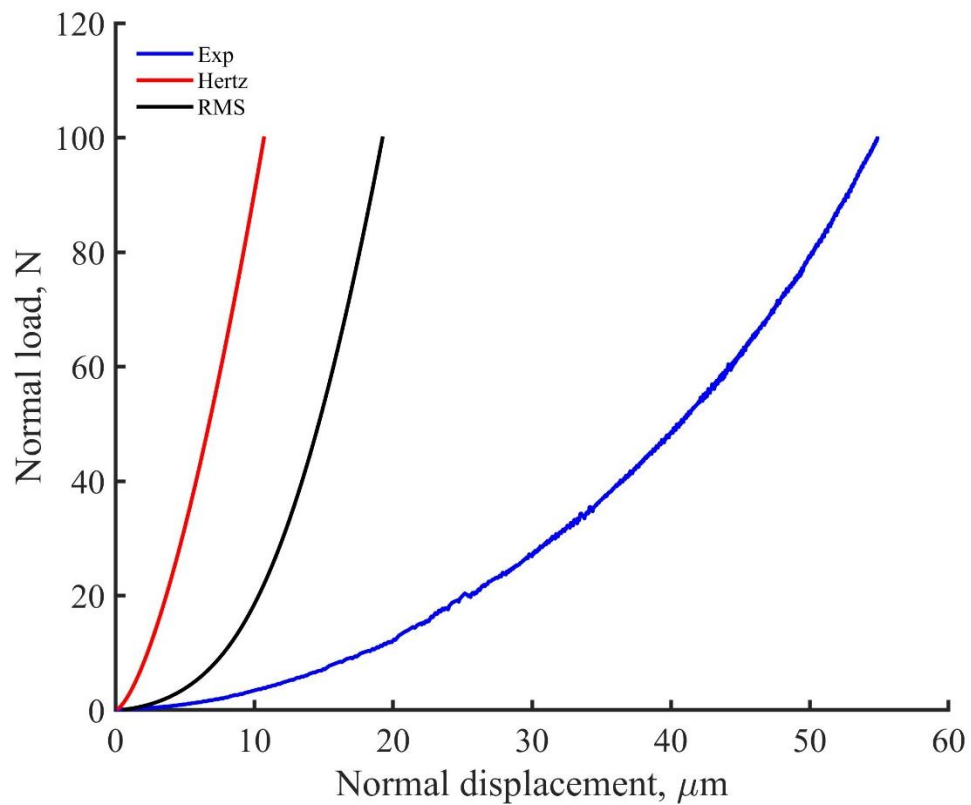
Figure 3.36 A comparison of the basalt particles under a normal loading of 100N with the Hertz and RMS.
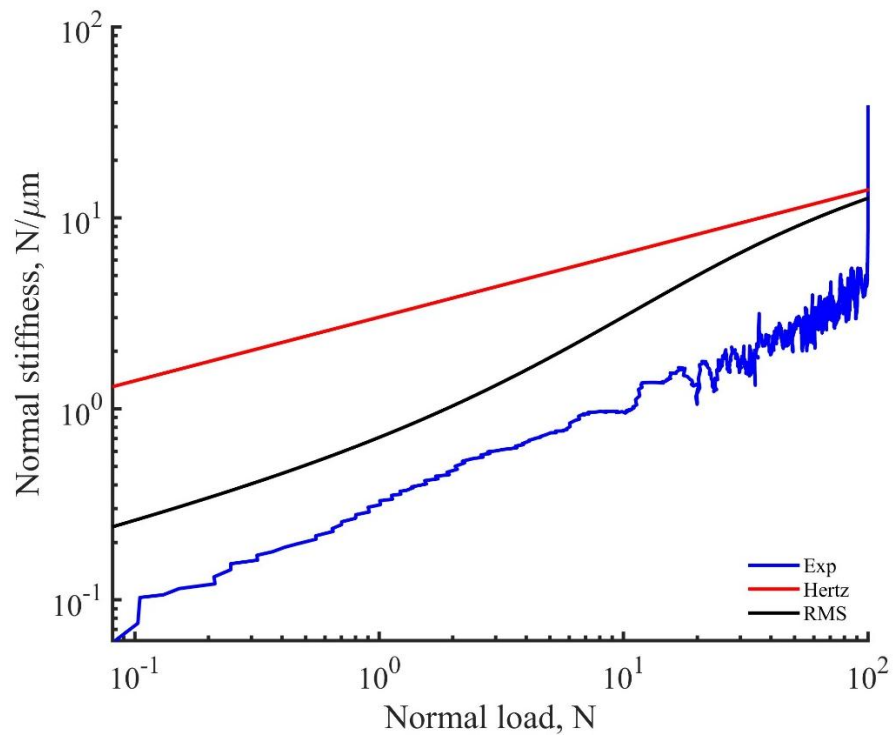
Figure 3.37 Normal stiffness of 100N in comparison with both Hertz and RMS.

Figure 3.38 The apparatus after disassembling for calibration
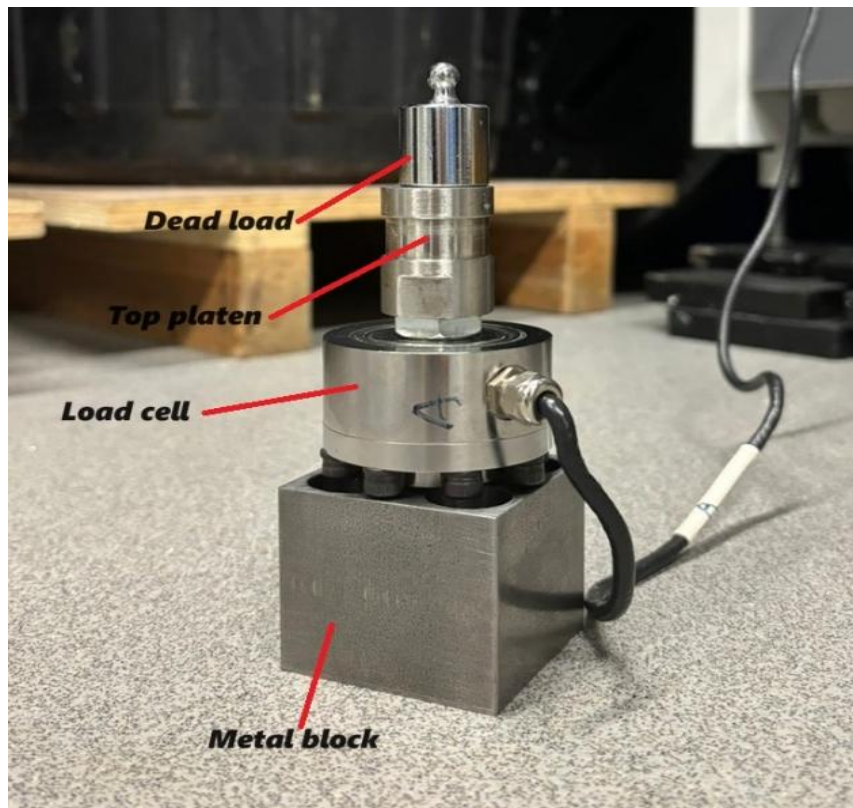
Figure 3.39 Initially small load of 5N applied to load cell.
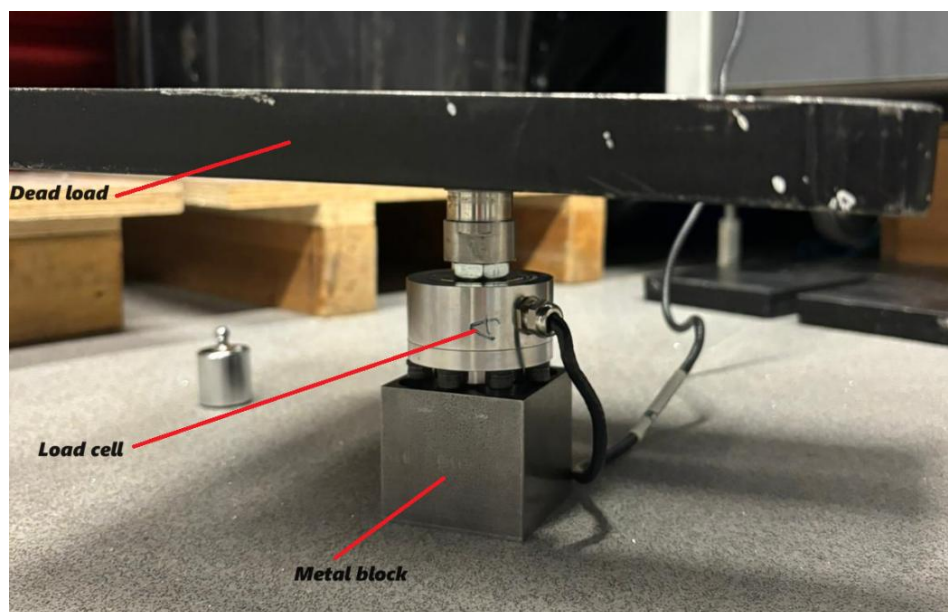
Figure 3.40 Large load of 200N applied to the load cell.
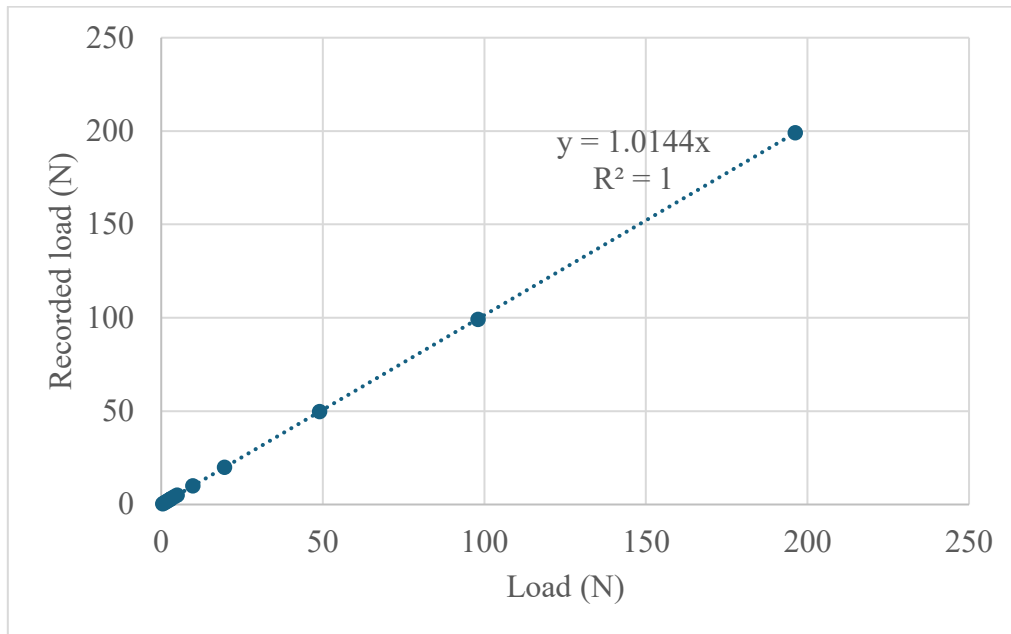
Figure 3.41 Recorded load from the vertical load cell versus applied dead load.
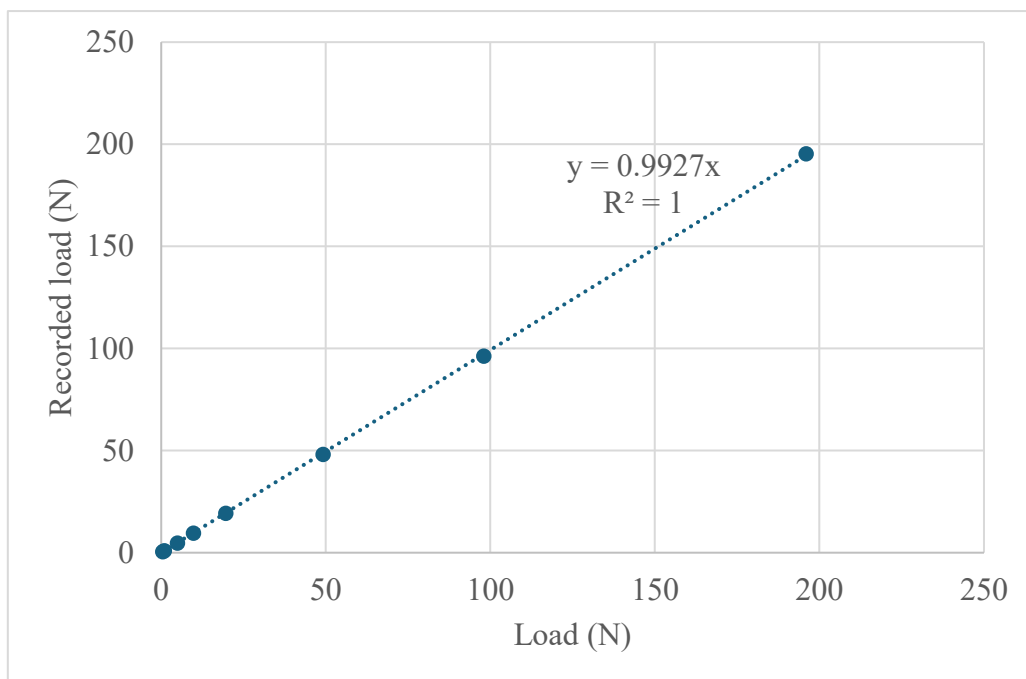
Figure 3.42 Recorded load from the H1 load cell versus applied dead load.
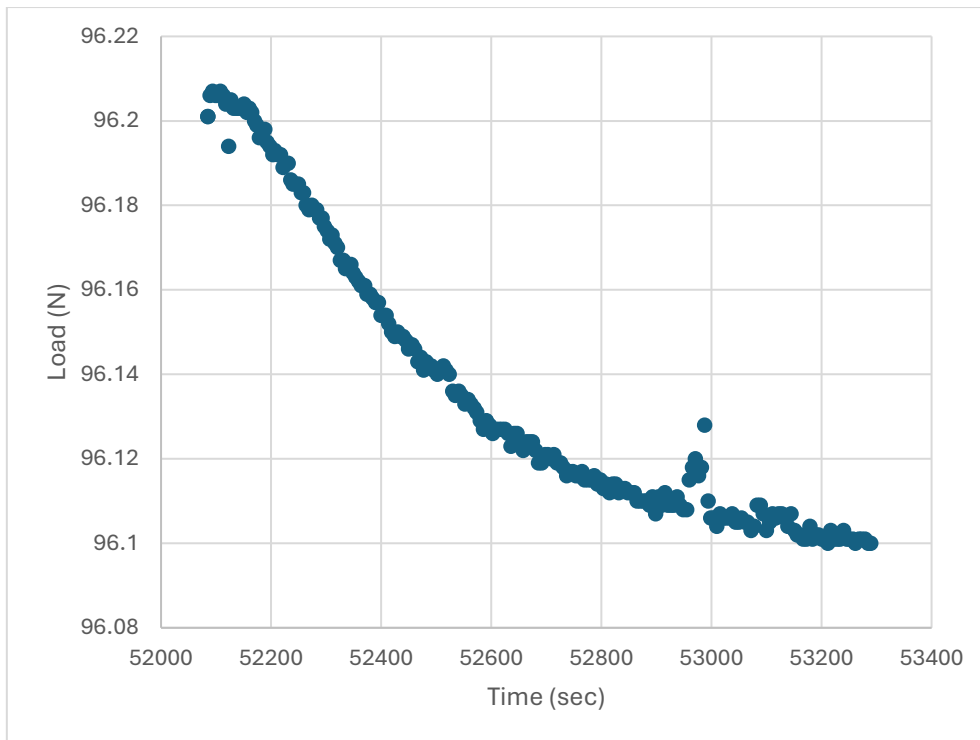
Figure 3.43 H1load cell under load of 10KG for 15 hours.

$$y = 1.0039x$$
$$R^2 = 1$$
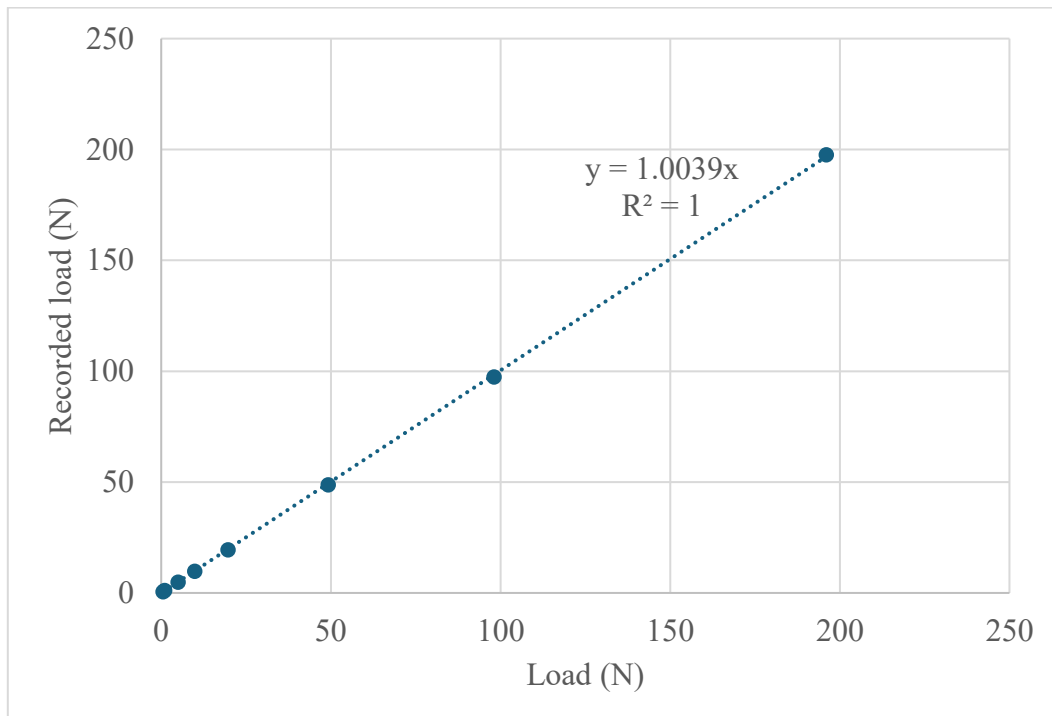
Figure 3.44 Recorded load from the H2 load cell versus applied dead load.
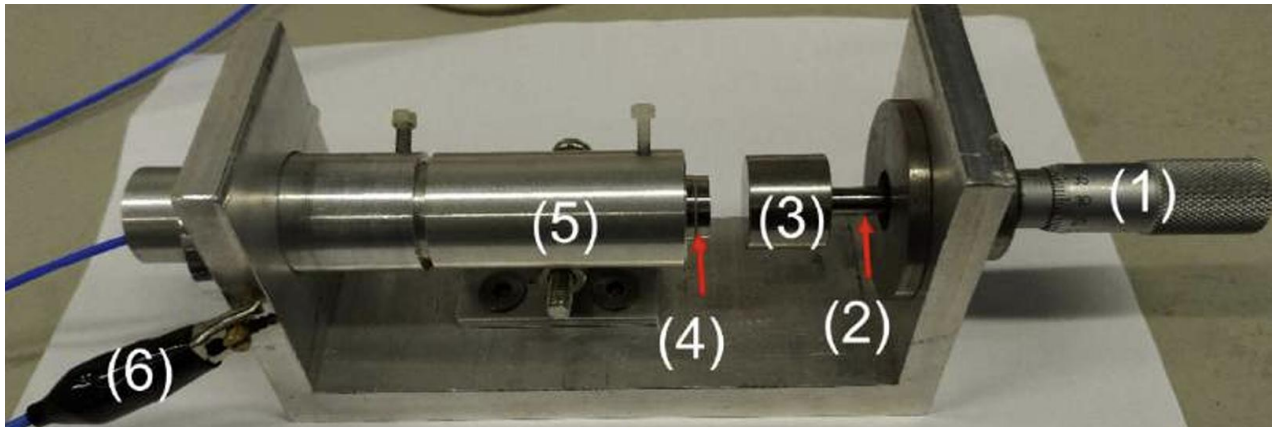
Figure 3.45 Custom-made calibrator for the capacitive non-contact displacement.
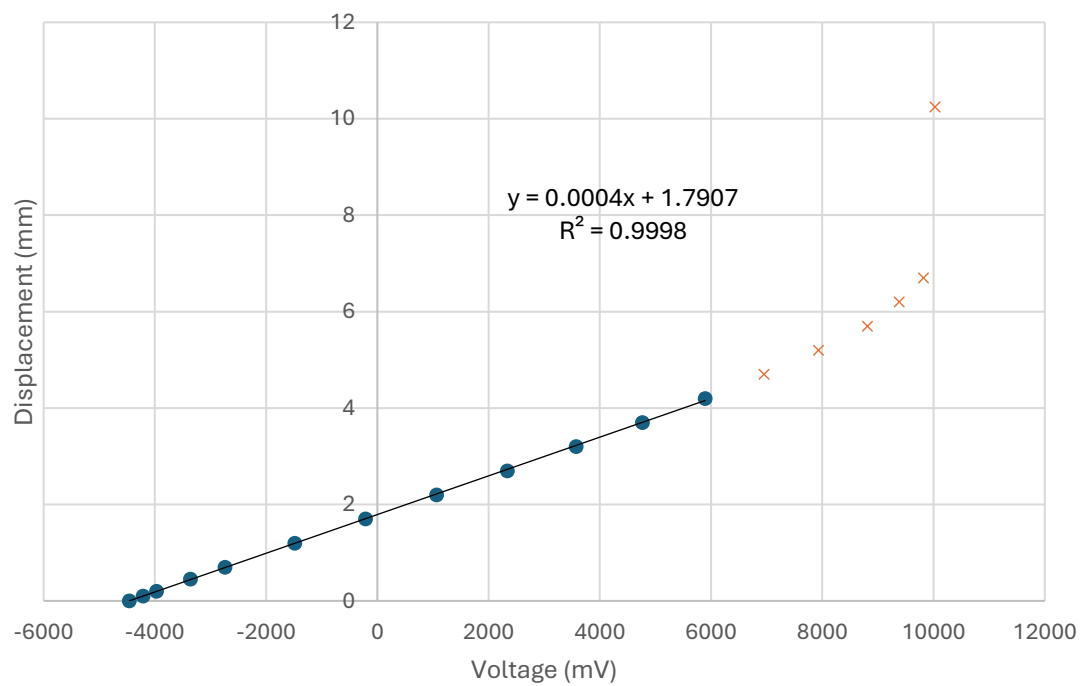
Figure 3.46 Calibration of vertical displacement transducer.
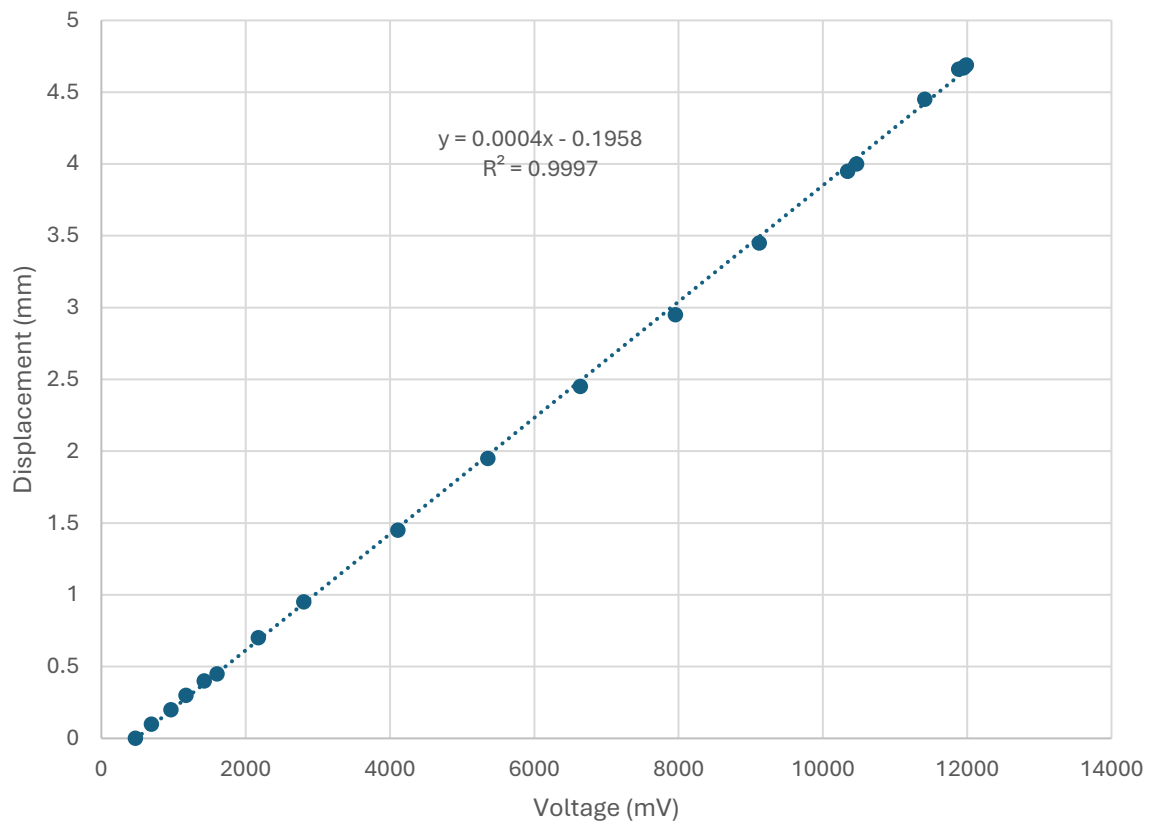
Figure 3.47 Calibration of H1 displacement transducer (new amplifier).
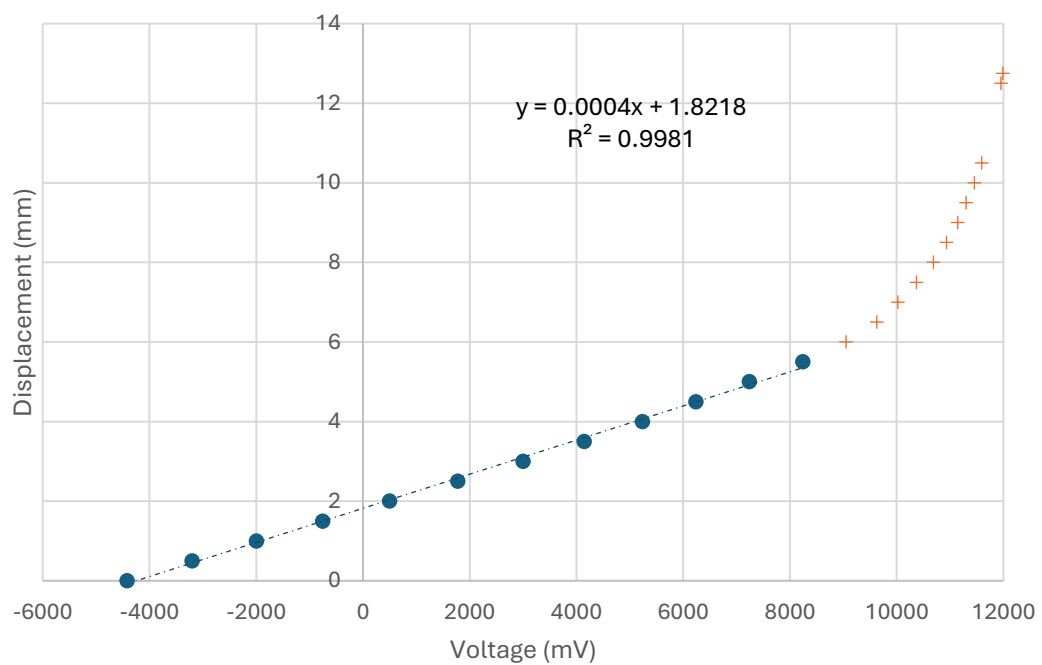
Figure 3.48 Calibration of H2 displacement transducer.

Figure 3.49 The 3-point bearing system to measure friction modified by the author and Dr Saurabh Singh.

4. Normal loading

This chapter is divided into three main sections, each addressing a different aspect of ballast particle testing and analysis.

The first section details the surface quantification of various types of ballast particles before and after testing. Advanced 3D methods and ConfoMap7 software were employed to analyse surface roughness, focusing on parameters such as root mean square roughness (Sq), average roughness (Sa), and fractal dimension (Df). Measurements were taken before initial contact to establish baseline roughness and monitor changes resulting from the tests.

The second section focuses on the contact behaviour under normal loadings (single particle testing and particle-to-particle testing), comparing experimental results with theoretical models. This section includes comparisons with the standard Hertz theory and a modified version of Hertz theory that incorporates roughness (RMS). It also addresses normal loading, examining the diameters of top particles and discussing individual and combined test results for normal stiffness, followed by an analysis of creep behaviour under sustained loading conditions. The last section covers the normal cyclic loading behaviours under different loads.

The chapter concludes with a summary of key findings, highlighting the significance of surface quantification and the implications of contact behaviour under varying load conditions. This summary integrates the results and insights gained from the different sections, providing a comprehensive understanding of ballast particle performance in railway applications.

4.1 Surface Quantification (Roughness)

The surface roughness of sand and ballast particles significantly affects their mechanical behaviour, but measuring this roughness is challenging due to the small size and irregular shapes of particles. Traditional methods include optical microscopy and stylus profilometry while modern techniques involve optical stereoscope (z-stack), laser confocal microscopy, and interferometry as described in the literature review.

In this research, the surface roughness of ballast particles was evaluated from the 3D surface, obtained using a Zeiss microscope or Keyence laser confocal microscope, after removing the

shape using the polynomial removal method (see Chapter 3). Key descriptors such as root mean square roughness (Sq), average roughness (Sa), fractal dimension (Df) and peak counts were evaluated.

Three different methods were used to find the right Sq, Sa and Df (as explained in Chapter 3), after and before the test, as there was no proper guidance on how to use the ConfoMap software. In particular, for railway ballasts, a method needed to be adopted which could be used throughout this PhD research. It was agreed to extract the area 200μm x 200μm just after applying the noise filter, measure the Df, remove the form with the polynomial degree of 9, remove the waviness, and measure the Sq and Sa. The single-particle tests are shown first, followed by inter-particle tests for each type of ballast.

4.2 Single particle testing

A set of single particle tests was carried out on each type of ballast (Andesite, Basalt, Chinese granite and granite from the UK) under normal loads of 1N, 5N, 10N, 20N, 50N, 100N, and 200N to check the difference in the contact area and changes in profile. One test dataset will be shown here.

Loading Procedures

Force was applied to the top platen at a 0.2 mm/hour rate until it reached 1N (displacement control command was used), ensuring precise control over contact force. The contact area radius was calculated by analysing microscope images of the contact imprint. The platen was then unloaded with the same rate (0.2 mm/hour) to capture elastic deformation, and the specimen was rescanned using the Zeiss microscope for earlier tests then the new microscope (Keyence) was used since it was much faster and had a better resolution, to assess deformation and ensure consistent positioning for accurate comparisons. After each loading/unloading cycle, the specimen was cleaned of dust and scanned to document surface changes, allowing analysis of contact area evolution and deformation behaviour under stress. The analysis of the 3D surface also allowed mapping of the deformation.

Stacked images from each load step were processed using ImageJ and ConfoMap to align scans and define contact area boundaries. MATLAB was then used to calculate contact areas and establish load-area relationships (Table 4.1).

4.2.1   Andesite (test AB1)

Chinese andesite ballast (Fig. 4.1a) features rough textures with plagioclase feldspar, pyroxene, and amphibole crystals (Fig. 4.1b). Its mineral diversity and surface roughness enhance interlocking and durability, ideal for railway ballast.

Load-deformation behaviour:

The andesite test (AB1) initially resisted deformation, with minimal displacement up to 20N, as illustrated in Fig. 4.2. As the load increased, the load-displacement curve showed a notable rise, reaching 220 μm at 200N. When compared with models, the data fit well with Hertz and modified Hertz (RMS) during unloading where a curvature of 1.38mm and different roughness were reused in the calculation for each load. As roughness could not be measured during the test, the initial Sq values were used.

A plateau around 100N suggested internal structural changes that allowed more deformation without a corresponding increase in load. Andesite particle approached its structural limit, with a sharp rise in displacement indicating potential failure. This behaviour aligns with Li et al. (2019), who found that microcracks and the material's mineral composition significantly influence load-bearing capacity and deformation under pressure.

Cross-section profile:

Fig. 4.3 illustrates the cross-section profile for andesite in both directions (X and Y), highlighting minimal displacement under low loads, reflecting the material's stiffness and resistance to initial deformation. Between 10N and 50N, the particle exhibited notable plastic deformation, with the profile showing a marked downward shift and reduced peak heights as surface roughness decreased. This transition from elastic to plastic behaviour is evident in the curve, where displacement increases substantially with rising load.

At higher loads (200N), the profile displayed a huge deformation, with peak heights reduced by nearly 150 microns. This indicated extensive plastic deformation and surface flattening, suggesting major internal structural changes, with the material nearing its load-bearing capacity.

Contact area:

Fig. 4.4 illustrates a smooth, linear relationship between load and contact area for the andesite particle, indicating a consistent and uniform deformation under increasing normal loads. This linearity suggests that the material's response is predictable, with deformation evenly distributed across the contact surface. Such behaviour highlights the andesite's unique balance of surface roughness and intrinsic material strength, which allows it to adapt to and accommodate higher loads without abrupt structural failure.

The gradual increase in contact area with rising load demonstrates the particle's ability to maintain integrity while redistributing stress, a characteristic differentiating it from more brittle materials. This combination of roughness and strength likely prevents sudden fractures, instead promoting controlled plastic deformation. Consequently, andesite proves effective in load-bearing applications where resilience and adaptability to stress are critical.

4.2.2 Basalt

The Australian basalt ballast (Fig. 4.5a and b) comprises plagioclase, pyroxene, olivine, and iron oxides, giving it a dense texture and dark colour. While generally strong, olivine increases brittleness (Winter, 2010; Boggs, 2009).

Load-deformation behaviour:

The load-displacement curve (Fig. 4.6) highlights basalt's tendency for an abrupt transition to plastic deformation. This is evident from the rapid increase in displacement after reaching peak load, likely due to the propagation of microcracks within the material under stress, as observed by Yang et al. (2023). At lower loads, the basalt ballast displayed minimal displacement, reflecting its initial stiffness. The plastic deformation is evident at approximately 200N, with a displacement of nearly 90 μm; however, this displacement was much lower than the andesite, for the same normal load. Unloading of basalt for higher loads is well fitting with the Hertz and RMS models, but at lower loads diverges from the models.

Cross-section profile:

Fig. 4.7 shows the profile reduction, which is minimal at low loads (between 1N to 10N), highlighting the basalt's stiffness. Between 20N and 50N, plastic deformation becomes evident, with the surface profile decreasing significantly by almost 20 μm along both axes. At higher loads (200N), deformation peaks, with an 80-90 μm reduction in height, indicate surface

flattening and nearing the material's load-bearing limit, which was much less than andesite.

Contact area:

At lower loads (1N to 50N), the contact area for basalt particles is small, typically under 0.1 mm² (Fig. 4.8), as only the highest surface asperities make contact. As the load increases, the rate of contact area growth varies among basalt and andesite particles. Basalt exhibits a gradual increase in contact area, reaching about 0.36 mm² at 200N. The relationship between load and contact area is nearly linear, similar to andesite, though basalt maintains a slightly smaller overall contact area than andesite.

4.2.3 Fresh granite

Fig. 4.9a shows granite (UK) in nature and under the microscope with a magnification of 10x (Fig. 4.9b).

Load-deformation behaviour:

The granite ballast exhibits minimal displacement under low loads (1N to 10N), showing greater resistance to deformation compared to andesite and basalt (Fig. 4.10). As the load increases (50N to 200N), noticeable displacement occurs, marking the onset of plastic deformation, similar to observations for andesite and basalt. The steep slopes in the load vs. displacement curves at higher loads indicate the samples nearing their structural limits and potential failure, consistent with findings by Mendoza-Chavez et al. (2012). Displacement at 200N for granite (125 µm) was lower than andesite (220 µm) but higher than basalt (90 µm) under the same normal load. During unloading at higher loads, the results align with Hertz and RMS models; however, deviations appear as the load decreases.

Cross-Section Profile:

Fig. 4.11 illustrates that the granite surface profile reduces as the load increases, with minor compression under low loads (1N to 10N), indicating elastic behaviour with minimal deformation. At moderate loads (50N to 100N), plastic deformation became evident, with peaks reducing and asperities collapsing. Higher loads (200N) caused significant flattening, with peak heights decreasing by nearly 100 µm, indicating extensive plastic deformation.

Contact Area:

Fig. 4.12 illustrates that at low loads (1N–5N), contact areas were minimal (0.06 mm²). For granite, the contact area increased linearly, reaching 0.36 mm² at 200N, similar to basalt but lower than andesite (0.55 mm²) under the same load. This behaviour indicates uniform

surface roughness and proportional load-to-contact area expansion, aligning with Røyne et al. (2015). Granite's contact area at 200N reflects its efficient stress distribution and notable load-bearing capacity through gradual surface compression.

In conclusion, the load-displacement curves for granite, basalt, and andesite show clear phases of deformation. Initially, all three materials behave elastically, meaning they resist deformation and return to their original shape when the load is removed. This elastic phase is marked by a linear relationship between load and displacement (e.g. insertion Fig.4.10). As the load increases, all materials enter a plastic phase, where permanent deformation occurs. Basalt shows a quicker transition to plasticity, with rapid displacement at higher loads, while granite and andesite exhibit a more gradual shift. During unloading at higher loads, all ballast results align with Hertz and RMS models; however, deviations appear as the load decreases for granite and basalt.

In terms of contact area, all ballast materials show a linear increase as the load rises, indicating that their rough surfaces are compressing to bear more load. At 200N, granite's contact area reaches 0.36 mm², similar to basalt, but much lower than andesite (0.55 mm²).

The cross-sectional profiles further confirm these findings, as the load increases, the profiles flatten, with andesite undergoing more significant deformation compared to basalt and granite. This indicates that andesite undergoes more compression and surface flattening under stress.

Overall, basalt and granite show the highest resistance to deformation and have a better capacity to distribute stress efficiently compared to andesite, making them more durable materials under normal load.

4.3 Inter-particle normal loading

Recent studies have shown that the surface roughness of sand particles significantly affects their contact behaviour and inter-particle friction (Altuhafi et al., 2024). This is important because these properties influence the overall load-bearing capacity of the material.

To better understand the behaviour of sand and ballast, researchers have been using advanced experimental techniques and computer simulations. These studies have revealed that traditional elastic models are often insufficient to accurately describe the contact behaviour of these materials. It is important to identify the significant micro-mechanical deformation

mechanisms of granular materials and employ or develop contact laws that reflect the actual material behaviour to obtain a reliable, discrete element analysis. This section will cover the experimental behaviour of normal loads with comparison to some theoretical models such as Hertz and the modified Hertz model (RMS).

At the beginning of this research, normal loading tests were carried out at different rates (speeds). It was subsequently decided to adopt a consistent loading rate for all materials to ensure comparability of results throughout the study. The agreed-upon rate was set at 150 mm/hr, reduced from the initial 300 mm/hr. Applying the load too slowly was found to cause creep, which could compromise the accuracy of the results. Therefore, it was determined that the loading rate should not be slower than 150 mm/hr. On the other hand, applying the load too quickly resulted in significant breakage of asperities during contact, leading to poor control over the experiments. Consequently, a loading rate of 150 mm/hr was established as an optimal balance, preventing creep while minimising asperity breakage. This consistent rate ensures reliable and comparable results across all ballast materials tested throughout the PhD research. All the tests presented in the following were performed on the flat-to-angular particle contact.

4.3.1   Andesite ballast

Individual test (AB-150N)

Test AB-150N initially exhibited a softer response and then stiffened at larger loads, Fig.4.13 illustrates how the response curve steepens steadily as the load increases in the load-displacement test, under a normal load of 150N. The data show that normal loading follows a line and there is regular breakage of asperities as the load increases. As the load increased, AB-150N displayed a noticeable rise in displacement, reaching approximately 90μm. A plateau observed at around 60N indicates internal structural changes that allowed the material to deform more without a corresponding increase in load. This behaviour is consistent with findings from Li et al. (2019), who studied the mechanical properties of thermally cracked andesite under pressure.

Furthermore, Nardelli and Coop (2019) and Wong and Coop (2024) observed that the initial portion of loading was soft compared to the larger displacement behaviour, which is in line with this study.

Stiffness and displacement have a linear relationship, as illustrated in Fig. 4.14 It was found that particles initially have small stiffness but then simply increase. This demonstrates that the normal stiffness increases with the normal load, as predicted by Hertz's (1882) theory and Yimsiri and Soga (2000).

Combined tests data

A total of five tests were carried out on andesite ballast which is illustrated in Fig. 4.15 and the curvatures (R) and roughness (Sq) of all the particles that have been tested are given in Table 4.2. There are many breakages of asperities happening during the tests (for all tests) which indicates that the andesite is very rough and has many peaks. As the load increases the normal displacement increases and it can be said that vertical displacement is dependent on normal load. Test AB-200N-1 (under normal load of 200N) shows completely different behaviour after reaching 100N, where the load dropped gradually reaching around 80N while the displacement was increasing, at 0.2 mm vertical displacement it increased back again. Similar behaviour was seen for test AB-050N (under normal of 50N), after reaching normal load of 30N then increased and then drooped again.

Figure 4. 16 shows, a linear relationship between stiffness and displacement, indicating that stiffness initially starts low and then increases with displacement. This aligns with the predictions of Hertz's theory (1882) and with Yimsiri and Soga (2000). The impact of normal load on stiffness is not evident: for instance, at 10N, the stiffness values vary among particles despite theoretical expectations of uniformity. This discrepancy could be from differences in particle shape and the specific contact points during loading, suggesting that the mineralogy and mechanical properties of ballast particles significantly influence normal stiffness. Tests under normal load of 100N, 150N and 200N exhibit similar normal stiffness which is around 3N/µm. Wong and Coop (2024) suggested that normal stiffness is dependent on normal loads for fresh granite from the UK and the normal stiffness values were higher than andesite.

4.3.2 Basalt ballast

Around 30 tests were conducted on basalt ballast from Australia. Most of the earlier tests were ignored due largely to inconsistencies (different rates, different methods of measuring the curvature, not applying correction and not adding loads from H2 and H1). Out of all the tests 11 tests were selected and the results are presented here.

Individual test

Test BB-100N-1 (under normal load of 100N) exhibited a similar response as andesite, softer at the start and then stiffened at higher loads. Figure 4.17 illustrates how the response curve becomes steeper (after 80N) as the load increases in the load-displacement test. The data show that normal loading follows a consistent pattern, with some asperity breakages as the load increases however the breakage is much less in comparison to the andesite. At 12 µm displacement, a plateau is noticed, suggesting that basalt deformed further without a significant increase in load.

A linear relationship between stiffness and load becomes evident (Fig. 4.18). Initially, particles display low stiffness, which then increases steadily. This trend supports Hertz's theory (1882) and findings by Yimsiri and Soga (2000), which state that normal stiffness increases proportionally with the applied normal load.

Nardelli and Coop (2019), as well as Wong and Coop (2024), similarly observed that initial loading often exhibits a softer response, which becomes stiffer with increasing displacement. This observation is consistent with the findings in the current study for basalt and andesite.

Combined Test Data

Curvatures (R) and roughness (Sq) for all tests on basalt are listed in Table 4.3, which were later used for the model predictions. Fig. 4.19 shows that frequent asperity breakages are seen throughout all tests, indicating that basalt, like andesite, however, the breakage is not large like what was noticed for andesite, except for test BB-150N after reaching 20N, the load gradually dropped to around 15N while the displacement continued to increase. At 25µm vertical displacement, the load began to rise again. As the load increased, so did the normal displacement, indicating a dependence of vertical displacement on normal load. It was found that tests with similar loads such as BB-200-1 and BB-200N-2 were giving different displacements. Also, for tests under normal loads of 100N, the deformation was different, so it can be concluded that load is not the only parameter that affects the deformation, there could be other factors such as the curvature of the particles.

Furthermore, when unloading was carried out (test BB-100N-Un100N) it was found that unloading didn't follow the loading path. It could be due to the smoothing surface and unloading being plastic.

Figure 4.20 shows the linear relationship between stiffness and load indicating that stiffness starts low but increases with load, consistent with predictions from Hertz's theory (1882). The influence of normal load on stiffness appears inconsistent, similar to what was noticed for andesite; however, the inconsistency was much less. Furthermore, basalt displays slightly higher stiffness values than andesite under the same loads, for example, tests under a normal load of 200N for basalt show stiffness of 8N/µm while andesite 3N/µm. Wong and Coop (2024) observed that granite from the UK has higher normal stiffness values than andesite and basalt. This highlights the influence of mineral composition and roughness in the deformation properties of ballast materials, with basalt demonstrating moderate stiffness between that of andesite and granite.

4.3.3   Chinese granite ballast

At least 10 tests were carried out on Chinese granite and only 7 tests with good data are presented here.

Individual test

Figure 4.21 illustrates the load-deformation behaviour of test CB-200N (normal load of 200N), which initially (under 5N) exhibited a remarkably softer response compared to andesite, basalt, and the granite tested by Wong and Coop (2024). As the load increased, the contact stiffness also increased, aligning with the behaviour observed in the andesite and basalt. After a 5 µm displacement, the response curve steepened, with fewer asperity breakages than in andesite and basalt, except around 150N, where a distinct breakage of asperities was noted. Figure 4.22 also shows a linear relationship between load and stiffness, consistent with Hertz's (1882) theory, which suggests that stiffness increases with load. Under the same 200N load, the stiffness of Chinese granite (20 N/µm) was substantially higher than that of basalt (8 N/µm) and andesite (3 N/µm).

Combined Test Data

Table 4.4 presents the contact curvatures and roughness for all tests conducted on Chinese granite. Asperity breakage was minimal for Chinese granite (Fig. 4.23), except in test CB-100N-2, contrasting with the more frequent breakages observed in andesite and basalt. During unloading (CB-200N-Un200N), the path diverged from the loading path, likely due to

surface smoothing; however, the slope during normal loading was significantly steeper than in other tests.

Chinese granite demonstrated considerably higher stiffness (Fig. 4.24) than basalt and andesite, reaching a stiffness of 20 N/µm under a normal load of 200N. This is higher than the stiffness values for granite reported by Wong and Coop (2024) under similar conditions, highlighting the influence of mineral composition and surface roughness. Among these materials, Chinese granite exhibited the highest stiffness, followed by basalt, then andesite. Notably, the expected relationship between normal load and stiffness was not observed in Chinese granite too, as tests under lower loads (20N and 50N) showed higher stiffness than those under a 100N normal load. However, tests under normal loads of 200N demonstrated higher stiffness, and there was minimal difference between loading and unloading stiffness values, both remaining nearly the same.

4.3.4   Fresh granite ballast

This is the same type of granite ballast that was tested by Wong and Coop (2024). The main difference will be the rate and the correction to normal load that was not done previously by Wong and Coop (2024). Table 4.5 provides the contact curvatures and roughness values for all tests conducted on fresh granite.

Individual test

The data of load-deformation behaviour for test GB-100N is illustrated in Figure 4.25 which initially exhibited a very soft response approximately after 2N till 15N and the particle deformed a lot about 40 µm and this behaviour was not seen for other ballasts. This makes fresh granite the softer material when the response is compared to andesite, basalt, and granite tested by Wong and Coop (2024). The response curve steepened consistently after a 40 µm displacement, with fewer asperity breakages than observed in Chinese granite, andesite and basalt. The large displacement could be due to early breakage of the small asperities broken under the small normal load.

As the load increased, contact stiffness improved, becoming similar to that of Chinese granite, andesite and basalt. Figure 4.26. shows a linear relationship between load and stiffness, aligning with Hertz's (1882) theory, which predicts that stiffness increases with load. Under the same normal load of 100N, fresh granite (5 N/µm) exhibited a slightly higher stiffness than andesite (3 N/µm) Chinese granite (2 N/µm) and basalt (4 N/µm).

Combined Test Data

Asperity breakages were generally higher in fresh granite in this study (Fig. 4.27) compared to the same type of granite ballast tested by Wong and Coop (2024), except for test GB-50N-2. These regular breakages were observed in andesites too, indicating that both types of ballasts have relatively less resistance to surface wear. Notably, the slope of GB-50N-2 was steeper than observed in other tests.

Fresh granite demonstrated significantly higher stiffness (Fig. 4.28) than andesite and slightly lower stiffness than basalt and Chinese granite. This underpins the impact of mineral composition and surface roughness on ballast stiffness, with fresh granite displaying intermediate stiffness—higher than andesite but lower than basalt and Chinese granite. Interestingly, the expected correlation between normal load and stiffness was not consistently observed in fresh granite, as a test under lower loads 50N displayed higher stiffness than those conducted under higher normal loads (100N, 200N), also GB-100N exhibited similar stiffness as GB-200N. This suggests that factors such as particle curvature and contact specifics may influence stiffness independently of normal load as found for other ballasts too.

4.3.5 Used granite ballast

Individual test

Test UG-100N under a normal load of 100N on used granite which is illustrated in Figure 4.29, exhibited a response similar to that of fresh granite, starting softer and then stiffening as the loads increased. The data indicate a consistent pattern in normal loading, with some asperity breakages occurring at approximately 8 and 48 μm displacement; however, these breakages were significantly less compared to those observed in fresh granite as well as other types of ballasts.

Upon examining the log-log plot, a linear relationship between load and stiffness becomes evident (Fig. 4.30). Initially, the particles display low stiffness, which then increases steadily. This trend supports Hertz's theory (1882) and findings by Yimsiri and Soga (2000), indicating that normal stiffness increases proportionally with the applied normal load. Wong and Coop (2024) similarly observed that the initial loading phase often exhibits a softer response that becomes stiffer with increasing load. This trend was seen in fresh granite and

other ballasts; however, the stiffness of used granite (8 N/µm) is higher than fresh granite (5 N/µm) for the same normal load (150N).

Combined Test Data

The combined test data for used granite is shown in Fig. 4.31. Less frequent asperity breakages throughout all tests indicate that used granite, like basalt, experiences fewer breakages; however, these were not as pronounced as those seen with andesite and fresh granite. Notably, in test UG-200N, after reaching a load of 60N, the load did not increase much while displacement continued to increase, however, the load began to rise again at the vertical displacement of 50 µm. As the load increased, so did the normal displacement, suggesting that vertical displacement is dependent on the normal load, which was seen for fresh granite as well as other type of ballasts.

During unloading (test UG-100N-Un100N), it was noted that the unloading path did not follow the loading path similarly to basalt and Chinese granite, which is likely due to surface smoothing. Figure 4.32 illustrates the linear relationship between stiffness and load, indicating that stiffness starts low but increases with load, consistent with Hertz's theory (1882). The influence of normal load on stiffness appears inconsistent, similar to what was observed for other ballasts, though the variability was less pronounced in this case. Furthermore, used granite displayed slightly higher stiffness values than fresh granite under the same normal loads (100N, 150N and 200N), for instance, tests under a normal load of 200N yielded stiffness values of 10N/µm while fresh granite 5N/µm exhibited 8N/µm for basalt compared to 3N/µm for andesite.

4.3.6 Washed used granite ballast

These ballasts are the same as used granite ballast but have been washed and some of them are treated, to see the difference between the washed and unwashed used granite. Also, the result will be compared with fresh granite as well as used granite.

Individual test

Figure 4.33 shows the load-deformation behaviour for test WUG-150N on washed used granite under a normal load of 150N, displaying an initially soft response, similar to fresh granite but less soft than used granite, that stiffened with increasing load. There is much less spherite breakage than in fresh granite, used granite and other ballasts. The log-log plot reveals a linear relationship between stiffness and displacement (Fig. 4.34), consistent with Hertz's theory (1882) and Yimsiri and Soga (2000), indicating that stiffness increases with load. Wong and Coop (2024) also observed this pattern, although washed used granite's stiffness (7 N/μm) was slightly lower than used granite (7 N/μm) but higher than fresh granite's (5 N/μm) at 150N.

Combined Test Data

Combined test data in Figure 4.35 shows that washed used granite had minimal asperity breakages compared to fresh granite and andesite, similar to basalt, except for one test (WUG-100N), where some asperity breakage is seen. Stiffness generally rose with load (Fig. 4.36), matching Hertz's theory, and remained slightly higher than in fresh granite across normal loads of 100N, 150N, and 200N, with WUG at 200N showing a stiffness of 10 N/μm versus 5 N/μm in fresh granite. However, used granite (not washed) showed higher stiffness than washed-used granite.

4.4   Comparison with theoretical models

4.4.1 Andesite

Fig.4.37 illustrates how the response curve steepens steadily as the load increases in the load-displacement test of 150N. Using the parameters given in Table 4.2, the data show that normal loading follows a line and does not follow the Hertz model; however, it is closer to RMS than Hertz shown in Fig. 4.37. Wong (2022) suggested that the Hertz model, with extremely low Young modulus (E) values, seems correct at small loads/displacements, but it seems too soft to capture the data at larger loads. The E value had to be increased (from 7GPa to 30GPa) in the current study for andesite as earlier studies suggested that E values for andesite lie 5-9 GPa as mentioned in Chapter 3. The curves still would not match at higher loads and have softer curves at the end of the loading process if lower values were used. In an earlier study, Cole et al. (2010) also used a lower E value to account for a smooth sphere-

sphere contact on gneiss, but the reduction was smaller than that used in this study. Nardelli and Coop (2019) observed that the initial portion of loading was soft compared to the larger displacement behaviour, which is in line with this study. While Nardelli and Coop (2019) found the Hertz model reasonable for large displacements in sands, clearly, this is not the case in this instance.

According to Wong (2022), the gradient of the slope before 5N of ballast particles is much less than Hertz, and after 5N, the values are approximately 2/3. Also, Cole and Peters (2008) found this gradient in crushed and milled gneiss. Despite that, our data indicate that the gradient is much less than 2/3 even after 5N.

Upon plotting the log-log plot, stiffness data follows both models and matches better with RMS at low loads, as illustrated in Fig. 4.38. It was found that particles initially have small stiffness but then simply increase. This demonstrates that the normal stiffness increases with the normal load, as predicted by Hertz's (1882) theory and Yimsiri and Soga (2000).

The combined test data for andesite illustrated in Fig. 4.39a, which represents the stiffness ratio (k/k_{Hertz}) as a function of normal load for different tests (Black: 100N, Blue: 150N, Green: 50N, Cyan: 200N, Red: 20N). The data demonstrates that for low normal loads, the experimental stiffness (k) is significantly lower than the Hertzian prediction (k_{Hertz}), evident from $k/k_{Hertz} < 1$. This indicates that the measured stiffness for all the ballast materials tested is lower than the stiffness predicted by the Hertzian model. This deviation is most likely due to the effects of surface texture and particle curvature, which reduce the effective contact area at lower normal loads. As the normal load increases, the ratio k/k_{Hertz} approaches 1, indicating better agreement with the Hertzian model at higher loads where surface roughness effects diminish.

Fig. 4.39b illustrates the stiffness ratio (k/k_{RMS}) below 1 for all tests at lower normal loads except for tests with normal loads of 100N and 200N, reflecting the reduced effective contact area caused by surface roughness, leading to lower stiffness values. At higher loads begins to converge towards Hertzian predictions as asperities flatten the contact area increases and k/k_{RMS} tends to approach or exceed 1, reflecting better alignment with the RMS-based model. This suggests that under higher loads, the contact surfaces experience sufficient deformation to smooth out asperities, making the contact behaviour more predictable and closer to theoretical models. The data also exhibits scatter for both models, especially in tests with lower loads.

4.4.2   Basalt

Fig. 4.40 illustrates the load-displacement behaviour, showing a steepening trend with increasing load. The results deviate from Hertz's model but align more closely with the RMS model. Basalt particles exhibited significantly less apex breakage under loading compared to andesite.

The log-log plots in Fig. 4.41 indicate a linear stiffness-displacement relationship, with stiffness increasing with load, consistent with Hertz's theory. However, while both models are followed, the data align more closely with the RMS model than the Hertz model.

Fig. 4.42a illustrates the combined test data for basalt and depicts the stiffness ratio (k/k_{Hertz}) as a function of normal load. At low loads, $k/k_{Hertz} < 1$, indicating lower stiffness than Hertzian predictions, as the load increases, k/k_{Hertz} advances towards 1, showing some alignment with the Hertzian model. However, basalt shows less agreement with the Hertz model compared to andesite, likely due to its higher Young's modulus, which results in stiffer behaviour and less surface deformation.

Fig. 4.42b shows k/k_{RMS} for all tests under different load levels, k/k_{RMS} converges to 1 and some test data exceed 1 (BB-050N), indicating improved agreement with RMS than Hertz. The effect of the load level was not seen and basalt data for all tests were less scattered than the andesite.

4.4.3   Chinese granite

Fig. 4.43 illustrates the load-displacement behaviour of Chinese granite with Hertz and RMS model predictions, using parameters given in Table 4.4. The results deviate from Hertz's model similarly to andesite and basalt but align more closely with the RMS model, especially at low load (under 20N), which was noticed for andesite and basalt. Chinese granite particles exhibited significantly less breakage compared to andesite and basalt, also it matches better with RMS compared to andesite and basalt.

Fig. 4.44 reveals a linear stiffness-displacement relationship similar to that found for andesite and basalt, with stiffness increasing with load, consistent with Hertz's theory. While both models are followed, the data align more closely with the RMS model (under low load up to 10N) than the Hertz model.

Fig. 4.45a presents the combined test data for Chinese granite, showing the stiffness ratio (k/k_{Hertz}) as a function of normal load. At low loads, $k/k_{Hertz} < 1$, indicating lower stiffness than Hertzian predictions. Tests with higher loads (150N and 200N), k/k_{Hertz} approaches 1, suggesting better agreement at higher loads. However, Chinese granite shows less alignment with the Hertz model than andesite, likely due to its curvature and surface texture, leading to stiffer behaviour. The results reveal that at low loads (0-10N), significant fluctuations in k/K_{Hertz}, as the load increases, K_{Hertz} stabilises, with lower initial loads (20N, 50N) converging earlier, while higher initial loads (150N, 200N) exhibit delayed stabilisation. At loads exceeding 100N, all curves converge near $K_{Hertz} \approx 1$, indicating a transition to bulk elastic deformation by Hertzian theory.

Fig. 4.45b demonstrates $k/k_{RMS} \approx 1$ for combined data and matches well with RMS predictions at low loads and higher loads except for test CB-100N. At low loads (1-10N) k/K_{RMS} exhibits pronounced fluctuations, reflecting sensitivity to surface effects such as roughness and asperity interactions. Stabilisation occurs as the load increases, but convergence is less uniform compared to k/K_{Hertz}, especially for higher initial loads (150N, 200N). At high loads (>100N), partial convergence is observed, though residual surface effects remain. The k/k_{RMS} exceeds 1, indicating better agreement with the RMS model than the Hertz model, which indicates that K_{RMS}-normalised stiffness provides greater sensitivity to surface irregularities than K_{Hertz}, making it valuable for analysing rough or fine-scale contact conditions.

4.4.4 Fresh Granite (UK)

Fig. 4.46 compares the experimental data for granite with the Hertz and RMS models using parameters from Table 4.5. The data aligns well with the RMS model, particularly at lower loads (0–1N), highlighting the RMS model's effectiveness in capturing surface effects and asperity contributions. However, fresh granite shows less agreement with both the RMS and Hertz models compared to Chinese granite and other ballast materials.

Fig. 4.47 demonstrates the relationship between normal load and normal stiffness with Hertz and RMS models for fresh granite. The experimental data deviates from the linear prediction of the Hertzian model. The RMS model, which includes surface roughness effects, provides a better fit to the experimental data; however, the agreement is less in comparison to Chinese granite, basalt, and andesite.

The normalised stiffness (k/K_{Hertz}) generally increases with increasing load (Fig. 4.48a), deviating from the linear prediction of the Hertzian model, and it tends to plateau or even decrease at higher loads for some curves (GB-020N, GB-050N). This behaviour might be attributed to plastic deformation, adhesive forces, or changes in contact geometry (from one mineral to another) at higher loads.

It was observed that higher loads generally result in higher normalised contact stiffness. For example, the test GB-200N curve exhibits the highest stiffness values, while the test GB-020N shows the lowest. This trend is consistent with the expectation that increased load leads to increased contact area and, consequently, higher stiffness. However, it is important to note that the influence of surface roughness can also affect this trend, as seen in the variations between the different tests and was noticed for other ballasts too.

Fig. 4.48b shows that k/k_{RMS} is less than 1 for combined data. At low loads (0N to 10N): GB-020N exhibited the most stable behaviour, while GB-050N and GB-150N showed noticeable degradation, indicating sensitivity to minor load changes. GB-150N displayed consistent performance with minimal decline, whereas GB-050N deteriorated sharply, highlighting the impact of load on its structural integrity. At higher loads (100-200N), GB-150N maintained stability, outperforming other tests. GB-200N fluctuated significantly, indicating inconsistency at extreme loads. Overall, GB-150N demonstrated the most robust performance ($k/k_{RMS} \approx 1$) across all load ranges, in contrast, GB-050N showed rapid property degradation.

4.4.5 Used granite (UK)

Figure 4.49 illustrates the comparison of used granite with Hertz and RMS model predictions, using parameters given in Table 4.6. The experimental data deviate from Hertz's model similarly to Chinese granita, fresh granite, andesite and basalt but align more closely with the RMS model, especially at low load (under 10N), which was less noticed for fresh granite. Used granite particles exhibited significantly less breakage compared to fresh granite and andesite, also it matches better with RMS compared to fresh granite and basalt.

Figure 4.50 demonstrates a linear load-stiffness relationship similar to that found for fresh granite, Chinese granite, andesite and basalt. While both models are followed, the data align more closely with the RMS model (under low load 10N) than the Hertz model and then diverge at a higher load. Used granite showed much better fitting with models than fresh granite and showed much similar behaviour to Chinese granite.

The normalised stiffness ratio (k/K_{Hertz}) of used granite is illustrated in Fig. 4.51a, revealing distinct trends for each test. At low loads (0N-10N), UG-020N and UG-100N exhibited relatively stable behaviour with minor fluctuations, whereas UG-050N and UG-150N showed significant variability.

In the intermediate load range (<100), UG-150N and UG-200N demonstrated a gradual increase in k/K_{Hertz}, in contrast, UG-050N experienced an initial decline followed by recovery. At higher loads (100N>), UG-200N displayed a rapid increase in k/K_{Hertz}, which may reflect enhanced stiffness under extreme conditions. UG-020N and UG-100N maintained stable performance across this range, while UG-050N and UG-150N showed inconsistent trends, limiting their reliability in high-load applications.

In comparison, UG-200N exhibited the most adaptive performance under higher loads, and UG-020N demonstrated consistent stability across all load ranges, on the other hand, UG-050N pronounced variability and showed an increase with increasing load.

The k/k_{RMS} of used granite is illustrated in Fig. 4.51b under different loads. UG-020N, UG-100N and UG-200N showed significant variability at low load (0.1 to 10N) and then stabilised at higher load, limiting their reliability under fluctuating. In contrast, UG-050N and UG-150N exhibited consistent stability across all load ranges. UG-200N demonstrated superior adaptability at high loads and it almost matched $k/k_{RMS} = 1$. It can be concluded that used granite showed similar behaviour to fresh granite.

4.4.6 Washed used granite

Figure 4.52 compares the experimental data for washed-used granite with predictions from the Hertz and RMS models. Similar to used granite, fresh granite and other ballasts, the experimental data deviates from the Hertzian model, particularly at lower loads (under 5N). However, the washed-used granite data aligns more closely with the RMS model, especially at low loads, which was less pronounced for fresh granite. Additionally, washed-used granite exhibited significantly less breakage compared to fresh granite and used granite, and its behaviour aligns more closely with the RMS model than fresh granite. At higher load, it aligned much better with the models than used granite and fresh granite.

Figure 4.53 demonstrates a linear stiffness-displacement relationship for washed-used granite, similar to that observed for used granite, Chinese granite, andesite, and basalt. While the data follow both the Hertz and RMS models to some extent, it aligns more closely with

the RMS model at lower loads and then diverges at higher loads. Interestingly, washed-used granite shows a better fit with the models compared to fresh granite and exhibits behaviour more similar to Chinese granite.

The results reveal distinct differences in the load-dependent behaviour of k/k_{Hertz} across the different tests (Fig. 4.54a). At low loads (0.1-5N), significant fluctuations are observed for all load levels, with the magnitude of fluctuations increasing with higher initial loads. WUG-020N and WUG-100N stabilise earlier and then unstable as the load increases, in contrast, WUG-150N and WUG-200N exhibit prolonged instability. At intermediate to high loads (>100N), tests WUG-150N and WUG-200N converge toward $k/k_{Hertz} \approx 1$, consistent with Hertzian contact theory.

The k/k_{RMS} behaviour diverges across tests for washed-used granite as illustrated in Fig 4.54b. At low loads (0.1-5N), all tests show fluctuations, with higher initial loads (WUG-150N, WUG-200N) exhibiting more instability due to surface effects. Stabilisation occurs faster for WUG-100N, while higher loads display prolonged instability. Unlike k/k_{Hertz} convergence at high loads (>100N) is partial, reflecting the sensitivity of k/k_{RMS} to surface roughness. These results highlight k/k_{RMS}'s ability to capture persistent surface effects, making it suitable for rough contact analysis.

4.5 Normal cyclic loading

The normal load was gradually increased from 0 to 20N, followed by normal cycles with a magnitude of ±5N. The normal load was then increased to 50N, and additional cycles were performed. This process was repeated at 100N, 150N, 200N, 250N and continued in the same manner until the load reached 300N. The figure 5.26 presents the variation of normal stiffness with cycle number under different normal loads. The stiffness is measured in N/μm, and the cycle number represents the progressive loading stages. At an initial load of 20N, the normal stiffness starts at approximately 4 N/μm and gradually stabilises after a few cycles. When the load is increased to 50N, a noticeable rise in stiffness is observed, indicating that a greater normal force enhances surface contact and structural rigidity. As the load further increases to 100N, the stiffness remains relatively stable with minor fluctuations, suggesting that the system is adapting to the increased load without significant structural changes.

Upon reaching 150N, another increase in stiffness is evident, followed by a more pronounced jump when the load is increased to 200N. This sudden rise in stiffness could be attributed to changes in surface interactions, increased real contact area, or material compaction under higher loads. A similar but slightly smaller increase occurs when the load is raised to 250N, followed by a final surge in stiffness as the load reaches 300N. The trend suggests a non-linear response, where higher loads result in more significant increases in stiffness, likely due to progressive asperity deformation and enhanced mechanical interlocking at the interface.

Overall, the figure 4.55 demonstrates that normal stiffness increases with normal load, with more pronounced changes occurring at higher loads. The stiffness evolution suggests that at lower loads, the contact interface undergoes gradual adaptation, while at higher loads, significant changes in material behaviour lead to abrupt stiffness increases. This response highlights the role of load-dependent deformation and contact mechanics in governing the stiffness characteristics of the system.

4.6 Summary

This study reveals key differences in the mechanical behaviour of various ballast materials, including andesite, basalt, Chinese granite, fresh granite, used granite, and washed-used granite, under normal loading conditions. Initially, all materials exhibit elastic behaviour; however, as the load increases, they all enter a plastic phase, where permanent deformation occurs. Basalt transitions to plasticity more rapidly, exhibiting significant displacement at higher loads, while granite and andesite undergo more gradual deformation. As the load increases, all ballast materials approach their structural limits, with basalt and granite showing higher resistance to deformation compared to andesite.

Among the materials tested, Chinese granite demonstrates the highest stiffness, reaching 20 N/µm at 200N, significantly outperforming basalt (8 N/µm) and andesite (3 N/µm). For the UK granites: Fresh granite shows the lowest stiffness, with values around 5 N/µm at 100N, while used granite exhibits slightly higher stiffness, especially at higher loads (8 N/µm at 150N). Washed-used granite performs better than fresh granite but slightly less than used granite, with stiffness values around 7 N/µm at 150N. The surface roughness and particle shape of each material play a key role in their deformation behaviour, influencing their stiffness and load-bearing capabilities.

In terms of contact area, all materials exhibit a linear increase as the load rises, with the rougher surfaces compressing to bear more load. At 200N, the contact area of granite reaches 0.36 mm², similar to basalt but much lower than andesite (0.55 mm²). Cross-sectional profiles reveal that andesite undergoes more significant deformation compared to basalt and granite, indicating higher compression and surface flattening under stress. This shows that while granite and basalt distribute stress more efficiently, andesite is more prone to deformation under similar loads.
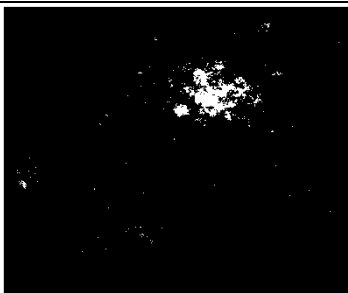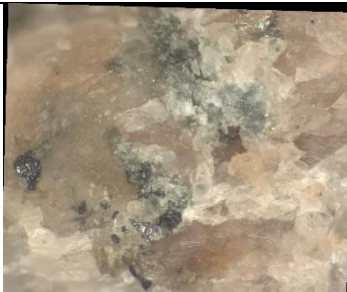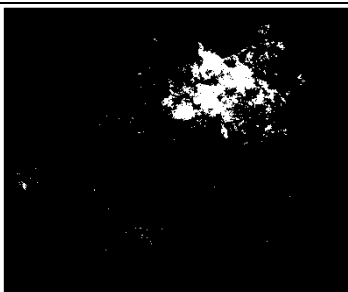
The RMS model, which better captures surface roughness and asperity interactions, demonstrates superior predictive capability at low loads, where surface effects dominate. Basalt and andesite align well with the RMS model, particularly at lower loads, while granite shows a more consistent alignment with both RMS and Hertz models as the load increases. Chinese granite performs exceptionally well in both models, with minimal particle breakage and better convergence with theoretical predictions, especially at lower loads. Washed-used granite also aligns well with the RMS model, offering stability and reliability across load conditions, outperforming fresh and used granite.

Comparing the granite types, Chinese granite and washed-used granite emerge as the most stable and reliable ballast materials, showing minimal scatter and superior consistency across all load ranges. Its stiffness and performance align better with theoretical models, demonstrating better load stability than both fresh granite and used granite. Used granite shows reduced variability compared to fresh granite, particularly at lower loads, but is slightly less stable under extreme loading conditions. Fresh granite, due to significant surface roughness and structural inconsistencies, exhibits higher variability and less agreement with both the Hertz and RMS models, especially at lower loads.

Overall, Chinese granite, basalt and washed-used granite are the most robust ballast materials, providing a superior balance of stiffness, durability, and match better than other ballasts with theoretical models under different load conditions. Its performance is more stable and reliable than other ballast materials, making it the most suitable choice for applications requiring consistent and efficient load-bearing properties.

Chapter 4 Tables and Figures

Table 4.1 Microscopic image of granite (left), and contact area (right)

Granite		
Load (N)	Original image	Thresholded
0		
1		
5		
10		
20		
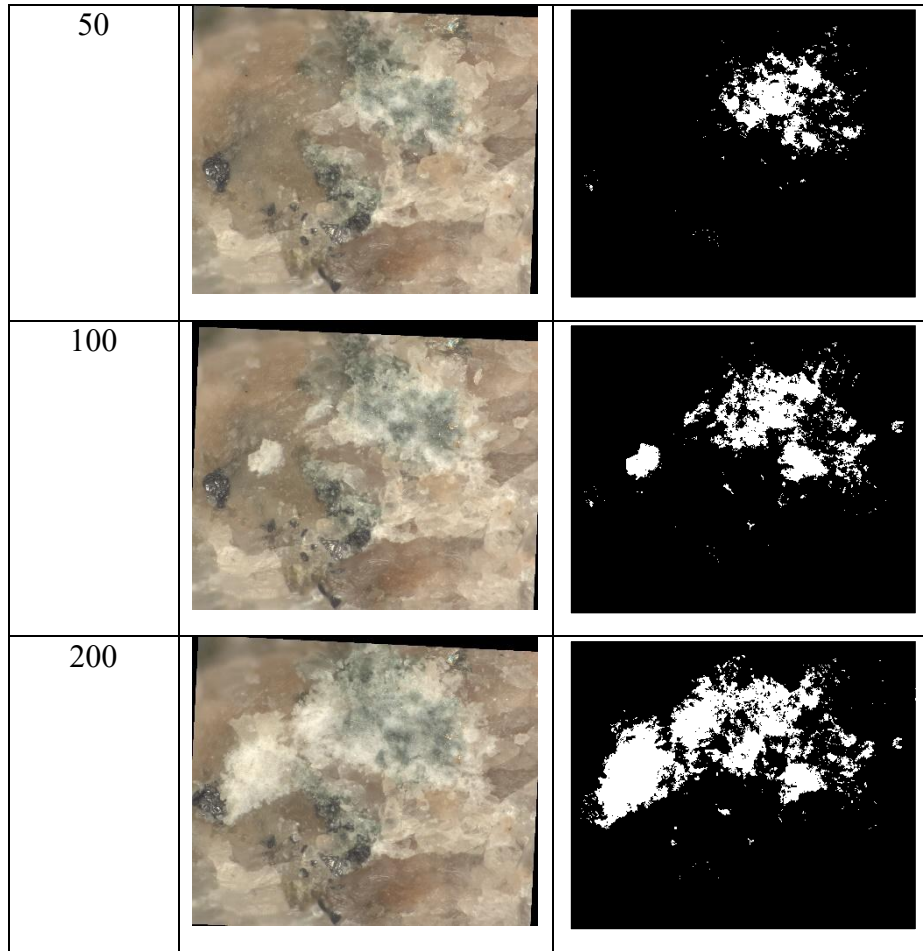
Table 4.2 Test matrix and surface parameters for normal loading on andesite.

Test	Normal load (N)	Contact R Top particle (mm)	Roughness (Sq)(µm)		Fractal dimension (D_f)	
			Top	Base	Top	Base
AB-020N-1	20	1.281	1.22	2.66	2.15	2.14
AB-050N	50	2.99	1.8	1.2	2.3	2.27
AB-100N	100	1.159	1.10	1.13	2.25	2.28
AB-150N	150	1.04	-	-	-	-
AB-200N-1	200	1.73	1.51	1.24	2.21	2.24
AB-200N-2	200	0.869	4.83	1.69	2.07	2.18
AB-020N-2	20	0.896	-	-	-	-

Table 4.3 Test matrix and surface parameters for normal loading on basalt.

Test	Normal load (N)	Contact R Top particle (mm)	Roughness (Sq)(µm)		Fractal dimension (D_f)	
			Top	Base		
BB-100N-1	100	4.22	5.65	3.89	-	-
BB-100N-2	100	2.80	4.11	9.11	-	-
BB-150N	150	2.94	7.22	10.70	2.07	2.15
BB-200N-1	200	1.032	2.41	2.65	2.27	2.24
BB-100N-3	100	1.616	3.12	10.8	2.29	2.24
BB-020N	20	0.706	-	3.22	-	2.12
BB-100N-Flooded	100	0.769	-	-	-	-

Table 4.4 Test matrix and surface parameters for normal loading on Chinese granite.

Test	Normal load (N)	Contact R Top particle (mm)	Roughness (Sq) (µm)		Fractal dimension (D_f)	
			Top	Base	Top	Base
CB-200N	200	2.04	1.32	1.4	2.22	2.19
CB-100N-1	150	2.319	-	1.29	-	2.2
CB-100N-2	100	1.520	16.2	4.15	2.27	2.37
CB-050N	50	-	1.41	1.4	2.24	2.22
CB8	20	-	1.49	3.2	2.09	2.13
CB-100N-Flooded	100	3.025	-	-	-	-

Table 4.5 Test matrix and surface parameters for normal loading on fresh granite.

Test	Normal load	Contact R Top particle (mm)	Roughness (Sq) (μm)		Fractal dimension (D_f)	
			Top	Base	Top	Base
GB-020N	20	1.649	0.689	0.73	2.03	2.30
GB-100N	100	1.53	1.65	13.6	2.17	2.11
GB-200N	200	1.453	4.29		2.60	
GB-50N-1	50	-	-	-	-	-
GB5-50N-2	50	-	-	-	-	-

Table 4.6 Test matrix and surface parameters for normal loading on used granite.

Test	Normal load (N)	Contact R Top particle (mm)	Roughness (Sq) (μm)		Fractal dimension (D_f)	
			Top	Base	Top	Base
UG-020N	20	1.468	2.36	4.03	2.26	2.16
UG-100N	100	0.989	3.5	2.92	2.1	2.24
UG-150N	150	1.745	2.28	2.24	2.18	2.18
UG-200N	200	1.072	2.16	2.09	2.24	2.28

Table 4.7 Test matrix and surface parameters for normal loading on washed used granite.

Test	Normal load (N)	Contact R Top particle (mm)	Roughness (Sq) (μm)		Fractal dimension (D_f)	
			Top	Base	Top	Base
WUG-100N	100	0.685	1.37		2.06	
WUG-020N-1	20	0.819	0.9	0.73	2.17	2.03
WUG-200N	200	1.073	0.92	0.87	2.03	2.08
WUG-020N-2	20	0.68	1.43	0.74	2.09	2.06

(a)
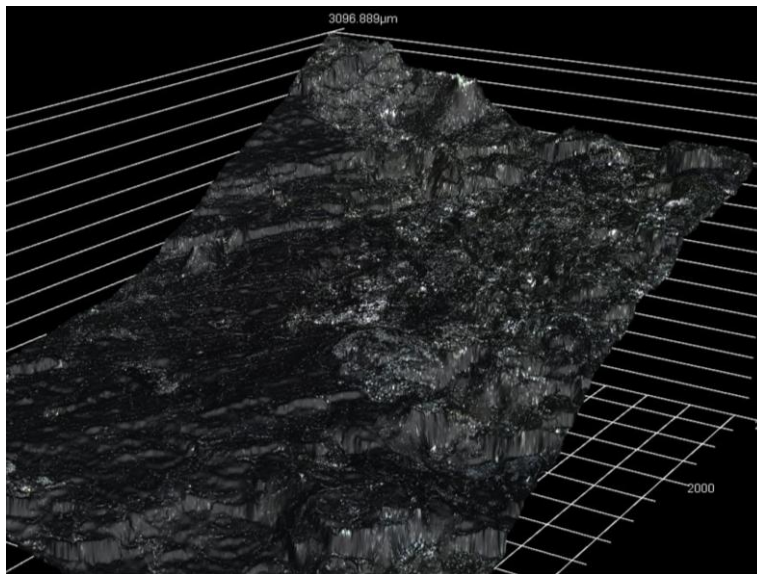
(b)

Figure 4.1 Chinese andesite in nature (a) and surface texture under the microscope with magnification of 10x (b).
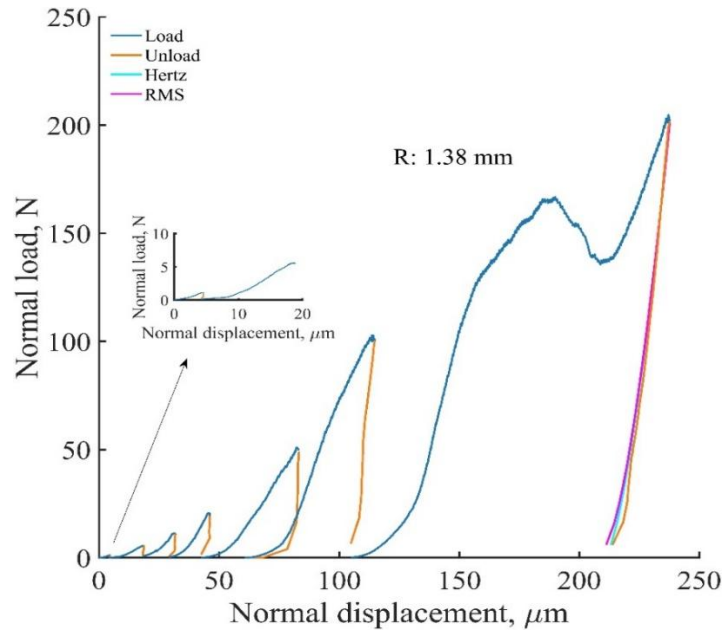
Figure 4.2 Load-displacement behaviour of Chinese andesite under different load levels.

(a)

(b)
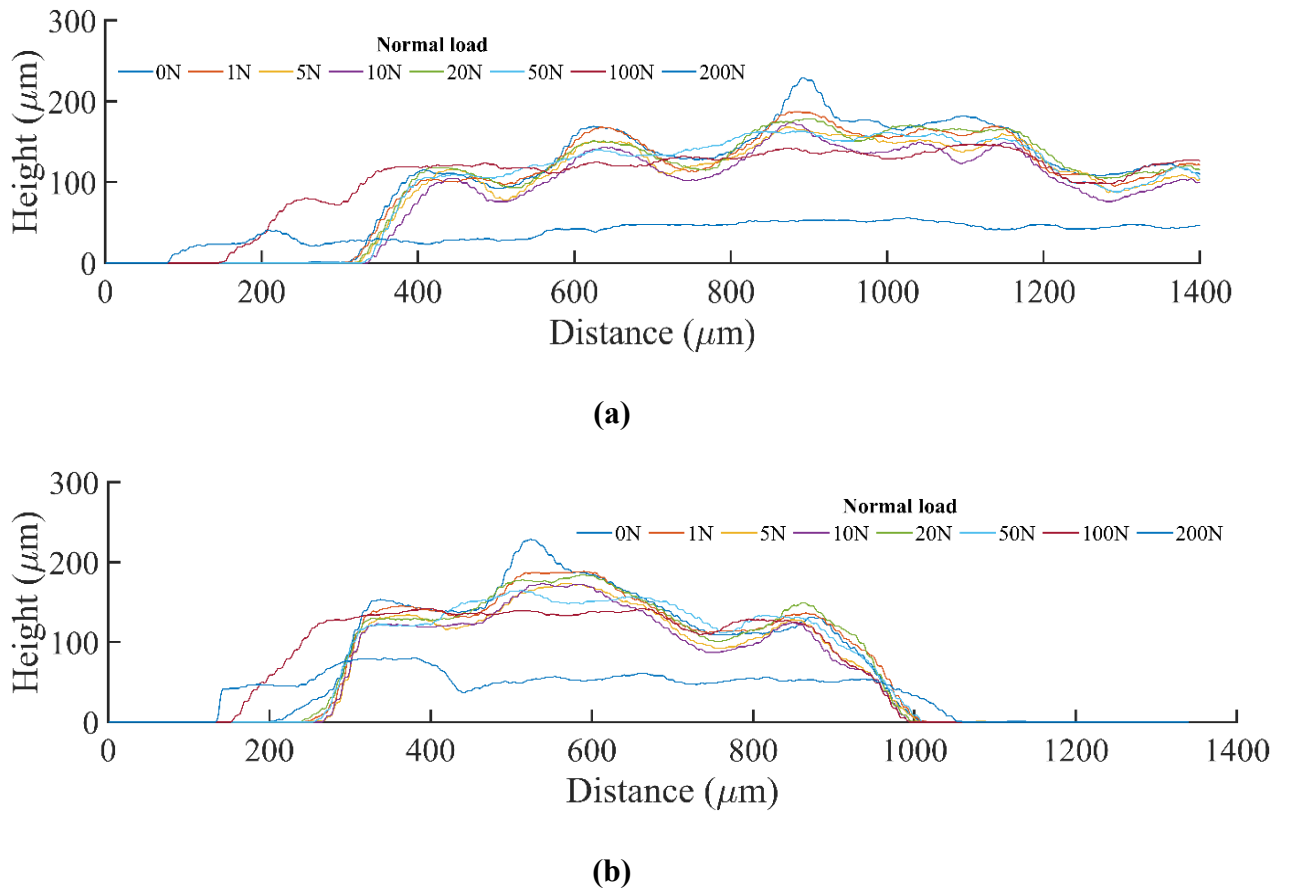
Figure 4.3 Crose-section of Chinese andesite for different normal loads in X-direction (a) and in Y-direction (b) (after Bagir and Singh, 2024).
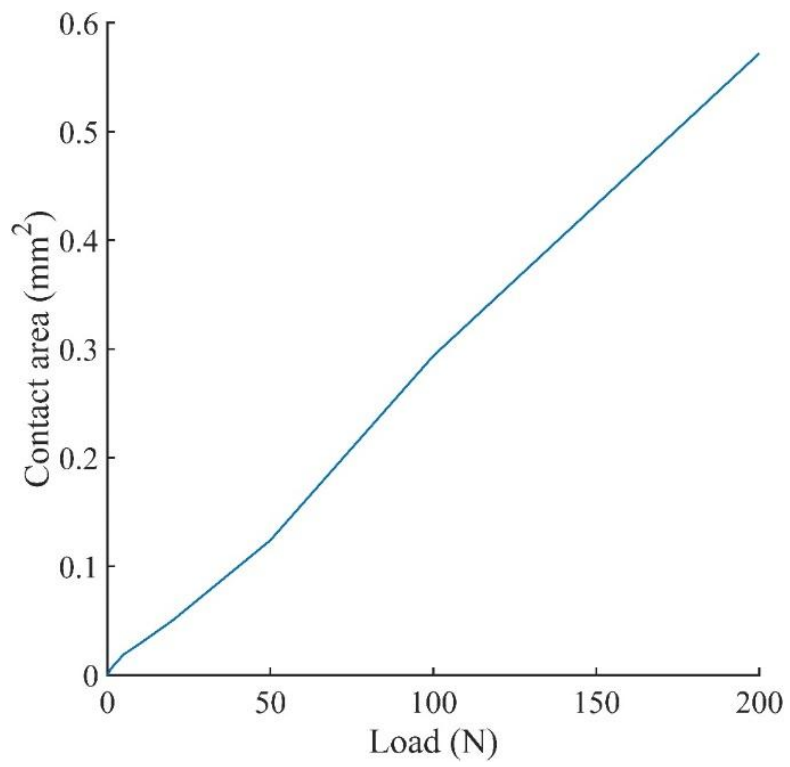
Figure 4.4 Measured contact area for Chinese andesite ballast.

(a)
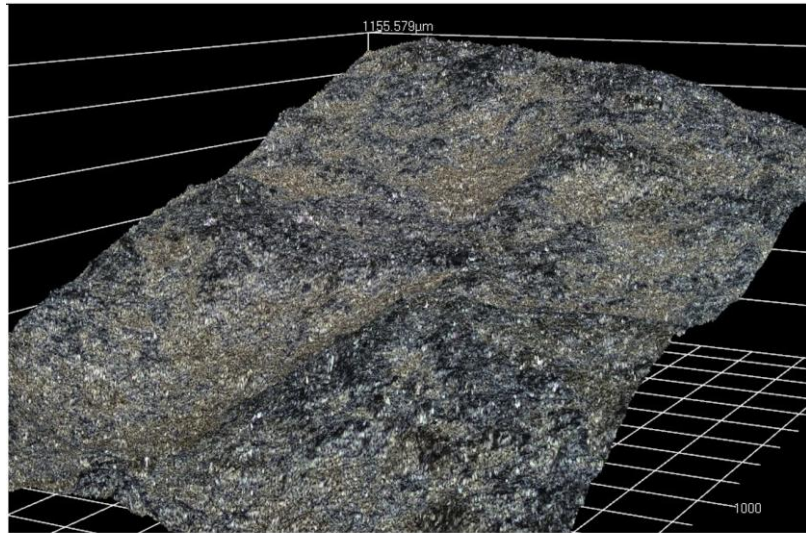
(b)

Figure 4.5 Basalt ballast (Australia) in nature (a) and under the microscope with magnification of 10x (b).
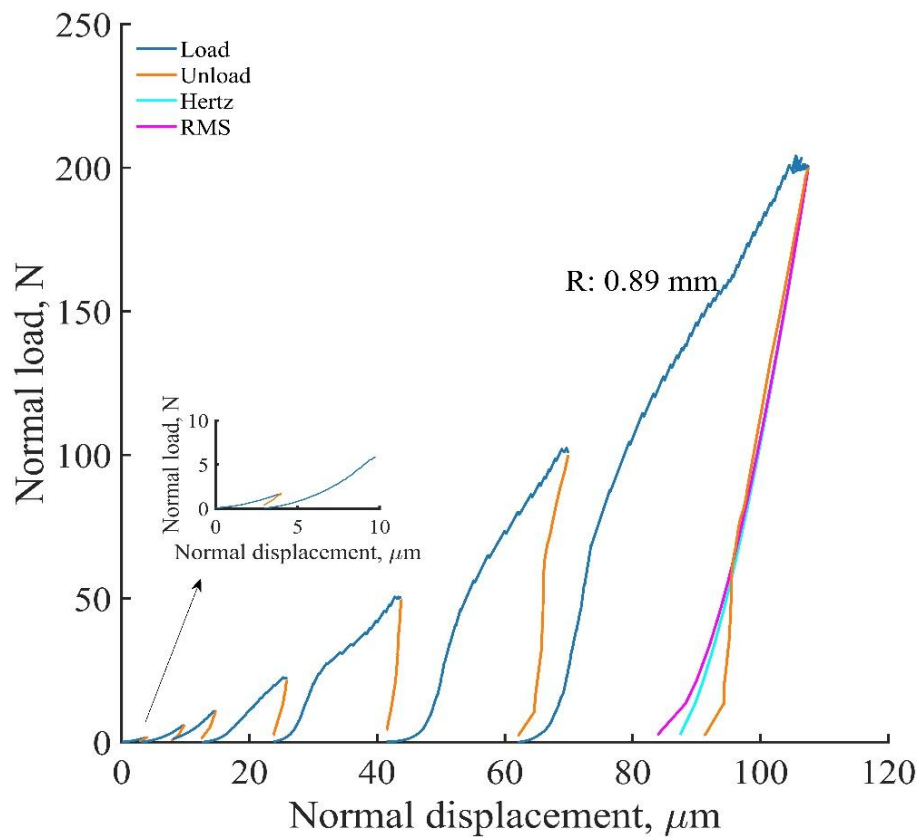
Figure 4.6 Load-displacement response of Australian basalt ballasts under different load levels. Modified by the author (after Bagir and Singh, 2024).

(a)

(b)
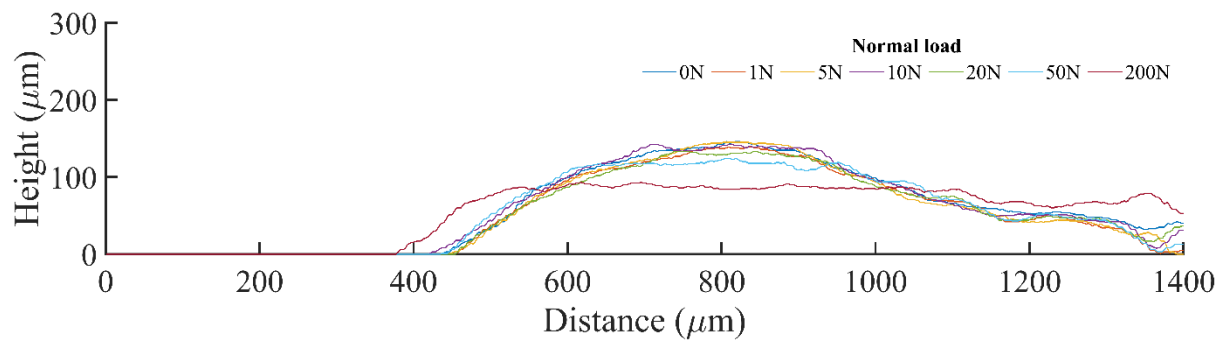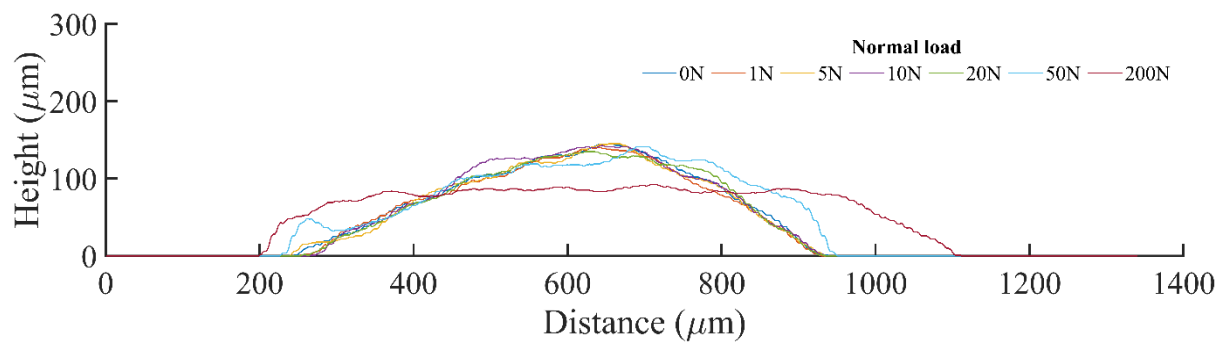
Figure 4.7 Crose-section of Australian granite for different normal loads in X-direction (a) and in Y-direction (b) (after Bagir and Singh, 2024).
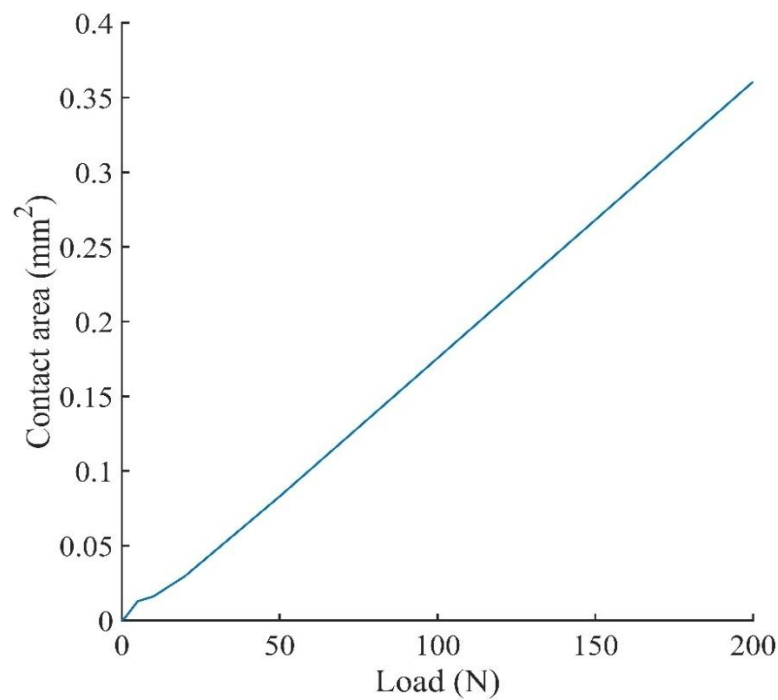
Figure 4.8 Load-contact area behaviour of basalt ballast.

(a)
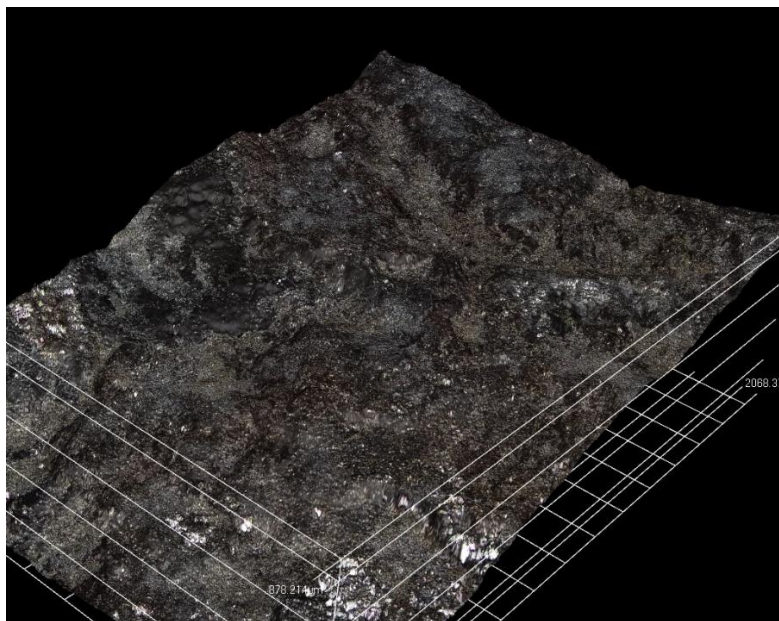
(b)

Figure 4.9 Granite (UK) in nature (a) and under the microscope with magnification of 10x (b).
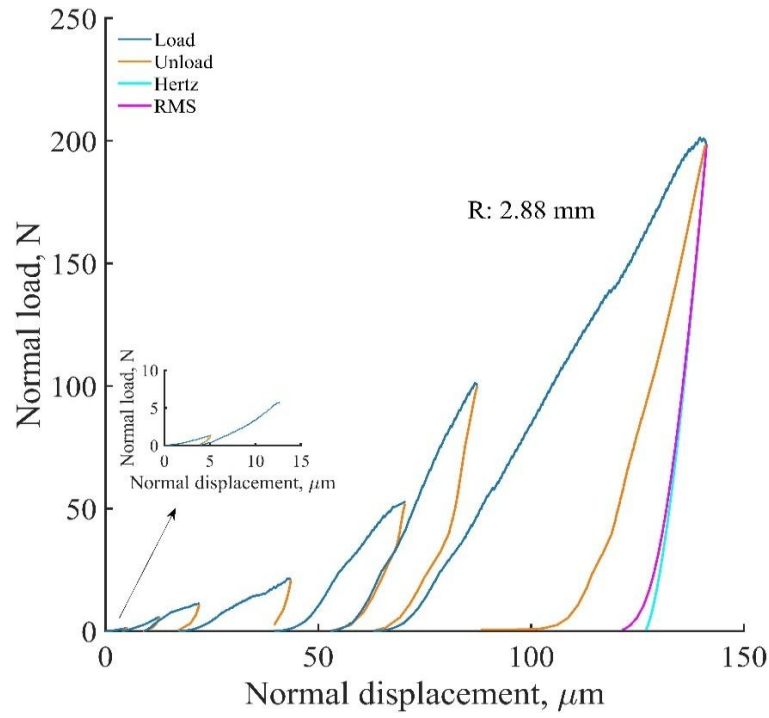
Figure 4.10 Load-displacement response of UK granite ballasts under different load levels.

(a)

(b)
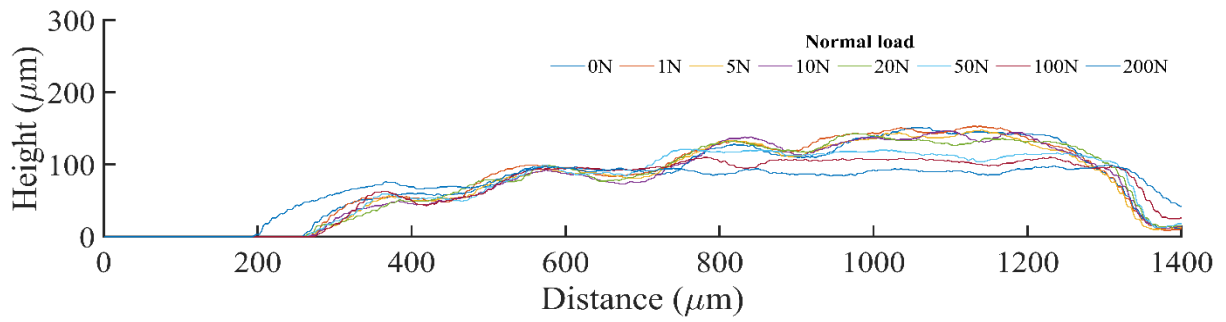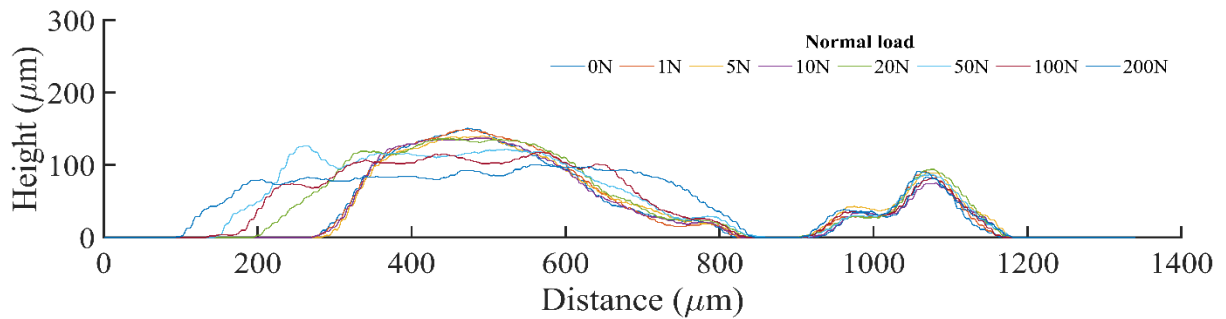
Figure 4.11Crose-section of UK granite for different normal loads in X-direction (a) and in Y-direction (b) (after Bagir and Singh, 2024).
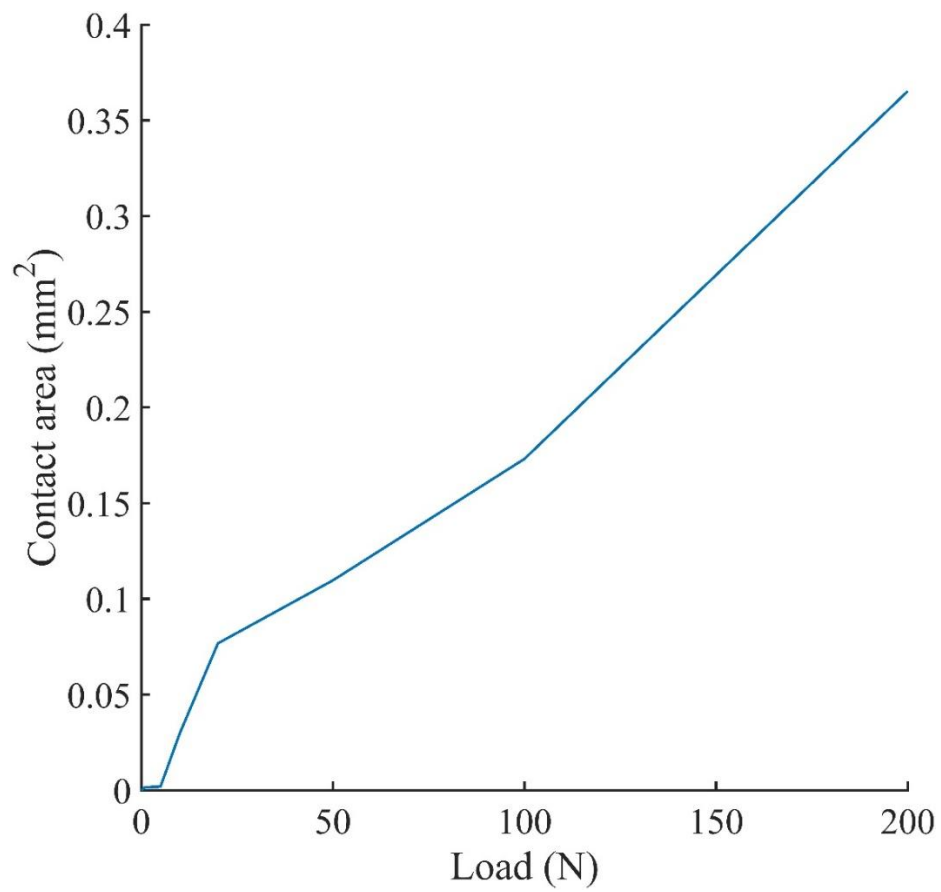
Figure 4.12 Load-contact area behaviour for UK granite ballast.
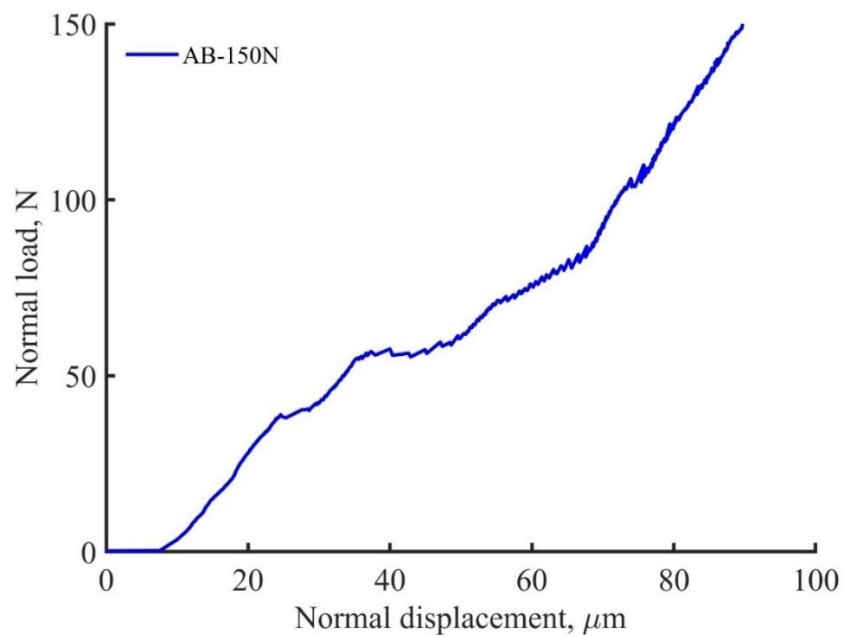
Figure 4.13 The load-deformation behaviour of andesite ballast under normal load of 150N.
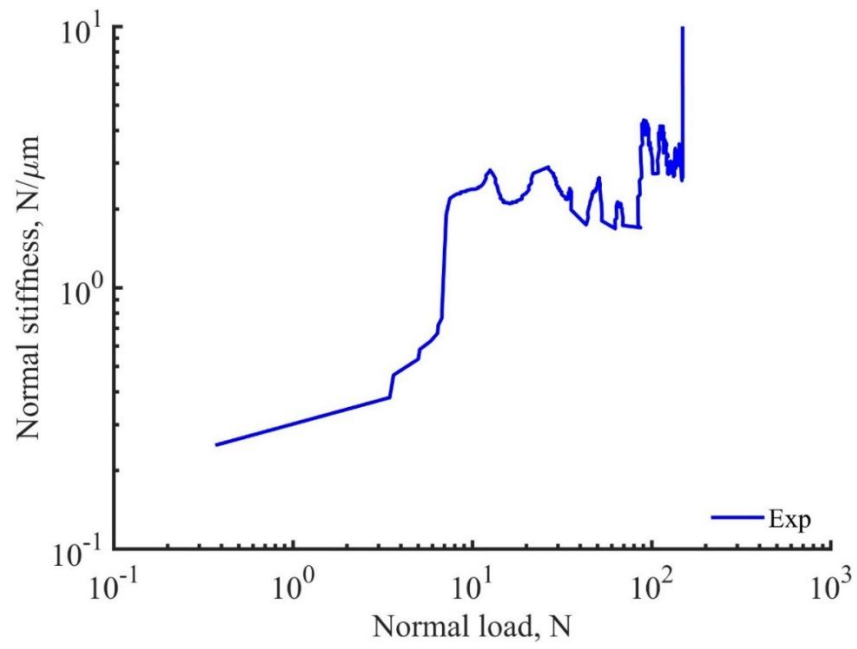
Figure 4.14 Normal stiffness behaviour of andesite ballast under the normal load of 150N.
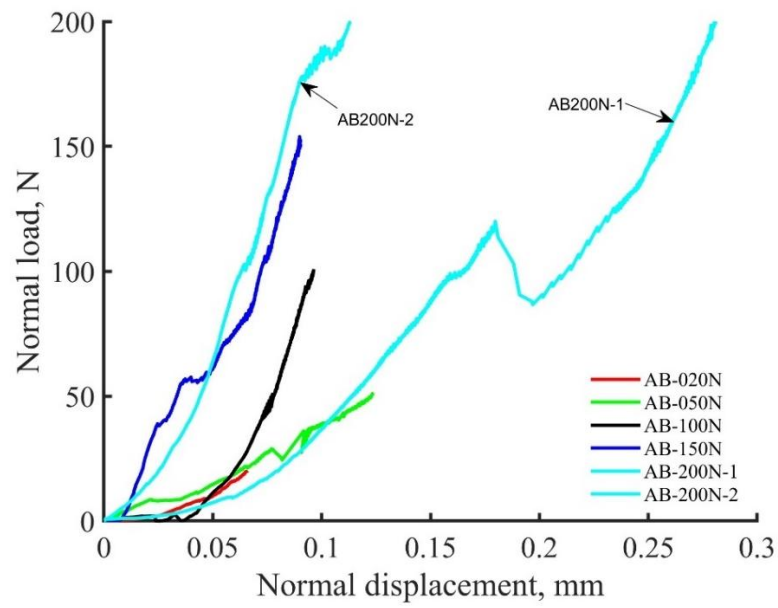
Figure 4.15 The load-deformation behaviour of basalt under different normal loads.
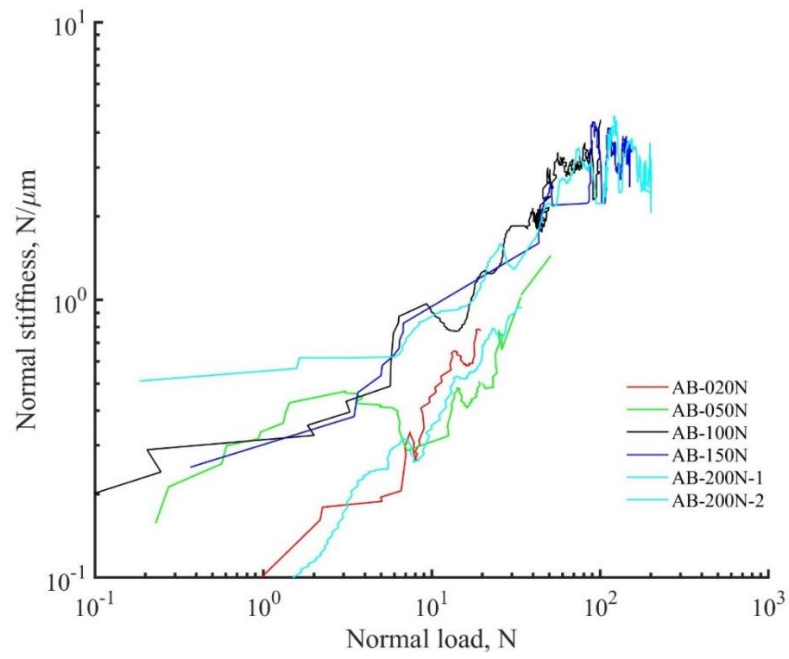
Figure 4.16 Normal stiffness of andesite ballast under different normal loads.
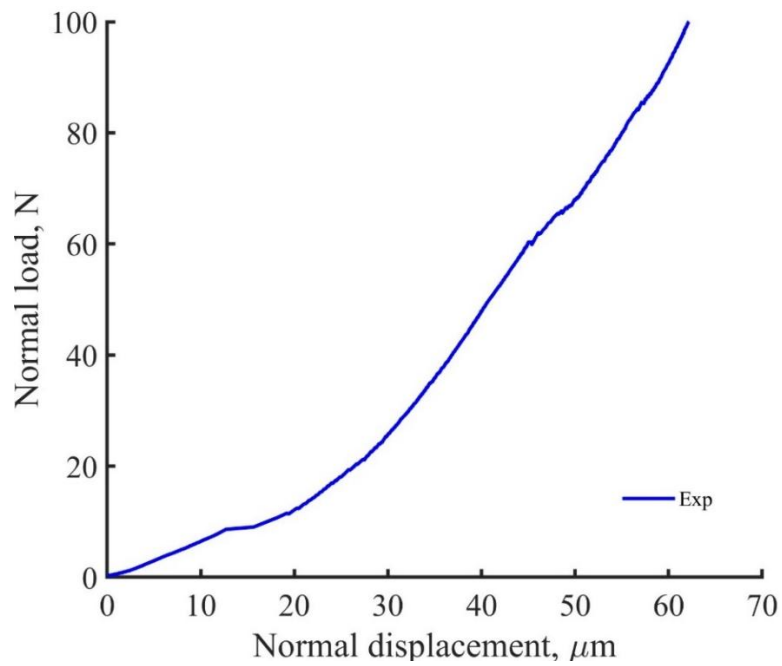
Figure 4.17 The load-displacement curve of basalt ballast under the normal load of 100N.
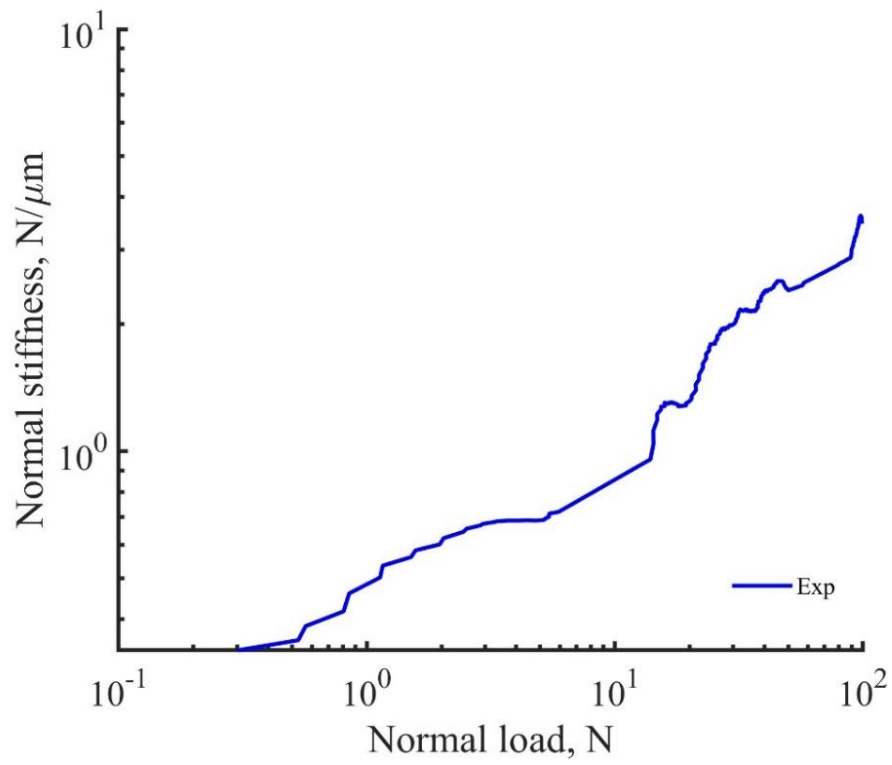
Figure 4.18 Normal stiffness of basalt ballast under the normal load of 100.
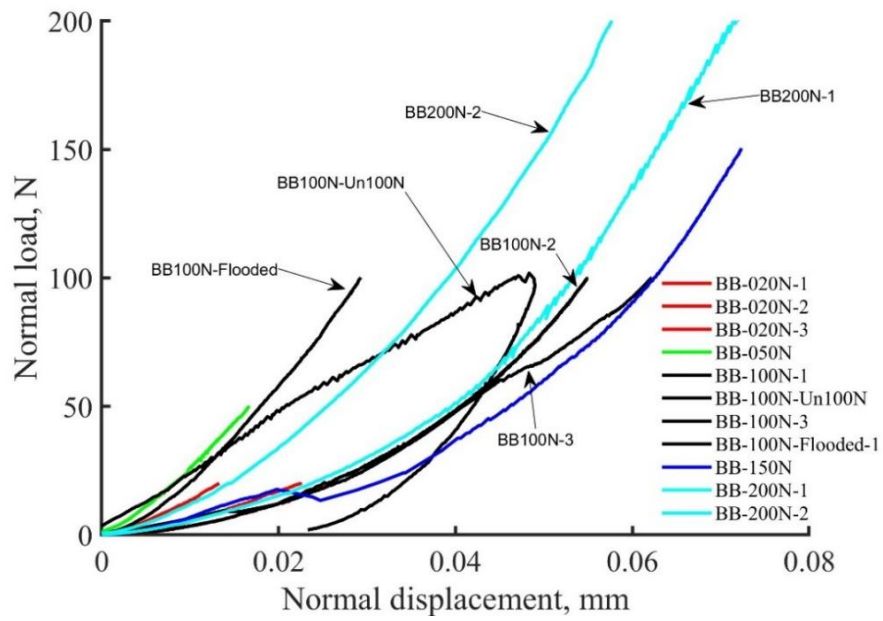
Figure 4.19 The load-deformation behaviour of basalt under different normal load levels.
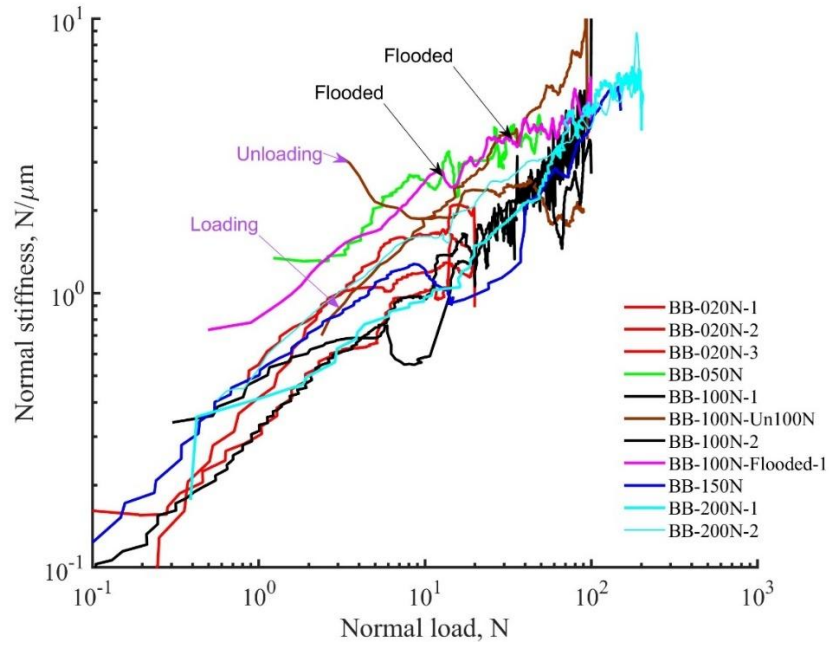
Figure 4.20 Normal stiffness of basalt ballast under different normal loads.
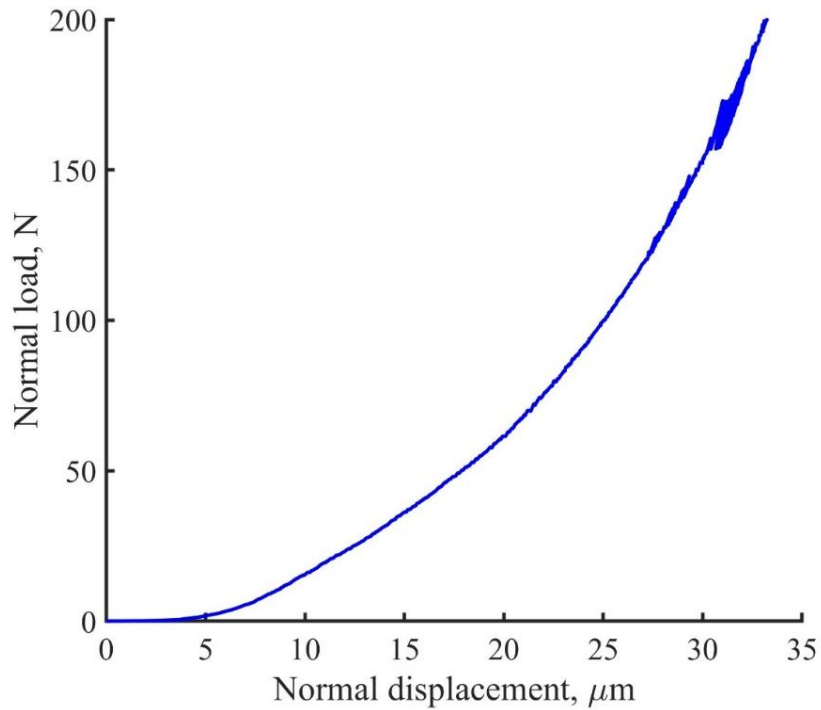
Figure 4.21 The load-deformation behaviour of Chinese granite under a normal load of 200N.
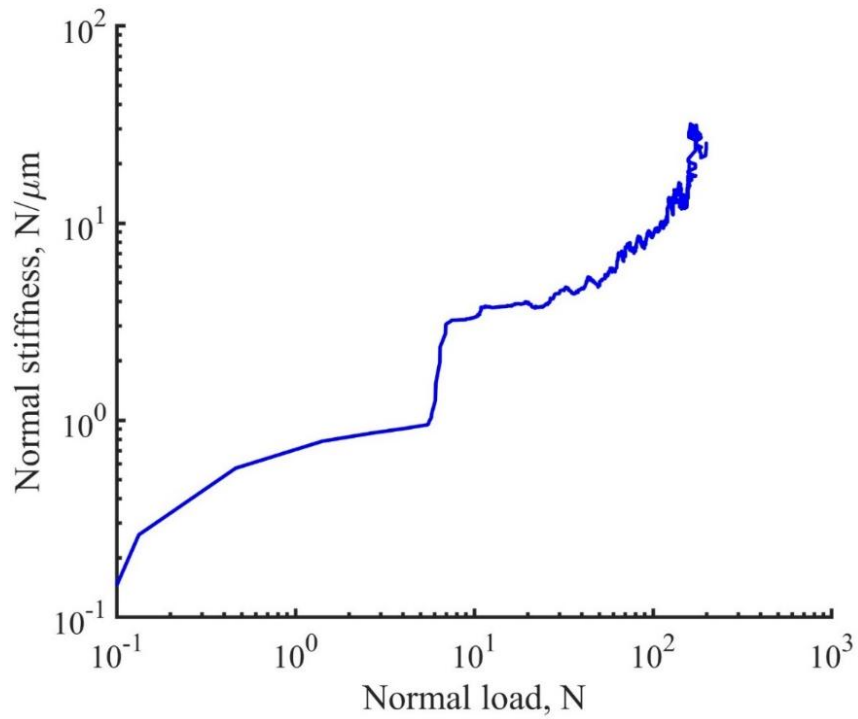
Figure 4.22 Normal stiffness of fresh granite ballast under normal load of 200N.
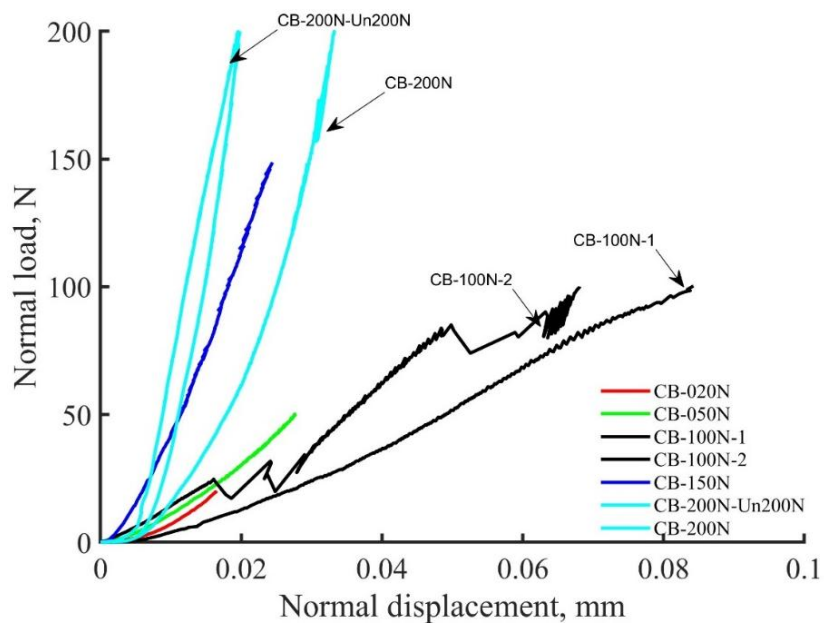
Figure 4.23 The load-deformation behaviour of Chinese granite under different normal load levels.
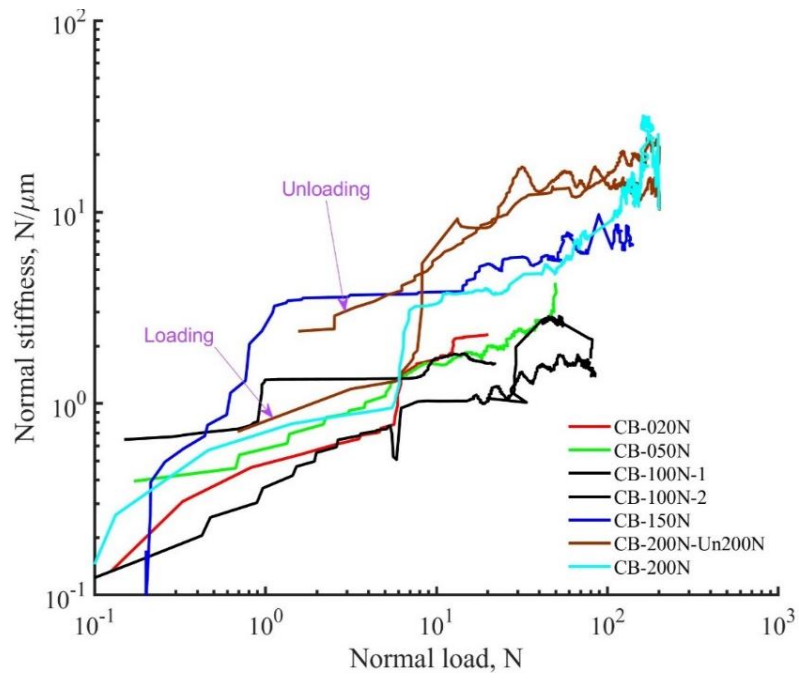
Figure 4.24 Normal stiffness of Chinese granite under different normal load levels.
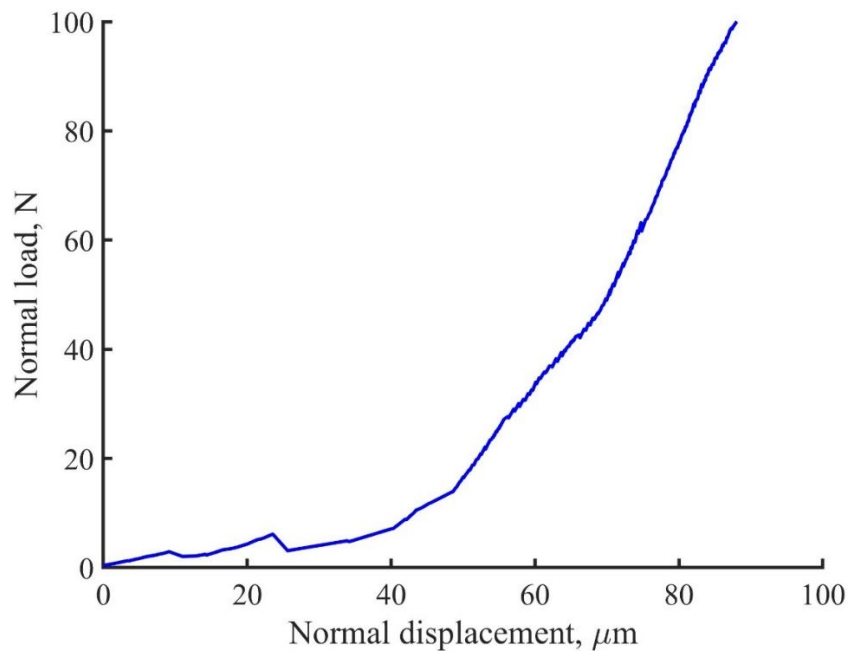
Figure 4.25 The load-deformation behaviour of fresh granite (UK) under normal load 150N.
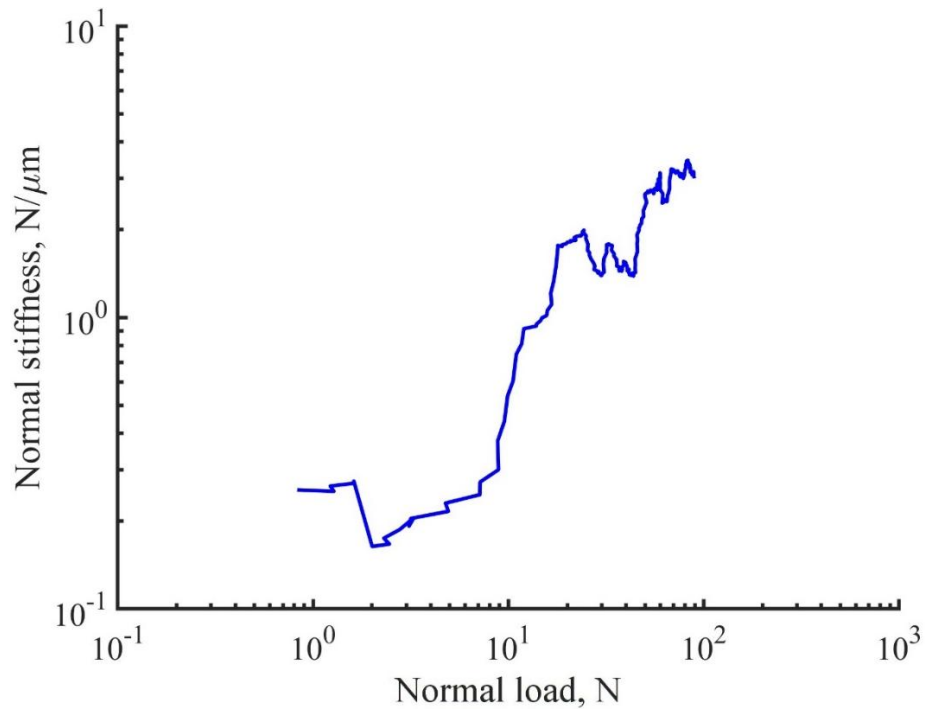
Figure 4.26 Normal stiffness of fresh granite ballast under a normal load of 200N.
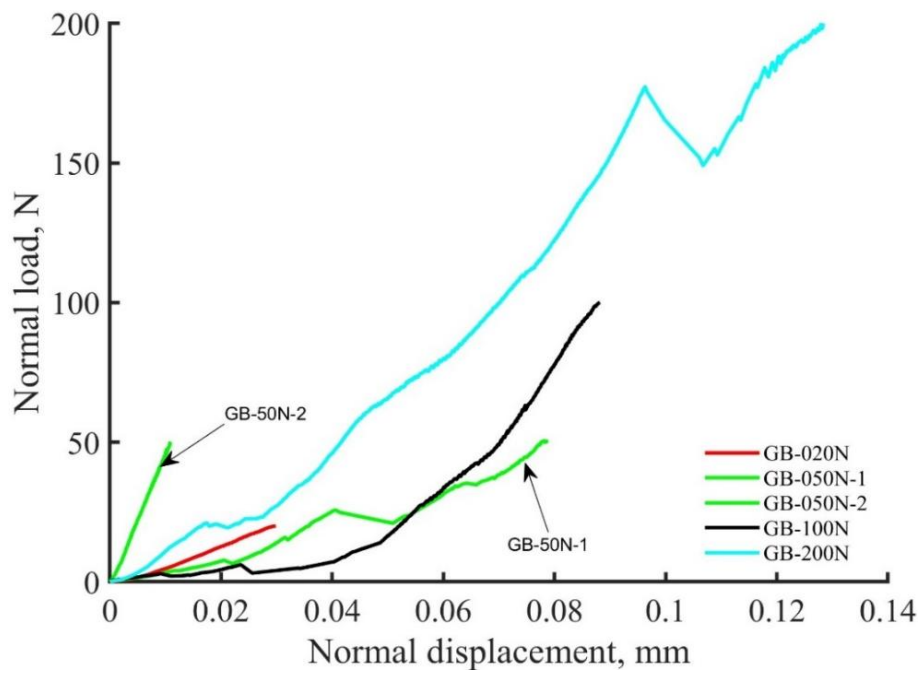
Figure 4.27 The load-deformation behaviour of fresh granite (UK) under different normal load levels.
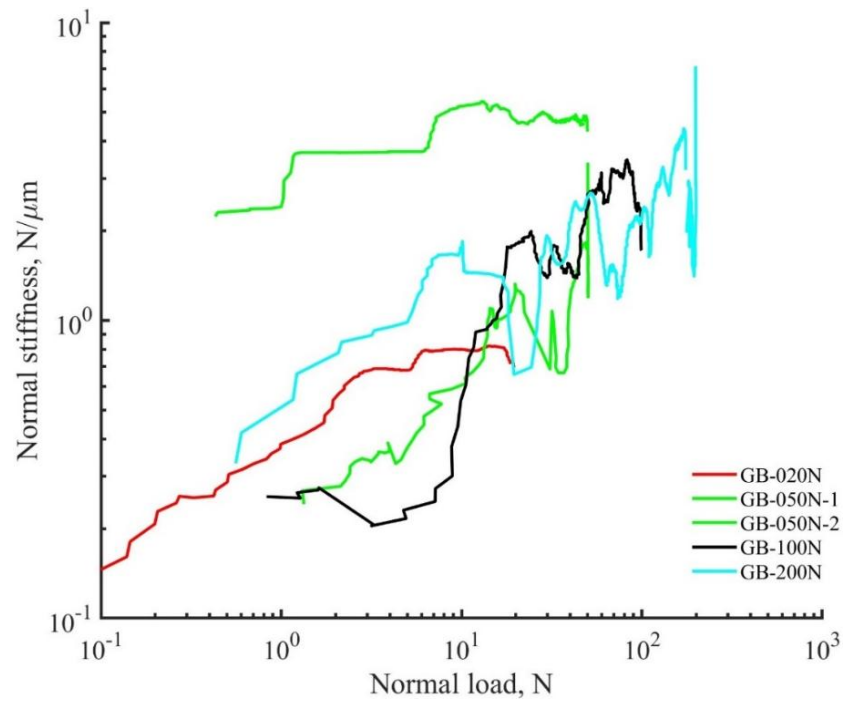
Figure 4.28 Normal stiffness of fresh granite ballast under different normal loads.
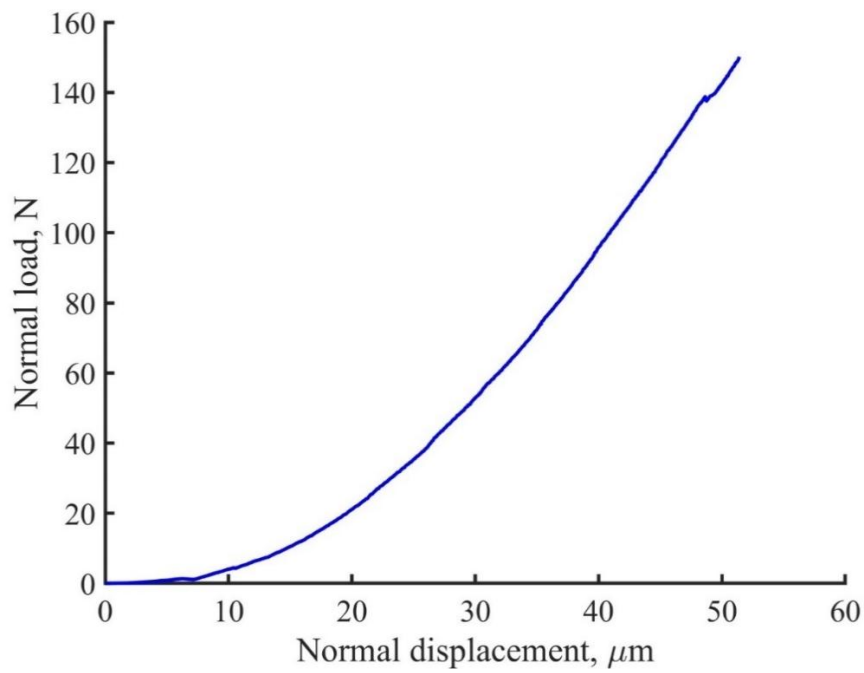
Figure 4.29 The load-deformation behaviour of used granite (UK) under normal load 150N.
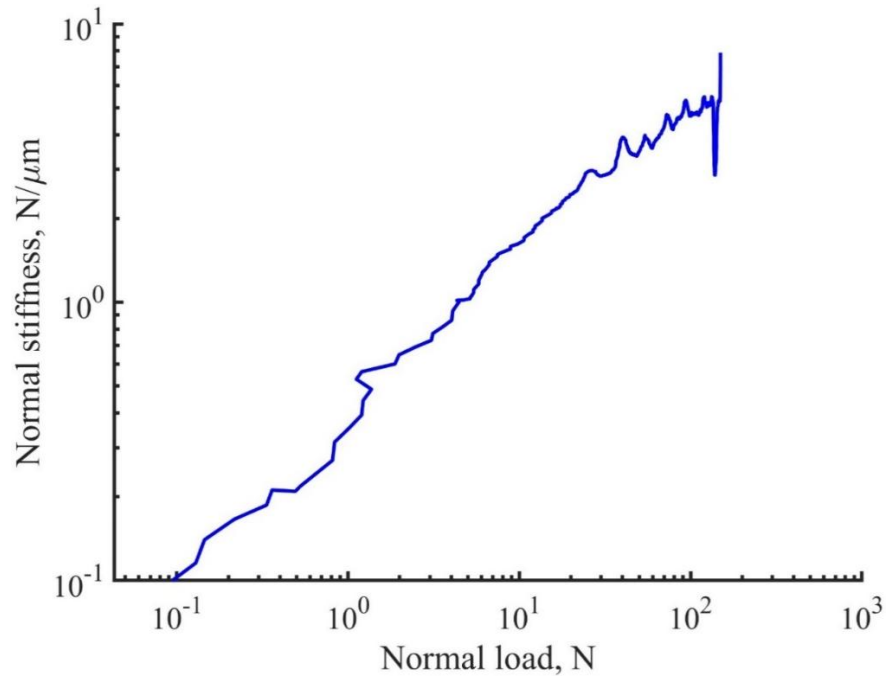
Figure 4.30 Normal stiffness behaviour of used granite (UK) under normal load 150N.
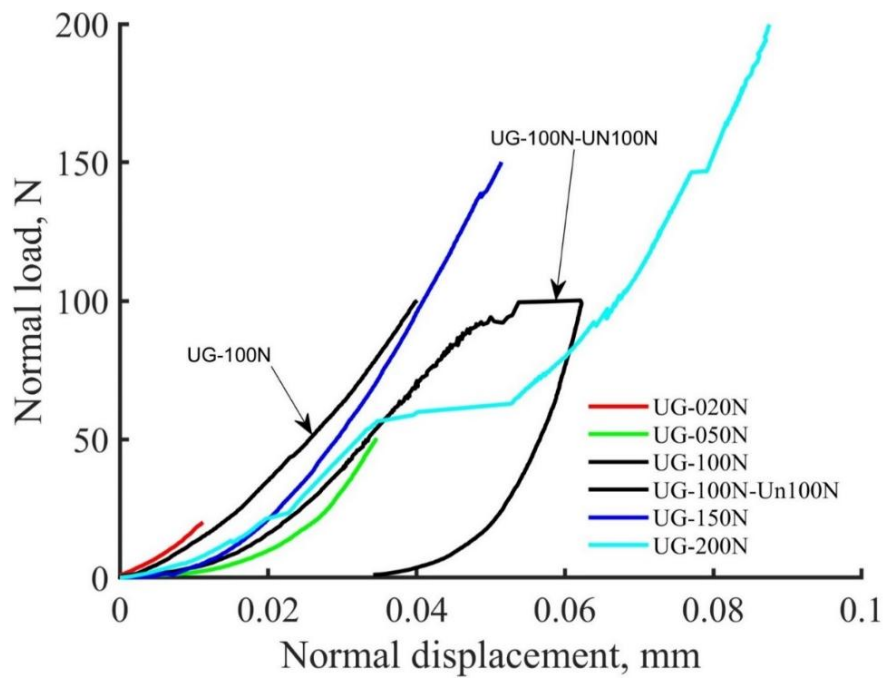
Figure 4.31 The load-deformation behaviour of used granite (UK) under different normal load levels.
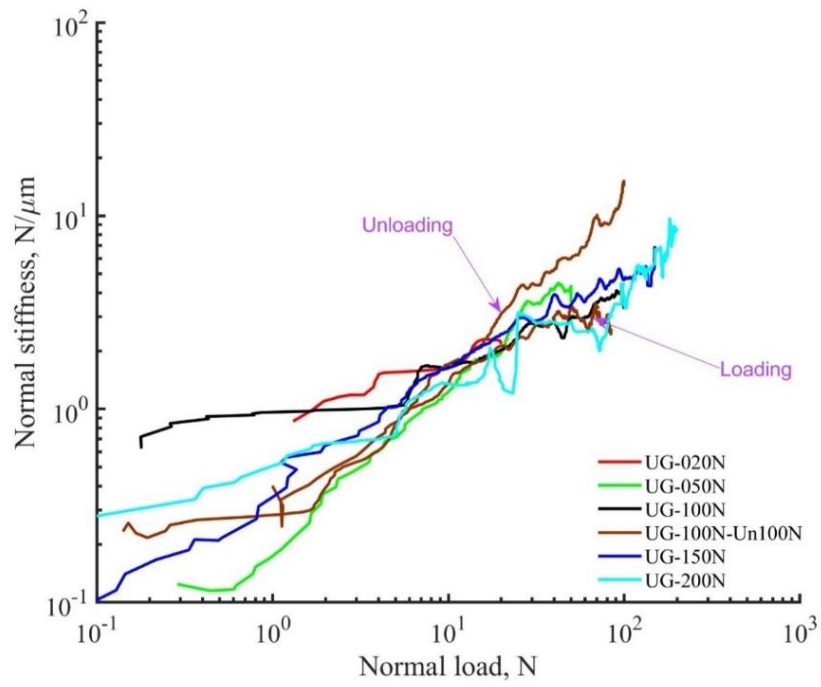
Figure 4.32 Normal stiffness behaviour of used granite (UK) under different normal loads.
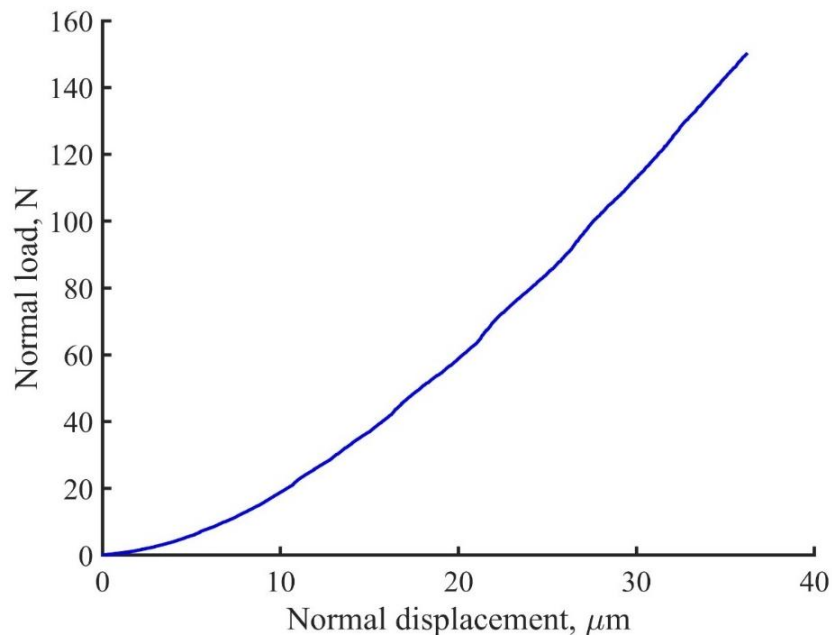
Figure 4.33 The load-deformation behaviour of washed granite (UK) under normal load 150N.
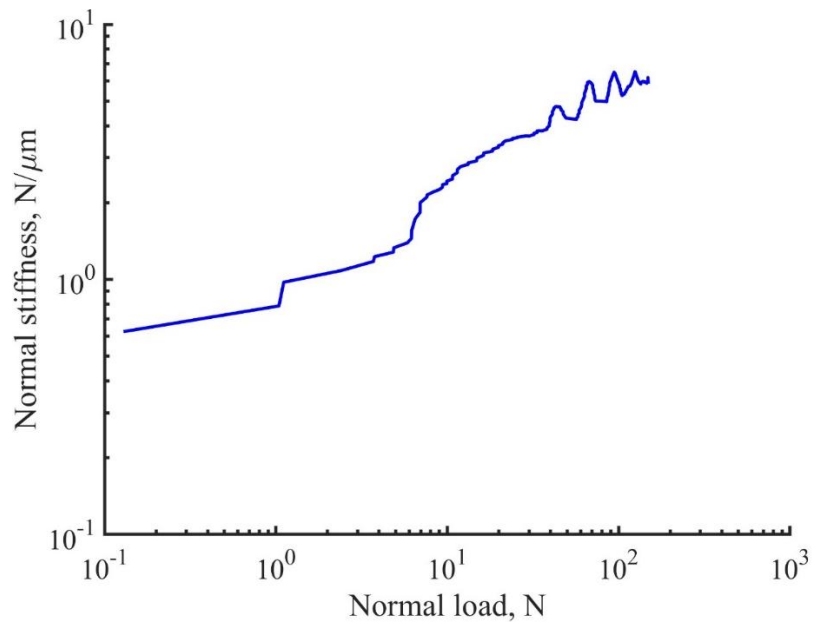
Figure 4.34 Normal stiffness behaviour of washed used granite (UK) under a normal load of 150N.
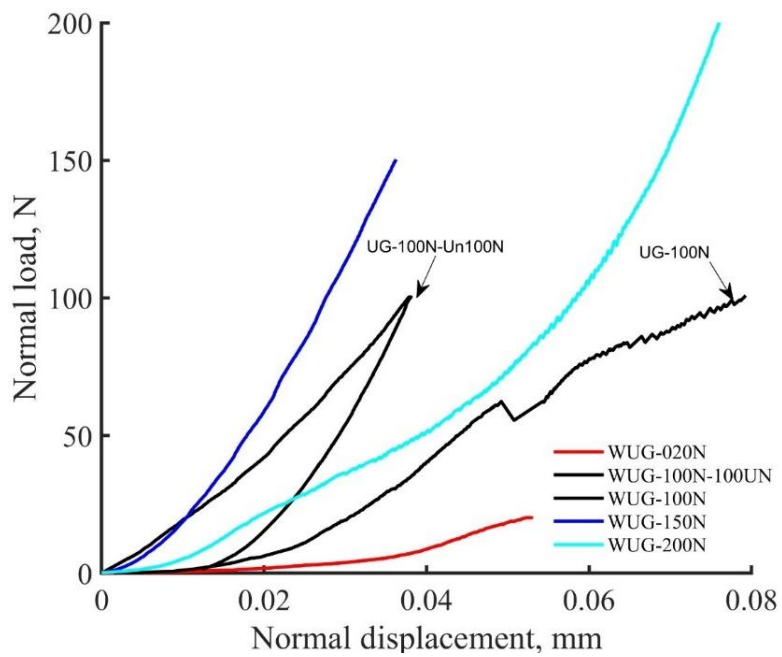
Figure 4.35 The load-deformation behaviour of washed used granite (UK) under different normal load levels.
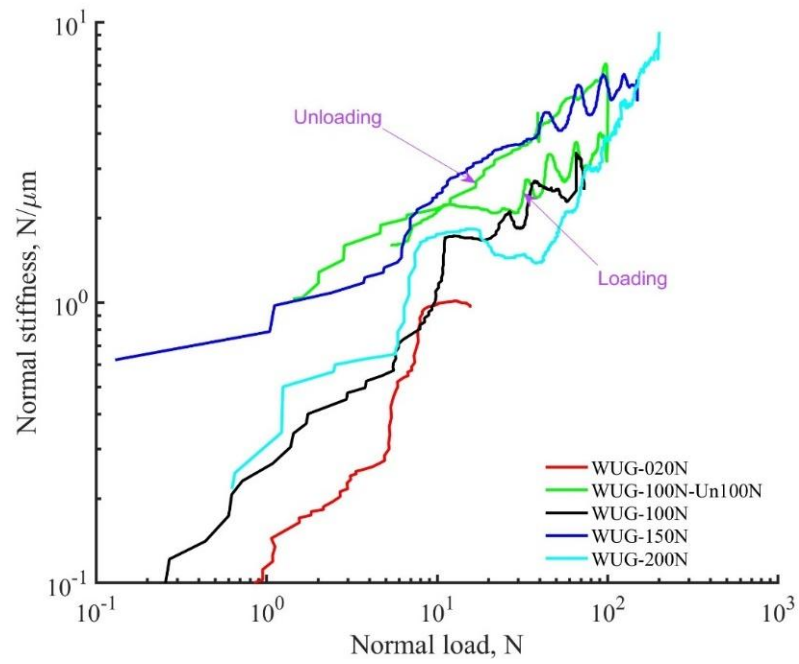
Figure 4.36 Normal stiffness behaviour of washed used granite (UK) under different normal loads.
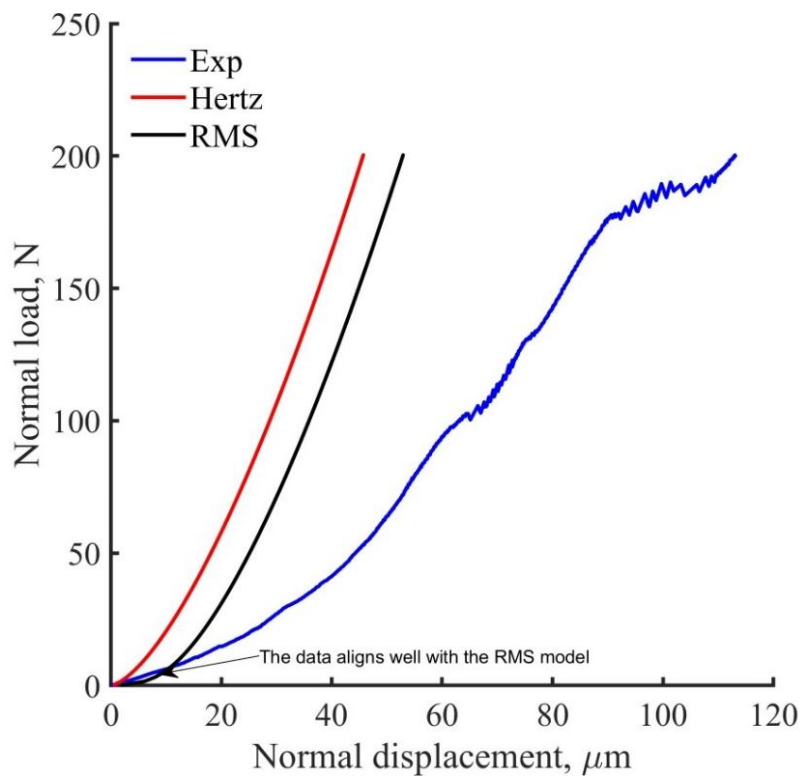
Figure 4.37 Comparison of andesite data with Hertz and RMS models.
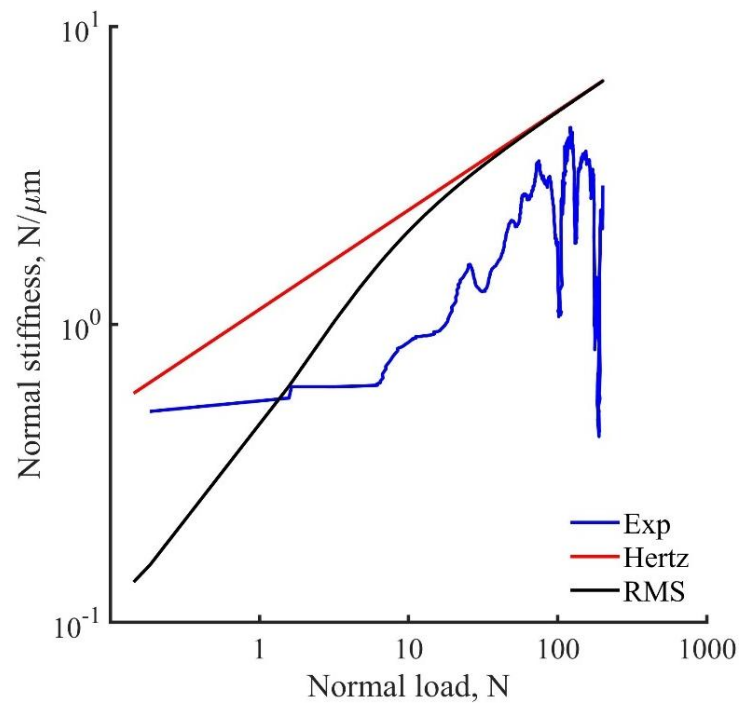
Figure 4.38 Comparison of andesites stiffness data with Hertz and RMS models.
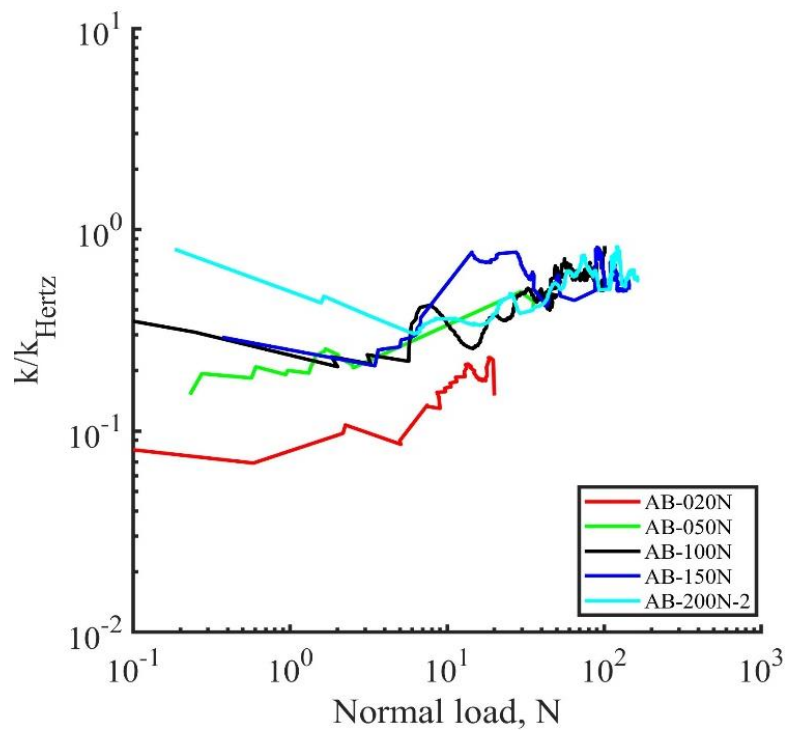
(a)
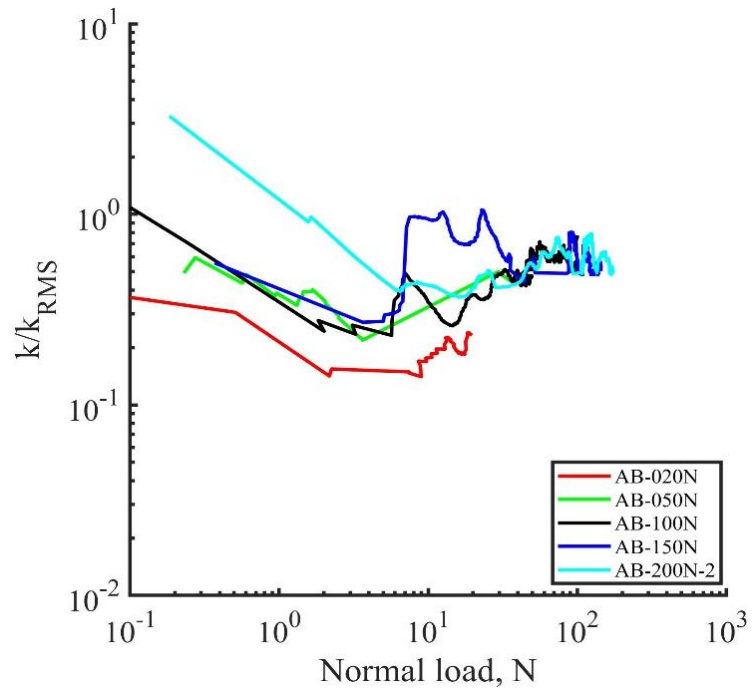
(b)

Figure 4.39 Comparison of andesites stiffness with Hertz (a) and RMS (b) models under different load levels.
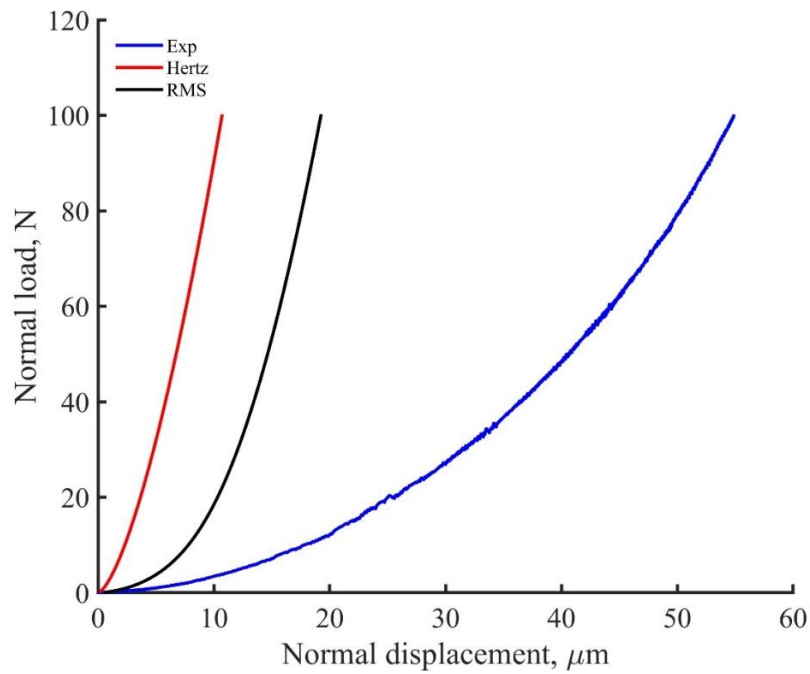
Figure 4.40 Comparison of basalt data with Hertz and RMS models.
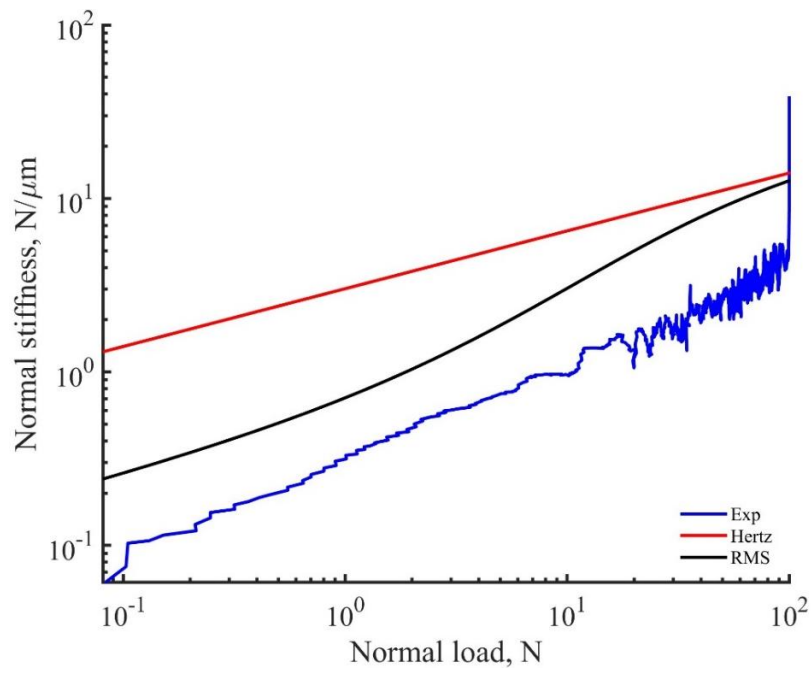
Figure 4.41 Comparison of basalt stiffness data with Hertz and RMS models

(a)

(b)
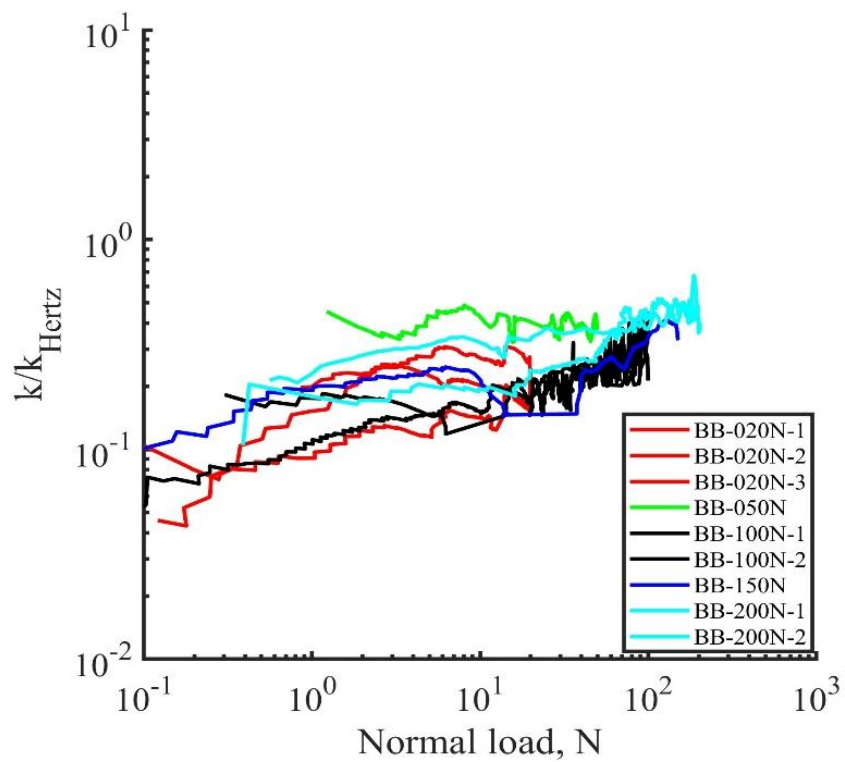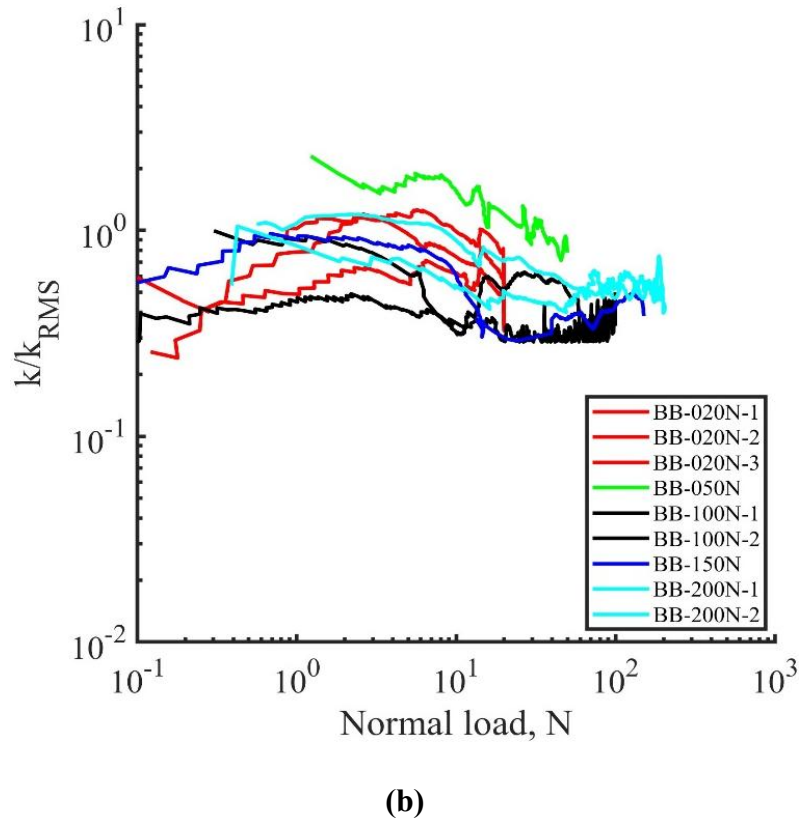
Figure 4.42 Comparison of basalt stiffness data with Hertz (a) and RMS (b) models under different load levels.
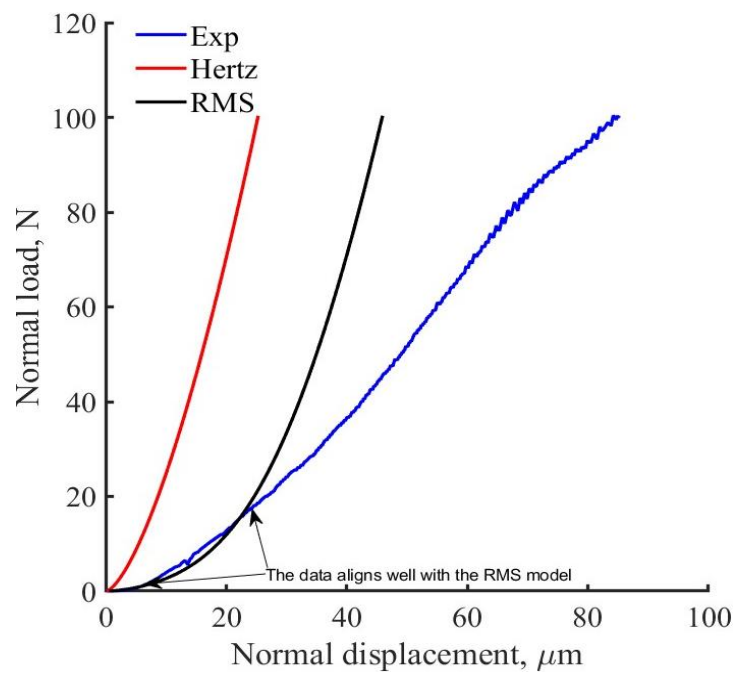
Figure 4.43 Comparison of Chinese granite data with Hertz and RMS models
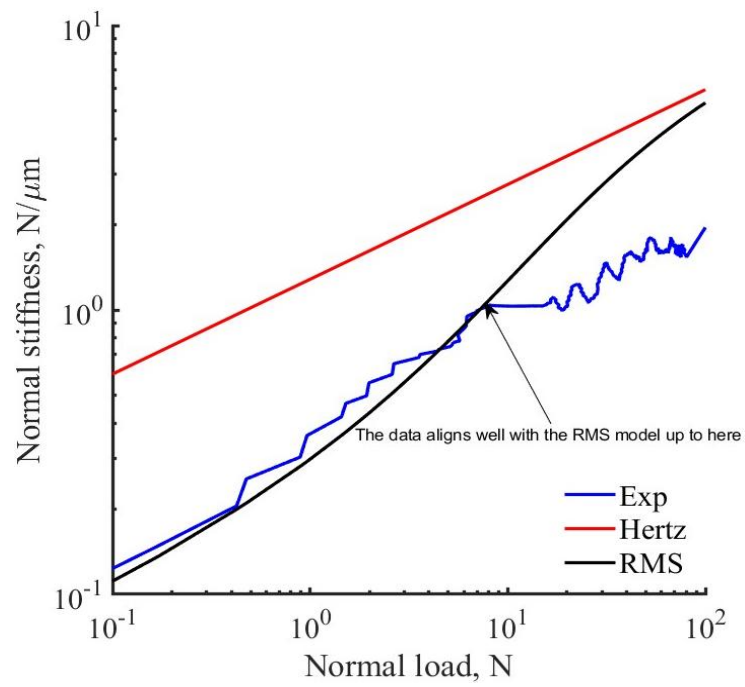
Figure 4.44 Comparison of Chinese granite stiffness data with Hertz and RMS models.
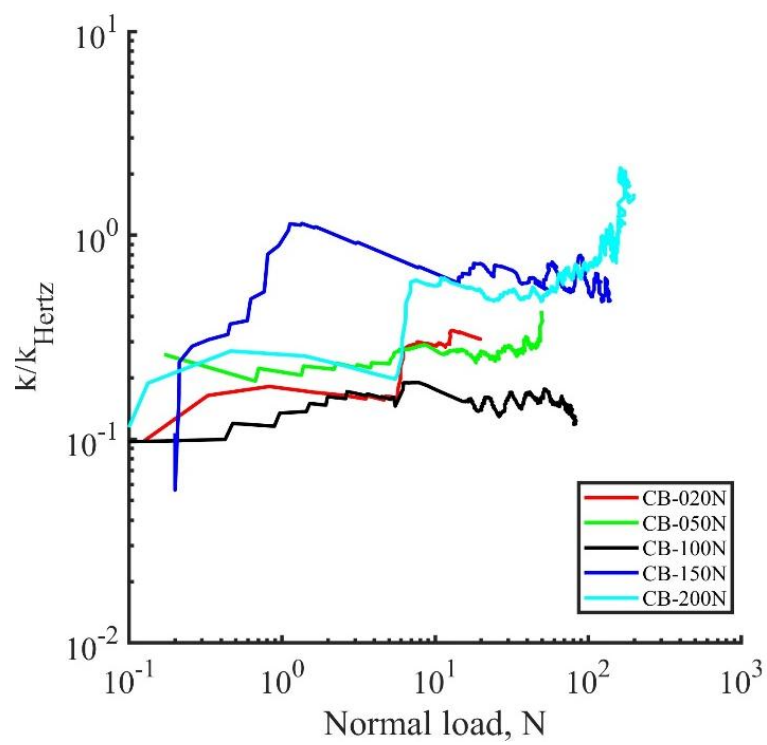
(a)
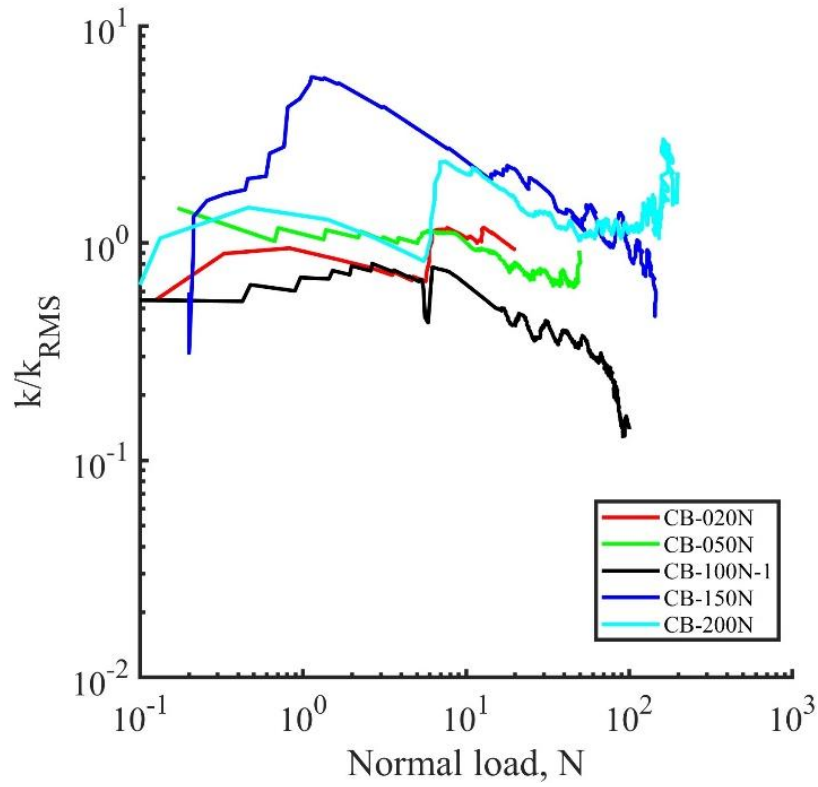
(b)

Figure 4.45 Comparison of Chinese granite stiffness data with Hertz (a) and RMS (b) models under different load levels.
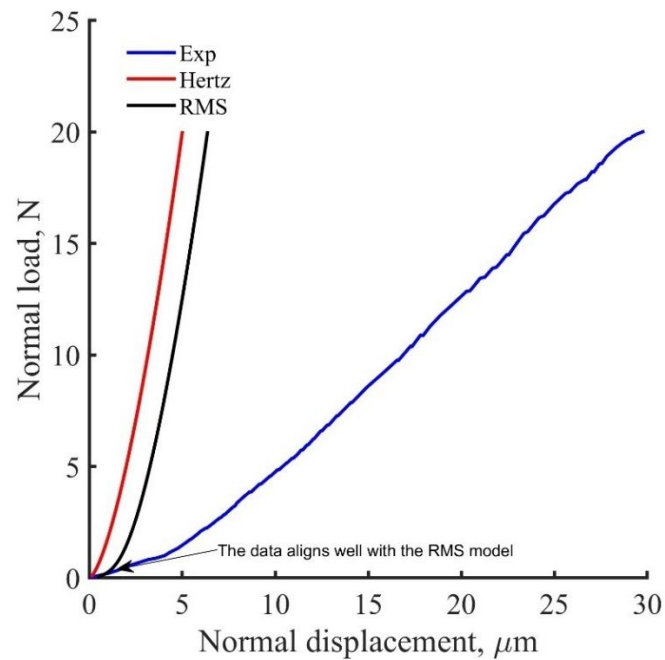
Figure 4.46 Comparison of fresh granite data with Hertz and RMS models.
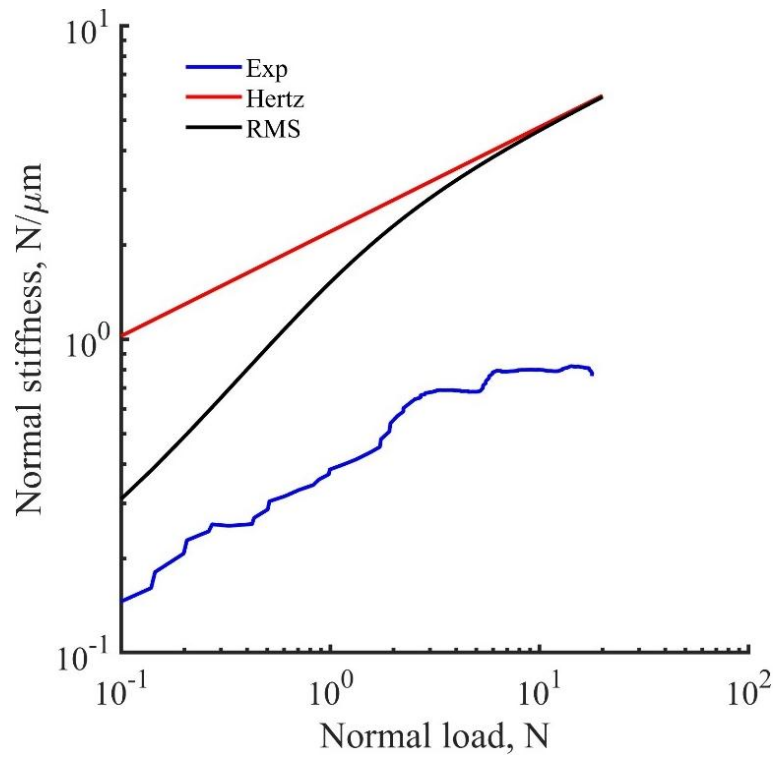
Figure 4.47 Comparison of fresh granite stiffness data with Hertz and RMS models.
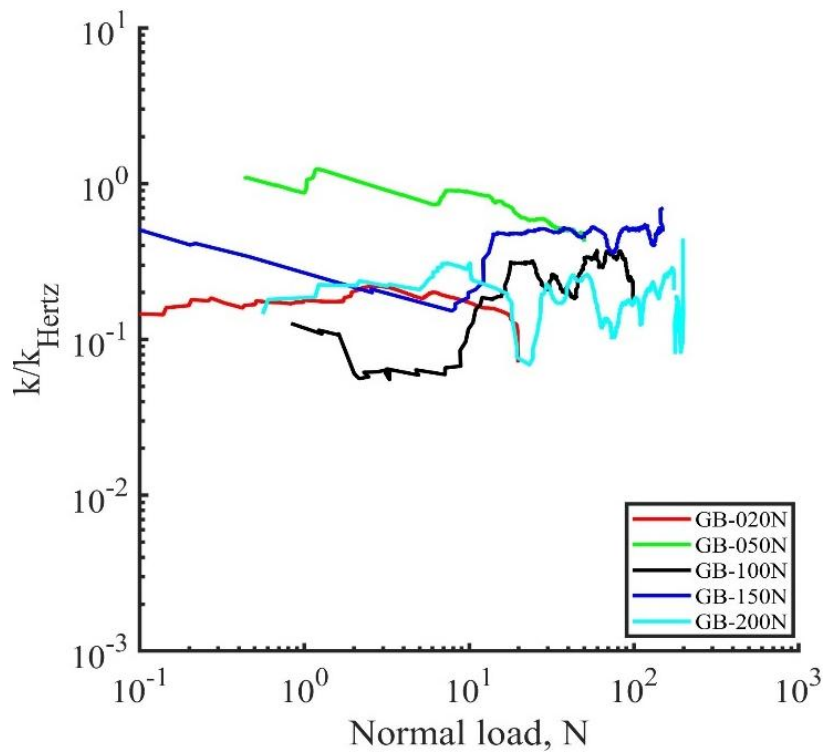
(a)
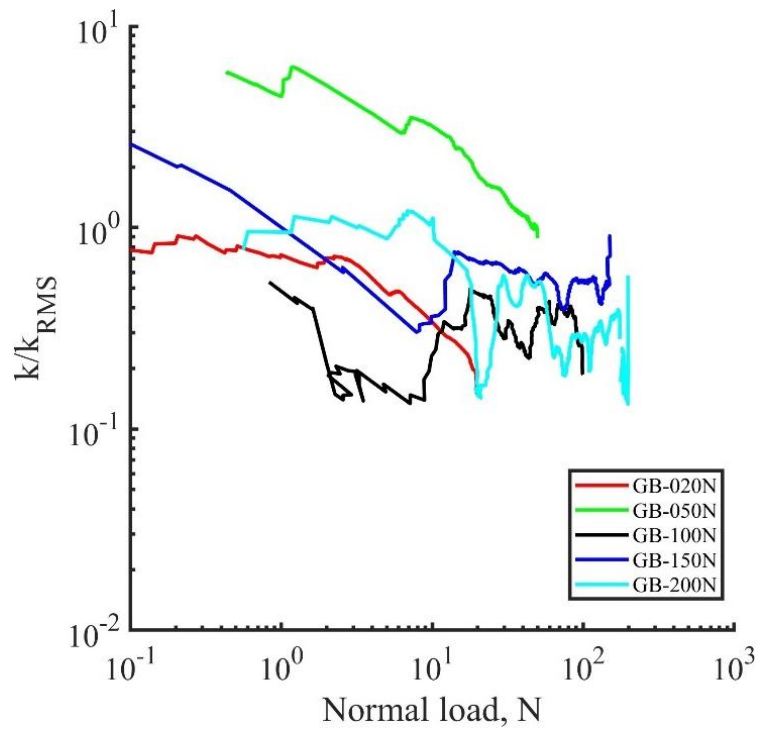
(b)

Figure 4.48 Comparison of fresh granite stiffness data with Hertz (a) and RMS (b) models
under different load levels.
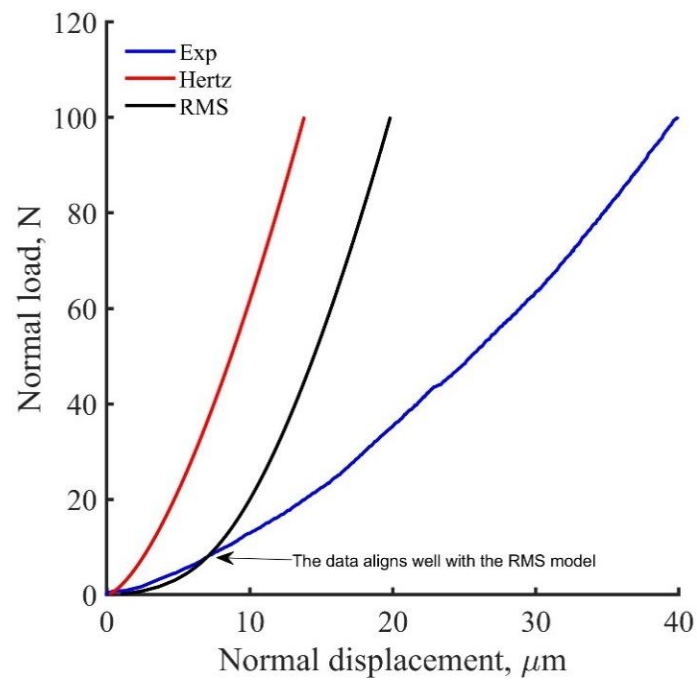
Figure 4.49 Comparison of used granite data with Hertz and RMS models.
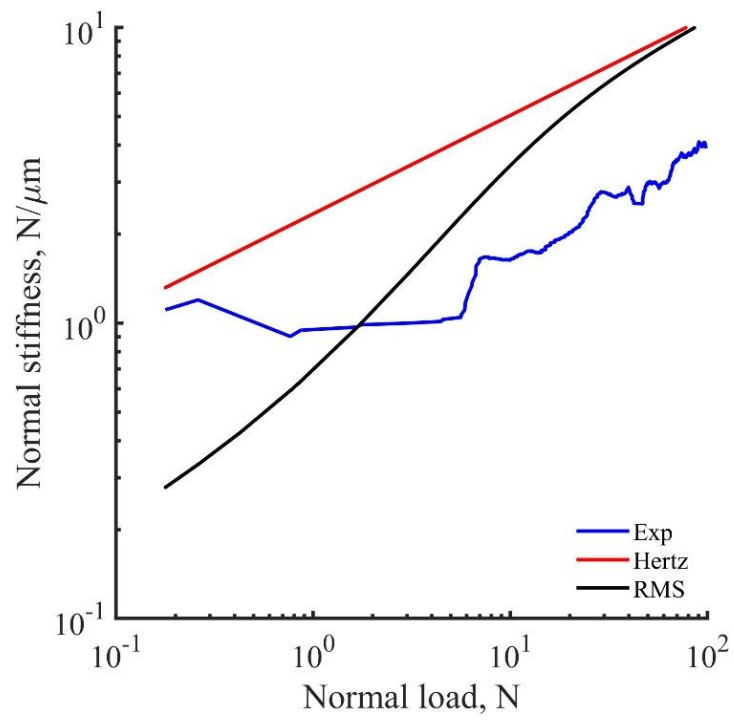
Figure 4.50 Comparison of used granite stiffness data with Hertz and RMS models.
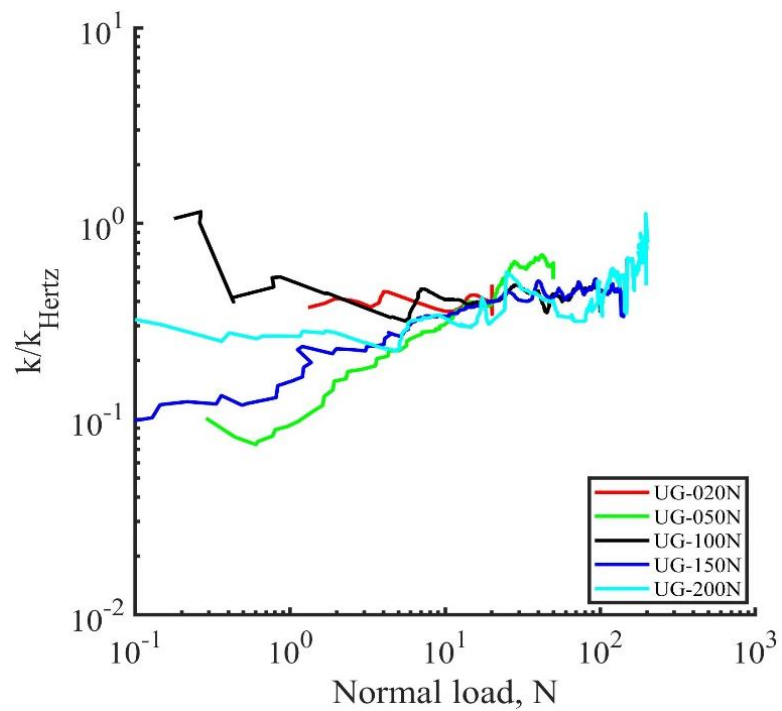
(a)
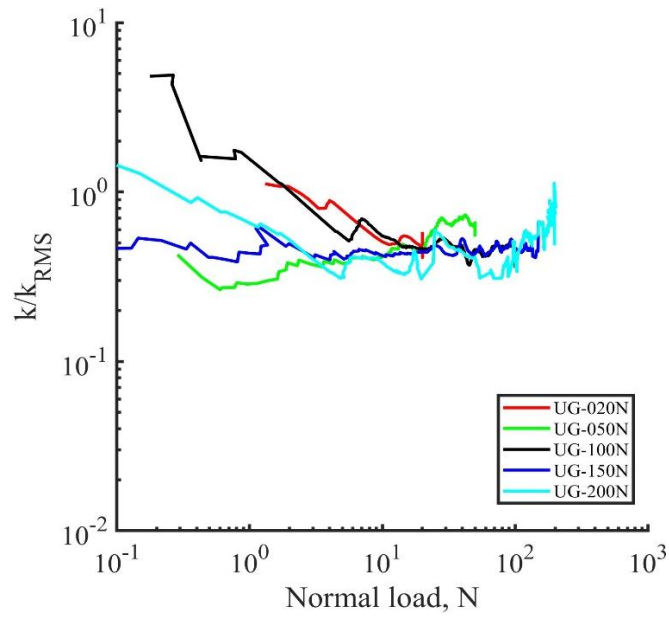
(b)

Figure 4.51 Comparison of used granite stiffness data with Hertz (a) and RMS (b) models under different load levels.
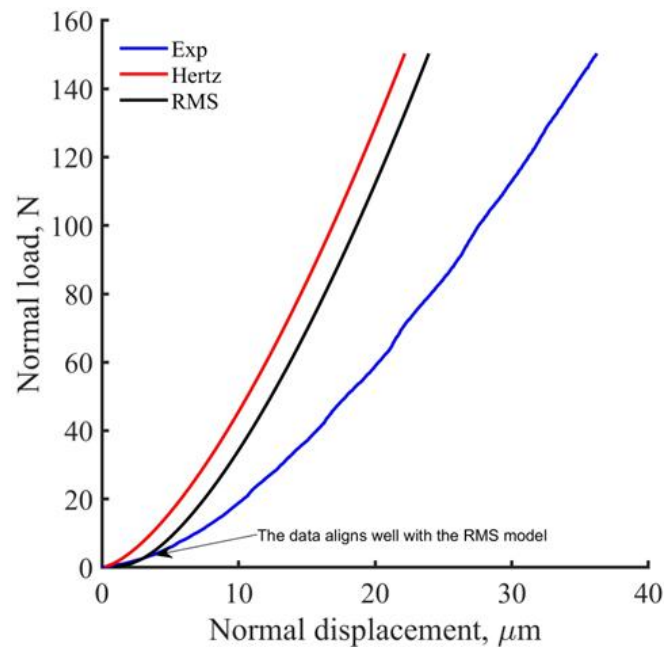
Figure 4.52 Comparison of washed used granite data with Hertz and RMS models
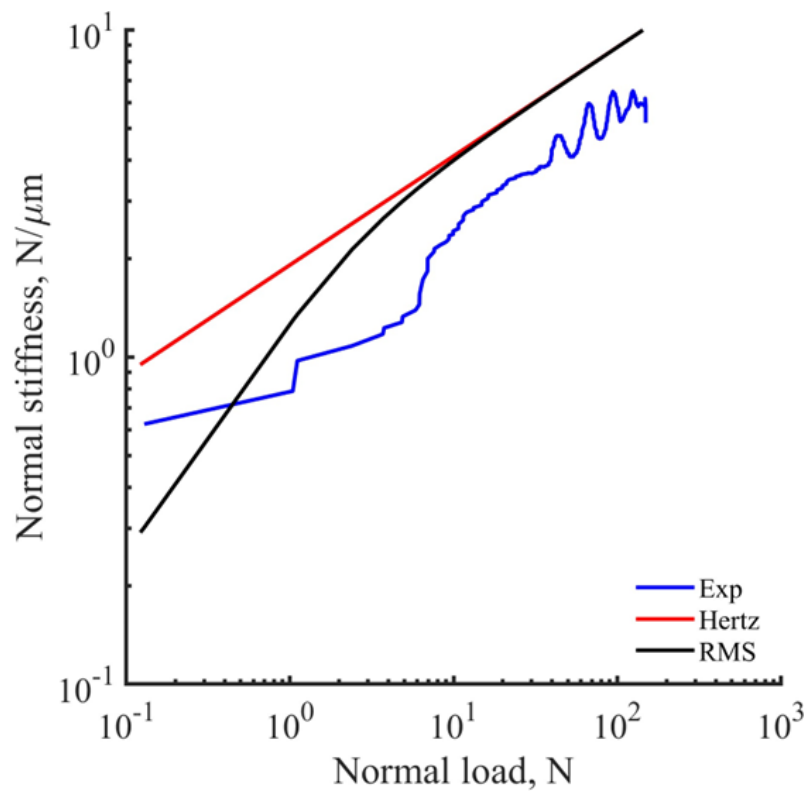
Figure 4.53 Comparison of washed used granite stiffness data with Hertz and RMS models.
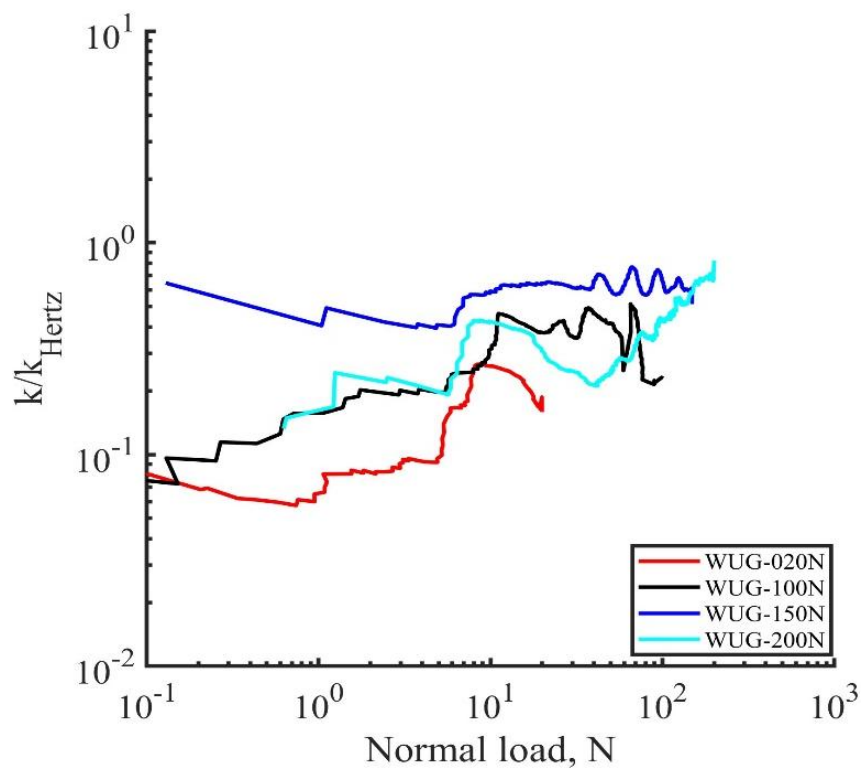
(a)
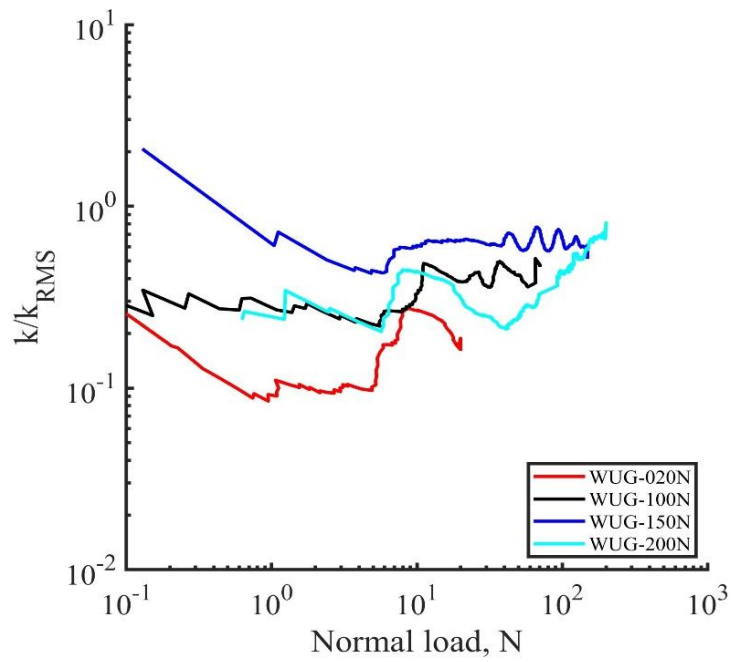
(b)

Figure 4.54 Comparison of washed used granite stiffness data with Hertz (a) and RMS (b) models under different load levels.
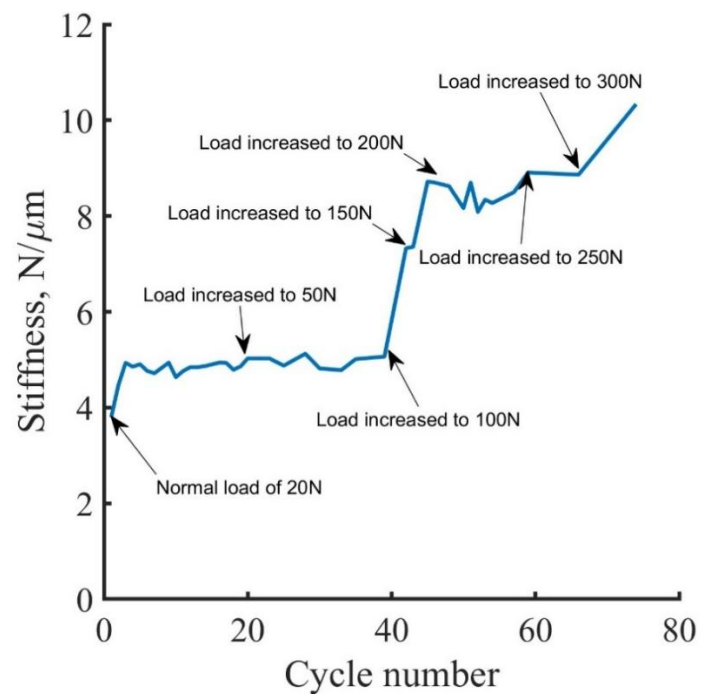
Figure 4.55 Normal stiffness of basalt increases with normal load, with more pronounced changes at higher loads due to surface deformation.

5. Monotonic Shearing Loading

After investigating the behaviour of railway ballasts under normal loading in the last chapter, this section presents results from monotonic shearing tests on the different ballast particles to see their behaviours under different normal load conditions. Cyclic shearing will be presented in the next chapter; however, this chapter will also include data from local shearing tests.

5.1 Monotonic shearing

This section covers the monotonic shearing behaviour of all types of ballasts. The tangential loading was usually carried out after normal loading to the desired load level. Some tangential loading tests on calcite particles were performed early in the PhD, and the results of the tests were not included. Chapter 3 briefly introduced the different types of ballasts in the materials section. Because of the large number of tests, for each ballast type, we will discuss the results for all types of ballasts by selecting figures from one test and then explaining the combined behaviours.

The methodology for the monotonic shearing is discussed first, and some examples are given from ballast particles.

Experimental Procedure:

The tests typically did not start with zero tangential force (T) due to the presence of a small horizontal load in one or more directions after applying the normal load, resulting from the contact surface not being perfectly horizontal. Tangential force and stiffness are dependent on the normal load (N), with higher normal loads generally leading to greater initial stiffness. The H1 and H2 direction displacements were set to zero at the start of shearing. Lower normal loads resulted in lower shear forces, but the gradients of most tests remained consistent across different normal load levels. Initial tangential load and stiffness were influenced by the normal load, with higher normal loads producing an expected increase in stiffness. As the testing program progressed and modifications reduced the apparatus's compliance, the reliability of the tests improved.

The mobilised T/N values for monotonic shearing were calculated by dividing the tangential force by the normal force. Stiffness values were derived by taking local gradients of the

force-displacement curve, using linear regression over several data points. These points were adjusted during each test to minimise value scatter while avoiding overly long intervals that could skew the calculations. The interval for regression ranged between 10 and 100 data points. The results of monotonic shearing tests for all types of ballast under normal loads of 20N, 50N, 100N, 150N, and 200N will be discussed. The discussion will be organised by selecting figures from one test and then explaining the combined behaviours, starting with andesite and following alphabetical order**.

5.1.1   Andesite ballasts

A total of 5 monotonic shearing tests (Table 5.1) were carried out on andesite ballasts under different normal loads to see the effect of normal load on the coefficient of inter-particle friction (μ) values and tangential stiffness.

Typical results (test AB-20N)

The monotonic shearing test AB-20N was conducted with a new pair of cleaned and dry andesite ballast particles under a constant vertical load of 20N, with a displacement of +0.5 mm.

Coefficient of Inter-particle Friction (μ) Values: The mobilised T/N values for test AB-20N increased with displacement, stabilising after 100 μm, as shown in Figure 5.1. At large displacements, the particles tended to slide at T/N values mostly between 0.5 and 0.8. Similar behaviour will be shown for cyclic shearing (see Chapter 6 for details). The displacements required to obtain the coefficient of friction values varied, and the T/N values were very scattered, similar to the findings of Cole (2015), Wong and Coop (2024), and Altuhafi et al. (2024).

Tangential Stiffness: Typically, tangential stiffness starts with a constant value and then decreases towards zero at large displacements (around 90 μm), as shown in Figure 5.2. The tangential stiffness values at small displacements were also scattered, the scatter reducing with increasing displacement. Some data points were removed for better presentation, as these points were likely caused by the breakage of the asperities or movement in the apparatus. The tangential stiffness of test AB-20N (0.85 N/μm) was very similar to the value Wong (2022) found under the same normal load (20N) for granite, which was 0.75 N/μm.

Combined test data

Coefficient of Inter-particle Friction (μ) Values: The mobilised T/N values for all five tests with different tangential displacements (+0.5 – 1 mm) increased with increasing displacement, usually stabilising after 100-200 μm (Fig. 5.3). At large displacements, the particles tended to slide at μ values mostly between 0.65 and 1. However, the μ values were very scattered, similar to the findings of Cole (2015), Wong (2022), and Altuhafi et al. (2024). Friction should not be dependent on the normal load, and test AB-150N showed higher T/N values than AB-200N, and test AB-20N showed higher μ values than AB-50N and AB-100N, in no particular trend. During the monotonic shearing, a common trend was observed: T/N values were higher at 100 μm displacement and then dropped, except in test AB-150N. This could be due to the breakage of asperities and peaks at the contact points.

The variability in μ values may also be influenced by the mineralogical composition and surface topology of the ballast particles. Andesite particles, being rougher and more angular, are likely to have more pronounced asperities that can interlock, leading to higher initial friction values. This interlocking effect can cause greater variability in the μ values compared to smoother particles like granite.

Additionally, the presence of powder due to abrasions and dust on the ballast surfaces might have contributed to the scattering of μ values. Cleaned and dry andesite particles were used in the tests to minimise this effect, but complete elimination was challenging. The role of particle shape and surface texture cannot be ignored either, as these factors significantly influence the contact mechanics and frictional behaviour of ballast materials. In conclusion, the μ values observed in the tests show a complex interplay of factors, including normal load, displacement, mineralogy, surface roughness, and the presence of powders.

Tangential Stiffness: The summary of the five tests is shown in Figure 5.4. Initially, tangential stiffness for all tests was higher and followed a similar trend, except for test AB-050N. The stiffness then decreased to near zero at approximately 100 μm. The tangential stiffness values at small displacements were scattered, and some data points were removed for better presentation, likely caused by the breakage of asperities or movement in the apparatus. Drops and negative values of stiffness, which were removed, occurred where particle breakages happened, causing the load to jump backwards.

The effect of normal loads on tangential stiffness was not consistent. Test AB-150N showed lower stiffness than test AB-100N, whereas test AB-200N exhibited higher stiffness, followed

by AB-100N. These stiffness values were generally lower than those found by (2022) for granite. Wong (2022) observed that increasing normal loads increased tangential stiffness, which would be expected for any granular soil.

The differences in stiffness and μ values could be influenced by the mineralogy of the particles and the surface topology, which play a significant role in the mechanical behaviour of the ballast. The rougher and more angular andesite particles likely contribute to the observed variability, highlighting the importance of particle characteristics in determining frictional and stiffness properties.

5.1.2 Basalt ballasts

Basalt ballasts were extensively tested in this experimental research project, serving as the core research material. Over 20 tests were conducted on basalt, with 12 tests selected for monotonic shearing, for better data presentation and the summary is shown in Table 5.2. Early tests were disregarded due to issues with the shearing rate and data reliability, and corrections for load in the H2 direction were excluded since the shearing was conducted in the H1 direction.

Topology and noise corrections were applied to the later tests, whereas only global corrections were used in the earlier tests, similar to the methods of Nardelli and Coop (2018) and Wong (2022). Following discussions and with the assistance of Dr Saurabh Singh, all necessary filters and corrections were applied systematically to the remaining tests on all types of ballasts. It was agreed that the shearing rate should be reduced at the beginning of the test (0.1mm/hr) to obtain more data points for better stiffness analysis before increasing the rate (0.5mm/hr) and the displacements in both directions (H1 and H2) were zeroed before starting monotonic shearing. This approach was missing in the earlier tests and previous research works.

Test BB1-100N-Flooded:

This test was conducted on basalt ballast particles under a constant vertical load of 100N with a displacement of +1.0 mm. The surfaces of the basalt ballast particles were washed and dried. During the test, water was added to the sample to observe the effect of water on the μ values and tangential stiffness.

Coefficient of Inter-particle Friction (µ) Values: The results of test BB1-100N are illustrated in Fig. 5.5. The mobilised values of T/N increased with displacement, similar to the trend observed for andesite ballasts, but stabilised after 300 µm, whereas andesite ballast stabilised more quickly at around 100 µm.

At 700 µm displacement, the sample was flooded to investigate the effect of water on the monotonic shearing µ. It was observed that flooding caused a clear drop in µ values. The µ values decreased significantly upon flooding and then returned to their previous levels once the sample dried. This change was immediate, indicating that the presence of water reduced the friction between the particles, but this effect was reversible once the water was removed.

The µ values for basalt were generally lower (around 0.65) compared to those for andesite ballast (around 0.8). Despite this, the µ values were higher than those obtained by Wong (2022) for other materials such as granite (0.45). This variation could be attributed to the interlocking of asperities and differences in mineralogy and angularity, as basalt ballasts are more angular than the granite ballasts tested by Wong (2022). The roughness and angularity of basalt and andesite particles likely contribute to higher friction values, as these characteristics enhance the mechanical interlock between particles.

Additionally, the presence of water likely reduced the inter-particle friction by acting as a lubricant, temporarily decreasing the µ values. This effect underscores the importance of considering environmental conditions, such as moisture, in the assessment of ballast materials for practical applications.

Tangential Stiffness: Tangential stiffness initially started higher and then decreased with increasing displacement, approaching zero at larger displacements around 100 µm (Fig. 5.6). Similar to the findings for andesite and granite by Wong (2022), the stiffness values for basalt at small displacements were also scattered.

The initial stiffness of test BB-100N (0.95 N/µm) was slightly lower than that of andesite (1.10 N/µm) for the same normal load (100N), but much lower than the values found by Wong (2022) for granite under the same normal load, which was 1.75 N/µm.

Furthermore, upon flooding at 700 µm a slight jump in the tangential stiffness values was observed, but the effect was not significant. This indicates that while water impacts the coefficient of inter-particle friction, its influence on tangential stiffness is less pronounced.

Combined Tests data

Coefficient of Inter-particle Friction (μ) Values:

The summary of mobilised T/N values for all 12 tests with different tangential displacements (+0.5 – 1 mm) is illustrated in Figure 5.7. The values of T/N increased with displacement and stabilised after 100-200 μm, with particles tending to slide at μ values mostly between 0.4 and 0.7. These values were lower than those for andesite ballast but were highly scattered, similar to the findings for andesite, as well as those of Cole (2015), Wong (2022), and Altuhafi et al. (2024).

The effect of normal load was not apparent, as tests with a normal load of 20N showed higher μ values than tests with 200N, consistent with Wong (2022). μ values were typically higher at 100-200 μm displacement before dropping, except for some tests like BB-50N, which could be due to the slow rate or the breakage of asperities. Initially, a slow rate of 0.1 mm/hr was used for better data, which was then increased to 0.5 mm/hr after 100-200 μm.

Basalt particles, being rougher and more angular, likely have more pronounced asperities that can interlock, leading to higher initial friction values. This interlocking effect causes greater variability in μ values compared to sub-angular particles like granite. This might explain why Wong (2022) found lower μ values for the monotonic shearing of granite ballast compared to basalt.

Additionally, water likely reduced inter-particle friction, possibly acting as a lubricant, temporarily decreasing μ values. This emphasises the importance of considering environmental conditions, such as moisture, in assessing ballast materials for practical applications. The scattering of μ values may also result from the breakage of the asperities and could be from debris or powders. While cleaned and dry basalt particles minimised this effect, complete elimination was challenging.

Tangential Stiffness:

Initially, tangential stiffness for all tests was higher and followed a trend similar to andesite, decreasing with increasing displacement as illustrated in Figure 5.8. The stiffness values decreased to near zero after 100 μm, whereas for andesite, this zeroing occurred earlier.

Tangential stiffness values at small displacements were scattered and influenced by particle breakages, which caused the load to jump backwards.

The effect of normal loads on tangential stiffness was not consistent. Tests with a normal load of 20N showed similar stiffness to tests with 100N, while test BB-200N-3 exhibited higher stiffness, followed by BB-100N-Flooded. Similarly to andesite ballast, differences in stiffness and μ values for basalt could be influenced by the mineralogy of the particles and surface texture.

5.1.3 Chinese ballasts

A total of seven tests were conducted on Chinese granite, and the results are presented in Table 5.3.

Individual Test (CB-150N)

CB-150N was conducted using a new pair of cleaned and dried Chinese granite ballast particles under a continuous normal load of 150N, with a displacement of + 1 mm

Coefficient of Inter-particle Friction (μ) Values: Test CB-150N yielded lower μ values compared to andesite and basalt ballasts, as shown in Figure 5.9. Initially, the values of T/N increased with displacement, reaching up to 0.3, but then dropped sharply after 50 μm to below 0.2. A slight increase was observed after 300 μm, with μ stabilising around 0.2. This stabilisation occurred much later compared to other ballasts like basalt, andesite, and granite, as reported by Wong (2022). A similar behaviour was noted in cyclic shearing (refer to Chapter 6), where μ started low but increased after 20 cycles.

The stabilised μ values for Chinese granite were not as scattered, unlike those found for other ballasts (basalt and andesite) and by previous research by Cole (2015), Wong (2022), and Altuhafi et al. (2024). The μ values observed during the monotonic shearing of Chinese granite ballast were generally similar to those seen in the first 10 cycles of cyclic shearing. During cyclic shearing, μ values were initially lower, then increased, eventually surpassing those observed during monotonic shearing. This difference could be attributed to variations in mineralogy and surface topology, as Chinese granite particles may have a different surface texture that influences frictional behaviour, as this behaviour was not seen for any other type of ballasts.

Tangential Stiffness: In test CB-150N, the tangential stiffness started at a constant value and decreased towards zero at 40 µm of tangential displacement, eventually dropping below zero after 70 µm (Fig. 5.10). The initial tangential stiffness values were scattered and were removed due to possible inaccuracies caused by the breakage of asperities or interruptions during testing. The tangential stiffness for test CB-150N was 3.25 N/µm, which is significantly higher than the values found for other ballasts like basalt and andesite under the same normal loads. It was even higher than the value reported by Wong (2022) for granite under a higher normal load of 200N, which was 2.25 N/µm. This suggests that Chinese granite exhibits superior stiffness properties compared to other ballast materials.

Combined Test data

Coefficient of Inter-particle Friction (µ) Values: The results of monotonic shearing tests on Chinese granite ballast, conducted under varying normal loads across seven tests with different tangential displacements (+0.5–1 mm), are shown in Figure 5.11. As with other ballast materials, the values of mobilised T/N initially increased with displacement but dropped significantly quite early, around 50 µm, except in a few cases, such as CB-020N and CB-100N-2. The µ values generally stabilised after 400 µm, with the particles typically sliding at µ values between 0.15 and 0.5. An exception was test CB-100N-Flooded, which exhibited higher µ values than the other tests, though these values were scattered and may have been influenced by the movement of the load cell when water was added.

A common trend observed with other ballasts was also noted here: µ values increased before dropping. The effect of the normal load was unclear; for instance, tests with smaller loads (20N and 50N) exhibited higher µ values than CB-150N and CB-200N. This pattern was also observed in basalt and andesite tests and aligns with findings by Wong (2022).

Additionally, Figure 5.11 shows that the stabilised µ values for Chinese granite were less scattered compared to other ballast materials like basalt and andesite and were consistent with previous research by Wong (2022) and Altuhafi et al. (2024) on granite ballasts. The µ values observed during the monotonic shearing of Chinese granite were generally similar to those seen during the early stage of cyclic shearing. During cyclic shearing, µ values were initially lower but increased over time, eventually surpassing those observed during monotonic shearing (see Chapter 6).

The effect of water was also evident; for instance, in test CB-100N-Flooded, the µ values dropped when water was added and increased again as the sample dried. In conclusion, the µ

values observed in these tests for Chinese granite were generally lower than those found for andesite, basalt, and the values found by Wong (2022).

Tangential Stiffness: Figure 5.12 provides a summary of the tangential stiffness observed across all tests on Chinese granite. The tangential stiffnesses were high initially for all tests and then decreased, following a similar trend observed for other ballasts, except for the flooded test (CB-100N-Flooded). Tangential stiffness decreased to near zero much faster than seen for other ballasts, typically around 50 μm of tangential displacement.

As shown in Figure 5.12, Chinese granite demonstrated higher tangential stiffness compared to basalt and andesite. While Wong (2022) noted that increasing normal loads generally led to increased tangential stiffness, the effect of normal loads on tangential stiffness for Chinese granite was inconsistent. For example, a test under the normal load of 150N (CB-150N) exhibited higher stiffness than a test under the normal load of 200N (CB-200N), followed by a test with a normal load of 100N (CB-100N-2). These stiffness values were generally higher than those reported by Wong (2022) for granite, indicating that Chinese granite may possess superior stiffness characteristics under similar conditions.

5.1.4 Fresh granite ballasts

Six tests were conducted on fresh granite ballast to investigate its micro-mechanical contact behaviour under varying loading conditions, focusing on the influence of normal load on tangential stiffness. The results provide valuable insights into the mechanical response of the material and are presented in Table 5.4.

Individual Test (GB-200N)

Test GB-200N was carried out on a new pair of fresh granite ballast particles under a constant vertical load of 200N, with a tangential displacement of +0.5 mm.

Coefficient of Inter-particle Friction (μ) Values: Figure 5.13 presents the mobilised T/N values from the monotonic shearing tests plotted against tangential displacement. The T/N values increased with displacement, consistent with trends observed in other ballast materials. Although the μ values were scattered, they eventually stabilised around 0.7. Notably, the μ values for fresh granite were higher during monotonic shearing compared to cyclic shearing

(as discussed in Chapter 6), likely due to the interlocking of asperities and the rougher surface texture of fresh granite. These values also exceeded those reported by Wong (2022) for fresh granite under similar conditions, suggesting that surface characteristics may significantly influence friction.

Tangential Stiffness: Similar to other railway ballasts, the tangential stiffness in the fresh granite tests started high and decreased as displacement increased, approaching zero around 80 µm (Figure 5.14). The tangential stiffness for test GB-200N was 1.35 N/µm, lower than that of andesite and Chinese granite, but higher than basalt. This stiffness value was also lower than what Wong (2022) reported for the same granite under the same normal load, indicating that factors beyond normal load, such as surface roughness and materials curvature, can significantly impact tangential stiffness.

Combined Test data

Coefficient of Inter-particle Friction (µ) Values: Across all five tests with varying tangential displacements (+0.5 – 1 mm), at small displacement, the values of T/N generally increased with displacement as seen in Figure 5.15. However, at large displacements (after 100 µm), the values of T/N were decreasing, and a big drop was seen for some tests (e.g., GB-50-2 and GB-100N). The stabilised µ values ranged between 0.4 and 0.7, though they were scattered and consistent with findings for other ballasts. The effect of the normal load was inconsistent; for instance, the test GB-050N-2 with a normal load of 50N demonstrated higher µ values than the tests with higher loads such as GB-100 and GB-200N. Test GB-20N with a normal load of 20N exhibited higher values than tests with a normal load of 50N (GB-050N-1) and similar values to test with a normal load of 100N (GB-100N).

Fresh granite, being rougher, likely has more pronounced asperities than interlock, leading to higher initial friction values. This interlocking effect results in greater variability compared to smoother particles like those tested by Altuhafi et al. (2024). Overall, fresh granite has higher monotonic shearing µ values than Chinese granite and the same granite tested by Wong et al.

Tangential Stiffness: Tangential stiffness with tangential displacement across all the tests on fresh granite is illustrated in Figure 5.16. Initially, tangential stiffness was high for all tests and then decreased, following a similar trend that was observed for other ballasts except for test GB-020N-1. The tangential stiffness of fresh granite was not affected by the normal loads and was inconsistent. For illustration, tests with lower loads (GB-020N-2, GB-050N-1 and GB-050-2), showed higher stiffness in tests with higher loads (GB-100N and GB-200N).

These stiffness values were generally higher than those reported by Wong (2022) for the same granite ballasts. The differences in stiffness values highlight the significant role of surface topology in the micro-mechanical behaviour of ballast.

5.1.5 Used granite ballasts

Used granite ballasts were the only ballasts that were not washed before the test as we wanted them to test them in their original state, to see the effect of fouling and the outside environment and then compare with fresh granite and washed used granite. Five tests were performed on used granite ballast, with the corresponding results shown in Table 5.5.

Individual Test (UG-050N)

The used granite ballast tested in UG-050N was not washed or cleaned but rather tested in its original condition as collected from the depot, with only minor alterations made to achieve the appropriate sizes. This approach aimed to assess the behaviour of used granite, facilitating a comparison with fresh granite, as both granite types were sourced from the UK. The test UG-050N was conducted using a new pair of used granite ballast particles under a constant vertical load of 50N, with a tangential displacement of +1 mm.

Coefficient of Inter-particle Friction (μ) Values: The mobilised values of T/N from test UG-050N increased with tangential displacement, consistent with trends observed in other ballast materials tested in this study (Fig. 5.17). Although the μ values were somewhat scattered at the beginning of the test, they eventually stabilised after sliding at an approximate displacement of 200 μm, with the measured μ values ranging between 0.4 and 0.5. These values closely align with fresh granite and those reported by Wong (2022) for fresh granite, underscoring the importance of testing used granite ballast.

Tangential Stiffness: Figure 5.18 illustrates the tangential stiffness of used granite under a normal load of 50N. The stiffness initially started high and then decreased with displacement, approaching zero at approximately 80 μm, similar to the behaviour observed in fresh granite and other ballast types. The measured tangential stiffness was 1.4 N/μm, which is higher than that of all other ballast types, including fresh granite under the same normal load of 50N. This value was comparable to what Wong (2022) reported for fresh granite under a normal load of 100N.

Combined Tests

Coefficient of Inter-particle Friction (µ) Values: The summary of the coefficient of inter-particle friction (µ) values for all five tests conducted on used granite ballast, with a tangential displacement of +1 mm, is illustrated in Figure 5.19. The T/N values generally increased with small displacements across all tests, eventually stabilising after 600 µm. Stabilised µ values ranged between 0.4 and 0.7, though they were somewhat scattered. Unlike other ballast materials, no data was removed or filtered, as the data for used granite was more consistent and readable. This may be attributed to the smoother surface of the used ballast due to broken asperities from previous railway operations. The influence of normal load on µ was unpredictable; for instance, UG-150N, tested under a 150N load, exhibited higher µ values than UG-200N, tested under a 200N load. Additionally, UG-200N displayed lower µ values than tests conducted under smaller normal loads, such as UG-20N and UG-50N. Overall, used granite demonstrated higher monotonic shearing µ values compared to Chinese granite and the granite tested by Wong (2022), although it was lower than andesite. The µ values were similar to those observed in basalt and fresh granite tested in this research.

Tangential Stiffness: Figure 5.20 presents the tangential stiffness for all tests on used granite ballast with tangential displacement. Initially, tangential stiffness was high across all tests but decreased as displacement increased, following trends observed in other ballast materials. Although tangential stiffness is theoretically dependent on normal load, the used granite showed inconsistencies at small displacements with varying normal loads. For example, the test with a lower load of 50N (UG-050N) exhibited higher stiffness than those with higher loads (UG-100N and UG-150N). However, at larger displacements, a clearer correlation emerged, with higher loads yielding higher stiffness, followed by the order of normal loads. These stiffness values were generally similar to those found for Chinese granite and those reported by Wong (2022) for fresh granite ballast, but higher than those observed in this research for fresh granite, andesite, and basalt.

5.1.6 Washed used granite ballasts

These are the same used granite however washed and treated with chemicals with different types of acids to see the difference between washed surface and not washed. Also, some of

the particles were cut and the used surface was removed to compare it with the fresh surface and used surface. Four tests were conducted on washed used granite ballast to examine its micro-mechanical contact behaviour under different loading conditions. The results are presented in Table 5.6.

Individual Test (WUG-20N)

Test WUG-20N was conducted on washed used granite ballast particles under a constant vertical load of 20N, with a tangential displacement of +0.5 mm, in the H2 direction as the H1 transducer was not functioning.

Coefficient of Inter-particle Friction (μ) Values:

The μ values of washed used granite for test WUG-20N under the normal load of 20N are shown in Figure 5.21. At small displacement T/N was increasing with tangential displacement, aligning with trends seen in other ballast materials including untreated used granite and fresh granite. Although the μ value stabilised almost at 200 μm the approximate value was close to 0.7. Notably, the μ values for washed used granite were higher than for unwashed used granite, likely due to the contaminated surface of used granite, indicating the significant influence of surface characteristics on friction.

Tangential Stiffness:

The washed-used granite's tangential stiffness, which was initially high but decreased with displacement and eventually approached zero around 100 μm, is shown in Figure 5.22. The tangential stiffness for test WUG-20N was 1.25 N/μm higher than untreated used granite, which shows that it can be reused. This value was also higher than what Wong (2022) reported for the fresh granite under the same normal load, suggesting that factors beyond normal load, such as particle curvature.

Combined Test data

Coefficient of Inter-particle Friction (μ) Values: The monotonic shearing behaviour of washed used granite under different normal loads is illustrated in Figure 5.23, with tangential displacements (+0.5 mm). At the start of the test, μ values generally increased with displacement but stabilised after 100 μm, except for test WUG-150N. The stabilised μ values ranged between 0.45 and 0.85, and the effect of normal load was not evident. For example, as shown in Figure 5.23, the test with a smaller load (e.g., WUG-020N with a normal load of 20N) exhibited higher μ values than tests with a higher load of 150N (like WUG-150N) and almost similar values to the test with 200N (WUG-200N). Test WUG-100N with a normal

load of 100N exhibited higher µ values than WUG-200N-1 (200N load). Overall, washed used granite exhibited higher monotonic shearing µ values than untreated used granite, fresh granite, Chinese granite, basalt, and the granite tested by Wong (2022), though it was similar to the andesite ballast tested by the author. The effect of washing is clear, indicating that washed used ballasts could perform similarly to fresh railway ballasts.

Tangential Stiffness: Washing and cleaning used granite have improved the stiffness, as illustrated in Figure 5.24. The tangential stiffness of washed used granite across all tests was higher than that found for other types of ballast, except for Chinese granite, which was similar. Consistent with other railway ballast, initially high tangential stiffness decreased as displacement increased. However, the relationship between normal load and stiffness was unpredictable at small displacements. For instance, test WUG-020N with a normal load of 20N exhibited higher stiffness than WUG-100N with a normal load of 100N. At larger displacements (after 5 µm), the correlation is evident as tests with higher loads showed higher stiffness, following the expected trend. These stiffness values were generally similar to those reported for Chinese granite but were higher than the values found for fresh granite, andesite, basalt, and fresh granite by Wong (2022). This highlights the significant role of surface topology in the micro-mechanical behaviour of washed used granite ballast after treatment and cleaning**.**

The study shows that washing used ballast significantly improves both its frictional performance and tangential stiffness, making it comparable to fresh railway ballast. The treatment enhances the interlocking of asperities and increases resistance to deformation, which improves the ballast's mechanical stability and extends its service life. Washed used ballast could serve as a sustainable alternative to fresh ballast, maintaining performance while reducing the need for new materials.

5.2 Local cyclic shearing

Local shearing was performed immediately after monotonic shearing at varying displacements, ranging from 5µm to 50µm, under different normal loads (20N, 50N, 100N, 150N, 200N, 250N and 300N for each type of ballast. Similar to monotonic shearing, local cyclic shearing was conducted on all ballast types. However, only the results from a few tests will be presented, as some tests were poorly controlled and might not cover all different types of ballasts. Further, it was agreed with the supervisor that only tests with different load stages

will be shown here, as there are many tests and most of the outcome is similar to the next chapter and will only be considered here the effect of normal load on the stiffness during normal cyclic loading and local shearing.

5.2.1 Basalt ballast

Basalt was the only material that was tested under different load levels during the local cyclic shearing test. Figure 5.25 illustrates the relationship between tangential secant stiffness and the number of cycles under varying normal loads. Initially, at a normal load of 20N, the tangential secant stiffness starts at a baseline value and exhibits a slight increase over the initial cycles. This minor change suggests surface adaptation or settling effects as the contact interface adjusts. When the load increases to 50N, a noticeable rise in stiffness is observed, indicating that a higher normal force enhances surface contact and results in a stiffer response.

As the load further increases to 100N, another increment in stiffness occurs, though the rate of increase is smaller compared to the previous transition. This suggests that while higher loads continue to influence stiffness, the effect may become less pronounced with each subsequent increment. However, when the normal load reaches 200N, a significant jump in stiffness is observed. This sharp increase is likely due to greater asperity deformation, increased real contact area, or enhanced interfacial interactions, which contribute to a much stiffer system.

Overall, the results demonstrate that tangential secant stiffness increases with normal load. The trend is non-linear, with a more pronounced change at the highest applied load. This behaviour may be attributed to the progressive deformation of surface asperities, and potential wear effects.

5.3 Normal cyclic loading

The normal load was gradually increased from 0 to 20N, followed by normal cycles with a magnitude of ±5N. The normal load was then increased to 50N, and additional cycles were performed. This process was repeated at 100N, 150N, 200N, 250N and continued in the same manner until the load reached 300N. The figure 5.26 presents the variation of normal stiffness with cycle number under different normal loads. The stiffness is measured in N/μm, and the cycle number represents the progressive loading stages. At an initial load of 20N, the normal

stiffness starts at approximately 4 N/μm and gradually stabilises after a few cycles. When the load is increased to 50N, a noticeable rise in stiffness is observed, indicating that a greater normal force enhances surface contact and structural rigidity. As the load further increases to 100N, the stiffness remains relatively stable with minor fluctuations, suggesting that the system is adapting to the increased load without significant structural changes.

Upon reaching 150N, another increase in stiffness is evident, followed by a more pronounced jump when the load is increased to 200N. This sudden rise in stiffness could be attributed to changes in surface interactions, increased real contact area, or material compaction under higher loads. A similar but slightly smaller increase occurs when the load is raised to 250N, followed by a final surge in stiffness as the load reaches 300N. The trend suggests a non-linear response, where higher loads result in more significant increases in stiffness, likely due to progressive asperity deformation and enhanced mechanical interlocking at the interface.

Overall, the figure 5.26 demonstrates that normal stiffness increases with normal load, with more pronounced changes occurring at higher loads. The stiffness evolution suggests that at lower loads, the contact interface undergoes gradual adaptation, while at higher loads, significant changes in material behaviour led to abrupt stiffness increases. This response highlights the role of load-dependent deformation and contact mechanics in governing the stiffness characteristics of the system.

5.4 Summary

Andesite exhibited slightly higher initial μ values of 0.7 to 0.95. Basalt demonstrated relatively high and scattered μ values, ranging from 0.4 to 0.7, due to its rough and angular surface, which enhances asperity interlocking. Fresh granite exhibited similar frictional behaviour to basalt, with slightly higher initial μ values (0.35 to 0.95) resulting from its pronounced angularity and asperities. In contrast, Chinese granite showed lower and more consistent μ values, stabilising between 0.15 and 0.5, reflecting its smoother, sub-angular surface texture. Fresh granite performed similarly to Chinese granite, with μ values stabilising much faster after 50 to 100 μm of tangential displacement.

Washed used granite in comparison to unwashed used granite, achieved higher μ values, ranging from 0.45 to 0.85, which were comparable to andesite and fresh granite. The washing process significantly improved the performance of the used granite by removing surface

powders and debris, enhancing asperity interlocking and reducing variability in µ values. This highlights the role of surface cleanliness in optimising ballast performance.

The tangential stiffness of basalt and andesite was initially high but decreased rapidly with displacement due to the breakage of asperities, showing greater variability than other ballast types. Basalt and fresh granite exhibited lower tangential stiffness overall, whereas washed-used granite outperformed all other ballast materials in terms of tangential stiffness. Washed used granite stiffness values comparable to Chinese granite but superior to fresh granite, unwashed used granite, basalt, and andesite. Also washed used granite showed slightly consistent behaviour across normal loads. The washing treatment improved the resistance of used granite to deformation and greater mechanical stability, resulting in higher tangential stiffness.

Overall, the results highlight distinct differences among the ballast materials, emphasising the influence of surface roughness, angularity, and treatment on frictional behaviour and stiffness. Rough and angular materials such as basalt and andesite displayed higher initial µ and stiffness values, but these properties degraded faster due to asperity breakage. Smoother materials like used granite and Chinese granite exhibited lower but more consistent performance. Washed-used granite demonstrated the best overall performance, combining high friction and stiffness with reduced variability, making it a sustainable alternative to fresh ballast.

During local shearing and cyclic normal loading, tests on basalt ballast showed that both tangential and normal stiffness increased as the applied load became higher. At lower loads, the stiffness changed gradually, but from 200N onwards, the increase was more noticeable. This suggests that the material surface adjusts more under heavier pressure due to better contact and surface changes.

These findings provide essential parameters for discrete element modelling (DEM) and offer valuable insights into optimising ballast materials for railway engineering applications.

Chapter 5 figures and tables

Table 5.1 Summary of monotonic shearing test results on andesite.

Test	Normal load (N)	Shearing to (mm)	Coefficient of friction	Stiffness N/μm
AB-020N	20	+ 0.5	0.8	1.0
AB-050N	50	+ 1.0	0.75	0.50
AB-100N	100	+ 0.5	0.7	1.15
AB-150N	150	+ 1.0	1.0	1.10
AB-200N	200	+ 0.5	0.85	1.6

Table 5.2 Basalt test results during monotonic shearing.

Test	Normal load (N)	Shearing to (mm)	Coefficient of friction	Stiffness N/μm
BB-020N (average all of tests under 20N)	20	+ 1.0	0.55-0.70	0.4-1.10
BB-050N	50	+ 1.0	0.65	0.70
BB-150N	150	+ 1.0	0.60	0.65
BB-200N (average all of tests under 200N)	200	+ 1.0	0.5-0.65	0.8-1.20
BB-100N	100	+ 1.0	0.4	0.8
BB-100N-Flooded-1	100	+ 1.0	0.5-0.6	1.1
BB-100N-Flooded-2	100	+ 1.0	0.5-0.6	1.4

Table 5.3 Summary of monotonic shearing test results on Chinese granite.

Test	Normal load (N)	Shearing to (mm)	Coefficient of friction	Stiffness N/µm
CB-020N	20	+ 1.0	0.35	2.2
CB-050N	50	+ 1.0	0.22	1.8
CB-100N-1	100	+ 1.0	0.5	1.8
CB-100N-2	100	+ 1.0	0.22	2.25
CB-150N	150	+ 1.0	0.15	3.2
CB-200N	200	+ 1.0	0.20	1.0
CB-100N-Flooded	100	+ 0.5	0.25	0.25

Table 5.4 Summary of monotonic shearing test results on fresh granite.

Test	Normal load (N)	Shearing to (mm)	Coefficient of friction	Stiffness N/µm
GB-020N-1	20	+ 1.0	0.63	0.10
GB-020N-2	20	+ 0.5	0.6	2.0
GB-100N	100	+ 1.0	0.75	1.10
GB-200N	200	+ 0.5	0.65	1.20
GB-50N-1	50	+ 0.5	0.4	1.0
GB-50N-2	50	+ 0.5	0.7	1.10

Table 5.5 Summary of monotonic shearing test results on used granite.

Test	Normal load (N)	Shearing to (mm)	Coefficient of friction	Stiffness N/μm
UG-020N	20	+ 1.0	0.55	1.0
UG-050N	50	+ 1.0	0.60	1.40
UG-100N	100	+ 1.0	0.58	1.40
UG-150N	150	+ 1.0	0.65	1.30
UG-200N	200	+ 1.0	0.55	1.90

Table 5.6 Summary of monotonic shearing test results on washed used granite.

Test	Normal load (N)	Shearing to (mm)	Coefficient of friction	Stiffness N/μm
WUG-100N	100	+ 0.5	0.8	0.50
WUG-020N	20	+ 0.5	0.63	1.50
WUG-200N	200	+ 0.5	0.65	3.40
WUG-150	20	+ 0.5	0.5	2.0
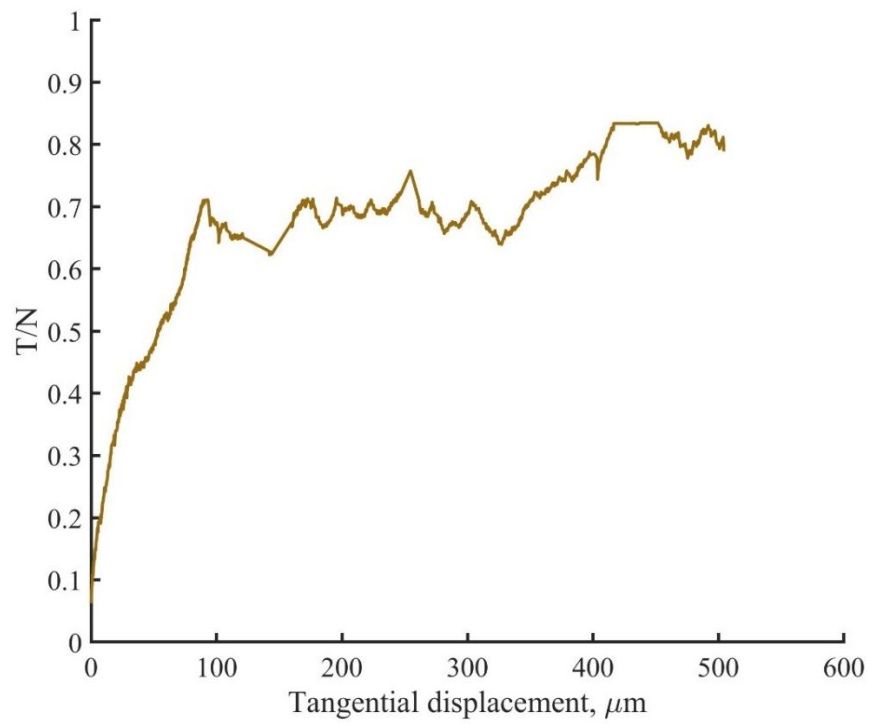
Figure 5.1 Monotonic shearing T/N of andesite ballast under normal load of 20N.
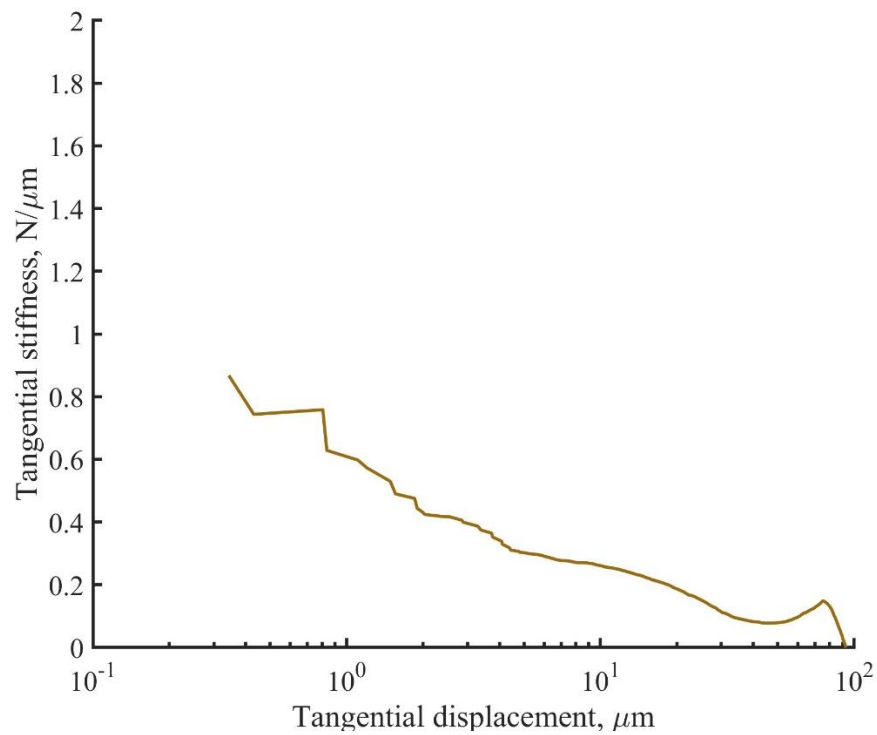
Figure 5.2 Tangential stiffness of andesite under normal load of 20N.
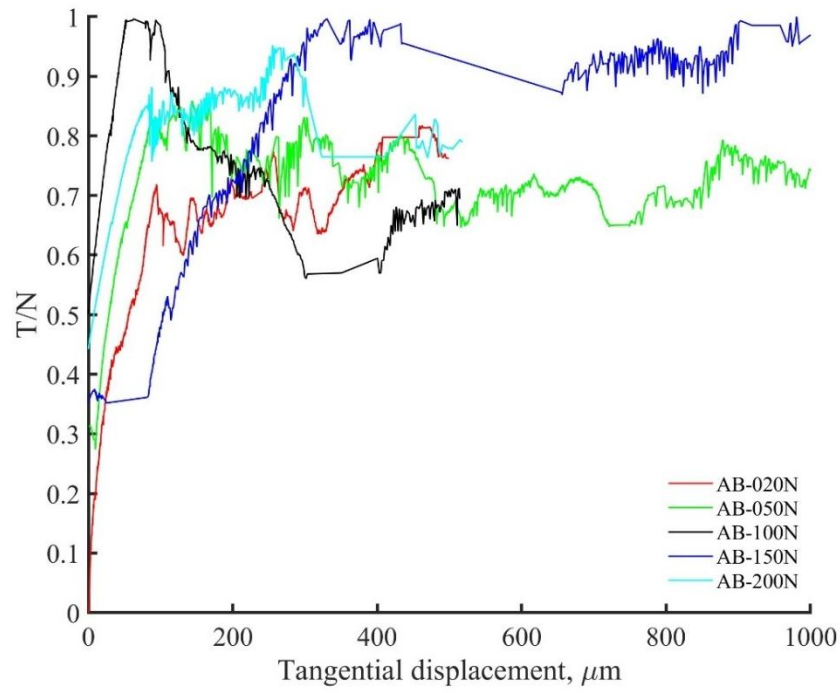
Figure 5.3 Monotonic shearing T/N under different normal loads of andesite ballasts.
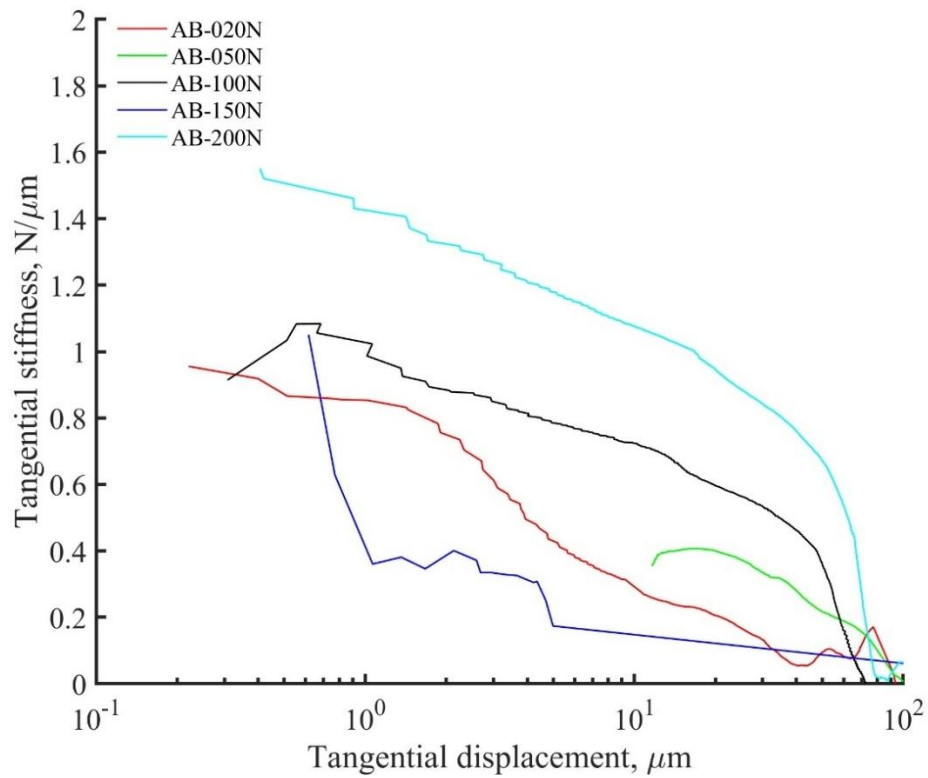
Figure 5.4 Tangential stiffness of andesite ballasts under normal loads.
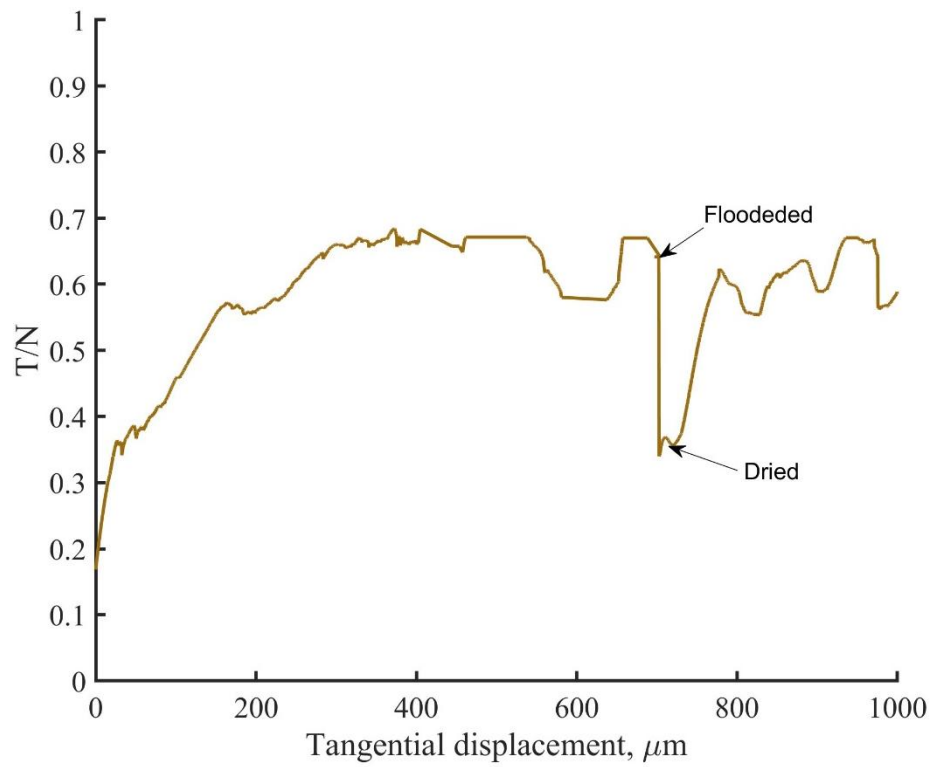
Figure 5.5 Monotonic shearing T/N of basalt ballast under normal load of 100N.
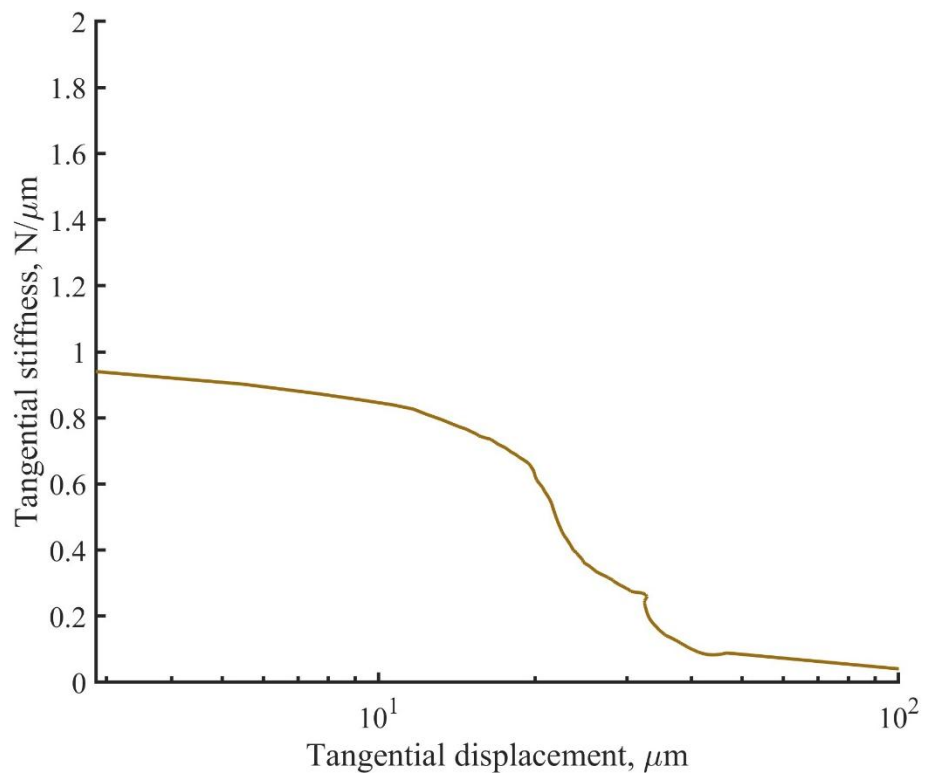
Figure 5.6 Tangential stiffness of basalt ballast under normal load of 100N.
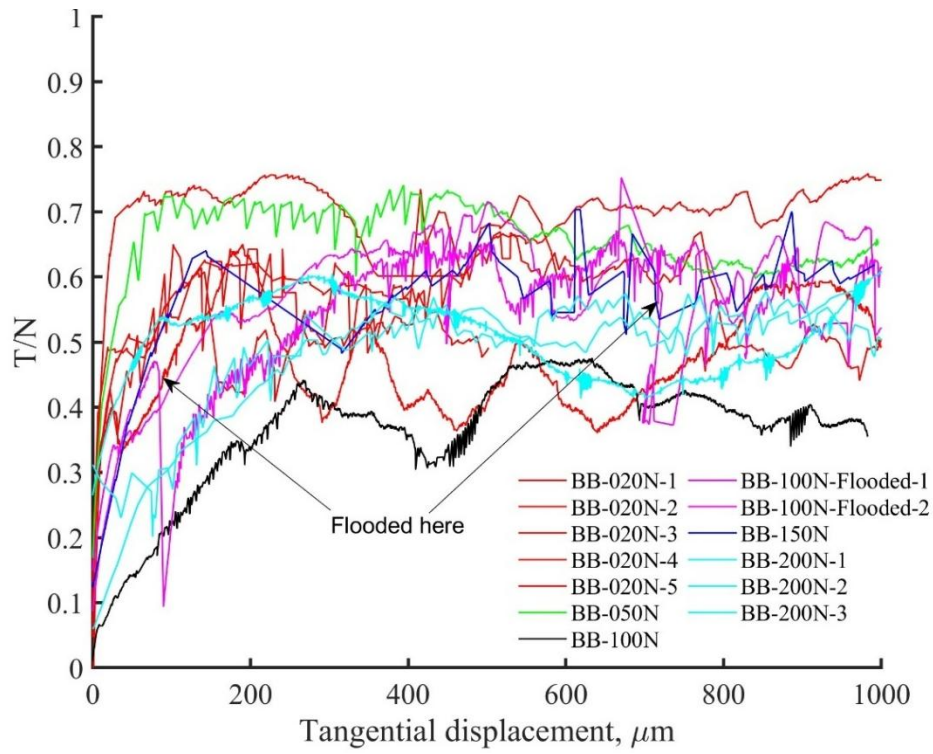
Figure 5.7 Monotonic shearing T/N under different normal loads (all the tests) of basalt ballast.
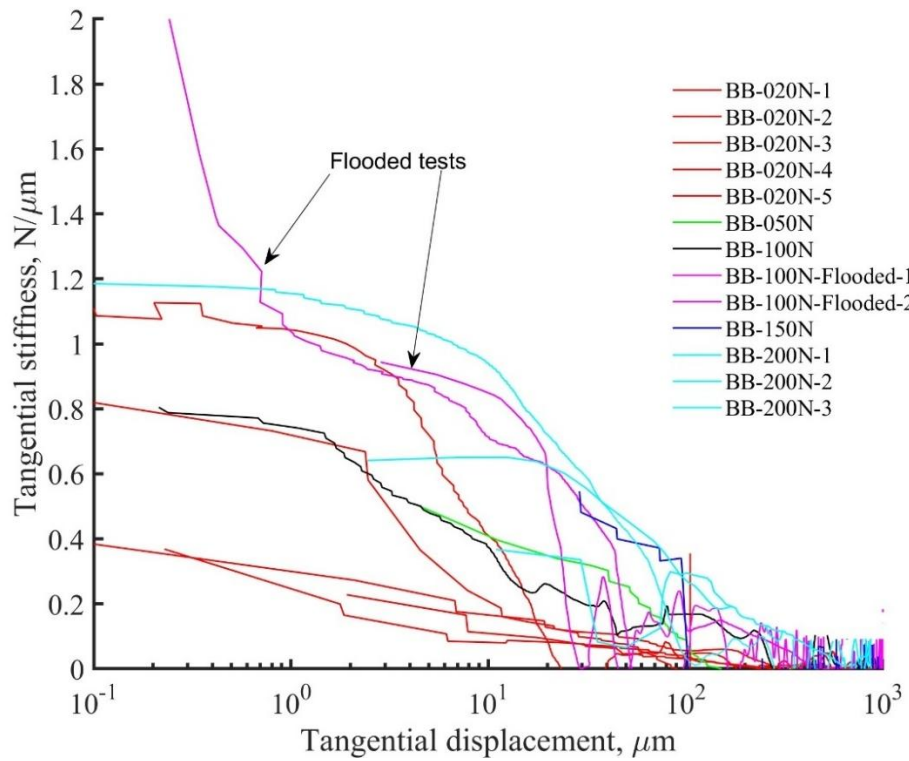
Figure 5.8 Tangential stiffness of basalt ballast under normal loads.
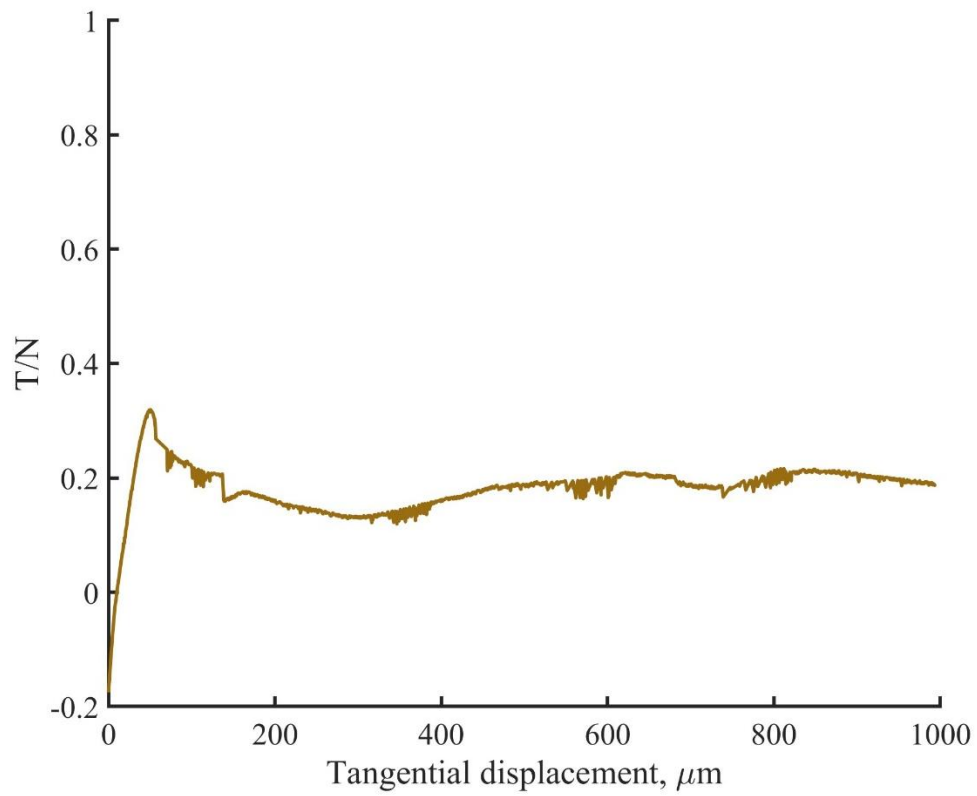
Figure 5.9 Monotonic shearing T/N of Chinese granite ballast under normal load of 150N.
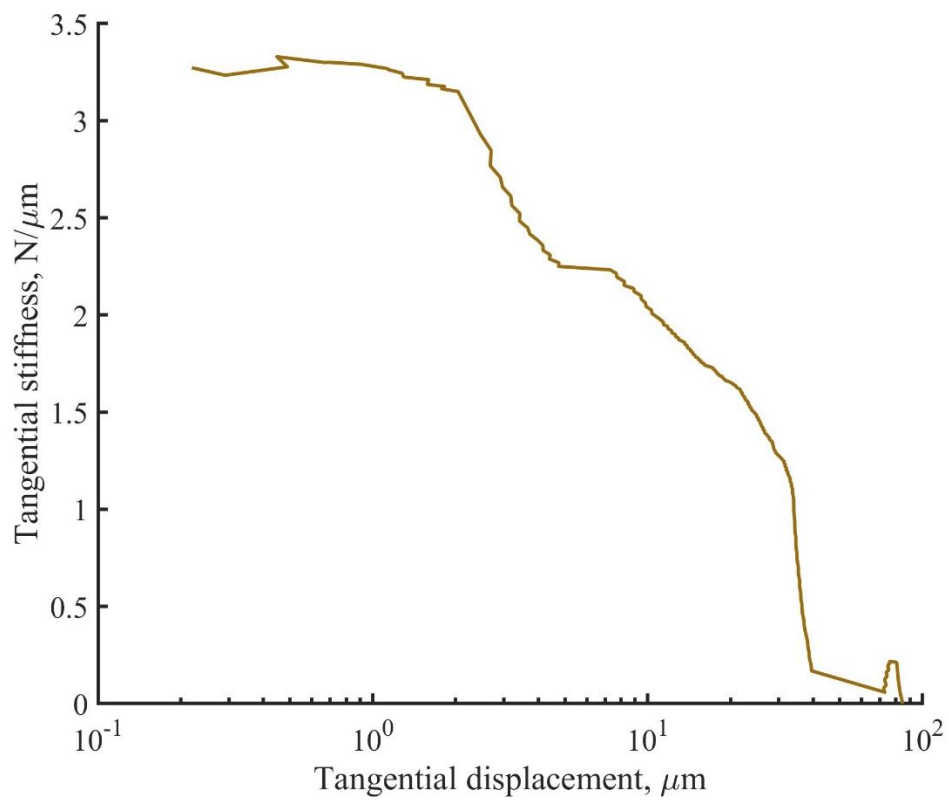
Figure 5.10 Tangential stiffness of Chinese granite ballast under normal load of 150N.
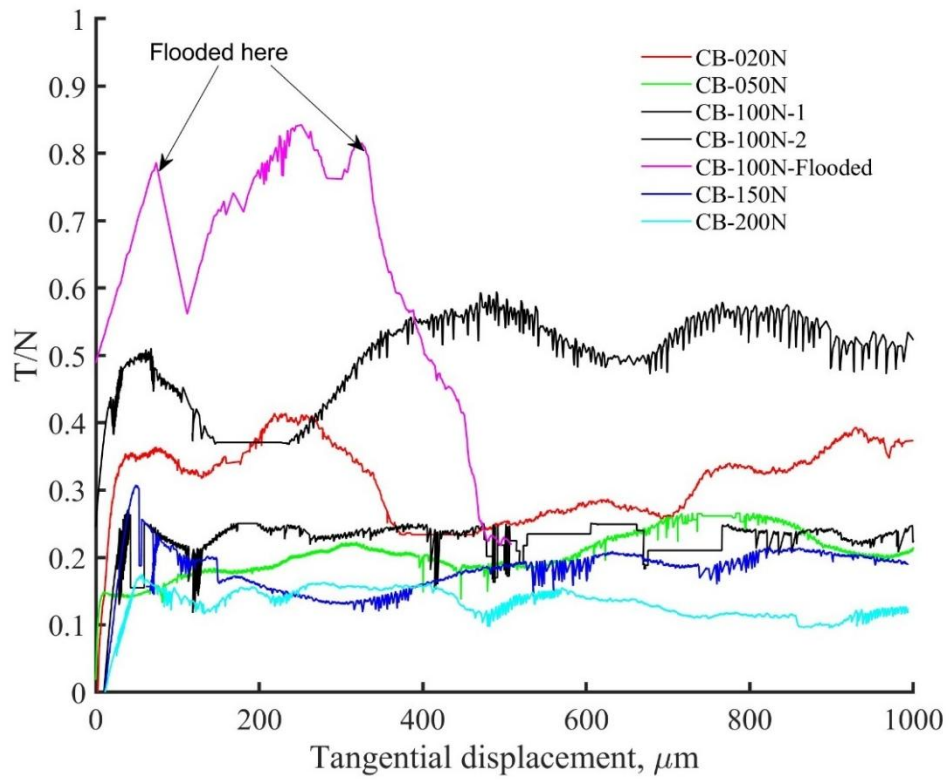
Figure 5.11 Monotonic shearing T/N under different normal loads of Chinese granite ballast.
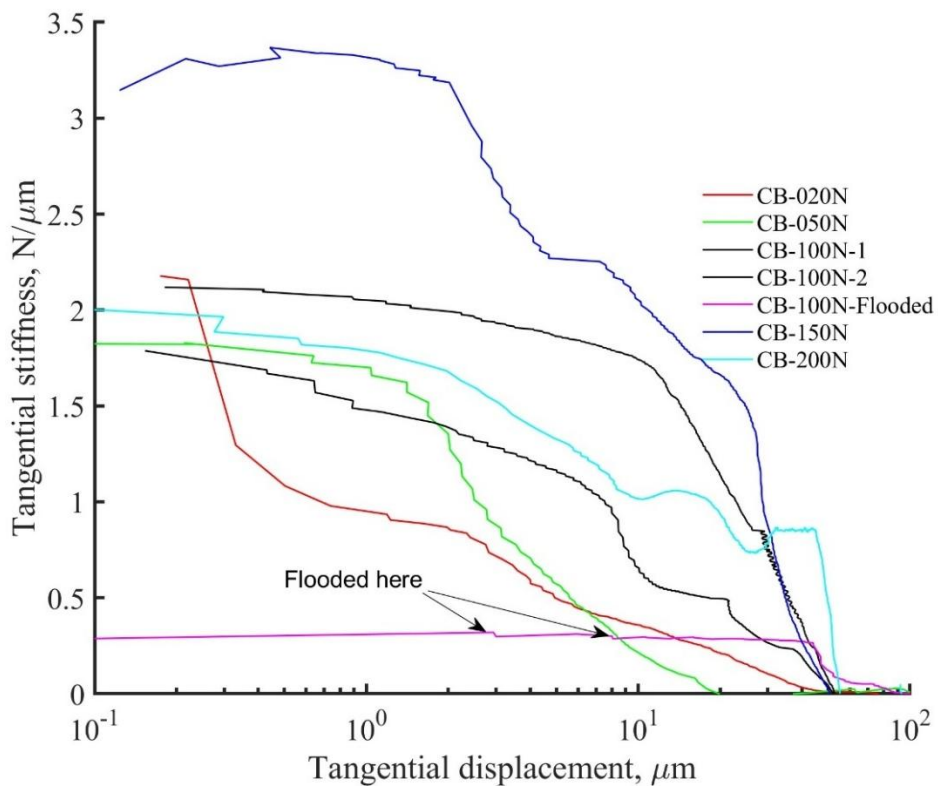
Figure 5.12 Tangential stiffness of Chinese granite ballast under normal loads.
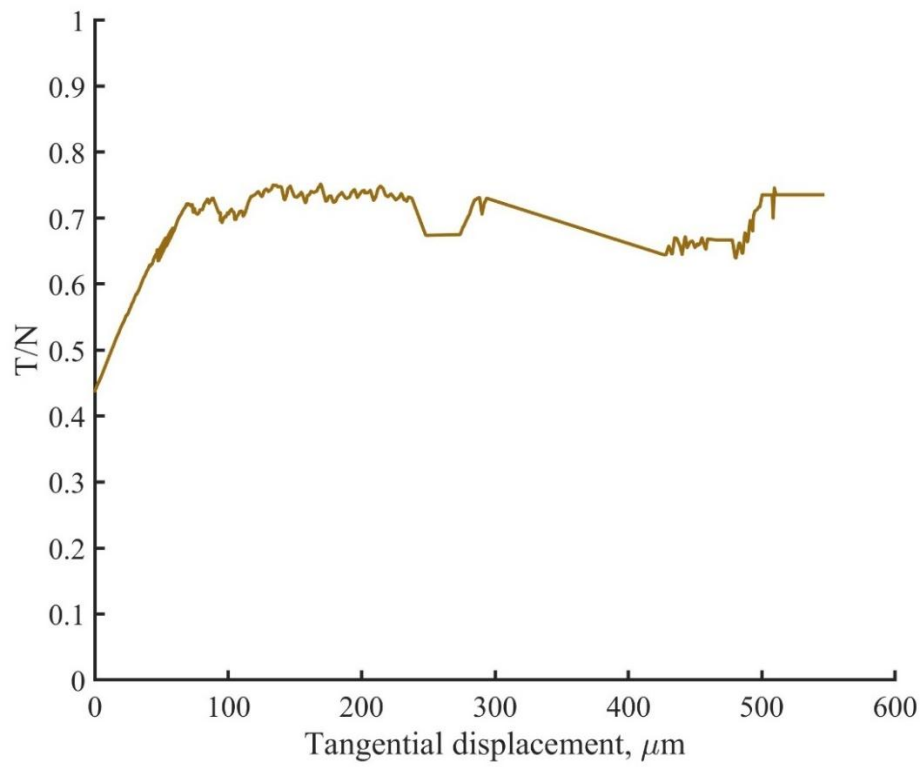
Figure 5.13 Monotonic shearing T/N of fresh granite ballast under normal load of 200N.
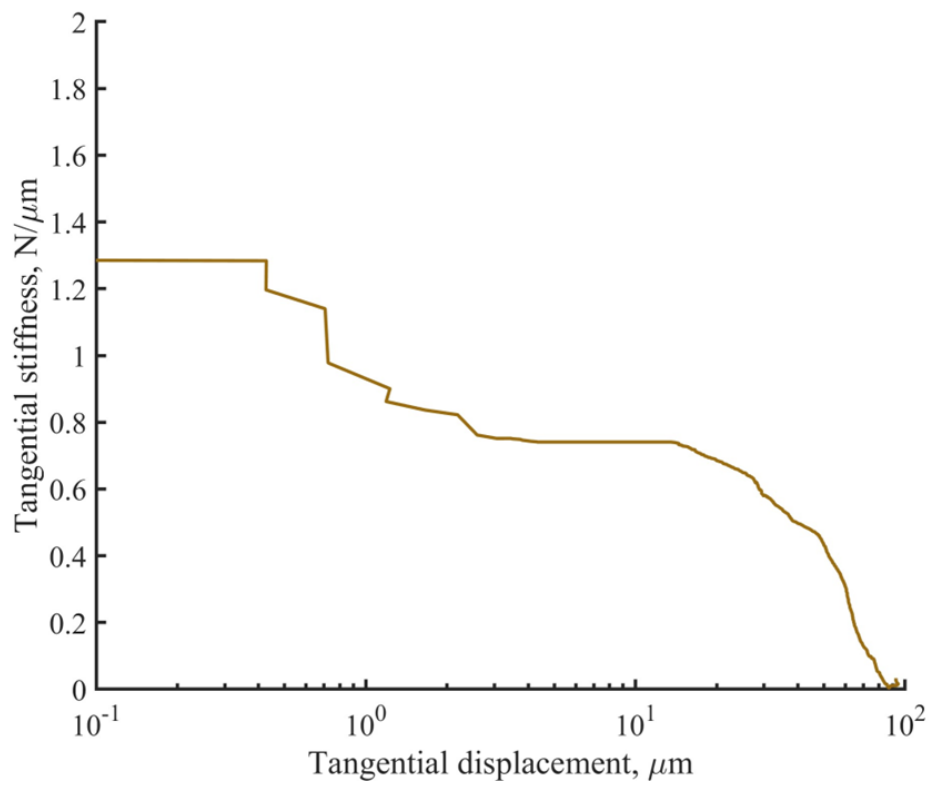
Figure 5.14 Tangential stiffness of fresh granite ballast under normal load of 200N.
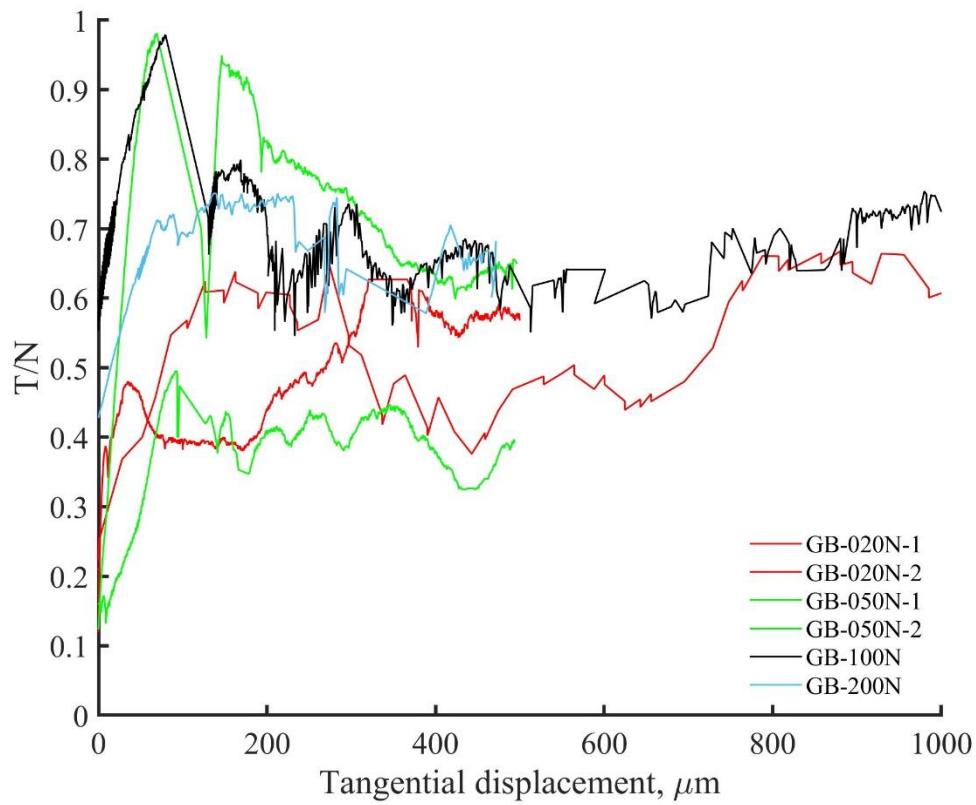
Figure 5.15 Monotonic shearing T/N under different normal loads of fresh granite ballast.
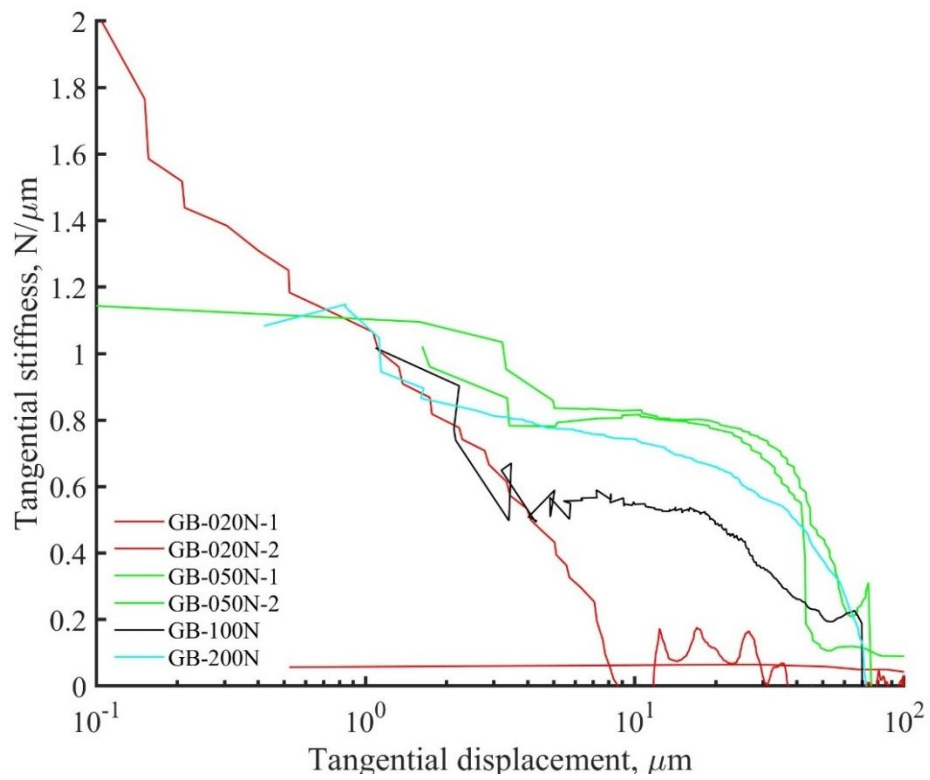
Figure 5.16 Tangential stiffness of fresh granite ballast under normal loads.
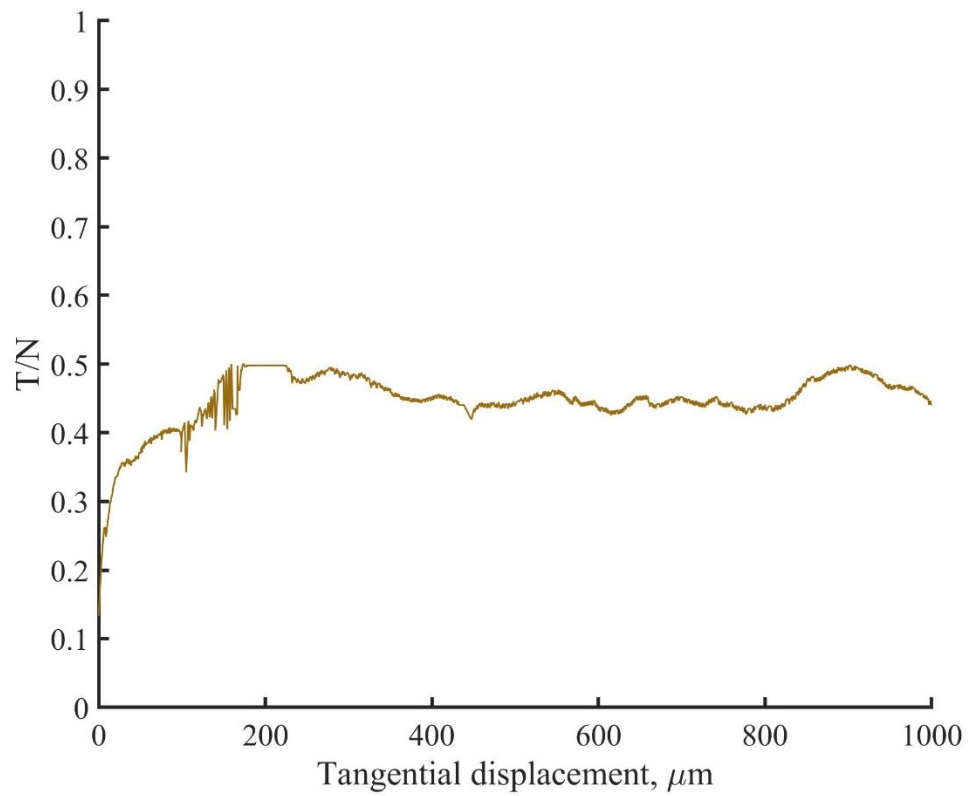
Figure 5.17 Monotonic shearing T/N of used granite under normal load of 50N.
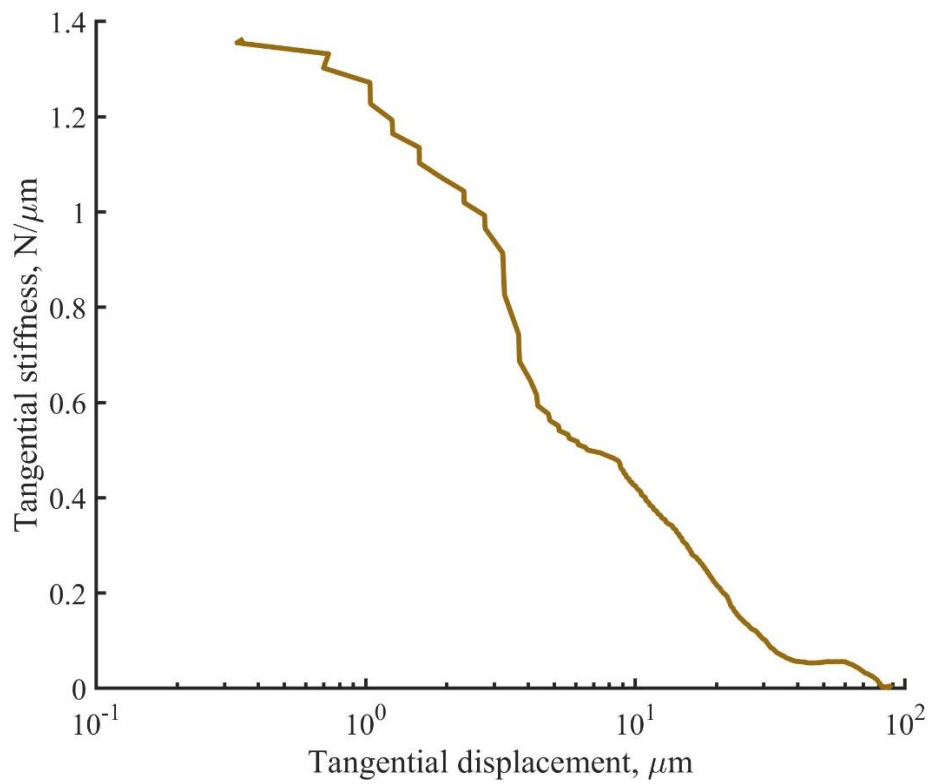
Figure 5.18 Tangential stiffness of used granite under normal load of 50N.
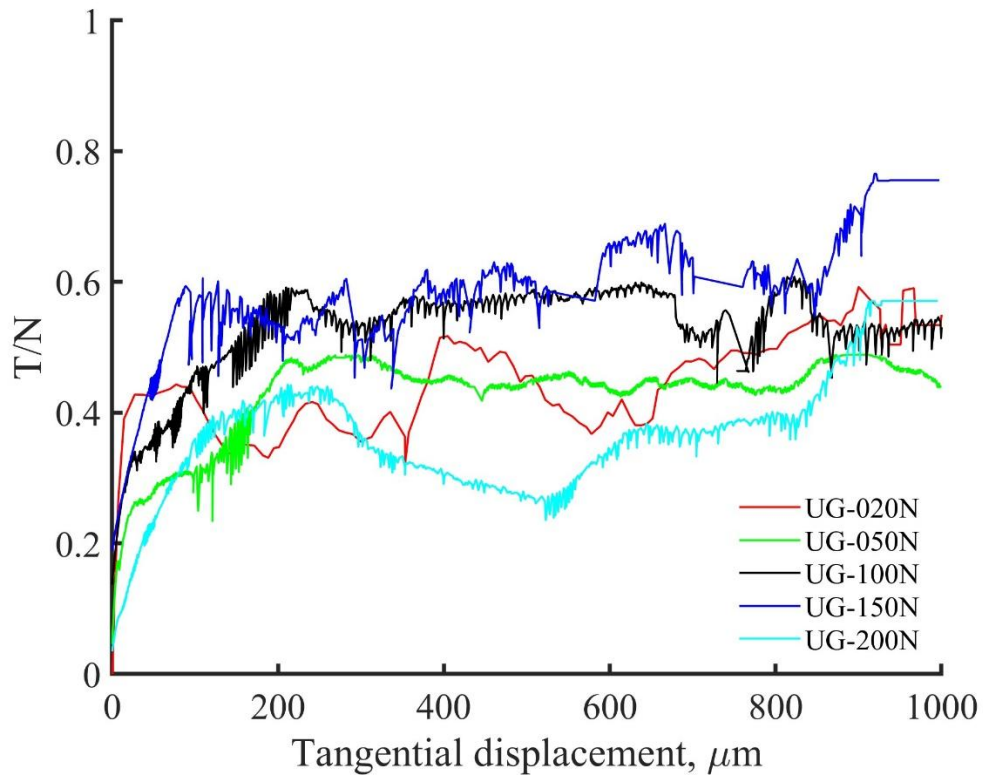
Figure 5.19 Combined monotonic shearing T/N of used granite ballast.
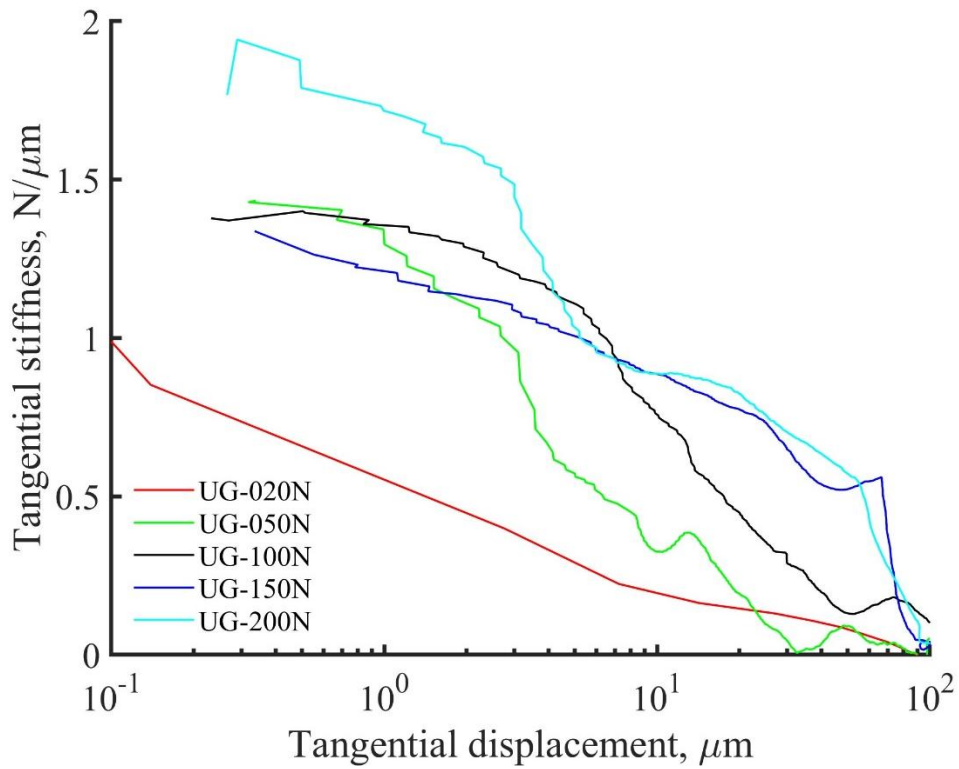
Figure 5.20 Tangential stiffness of used granite ballast under different normal loads.
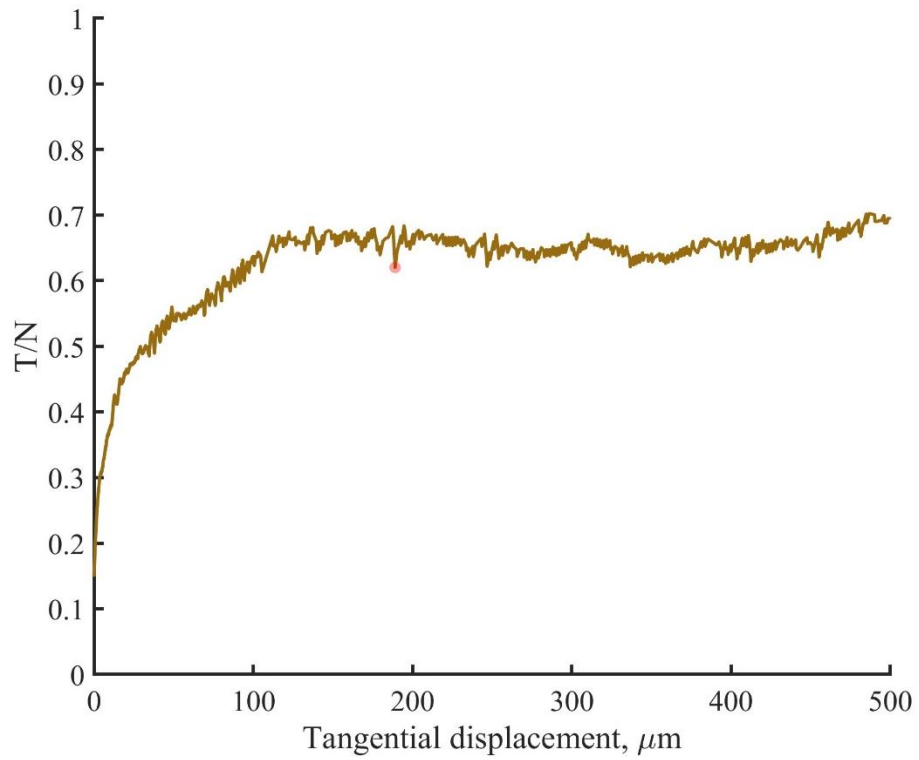
Figure 5.21 Monotonic shearing T/N of washed used granite ballast under normal load of 20N.
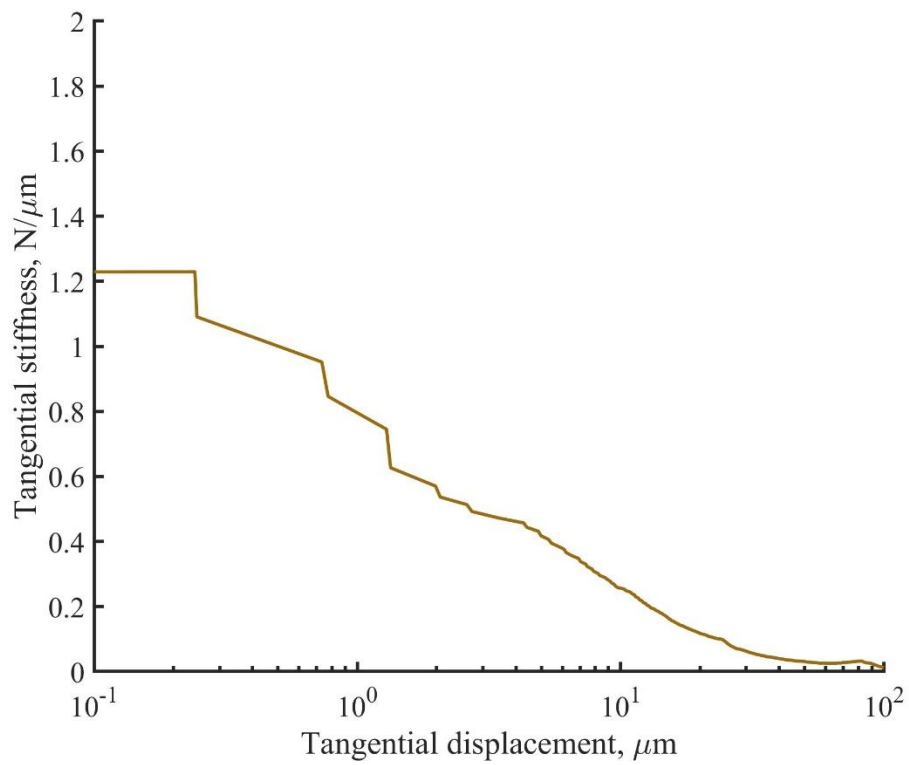
Figure 5.22 Tangential stiffness of washed used granite ballast under normal load of 20N.
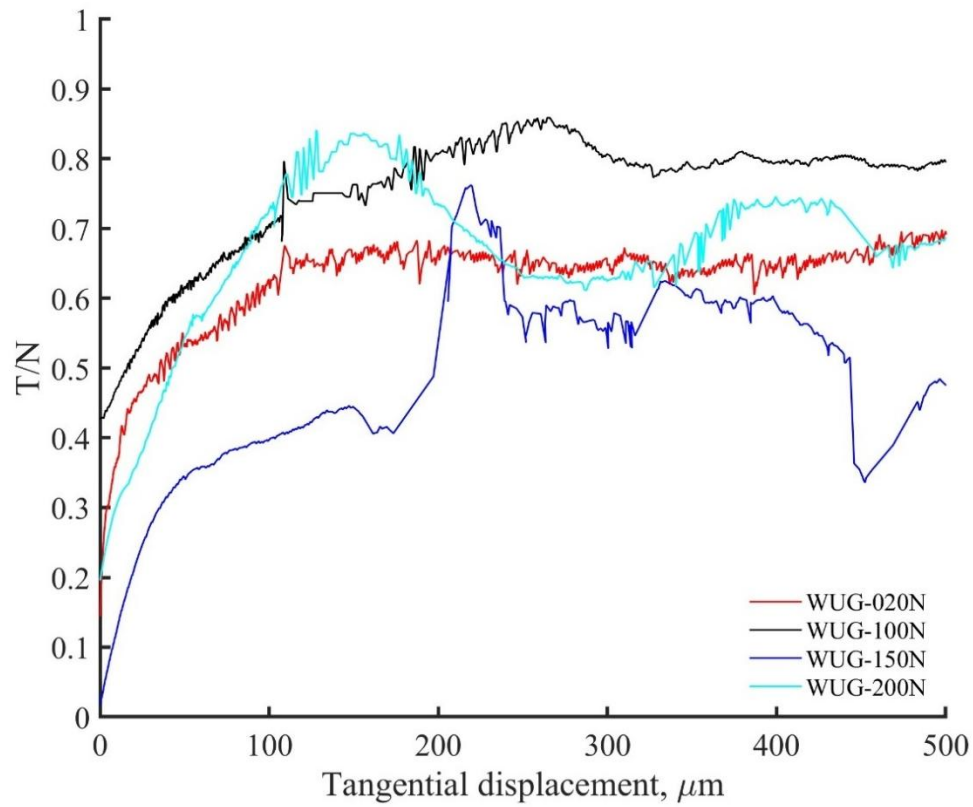
Figure 5.23 Monotonic shearing T/N under different normal loads of washed used granite ballast.
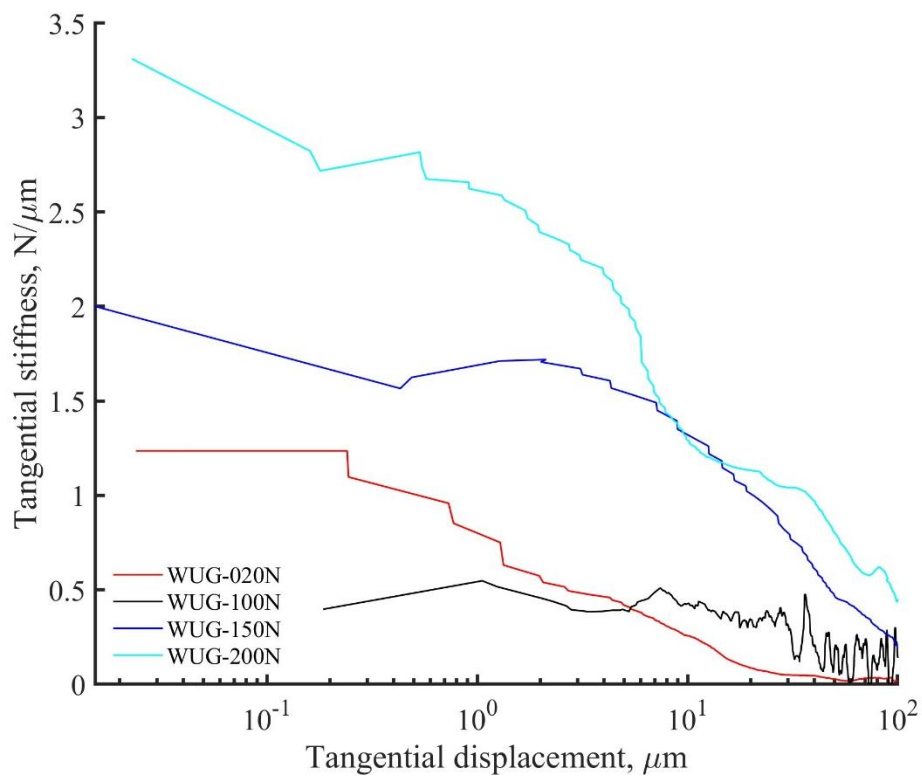
Figure 5.24 Tangential stiffness of washed used granite ballast under different normal loads.
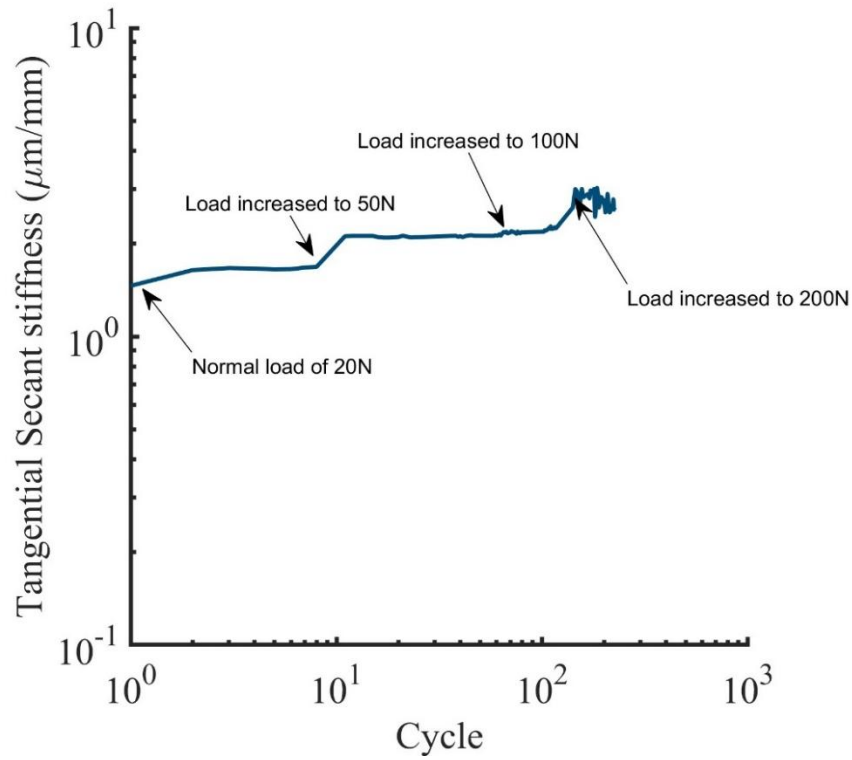
Figure 5.25 Tangential secant stiffness increases with cycle number as the normal load increases, showing a non-linear response with significant jumps at higher loads.
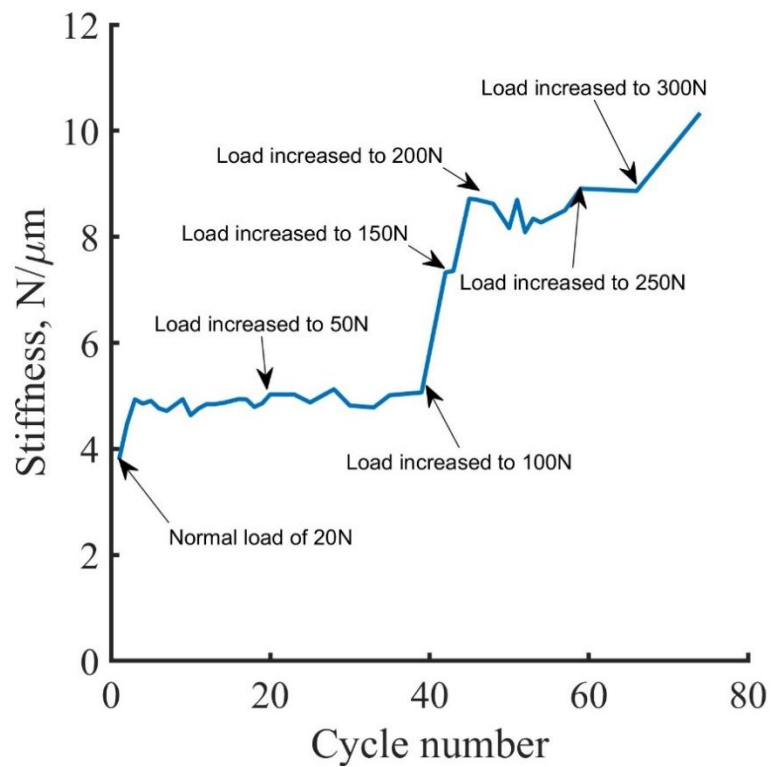
Figure 5.26 Normal stiffness of basalt increases with normal load, with more pronounced changes at higher loads due to surface deformation.

6. Cyclic Shearing

Railway ballasts undergo cyclic loading, and therefore, the behaviour at the contact between ballast particles was investigated in the IP apparatus by performing a series of cyclic shearing tests. Surface quantification before and after the test was also done to see surface texture or roughness changes. The tangential stiffness and the mobilised inter-particle friction (μ) values were determined, and their evolution during cycling was studied. Five different types of ballasts (andesite, basalt, Chinese granite, fresh granite, used granite, and washed used granite) were tested under various load conditions. Typical sample preparation and testing procedures for these tests were described in Chapter 3. A summary of the loading information for all the cyclic shearing tests on ballasts is presented in Tables 6.1 to 6.6.

In this chapter, the influence of various factors such as the number of cycles, conditions of the loading interfaces, normal load level, and shearing rate on the mobilised inter-particle friction values, vertical displacement, rate of abrasion and stiffness are examined. More limited focus has been made on the effects of water immersion, the presence or absence of powder generated at the contact, and pre-sheared surfaces on frictional behaviour.

Due to the large amount of data obtained, the chapter is organised as follows: initially, data from one individual test will be shown for each type of ballast, and then combined test data (showing all tests on a given ballast) will be shown to see the difference under different normal loading conditions. A comparison between ballasts will be given at the end of the chapter.

Data analysis and procedures of experiments

The methodology for data analysis and the presentation of individual test results are described in detail in Section 6.1. In the context of cyclic shearing analysis, data points were systematically recorded at intervals ranging from 3 to 7 seconds throughout the testing process, facilitated by the program and stored in files updated every 1000 lines. Owing to the extensive duration of the tests, each generating a substantial volume of data, a typical examination comprised approximately 10 to 50 files, equating to approximately more than 100,000 lines. In some instances, particularly prolonged tests (tests with slow cycles), this amount exceeded twice the standard volume. Consequently, to streamline the process and

mitigate the laborious nature of manual data handling in Excel, a MATLAB script was developed for both data analysis and graph plotting. The corner points were manually picked up for a better representation of μ and stiffness.

The inter-particle apparatus records vertical and horizontal displacements, as well as vertical and horizontal loads. In inter-particle experiments, horizontal displacements are constrained, and any resulting horizontal loads are measured that come from the topography of the particle contacts. The resultant normal force and displacement are calculated based on the recorded data. This information is crucial for understanding the mechanical behaviour of particles during inter-particle testing, as described by Singh et al. (2024).

Some of the early test data exhibited variability due to intermittent slippage during testing. To address this issue, a comprehensive data filtering process was implemented. This process included removing noise from H1 and H2 for forces and μ, applying slope corrections, and making topographical corrections in terms of profile and topography. Additionally, some data points were manually removed to improve the results, as they could have been affected by the irregularities in testing. A number of points were skipped from the corners to measure μ at the start and end of sliding was also adjusted. It is worth noting that the instances of slippage-induced unloading data points were relatively minor compared to the overall dataset, and the slippage phenomenon diminished as testing progressed, particularly following changes made to enhance the apparatus's rigidity. The cycle rate initially used 1 cycle/hour then it was slowed down from cycle/0.5hour and cycle/0.25 hour.

A compliance check was carried out on the apparatus to see if the apparatus is functioning correctly during the final stage, resulting in no significant changes. A small difference was seen between the actual load and the load shown by the load cell in the H1 direction, therefore, corrections were applied to tests that were done in the H1 direction for most of the early test, and for the last few tests, shearing was conducted in the direction of H2. Load cells and sliding friction were corrected accordingly.

6.1. Andesite Ballast

Five cyclic shearing tests were conducted on andesite ballast to investigate its micro-mechanical response under repeated loading conditions. The results of these tests are presented in Table 6.1.

6.1.1 Individual test (AB1-20N)

A brief introduction was given to the different types of ballasts in Chapter 3 under the materials section. Here, the results will be discussed by choosing figures from one test and then explaining the behaviour from the combined tests. The cycle regime begins with a dark colour at low cycle numbers and transitions to a light yellow, making the light colour more predominant as these represent the final cycles plotted and stabilised, a detail that will be elaborated upon later.

Vertical displacement: Test AB1-20N was conducted under a constant vertical load of 20N, with a new pair of andesite ballast particles. Figure 6.1 shows a typical angular-flat contact before and after approximately 100 cycles under a normal load of 20N. The contact points became flattened due to abrasion (as shown in Fig.6.1b), which increases with the number of cycles. Figure 6.2a illustrates the change of vertical displacement during cyclic shearing, increasing with the number of cycles. The experiment reveals a noticeable pattern: initially, there is a clear spacing between cycles, which gradually reduces with each continuous cycle. Eventually, the inter-cycle distance approaches minimal levels, nearly reaching zero. This gradual reduction in spacing between cycles highlights the importance of the contacts of frictional behaviour between two particles.

Normal force and tangential force consistency: Normal force and tangential force (normal and tangent to the surface) demonstrated high stability throughout the test (Fig.6.3a & 6.3b). This consistency is crucial for ensuring the reliability and repeatability of the results. In some tests, there was a small jump seen in the normal force, which affected the tangential force (either an increase or a decrease due to the nature of the particle surface). The observation of the forces remained stable even after the removal of abraded particles (powders), indicating robust experimental conditions and procedures. However, when removing powders caused a move or jump and affected the result, a correction was applied. The test was repeated if there were no consistency in the data or would be filtered and removed from the data.

Cyclic paths consistency: The cycling paths exhibited high consistency throughout the test, including features in the corners (Fig. 6.4a). The cycles and their return paths are remarkably similar, with the unloading and reloading paths at the end of the cycles being very consistent. The T/N values (ratio of shear force to normal force) in the corners for the forward and backwards directions initially differed significantly but intersected after cycle 20, following a similar trend thereafter. This merging suggests a stabilisation of the contact mechanics after

the initial cycles (Fig. 6.4b). This observation that the paths converge remained stable even after the removal of abraded particles.

Similar trends were observed by Wong (2022) in her PhD on granite ballast particle behaviour under varying load conditions, where initial discrepancies in T/N values became negligible after a series of cycles, indicating an adaptation period for the materials involved.

Stiffnesses: A representation of stiffness at the forward end of cyclic shearing is shown in Figure 6.5a. This illustration includes cycles 2, 10, 50, and 100, for which the stiffnesses were measured. Due to the extended test durations at the beginning of the study, fewer readings were obtained during cyclic loading, resulting in fewer data points. To acquire additional data points, tests were conducted at a slower rate of one cycle per hour.

The estimated stiffnesses in the forward direction for each cycle are shown in Figure 6.5b. The limited number of data points resulted in some scattering of the stiffness values. Consequently, the author's judgment was employed to interpret smooth lines through each data set, and some outlier points were removed to better represent the trends.

Figure 6.6a presents a plot of the stiffnesses in the backwards direction of the reversal for cycles 2, 10, 50, and 100. In both the forward and backwards directions, the stiffness increases with the cycle number within the first 80 μm but converges at larger displacements. Despite the data points being somewhat dispersed, this does not significantly alter the stiffness.

As horizontal displacement increased, there was a general tendency for the stiffness to decrease across all cycles in both directions, as illustrated in Figure 6.6b. It is also possible that stiffness increases with the number of cycles. However, there are minor peaks and drops in stiffness, which could suggest microfractures or other alterations on the particle surface.

6.1.2. Combined analysis of andesite ballasts

Coefficient of inter-particle friction (μ): Figure 6.7 provides a summary of the change in μ value for each cyclic shearing test, with monotonic shearing represented as the first cycle. The majority of these values were derived from the average of the forward and backwards directions during sliding. However, in certain experiments, data from one direction was adjusted due to an excessive number of dispersed data points. Most testing was completed at

approximately 100 cycles due to the early stabilisation, and there was no need for further cycles. Some tests were longer than 100 cycles, but only data to 100 cycles are shown, as no difference was noticed for further cycles. This shouldn't mean that there was no need to run longer tests.

The μ values for both forward and backwards directions were generally similar. In some tests, such as AB-150N, AB-05N, and AB-200N-2, the values from monotonic shear were higher than in the first cycle. However, this was not the case for all tests, with tests like AB-200N and AB-100N showing different trends. Drops in μ values were observed in cycles following the cleaning of the contact. These drops were likely due to small movements or touching the transducers during the cleaning process, an effect that will be discussed in detail later in this chapter.

Overall, there is a tendency towards more stable μ values after a few cycles, although some tests did not reach stable values by the end of the testing period. In the tests where sliding failure occurred, the average μ values for the monotonic shear preceding cyclic shearing were determined. The monotonic shear μ values ranged from 0.60 to 0.80, with an average of 0.70, while the cyclic shearing μ values ranged from 0.60 to 0.75, with an average of 0.65. For this material, both values were very close, with no significant differences as found by other researchers (Wong, 2022; Nardelli et al., 2018; Altuhafi et al., 2024).

The impact of flooding was seen, as when water is added, the μ value is reduced, and the effect was immediate (test AB-100N). Therefore, it can be concluded that water reduces the μ; however, slow or fast rates do not seem to have a significant effect on μ. Wong (2022) highlighted the sensitivity of μ values to cleaning processes. In their studies, even minimal water application during cleaning resulted in a temporary reduction in μ, which recovered after several cycles as the interface readjusted. This finding underscores the importance of considering the impact of cleaning procedures. To mitigate this issue in the present research, it was decided to avoid using water for cleaning and instead use a small brush to prevent significant fluctuations in the data. However, minor jumps in the data could not be entirely avoided.

Similarly to Wong (2022) and Altuhafi et al. (2022), who tested granite ballasts, it is observed that normal load and rate have no significant effect on μ values of andesite ballast, as displayed in Figure 6.7.

Vertical Displacement: Vertical displacement plays a critical role in the slope calculation; therefore it was important to see the changes in the vertical displacements during the cyclic shearing.

As the normal load increases the vertical displacement increases apart from one of the tests as there was some noise in the data and corrections were applied where it affected the vertical displacement (AB-100N). It can be concluded that normal load levels affect vertical displacement.

Significant effect on the vertical displacement was recorded primarily within the first few cycles, which showed a notable increase due to breakage of the asperities at the contact. It is clear from the Figure. 6.8 that the vertical displacement increases with the number of cycles. This behaviour aligns with findings by other researchers, such as Nardelli et al. (2018), Wong (2022), and Altuhafi et al. (2024), who noted that early cycles in similar inter-particle tests on various materials often show more substantial changes as the contact interface adjusts to the applied load.

Vertical displacement also depends on the nature of the particles. Asperity, in particular, plays a significant role in the steady increase of vertical load observed in test AB-100N. Initially, the vertical load increases rapidly, but then slows down after the 10th cycle. This behaviour could be attributed to the breakage of asperities; once the surface flattens, it resists the load more effectively, resulting in a reduced rate of increase in vertical displacement.

The rate of abrasion also plays a crucial role during cyclic loading. As the number of cycles increases, the rate of abrasion reduces, as illustrated in Figure 6.9. This reduction suggests that the initial high rate of abrasion diminishes as the particles wear down and the surface becomes smoother. In the early cycles, the rough nature of the particles causes higher rates of abrasion due to increased friction and particle breakage. Over time, as these asperities are worn down, the contact surfaces become smoother, resulting in a decreased rate of material removal and a stabilisation of the wear process.

Additionally, it appears that the load level has no clear effect on the rate of abrasion. This lack of a clear correlation could be related to the shape or the mineralogy of the particles. Angular particles may initially abrade more rapidly due to their sharp edges, but as these edges are worn away, the rate of abrasion decreases. Similarly, the mineralogical composition of the andesite particles could influence how they wear; for instance, harder minerals might resist abrasion better than softer ones, leading to variations in wear rates that are not solely

261

dependent on the applied load. While the load level does not show a straightforward effect, the combined influence of shape and mineralogy likely dictates the overall wear behaviour under cyclic loading conditions. This understanding is crucial for accurately assessing the long-term performance and durability of materials subjected to repeated loads. It was suggested that for a better understanding of the rate of abrasion behaviours, tests AB-200N-1 and AB-200N-2 should be run for longer periods.

Tangential stiffness: Stiffnesses were calculated under different displacements during cyclic shearing at 5, 10, and 50 μm, and the results of seven tests are compared in Figures 6.10 to 6.12. Observations revealed that stiffnesses are higher at the start of the test and decrease as displacement increases, becoming almost zero at 50 μm. This trend indicates that as particles undergo repeated shearing, the initial resistance to deformation is higher but diminishes with increased displacement. This reduction in stiffness can be attributed to the gradual wear and smoothing of the contact surfaces, as well as the breakage of asperities until sliding occurs.

The tangential stiffness calculated from the monotonic tests is much lower than cyclic stiffness and increasing the number of cycles has no effect on cyclic stiffness after a few cycles.

In theory, stiffness should be dependent on load levels, with higher loads resulting in greater resistance to deformation. However, this relationship was not clear for this ballast at smaller displacement. For example, Test AB-150N (under normal load of 150N) shows higher stiffness than Tests AB-200N-1 and AB-200N-2, (under normal load of 200N) and Test AB-100N shows lower stiffness at 5, 10 μm displacement (Figures 6.10 and 6.11).

Generally, lower loads show lower stiffness and, as the load increases stiffness increases. This correlation is only seen for andesite at larger displacement (50 μm) where the stiffness increases with normal load. Figure 6.12 represents this trend better if Test AB-150N is ignored. The lack of a clear correlation could be due to the combined effects of particle shape and mineralogical composition. While load levels are expected to influence stiffness, the observed data suggest that particle characteristics and their evolving surface conditions play a more dominant role in determining stiffness under cyclic loading.

6.2. Basalt ballast (BB)

The basalt ballasts were briefly described in Chapter 3 under the materials heading. Here, the cyclic shearing results will be discussed, choosing figures from one individual test and then explaining the combined behaviour of basalt. At least 23 tests were carried out on basalt ballasts under normal loading and different conditions (dry and wet) with different rates (fast and slow) and the results are shown in Table 6.2. Additionally, load stages took place during the tests on basalt to see the effect of load on the inter-particle friction of the same ballast particles (e.g. with same contact). It was found that basalt ballast particles had large vertical displacements during the cyclic shearing as most of the particles were very angular compared to andesite and granite. Therefore, several trials were conducted in the early stages of this experimental research, where the rate of the cycles played a significant role due to the angularity of basalt ballast. After testing different rates, it was decided that the remaining tests should be conducted at a rate of one cycle per hour (cycle/hour). Consequently, the earlier tests (which were done at the very beginning of this thesis) were ignored and repeated using this agreed-upon rate. Figure 6.13 shows a typical angular-flat contact before and after approximately 65 cycles under a normal load of 20N.

6.2.1. Individual test

Test BB22F-100N was conducted under a constant vertical load of 100N with a new pair of basalt ballast particles. The test commenced in a dry state and was subsequently flooded twice: initially from cycle 10 to 15, and then again during the final cycle.

Vertical displacement: As previously mentioned, the test exhibited significant vertical displacements, likely attributable to the angularity of the basalt ballast particles, which were markedly more angular compared to andesite and granite. As the number of cycles increased, the vertical displacement also increased at a consistently rapid rate, and the vertical displacement of basalt is larger than andesite and granite as illustrated in Figure 6.14.

Normal force and tangential force consistency: Throughout the test, both normal and tangential forces remained stable (Figs. 6.15a & 6.15b), ensuring reliable results. Occasionally, a slight jump in normal force affected the tangential force, depending on particle surface characteristics. Even after removing abraded particles, forces remained stable, confirming the robustness of the experimental setup. If data inconsistency occurred, the powders were cleaned and removed, corrections were applied if necessary and the data at

the corner was ignored during the calculation of T/N values. If removing the powders altered the results, or the test was stopped due to the presence of powders, the test was repeated on new particles to avoid pre-shearing effect on the results.

Cyclic paths consistency: It was found that basalt ballast stabilised more quickly, just after 20 cycles (Fig. 6.16a), compared to andesite and granite. Wong (2022) observed that fresh granite from the UK required up to 100 cycles during cyclic shearing to reach stabilisation. Their study indicated that the angularity and mineral composition of granite contributed to its longer stabilisation period. Altuhafi et al. (2022) reported that granite samples exhibited significant particle breakage and rearrangement during the initial cycles, which could have delayed stabilisation. The rate used for cyclic shearing could have also played a role. In contrast, basalt ballast demonstrated quicker stabilisation, suggest that the characteristic properties of basalt, such as its mineralogy (Plagioclase Feldspar, Pyroxene, Olivine, Iron Oxides) and particle shape, contribute to its performance in stabilising under cyclic loading. Values of µ for both directions (backwards and forward) were quite similar and average values are shown in Figure 6.16b. It was noticed that basalt ballast has a slightly lower µ compared to andesite (0.7) and granite (0.8).

Stiffness degradation: Figure 6.17a illustrates the stiffness at the forward end of cyclic shearing for cycles 2, 10, and 50. Usually, as the cycles increased the stiffness degradation increases as shown for andesite ballast. However, it was not clear in this test, although, it was clear when all cycles are shown instead of selected cycles which can be noticed in Figure 6.17b.

Figure 6.18a shows stiffness in the backward direction for the same cycles. The stiffness increased with cycle number within the first 200 µm displacements, where cycle 50 gives higher stiffness compared to cycles 2 & 10 but converged at larger displacements. As tangential displacement increased, stiffness mostly decreased across all cycles in both directions, with minor variations suggesting particle surface changes, as seen in Figure 6.18b. Despite some filtering of the data, the scattering is still seen in both directions. The author's judgement was used to smooth data trends, removing outliers.

These findings align with Wong (2022), who also observed on granite ballast that stiffness increases with the number of cycles but saturates after a certain point. Similarly, our results show that stiffness converges at larger displacements, indicating a consistent trend across different materials and conditions.

6.2.2. Combined analysis

Coefficient of inter-particle friction (μ) values: Figure 6.19 summarises μ values for each cyclic shearing test, with monotonic shearing as the first cycle. Most μ values were averaged from forward and backward directions. However, some experiments required adjustments due to data scattering (median was taken instead of average). Tests generally reached about 100 cycles, and a few longer tests were run to see if the inter-particle friction increased with increasing cycles as Wong (2022) suggested in her PhD thesis that μ was increasing with increasing cycles. However, basalt ballast was stabilising much quicker and it was not observed during our experimental research for all types of ballast and due to time limitations longer tests were not done.

In tests like BB-20N, BB-150N and BB-200N-Flooded, monotonic shear μ was higher than in the first cycle, unlike for the remaining tests, which showed different trends. Drops in μ values were seen after cleaning the contact, likely due to minor disturbances during the process of cleaning as indicated for test BB-150N. The amounts of powder due to abrasion of basalt ballasts were quite higher than for the andesite.

Water seems to significantly impact the μ values for basalt ballast as μ drops as soon the water is added, and when it dried μ increased quickly (as seen for tests BB-050N-Flooded, BB-100N-Flooded and BB-200N-Flooded). This is unlike the minimal effects observed for natural sand by Nardelli and Coop (2019). This difference may be due to abrasion on the ballast interface during cyclic shearing, creating a fine powder that affects results when water is added. Additionally, varying material roughness could contribute to the differing outcomes. Wong (2022) highlighted μ sensitivity to cleaning, noting temporary reductions with water application, which recovered after several cycles. To minimise this effect, our research avoided water and used a small brush for cleaning, though minor data jumps persisted during the cleaning. Our findings agree with Wong (2022) and Altuhafi et al. (2022), showing that water affects μ while normal load and rate have little or no effect on μ values.

Vertical Displacement: Vertical displacement is crucial for slope calculation as the correction is applied to the data before calculating μ. Increased normal loads generally led to greater vertical displacements (Fig. 6.20), except for tests under normal loading of 100N showing larger displacement than tests under normal loading of 150N and 200N. Test BB-100N-Flooded had a large displacement compared to the remaining tests, possibly due to

some jump or noise when it was flooded and the right corrections were not applied. Alternatively, the significant effect of water is shown in Figure 6.20, where vertical displacement decreases when the sample is flooded except in test BB-100N-Flooded, where correction was applied due to the touching transducer during the test.

Particle angularity significantly influenced vertical load increase. Initially, displacement rose quickly but slowed after a few cycles, likely due to asperity breakage and surface smoothening. It is also understood that vertical displacement increases with cycle numbers which was found for andesite ballasts. This matches the findings of Wong (2022), and Altuhafi et al. (2022), who observed substantial changes in early cycles as the contact interface changed.

The abrasion rate also decreased with increasing cycles, indicating initial high abrasion due to rough particles that smooth over time (Figure 6.21). The effect of load level is clear on the abrasion rate and is likely influenced by particle angularity and mineralogy. Angular particles initially abrade faster, but this slows down as edges wear down. The mineral composition also affects wear; basalt ballasts resist abrasion better than andesite ballasts.

Tangential Stiffness: forward and backward stiffness was measured at different displacements (5, 10, and 50 μm) during cyclic shearing across all the tests, similar to andesite ballasts (Fig. 6.22). Initially, the stiffness was scattered (first few cycles) and then stabilised with increasing cycles. This indicates reduced resistance due to wear and surface smoothing.

Monotonic stiffness was lower than cyclic stiffness, with the cycle number having minimal effect after initial cycles. Load levels theoretically affect stiffness, but this was not seen for basalt ballasts. For instance, Tests BB-50N (under normal load of 50N) showed higher stiffness than BB-150N, and AB-100N at 5 μm tangential displacement (Fig. 6.22). Similar behaviour was seen at 10 μm displacement too. The tangential stiffness of basalt is more scattered than andesite, as illustrated in Figure 6.23 and Figure 6.24.

The expected correlation between load level and stiffness is complicated, however, it can be said that small loads such as 20N and 50N stiffnesses tend to be equal to zero or below, and in tests at higher normal loads (100N, 150N, 200N) stiffnesses are around 2N/ μm (Fig. 6.24).

6.3 Chinese granite ballast (CB)

Chinese granite ballasts (CB) were briefly described in Chapter 3. This section investigates the cyclic shearing results of Chinese granite. Specific figures were selected to explain the individual test and combined behaviour of this Chinese granite. At least 7 tests were conducted (Table 6.3) on Chinese granite ballasts under different conditions (dry and wet), varying the normal load to study its effect on inter-particle friction. Figure 6.25 illustrates typical Chinese granite particles with angular-flat contact geometry, shown before and after undergoing 65 cycles under a normal load of 200 N. Chinese granite ballast exhibits a transition from sub-angular to more spherical shapes, particularly when compared to the sharper profiles of basalt and andesite.

6.3.1 Individual test (CB6-100N)

This test (CB6-100N) was conducted under a constant vertical load of 100N using new pairs of Chinese granite ballast particles.

Vertical Displacement: Significant vertical displacements were observed during the shearing however not as large a displacement as that which was observed for basalt ballasts (Fig. 6.26a). The vertical displacement increased with increasing cycles, as shown in Figure 6.26.

Force Consistency: Both normal and tangential forces remained stable throughout the test (Figs. 6.27a & 6.27b) apart from the few cycles at the beginning of the test. Occasional slight jumps in normal force due to the roughness, affecting tangential force, were noted but did not compromise the results.

Cyclic Paths: Chinese granite ballast stabilised after just 20 cycles (Fig. 6.28a), however, it was noticed that at the start of the test, T/N was very low and then it would increase with increasing cycle number until stabilised. This behaviour was not observed for other railway ballasts by the author and Wong (2022), likely due to its mineral composition and surface texture. Wong (2022) also observed significant breakage in UK granite during initial cycles, which stabilised after 100 cycles. The average μ values for forward and backward directions were similar (Fig. 6.28b), with Chinese granite showing a slightly higher μ compared to basalt ballast.

Stiffness Degradation: Stiffness typically degraded with more cycles, although it wasn't clear at larger tangential displacement. Figure 6.29a shows stiffness at the forward end of cyclic shearing for cycles 2, 10, and 50, with an obvious trend, as the cycles increase the

stiffness increases. The same trend was noticed when all cycles are shown (Fig. 6.29b). Stiffness in the backwards direction (Fig. 6.30a) also increased with cycle number within the first 100 μm displacements but converged at larger displacements. Across all cycles, stiffness increases with increasing cycles (Fig. 6.30b), suggesting that the surface is changing. Data trends were smoothed by removing outliers, as some cycles had jumps and noise.

6.3.2. Combined data analysis

Coefficient of inter-particle friction (μ): Figure 6.31 summarises μ values for each cyclic shearing test, averaging the results from both forward and backwards directions, similar to the analysis done for basalt and andesite ballasts. The results show that monotonic shear and the initial 10 cycles of cyclic shearing exhibited lower μ values. The Chinese granite ballasts underwent a transition period and tended to stabilise after approximately 30 cycles. In Test CB-200N, μ was particularly low, around 0.15, during the first 25 cycles. However, after this initial period, μ increased significantly to 0.7. This distinct behaviour was not observed in other ballast types. The initial low μ values could be attributed to the surface roughness of the Chinese granite particles, in addition to the different grains (minerals) that Chinese granite is formed from. As the test progressed, wear and abrasion likely altered (changed) the surface, resulting in higher friction values. This hypothesis is supported by the fact that surface roughness and its changes due to wear play a significant role in the frictional behaviour of ballast materials.

Test CB-150N-Flooded exhibited behaviour consistent with other ballast types when exposed to water. Upon flooding, μ dropped immediately, which could be explained by the lubricating effect of water reducing friction between the particles. Once the sample dried, μ increased again as the water's lubricating effect was removed. This behaviour aligns with the findings of Wong (2022) on UK granites, who also reported immediate drops in μ upon water application, followed by a recovery once the material dried.

While Wong (2022) suggested that μ increases with the number of cycles due to progressive particle rearrangement and surface smoothing, these experiments with Chinese granite ballast showed that this trend is less evident due to slower stabilisation. The transition period before stabilisation suggests that the particles initially undergo significant changes in their contact surfaces and positions. Once these changes reach a steady state, the friction values (μ) stabilise. This gradual increase and stabilisation of μ highlight the importance of particle

mineralogy, surface roughness, and the effects of wear in determining the frictional properties of ballast materials.

Additionally, the findings presented here indicate that the normal load has no significant effect on μ, which aligns with the suggestions made by Wong (2022). Despite varying the normal load in our tests, μ values remained largely unaffected as expected. This suggests that factors such as surface roughness and wear play more critical roles in determining frictional behaviour than the magnitude of the normal load. Overall, the behaviour of Chinese granite ballast under cyclic shearing tests demonstrates the complex interplay between material properties and external conditions. The initial period of low μ followed by a significant increase indicates a phase of surface change and μ values (0.75) were higher than basalt ballasts.

Vertical Displacement: The vertical displacement of all tests involving Chinese granite ballasts is much lower compared to basalt ballasts, as shown in Figure 6.32. Increased normal loads generally led to greater vertical displacements, except for the test CB-100N-1, which exhibited higher displacement than the CB-150N and CB-200N tests. Test CB-100N-Flooded showed significant displacement, but it was unclear whether water reduced vertical displacement.

The rate of abrasion decreased with increasing cycles, indicating initially high abrasion due to rough particles that smoothed over time (Figure 6.33). It was found that Chinese granite resists abrasion better than basalt ballasts. Load level, particle angularity, and mineralogy influenced vertical displacement and abrasion rates. Angular particles initially abrade faster, which significantly influences vertical displacement, with rapid initial increases slowing after a few cycles due to asperity breakage and surface flattening. This trend aligns with findings for andesite ballasts by Wong (2022). There was no indication that load levels affected the rate of abrasion in tests CB-20N-1 and CB-100N-1, which exhibited a higher rate of abrasion than the remaining tests. The CB-200N test had a lower rate of abrasion and lower vertical displacement, which could be due to the transition period.

Tangential Stiffness: Similar to other ballasts, stiffness was determined during cyclic shearing at various displacements (5, 10, and 50 μm). A decrease in resistance due to wear and surface smoothing was evident in the initial stiffness, which initially showed variability but stabilised with an increasing number of cycles (Figure 6.34). As wear increased, the initial stiffness of Chinese granite particles decreased. Beyond the first few cycles, the cycle

number had little influence on stiffness, with monotonic stiffness consistently less than cyclic stiffness, apart from the initial cycles.

Although load levels theoretically affect stiffness, this effect was not consistently observed in the experiments. For example, Tests CB-50N and CB-20N-1 exhibited higher stiffness than CB-200N at 5 and 10 μm tangential displacement (Figures 6.34 and 6.35). Generally, higher loads resulted in higher stiffness at 50 μm tangential displacement after 10 cycles, although there were some irregularities in the data. Tangential stiffness tended to decrease with increasing displacement and was near zero at 50 μm (Figure 6.36). Notably, stiffness increased with the number of cycles under different normal loads.

The initial variability in stiffness is due to the roughness and angularity of the Chinese granite particles. As cyclic shearing progressed, wear and surface smoothing led to more stable stiffness measurements, reflecting the dynamic nature of contact surfaces in early cycles.

The inconsistencies in stiffness maybe different load levels suggest that factors other than normal load, such as particle shape (contact curvature) and surface characteristics, play a significant role in determining the stiffness of the ballast. The higher stiffness observed in lower load tests (CB-50N and CB-20N-1) compared to higher load tests (CB-200N) at specific displacements indicates that the relationship between load and stiffness is complex and influenced by multiple variables. At larger displacements, tangential stiffness decreased significantly, approaching zero at 50 μm due to increased wear and smoothing. Overall the Chinese granite had a slightly lower stiffness in comparison to basalt ballasts.

6.4. Fresh Granite UK

It is the same fresh granite (GB) ballasts that were tested previously by Wong (2022) during her PhD. They were tested to see the difference between their method and the current one used for this research. The current research takes into consideration the load in both horizontal directions (H1 and H2) as well as the local topology and noise corrections, in which the rate of shearing was also different. In total 8 tests were conducted on this fresh granite and the results are shown in Table 6.4. It was found that some of the tests were showing lower μ therefore they were repeated. Fresh granite particles with an angular-flat contact geometry, before and after a test involving 90 cycles under a normal load of 20 N are illustrated in Figure 6.37.

6.4.1. Individual test

For the analysis of fresh granite, the GB-100N testing apparatus was selected, and the results are presented. The test was conducted under a normal load of 100 N.

Vertical Displacement: The fresh granite ballasts initially exhibited significantly larger spacing between the cycles in comparison to andesite and Chinese granite (Fig. 6.38a). At the onset of the test, the inter-cycle spacing was greater, progressively diminishing with subsequent cycles until reaching minimal levels, nearly approaching zero distance. This was likely due to the angularity of the fresh granite. As the number of cycles increased, the vertical displacement also increased at a consistently rapid pace, with the vertical displacement of fresh granite being larger than that of andesite and Chinese granite, as illustrated in Figure 6.38b. Additionally, it was found that fresh granite and basalt had almost the same vertical displacement.

Normal Force and Tangential Force Consistency: Throughout the test, both normal and tangential forces remained stable (Figs. 6.39a & 6.39b), ensuring reliable results. Even after removing abraded particles, the forces remained stable apart from the first few cycles, confirming the robustness of the experimental setup. If consistency was not maintained, which could have altered the results, or if the test was stopped due to the presence of powders, the test was repeated using new particles to avoid pre-shearing, similar to the approach taken with other ballasts.

Cyclic Paths Consistency: It was found that fresh granite ballast stabilised more quickly, after just a few cycles (Fig. 6.40a), compared to andesite and Chinese granite. Additionally, μ values for both directions (backwards and forwards) were quite similar. Wong (2022) observed that fresh granite required up to 100 cycles to stabilise, with μ increasing with increasing cycles. However, our experimental findings did not align with this, potentially due to the slower rate used for cyclic shearing. It was noted that this fresh granite ballast has a slightly lower μ values (Fig. 6.40b) compared to andesite (0.7) and Chinese granite (0.75). Additionally, the μ values were lower than those reported by Wong (2022) for the same type of granite.

Stiffness Degradation: Figure 6.41a illustrates the stiffness at the forward end of cyclic shearing for cycles 2, 10, and 50, showing that as the number of cycles increases, tangential stiffness also increases, similar to other ballasts. This trend is more evident when all cycles

are shown within the first 100 μm displacements, although stiffness values converge at larger displacements (Fig. 6.41b).

Stiffness in the backward direction (Fig. 6.42a) for the same cycles exhibits a similar trend as in the forward direction. As tangential displacement increases, stiffness generally decreases across all cycles in both directions, with minor variations indicating particle surface changes (Fig. 6.42b). Despite some data filtering, scattering remains visible in both directions, which was also observed for other ballasts.

These findings align with Wong (2022), who observed that stiffness increases with the number of cycles but eventually saturates. Similarly, our results demonstrate that stiffness converges at larger displacements, indicating a consistent trend across different materials and conditions.

6.4.2. Combined analysis

Coefficient of inter-particle friction (μ): The μ values were averaged from forward and backward directions, and the summary of μ values for each cyclic shearing test, with monotonic shearing as the first cycle, is illustrated in Figure 6.43. Tests usually reached about 100 cycles, with a few longer ones to see if μ increased with cycles, however, fresh granite ballast stabilised faster, so longer tests were not required. Wong (2022) reported that fresh granite required up to 100 cycles to stabilise, with μ increasing with the number of cycles. Our experimental results, with a lower cyclic shearing rate showed stabilisation at 30 cycles.

In most of the tests, the monotonic shear μ values were higher than the first cycle of cyclic shearing, except for test GB-20N-1. Additionally, the average μ (0.6-0.7) was lower than that found by Wong et al (0.65-0.85) for the same ballasts.

Vertical displacement: It was observed that increasing normal loads generally led to greater vertical displacements (Fig. 6.44) during the cyclic shearing. Initially, displacement rose quickly but slowed after a few cycles, likely due to asperity breakage and surface flattening which was seen for other ballasts too. Vertical displacement increases with cycle numbers, a finding consistent with Wong (2022)

The impact of load level on the rate of abrasion is evident. In addition, the number of cycles increased, the abrasion rate likewise dropped, suggesting that the rough particles causing the initial high abrasion were eventually smoothed (Fig. 6.45). Compared to basalt ballast, fresh granite ballast is more abrasion resistant.

Tangential stiffness: Stiffness was measured at different displacements (5, 10, and 50 µm) during cyclic shearing across all tests, similar to other ballasts (Fig. 6.46). Initially, stiffness was scattered in the first few cycles and then stabilised with increasing cycles, indicating reduced resistance due to wear and surface smoothing. Monotonic stiffness was lower than cyclic stiffness, with the cycle number having minimal effect after initial cycles.

Load levels theoretically affect stiffness, but this was not observed. For instance, test GB-50N showed higher stiffness than GB-200N at 5 and 10 µm tangential displacement (Fig. 6.46 and Fig. 6.47). Generally, at 50 µm, higher loads have higher stiffness, and the impact of load level is evident (Fig. 6.48).

6.5. Used granite (UG)

Used granite ballast (UG) was recovered from existing tracks (from Nottingham network rail depot). A total of five tests were conducted on used granite (UG) to evaluate its micro-mechanical contact behaviour under varying loading conditions. The results are summarised in Table 6.5. The particle can be described as spherical and sub-angular as illustrated in Figure 6.49a.

6.5.1. Individual test

Test UG-100N was conducted under a constant vertical load of 100N, using a new pair of used granite ballast particles. The contact points become flattened due to abrasion, which increases with the number of cycles (Fig. 6.49b).

Vertical displacement: Figure 6.50a illustrates the effect of normal load on normal displacement during cyclic shearing, showing that vertical displacement increases with the number of cycles. It was found that used granite had lower vertical displacement in contrast to other type of ballasts (Fig. 6.50b). The data is presented only up to 45 cycles due to the stop-and-start nature of the test conducted at a slow rate.

Normal force and tangential force consistency: As shown in Figures 6.51a & 6.51b, both normal and tangential forces remained stable throughout the experiment, providing reliable results. The forces remained stable even after abraded particles were removed, indicating robust experimental conditions.

Cyclic Paths Consistency: The cycling paths showed high consistency throughout the test, except during the slow cycle (Fig. 6.52a). Initially, µ values for the forward and backward directions differed slightly but converged after cycle 20, following a similar trend thereafter. Wong (2022) observed similar trends with granite ballast, where initial discrepancies in µ values normalised after several cycles. It was noted that slowing the rate of cycles increased µ (Fig. 6.52b), but this effect was not observed consistently upon repetition and was therefore disregarded.

Stiffness: Stiffness at the forward end of cycles 2, 10, 50, and 100 suggests a correlation with the number of cycles (Fig. 6.53a). The estimated stiffness in the forward direction for each cycle is shown in Figure 6.53b, with some scattering and no clear indication of the cycle numbers' impact. However, the impact is seen in backward directions (Fig. 6.54a) for cycles 2, 10, 50, and 100, where stiffness increases with cycle number but converges at larger displacements. As tangential displacement increases, stiffness generally decreases across all cycles in both directions, as shown in Figure 6.54b. Minor peaks and drops in stiffness suggest changes on the particle surface.

6.5.2. Combined tests analysis

Coefficient of inter-particle friction (µ): The change in µ value for each cyclic shearing test, with monotonic shearing represented as the first cycle, is presented in Figure 6.55. Most of the cyclic shearing µ values were similar to the monotonic shearing µ values. However, some tests, such as UG-20N and UG-100N, showed higher monotonic shear values than the first cycle (which is now plotted as the second cycle). This suggests that these specific tests experienced an increase in friction over the initial cycles.

Notably, the effect of normal load on µ values was not consistently observed. For example, test UG-100N exhibited higher µ values compared to the other tests, regardless of the normal load applied. This anomaly indicates that other factors besides normal load might be influencing the µ values, such as surface roughness and material composition. Additionally, it was observed that µ values tended to increase with the number of cycles, suggesting a possible stabilisation or conditioning of the particle surfaces through repeated shearing.

Drops in µ values were observed after cleaning the contact surfaces between particles. This phenomenon is likely due to small disturbances or movements caused by the cleaning

process, which may have momentarily altered the contact conditions or slightly repositioned the transducers as previously mentioned. Moreover, it was noted that used granite had the lowest μ values compared to other ballasts. This could be attributed to the weathering and surface wear of the used granite particles. Over time, weathering can smooth the surfaces of the granite particles, reducing their roughness and consequently their inter-particle friction. Surface wear, resulting from repeated shearing and abrasion, can also contribute to lower μ values by further smoothing the particle surfaces and reducing their ability to interlock or resist relative movement.

Vertical Displacement: It was observed that increasing normal loads generally led to greater vertical displacements during cyclic shearing (Fig. 6.55). Initially, the displacement rose quickly but then slowed after a few cycles, likely due to the surface flattening, a trend seen with other ballasts as well. Vertical displacement increases with the number of cycles, and higher loads lead to larger displacements. This finding aligns with the observations of Wong (2022). The vertical displacement of used granite was lower than that of basalt but higher than for other ballast particles and double that of fresh granite.

The rate of abrasion of used granite is also influenced by normal load levels, similar to fresh granite, however, the used granite had a higher rate of abrasion compared to fresh granite. Figure 6.56 shows how the abrasion rate decreased with increasing cycles, suggesting that the rough particles initially causing high abrasion were gradually smoothed out, this behaviour was seen for fresh granite too. Used granite ballast is less durable under cyclic loading conditions than fresh granite ballast, making it less resistant to abrasion. Fresh granite ballast, by contrast, maintained its structural integrity better and experienced less surface wear, highlighting the significant difference in durability between the two types of granite ballast (Chinese and fresh granite).

Tangential Stiffness: Stiffness of used granite was measured at different displacements (5, 10, and 50 μm) during cyclic shearing across all tests, similar to other ballasts (Fig. 6.58). The distinction between monotonic and cyclic stiffness was significant, with monotonic stiffness consistently lower than cyclic stiffness. After the initial cycles, the number of additional cycles had minimal impact on the stiffness values and stabilised quickly under repeated shearing.

While theoretically, load levels should affect stiffness, this was not consistently observed in the tests. For instance, the stiffness observed in tests of UG-50N was similar to that in tests of

UG-200N at 5 and 10 µm tangential displacement (Fig. 6.58 and Fig. 6.59). This similarity suggests that within this range, the normal load did not significantly alter the inter-particle contact conditions enough to impact stiffness significantly. In contrast, test UG-20N exhibited much lower stiffness compared to the other tests and the impact of load level was most evident only at the larger displacement of 50 µm (Fig. 6.60).

6.6. Washed-used granite (WUG)

Washed-used granite refers to used granite that was treated and cleaned in the environmental laboratory to assess the differences between it and untreated used granite. The cleaning process involved removing accumulated debris, fine particles, and contaminants (using acid) that could affect the material's performance. By comparing the washed-used granite with untreated used granite, the study aimed to understand the impact of these treatments on various properties such as friction (µ values), vertical displacement, abrasion resistance, and stiffness. The results of all the tests are summarised in Table 6.6.

Coefficient of interparticle friction (µ): The tests showed that washed-used granite behaved differently from unwashed granite in cyclic shearing tests, and cleaning improved the surface of the granite particles, leading to higher friction values (Fig 6.61), possibly due to the roughness and the smoother surface (the surface was smoothened to see the changes between rough and smooth). Washed-used granite showed that the µ values are not affected by increasing cycles, but normal load had contradictory effects. For instance, WUG-150N had higher µ values regardless of the normal load. When increasing load during the test it would marginally change the µ as shown for test WUG-20-100N. Washed-used granite had the highest µ values compared to used granite and fresh granite ballasts.

Vertical displacement: Washed used granite had lower vertical displacement (Fig 6.62) than other ballasts (except WUG-20-100N). The impact of load levels was evident as increased normal loads led to greater vertical displacements, which initially rose quickly but then slowed due to surface flattening, similar to other ballasts. When compared to used granite (not washed) the vertical displacement of washed used granite was much less.

The abrasion rate decreased with more cycles, it was much lower in comparison to unwashed used granite, this could be due to the smoothing of the surface. Washed used granite was

more durable under cyclic loading than used granite and fresh granite, showing less wear (Fig 6.63).

Tangential Stiffness: Stiffness measurements at different displacements (5, 10, and 50 µm) showed that the effect of load levels on stiffness was apparent, with increasing normal load causing stiffness to increase (Fig 6.64 and Fig 6.65). This was not seen for other types of ballasts including used granite. At larger displacements (50 µ) stiffness was weak, similar behaviour was observed for other ballasts. These findings highlight the importance of cleaning and treating granite to evaluate its performance and durability in railway tracks and other uses.

6.7 Summary

This section summarised the behaviour of different ballast materials under cyclic shearing conditions, aiming to understand the effects of normal load, particle angularity, surface roughness, and environmental conditions on the coefficient of inter-particle friction (μ), vertical displacement, and tangential stiffness.

The μ values were averaged from forward and backward directions for each test, with monotonic shearing considered the first cycle. Most tests reached around 100 cycles and stabilised, therefore longer tests were unnecessary. Contrary to Wong (2022), who suggested that μ increases with cycles and stabilises after 100 cycles for fresh granite, this trend was not observed in our tests, possibly due to the shearing rate used. Generally, monotonic shear μ values were higher than the first cycle of cyclic shearing (the second cycle in the Figures), and the average μ for fresh granite was lower than that found by Wong et al. Water significantly impacted μ values for basalt ballast, reducing μ immediately upon flooding and increasing again as it dried. This effect was not seen for natural sand, as noted by Nardelli and Coop (2019). There was no clear indication that the rate has any impact on the μ and drops in μ were observed after cleaning the contact surfaces, likely due to minor disturbances, which aligns with findings by Wong (2022) and Altuhafi et al. (2022), who noted that normal load and cycle rate had little effect on μ values. Andesite had the highest μ values (0.6- 0.8), while used granite demonstrated the lowest μ values (0.55-0.7) compared to other ballasts (Table 6.1), likely due to weathering and surface wear. Fresh granite also showed lower μ values compared to what was found by Wong (2022). Chinese granite ballast under cyclic shearing tests shows a complex interplay between material properties and external conditions.

Initially (at low cycles), low μ values increase significantly, reaching 0.75, higher than basalt ballasts.

Increasing normal loads generally led to greater vertical displacements during cyclic shearing. Initially, displacement rose quickly but slowed after a few cycles due to asperity breakage and surface flattening, a trend that was observed in all types of ballasts. Vertical displacement increased with the number of cycles, consistent with Wong (2022). Chinese granite had a lower rate of abrasion and lower vertical displacement, which could be due to the transition period. Used granite had lower vertical displacement than basalt but higher than other ballast particles. Normal load levels affected the rate of abrasion. As cycles increased, the abrasion rate decreased, indicating that the rough particles causing high initial abrasion were smoothed over time. Used granite ballast was more durable to abrasion than fresh granite ballast.

Stiffness was measured at different displacements (5, 10, and 50 μm) during cyclic shearing across all tests for all types of ballast particles. Monotonic stiffness was consistently lower than cyclic stiffness, with minimal effect from the number of cycles after the initial ones. Although load levels theoretically affect stiffness, this was not consistently observed. For example, test UG-50N showed similar stiffness to UG-200N at 5 and 10 μm tangential displacement, while test UG-20N had much lower stiffness compared to other tests. The impact of load level was evident only at 50 μm tangential displacement, indicating a complex correlation between load levels and stiffness.

Furthermore, washed-used granite (WUG) was cleaned in a lab to compare its properties with untreated used granite. The cleaning process removed debris and contaminants, improving the material's performance. WUG had higher friction values than untreated granite, with these values remaining stable across cycles. Normal load effects varied, with WUG-150N showing high friction regardless of load. WUG exhibited lower vertical displacement than other ballasts due to its cleaned surface. Increased normal loads led to greater vertical displacements initially, then slowed due to surface flattening. WUG was more durable under cyclic loading, with a reduced abrasion rate over time. Stiffness increased with higher normal loads, a trend not seen in other ballasts, but decreased at larger displacements. These results highlight the benefits of cleaning and treating granite for better performance and durability in railway tracks and other applications.

In conclusion, the study found that factors such as particle shape at the contact, surface texture, and wear seem to play more significant roles in determining the contact behaviour of railway ballasts than normal load levels. These findings enhance the understanding of ballast performance under cyclic loading conditions, which is crucial for railway track stability and maintenance, and suggest that more research should be caried out on the micro-mechanical features of ballasts and their impact on the contact behaviour.

Chapter 6 Figures and Tables

Table 6.1 Summary of cyclic shearing test results on andesite.

Test	Normal load (N)	Shearing (mm)	Coefficient of friction	Stiffness at 5 μm (N/μm)
AB-020N	20	± 0.5	0.63	1.2
AB-050N	50	±1.0	0.6	1.3
AB-100N	100	± 0.5	0.75	1.1
AB-150N	150	± 1.0	0.75	2.1
AB-200N	200	± 0.5	0.75	2.0

Table 6.2 Summary of cyclic shearing test results on basalt.

Test	Normal load	Shearing to (mm)	Coefficient of friction	Stiffness N/μm
BB-100N-1	100	± 1.0	0.6	1.0
BB-100N-2	100	±1.0	0.65	1.5
BB-150N	150	± 1.0	0.65	1.8
BB-200N-1	200	± 1.0	0.7	2.0
BB-100N-3	100	± 1.0	0.75	1.6
BB-020N (average all of tests under	20	± 1.0	0.6	1-2
BB-050N-Flooded	50	± 1.0	0.6	1.0
BB-200N-Flooded	200	± 1.0	0.62	1.7
BB-050N (average all of tests under	50	± 1.0	0.6-0.8	1.0-2.0
BB-100N-Flooded	100	± 1.0	0.65	1.7

Table 6.3 Summary of cyclic shearing test results on Chinese granite

Test	Normal load (N)	Shearing to (mm)	Coefficient of friction	Stiffness N/µm
CB-020N	50	± 1.0	0.65	1.0 - 2.0
CB-050N	50	± 0.5	0.75	2.0
CB-100N-Flooded	100	± 0.5	0.72	2.0
CB-100N-2	100	± 0.5	0.7	1.0
CB-150N	150	± 1.0	0.65	3.0
CB-200N	200	± 1.0	0.75	1.0

Table 6.4 Summary of cyclic shearing test results on fresh granite.

Test	Normal load (N)	Shearing to (mm)	Coefficient of friction	Stiffness N/µm
GB-020N-1	20	± 0.5	0.62	1.0
GB-100N	100	± 1.0	0.6	0.90
GB-200N	200	± 0.5	0.63	1.5
GB-50N	50	± 1.0	0.68	2.0
GB-020N-2	20	± 0.5	0.68	1.4

Table 6.5 Summary of cyclic shearing test results on used granite.

Test	Normal load (N)	Shearing to (mm)	Coefficient of friction	Stiffness N/µm
UG-020N	20	± 0.5	0.6	1.0
UG-100N	100	± 1.0	0.73	1.9
UG-150N	150	± 0.5	0.65	1.8
UG-200N	200	± 1.0	0.7	2.0
UG-050N	50	± 1.0	0.6	1.8

Table 6.6 Summary of cyclic shearing test results on washed used granite.

Test	Normal load (N)	Shearing to (mm)	Coefficient of friction	Stiffness N/µm
WUG-100N	100	± 0.5	0.65	2.0
WUG-020N-1	20	± 1.0	0.65	1.9
WUG-200N	200	± 0.5	0.6	2.9
WUG-150N	20	± 1.0	0.7	2.4

(a) Before

(b) After approximately after 100 cycles under a normal load of 20N)

Figure 6.1 A typical angular-flat contact of andesite ballast before the test and after the test
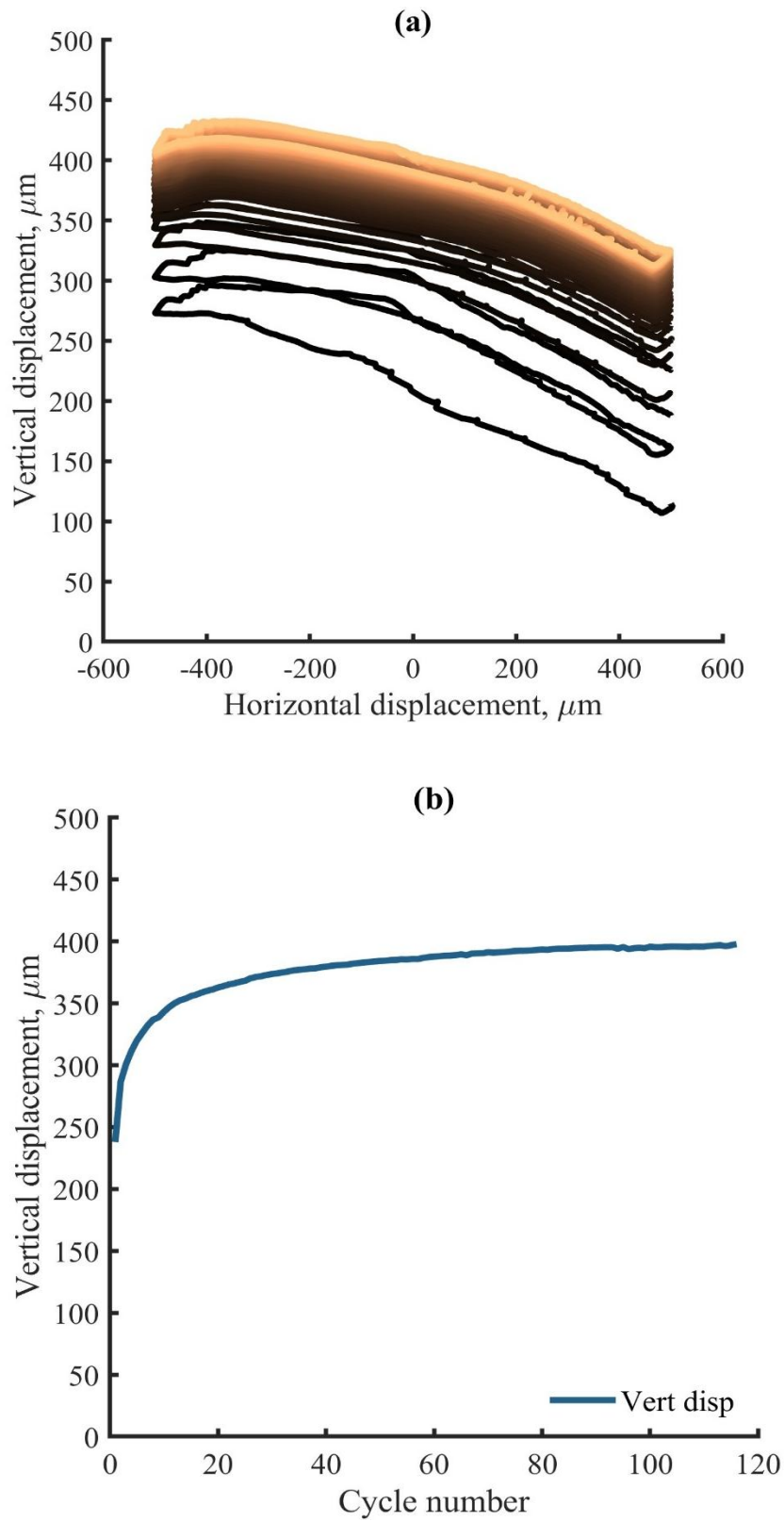
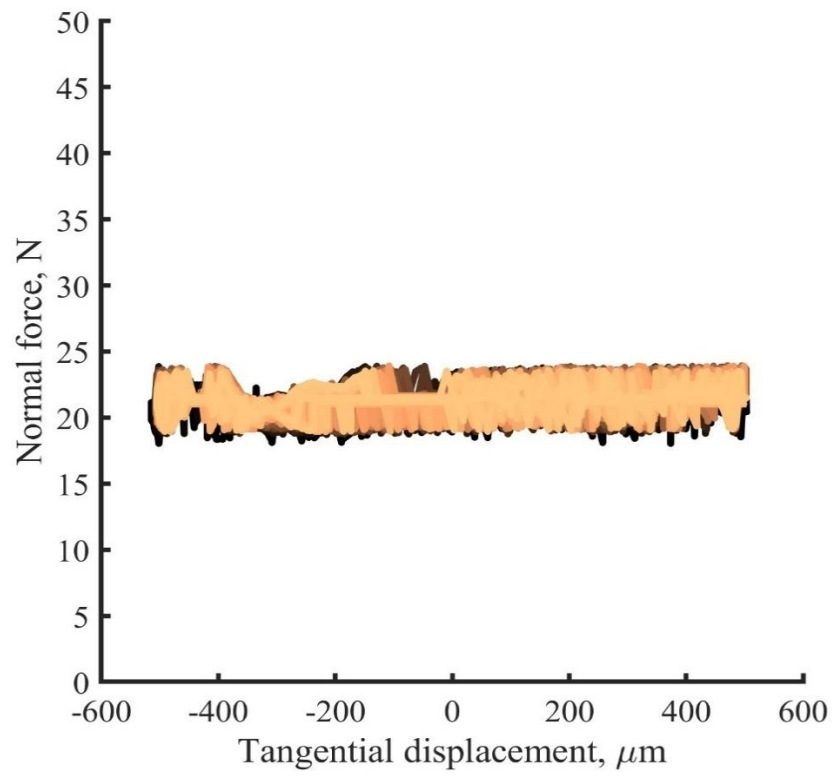Figure 6.2 Vertical displacement of andesite ballasts, initially, at the onset of the test, the inter-cycle spacing is greater, progressively diminishing with subsequent cycles until reaching minimal levels, nearly approaching zero distance (a), as the cycles increase the normal displacement increases (b).

(a)
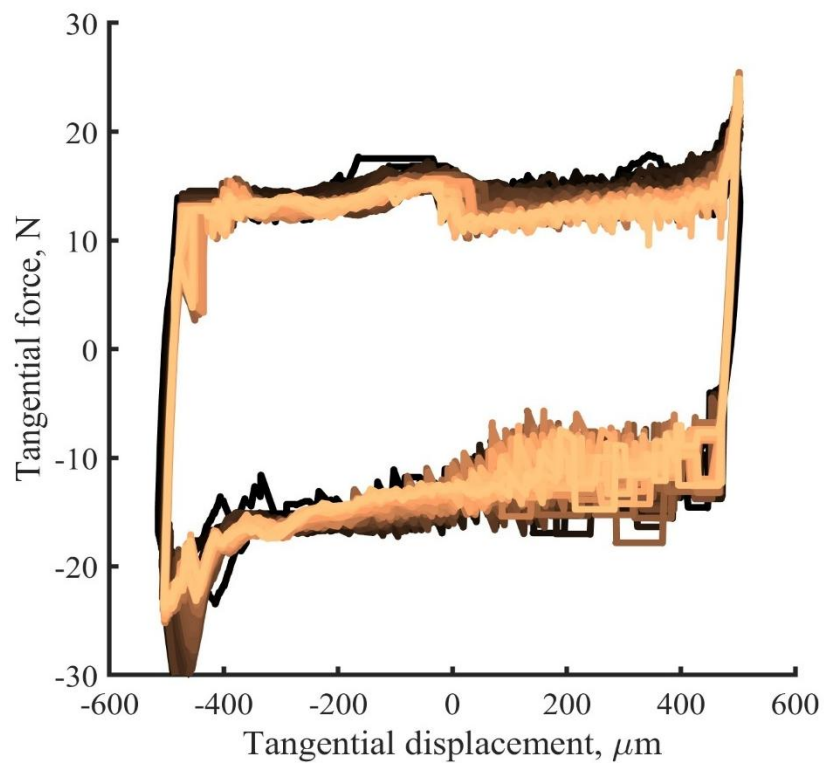
(b)

Figure 6.3 Normal force (a) and Tangential force (b) of andesite ballasts during cyclic
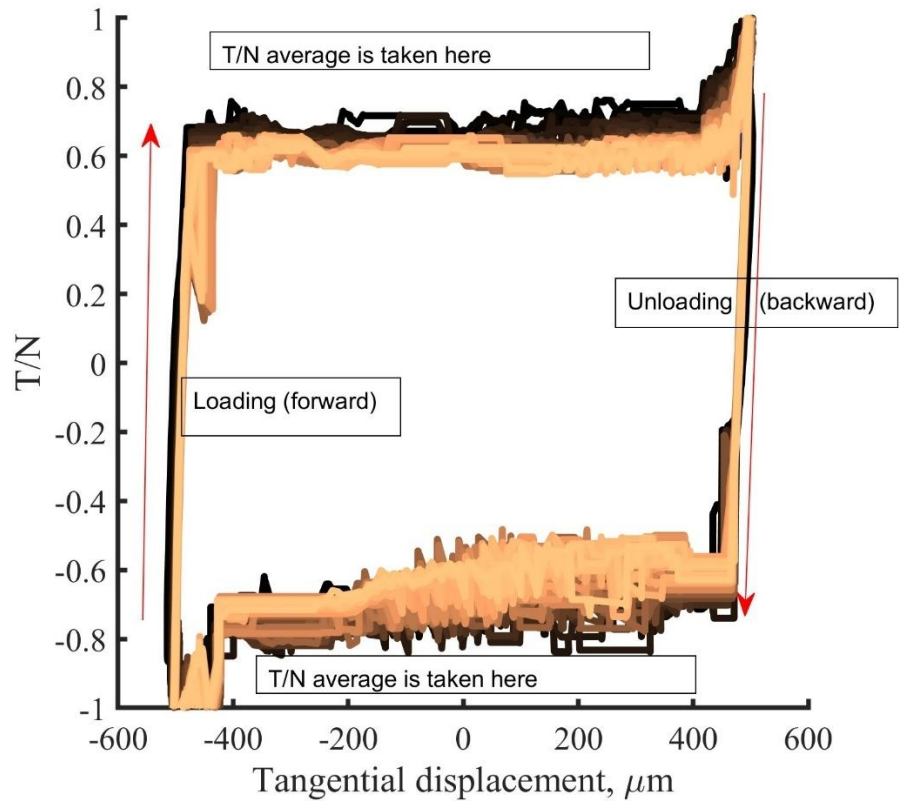
shearing.

(a)
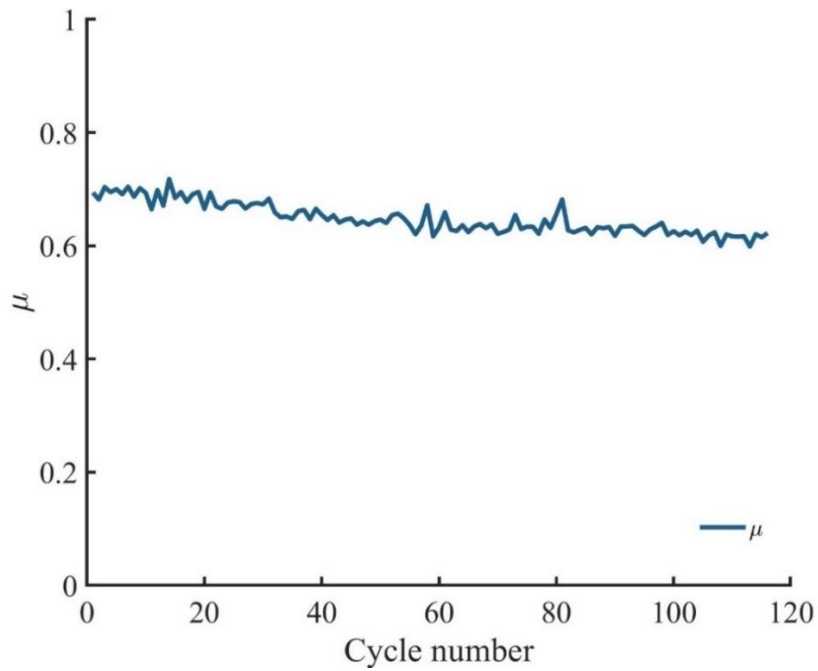
(b)

Figure 6.4 Tangential force to normal force ratio (T/N) versus tangential displacement (a) and friction coefficient (μ) versus cycle number (b) for andesite ballast during cyclic shearing.
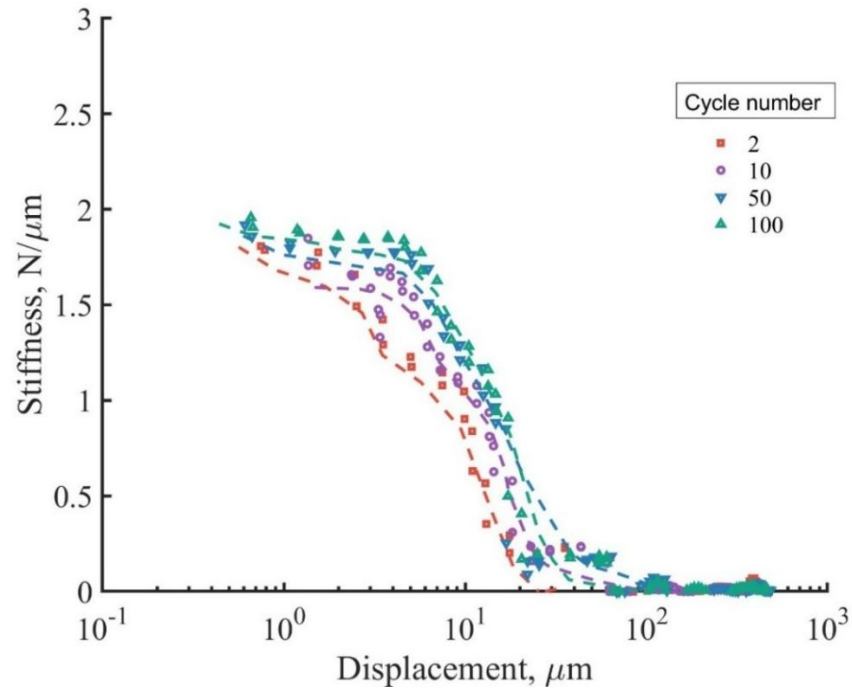
(a)
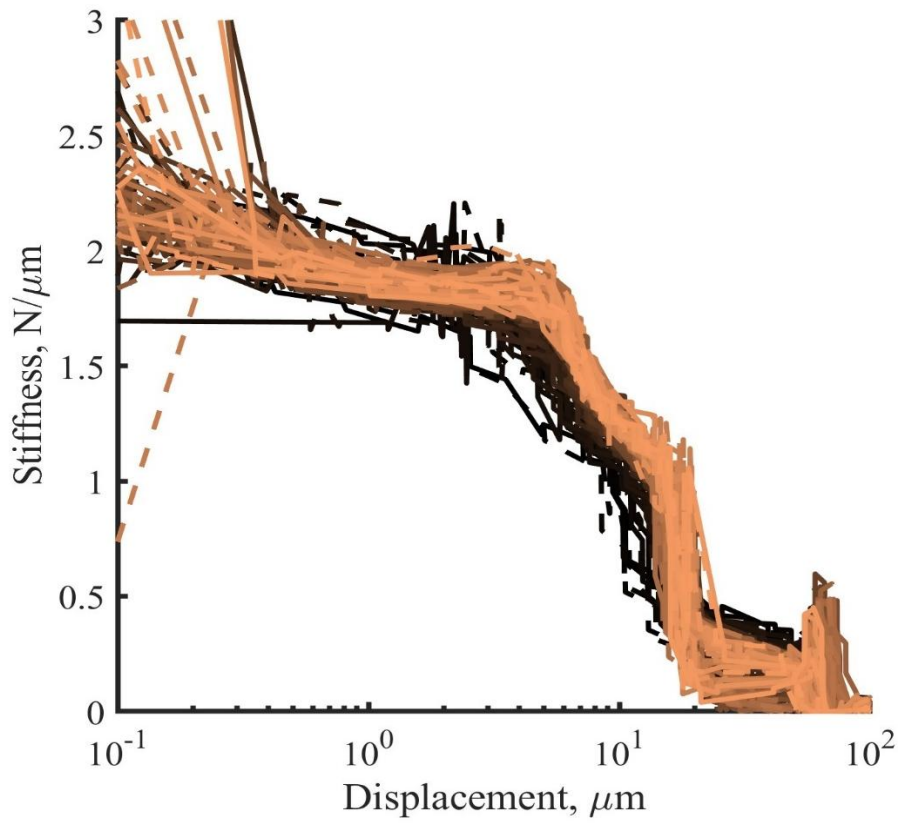
(b)

Figure 6.5 Stiffness of andesite ballasts during cyclic shearing, display of stiffness after a few cycles (a), stiffness across all cycles (b) in a forward direction.
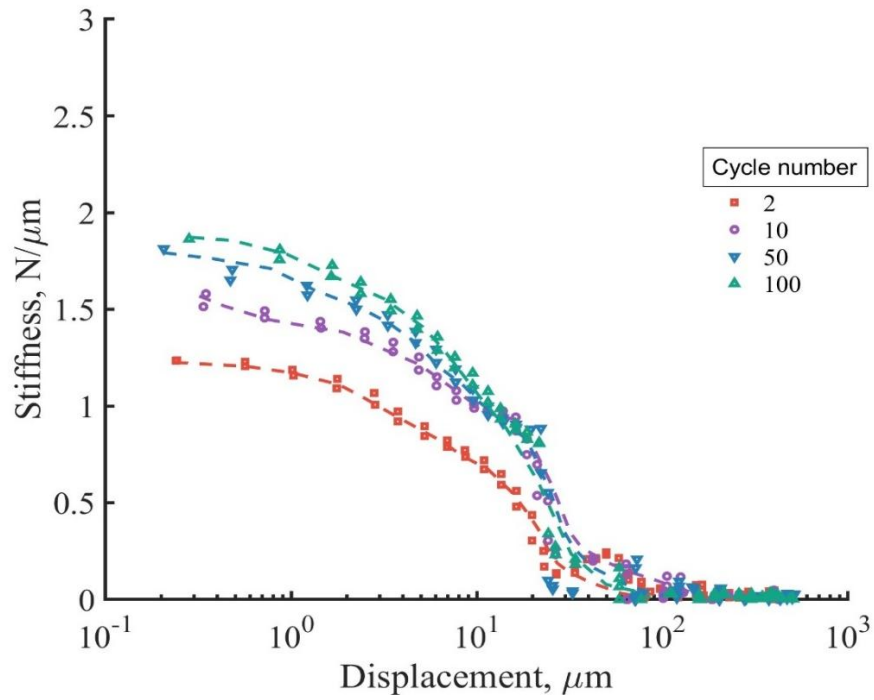
(a)
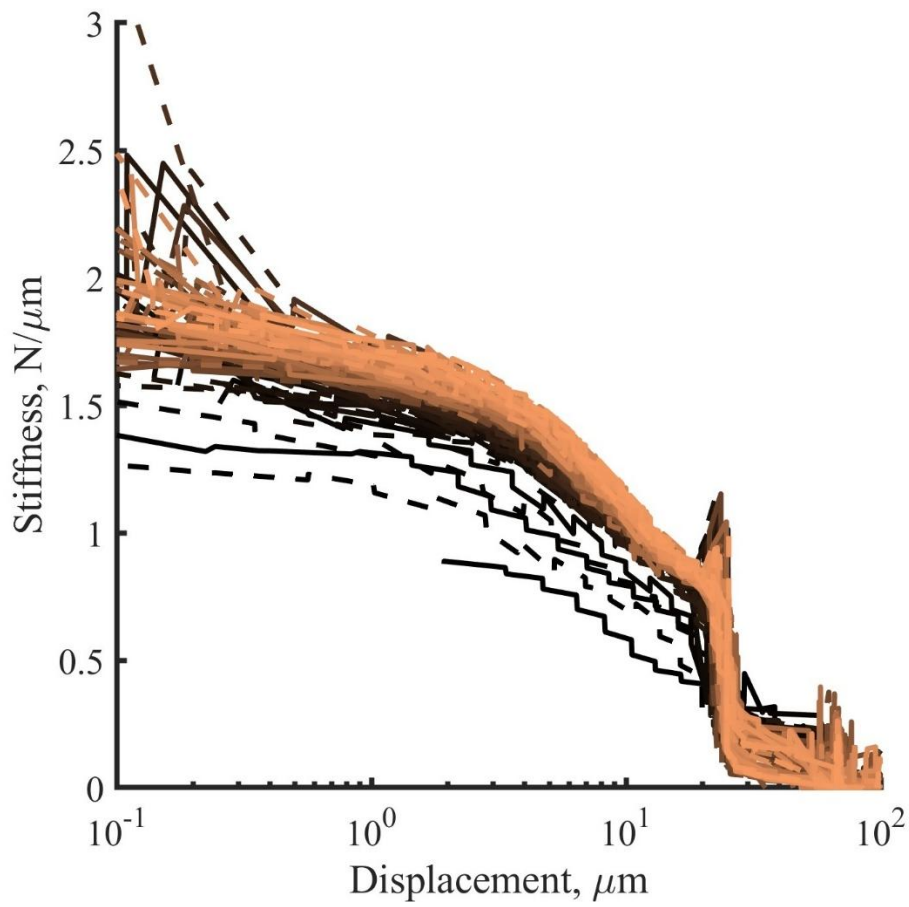
(b)

Figure 6.6 Backwards stiffness of a few cycles (a) and the stiffness of all cycles.

Figure 6.7 Coefficient of inter-particle friction (μ) with monotonic shear shown as the first cycle, under different levels of loads on andesite ballasts.

Figure 6.8 Vertical displacements of andesite ballasts under different normal load levels.
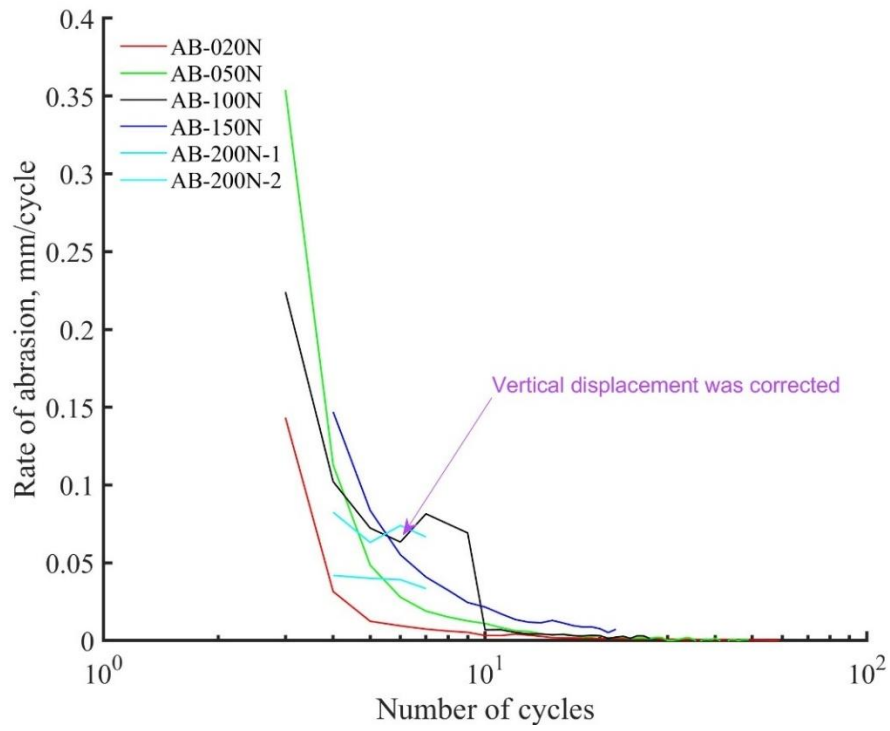
Figure 6.9 Rate of abrasion of andesite during cyclic shearing.
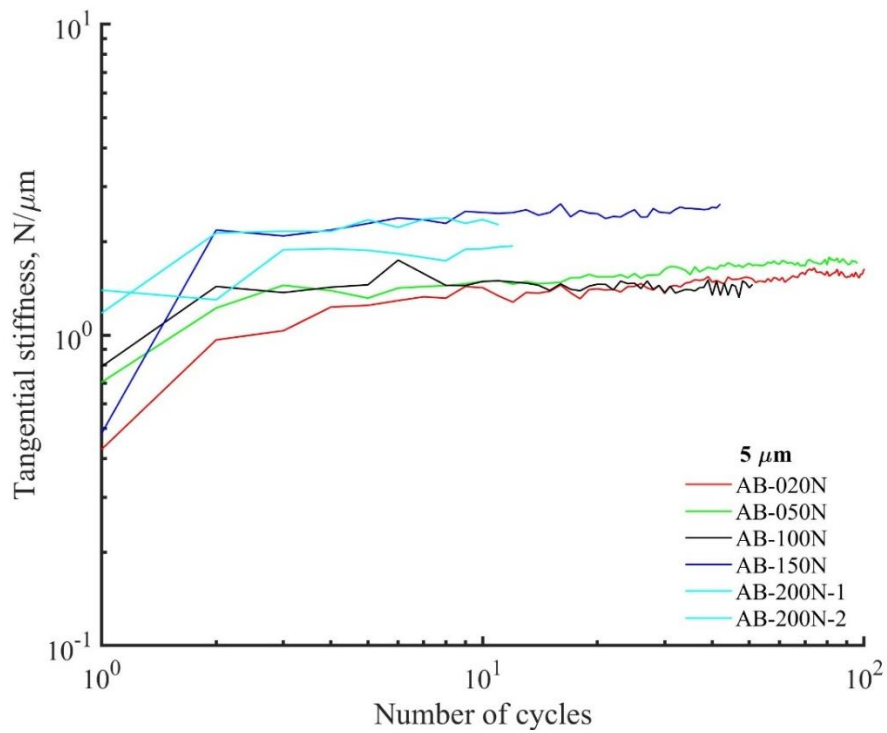
Figure 6.10 Cyclic stiffness of andesite at 5 μ under different normal loading conditions.
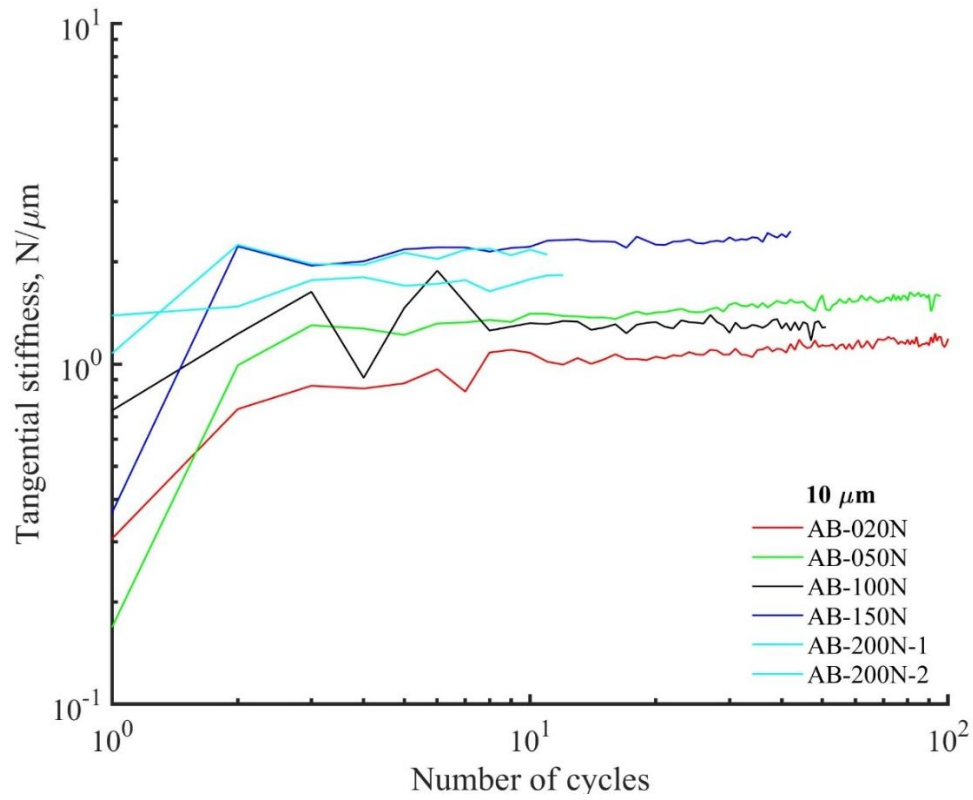
Figure 6.11 Cyclic stiffness of andesite at 10 μ under different normal loading conditions.
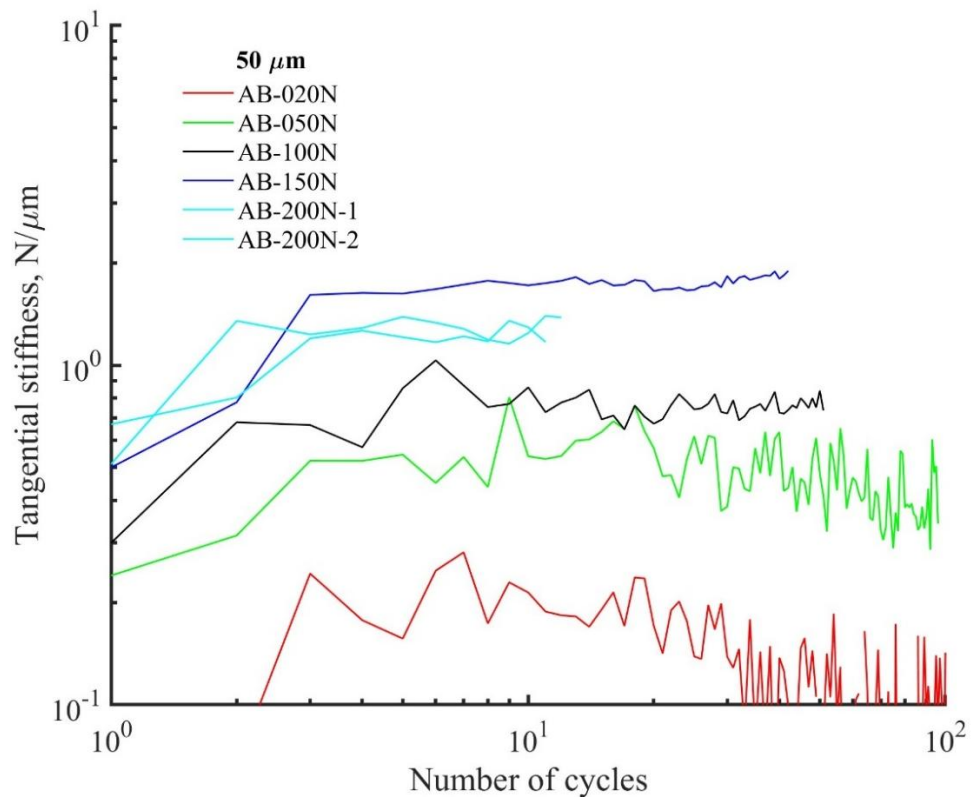
Figure 6.12 Cyclic stiffness of andesite at 50 μ under different normal loading conditions.
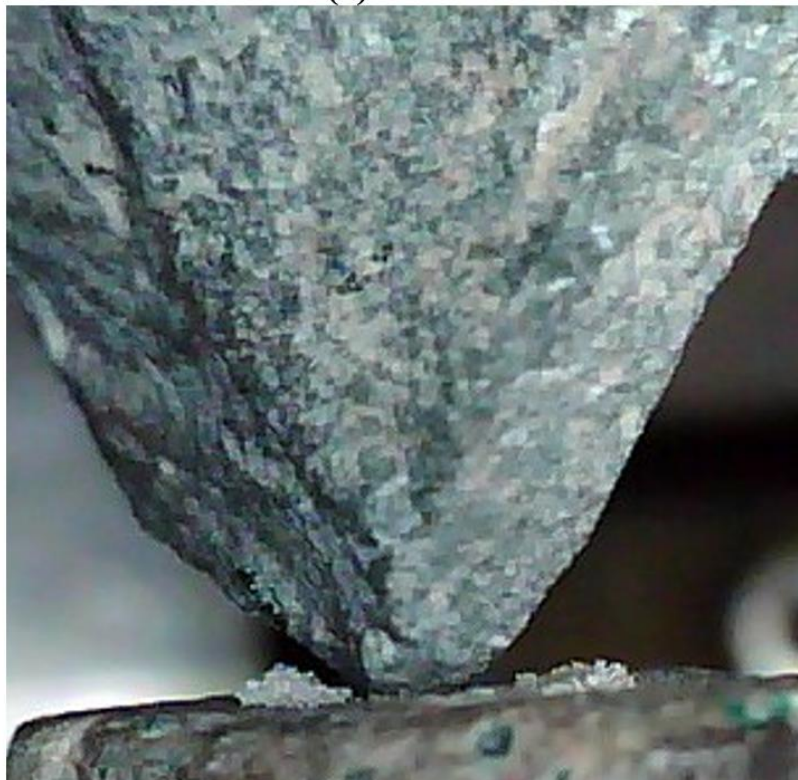
(a) Before

(b)

Figure 6.13 Basalt particles with an angular-flat contact geometry, before and after a test of 65 cycles under a normal load of 20N.
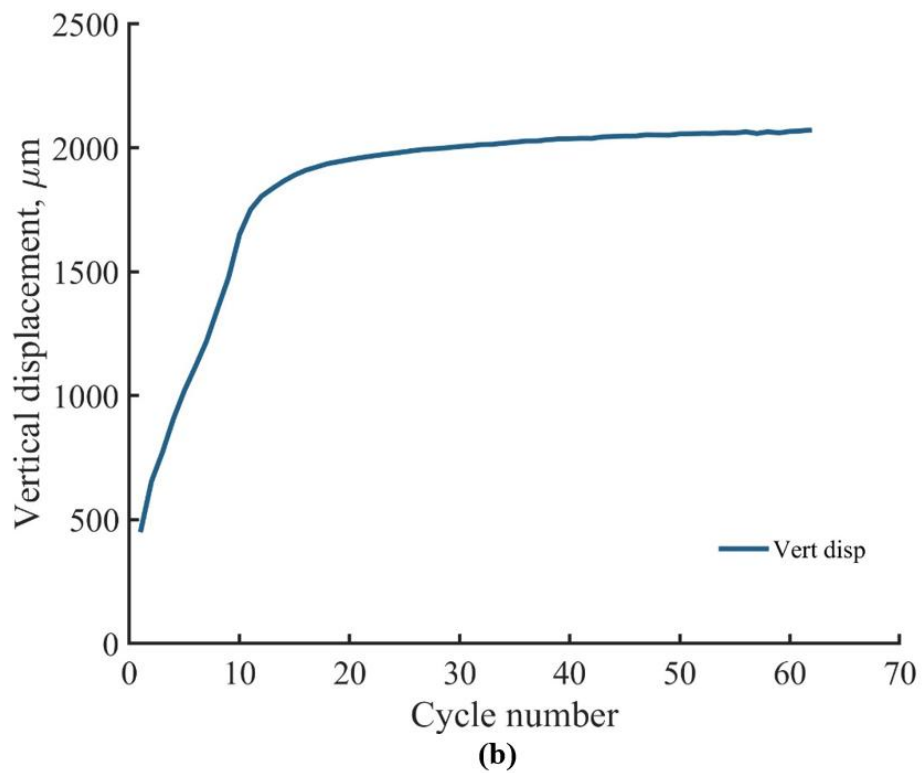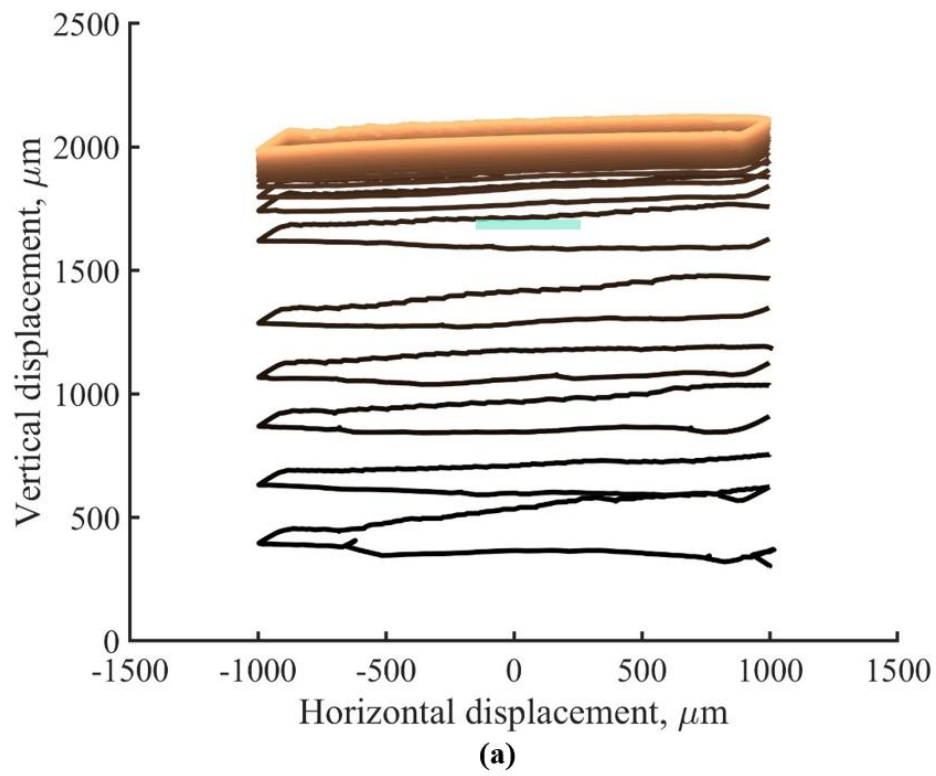
Figure 6.14 Vertical displacement of basalt during cyclic shearing(a) as the cycles increase the normal displacement increases (b).
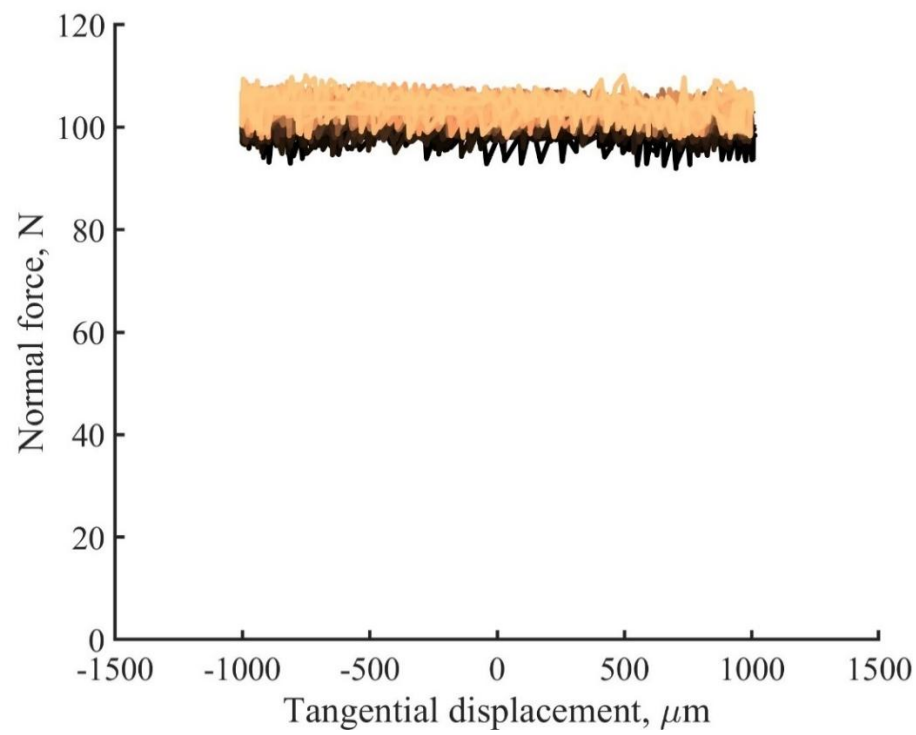
(a)
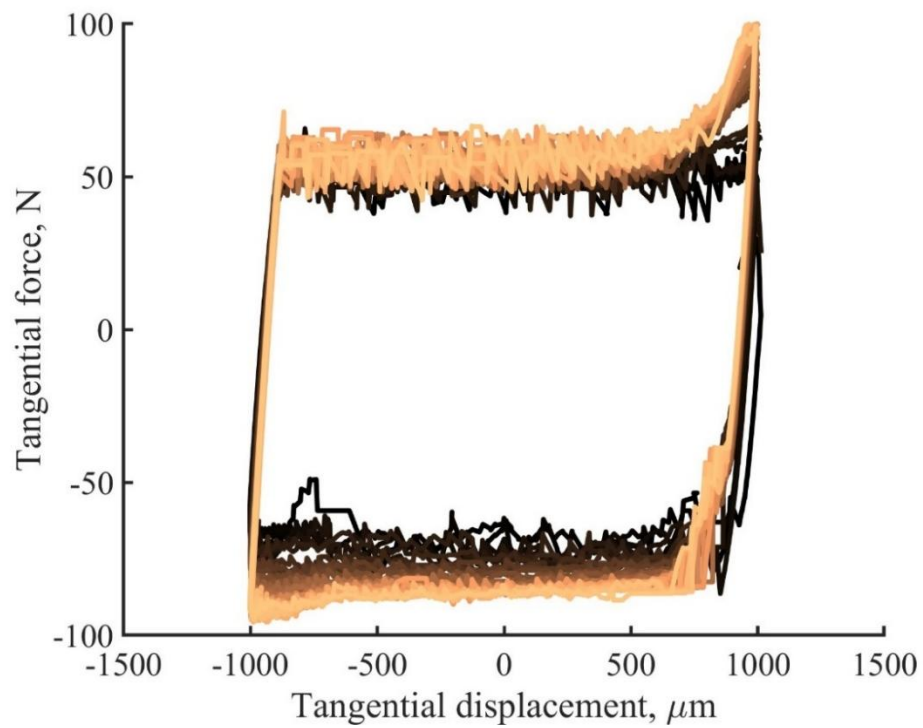
(b)

Figure 6.15 The normal force (a) and tangential force (b) during cyclic shearing of basalt ballast.
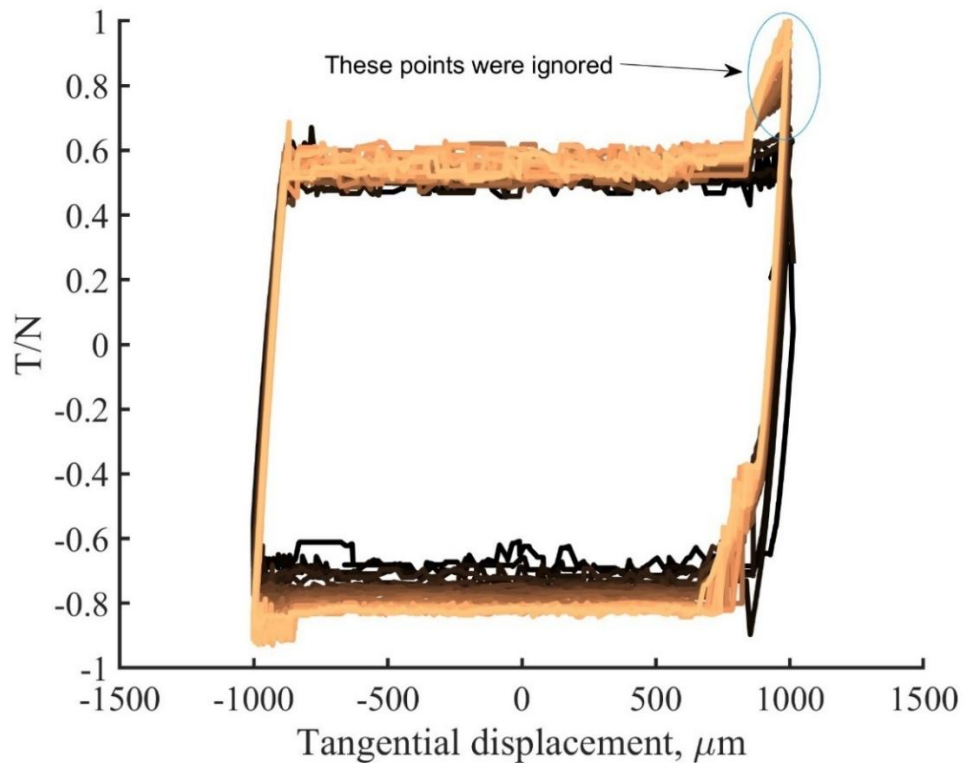
(a)
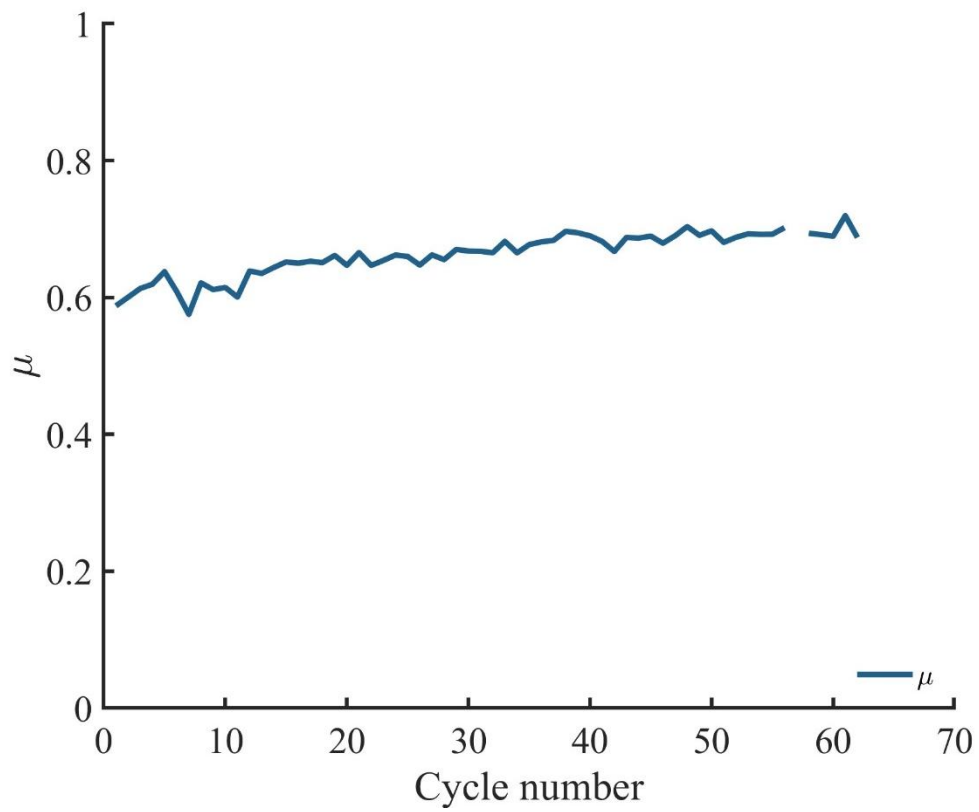
(b)

Figure 6.16 Force ratio (a) and μ (b) with cycle number of basalt ballast.

(a)

(b)
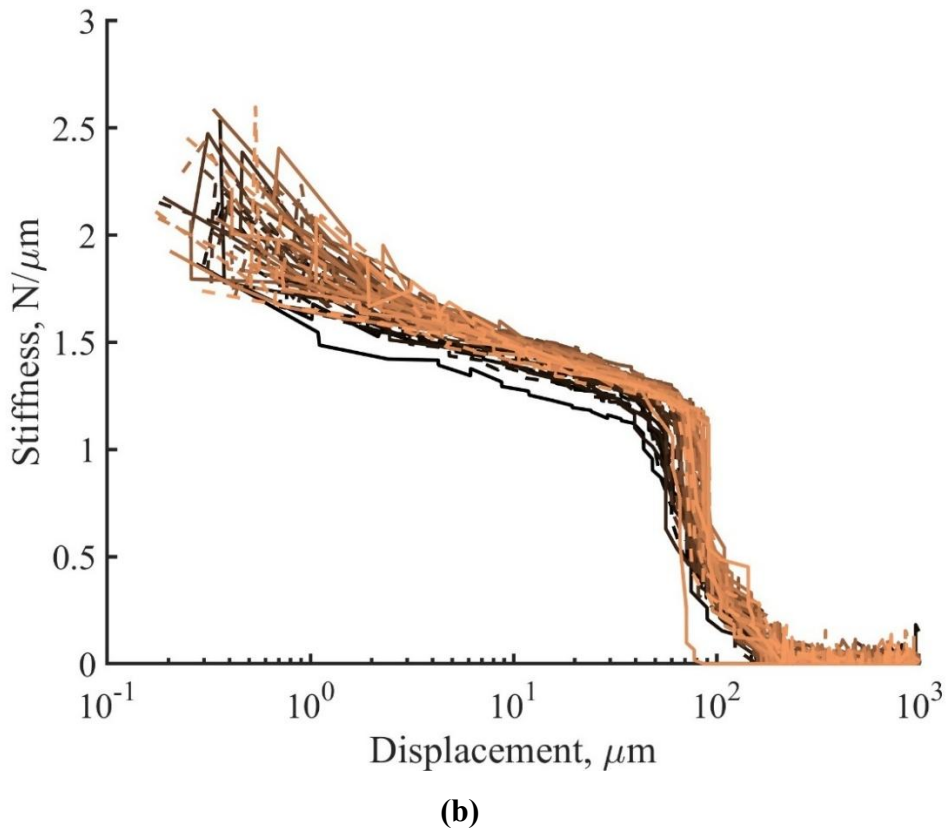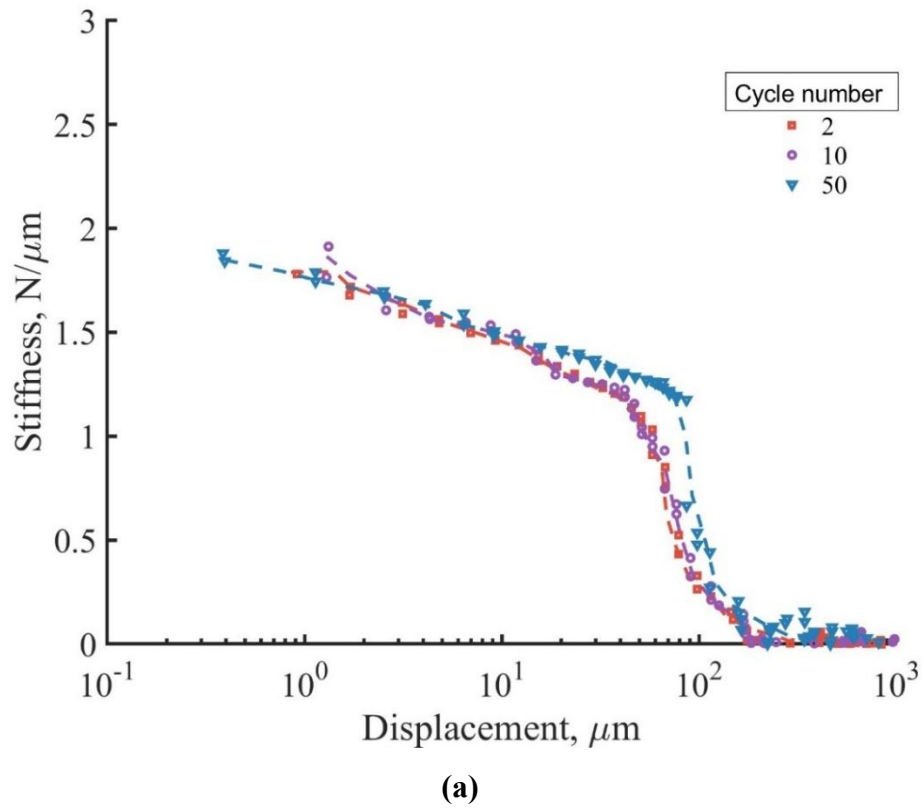
Figure 6.17 Stiffness degradation of basalt ballast in the forward direction for cycles 2, 10 and 50 (a), and all cycles (b).
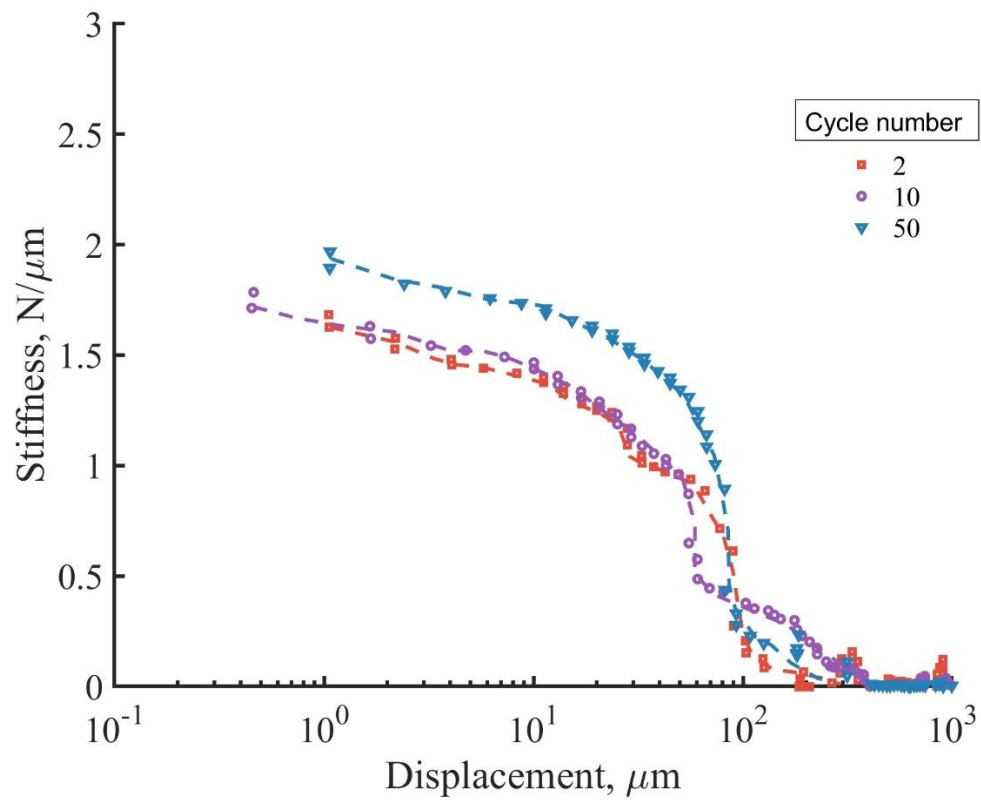
(a)
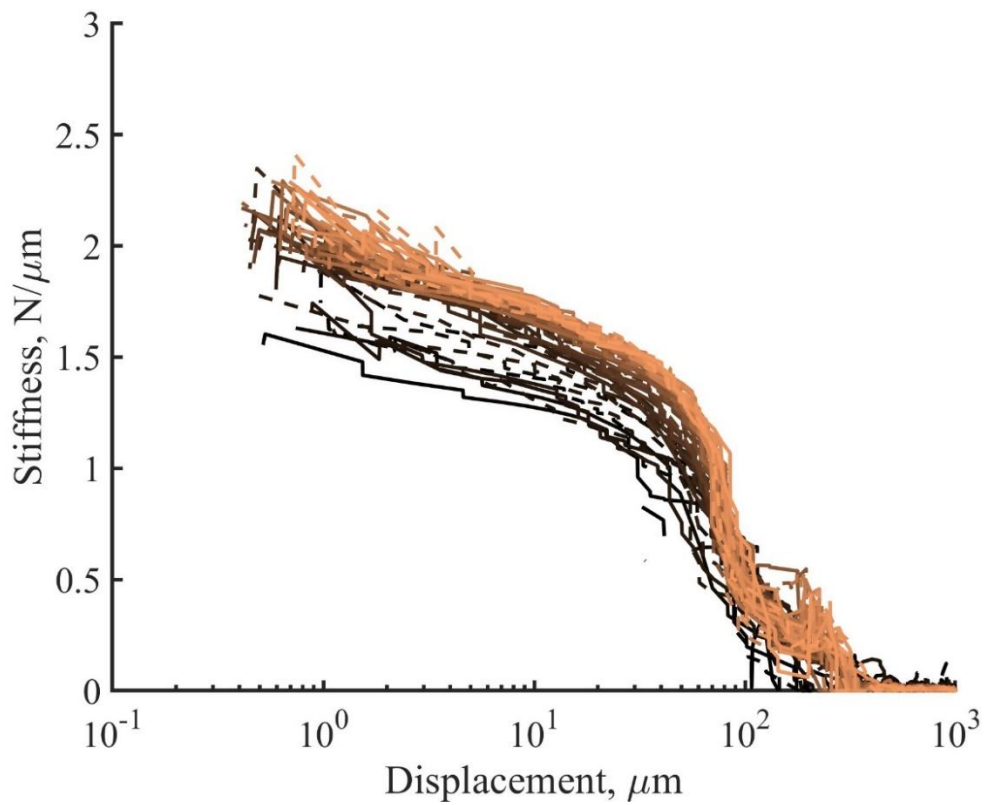
(b)

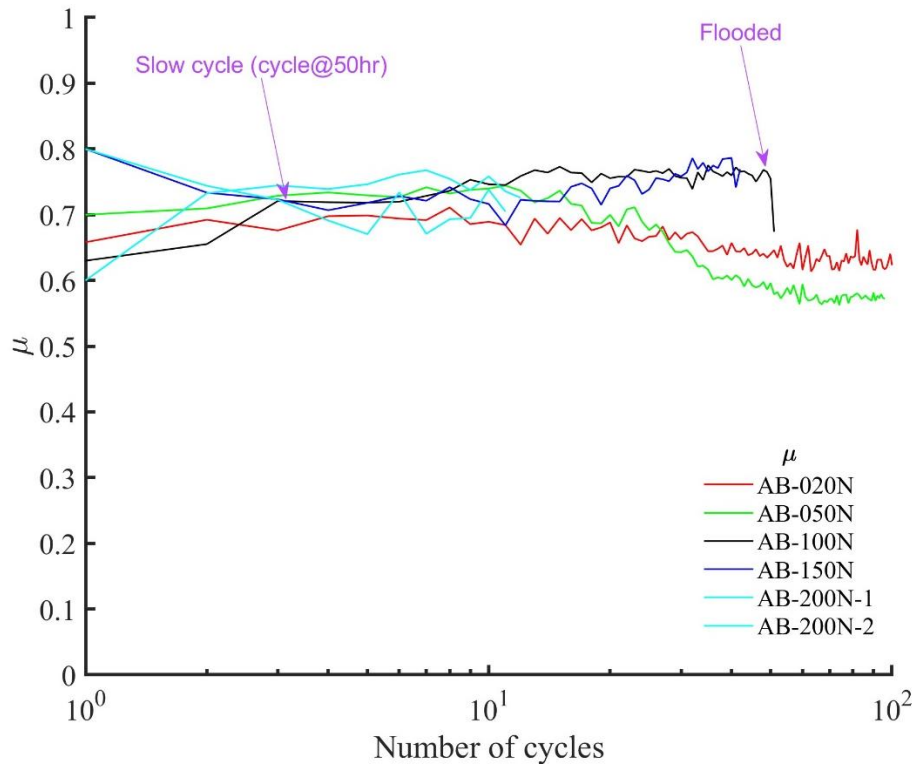Figure 6.18 Backwards stiffness of a few cycles (a) and the stiffness of all cycles.

Figure 6.19 Coefficient of inter-particle friction (μ) with monotonic shear shown as the first cycle, under different levels of loads on basalt ballasts.
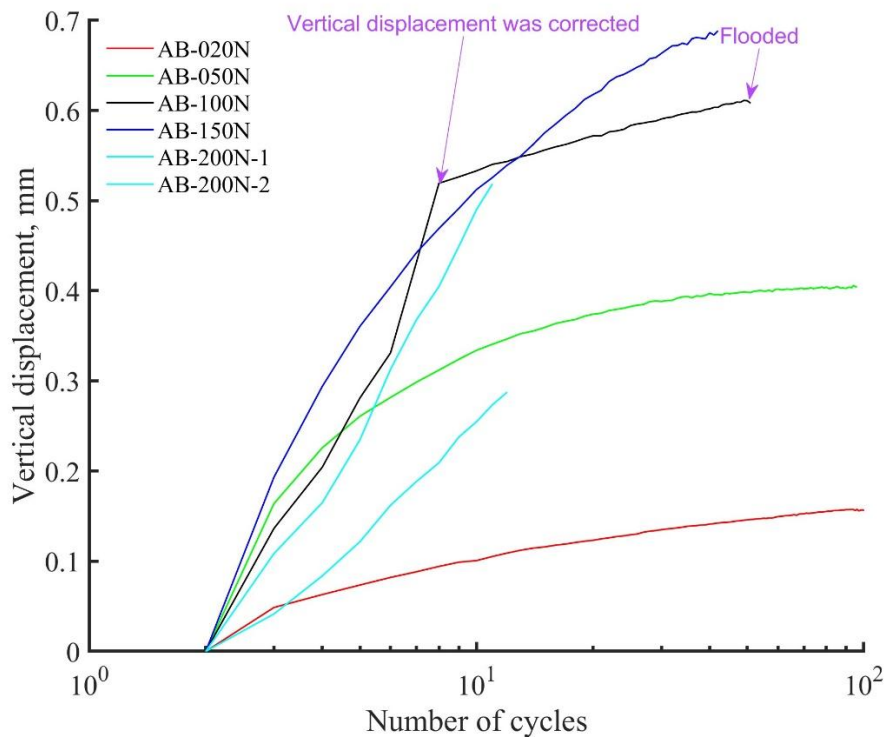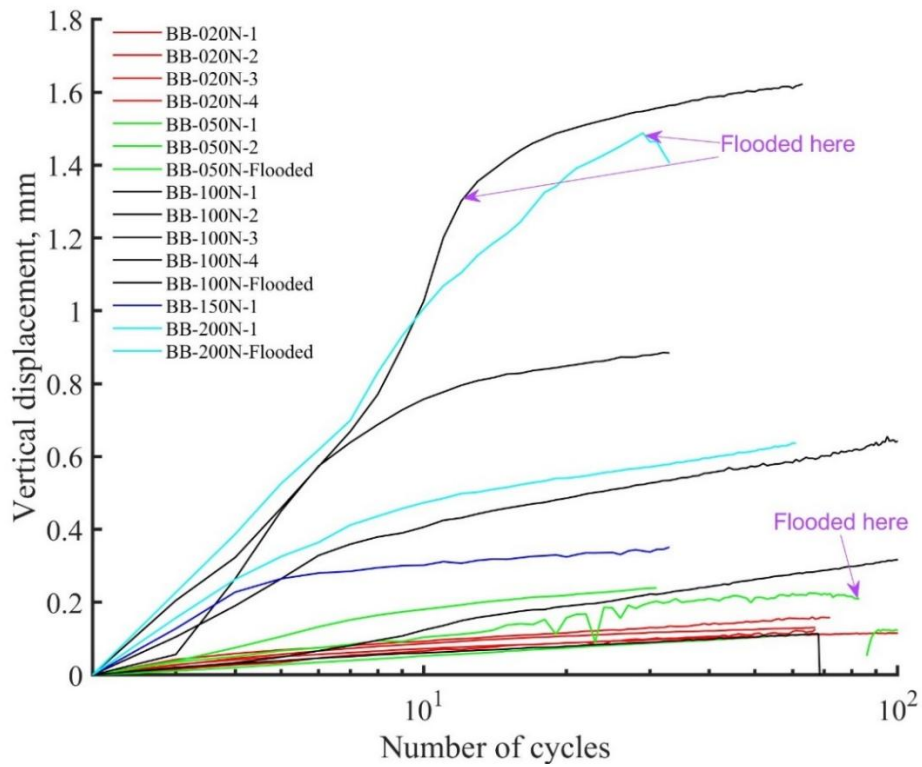

Figure 6.20 Vertical displacements under different levels of loads on basalt ballasts.
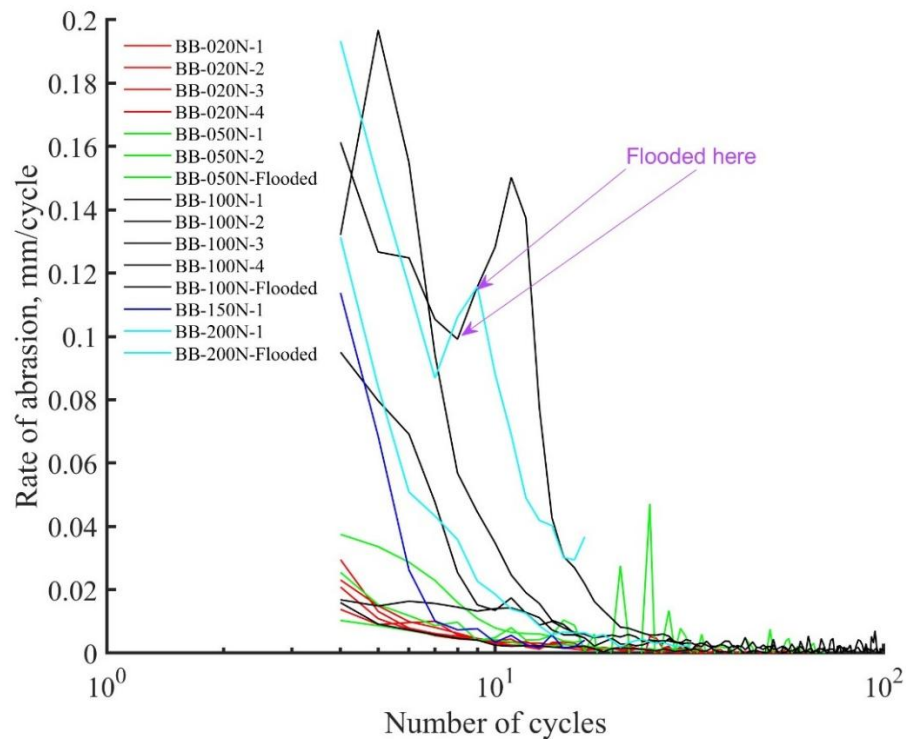
Figure 6.21 Rate of abrasion during cyclic shearing of basalt ballasts.
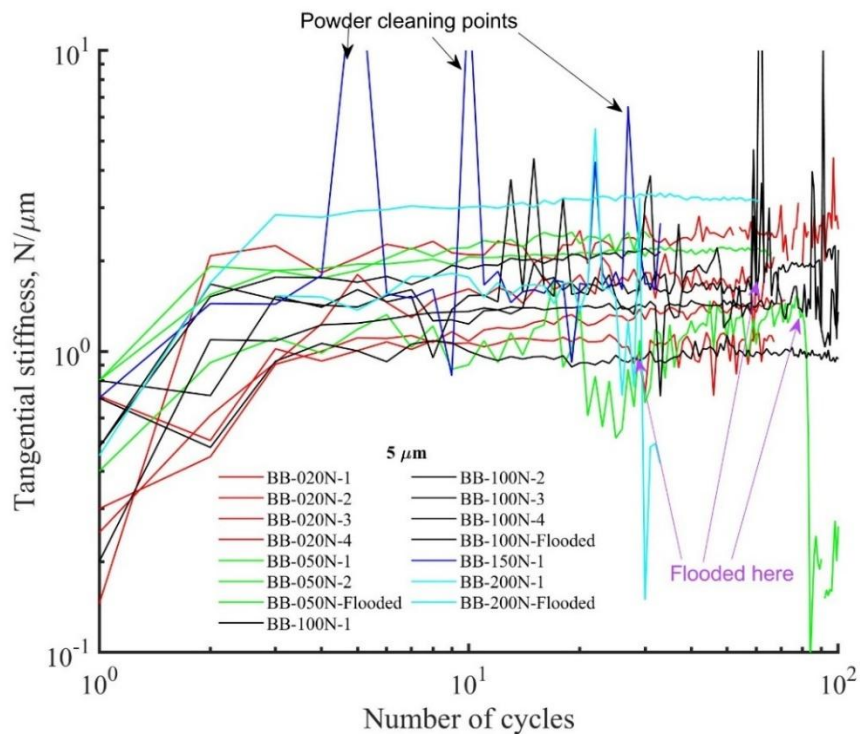
Figure 6.22 Cyclic stiffness of basalt ballasts at 5 μ under different normal loadings.
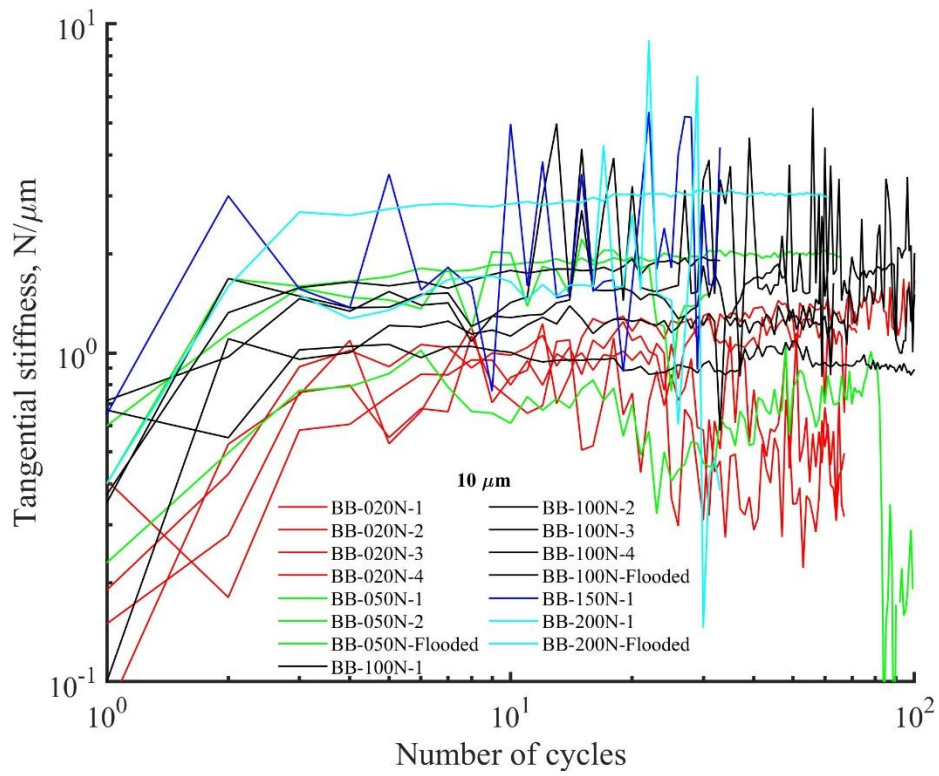
Figure 6.23 Cyclic stiffness of basalt ballasts at 10 μ under different normal loading conditions.
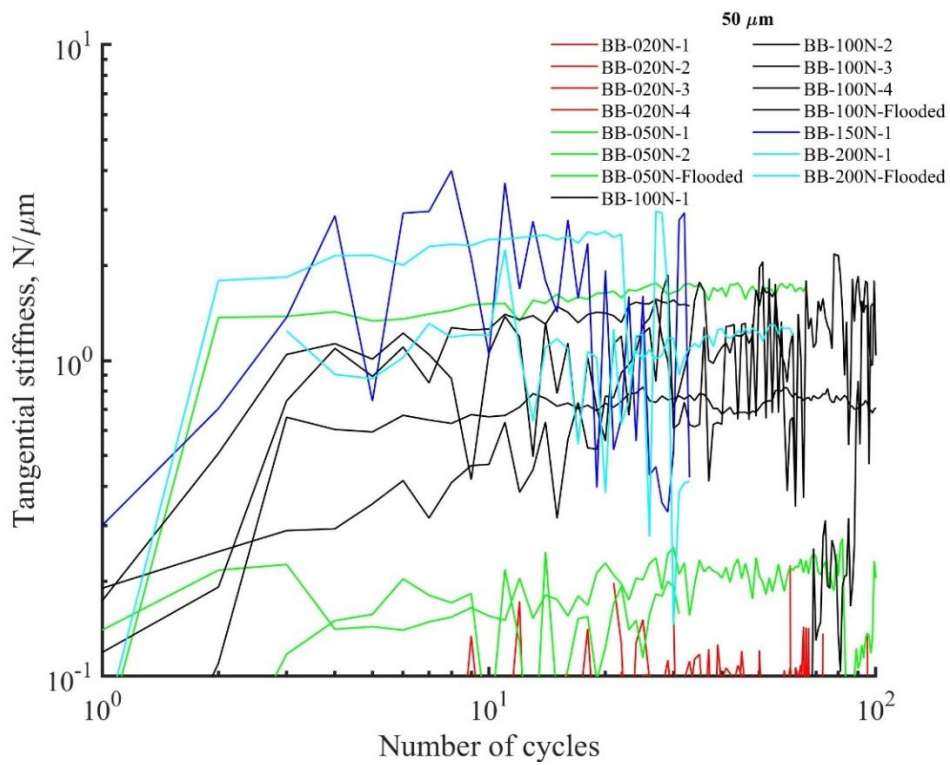
Figure 6.24 Cyclic stiffness of basalt ballasts at 50 μ under different normal loading conditions.

(a)

(b)

Figure 6.25 Typical Chinese granite particles with an angular-flat contact geometry, before and after a test involving 65 cycles under a normal load of 200 N.

(a)

(b)
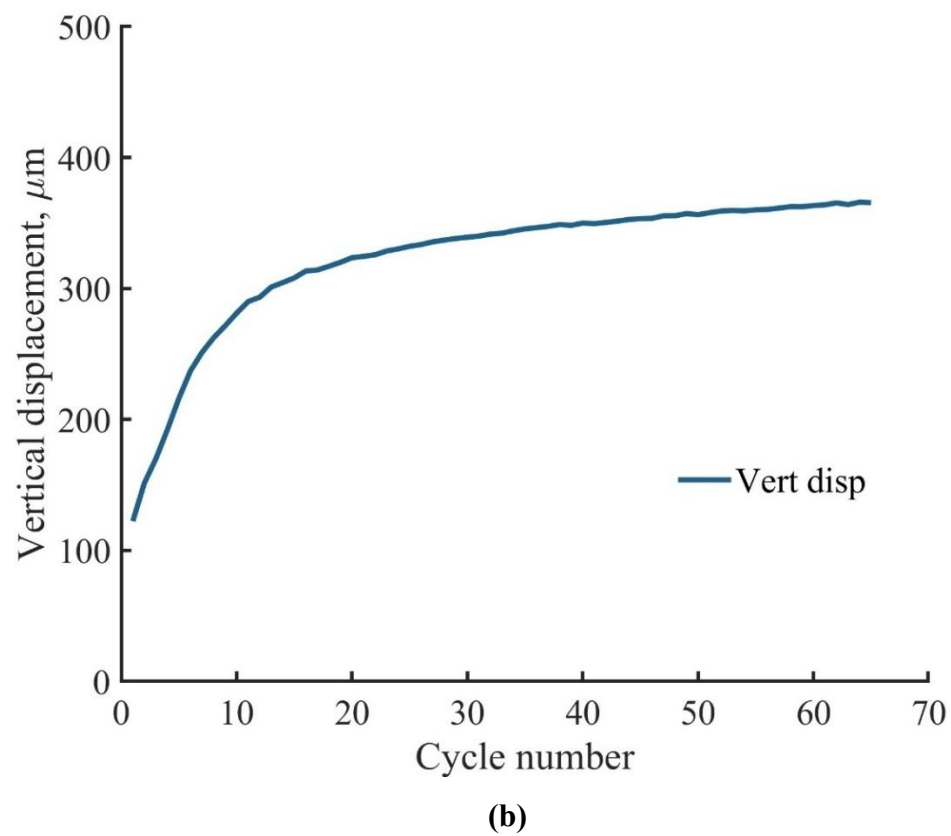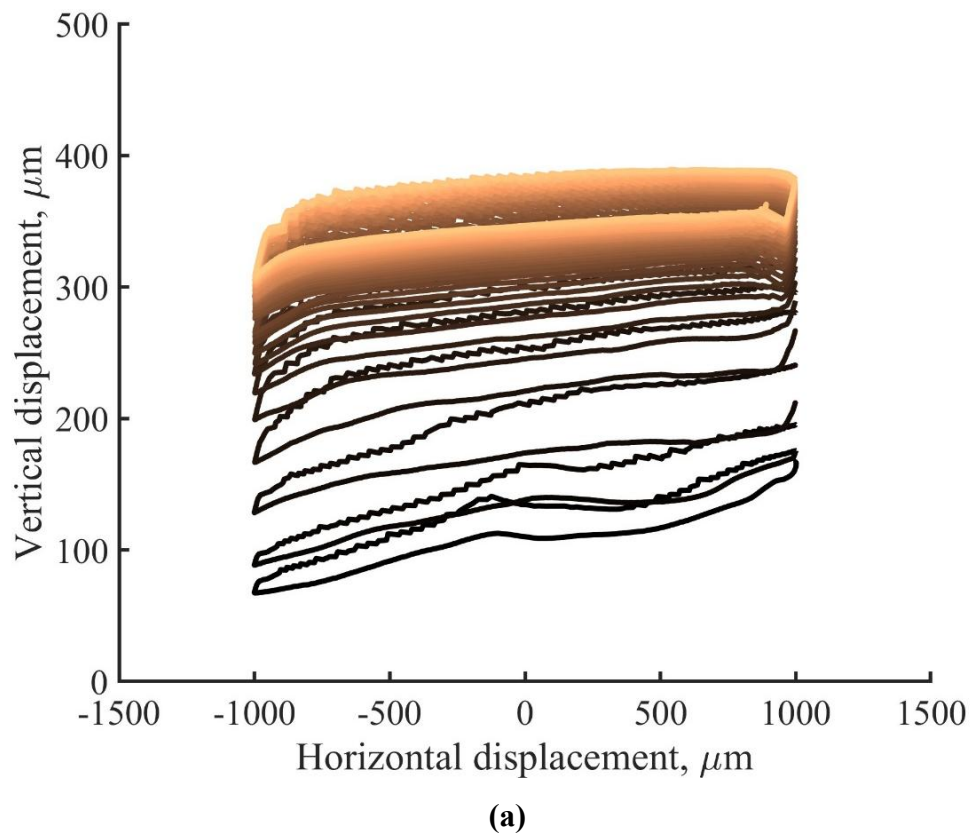
Figure 6.26 Initially, the inter-cycle spacing of Chinese granite is greater and then nearly approaching zero distance (a), as the cycles increase the normal displacement increases (b).
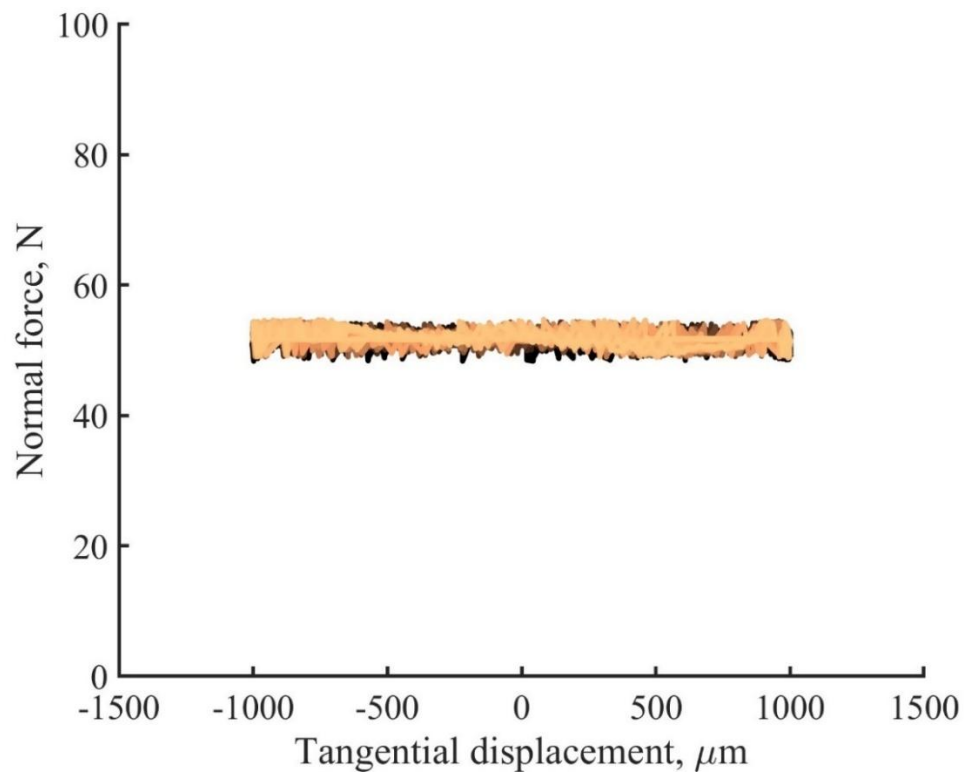
(a)
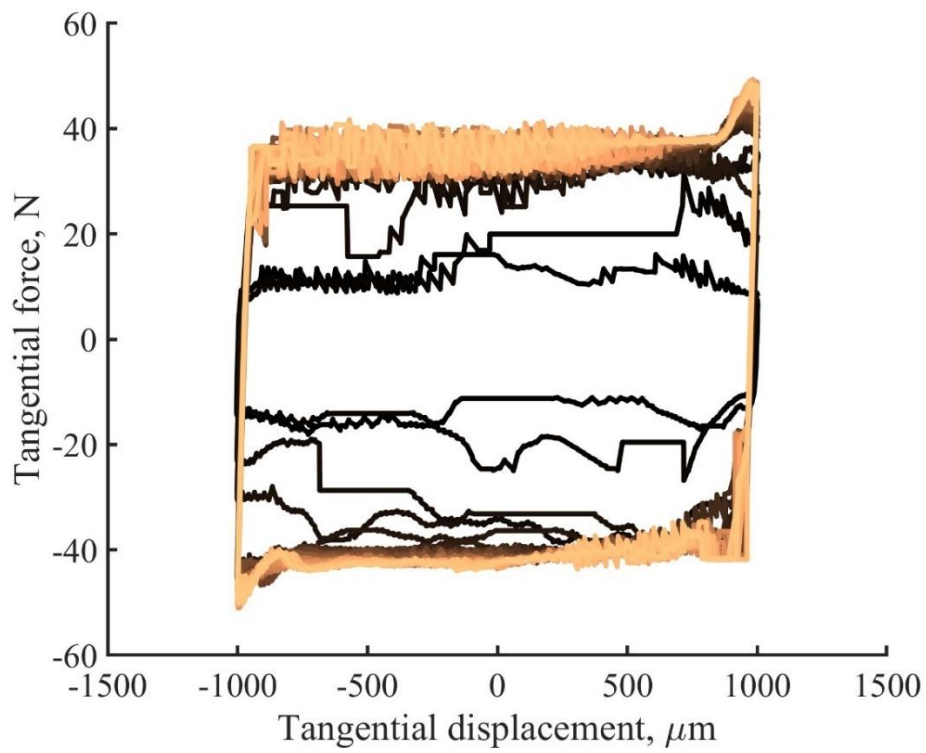
(b)

Figure 6.27 Normal force (a) and Tangential force (b) of Chinese granite during cyclic shearing.
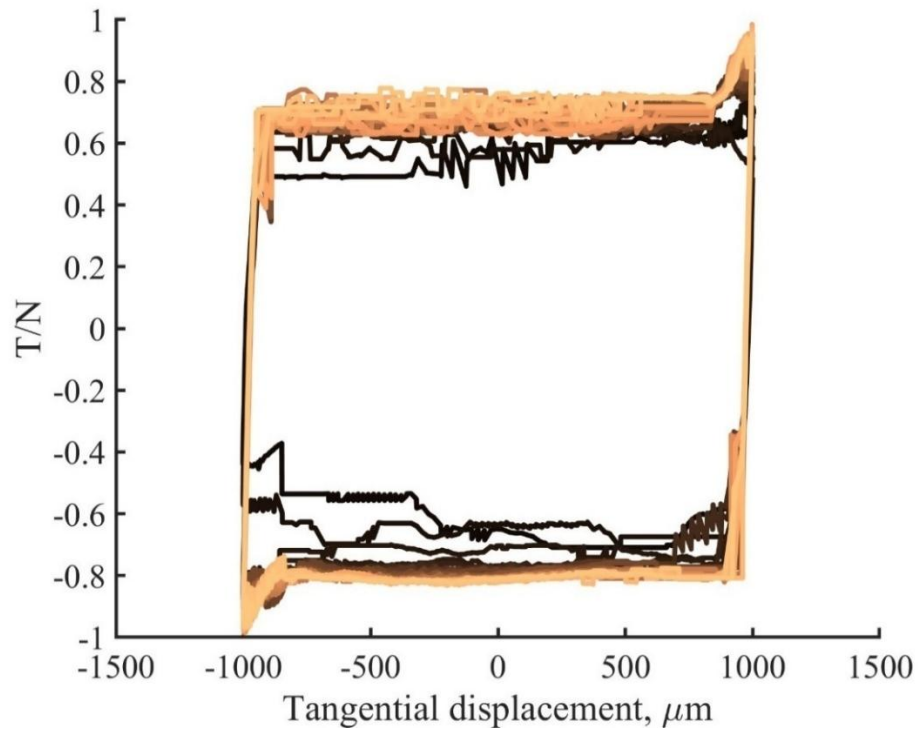
(a)
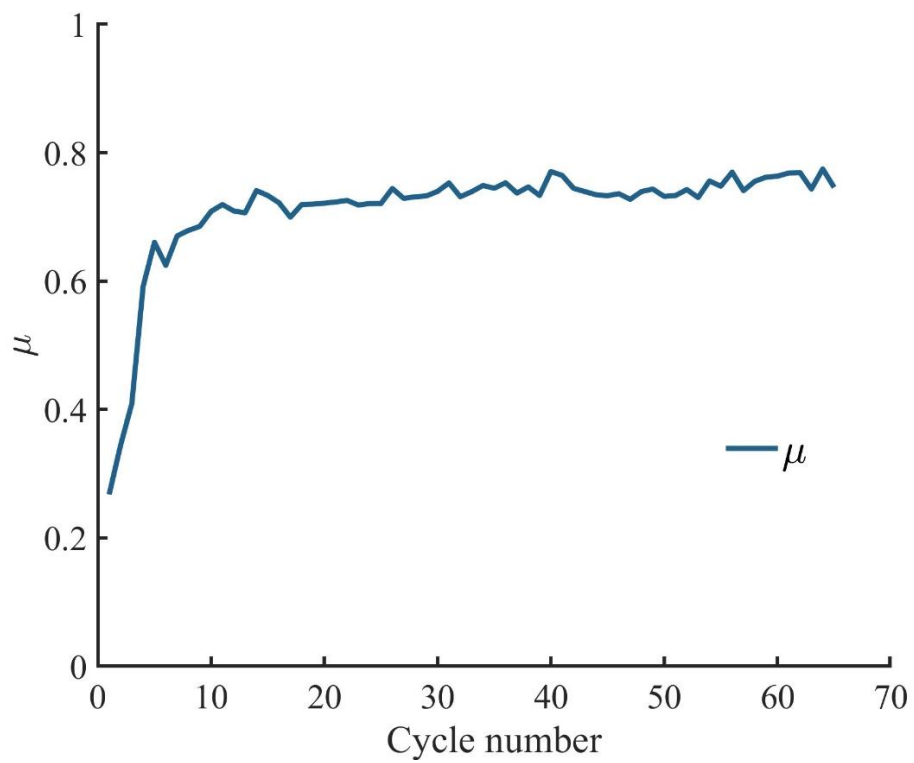
(b)

Figure 6.28 Force ratio (a) and μ (b) with cycle number of Chinese granite ballasts.
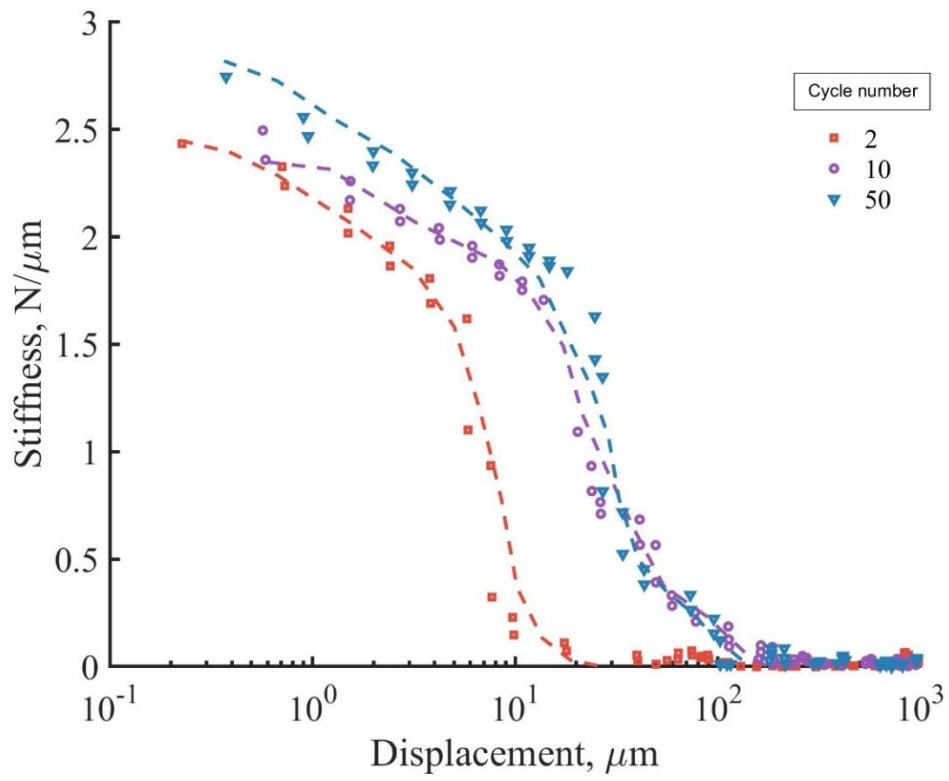
(a)
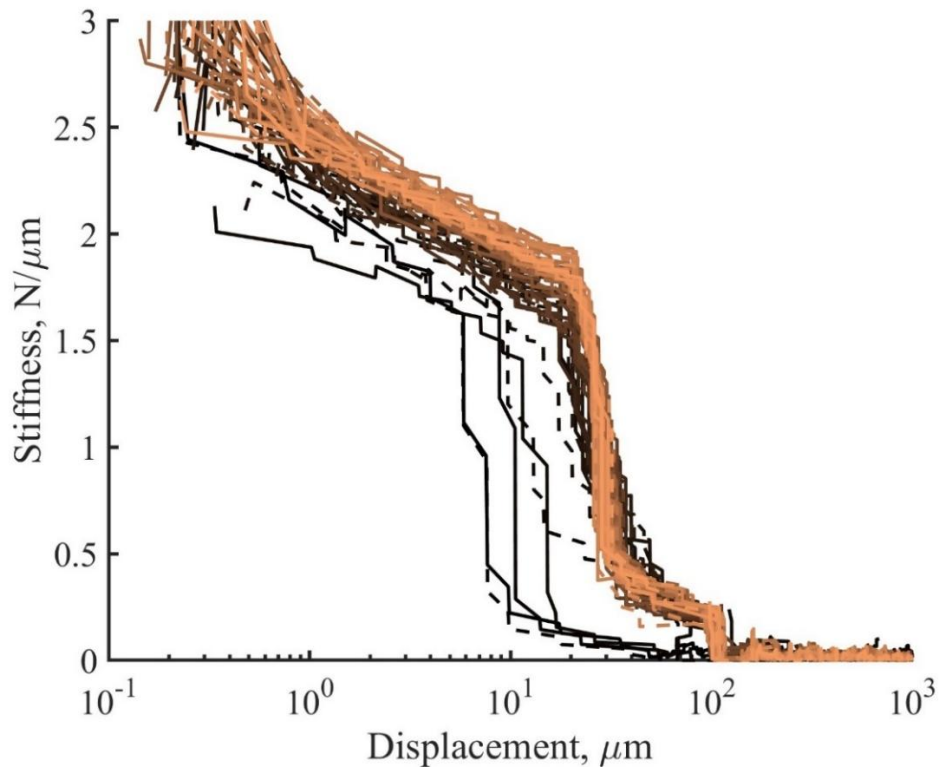
(b)

Figure 6.29 Chinese granite ballast stiffness in the forward direction of 2, 10 and 50 cycles (a) and for all cycles (b).
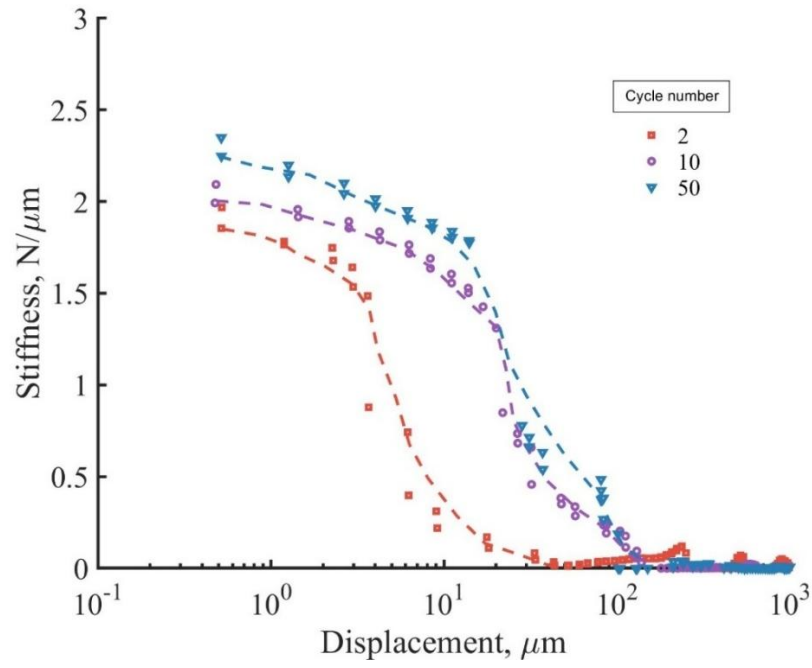
(a)
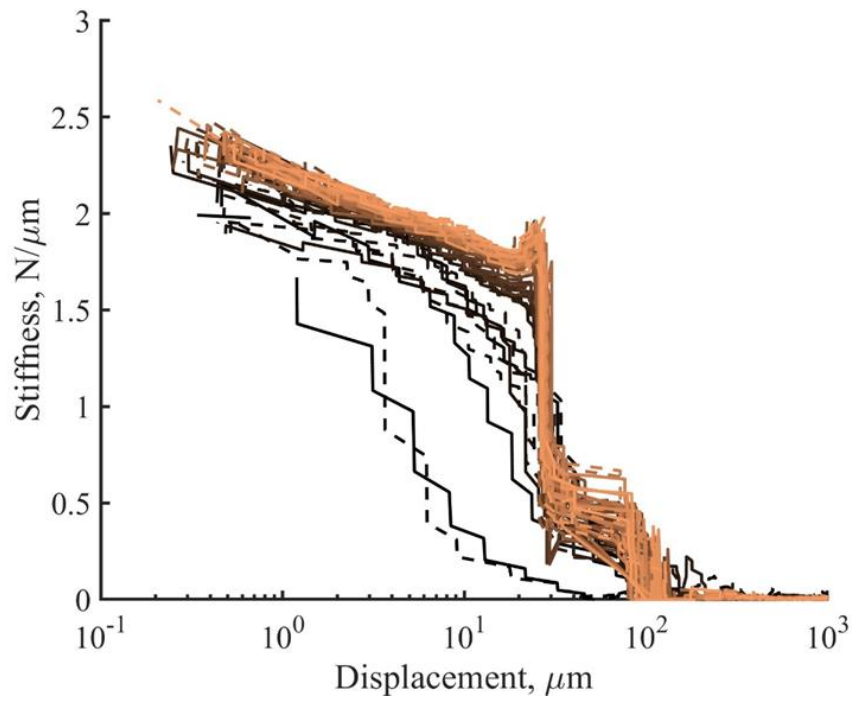
(b)

Figure 6.30 Chinese granite ballast stiffness in the backward direction of 2, 10 and 50

cycles (a) and for all cycles (b).
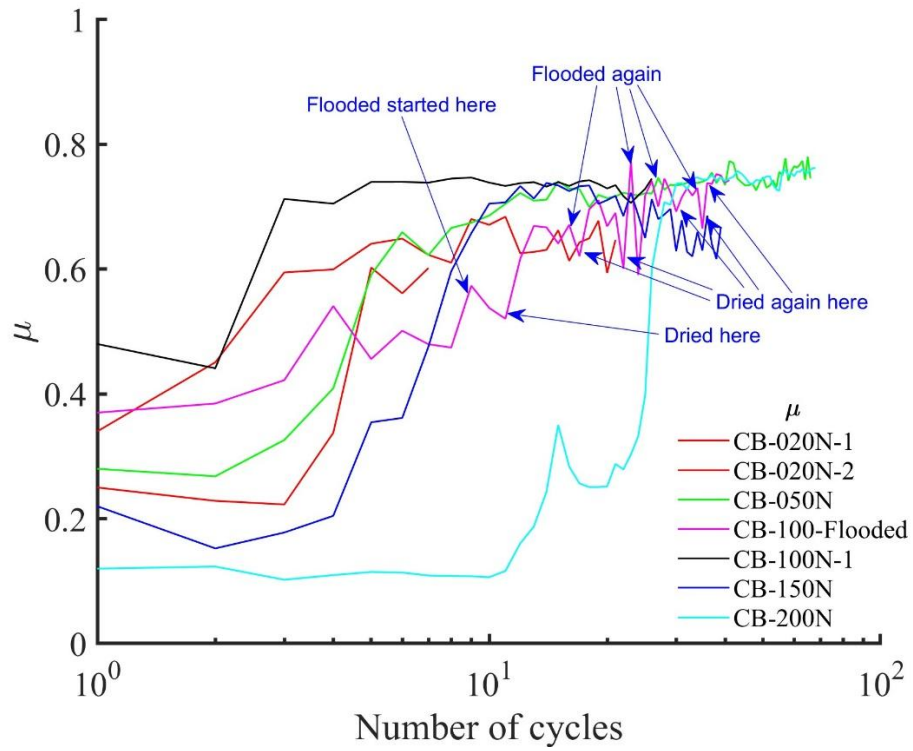
Figure 6.31 Coefficient of inter-particle friction (μ) with monotonic shear shown as the first cycle, under different levels of loads on Chinese granite ballasts.
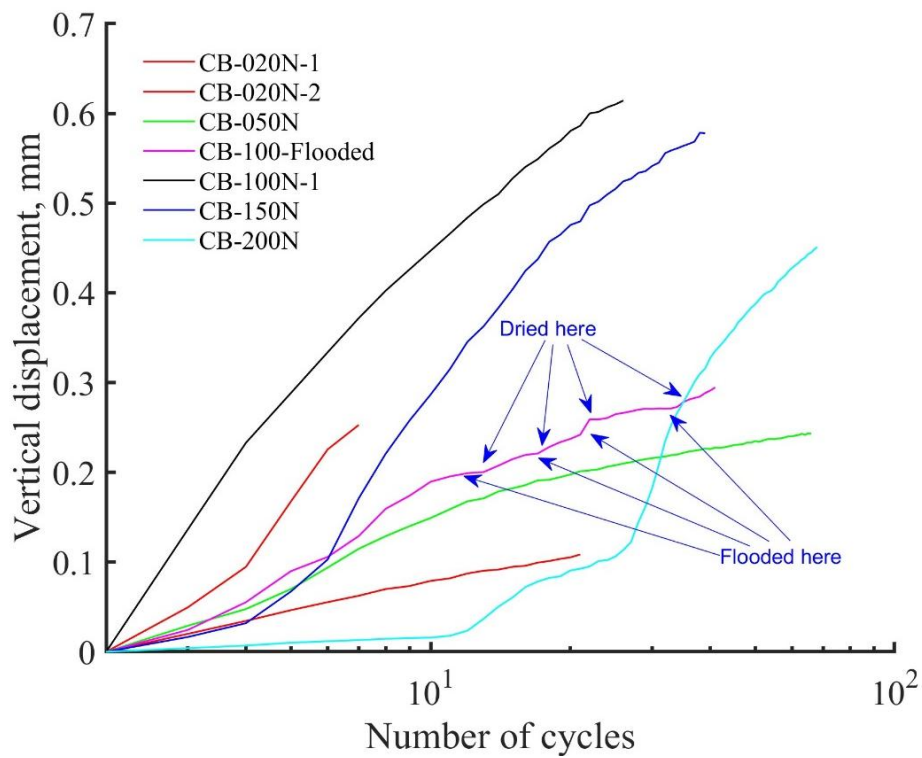
Figure 6.32 Vertical displacements under different levels of loads on Chinese granite ballasts.
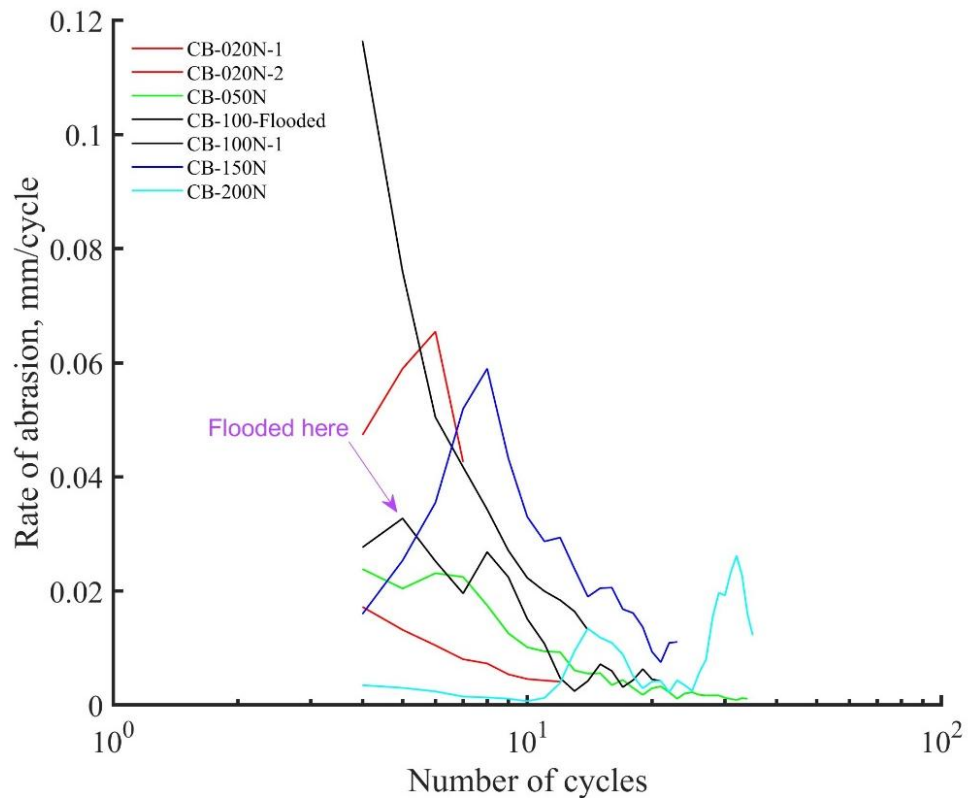
Figure 6.33 Rate of abrasion during cyclic shearing of Chinese granite.
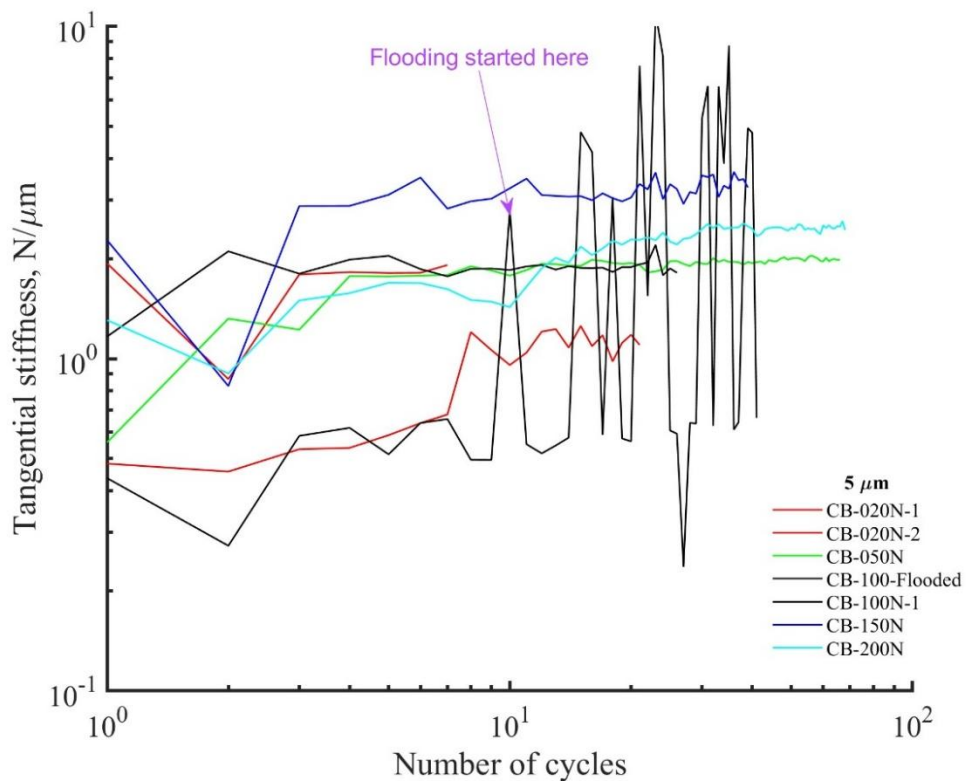
Figure 6.34 Cyclic stiffness of Chinese granite at 5 μ under different normal loadings.
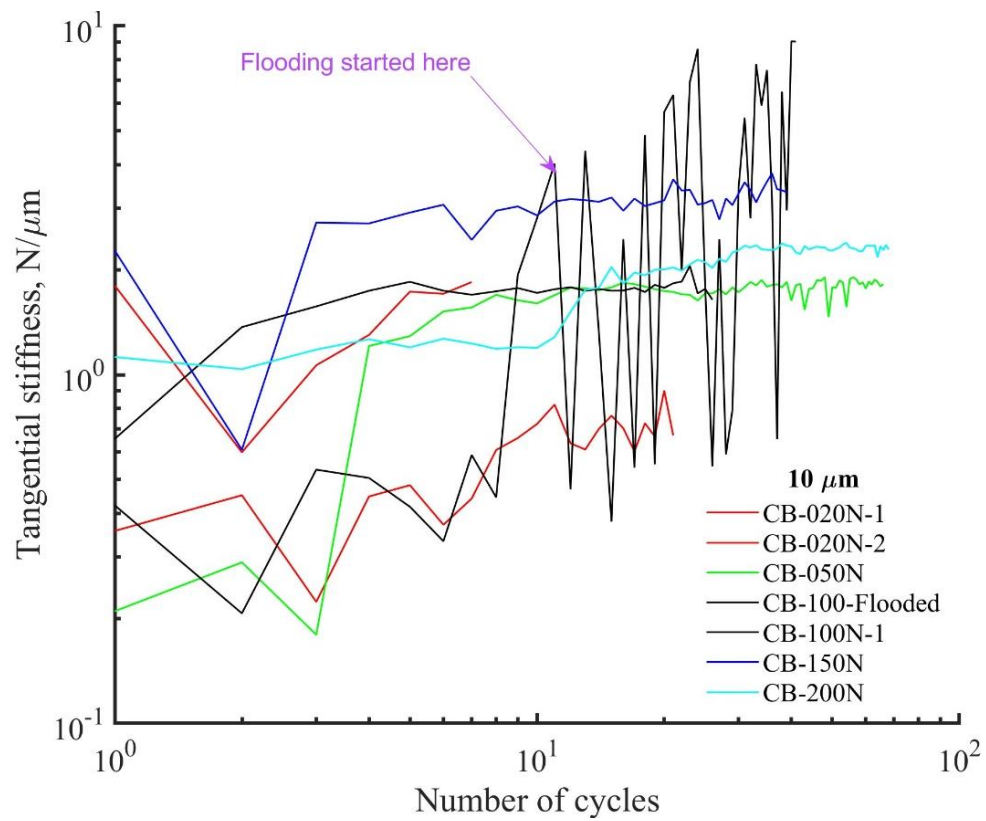
Figure 6.35 Cyclic stiffness of Chinese granite at 10 μ under different normal loading conditions.
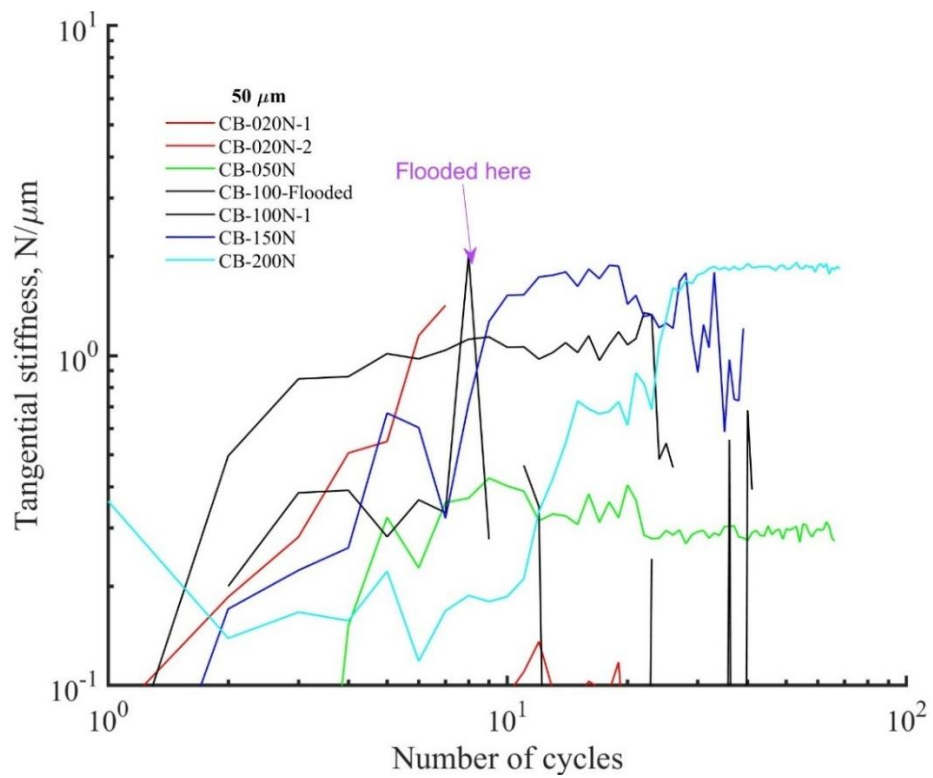
Figure 6.36 Cyclic stiffness of Chinese granite at 50 μ under different normal loading conditions.

(a) Before
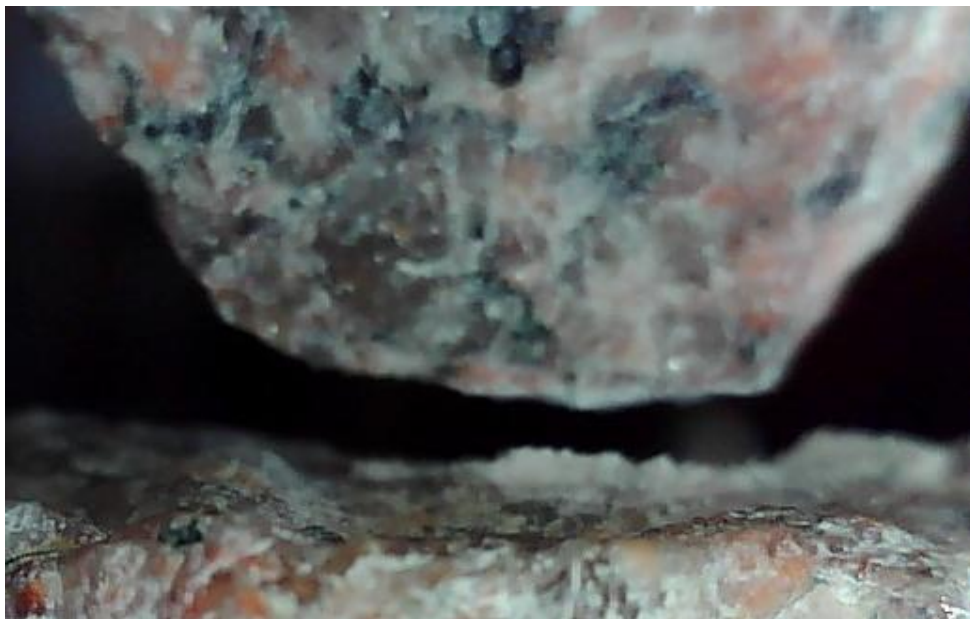
(b) After 90 cycles

Figure 6.37 During a cyclic loading test on fresh granite particles (angular-flat geometry), subjected to 90 cycles under 20 N normal load.
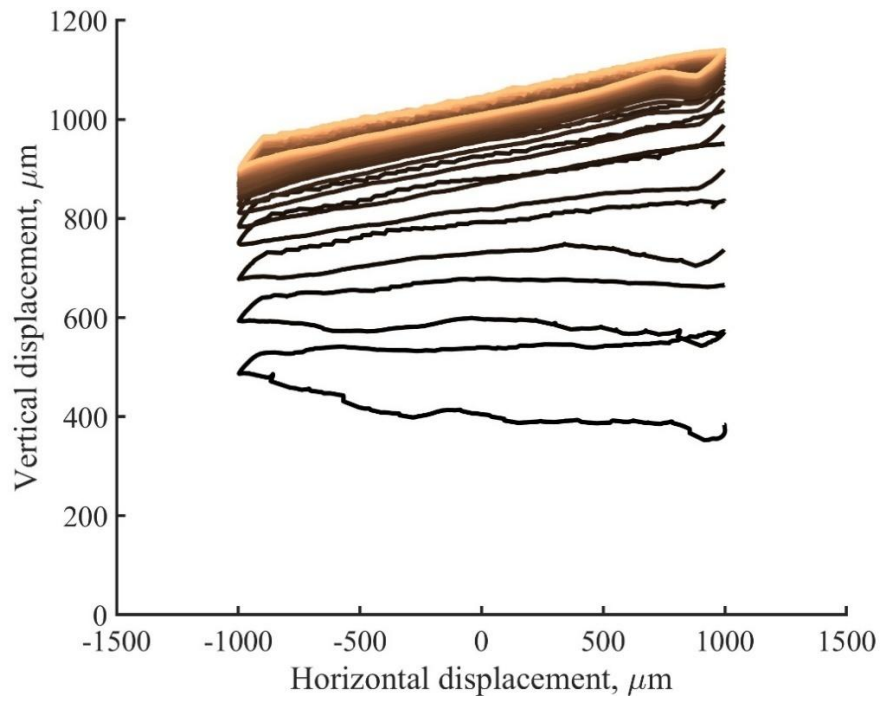
(a)
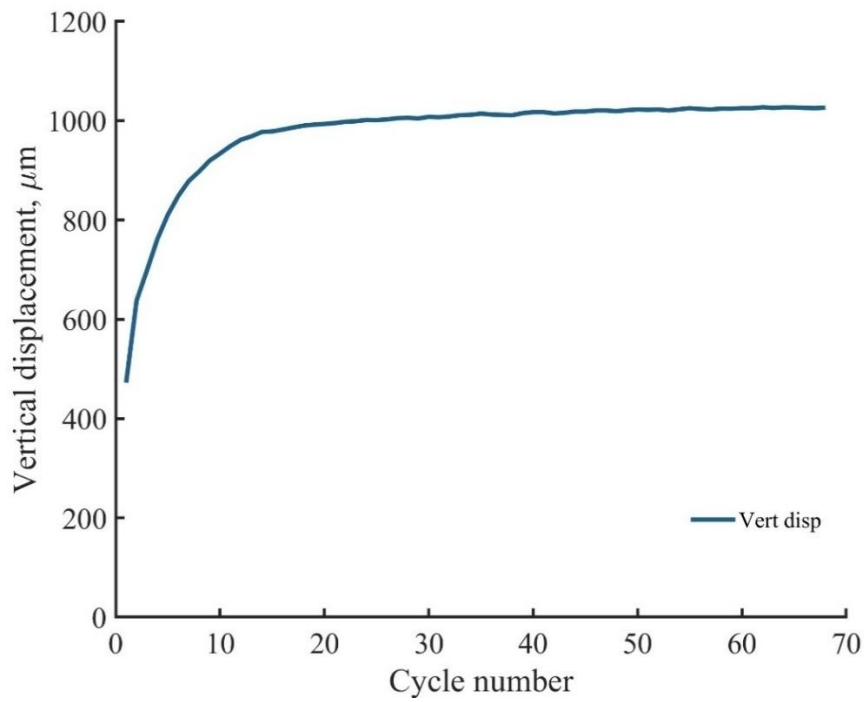
(b)

Figure 6.38 During a cyclic loading test on fresh granite, the intracycle spacing progressively shrinks (a), while the normal displacement conversely increases with more cycles (b).
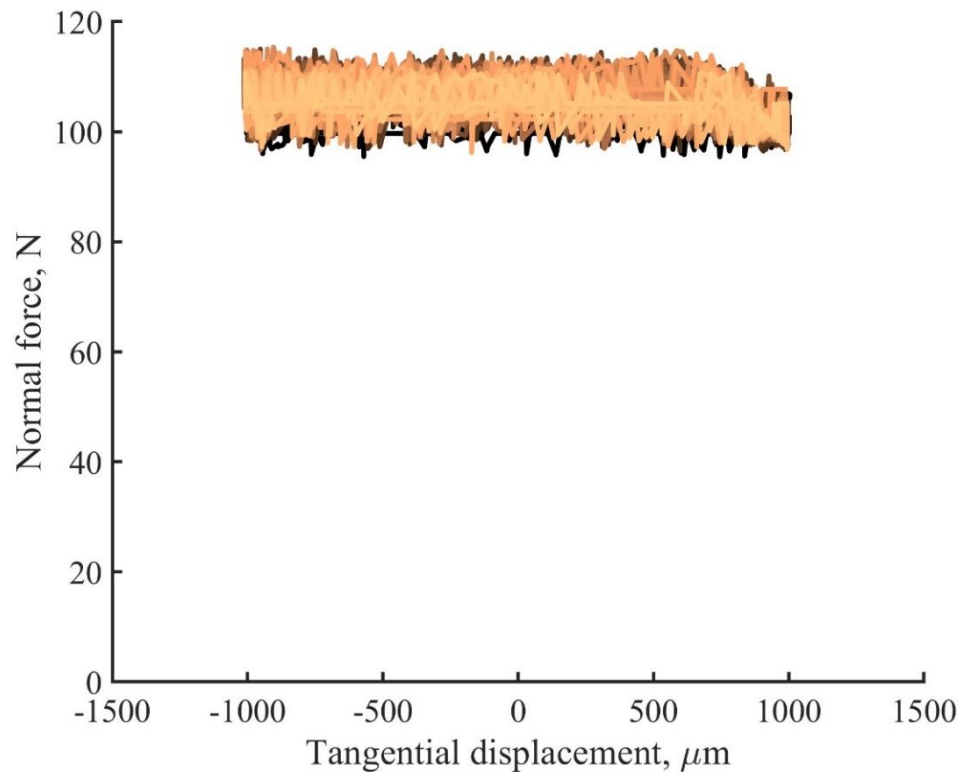
(a)
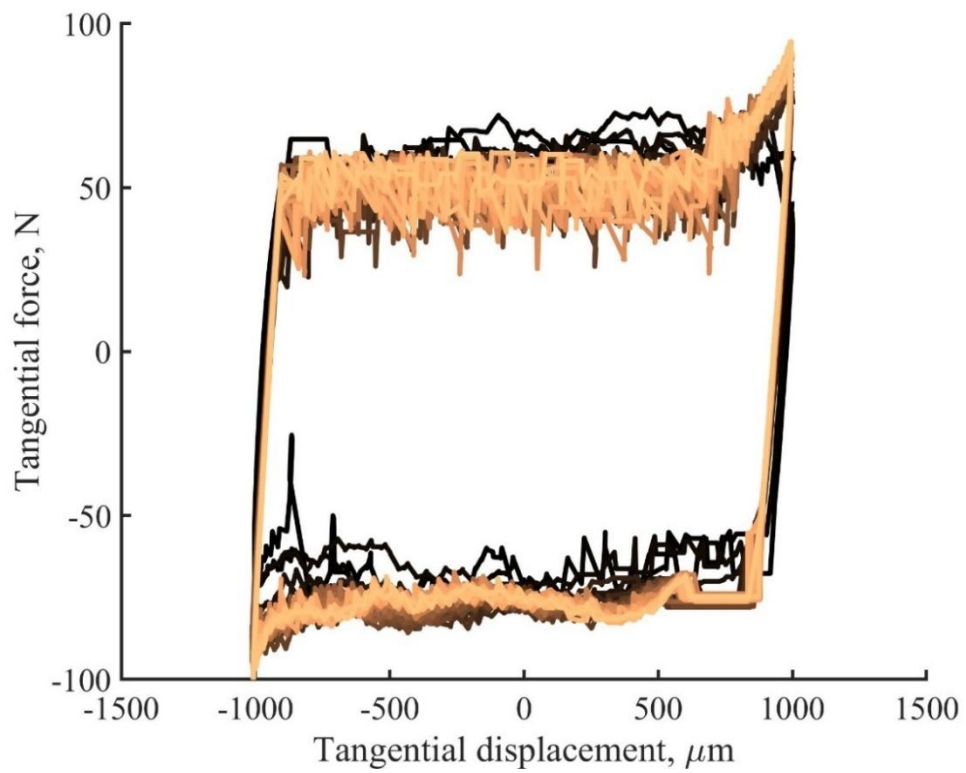
(b)

Figure 6.39 Normal force (a) and Tangential force (b) during cyclic shearing of fresh granite from the UK.

(a)

(b)
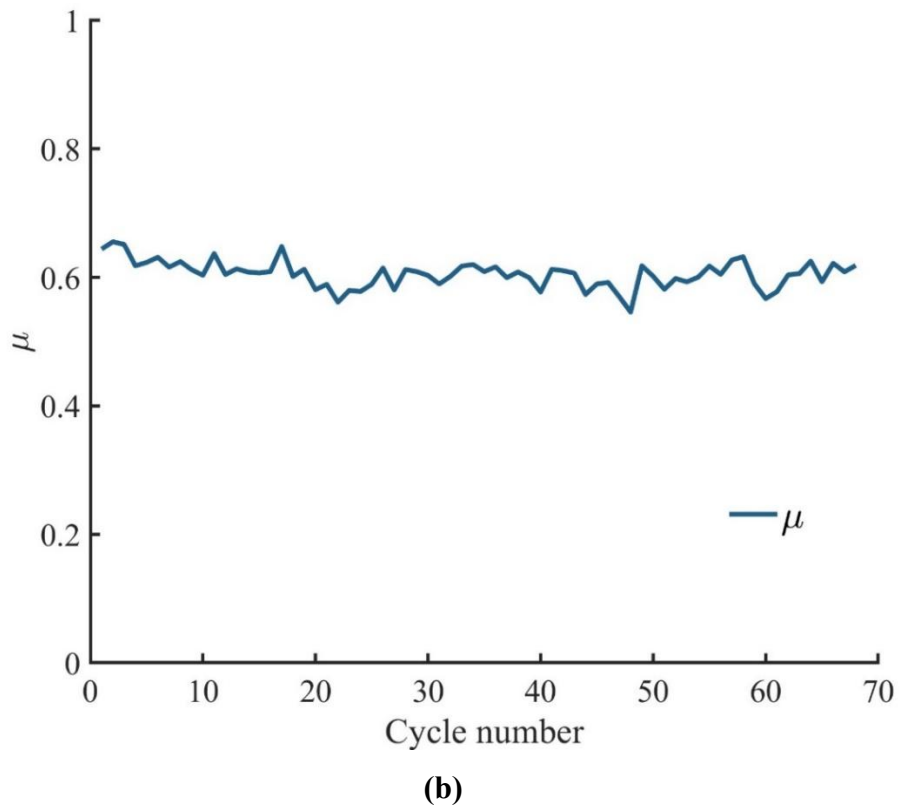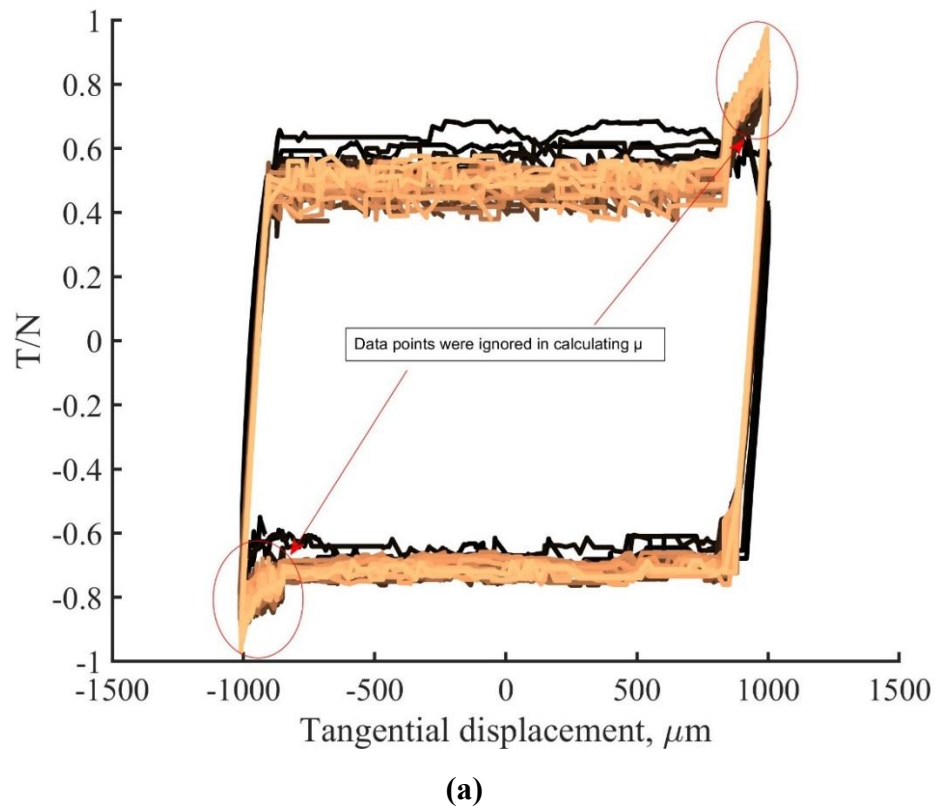
Figure 6.40 The force ratio of fresh granite ballasts (a) and the cyclic shearing μ (b) with

cycle numbers.
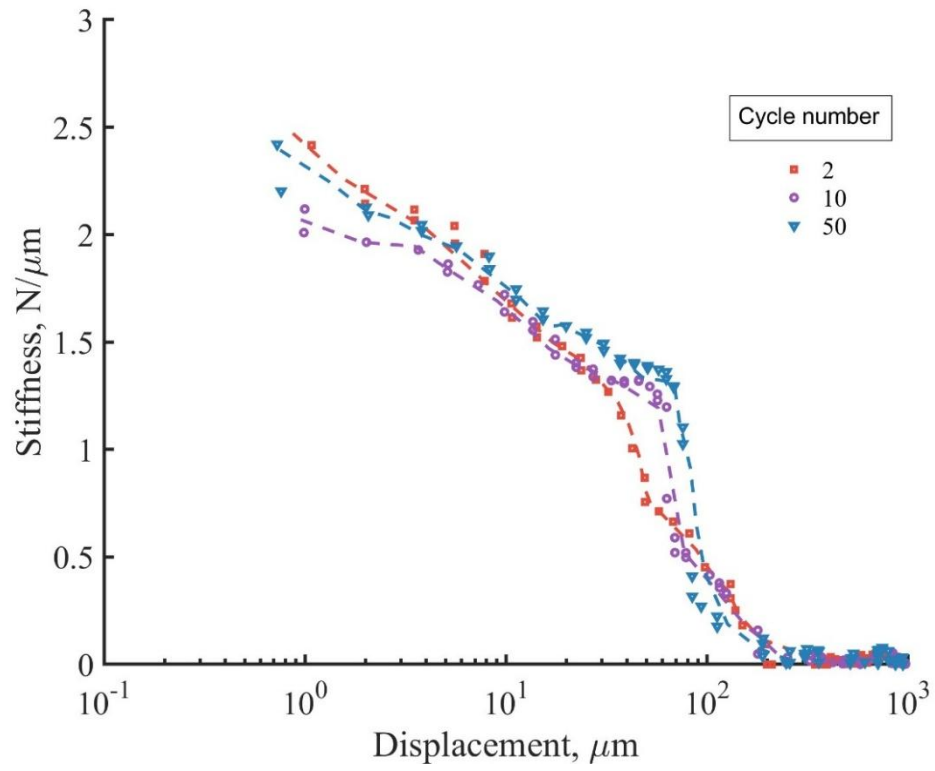
(a)
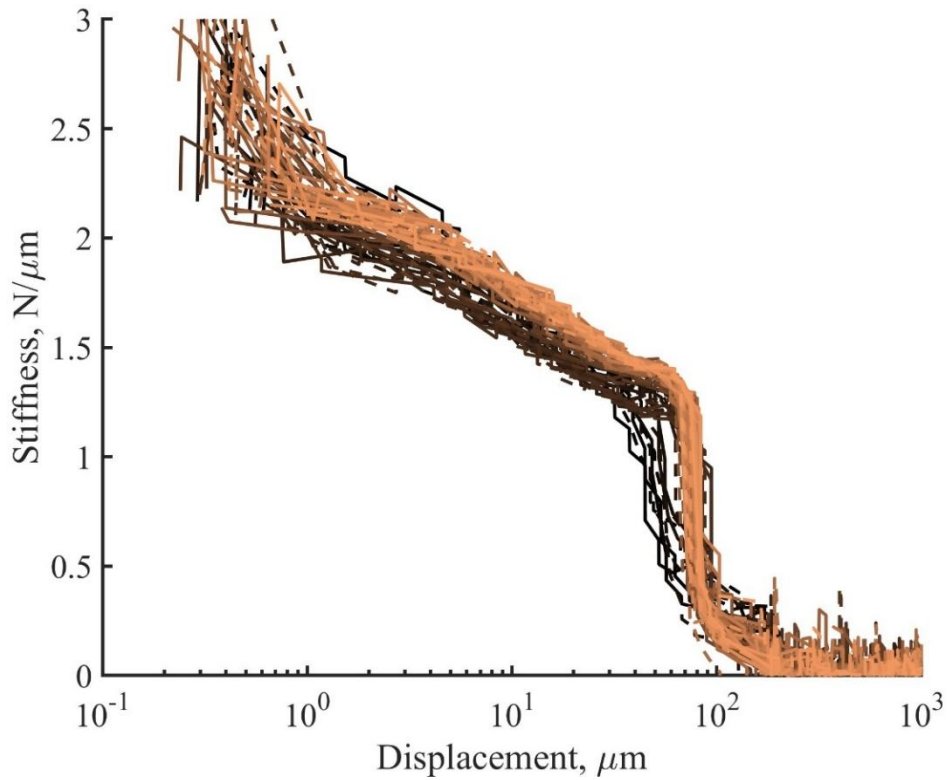
(b)

Figure 6.41 Fresh granite ballast stiffness in the forward direction: 2, 10, and 50 cycles (a)

and all cycles (b).

315
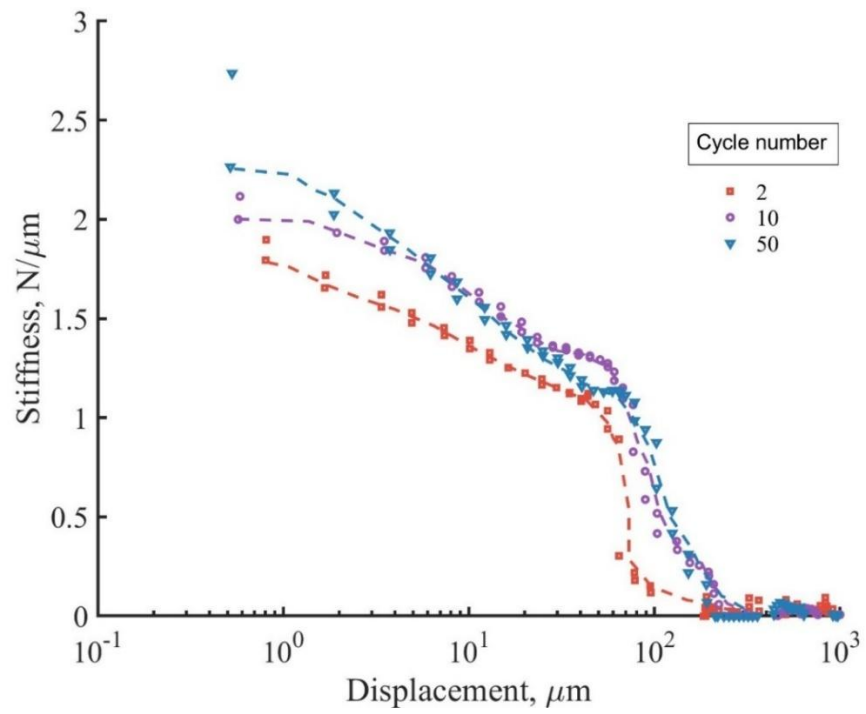
(a)
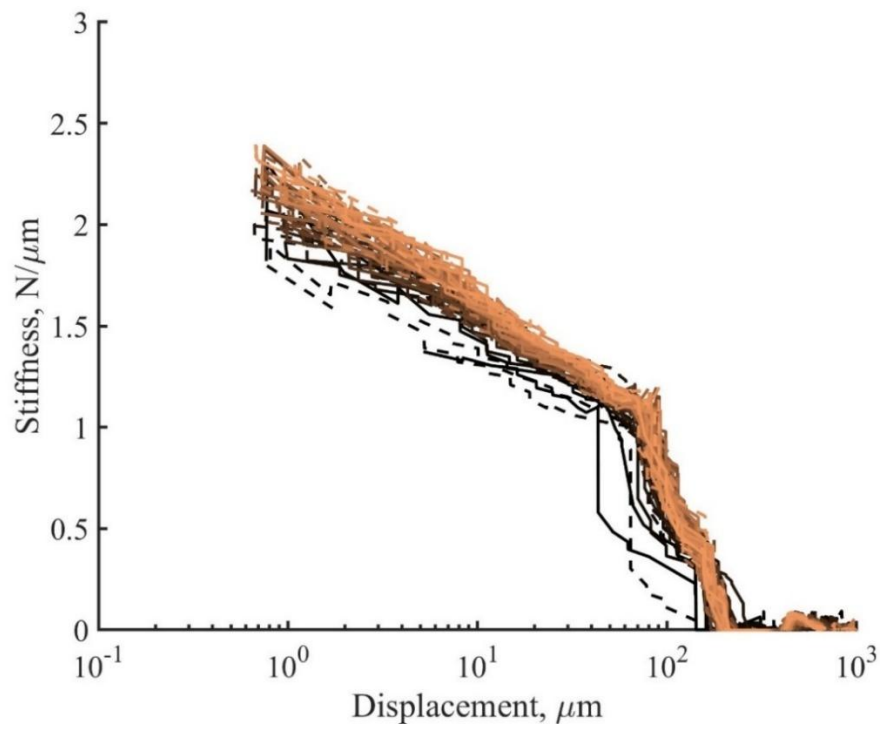
(b)

Figure 6.42 Fresh granite ballast stiffness in the backward direction: 2, 10, and 50 cycles
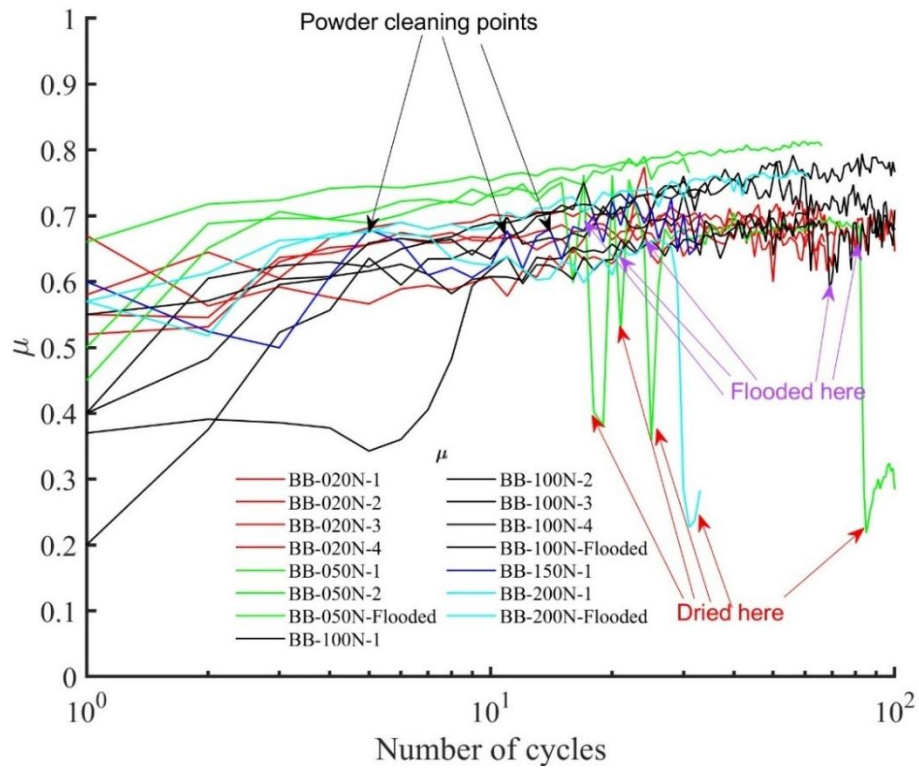
(a) and all cycles (b).
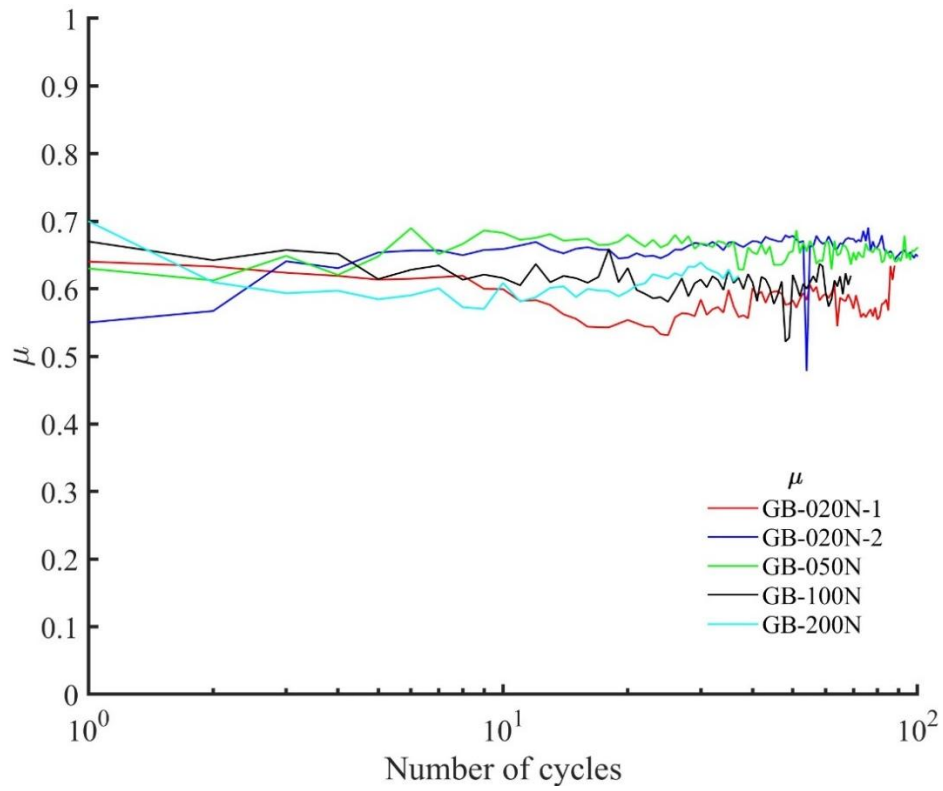
Figure 6.43 Coefficient of inter-particle friction (μ) with monotonic shear shown as the first cycle, under different levels of loads on fresh granite ballasts.
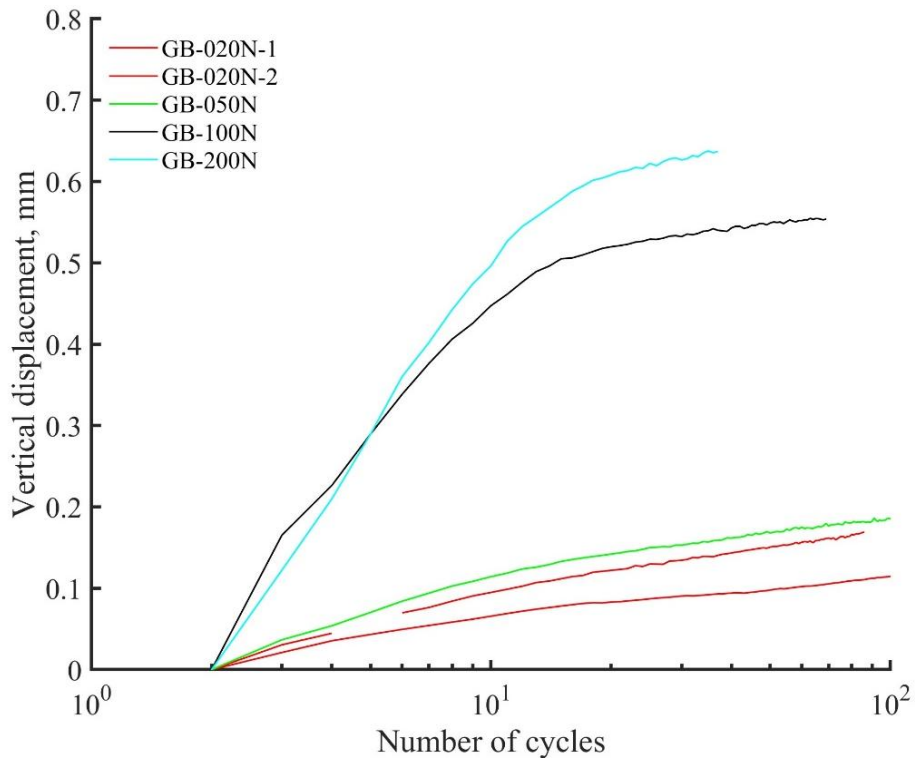
Figure 6.44 Vertical displacements under different levels of loads on fresh granite ballasts.
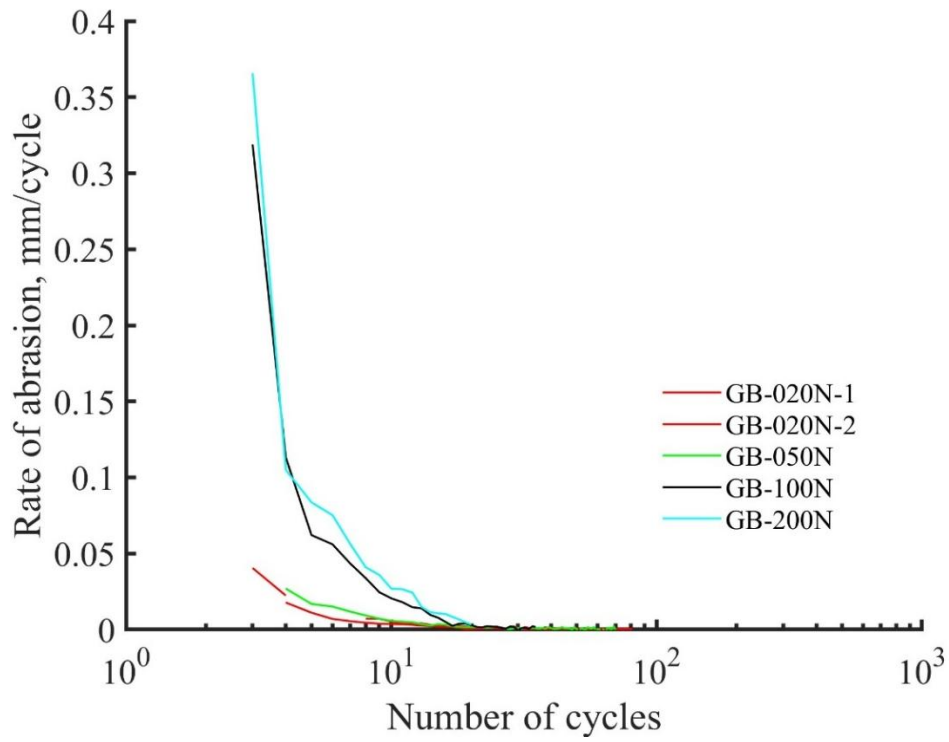
Figure 6.45 Rate of abrasion of fresh granite during cyclic shearing.
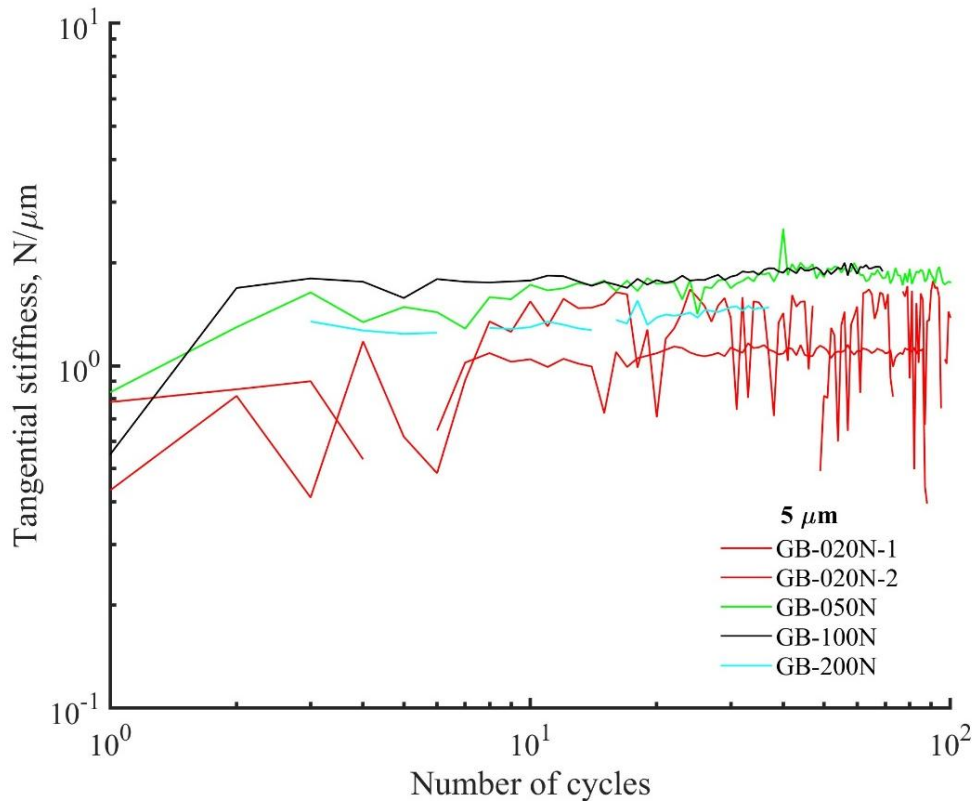
Figure 6.46 Cyclic stiffness of fresh granite at 5 μ under different normal load levels.
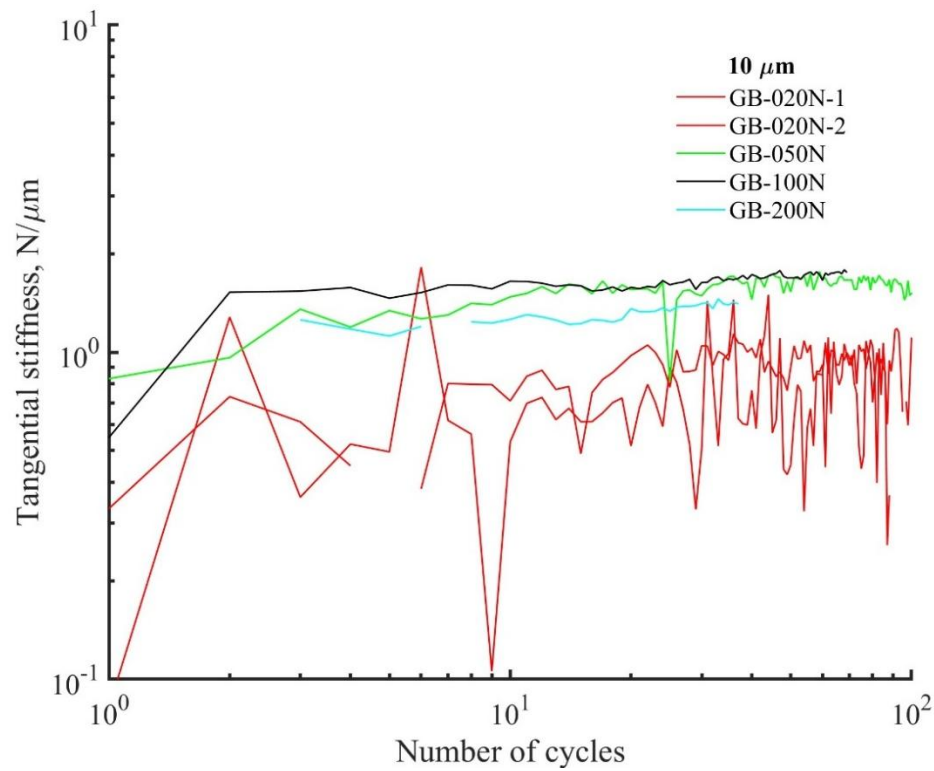
Figure 6.47 Cyclic stiffness of fresh granite at 10 μ under different normal loading
conditions.
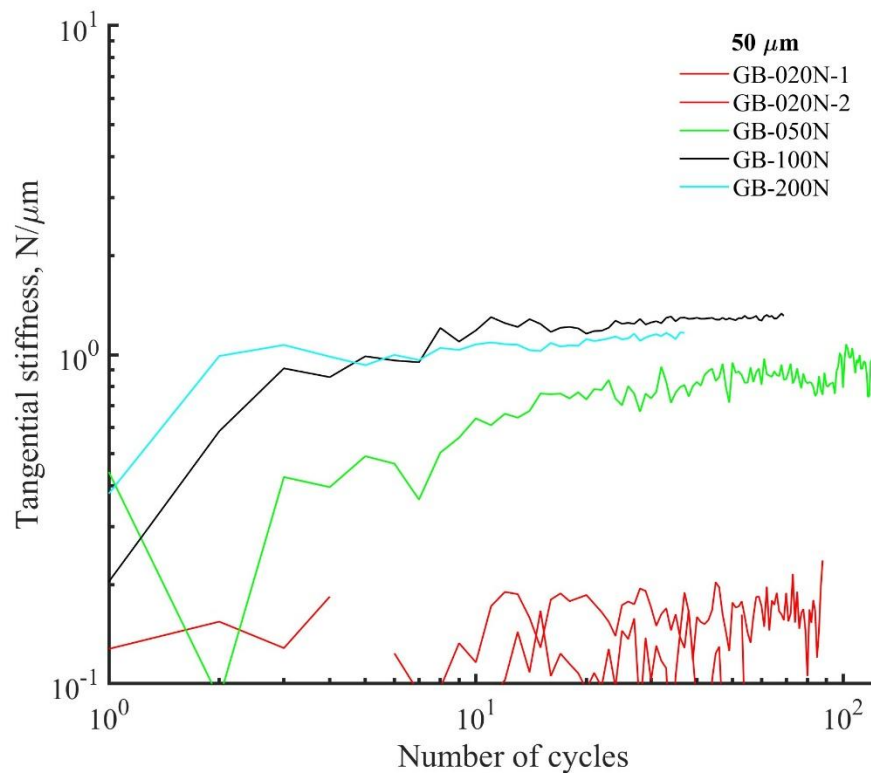
Figure 6.48 Cyclic stiffness of fresh granite at 50 μ under different normal loading
conditions.

(a) Before

(b) After 150 cycles

Figure 6.49 Used granite particles with an angular-flat contact geometry, before and after a test involving 150 cycles under a normal load of 100 N.
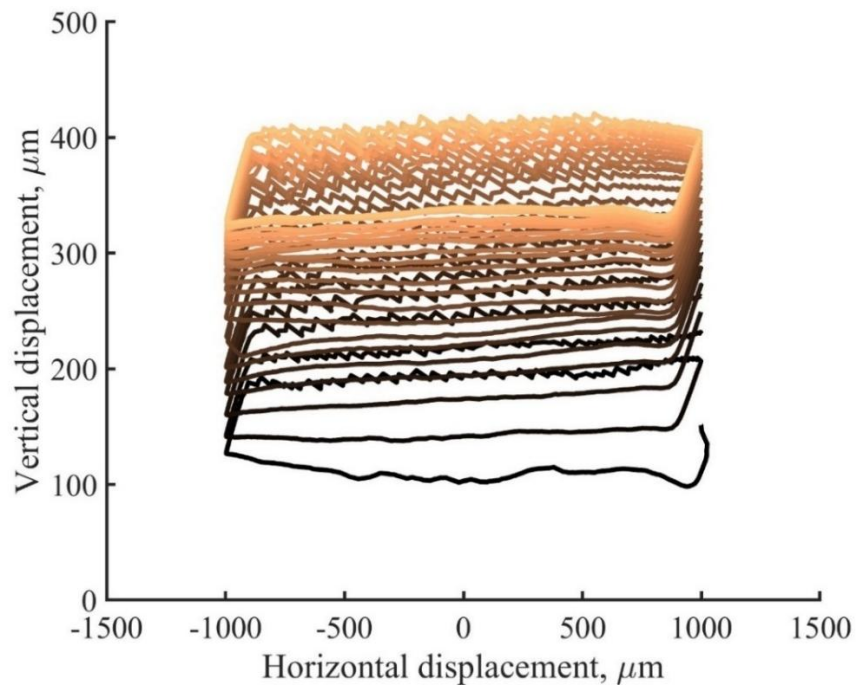
(a)
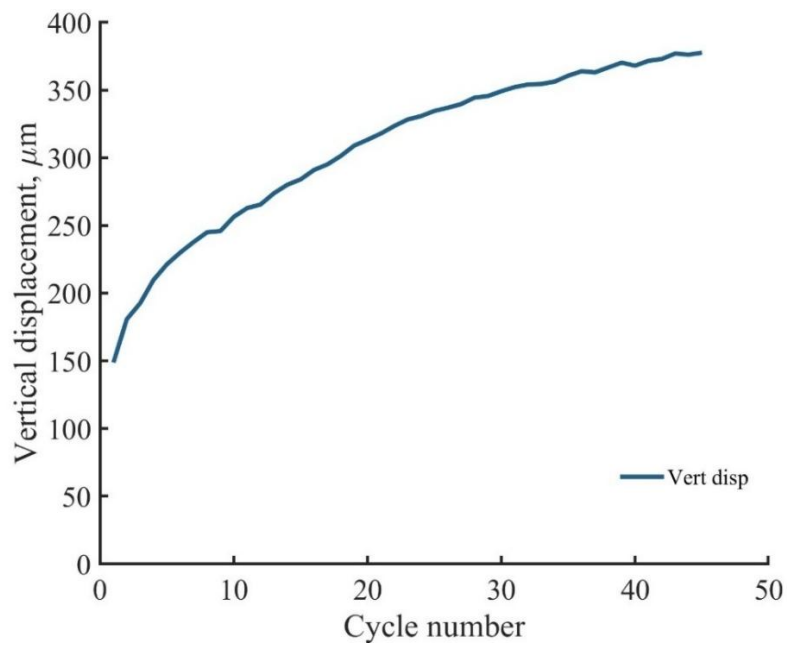
(b)

Figure 6.50 Initially, the inter-cycle spacing of used granite is greater, progressively diminishing with cycles until reaching minimal levels (a), as the cycles increase the normal displacement increases (b).

(a)

(b)
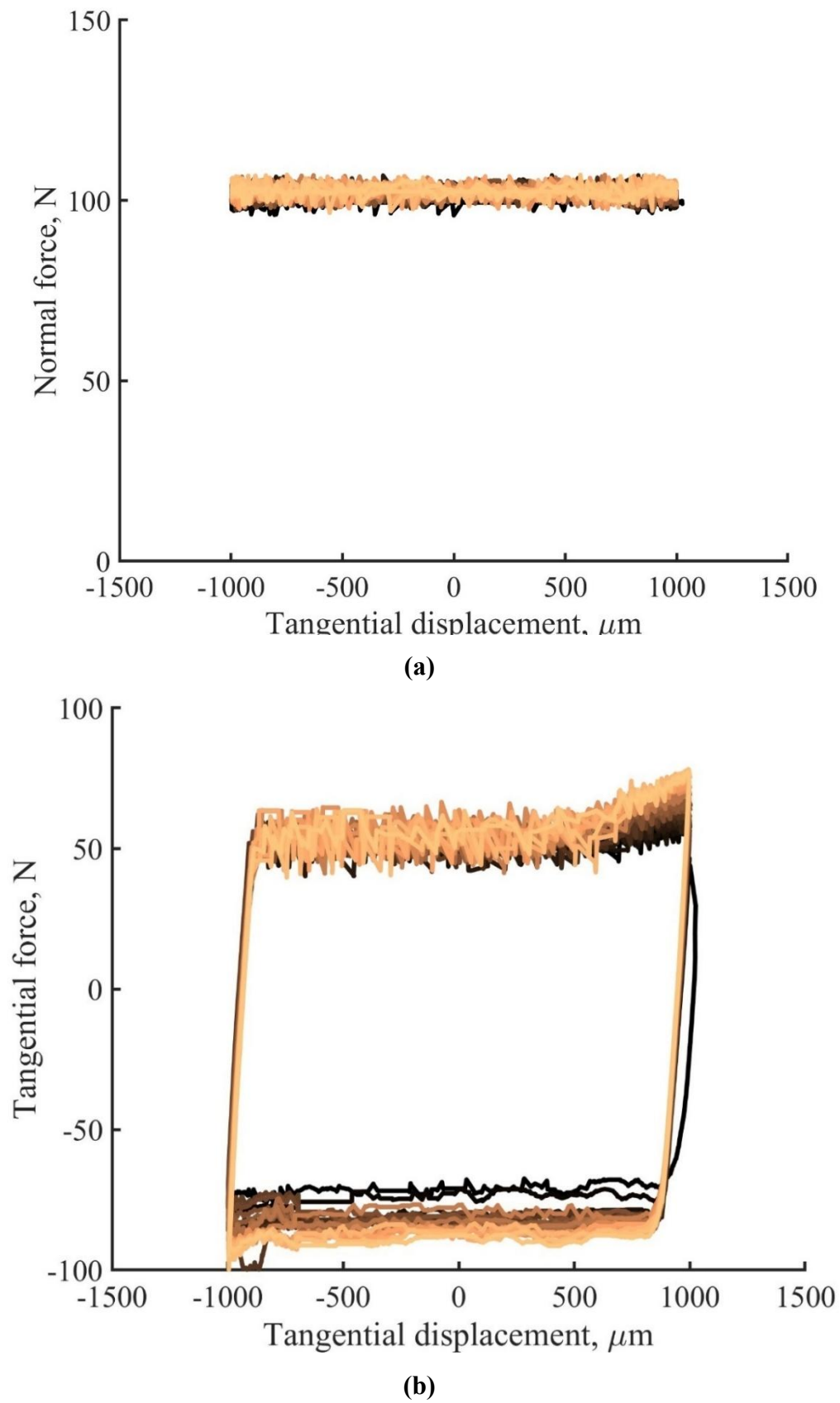
Figure 6.51 Normal force (a) and Tangential force (b) of used granite during cyclic shearing.

(a)

(b)
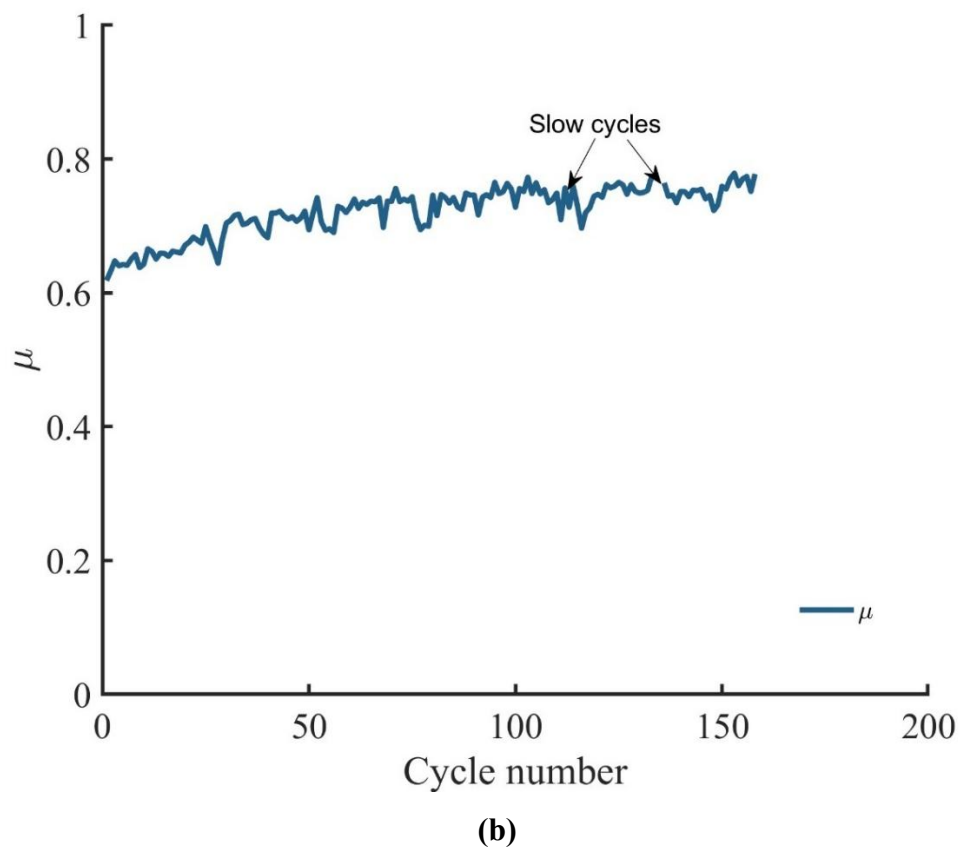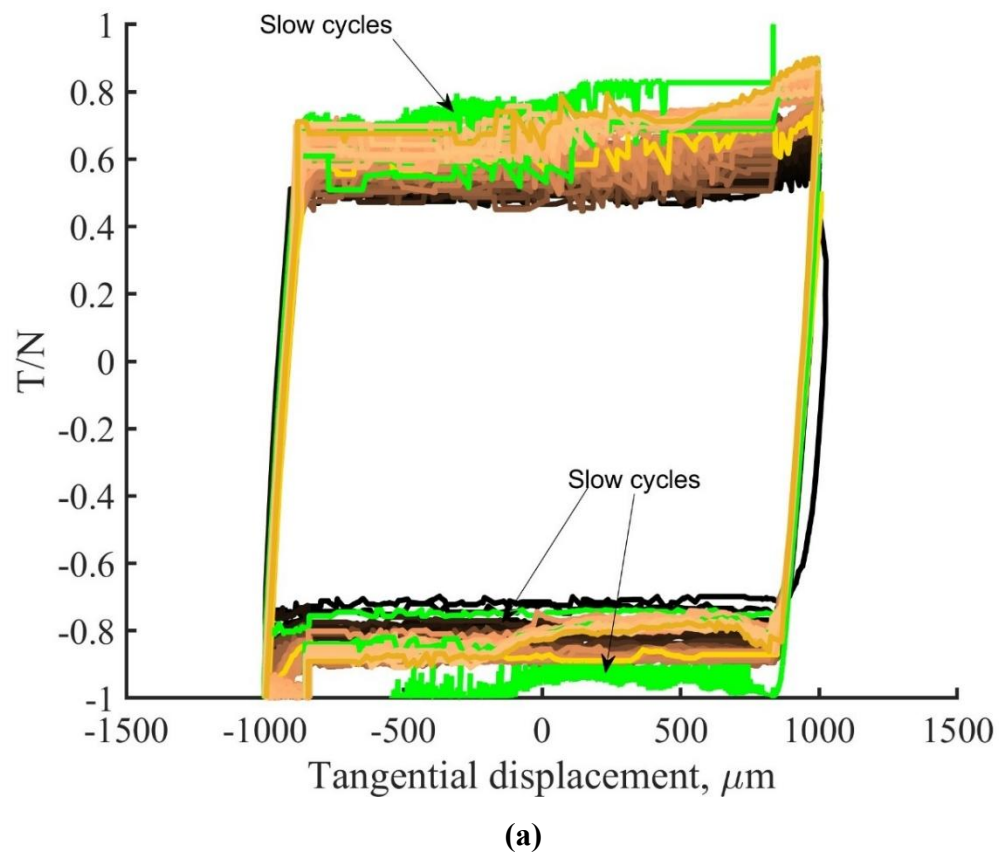
Figure 6.52 Force ratio (a) and μ (b) with cycle number of used granite.

(a)

(b)
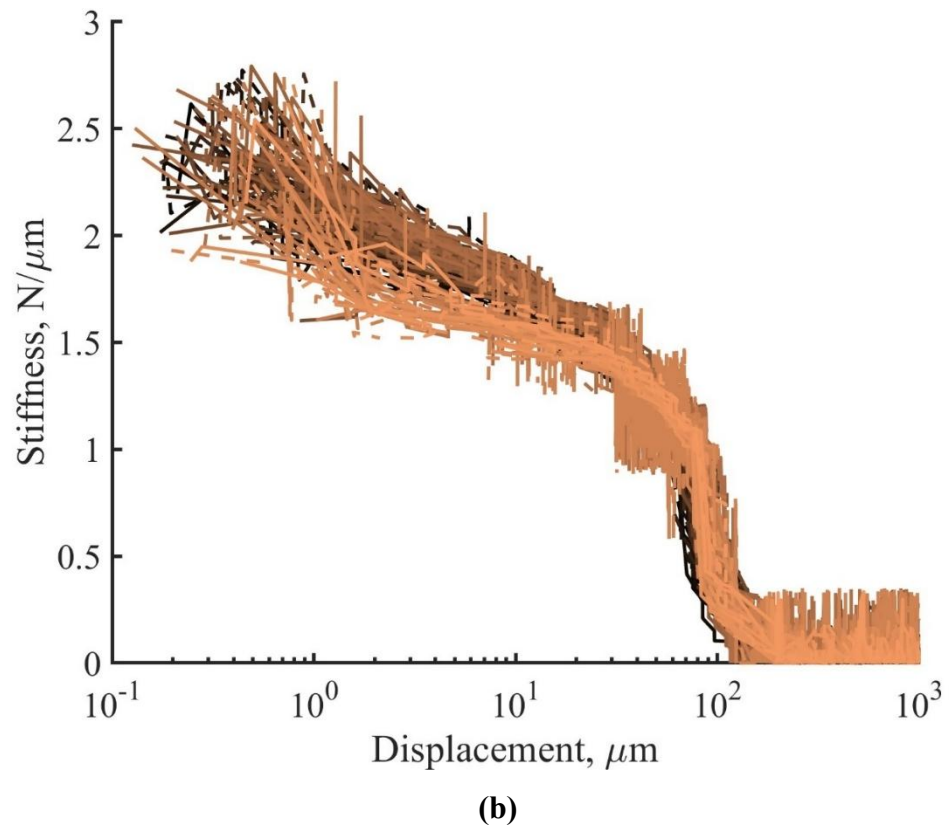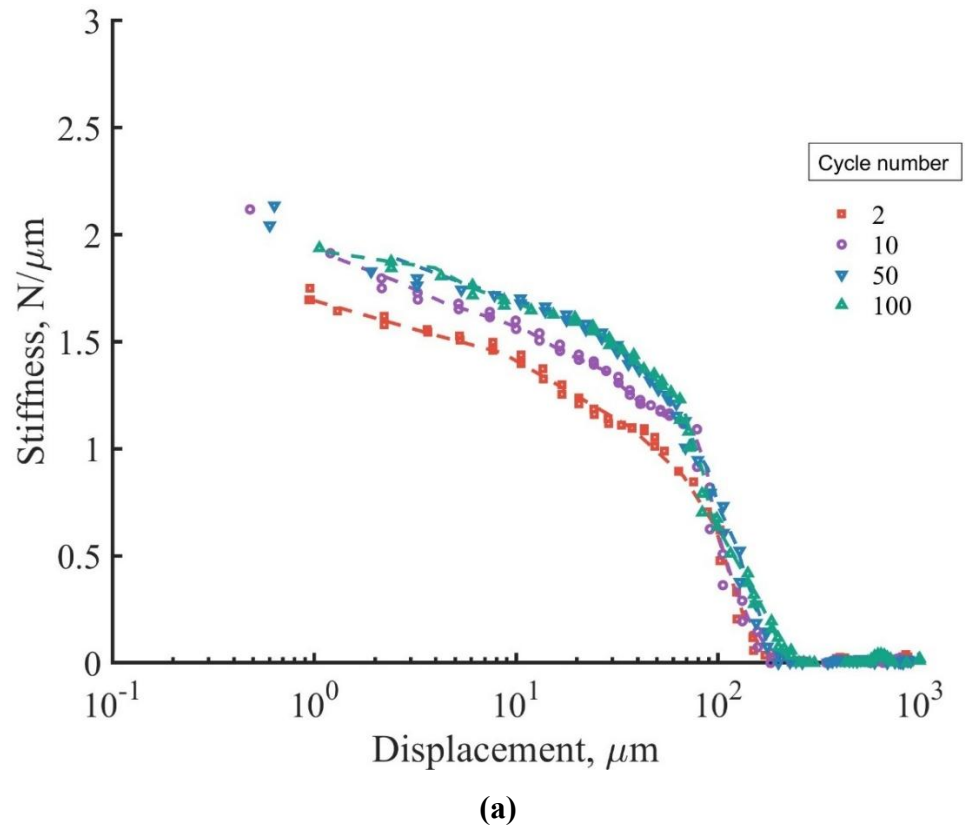
Figure 6.53 Used granite stiffness in the forward direction of a few cycles (a) and all cycles (b).
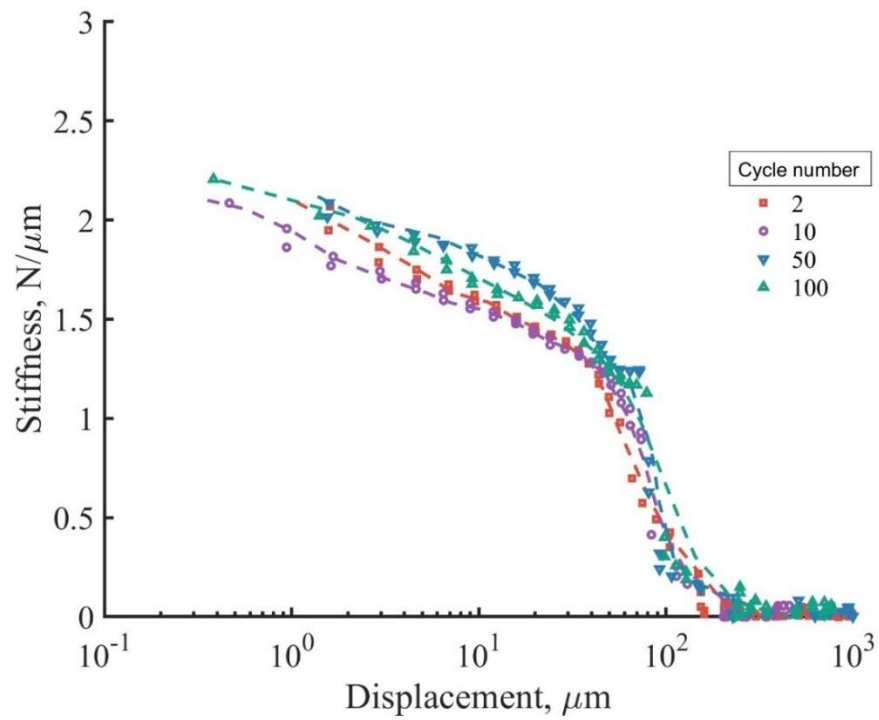
(a)
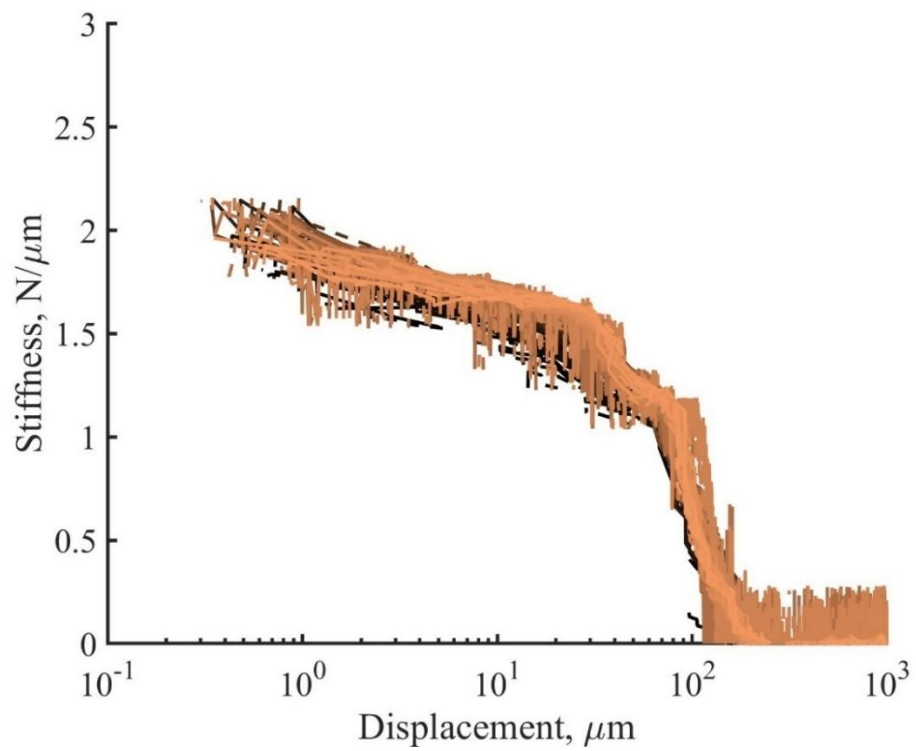
(b)

Figure 6.54 Used granite stiffness in the backward direction of a few cycles (a) and all cycles (b).
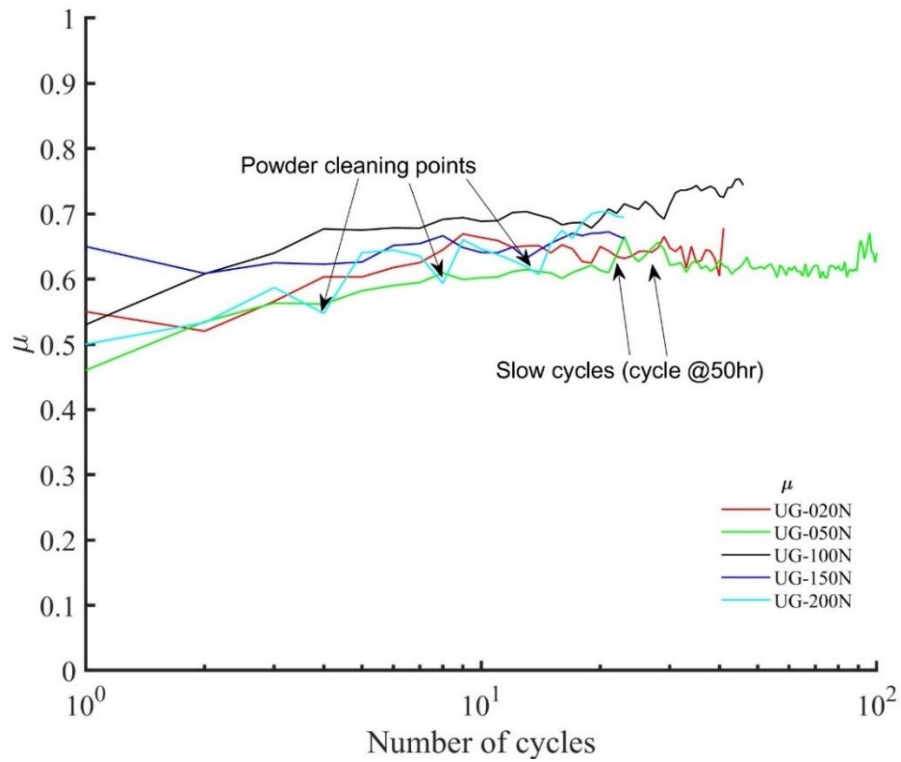
Figure 6.55 Coefficient of inter-particle friction (μ) with monotonic shear shown as first cycle, under different levels of loads on used granite ballasts.
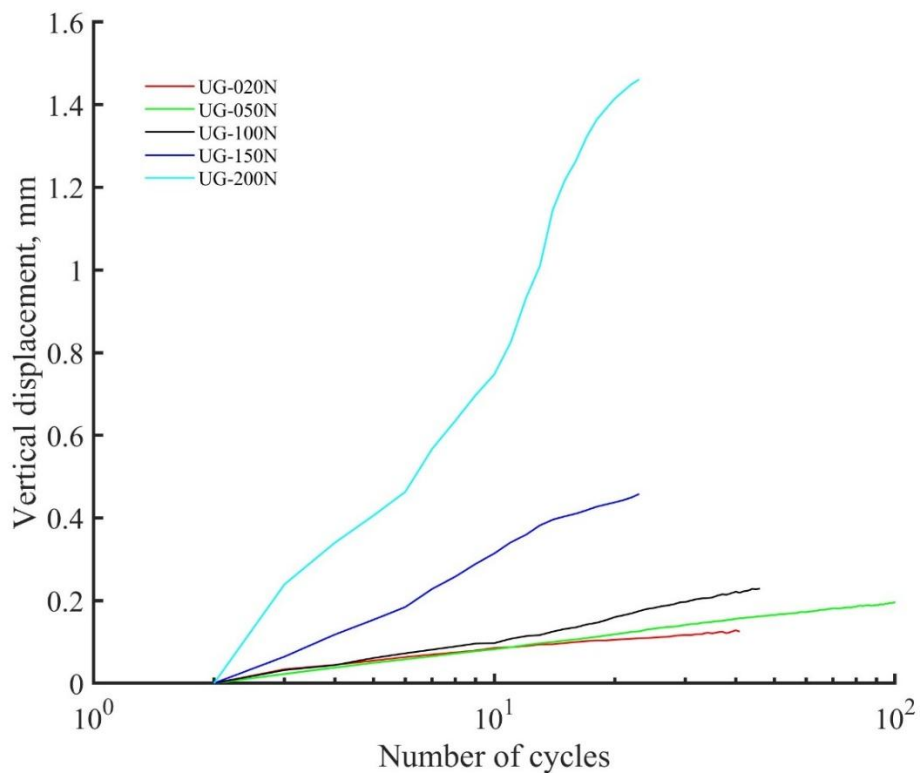
Figure 6.56 Vertical displacements under different levels of loads on used granite ballasts.
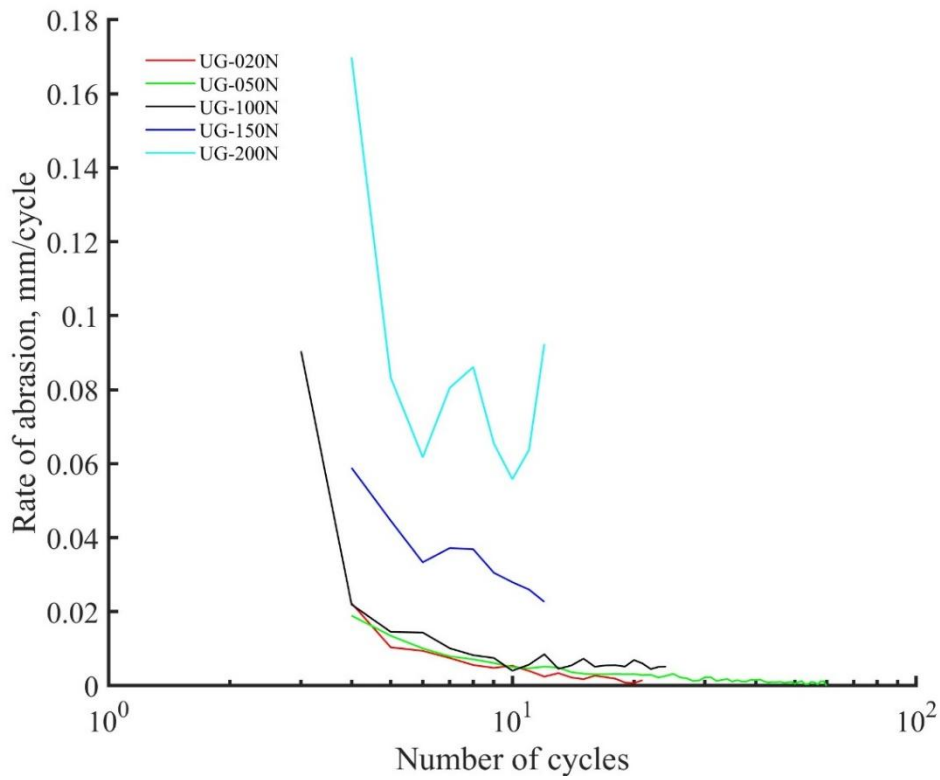
Figure 6.57 The rate of abrasion of used granite during cyclic shearing.
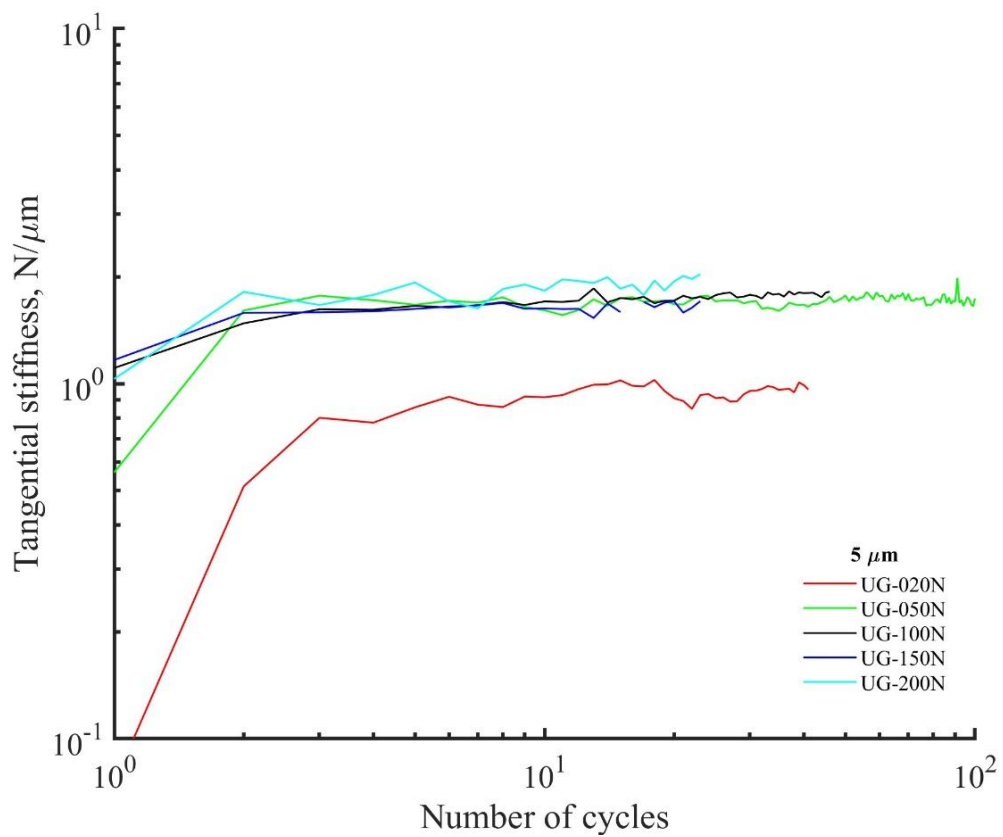
Figure 6.58 Cyclic stiffness of used granite at 5 μ under different normal loading conditions.
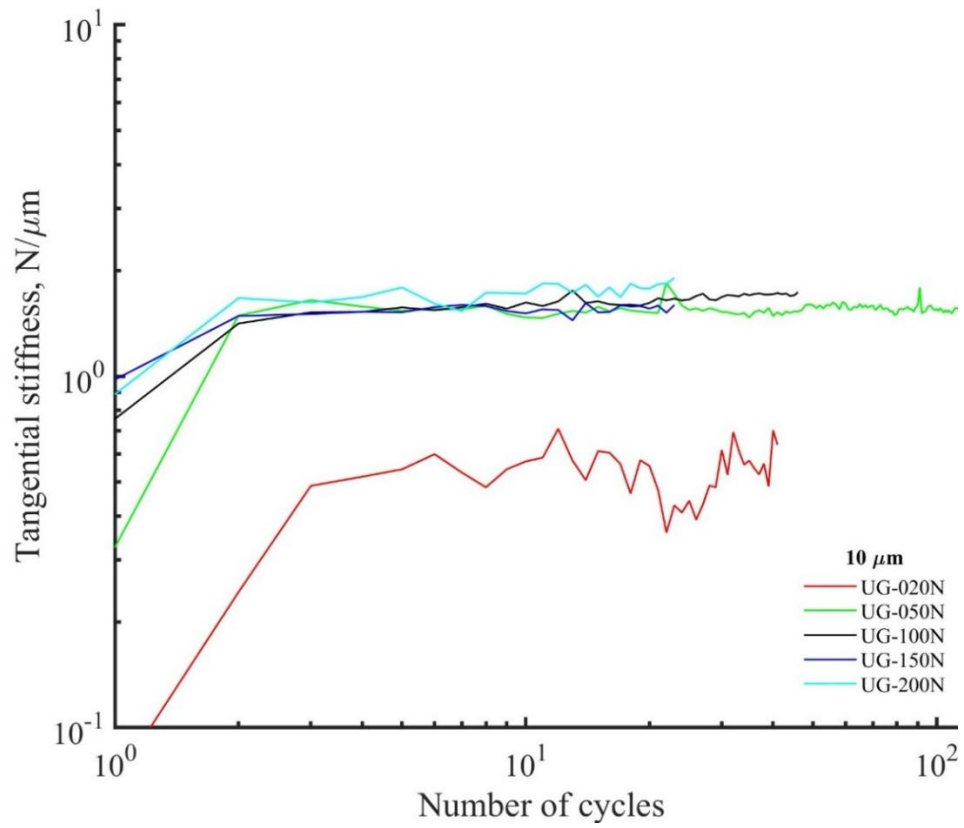
Figure 6.59 Cyclic stiffness of used granite at 10 μ under different normal loading conditions.
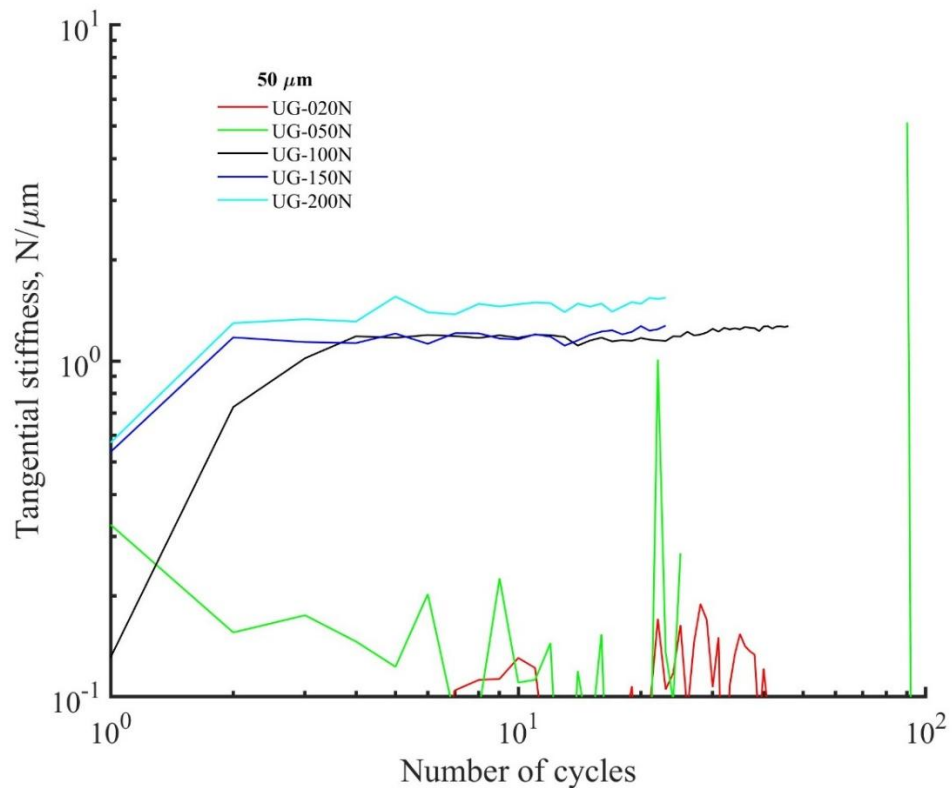
Figure 6.60 Cyclic stiffness of used granite at 50 μ under different normal loading conditions.
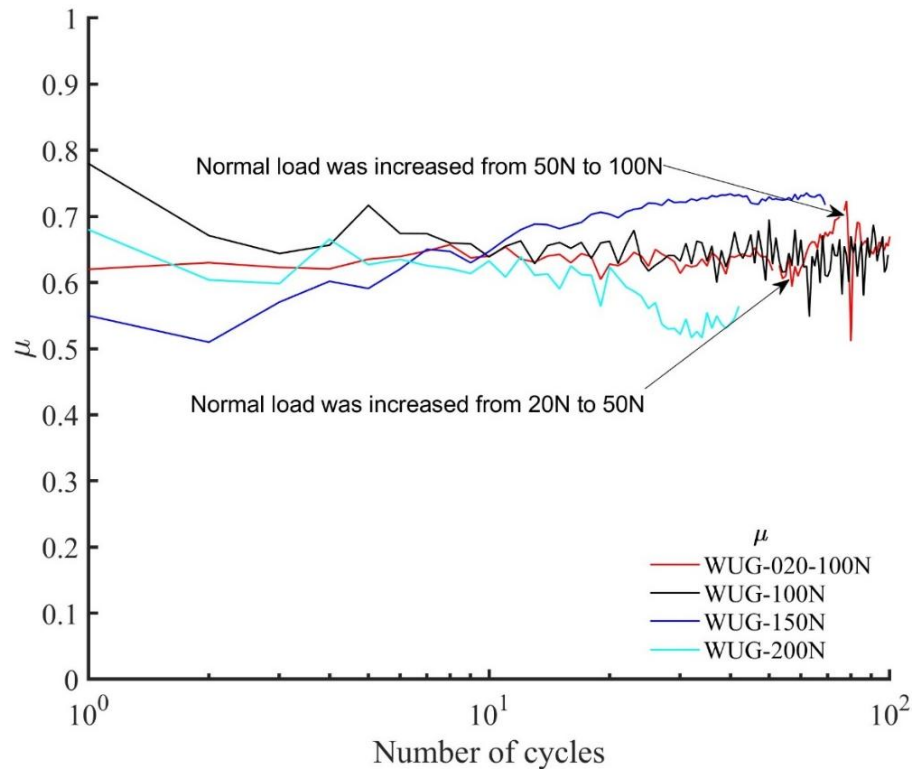
Figure 6.61 The coefficient of inter-particle friction (μ) of washed used granite ballasts with monotonic shear displayed as the first cycle, under various loads.
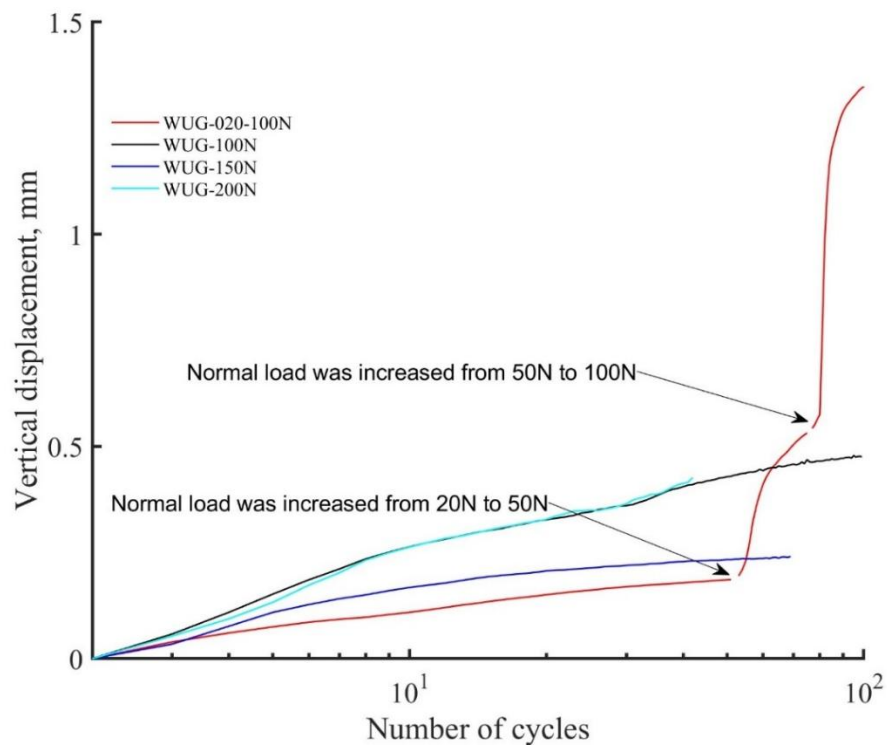
Figure 6.62 Vertical displacements of used washed granite ballasts under various loads.
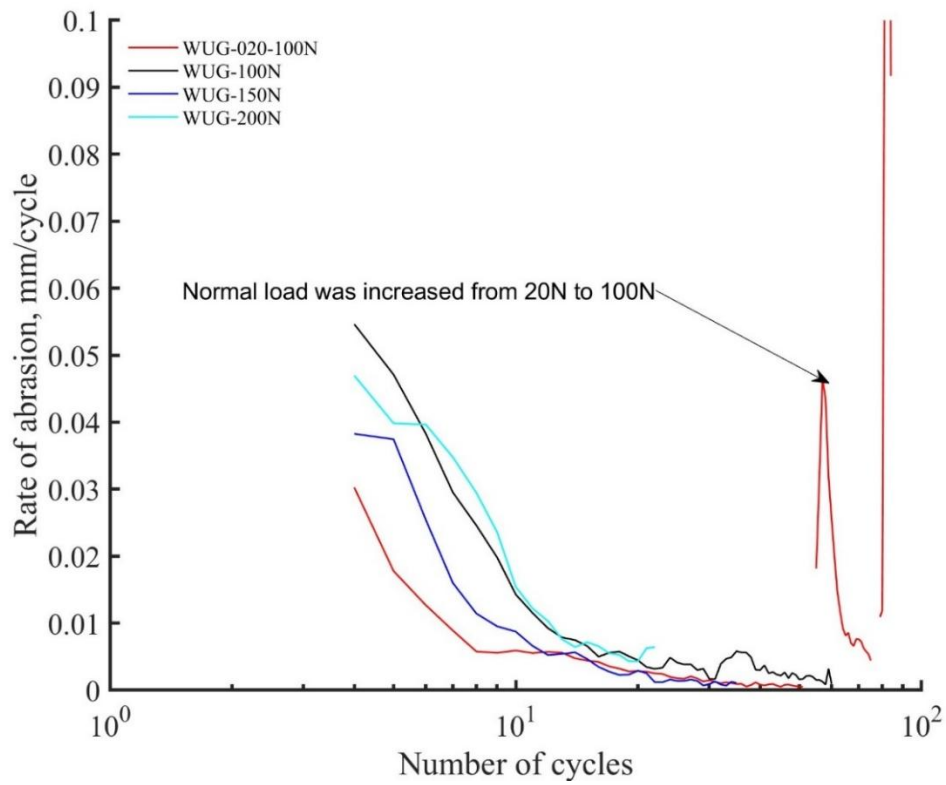
Figure 6.63 Rate of abrasion of washed used granite during cyclic shearing.
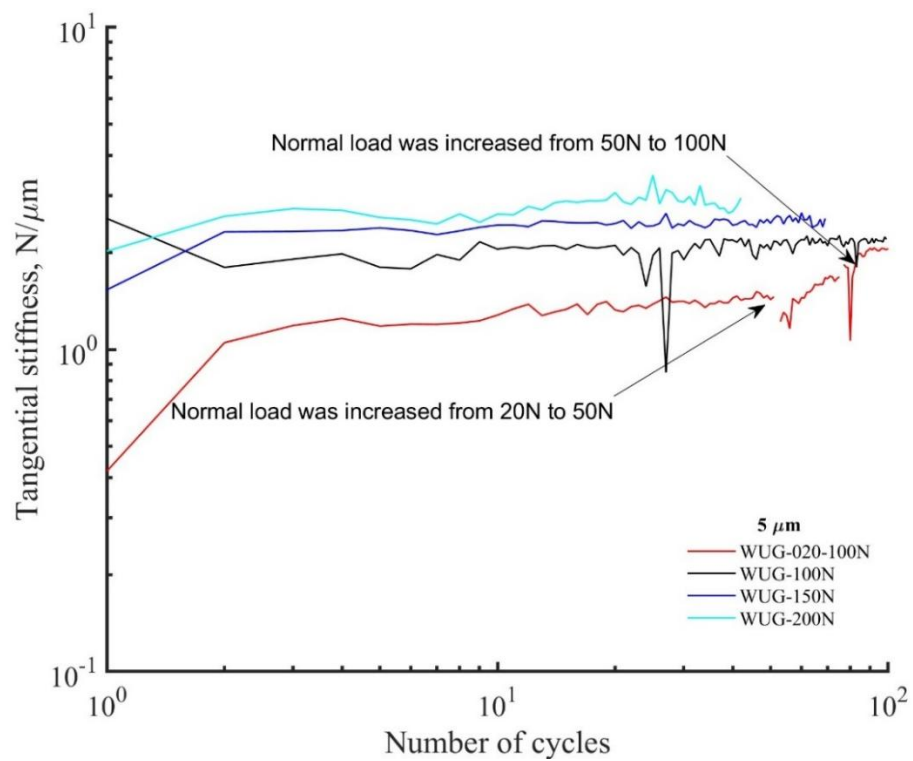
Figure 6.64 The tangential stiffness of washed granite was at 10 μm tangential displacement under different loadings.
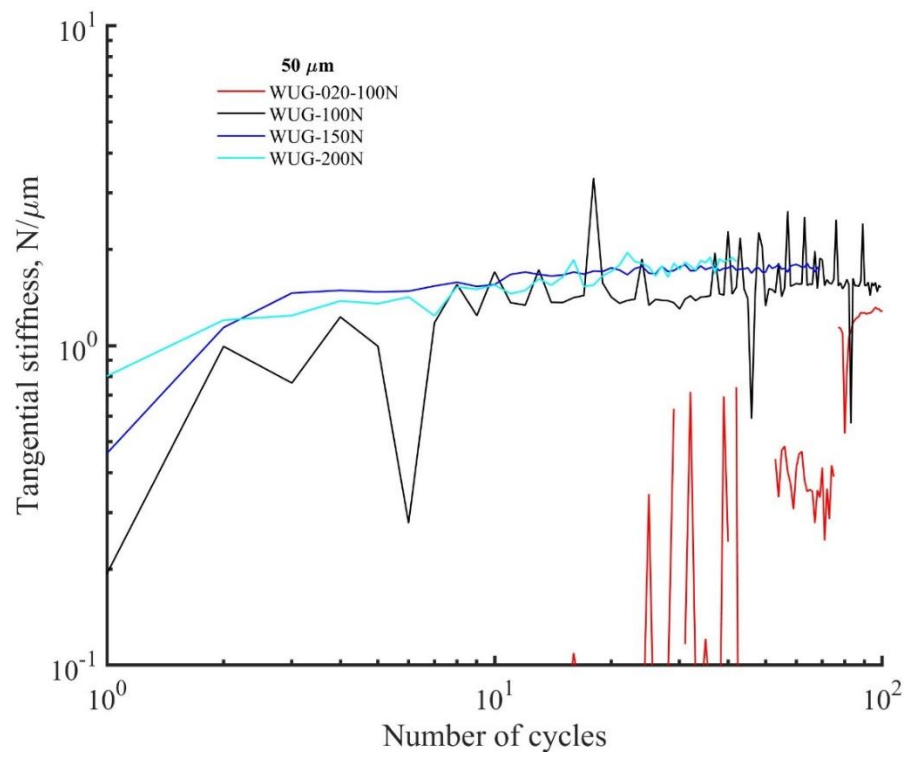
Fig. 6.65 Washed used granite's cyclic stiffness at 50 µm, under different loadings.

7. Comparison of the railway's ballasts

This chapter provides a comprehensive comparison of the mechanical behaviour of the ballast materials tested, including Chinese granite, basalt, andesite, fresh granite, used granite, and washed-used granite. Highlighting the influence of mineralogical composition, particle condition, and loading history on their micro-mechanical response. This comparative analysis offers new insights that broaden the current understanding of ballast behaviour, which has not been systematically examined across such a diverse range of materials in previous research.

The first section presents a summary of behaviours under varying monotonic normal load conditions. The analysis examines stiffness, deformation, and stability across low, medium, and high load ranges.

The second section presents a comparison of the different types of railway ballast under monotonic shearing, focusing on the coefficient of friction and monotonic tangential stiffness across varying load levels.

The final section of the chapter examines cyclic shearing behaviour for all ballast types under different load conditions. This comparison considers the ballast coefficient, vertical displacement, rate of abrasion, and tangential stiffness, under different normal loading conditions.

7.1 Comparison of different railway ballasts under monotonic normal load levels

The comparison of normal loading behaviour is discussed here under different load levels.

Behaviour under low loads (20N)

Fig. 7.1 illustrates the comparison of different ballasts under a normal load of 20N. At low loads (under 2N), the mechanical response of ballast materials is primarily influenced by surface roughness and initial particle contacts. Basalt, Chinese granite and used granite exhibit minimal deformation, with high resistance to early asperity wear. Basalt, while initially softer, stiffens gradually and shows linear load-displacement behaviour. Andesite, the softest material followed by washed-used granite, experiences significant deformation and scatter due to its rough surface. Fresh granite displays significant plastic deformation and variability, attributed to high surface roughness and asperity breakage.

Fig. 7.2 shows that Chinese granite and used granite exhibit higher stiffness followed by basalt. Used granite exhibits greater stiffness stability than fresh granite and washed-used granite which is not expected. Data for all types of ballasts were not very scattered, with minimal asperity breakage except for andesite and washed-used granite. All the different ballasts aligned well with theoretical predictions by Hertz that as the load increases the stiffness increases.

Overall, Chinese granite, used granite and basalt demonstrate superior performance at low loads due to their higher stiffness and resistance to asperity deformation. In contrast, andesite, washed-used granite and fresh granite exhibit significant variability and lower stability, limiting their suitability. Used granite offers a promising result compared to fresh granite, with improved performance in terms of stiffness, stability, and alignment with theoretical models.

Behaviour under medium-high loads (100N)

Fig. 7.3 illustrates the load-displacement behaviour of different ballasts under a normal load of 100N, where the mechanical response of ballast materials becomes more pronounced. While Chinese granite continues to exhibit the highest resistance to deformation, basalt stiffens gradually followed by washed-used granite. At low load andesite and fresh granite experience noticeable compression and flattening of asperities, reflecting their limited durability, as the load increases (>10N) andesite and fresh granite display a gradual increase in stiffness but remain less stiff than basalt and Chinese granite, with continued deformation. Used granite outperforms fresh granite and andesite, achieving a higher stiffening curve. Washed-used granite performs similarly to used granite, with slightly less deformation but much-reduced scatter and better alignment with Chinese granite and basalt.

Fig. 7.4 Shows the stiffness-deformation curves of different ballasts under a normal load of 100N. Chinese granite continues to display the highest stiffness of 10 N/μm while basalt (BB-100N-2) stiffens gradually and slightly less than Chinese granite, exhibiting stiffness of 6 N/μm. Andesite and fresh granite demonstrate a gradual increase in stiffness but remain less stiff than Chinese granite. Washed-used granite performs similarly to basalt, with a slightly lower stiffness of 5N/μm but higher than used granite and fresh granite. Used granite and washed-used granite outperforms fresh granite, achieving a higher stiffness.

Overall, Chinese granite and basalt remain the most robust materials under medium-high loads, maintaining high stiffness and resistance to deformation. Unlike at the low load, washed-used granite offers consistent and reliable performance, making it an effective alternative to fresh and used granite.

Behaviour under very high loads (200 N)

At high loads, the structural integrity of ballast materials is severely tested. Key factors such as stiffness stability and resistance to breakage become paramount in determining their suitability.

Fig. 7.5 illustrates the load-deformation response of ballasts under the higher load of 200N. Chinese granite consistently demonstrates exceptional performance, compared to all the remaining ballasts, showing minimal breakage during normal loading and the data is less scattered. Basalt, while slightly less stiff than Chinese granite, exhibits strong resistance to stress. Washed-used similar behaviour to basalt and exhibited better performances than used granite and fresh granite. This means the washing has improved the performance.

In contrast, andesite undergoes significant deformation and flattening, limiting its applicability in high-stress environments. Fresh granite, characterised by substantial deformation and variability, proves less reliable. Used granite, while showing improved performance over fresh granite, still exhibits limitations.

Fig. 7.6 shows a comparison of the load-stiffness ballasts under a higher load of 200N. Again Chinese granite maintains high stiffness. Washed-used granite and used granite emerged, achieving superior stiffness and stability versus fresh granite. Basalt followed them and showed higher stiffness than fresh granite and andesite. Once again andesite and fresh granite showed a lower stiffness than other ballasts.

In conclusion, Chinese granite and basalt remain the top-performing materials, offering optimal performance under high-load conditions. Washed-used granite presents a viable alternative, providing a balance between performance and cost-effectiveness. Fresh granite and andesite, however, exhibit limitations that restrict their suitability for high-stress applications. Table 7.1 summarises the performance of ballast materials under varying load conditions.

7.2 Monotonic shearing

After comparing the behaviour of railway ballasts under monotonic normal loading in the first part of this chapter, this section presents results from monotonic shearing tests, performed on the different ballast particles under different normal load conditions. The comparison will be based on the different types of ballast coefficient of friction and monotonic tangential stiffness, under different load levels.

Comparison of tangential monotonic shearing of different under normal load of 20N

Fig. 7.7 illustrates the monotonic T/N values for all ballasts with tangential displacements (+0.5-1 mm), showing an increase with tangential displacement and stabilising after 100-200 μm. At large displacements, all ballast particles tended to slide at μ values mostly between 0.25 and 0.8. The coefficient of inter-particle friction (μ) exhibited considerable variation across ballast types, similar to the findings of Cole (2015), Wong (2022), and Altuhafi et al. (2022). Andesite ballast demonstrated relatively high stabilised μ values ranging from 0.65 to 0.8, attributed to its pronounced asperities and surface texture. However, these values were accompanied by significant scatter, reflecting the variability in surface characteristics. Basalt ballast displayed slightly lower μ values than andesite, stabilising within the range of 0.4 to 0.75 for different tests. The stabilisation for basalt occurred at a greater displacement (except for test BB-20N-2) due to its smoother surfaces and angularity. Chinese granite exhibited the lowest μ values under this load, stabilising between 0.2 and 0.3. The smoother topology of the Chinese granite particles resulted in minimal scatter in the friction values. Fresh granite showed μ values comparable to basalt, ranging between 0.4 and 0.6, but with greater variability arising from the interlocking of angular asperities. Used granite behaved similarly to fresh granite and basalt (BB-20N-1), with μ values stabilising around 0.5-0.6 slightly lower than fresh granite, although smoother particle surfaces from railway operation reduced the observed scatter. Washed used granite demonstrated stabilised μ values between 0.6 to 0.7 much higher than used granite, fresh granite and Chinese granite and similar to basalt, with the cleaning and chemical treatment appearing to have minimal impact on the frictional behaviour, as the surface asperities were already smoothed by prior use (in railways).

Fig. 7.8 demonstrates the tangential stiffness of different ballasts under a normal load of 20N. Initially, tangential stiffness for all ballasts was high and followed a similar trend, and then stiffness decreased to near zero at approximately 100 μm. Chinese granite exhibited higher (2.25 N/μm) initial stiffness that decreased with displacement, approaching near-zero at

around 40 µm. Fresh granite demonstrated a similar tangential stiffness (2.05 N/µm) to Chinese granite but decreased to zero more quickly, typically within 10 µm of displacement. Basalt displayed slightly lower tangential stiffness (0.8-1.15 N/µm) than Chinese granite and fresh granite, with relatively higher tangential stiffness compared to used granite and andesite but decreased to zero much faster, typically within 20 µm of displacement (for BB-20N-2). Used granite showed stiffness behaviour was comparable to andesite (1.25 N/µm), though the smoother particle surfaces led to more consistent trends. Washed-used granite displayed tangential stiffness patterns (1.25 N/µm) similar to basalt just lower than Chinese granite and fresh granite but higher than used granite and andesite, with only minor inconsistencies observed at smaller displacements.

At medium-high loads of 100N

At medium loads of 100N, the coefficient of inter-particle friction for andesite remained high, with stabilised values ranging between 0.65 and 1, as illustrated in Fig. 7.10. Despite the higher load, significant scatter persisted, driven by the material's rough and angular surfaces. Basalt ballast stabilised at slightly lower µ values, between 0.4 and 0.7, with delayed stabilisation at approximately 300 µm displacement. The angularity of basalt contributed to higher µ values compared to smoother materials. Due to its smoother surface texture, Chinese granite recorded lower and less consistent µ values, stabilising between 0.15 and 0.5. Fresh granite displayed similar µ values to basalt, ranging between 0.4 and 0.7, with variability arising from its angular asperities. Used granite demonstrated stabilised µ values consistent with fresh granite, ranging between 0.4 and 0.7, though with less scatter due to the smoother surfaces produced by operational wear. Washed used granite exhibited µ values aligning with untreated used granite, stabilising around 0.7, with no substantial effect from cleaning or chemical treatment.

The tangential stiffness under medium loads revealed similar patterns to those observed under low loads (Fig. 7.10). Andesite ballast retained high initial stiffness, which decreased with displacement, reaching near-zero by approximately 100 µm. There was no consistent trend regarding the influence of increased load on stiffness. Basalt exhibited slightly lower stiffness than andesite, with a similarly rapid decline as displacement increased. Chinese granite demonstrated higher tangential stiffness than basalt and andesite but exhibited a faster reduction to zero, generally at around 50 µm of displacement. Fresh granite followed stiffness trends similar to basalt, with rapid decreases and some variability attributable to surface

roughness. Used granite exhibited higher stiffness values than basalt and fresh granite, reflecting the compacted and smoother surface characteristics. Washed used granite displayed stiffness trends consistent with untreated used granite, with minimal changes due to surface treatments.

Under higher loads of 200N

Fig. 7 .11 illustrates the coefficient of inter-particle friction of all ballast materials under high load. Andesite demonstrated the highest μ values stabilised between 0.6 and 0.9, though the μ values were slightly lower than under lower loads. Fresh granite recorded μ values comparable to andesite, stabilising within the range of 0.7 to 0.9, but with slightly higher variability due to angular surface asperities. Basalt displayed stabilised μ values between 0.5 and 0.6. Used granite also stabilised within the same range as basalt, between 0.4 and 0.6, though with less scatter due to its smoother surfaces. Chinese granite, owing to its smoother surface, retained the lowest but less consistent μ values, stabilising between 0.15 and 0.5. Washed-used granite continued to exhibit stabilised μ values of approximately 0.7 to 0.8, which is higher than used granite and almost similar to fresh granite, with cleaning having a clear effect on the frictional characteristics.

The tangential stiffness under high loads generally followed the patterns observed under lower and moderate loads as demonstrated in Fig. 7.12. Washed-used granite exhibited the highest stiffness under high loads, outperforming fresh granite and used granite, likely due to the compacted and smoothed surfaces from operational use and substantial changes arising from cleaning or chemical treatment. Used granite displayed stiffness values slightly lower than washed-used granite. Andesite exhibited a decrease in stiffness with displacement, reaching near-zero at around 80 μm, with no clear evidence of increased stiffness under higher loads. Basalt showed similar trends, with slightly lower stiffness compared to andesite and rapid reductions over displacement. Chinese granite demonstrated similar tangential stiffness to basalt and andesite, with a decrease observed under the high load compared to moderate load. Fresh granite displayed stiffness trends consistent with basalt, with slightly improved load-bearing performance under high loads.

The experimental findings across different ballast materials reveal the complexity of factors influencing friction and stiffness. Particle characteristics such as angularity, surface roughness, mineralogy, and environmental conditions like moisture play significant roles. Materials like andesite and basalt, with higher angularity and roughness, exhibit higher μ

values and greater variability. Granite, both fresh and used, demonstrated more stable behaviour with less scattering.

7.3 Cyclic shearing

Cyclic shearing tests were carried out after monotonic shearing to check the performance of ballast materials andesite, basalt, Chinese granite, fresh granite, used granite, and washed-used granite. They were evaluated under three main parameters: coefficient of inter-particle friction (μ), vertical displacement and abrasion rate, and tangential stiffness, under different normal loads. Each ballast type demonstrated unique characteristics shaped by its geological properties, surface roughness, angularity, and prior usage or maintenance degree.

7.3.1 Comparison of cyclic shearing coefficient of inter-particle friction (μ) of different ballasts under various load levels

Fig. 7.13 illustrates the coefficient of inter-particle friction (μ) for various ballast types subjected to cyclic loading under a low normal load of 20 N. Each ballast type demonstrated unique frictional behaviour, influenced by its material properties and environmental conditions.

Andesite, represented by the blue curve, initially showed a consistent and stable response then dropped and stabilised around 0.6. Basalt, described by the red curve, exhibits the highest frictional coefficients among the ballast types. Its μ stabilises in the range of 0.65-0.7, reflecting its superior angularity and rough particle texture, which promote strong inter-particle locking. However, under flooded conditions, basalt demonstrated a significant reduction in frictional performance, with μ dropping to approximately 0.35 due to the lubricating effects of water, underscoring the sensitivity of basalt to environmental conditions. This reduction was seen for other ballasts too and in later tests, which is not shown here. Chinese granite, (shown by the black curve), demonstrated a gradual increase in μ during the initial cycles before stabilising around 0.6 which is similar to andesite. This trend suggests that particle rearrangement and interlocking occur progressively under repeated loading. Although its final μ is slightly lower than that of basalt, Chinese granite provides stable frictional performance, suitable for general ballast applications.

Fresh granite, (represented by the pink curve), exhibits the lowest frictional coefficients, stabilising around 0.5. This is likely due to surface texture and reduced angularity of the

particles, which result in less effective inter-particle locking. As such, fresh granite may have limited suitability for applications requiring high stability under load.

Used granite, illustrated by the green curve, demonstrates stabilised µ values similar to those of andesite, at approximately 0.6. This indicates that prior use or weathering does not significantly degrade the material's frictional performance. Used granite remains a reliable choice for ballast applications, particularly under low-loading conditions.

Washed-used granite, represented by the cyan curve, exhibits slightly higher frictional coefficients than used granite and much higher than fresh granite, stabilising at around 0.65-0.7. This improvement suggests that the washing process enhances inter-particle friction, likely by removing fine particles or debris that may otherwise act as lubricants.

Overall, basalt and washed-used granite exhibit the highest frictional coefficients, making them well-suited for applications requiring strong inter-particle locking and stability. Andesite, Chinese granite, and used granite demonstrate moderate frictional performance, offering reliable but less robust interlocking compared to basalt. In contrast, fresh granite exhibits the lowest frictional coefficients, limiting its effectiveness in scenarios demanding high stability. Under flooding conditions, all ballast types experienced reductions in µ, highlighting the detrimental effect of water on frictional performance, reinforcing the need to consider environmental conditions when selecting ballast materials.

Fig. 7.14 illustrates the comparison of µ for all ballasts under moderate normal load (100N). Andesite and basalt emerged as the most effective ballast materials under a 100 N load, demonstrating superior frictional performance and remarkable stability across the range of load cycles. Their ability to maintain high µ with minimal fluctuation highlights their resilience to wear and degradation under repeated stress. These characteristics suggest that these materials possess excellent structural integrity and inter-particle interactions, making them highly reliable for long-term use in high-load railway applications.

Used granite and Chinese granite exhibit similar coefficients of friction, stabilising around 0.7. Chinese granite showed significant sensitivity to environmental conditions, particularly flooding, which severely compromised their performance. While these materials exhibited moderate stability under dry conditions, the introduction of water led to pronounced reductions in µ and increased variability across load cycles which was seen for basalt too under low normal load. Fresh granite and washed used granite displayed consistent but

moderate performance under a 100 N load, stabilising at intermediate μ levels around 0.6 which was much lower than other types of ballasts.

Under a normal load of 200N, the performance of various ballast materials demonstrates distinct characteristics as illustrated in Fig. 7.15. Andesite exhibited strong frictional performance with high coefficients of friction (0.7-0.8) maintained throughout most cycles. Periodic dips in μ were observed at the marked "Powder cleaning points," indicating that accumulated debris or particulate matter impacted performance temporarily. However, the friction recovered swiftly post-cleaning, highlighting the resilience of this material under operational conditions.

Basalt displayed stable performance in its non-flooded state, with μ stabilising within the range of 0.65–0.8 which is similar to andesite. However, when subjected to flooding, basalt showed a catastrophic drop in μ, indicating a severe sensitivity to water exposure. Chinese granite exhibited moderate stability after a transition period, with frictional coefficients consistently remaining within the range of 0.5–0.6. Compared to the top-performing materials, Chinese granite lacked at early cycles, however, it showed superior frictional performance and stability observed in andesite and basalt. Chinese ballast emerged as one of the top-performing materials under the 200N load. It demonstrated consistently high frictional coefficients, which suggests strong inter-particle interactions, and suitability for heavy-load applications.

Fresh granite, used granite and washed-used granite displayed moderate but consistent performance, with μ stabilising in the range of 0.5–0.6. While they did not match the performance levels of andesite, basalt and Chinese granite, their stable behaviour indicates that they may be suitable for less demanding applications or secondary railway lines.

Flooding emerged as a significant factor affecting ballast performance, with basalt being the most severely impacted, highlighting the necessity for water-resistant properties in ballast materials, especially for tracks in wet environments. Periodic dips in μ for andesite at cleaning points underscore the influence of debris accumulation on performance, indicating a need for regular maintenance or materials that resist particulate build-up to enhance long-term stability. Under a 200N load, andesite, Chinese granite, and basalt exhibited the best performance, maintaining high frictional coefficients and stability. In contrast, fresh granite used granite, and washed-used granite delivered consistent but lower performance, with washed-used granite unexpectedly failing to outperform used granite and fresh granite.

7.3.2 Comparison of vertical displacement of different ballasts during cyclic loading

Vertical displacement, which reflects compaction and abrasion, varied considerably across the ballast types during cyclic loading. The comparison of vertical displacement will be discussed under different normal load levels, (low load (20N), moderate load (100N) and higher load (200N).

Vertical displacement under low load (20N)

Fig. 7.16 presents the vertical displacement during cyclic shearing under low load, where fresh granite displayed the highest vertical displacement, with moderate initial displacement due to its high angularity and interlocking particles. Vertical displacement increased with increasing cycles however displacement rates reduced rapidly over successive cycles. Washed-used granite exhibited second second-highest displacement behaviour slightly lower than fresh granite and over successive cycles, washed-used granite's displacement trends closely approached those of fresh granite.

Basalt and andesite demonstrated slightly lower displacement compared to fresh granite and washed-used granite but showed a similar reduction over time, achieving stability after fewer cycles. For used granite and Chinese granite attributed to their relatively lower angularity and mixed particle shapes, over repeated cycles, the displacement stabilised but remained lower than fresh granite, andesite, and washed-used granite.

Chinese granite, basalt, and used granite were the most resistant to settlement, while andesite, washed-used granite, and especially fresh granite showed progressively higher displacement under tangential loading. Among these, washed-used granite surprisingly exhibited greater displacement than used granite, contrary to expectations. This indicates that the washing process may not effectively restore its original stability and could even degrade its structural integrity.

Under an intermediate normal load (100N)

Fig. 7.17 demonstrates the vertical displacement performance of different ballast types under moderate load, revealing notable differences in their mechanical stability and resilience. Used granite, Chinese granite flooded test and basalt demonstrated superior performance with the lowest vertical displacement across cycles, signifying their high resistance to deformation. Fresh granite from the UK showed moderate displacement levels, performing better than Chinese granite (dry test) and andesite.

Among these, washed-used granite surprisingly exhibited greater displacement than used granite, contrary to expectations, suggesting that washing may have negatively impacted the ballast's performance.

Used granite and basalt emerged as the most stable under a 100N load, followed by Chinese granite, while andesite and fresh granite demonstrated reduced performance. Washed-used granite materials showed limited resilience, and washing failed to sufficiently restore performance, raising questions about its cost-effectiveness for reuse.

Under higher normal load (200N)

Fig. 7.18 illustrates the vertical displacement performance of various ballast types, revealing notable differences in their deformation resistance under a 200N load. Chinese granite, washed-used granite, and andesite demonstrated superior performance with the lowest vertical displacements, indicating high stability and suitability for applications requiring minimal settlement. Among these, Chinese granite exhibited the highest resistance to deformation, making it particularly effective for long-term stability. Fresh granite performed moderately, surpassing used granite and basalt instability. In one test basalt, higher displacement was found, however, it showed reduced performance under flooded conditions. This underscores the detrimental effect of water infiltration on basalt's structural integrity.

Used granite materials displayed higher displacement due to prior wear, while washed-used granite improved performance but did not fully restore its original resilience. These findings suggest that while washing enhances used granite's suitability, it may not always achieve the desired performance levels. Chinese granite and andesite emerged as the most stable ballast types under cyclic loading, while basalt and used granite exhibited limitations, particularly in

adverse conditions like flooding. Proper selection of ballast materials should account for environmental factors and previous usage to ensure optimal railway track performance.

Overall, all ballast types show increasing displacement with cycles. Material properties significantly impact displacement magnitude. A higher normal load leads to greater displacement.

7.3.3 Comparison of rate of abrasion of all ballasts during cyclic shearing under different load levels

Fig. 7.19 illustrates the abrasion behaviour of various ballast types under cyclic shearing under a low load of 20N. This was calculated as the gradient of vertical displacement vs cyclic number. Results demonstrate that the rate of abrasion diminishes with increasing cycles due to the formation of a wear layer. Used granite and Chinese granite exhibited the lowest abrasion rate, indicating superior abrasion resistance compared to fresh granite and andesite. Basalt showed slightly lower abrasion resistance compared to used granite and Chinese granite. Washed-used granite displayed higher abrasion rates, suggesting potential degradation in abrasion resistance resulting from previous use or washing.

Under a moderate normal load of 100N, the abrasion resistance trends for ballast materials generally align with those observed at 20N, though the rate of abrasion increases across all types (Fig. 7.20). Used granite and Chinese granite remained the most abrasion-resistant, while basalt shows moderate performance with a slightly increased abrasion rate. Andesite and fresh granite, being softer, are likely to experience a more significant increase in abrasion, making them less suitable for high-stress environments. Washed-used granite demonstrated better resistance than used granite and fresh granite.

Under a high normal load of 200N, all ballast types are expected to experience a significant increase in abrasion rates due to elevated stresses (Fig. 7.21), as seen for moderate load showing a higher rate of abrasion than low load. Chinese granite will likely retain its status as the most abrasion-resistant material, followed by washed-used granite. Fresh granite and andesite once again showed less resistance, while they were expected to exhibit the highest wear due to their lower hardness. Basalt was not expected to exhibit a higher rate of abrasion. Washed-used granite outperforms used granite and fresh granite under a higher load of 200N.

Chinese granite and used granite consistently exhibited the highest resistance, while basalt showed moderate performance. Softer materials like andesite and fresh granite experienced

greater wear, particularly under higher loads. Washed-used granite was moderately vulnerable under low load, with increased degradation due to prior wear however the performance of washed-used granite was improved with higher load. Furthermore, the rate of abrasion is dependent on normal load levels, the higher load will induce greater stresses and strains within the ballast material, leading to increased wear and tear.

7.3.4   Comparison of tangential stiffness of different ballasts during cyclic shearing

Cyclic tangential stiffness will be compared under different normal load levels (20N, 100N and 200N) at different tangential displacements (5μ, 10μ, 50μ)

Comparison of cyclic tangential stiffness of all ballasts under low normal load of 20N

Fig. 7.22 shows the cyclic stiffness of ballast materials at a tangential displacement of 5 μm under a normal load of 20N. Although varying significantly, basalt and washed-used granite demonstrated the highest stiffness (2 N/μm), stabilising rapidly and indicating superior resistance to deformation under repeated loading. Andesite showed moderate stiffness with steady improvement over cycles, suggesting consistent structural integrity. Conversely, fresh granite and Chinese granite started with lower stiffness but stabilised at mid-range levels, while used granite exhibited the lowest stiffness, reflecting material fatigue from prior use. These results reinforce the superior performance of Basalt and washed-used granite under cyclic loading at 5 μm.

Cyclic stiffness of ballast materials at 10 μm tangential displacement under a normal load of 20 N exhibited similar behaviours to those observed at 5 μm as illustrated in Fig. 7.23. Basalt and washed-used granite maintained the highest stiffness and early stabilisation followed by andesite, while Chinese granite and fresh granite showed moderate stiffness and used granite (UK) displayed the lowest stiffness, indicating material fatigue. These results highlight basalt's durability as a premium ballast material under cyclic loading at 5 μm and 10 μm tangential displacement and washed-used granite could be the best alternative as demonstrated higher stiffness than used granite and fresh granite.

Fig. 7.24 shows that the cyclic stiffness of all ballast materials at 50 μm tangential displacement consistently falls below zero, indicating reduced stiffness across the board. andesite and fresh granite show slightly higher values compared to others, but the overall stiffness remains negative. This suggests that at larger displacements, the materials

experience significant softening or slippage. This behaviour contrasts with earlier trends at 5 and 10 µm, where variability and material differences were more pronounced.

Overall, basalt performed the best, demonstrating the highest stiffness, followed by washed-used granite which also showed relatively good performance, particularly in comparison to fresh granite and used granite with lower stiffness. The washing process likely contributed to its improved stiffness.

Comparison of cyclic tangential stiffness of all ballasts under moderate load of 100N

Under a moderate load (100N) at 5 µm, the ballast materials show distinct stiffness behaviours over the cycles (Fig. 7.25), which was observed under low load too. Washed-used granite exhibited the highest stiffness, followed by basalt, Chinese granite, fresh granite and used granite, while andesite and basalt (one test) have lower stiffness values. The Chinese granite-flooded test showed significant stiffness fluctuations that do not stabilise, unlike other materials. Washed-used granite exhibited a higher stiffness, with minimal difference compared to used granite and fresh granite. Overall, most materials stabilised after the 10th cycle, with their stiffness values becoming more consistent under the 100N load.

Fig. 7.26 illustrates cyclic tangential stiffness at 10 µm displacement, washed-used granite and basalt exhibited the highest tangential stiffness among all ballasts, stabilising at consistently elevated levels. Fresh granite showed similar stiffness to used granite, while Chinese granite and andesite displayed moderate stiffness, with fluctuations during the flooded test before stabilising. In contrast, one of the basalt test data had the lowest stiffness, which remained significantly below the other materials.

At 50 µm displacement under a normal load of 100 N, the cyclic stiffness of the ballast materials exhibited clear distinctions (Fig. 7.27). Washed-used granite demonstrated the highest stiffness once again, stabilising quickly and maintaining superior performance throughout the cycles. Fresh granite and Chinese granite followed closely, showing similar stiffness to used granite. Basalt displayed moderate stiffness, comparable to Chinese and UK granites, which stabilised after initial fluctuations (except one test). In contrast, andesite consistently showed the lowest stiffness, exhibited delayed stabilisation and significantly reduced stiffness compared to the granitic materials. This suggests that granite-based ballasts, especially washed-used granite and fresh granite, are more resilient and better suited for applications requiring higher stiffness and durability under repeated loading.

Under a moderate load of 100N, washed-used granite demonstrated the highest stiffness across all displacements, outperforming other materials. Fresh granite and Chinese granite followed closely, showing good stability. Basalt exhibited moderate stiffness, while andesite also showed lower stiffness. Overall, granite-based materials, particularly washed-used and fresh granite, are the most resilient and suitable for applications requiring high stiffness and durability.

Comparison of cyclic tangential stiffness of all ballasts under higher load of 200N

At a displacement of 5 μm under a normal load of 200 N, all ballast types show a similar trend of increasing tangential stiffness with the number of cycles as illustrated in Fig. 7.28 However, the magnitude of stiffness varies significantly across different materials which was seen for low and moderate normal loads. Basalt demonstrated the highest stiffness, closely followed by washed-used granite and Chinese granite. Andesite and used granite exhibited moderate stiffness, suggesting a balanced performance in terms of stiffness and resilience. The flooded basalt shows reduced stiffness, possibly indicating that water infiltration negatively impacts its performance. Fresh granite displayed the lowest stiffness similar to the flooded basalt test.

Fig. 7.29 demonstrates the cyclic stiffness at 10 μm displacement under a normal load of 200 N, all ballast types show a similar trend that was found for 5 μm. The stiffness increased with the number of cycles which was seen under low and medium-high loads. Basalt, Chinese granite and washed-used granite demonstrated the highest stiffness, similar to what was observed at 5μm displacement. Andesite and used granite showed moderate stiffness. Flooded basalt exhibited higher stiffness then reduced after 20 cycles, while fresh granite displayed the lowest.

At a displacement of 50 μm under a normal load of 200 N, all ballast types show a similar trend that was found for 5 μm displacement as demonstrated in Fig. 7.30. Chinese granite and washed-used granite demonstrated the highest stiffness. Basalt exhibited higher stiffness then reduced after 20 cycles, while the flooded basalt showed lower stiffness, indicating that water infiltration negatively impacts its performance. Andesite and used granite showed moderate stiffness while fresh granite displayed similar stiffness to the flooded basalt test.

In conclusion, across all displacement levels (5 µm, 10 µm, and 50 µm) and normal loads (20 N, 100 N, and 200 N), basalt consistently exhibited the highest stiffness, followed by washed-used granite and Chinese granite. Andesite and used granite displayed moderate stiffness, while flooded basalt and fresh granite showed lower stiffness, particularly at higher displacements. At 50 µm, Chinese granite and washed-used granite maintained the highest stiffness, while basalt and flooded basalt experienced reduced stiffness, indicating the detrimental effect of water infiltration. These findings underscore the importance of material selection and maintenance in ensuring the long-term functionality of ballast under cyclic loading.

7.4. Summary

During monotonic normal loading, Chinese granite and basalt consistently exhibited superior stiffness, minimal deformation, and excellent stability across low (20N), moderate (100N), and high (200N) loads. Washed-used granite also performed well, surpassing fresh granite in stiffness and stability under high loads. Andesite and fresh granite demonstrated greater deformation and variability, particularly under higher stress, indicating limited suitability for demanding applications.

The monotonic shearing behaviour of ballast materials showed that andesite consistently exhibited the highest friction (0.65–1.0) due to its rough texture, while Chinese granite had the lowest (0.15–0.5) owing to its smooth surface. Basalt and fresh granite showed moderate friction (0.4–0.7), with used granite performing similarly but more consistently due to wear. Washed-used granite achieved higher friction (0.7–0.8), reflecting improved stability after cleaning. Tangential stiffness for Chinese granite and fresh granite initially demonstrated higher stiffness but degraded rapidly. Andesite and basalt displayed steadier but lower stiffness, while washed-used granite maintained the highest stiffness across all conditions.

Tangential cyclic shearing tests revealed the highest coefficients of friction (0.65-0.7) for basalt and washed-used granite, with basalt's performance decreasing significantly under flooding. Andesite and Chinese granite exhibited moderate coefficients of friction (0.6), while fresh granite had the lowest (0.5). Used granite, with µ comparable to andesite, proved its durability despite prior usage.

Vertical displacement analysis showed that Chinese granite had the least settlement across all load levels, while fresh granite experienced the most displacement due to high angularity. Basalt and used granite demonstrated good resistance to deformation, while washed-used

granite showed higher displacement than expected, possibly due to degradation from washing.

Abrasion resistance testing highlighted Chinese granite and used granite as the most resistant material. Washed-used granite displayed moderate resistance but experienced wear degradation. Fresh granite and andesite, with lower hardness, exhibited significant wear at high loads.

Tangential stiffness varied with material and load. Basalt and washed-used granite consistently exhibited high stiffness, while fresh granite showed the lowest. Flooding significantly reduced stiffness in basalt and washed-used granite.

In conclusion, Chinese granite, basalt, and washed-used granite emerged as the most reliable materials for demanding railway ballast applications, combining high friction, stability, and stiffness. Andesite and used granite provided moderate performance, suitable for general use, while fresh granite's lower stability and wear resistance limited its applicability. These findings underscore the importance of material properties, prior usage, and environmental conditions in selecting suitable ballast materials.

Chapter 7 Figures and Tables

7.1 The performance of ballast materials under different normal loading.

Material	Low Load (20 N)	Medium Load (100 N)	High Load (200 N)
Chinese Granite	High stiffness, minimal scatter	Superior stiffness, durable	Most rigid, minimal deformation
Basalt	Gradual stiffening, durable	Linear stiffness, resilient	Stable, high resistance to stress
Andesite	Soft, significant scatter	Flattening under stress, less durable	Significant compression, not durable
Fresh Granite	High variability, less reliable	Inconsistent stiffness	Significant deformation, less durable
Used Granite	Reduced scatter, more stable	Improved stiffness, elastic behaviour	Reliable, better than fresh granite
Washed-Used Granite	Minimal scatter, balanced	Consistent stiffness, reduced breakage	Robust, aligns well with models

7.2 Shows the μ values for all ballasts from cyclic shearing

Material	μ values
Andesite	0.6 - 0.8
Basalt	0.6 - 0.75
Chinese granite	0.65 - 0.75
Fresh Granite	0.6 – 0.7
Used Granite	0.55 – 0.7
Washed Used Granite	0.65-0.85

7.3 Stiffness values of different materials under normal loadings.

Material	Stiffness (N/µm) - 20N	Stiffness (N/µm) - 100N	Stiffness (N/µm) - 200N
Andesite	0.6	1.80	1.5
Basalt	1.8	3.50	5.0
Chinese Granite	1.70	10.0	20.0
Fresh Granite	0.80	1.80	3.50
Used Granite	1.50	2.0	9.0
Washed Used Granite	0.90	2.10	9.0

7.4 Stiffness values of different materials during monotonic shearing.

Material	Stiffness (N/µm) - 20N	Stiffness (N/µm) - 100N	Stiffness (N/µm) - 200N
Andesite	1.0	1.15	1.6
Basalt	0.4 – 1.10	0.8 – 1.14	0.8 – 1.20
Chinese Granite	2.2	1.8 – 2.75	1.0
Fresh Granite	0.10 – 2.25	1.10	1.20
Used Granite	1.0	1.40	1.90
Washed Used Granite	1.50	0.50	3.40

7.5 Stiffness values of different materials during cyclic shearing.

Material	Stiffness (N/µm) - 20N	Stiffness (N/µm) - 100N	Stiffness (N/µm) - 200N
Andesite	1.20	1.10	2.0
Basalt	1.20	1.50 – 1.70	2.0
Chinese Granite	1.0 – 2.0	1.0 – 2.0	1.0
Fresh Granite	1.0	0.90	1.50
Used Granite	1.0	1.9	2.0
Washed Used Granite	1.9	2.0	2.90
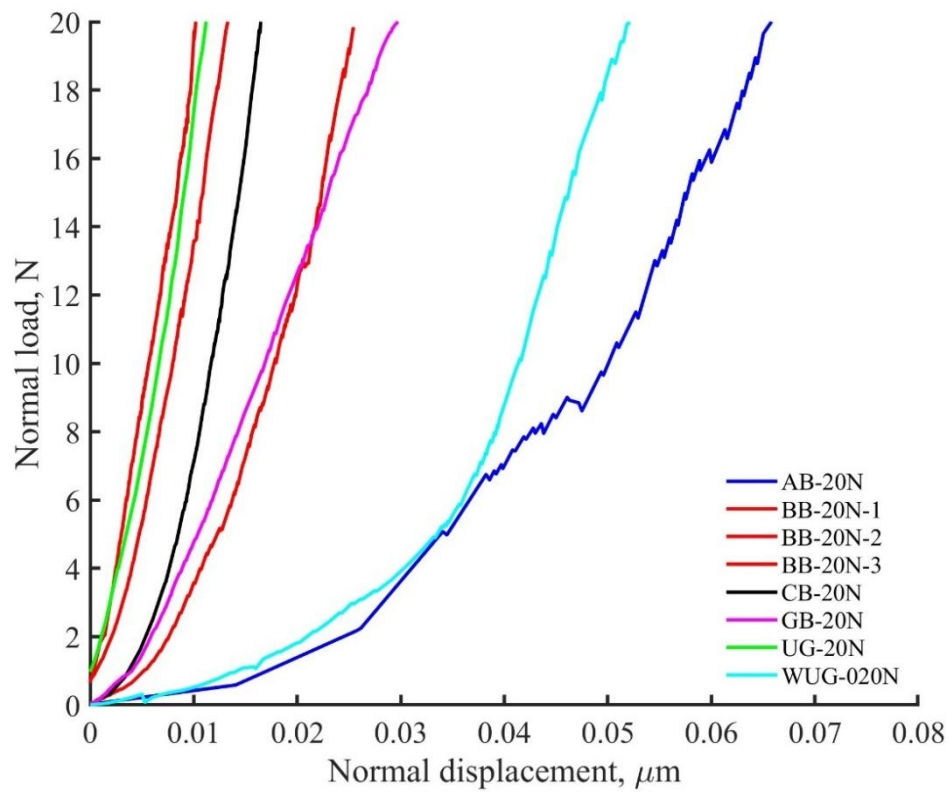
Figure 7.1 Load-deformation behaviour of all types of ballasts under a normal load of 20N.
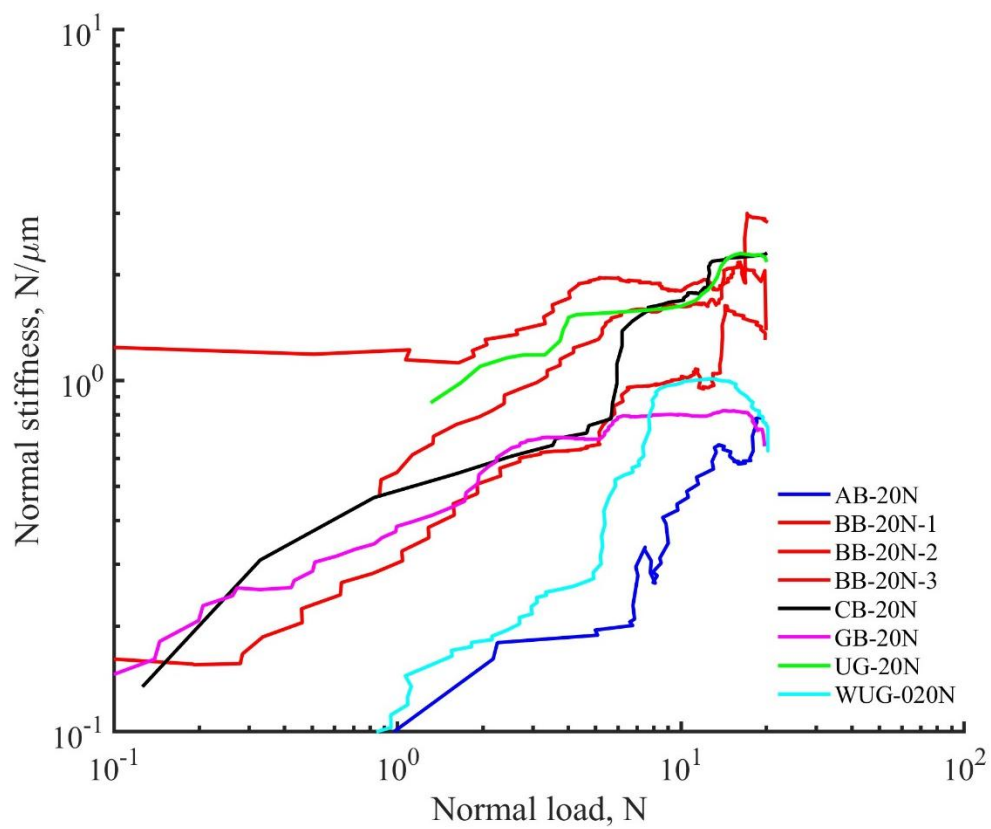
Figure 7.2 Stiffness-deformation curves for normal loading of 20N for all types of ballasts.
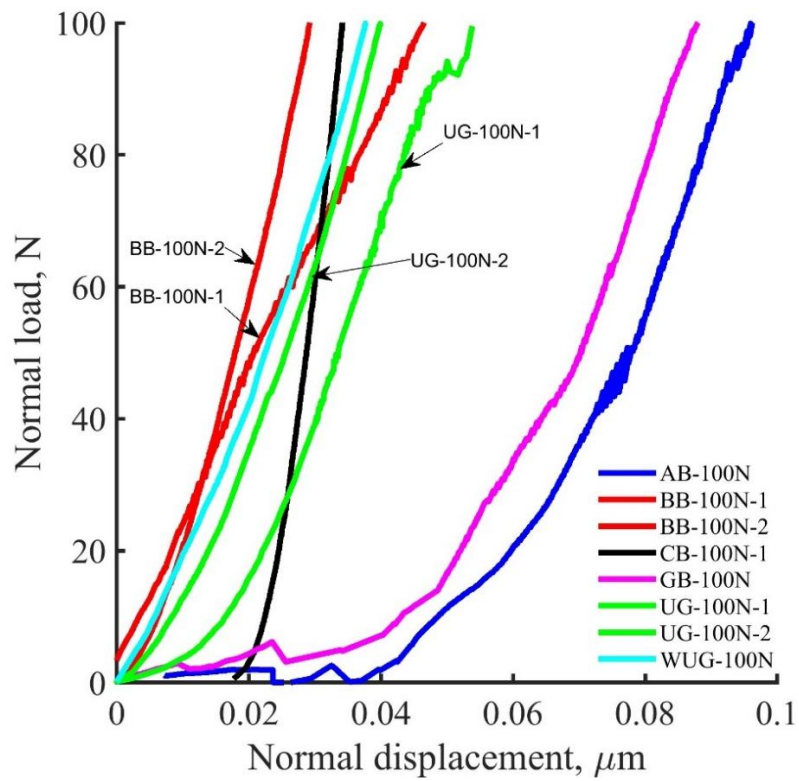
Figure 7.3 Load-displacement behaviour of different ballast materials under a normal load of 100N.
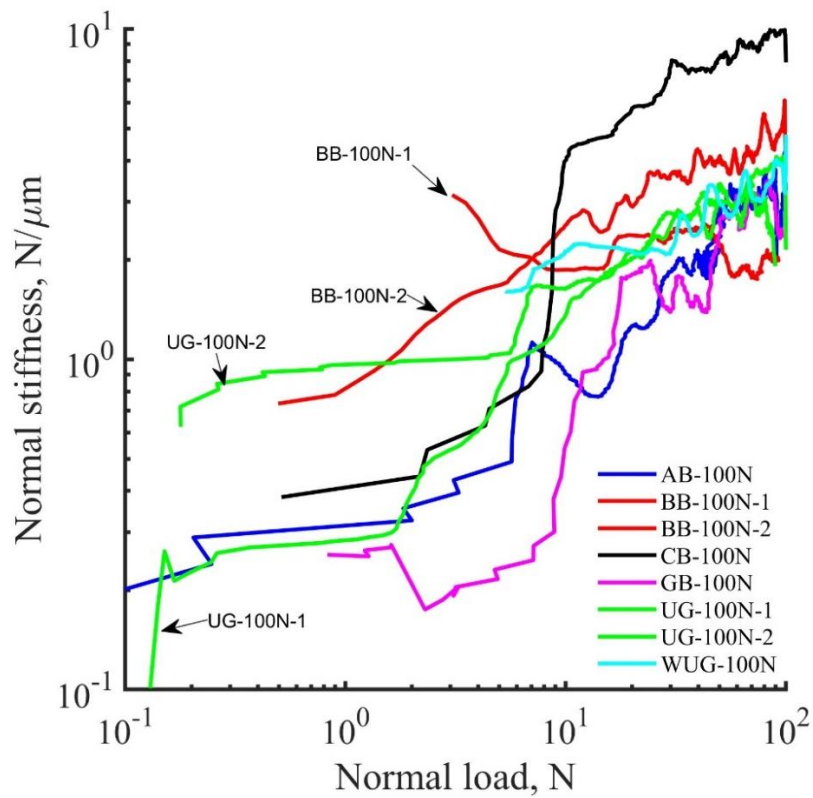
Figure 7.4 Stiffness-deformation curves of different ballasts under a normal load of 100N.
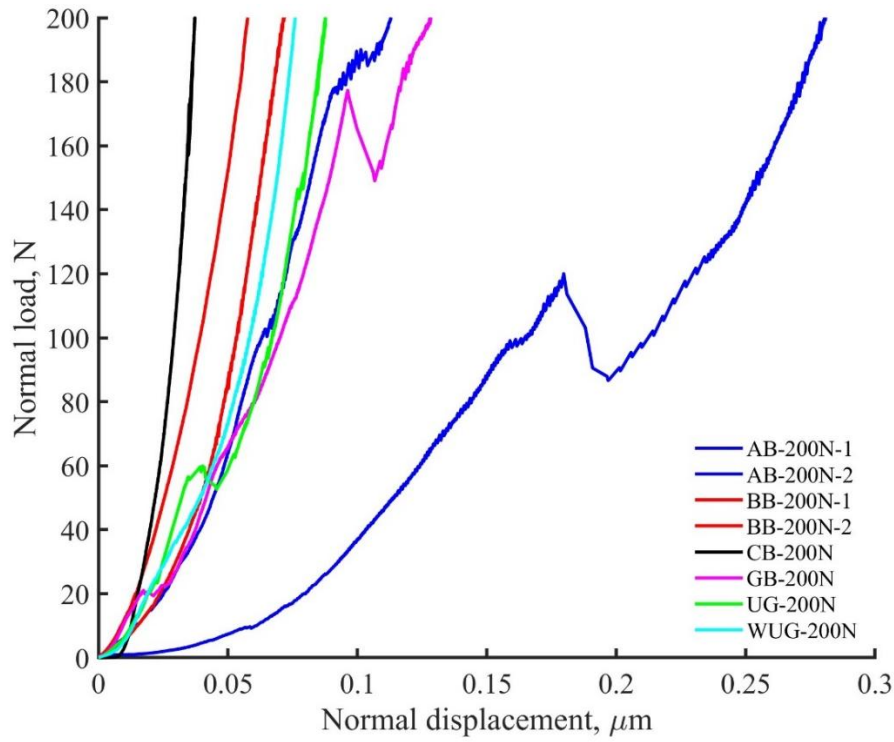
Figure 7.5 Load and deformation comparison of different ballasts under a normal load of 200N.
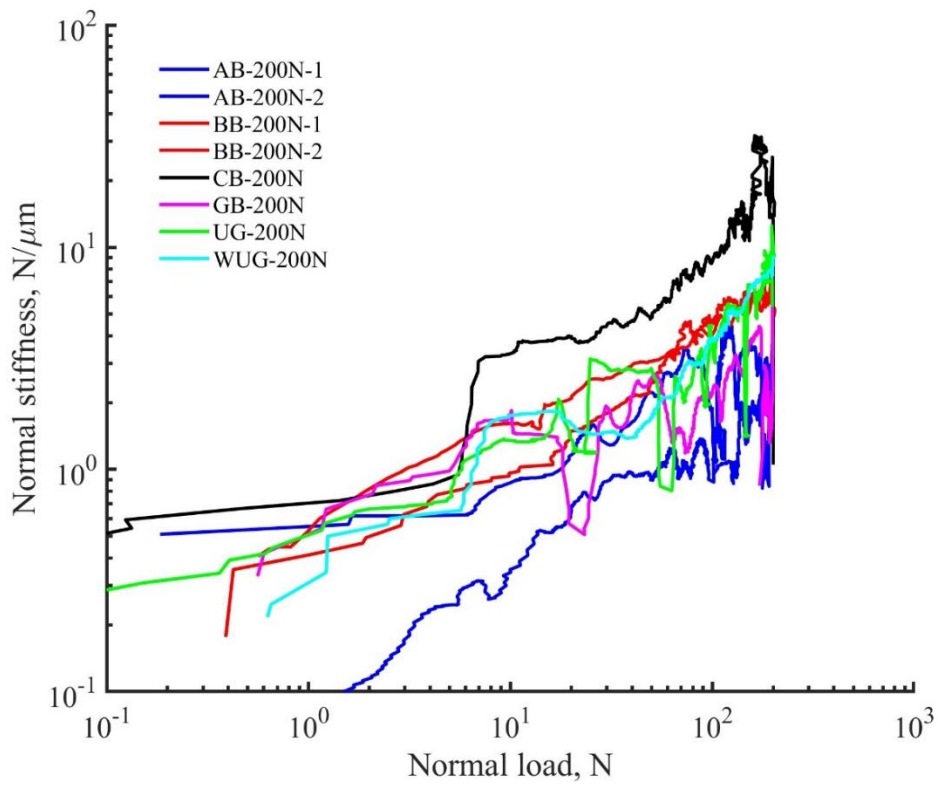
Figure 7.6 Normal stiffness of different ballasts under normal loading of 200N.
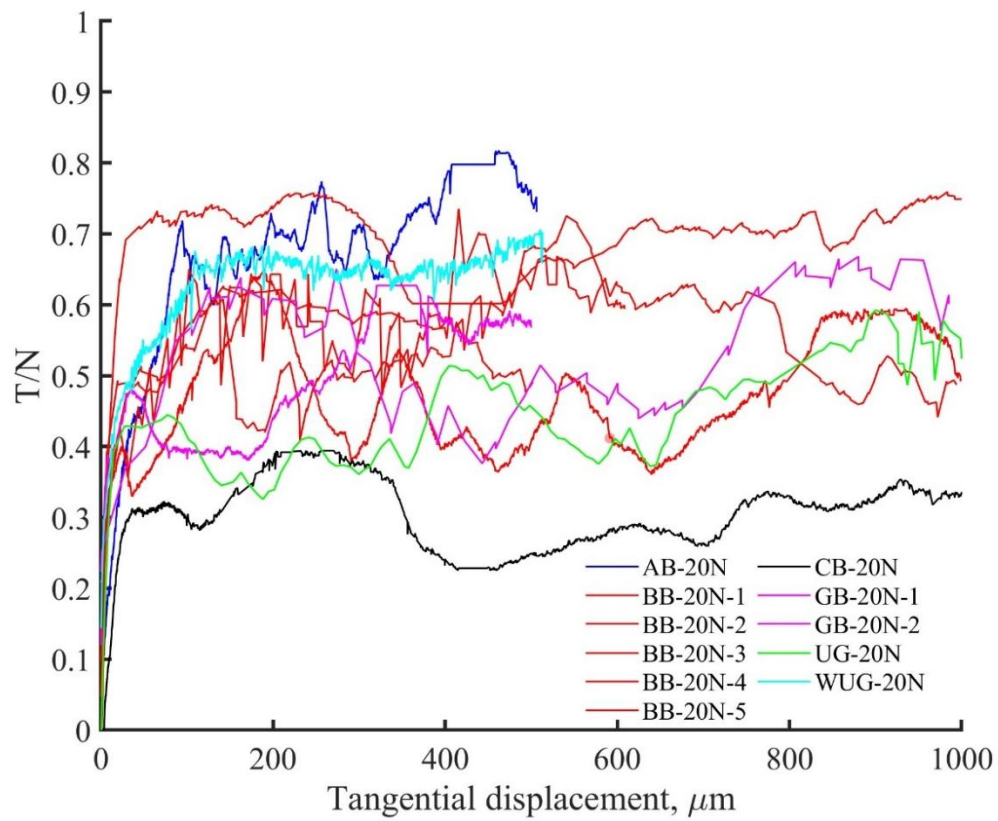
Figure 7.7 Monotonic shearing T/N of different ballasts under normal load of 20N.
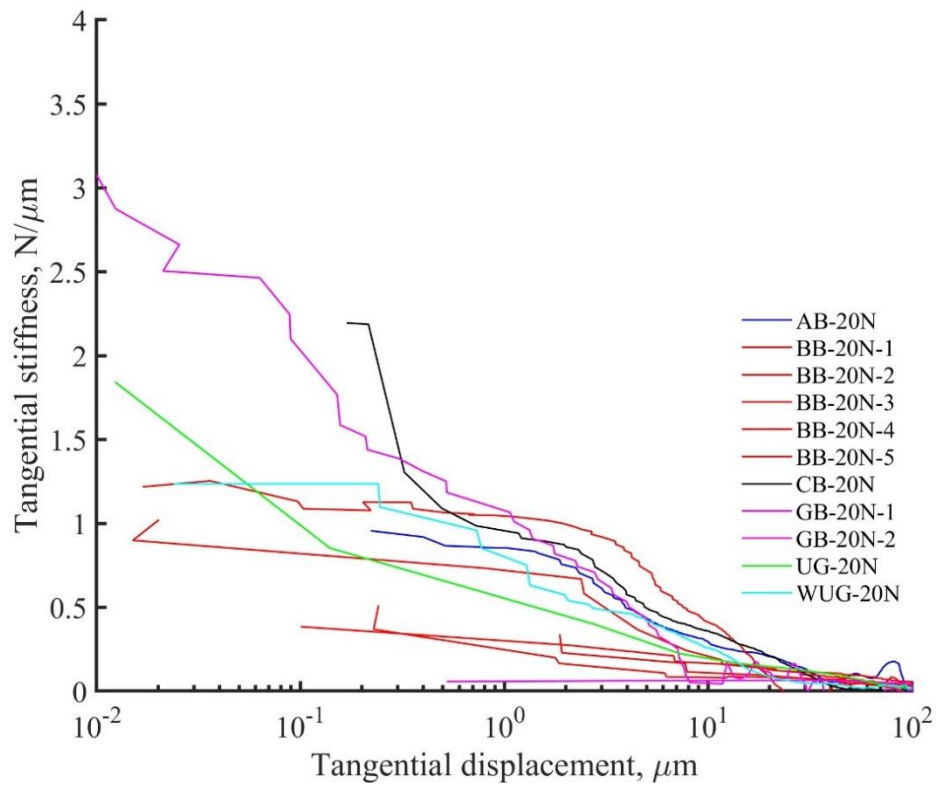
Figure 7.8 Tangential stiffness of different ballasts under normal load of 20N.
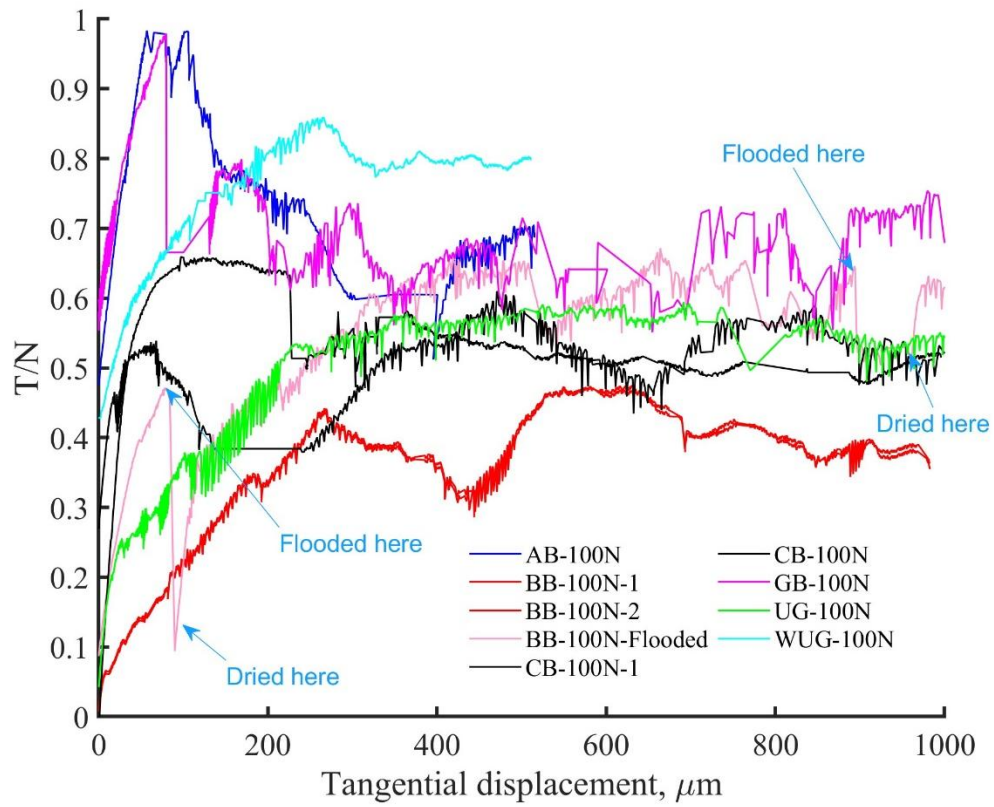
Figure 7.9 Monotonic shearing T/N of different ballasts under normal load of 100N.
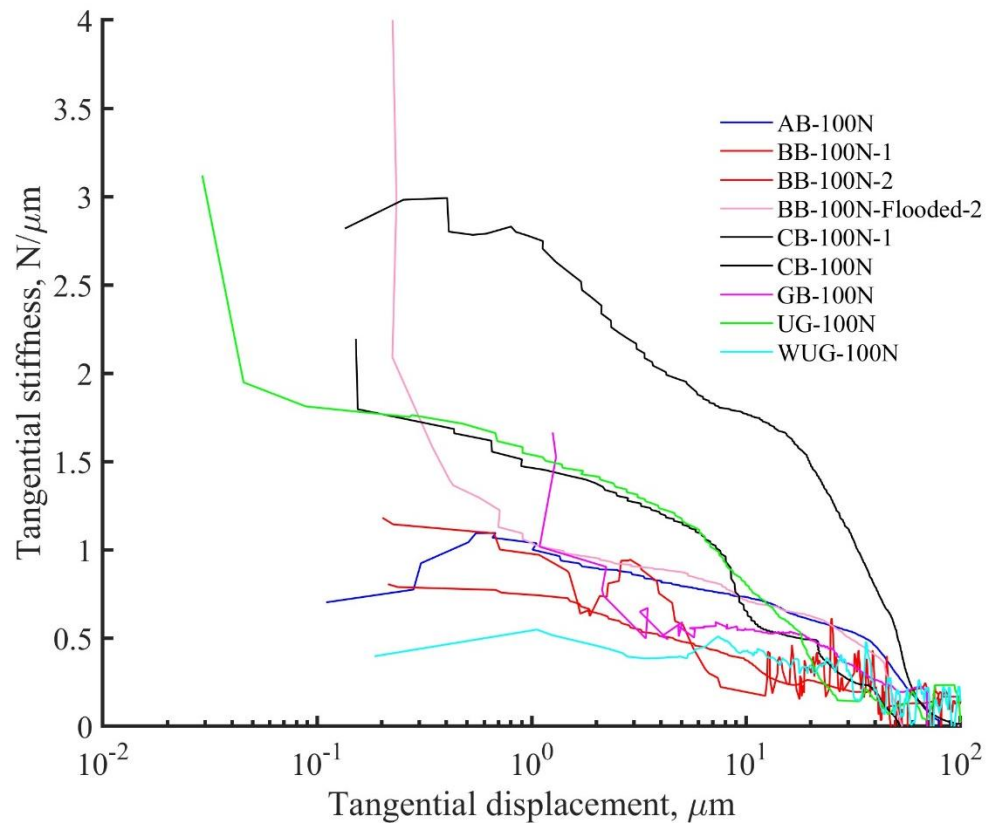
Figure 7.10 Tangential stiffness of different ballasts under normal load of 100N.
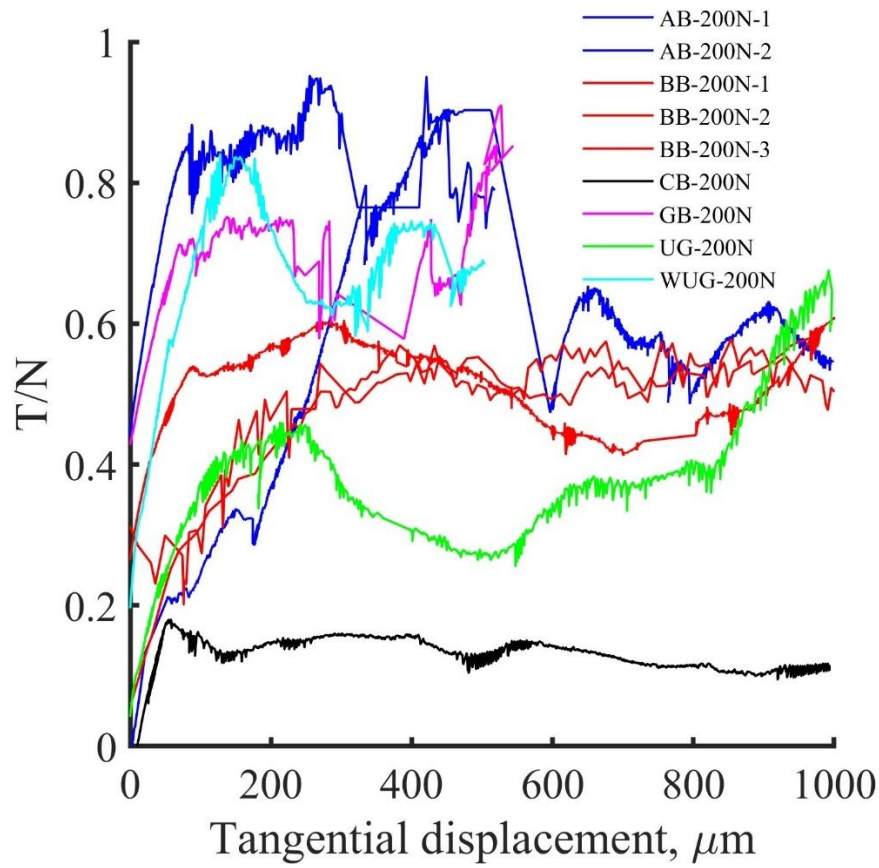
Figure 7.11 Monotonic shearing T/N of different ballasts under normal load of 200N
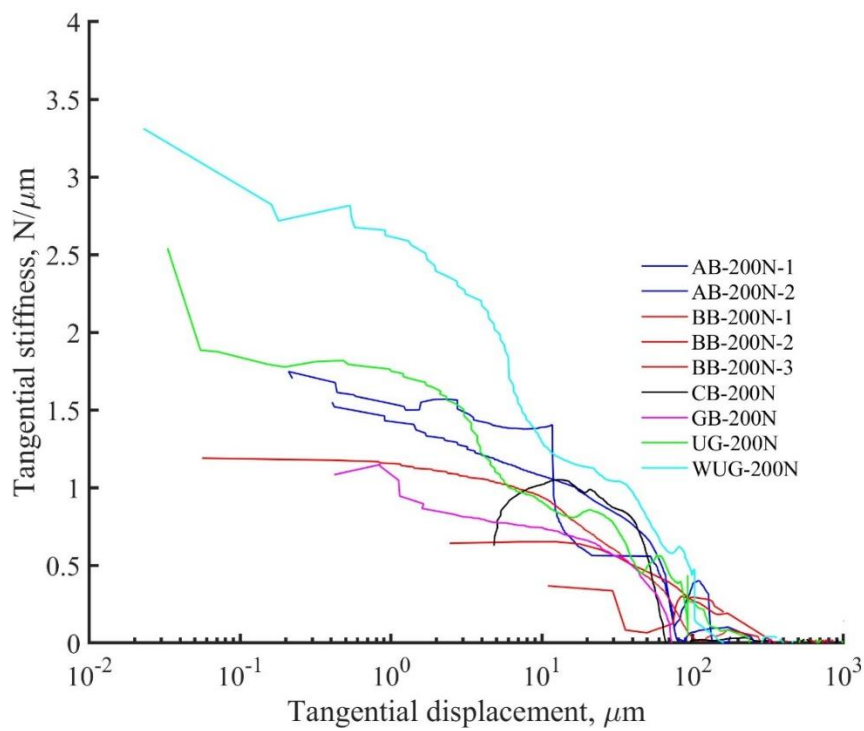
Figure 7.12 Tangential stiffness of different ballasts under normal load of 200N.

357
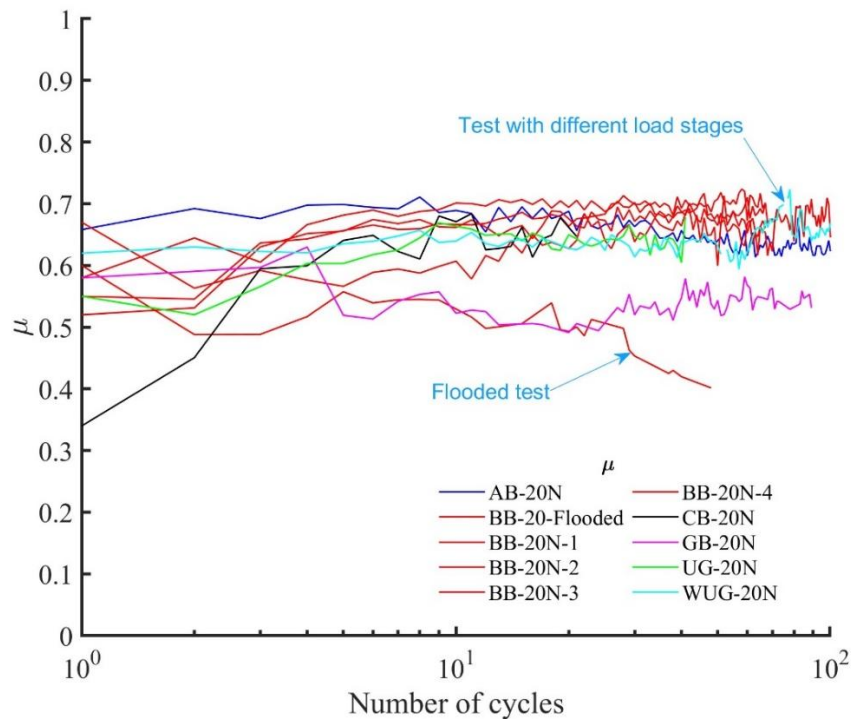
Figure 7.13 Coefficient of inter-particle friction (μ) with linear shear shown as first cycle, under normal load of 20N for all types of ballasts.
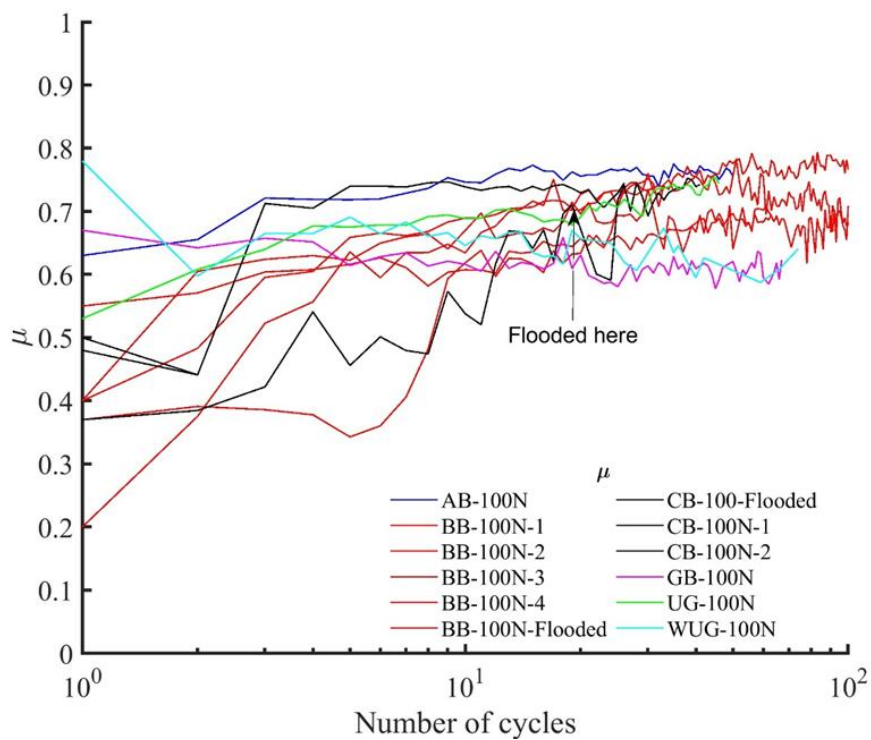
Figure 7.14 Coefficient of inter-particle friction (μ) with linear shear shown as first cycle, under normal load of 100N for all types of ballasts.
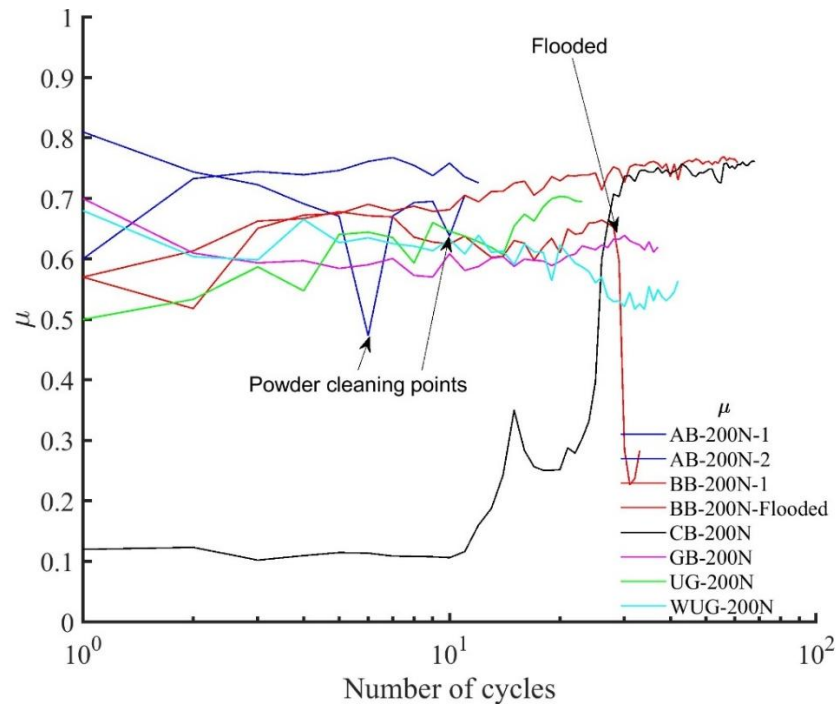
Figure 7.15 Comparison of cyclic shearing μ with linear shear shown as first cycle, under normal load of 200N for all types of ballasts.
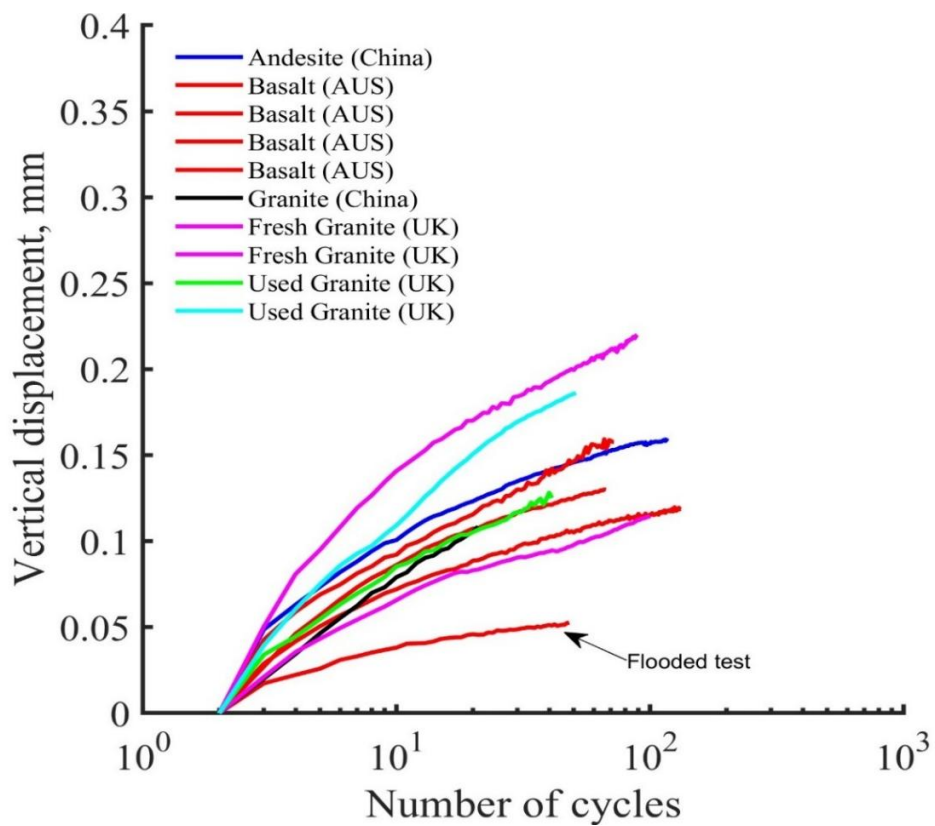
Figure 7.16 Comparison of vertical displacements under normal load of 20N for all types of ballasts.
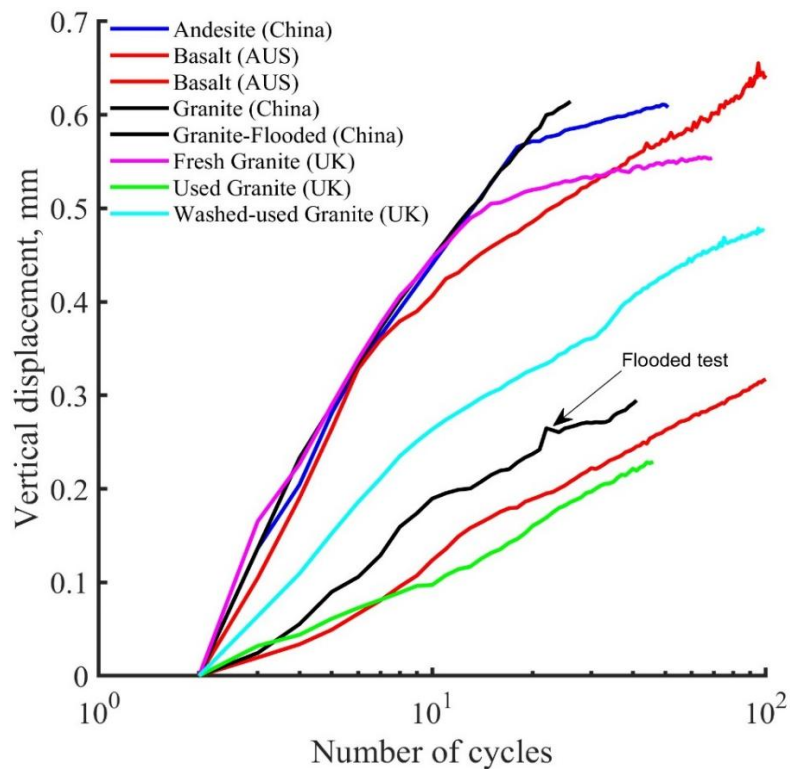
Figure 7.17 Comparison of vertical displacements under normal load of 100N for all types of ballasts.
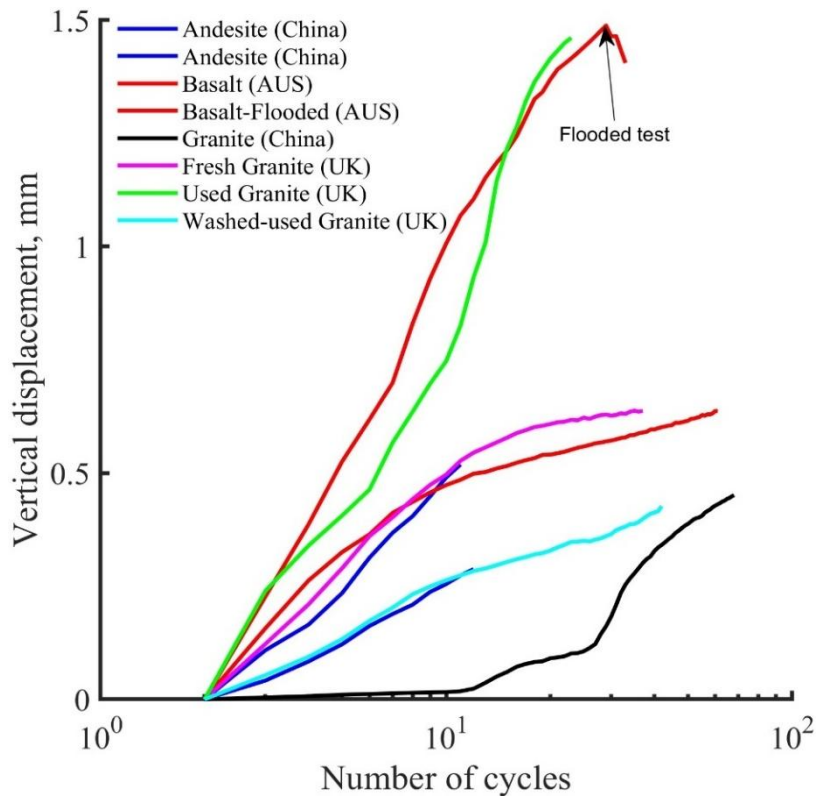
Figure 7.18 Comparison of vertical displacements under normal load of 200N for all types of ballasts.
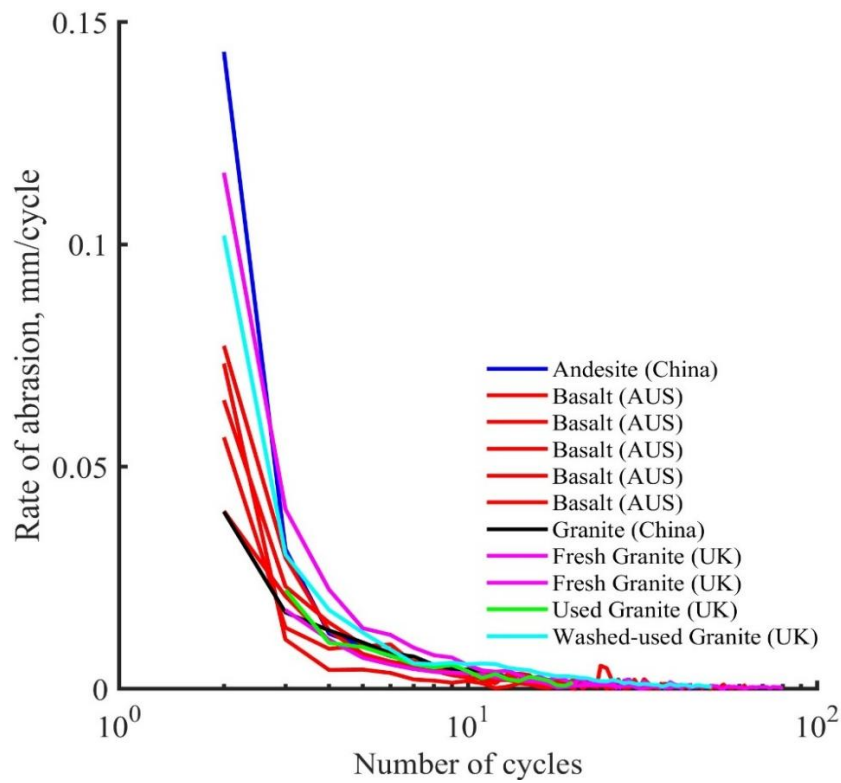
Figure 7.19 Comparison rate of abrasion during cyclic shearing for all ballasts under a normal load of 20N.
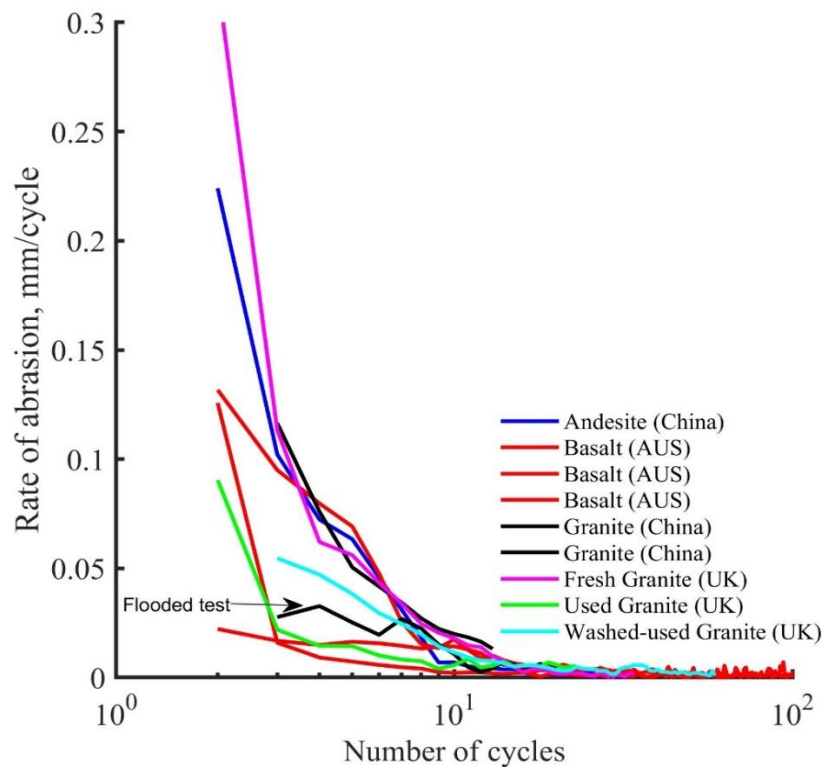
Figure 7.20 Compare of rate of abrasion during cyclic shearing for all ballasts under a normal load of 100N.
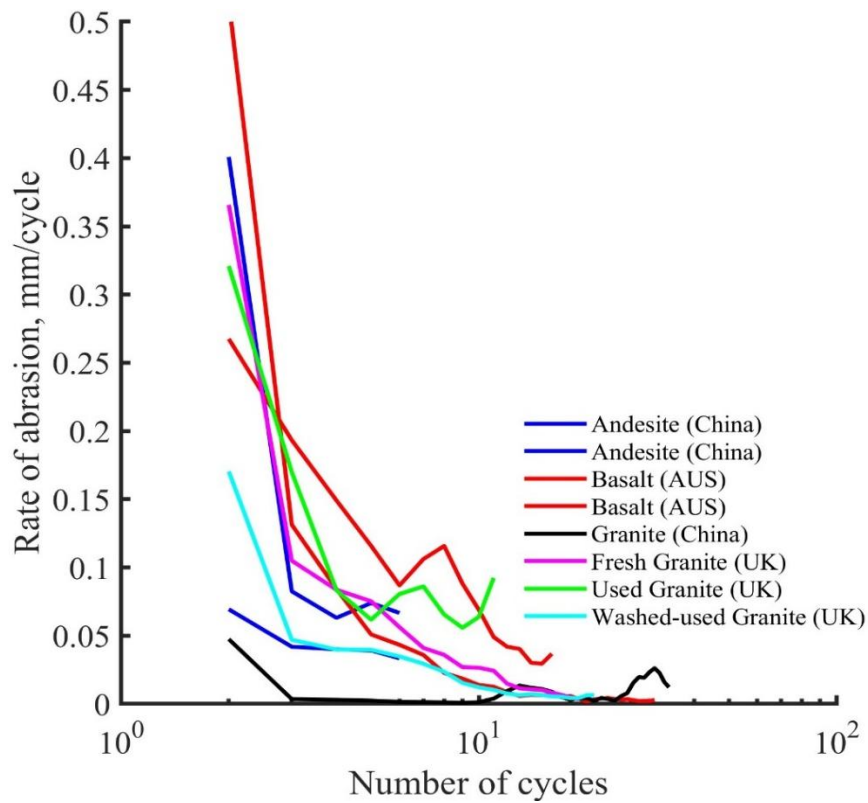
Figure 7.21 Rate of abrasion during cyclic shearing for all ballasts under normal load of 200N.
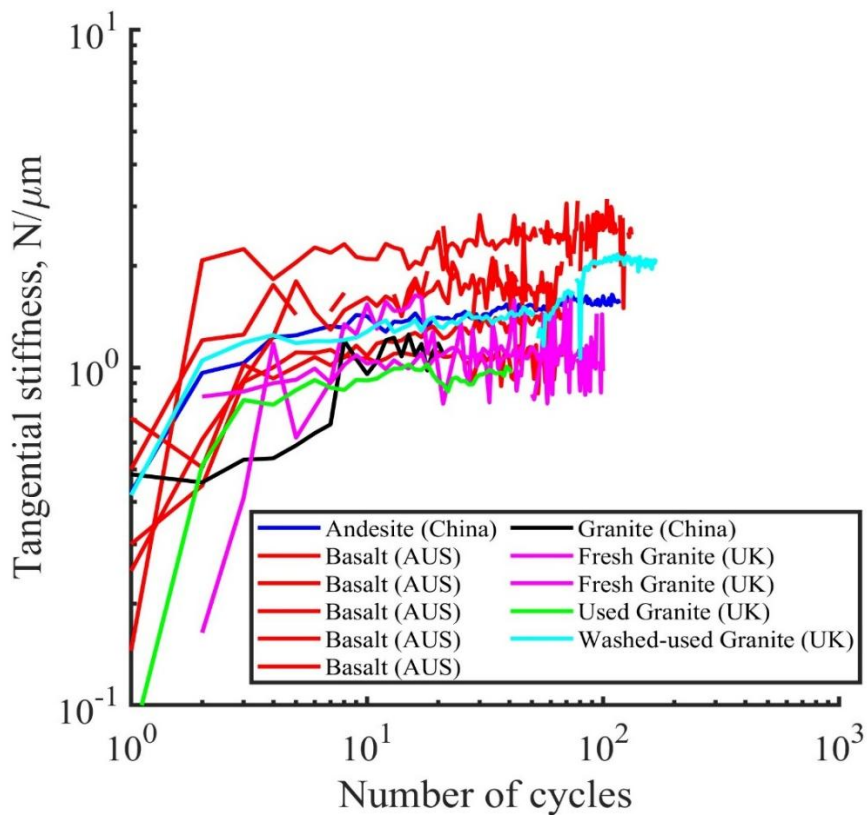
Figure 7.22 Comparing of cyclic stiffness of all ballasts at 5 μ under a normal load of 20N.
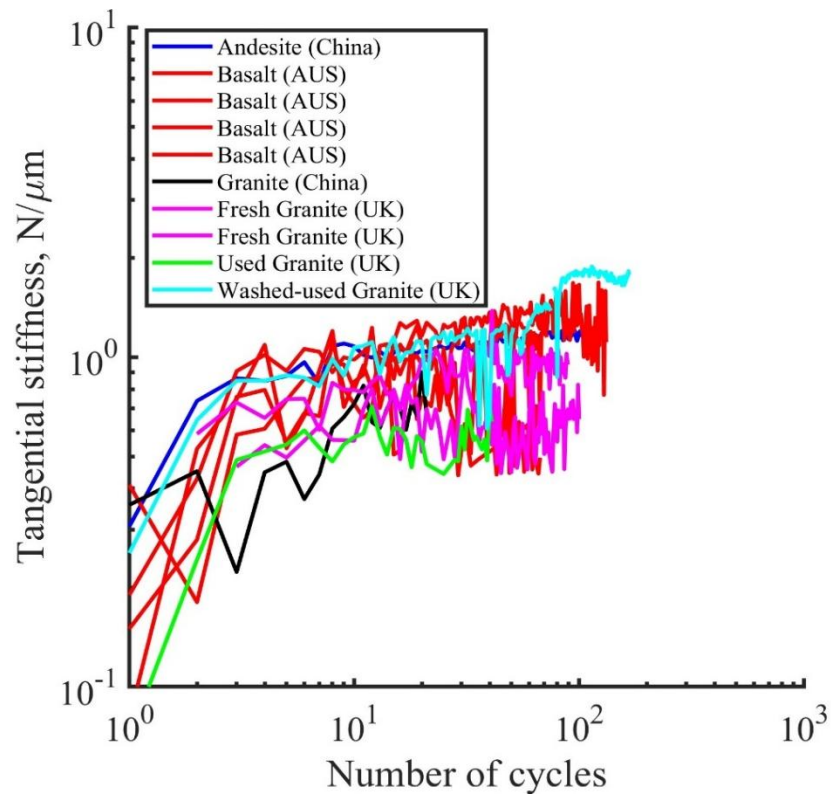
Figure 7.23 Comparison of cyclic stiffness of all ballasts at 10μ under a normal load of 20N.
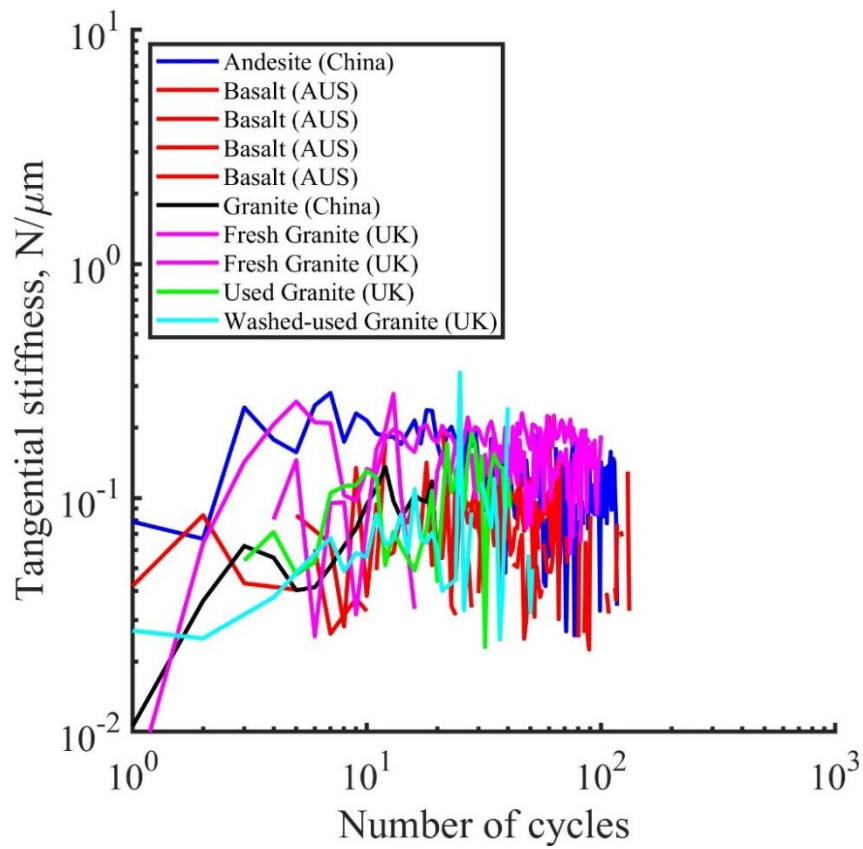
Figure 7.24 Comparing of cyclic stiffness of all ballasts at 50μ under a normal load of 20N.

363
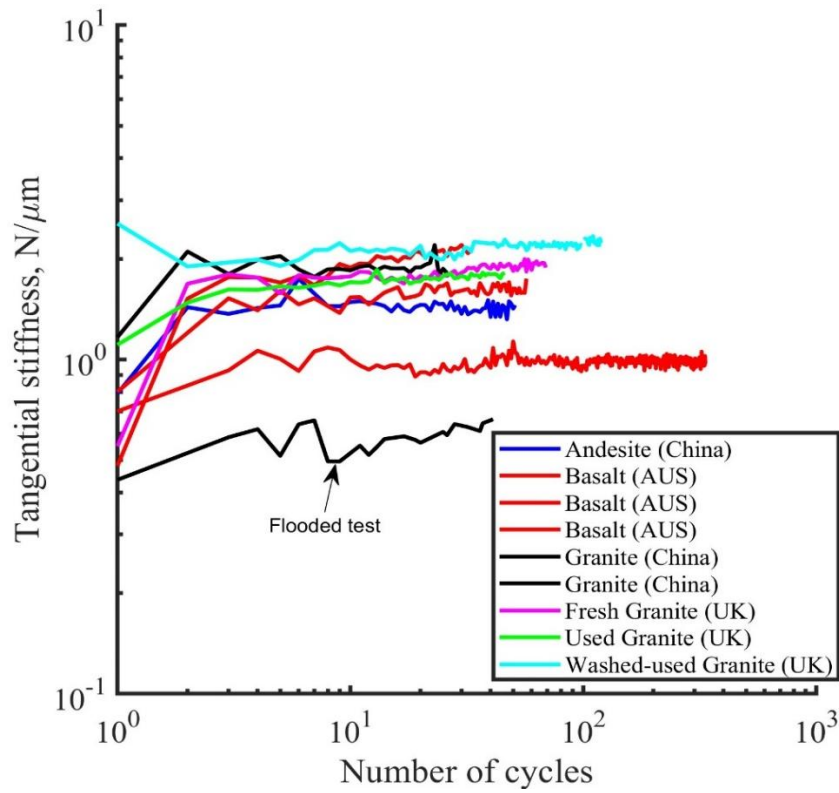
Figure 7.25 Comparing of cyclic stiffness of all ballasts at 5μ under a normal load of 100N.
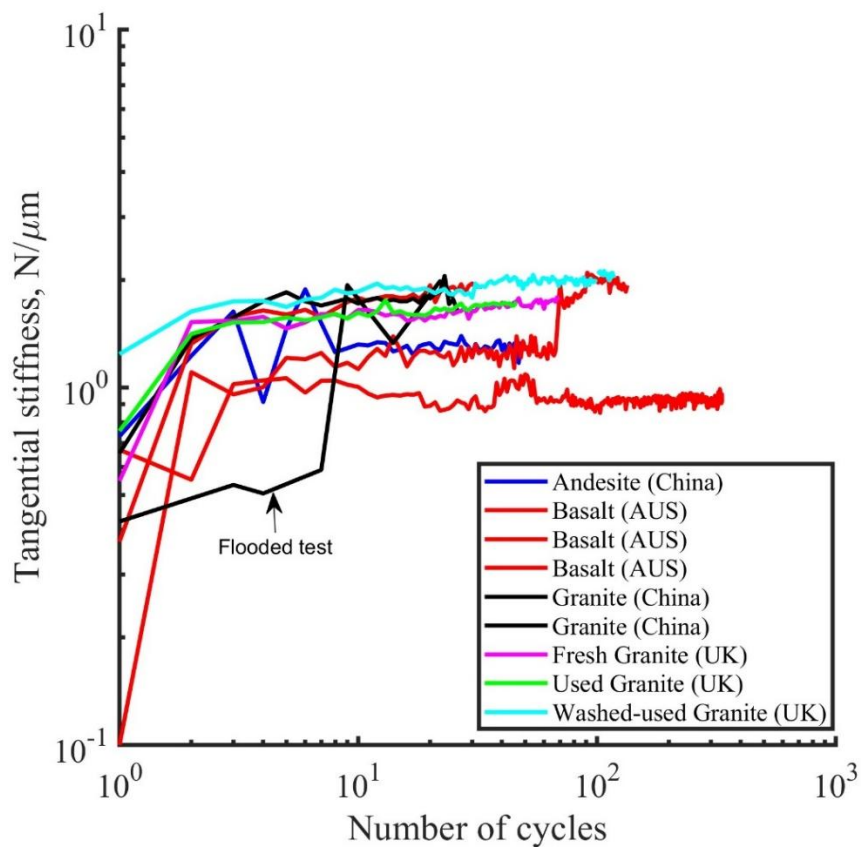
Figure 7.26 Comparing of cyclic stiffness of all ballasts at 10μ under a normal load of 100N.
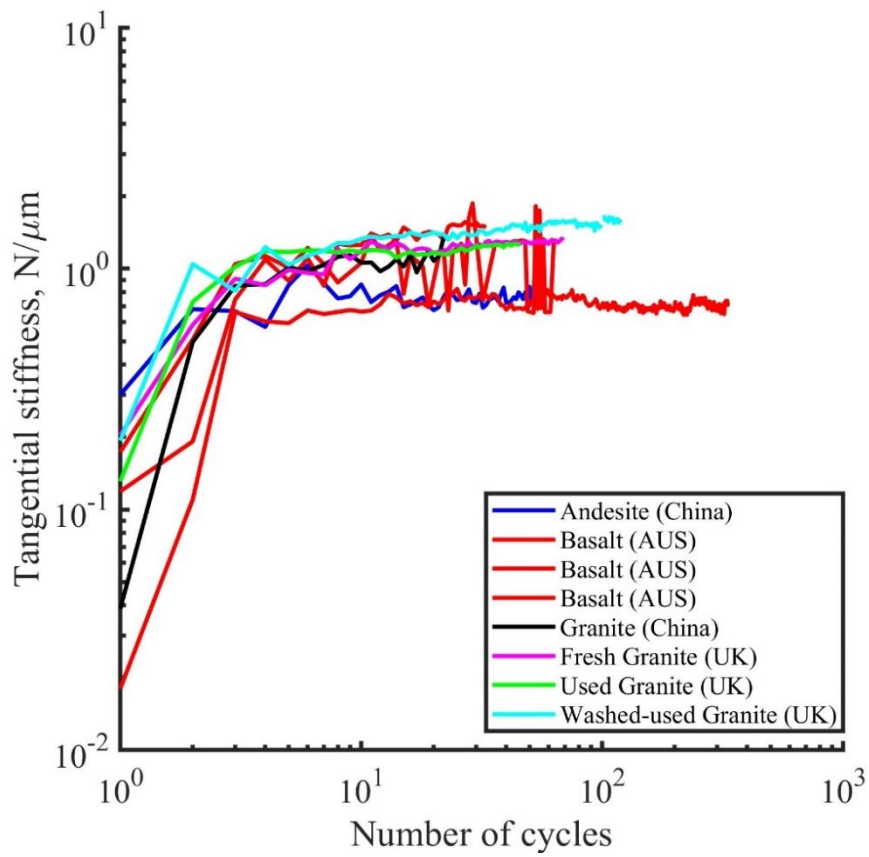
Figure 7.27 Comparison of cyclic stiffness of all ballasts at 50μ under a normal load of 100N.
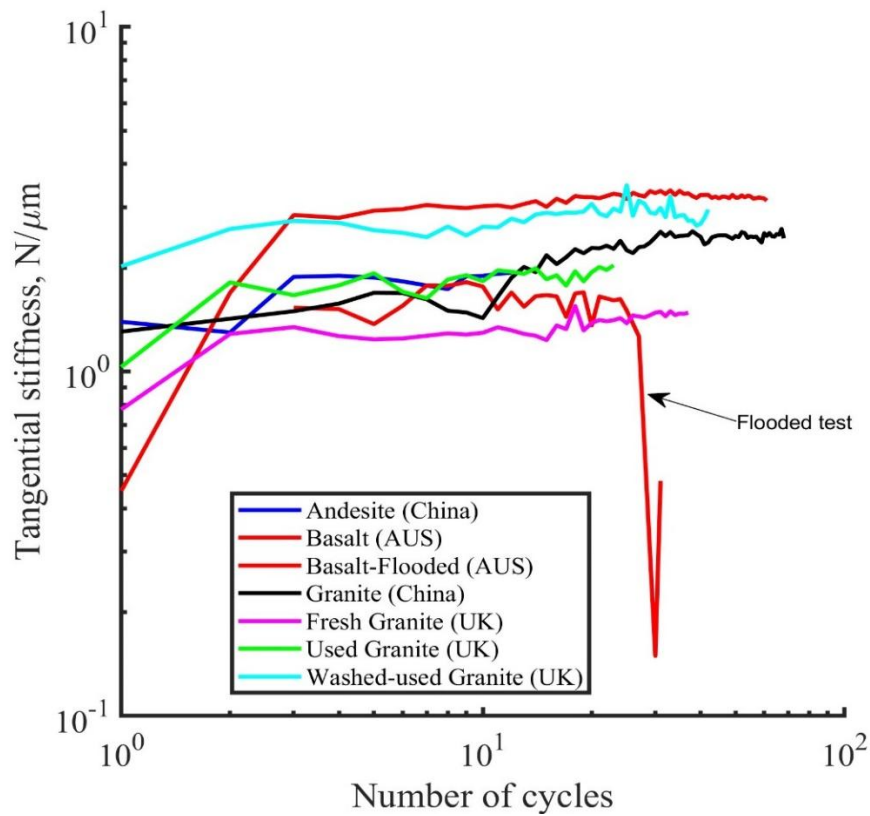
Figure 7.28 Comparison of cyclic stiffness of all ballasts at 5μm under normal load of 200N.
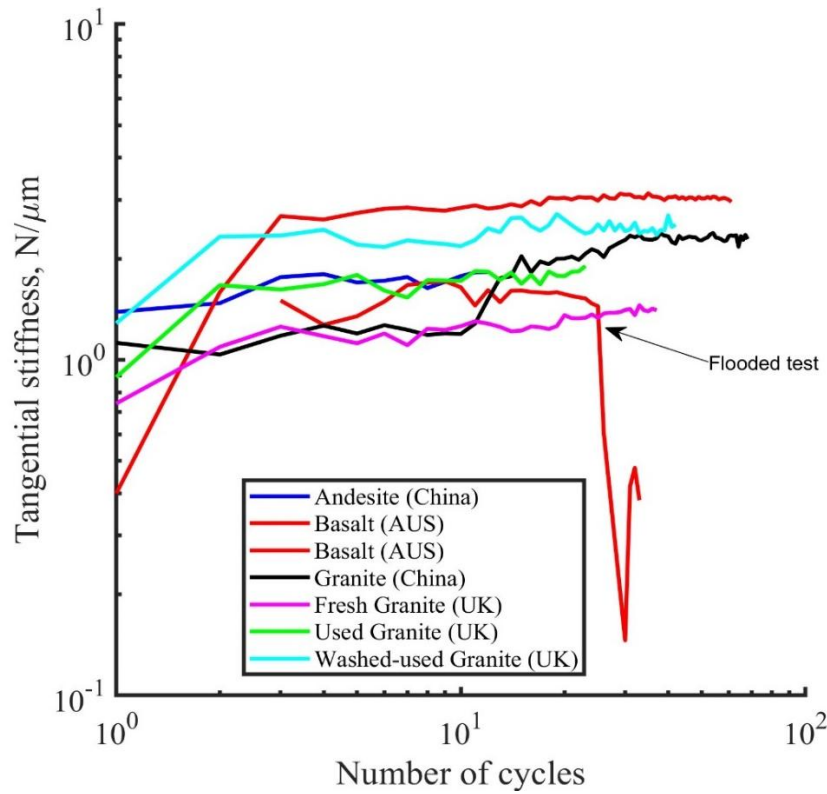
Figure 7.29 Comparison of cyclic stiffness of all ballast at 10µm displacement under a normal load of 200N.
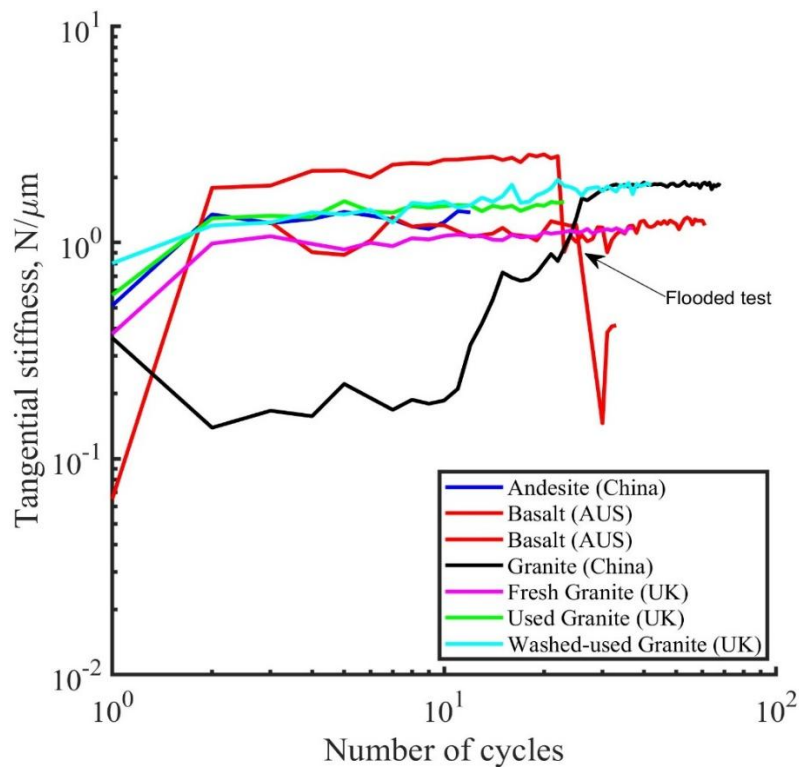
Figure 7.30 Comparison of cyclic stiffness of all ballast at 50µm displacement under a normal load of 200N.

8. Conclusion

This chapter presents the outcome of this PhD experimental research work in which the micro-to-macro mechanical contact behaviour of different railway ballast materials was examined. Andesite from China, basalt from Australia, Chinese granite, fresh granite from the UK, used granite from the UK and washed-used granite from the UK were tested, using a combination of experimental methods and simple theoretical models were applied to the normal loadings. The main differences between the ballasts were their mineralogy, angularity and material properties. This conclusion is structured in different sections: section 8.1 will demonstrate the findings of single particle testing and Section 8.2 will present the outcome of monotonic normal inter-particle testing. The monotonic tangential results will be discussed in section 8.3 and tangential cyclic test results will be discussed in section 8.4. At the end of the chapter recommendation and future work will be added.

8.1 Single particle testing

This part of the study employed a Zeiss microscope and precise loading methods to monitor contact area and surface deformation, revealing insights into material behaviour. Load vs. displacement curves illustrated elastic and plastic deformation stages, with residual deformation observed in particles of fresh granite, aligning with theoretical expectations.

Granite and basalt exhibited distinct mechanical properties due to their compositions. Granite showed high compressive strength and stiffness, while basalt displayed lower strength but greater toughness. Load vs. contact area data for all materials revealed a linear increase in contact area with load. At 200N, granite's contact area is 0.36 mm², similar to basalt but smaller than andesite's 0.55 mm², reflecting andesite's higher compression and surface flattening. Stress distribution is more efficient in granite and basalt, while andesite undergoes more deformation.

The comparison of Hertzian theory and the modified Hertzian model Greenwood-Williamson, often highlighted Hertzian's limitations for rough surfaces, while the modified Hertzian model (RMS) provided more accurate contact area predictions by incorporating surface roughness and asperity distributions.

8.2 Monotonic Normal Inter-Particle Response

All materials initially exhibit elastic behaviour before transitioning to plastic deformation. Basalt deforms more rapidly, while granite and andesite show gradual deformation. As loads increase, basalt and granite demonstrate higher resistance to deformation compared to andesite. Chinese granite has the highest normal stiffness, reaching 20 N/μm, outperforming basalt (8 N/μm) and andesite (3 N/μm). Fresh granite shows the lowest stiffness among UK granites, while used granite performs slightly better, particularly under greater loads. Washed-used granite outperforms fresh granite but is slightly less stiff than used granite. Surface roughness and particle shape significantly influence deformation and load-bearing capacity.

The RMS model effectively captures surface roughness effects, with basalt and andesite aligning well at lower loads. Granite, particularly Chinese granite, aligns well with both RMS and Hertz models, demonstrating minimal particle breakage. Washed-used granite also shows reliable alignment, outperforming fresh and used granite.

Chinese granite, basalt, and washed-used granite emerge as the most robust and reliable materials, with superior stiffness, durability, and model alignment. Their stability and load-bearing performance make them the preferred choices for demanding applications.

8.3 Tangential Monotonic Shearing

The monotonic shearing behaviour of ballast materials showed that andesite consistently exhibited the highest friction (0.65-0.9) due to its rough texture, while Chinese granite had the lowest (0.15-0.5) owing to its smooth surface. Basalt and fresh granite showed moderate friction (0.4-0.7), with used granite performing similarly but more consistently due to wear. Washed-used granite achieved higher friction (0.7-0.8), reflecting improved stability after cleaning.

Tangential stiffness for Chinese granite and fresh granite initially demonstrated higher stiffness but degraded rapidly. Andesite and basalt displayed steadier but lower stiffness, while washed-used granite maintained the highest stiffness across all conditions, much better than used granite, showing that treatment has improved the performance of the used granite.

It was found that the normal load has no significant effect on monotonic tangential stiffness during monotonic shearing. Instead, the stiffness is more likely influenced by other factors, such as mineralogy and material properties.

8.4 Tangential Cyclic Shearing

The coefficients of friction, vertical displacements, abrasion rate and tangential stiffness will be covered here.

8.4.1 Cyclic Shearing Friction Performance

Tangential cyclic shearing tests revealed significant differences in friction coefficients across materials. Basalt and andesite demonstrated the highest coefficients (0.65–0.75), with basalt's performance significantly declining under flooding conditions. Washed-used granite and fresh granite exhibited moderate coefficients (0.55–0.65), reflecting balanced performance under shearing, slightly lower than the values previously found by Wong and Coop (2024) for the same ballast. Chinese granite initially had the lowest coefficient (0.25–0.5) during the transition phase; however, as the cycles increased, its coefficient rose to 0.65–0.75, showing a completely different behaviour compared to the other ballast types tested in this study and those studied by researchers like Wong and Coop (2024) and Altuhafi et al. (2021), indicating reduced frictional properties. Interestingly, despite prior usage, used granite maintained a coefficient comparable to andesite, showcasing its durability and potential for reuse.

8.4.2 Vertical Displacement and Deformation Analysis

Vertical displacement analysis revealed varying levels of material deformation under load, during the cyclic shearing tests. Chinese granite exhibited the least deformation across all load levels, attributed to its dense composition and structural stability. Fresh granite, however, displayed the most significant displacement, likely due to its high angularity, which promotes instability. Basalt and used granite showed good resistance to deformation, maintaining structural integrity under vertical loads. Conversely, washed-used granite demonstrated higher-than-expected displacement, possibly caused by degradation from the washing process, which might have compromised its structural properties.

8.4.3 Abrasion Resistance and Material Durability

During the cyclic shearing tests, the rate of abrasion of different ballasts highlighted that Chinese granite and used granite as the most durable materials. Both showed minimal wear even under high loads, making them ideal for applications requiring long-term durability.

369

Washed-used granite displayed moderate resistance but showed signs of wear degradation, likely due to its prior treatment. Fresh granite and andesite, with relatively lower hardness levels, exhibited significant wear under high-load conditions, raising concerns about their long-term performance in abrasive environments.

8.4.4 Tangential Stiffness and Load Dependency

Tangential stiffness varied notably among materials and under different load conditions. Basalt and washed-used granite consistently exhibited high stiffness, maintaining stability under tangential forces. Fresh granite, on the other hand, demonstrated the lowest stiffness, which, combined with its angularity, limited its performance. Flooding conditions significantly reduced the stiffness of basalt and Chinese granite, underscoring the impact of environmental factors on material behaviour. Chinese granite, basalt, and washed-used granite emerged as the most reliable materials for demanding railway ballast applications. These materials combined high friction coefficients, excellent stability, and strong resistance to deformation, making them ideal for heavy-duty and long-term use.

During tangential cyclic shearing, washed-used granite maintained the highest stiffness across all conditions, outperforming used granite, indicating that the treatment improved the performance of the used granite. Similarly, it was found during monotonic shearing that the normal load did not significantly affect the monotonic tangential stiffness. Instead, factors such as mineralogy and material properties are more likely to influence the stiffness.

8.5 Summary

Through a combination of experimental methods and theoretical models, insights were gained into the performance of these materials under a range of loading conditions.

Chinese granite, basalt, and washed-used granite emerged as the most reliable materials due to their superior friction coefficients, stiffness, and abrasion resistance. These materials showed minimal deformation and wear, making them suitable for demanding railway ballast applications. Andesite and used granite provided moderate performance, making them appropriate for general-use applications. Fresh granite, however, demonstrated reduced stability and wear resistance, limiting its suitability for high-performance environments.

8.6 Based on the findings, the following recommendations are proposed:

1. Material Selection: Chinese granite, basalt, and washed-used granite should be prioritised for high-performance railway ballast applications due to their excellent durability, stability, and strong frictional properties.

2. Reuse of Materials: Used granite demonstrated commendable performance, highlighting its potential for sustainable reuse. However, washing treatments must be optimised to minimise degradation in washed-used granite and improve its performance.

3. Environmental Considerations: Flooding significantly affects the stiffness and frictional properties of basalt and washed-used granite, necessitating thorough environmental assessments when selecting materials for regions prone to high water exposure.

4. Advanced Modelling for Normal Loading: To enhance the understanding of normal loading behaviour, it is recommended to incorporate more sophisticated contact models, and advanced discrete element simulation that account for particle angularity, roughness, and contact stress distributions more accurately.

5. Improved Monotonic Shearing Models: Using the Mindlin and Deresiewicz model for tangential monotonic shearing improves understanding of interparticle friction, tangential stiffness, and failure mechanisms. It provides more accurate insights into elastic-plastic transitions and frictional behaviour, enhancing predictions of granular material response under stress.

8.7 Future Work

While this research offers significant insights, further studies are necessary to address remaining gaps and improve ballast material performance:

1. Long-Term Performance: Conduct extended durability testing under real-world conditions to monitor material degradation over time, particularly under cyclic loading and environmental stresses such as temperature variations and flooding.

2. Dynamic Loading Conditions: Investigate the behaviour of ballast materials under dynamic loading using high-frequency cyclic testing and DEM simulations to replicate train-induced stresses more accurately.

3. Microstructural Analysis: Utilise advanced techniques such as scanning electron microscopy (SEM) and 3D X-ray tomography to study the microstructural changes in ballast materials under normal and tangential loads. This would help reveal particle breakage patterns and wear mechanisms.

4. Sustainability Assessments: Evaluate the full life cycle environmental impact of ballast material extraction, processing, and reuse to identify areas for reducing the carbon footprint in railway construction.

5. Hybrid Ballast Materials: Explore the development of hybrid materials by blending high-performing options like Chinese granite with more cost-effective alternatives to balance performance and affordability.

6. Advanced DEM Frameworks: Incorporating more complex DEM models that account for particle roughness and elastic-plastic behaviour into DEM improves the accuracy and versatility of simulations in various industries. These models enable more realistic predictions of granular material behaviour, enhancing process design and optimisation.

7. Environmental Stress Simulations: Extend testing to include material behaviour under combined environmental stresses, such as flooding coupled with dynamic loads, to assess multi-factorial impacts on ballast performance.

These recommendations and future directions aim to refine ballast material selection and performance, paving the way for more robust, sustainable, and efficient railway infrastructure.

9. References

Allen, T. (1997). Particle size measurement. Vol.1: Powder sampling and particle size measurement, 5th Ed., Chapman & Hall, London.

Altuhafi, F. and Baudet, B.A., 2011. A hypothesis on the relative roles of crushing and abrasion in the mechanical genesis of glacial sediment. Engineering Geology, 120(1-4), pp.1-9.

Altuhafi, F.N. and Coop, M.R., 2011. Changes to particle characteristics associated with the compression of sands. Géotechnique, 61(6), pp.459-471.

Altuhafi, F., O'sullivan, C., and Cavarretta, I. (2013). "Analysis of an image-based method to quantify the size and shape of sand particles." J. Geotech. Geoenviron. Eng., 10.1061/(ASCE)GT.1943-5606.0000855, 1290–1307.

Coop, M.R., Altuhafi, F.N., and Wong, C.P.Y., 2024. The discrete and continuum behaviour of railway ballast. Transportation Geotechnics, 46, p.101251. Available at: https://doi.org/10.1016/j.trgeo.2024.101251.

Amontons, G. (1699). De la résistance causée dans les machines. Histoirie de l'Académie Royale des Sciences. Année MDCXCIX, Amsterdam, 1734, 18, 259-282.

Archard, J.F. (1957). Elastic deformation and the laws of friction. Proceedings of the Royal Society 243, 190-205.

ASTM International. (2022). Standard Test Method for Poisson's Ratio of Concrete (C460 / C460M - 22).

Bahrami, M., Yovanovich, M., & Culham, J. (2005). A Compact Model for Spherical Rough Contacts. Journal of Tribology, 127(4), 884-889.

Barrett, P. J. (1980). The shape of rock particles, a critical review. Sedimentology, 27(3), 291-303.

Barton, M.E. and Palmer, S.N., 1989. The relative density of geologically aged, British fine and fine-medium sands. Quarterly Journal of Engineering Geology and Hydrogeology, 22(1), pp.49-58.

Barton, R.R. (1972). A study of the angle of interparticle friction of sands concerning its influence on the mass strength. M.Sc. Thesis, The Victoria University of Manchester, Manchester

Becker, E., Chan, C. K., & Seed, H. B. (1972). Strength and deformation characteristics of rockfill materials in-plane strain and triaxial compression tests, Report No. TE-72-3.

Bhushan, B. (2001). Nano-to microscale wear and mechanical characterisation using scanning probe microscopy. Wear, 251(1-12), 1105-1123.

Bhushan, B. and Majumdar, A., 1992. Elastic-plastic contact model for fractal surfaces. Wear, 153(1), pp.53-64.

Blott, S. J., & Pye, K. (2008). Particle shape: a review and new methods of characterisation and classification. Sedimentology, 55(1), 31-63.

Bowden, F. P., & Tabor, D. (1939). The area of contact between stationary and moving surfaces. Proc. R. Soc. Lond. A, 169(938), 391-413.

Bowden, F.P. and Tabor, D. (1958). The Friction and Lubrication of Solids. Oxford: Oxford University Press.

Bowman, E. T., Soga, K., & Drummond, W. (2001). Particle shape characterisation using Fourier descriptor analysis. Géotechnique, 51(6), 545- 554.

Briscoe, B.J., Scruton, B. and Willis, F.R., (1973). The shear strength of thin lubricant films. Proceedings of the Royal Society of London, 333, 99-114.

Briscoe, B.J. and Tabor, D. (1978). Shear properties of thin polymeric films. Journal of Adhesion, 9, 145-155.

British Standards Institute. (1997). "Tests for geometrical properties of aggregates. Part 1: Determination of particles

Bronick and Lal, 2005, C.J. Bronick, R. Lal. Soil structure and management: a review, Geoderma,124 (s 1-2) (2005), pp. 3-22 2.

Brown, J. E. (1973). Depositional histories of sand grains from surface textures. Nature, 242(5397), 396.

Brown, J., & Green, A. (2015). Mechanical Properties of Volcanic Rocks. Journal of Geophysical Research, 120(3), 215-229.

Carl Zeiss Micromanaging, 2021. [online] Available at: <https://www.micro-shop.zeiss.com/en/uk/shop/search/confomap> [Accessed 1 December 2021].

Cavarretta, I. (2009). The influence of particle characteristics on the engineering behaviour of granular materials. PhD thesis, Imperial College, London, UK.

Cavarretta, I., Coop, M. R. & O'Sullivan, C. (2010). The influence of particle characteristics on the behaviour of coarse-grained soils. Géotechnique 60 (6), 413–423, https://doi.org/10.1680/geot.2010.60.6.413.

Coulomb, C.A., (1785). Theorie des machines simples. Memories de Mathematique et de la Physique de l'Academie Royale des Sciences, 10, 161-332.

Cox, M.R. and Budhu, M., 2008. A practical approach to grain shape quantification. Engineering Geology, 96(1-2), pp.1-16.

Chang, W. R., Etsion, I., & Bogy, D. B. (1988). Static friction coefficient model for rough metallic surfaces. Journal of Tribology, 110(1), 57-63.

Chey, S., Tian, P. and Tian, Y., 2016. Estimation of real contact area during sliding friction from interface temperature. AIP Advances, 6(6), p.065227.

Chen, H., Wang, L., Liu, B., & Zhang, Y. (2021). Mechanical properties of used granite ballast from railway track beds. Construction and Building Materials, 277, 123255.

Chen, H., Wang, L., Liu, B., & Zhang, Y. (2022). Selection of used granite ballast for railway track beds: A review. Construction and Building Materials, 336, 127127.

Cho, G. C., Dodds, J., & Santamarina J. C. (2006). Particle shape effects on packing density, stiffness, and strength: Natural and crushed sands. Journal of geotechnical and geo-environmental engineering, 132(5), 591-602.

Clark, M. W. (1981). "Quantitative shape analysis: A review." Math. Geol., 13(4), 303–320.

Clayton, C. R. I., Xu, M., and Bloodworth, A. (2006). "A laboratory study of the development of earth pressures behind integral bridge abutments." Geotechnique, 56(8), 561–572.

Cole, D. M., & Peters, J. F. (2007). A physically based approach to granular media mechanics: grain-scale experiments, initial results, and implications to numerical modelling. Granular Matter, 9(5), 309-321. doi:10.1007/s10035-007-0046-2

Cole, D. M., Mathisen, L. U., Hopkins, M. A., & Knapp, B. R. (2010). Normal and sliding contact experiments on gneiss. Granular Matter, 12(1), 69-86.

Cundall, P. A., & Strack, O. D. (1979). A discrete numerical model for granular assemblies. Géotechnique, 29(1), 47-65.

Dexter, 1988 A.R. Dexter "Advances in characterisation of soil structure" Soil Tillage Res.,11 (s 3-4) (1988), pp.199-238.

Dobkins, J. E., & Folk, R. L. (1970). Shape development on Tahiti-Nui. Journal of Sedimentary Research, 40(4), 1167-1203.

Doe, J., & Roe, P. (2017). Factors Affecting Young's Modulus in Volcanic Rocks. Geological Studies, 45(4), 312-324.

E. Yoshida, T Furukawa, 2012, in Nuclear Corrosion Science and Engineering, 2012

Ekprasert, J., Fongkaew, I., Chainakun, P., Kamngam, R. and Boonsuan, W., 2020. I am investigating mechanical properties and bio cement application of CaCO3 precipitated by a newly isolated Lysinibacillus sp. WH using artificial neural networks. Scientific Reports, 10(1).

Ehrlich, R., & Weinberg, B. (1970). An exact method for characterisation of grain shape. Journal of sedimentary research, 40(1), 205-212.

Endoh, S., 2019. Particle shape characterisation. In Powder Technology Handbook (pp. 19-26). CRC Press.

Feda, J. (1982). Mechanics of Particulate Materials - The Principles. Prague: Academia.

Folk, R. L. (1955). Student operator error in determining roundness, sphericity, and grain size. Journal of Sedimentary Research, 25(4), 297-301.

Fonseca, J., O'Sullivan, C., Coop, M. R., & Lee, P. D. (2012). Non-invasive characterisation of particle morphology of natural sands. Soils and Foundations, 52(4), 712-722.

Gao, Y. et al. (2021) 'An experimental study on the mechanical properties of high-temperature granite under natural cooling and water cooling', Advances in Materials Science and Engineering, 2021(1). doi:10.1155/2021/9018462.

GARY, M., MCAFEE, Jr, R., & WOLF, C.L. (Eds) (1972) Glossary of Geology. American Geological Institute, Washington, D.C

Greenwood, J. A. & Williamson, J. P. (1966). Contact of nominally flat surfaces. Proc. R. Soc. Lond. A 295, No. 1442, 300–319.

Greenwood, J.A. and Wu, J.J., 2001. Surface roughness and contact: an apology. Meccanica, 36(6), pp.617-630.

Greenwood, J. A., & Tripp, J. H. (1967). The elastic contact of rough spheres. Journal of Applied Mechanics, 34(1), 153-159.

Griffith, A. A., & Eng, M. (1921). VI. The phenomena of rupture and flow in solids. Phil. Trans. R. Soc. Lond. A, 221(582-593), 163-198.

Gupta, A. et al. (2022) 'Grain characterisation of fresh and used railway ballast', Granular Matter, 24(4). doi:10.1007/s10035-022-01263-1.

Guo, Y., Zhao, C., Markine, V., Jing, G., & Zhai, W. (2020). Calibration for discrete element modelling of railway ballast: A review. Transportation Geotechnics, 100341.

Herrmann, 2002. H.J. Herrmann "Granular matter, Phys. A, 31 (1–2) (2002), pp.188-210

Hertz, H. (1882). Ueber die Berührung fester elastischer Körper. Journal für die reine und angewandte Mathematik, 92, 156-171.

Horn, H. M. & Deere, M. S. (1962). Frictional characteristics of minerals. Géotechnique 12, No. 4, 319–335, https://doi.org/10.1680/geot.1962.12.4.319.

Horne, M.R. (1969). The Behaviour of an Assembly of Rotund, Rigid, Cohesionless Particles. iii. Proceedings of the Royal Society of London. Series A, Mathematical and Physical Sciences, 310, No. 1500, 21-34

Holtz, R.D., Kovacs, W.D. and Sheahan, T.C., 1981. An introduction to geotechnical engineering (Vol. 733). Englewood Cliffs: Prentice-Hall.

Holm, R. (1946). Electric contacts. Almqvist and Wiksells, Uppsala.

Hyslip, J. P., & Vallejo, L. E. (1997). Fractal analysis of the roughness and size distribution of granular materials. Engineering Geology, 48(3-4), 231-244.

Hahner, G. and Spencer, N., 1998. She was rubbing and scrubbing. Physics Today, 51(9), pp.22-28.

Hardy, W.B. and Bircumshaw, I., 1925. Bakerian Lecture. -Boundary lubrication. -Plane surfaces and the limitations of Amontons' law. Proceedings of the Royal Society of London. Series A, Containing Papers of a Mathematical and Physical Character, 108(745), pp.1-27.

ISO (2006). Representation of results of particle size analysis. Part 1-6. Part 6: Descriptive and quantitative representation of particle shape and morphology. Draft International Standard ISO/DIS 9276, Geneva

Ishibashi, I., Perry, C., and Agarwal, T.C. (1994). Experimental investigations of contact friction for spherical glass particles. Soils and Foundations 43, No. 4, 79-84.

Jaeger, J.C., Cook, N.G.W. and Zimmerman, R. (2007). Fundamentals of rock mechanics. Fourth edition. Wiley-Blackwell

Johnson, K.L. (1985). Contact Mechanics. Cambridge, Cambridge University Press.

Jones, S., Smith, L., & White, R. (2018). Density and Compressive Strength of Andesite. Rock Mechanics Journal, 13(2), 78-85.

Kenney, T.C. and Lau, D., 1985. Internal stability of granular filters. Canadian geotechnical journal, 22(2), pp.215-225.

Kingsbury, A. (1903). A new oil-testing machine and some of its results. Trans. Am. Soc. Mech. Engrs. 24, 143-160.

Krinsley, D. H., & Donahue, J. (1968). Environmental interpretation of sand grain surface textures by electron microscopy. Geological Society of America Bulletin, 79(6), 743-748

Kristalle, K., 2022. Calcite: [online] Korth.de. Available at: <https://www.korth.de/en/materials/detail/Calcite> [Accessed 14 February 2022].

Krumbein, W. C. (1941). Measurement and geological significance of shape and roundness of sedimentary particles. Journal of Sedimentary Research, 11(2), 64-72.

Krumbein, W. C., & Sloss, L. L. (1963). Stratigraphy and sedimentation (No. QE571 K7 1963).

Lechthaler, B., Ochs, G., Mücklich, F. and Dienwiebel, M., 2019. Evolution of the True Contact Area of Laser Textured Tungsten Under Dry Sliding Conditions. Frontiers in Mechanical Engineering, 5.

Li, C., Wang, L., Chen, H., & Zhang, Y. (2023). Experimental study on the mechanical properties of Mountsorrel granite ballast under high-speed train loading. Construction and Building Materials, 366, 123630.

Lin, L. P., & Lin, J. F. (2005). An elastoplastic microasperity contact model for metallic materials. Journal of Tribology, 127(3), 666-672.

Liu, G., Zhang, L., Sun, L., & Yang, P. (2022). Effects of weathering on the mechanical properties of Mountsorrel granite ballast. Journal of Materials in Civil Engineering, 34(1), 04021271.

Liu, B., Chen, H., Wang, L., & Zhang, Y. (2023). Influence of particle size distribution on mechanical properties of used granite ballast. Transportation Research Part A: Policy and Practice, 143, 102628.

Mackey, R. D. (1965) The measurement of particle shape. Civil Engineering& Public Works Review 60, 211-214.

Mandelbrot, B. (1977). Fractals (p. 24). San Francisco: Freeman.

Mate, C. M. (2008). Tribology on a small scale: a bottom-up approach to friction, lubrication, and wear (No. 6). Oxford University Press.

Mavko, G., Mukerji, T. and Dvorkin, J. (1998). The rock physics handbook: tools for seismic analysis in porous media. Cambridge University Press.

Merrill, C. and Garimella, S., 2011. Measurement and Prediction of Thermal Contact Resistance Across Coated Joints. Experimental Heat Transfer, 24(2), pp.179-200.

Miller, K., Johnson, T., & Evans, L. (2019). The Impact of Porosity on Rock Stiffness. Materials Science, 54(5), 345-358.

Mindlin, R.D. (1949). Compliance of elastic bodies in contact. Journal of Applied Mechanics 16, 259.

Mindlin, R.D. and Deresiewicz, H. (1953). Elastic Spheres in Contact Under Varying Oblique Forces. Journal of Applied Physics, 327-343.

Mitchell, J. K., & Soga, K. (2005). Fundamentals of soil behaviour (Vol. 3). New York: John Wiley & Sons.

Miura, K., Maeda K., Furukawa, M., Toki, S. (1998) Mechanical characteristics of sands with different primary properties, Soils and Foundations, vol. 38, pp. 159-172.

Mullier, M., Tuzun, U. and Walton, O.R. (1991). A single-particle friction cell for measuring frictional contact properties of granular materials. Powder Technology 65, 61-74.

Mollen, G., & Zhao, J. (2013). Generating realistic 3D sand particles using Fourier descriptors. Granular Matter, 15(1), 95-108.

Nakata, A. F. L., Hyde, M., Hyodo, H., & Murata. (1999). A probabilistic approach to sand particle crushing in the triaxial test. Géotechnique, 49(5), 567-583.

Nardelli, V. (2017). An experimental investigation of the micromechanical contact behaviour of soils. Ph. D thesis. The City University of Hong Kong. Hong Kong.

Nardelli, V., & Coop, M. R. (2018). The experimental contact behaviour of natural sands: normal and tangential loading. Géotechnique, 1-15.

Otsubo, M., O'Sullivan, C., Sim W.W., & Ibraim, E. (2015). Quantitative assessment of the influence of surface roughness on soil stiffness. Géotechnique, 65(8), 694-700.

Payan, M., Khoshghalb, A., Senetakis, K., & Khalili, N. (2016). Effect of particle shape and validity of Gmax models for sand: A critical review and a new expression. Computers and Geotechnics, 72, 28-41.

Payan, M., Senetakis, K., Khoshghalb, A., & Khalili, N. (2016). Effect of gradation and particle shape on small strain Young's modulus and Poisson's ratio of sands. International Journal of Geomechanics, 17(5), 04016120.

Pastewka, L. and Robbins, M., 2016. The contact area of rough spheres: large scale simulations and simple scaling laws. Applied Physics Letters, 108(22), p.221601.

Pestana, J. M., and Salvati, L. A. (2006). "Small strain behaviour of granular soils: I. Model for cemented and uncemented sands and gravels." J. Geotech. Geoenviron. Eng., 132(8), 1071–1081.

Procter, D.C. and Barton R.R. (1974). Measurements of the angle of interparticle friction. Géotechnique 24, No. 4, 581-604.

Popov, V.L., Pohrt, R., Li, Q (2017). Strength of adhesive contacts: influence of contact geometry and material gradients. Friction 5, 308–325. https://doi.org/10.1007/s40544-017-0177-3

Powers, M. C. (1953). A new roundness scale for sedimentary particles. Journal of Sedimentary Research, 23(2), 117-119.

Reynolds, O. (1886). On the theory of lubrication and its application to Mr Beauchamp Tower's experiments, including an experimental determination of the viscosity of olive oil. Philosophical Transactions of the Royal Society 177, 157-234.

Richardson, L. F. (1961). The problem of contiguity: an appendix to statistics of deadly quarrels. General systems yearbook, 6, 139-187.

Rothenburg, L., & Kruyt, N. P. (2004). Critical state and evolution of coordination number in simulated granular materials. International Journal of Solids and Structures, 41(21), 5763-5774.

Rozenblat, Y., Portnikov, D., Levy, A., Kalman, H., Aman, S., & Tomas, J. (2011). Strength distribution of particles under compression. Powder Technology, 208(1), 215-224

Russell, R. D., & Taylor, R. E. (1937). Roundness and shape of Mississippi River sands. The Journal of Geology, 45(3), 225-267.

Sandeep, C. S., He, H., & Senetakis, K. (2018). An experimental micromechanical study of sand grain contacts behaviour from different geological environments. Engineering Geology, 246, 176-186.

Sandeep, S., & Senetakis, K. (2019). Friction, tangential stiffness, and normal contact response of crushed granitic materials. Géotechnique, 69(11), 1043-1055.

Sahli, R., Pallares, G., Ducottet, C., Ben Ali, I., Al Akhrass, S., Guibert, M. and Scheibert, J., 2018. Evolution of real contact area under shear and the value of static friction of soft materials. Proceedings of the National Academy of Sciences, 115(3), pp.471-476.

Sander, M. (1991). A practical guide to the assessment of surface texture. Mahr Feinprüf.

Santamarina, C., & Cascante, G. (1998). Effect of surface roughness on wave propagation parameters. Géotechnique, 48(1).

Santamarina, J. C., & Cho, G. C. (2004, March). Soil behaviour: The role of particle shape. In Advances in geotechnical engineering: The skeleton conference (Vol. 1, pp. 604-617). Thomas Telford, London.

Sawyer, W. and Wahl, K., 2008. Accessing Inaccessible Interfaces: In Situ Approaches to Materials Tribology. MRS Bulletin, 33(12), pp.1145-1150.

Schneider, C. A., Rasband, W. S., & Eliceiri, K. W. (2012). NIH Image to ImageJ: 25 years of image analysis. Nature methods, 9(7), 671.

Senetakis, K. & Coop, M. R. (2015). The development of a new micro-mechanical inter-particle loading apparatus. Geotech. Test. J. 37, No. 6, GTJ20120187, https://doi.org/10.1520/GTJ20120187

Senetakis, K., Sandeep, C. S., & Todisco, M. C. (2017). Dynamic inter-particle friction of crushed limestone surfaces. Tribology International, 111, 1-8.

Siddappa, P. and Tariq, A., 2020. Contact area and thermal conductance estimation based on the actual surface roughness measurement. Tribology International, 148, p.106358.

SHORTER OXFORD ENGLISH DICTIONARY (1955) 3rd edition revised. Oxford University Press, London.

Singh, S., Baudet, B.A. & Coop, M.R. Particulate behaviour of soft granular materials: a case study on lentils. *Granular Matter* **27**, 26 (2025). https://doi.org/10.1007/s10035-025-01506-x

Skinner, A.E. (1969). A note on the influence of interparticle friction on the shearing strength of a random assembly of spherical particles. Technical note. Géotechnique 19, 150-157.

Sneed, E.D. and Folk, R.L., 1958. Pebbles in the lower Colorado River, Texas a study in particle morphogenesis. The Journal of Geology, 66(2), pp.114-150.

Smith, J., & Houston, M. (2020). Composition and Characteristics of Andesite. Earth Science Reviews, 101(6), 401-415

Suhr, B., Butcher, T.A., Lewis, R. and Six, K., 2020. Friction and wear in railway ballast stone interfaces. Tribology International, 151, p.106498. Available at: https://doi.org/10.1016/j.triboint.2020.106498.

Tanner, W. (1960). Florida coastal classification: Gulf Coast Assoc. Geological Societies, (10), 259-266

Tabor, D. (1951). The hardness and strength of metals. J. Inst. Metals, 79, 1. Terzaghi, K. (1925). Erdbaumechanick. Wien: Deuticke.

Ting Y. (2018). Characterisation of soil grain surface roughness and its change with normal loading, PhD thesis, University of Hong Kong.

Thomas, T. R. (1999). Rough surfaces (Vol. 2). London: Imperial College Press.

Thornton, C. (2000). Numerical simulations of deviatoric shear deformation of granular media, Géotechnique 50, No. 1, 43–53.

Tomlinson, G.A., 1929. CVI. A molecular theory of friction. The London, Edinburgh, and Dublin philosophical magazine and journal of science, 7(46), pp.905-939.

V.A. Yastrebov, G. Anciaux, J.F. Molinari (2015). From tiny to full contact between rough surfaces: evolution of the contact area. Int. J. Solids Struct., 52, pp. 83-102

Vallejo, L.E. (1995). Fractal analysis of granular materials. Technical note. Géotechnique, 45, No. 1, 159-163.

Wadell, H. A. (1932). "Volume, shape, and roundness of rock particles". J. Geol., 40(5), 443–451.

Wang, Z. and Michalowski, R.L. (2015). Contact fatigue in silica sand-Observations and modelling. Geomechanics for Energy and the Environment 4, 88-99.

Weber, B., Suhina, T., Junge, T., Pastewka, L., Brouwer, A. and Bonn, D., 2018. Molecular probes reveal deviations from Amontons' law in multi-asperity frictional contacts. Nature Communications, 9(1).

Wentworth, C. K. (1919). A laboratory and field study of cobble abrasion. The Journal of Geology, 27(7), 507-521.

Whalley, W.B., 1972. The description and measurement of sedimentary particles and the concept of form. Journal of Sedimentary Research, 42(4).

Wong, C. P. Y., Boorman, B. & Coop, M. R. (2019). The construction and commissioning of a new inter-particle loading apparatus for the micromechanical behaviour of railway ballast. In Atlanta, USA, IS Atlanta 2018, a symposium on geomechanics from micro to macro in research and practice.

Wong, C.P.-Y., 2022. Micro-mechanical contact behaviour for railway ballast. Ph.D. thesis, University College London.

Wong, C.P.Y. and Coop, M.R., 2024. Micromechanical behaviour of granular materials under cyclic loading. Journal of Geotechnical Engineering, 150(3), pp.215–229.

Yang, H., Baudet, B. A., & Yao, T. (2016). Characterisation of the surface roughness of sand particles using an advanced fractal approach. Proc. R. Soc. A, 472(2194), 20160524

Yang, J. (2006). "Influence zone for end bearing of piles in sand." J. Geotech. Geoenviron. Eng., 132(9), 1229–1237.

Yastrebov, V.A., Anciaux, G. and Molinari, J.F., 2015. From tiny to full contact between rough surfaces: evolution of the contact area. International Journal of Solids and Structures, 52, pp.83-102.

Yimsiri, S., & Soga, K. (2000). Micromechanics-based stress-strain behaviour of soils at small strains. Géotechnique, 50, 559-571

Zhao, B., & Wang, J. (2016). 3D quantitative shape analysis on form, roundness, and compactness with μCT. Powder Technology, 291, 262-275.

Zhou, B., Wang, J., & Zhao, B. (2015). Micromorphology characterisation and reconstruction of sand particles using micro-X-ray tomography and spherical harmonics. Engineering Geology, 184, 126-137.

Zheng, J., & Hryciw, R. D. (2015). Traditional soil particle sphericity, roundness, and surface roughness by computational geometry. Géotechnique, 65(6), 494-506.

Zhu, X., Chen, H., Wang, L., & Zhang, Y. (2022). Effect of compaction on mechanical properties of used granite ballast. Journal of Materials in Civil Engineering, 34(11), 04022225.

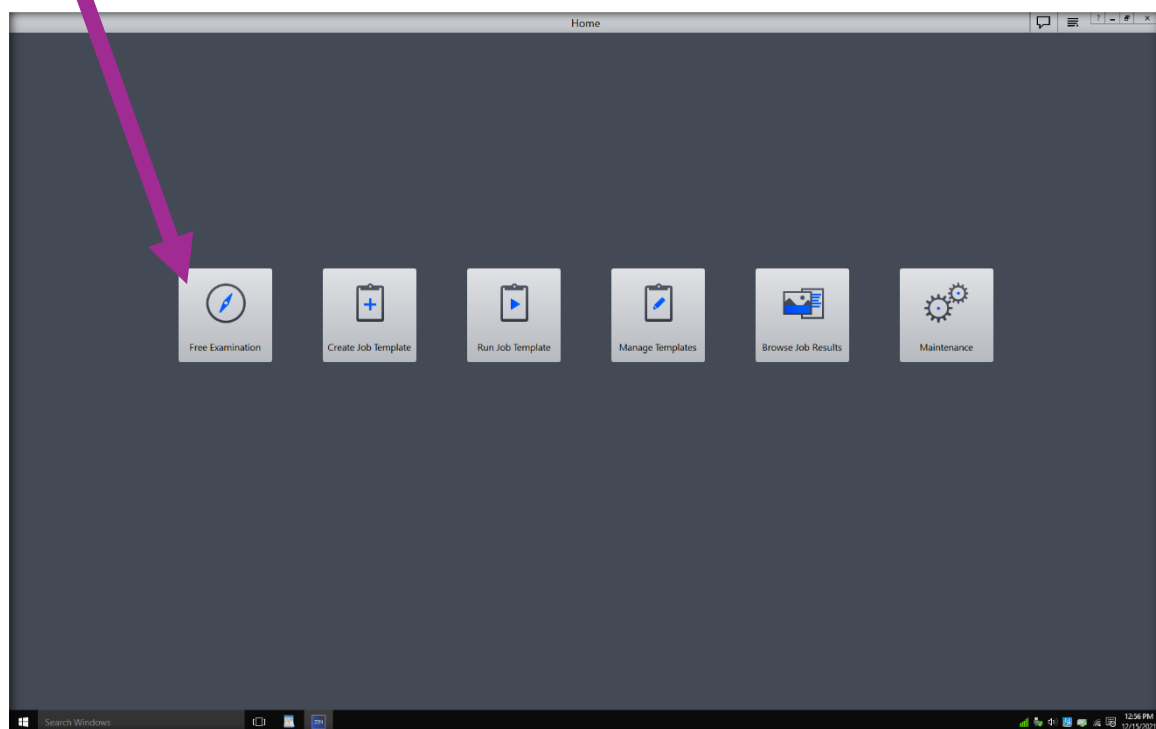Zingg, T. (1935) Beitrag zur schotteranalyse. Schweiz. Mineral. Petrograd. Mitt.15, 39-140.

10.   Appendix

**Constructing 3-D images using Z-stack images of an optical microscope**

1-Fist click on the ZEISS ICONE (Zen core 2.6) to run the software.

Once you click it will open the software
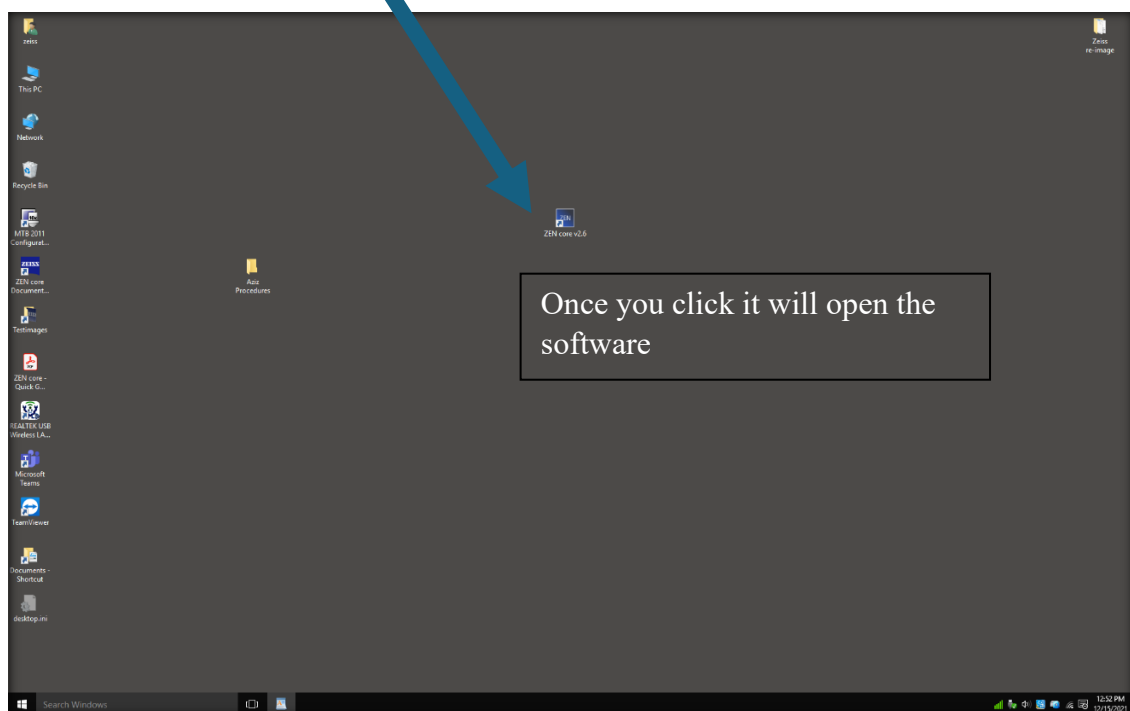
2- Click on the free examinations and wait for the software to open.

3- Skip Collaboration; Unless you are using the software for the first time, more likely after the update (you may skip calibration for fast access to the software, however, if you chose to run the calibration make sure that there is no sample on the stage as the camera and lenses will travel all the height intervals when you start running it)
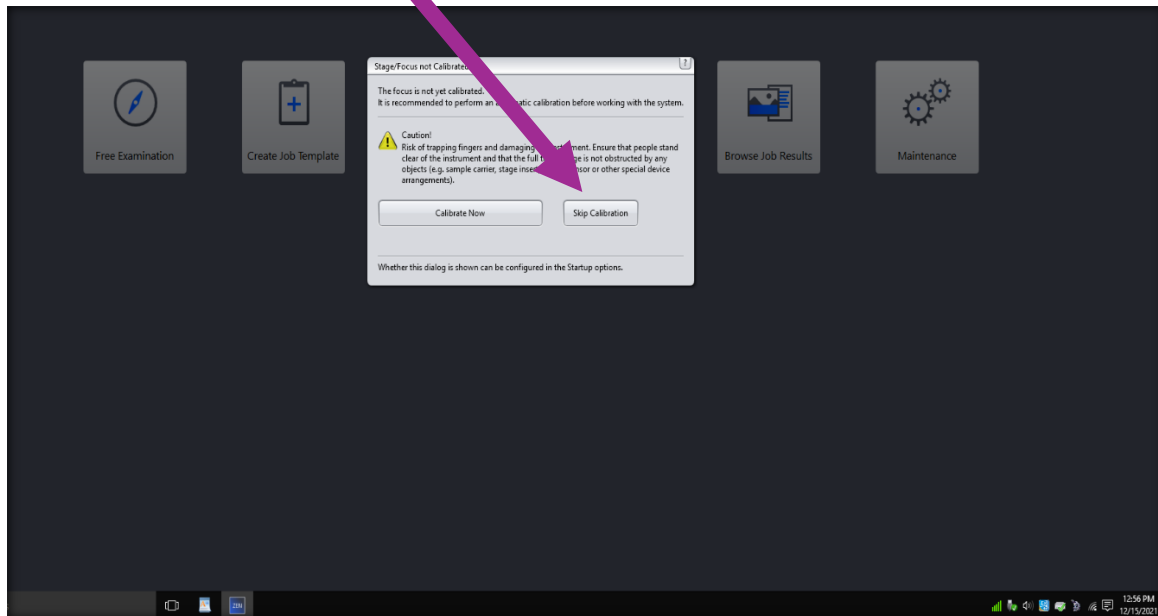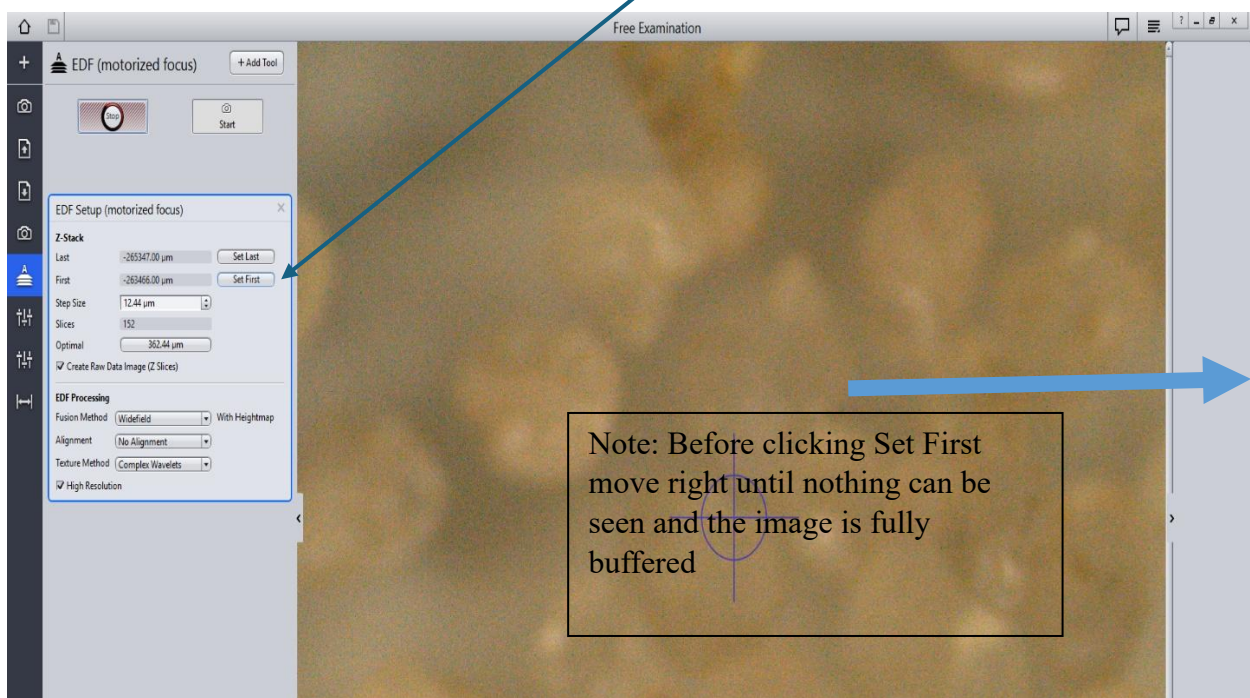

4 - Depending on your choice of magnification, select the right magnification (1-8) before you obtain any image to get the right scale for your measurements.
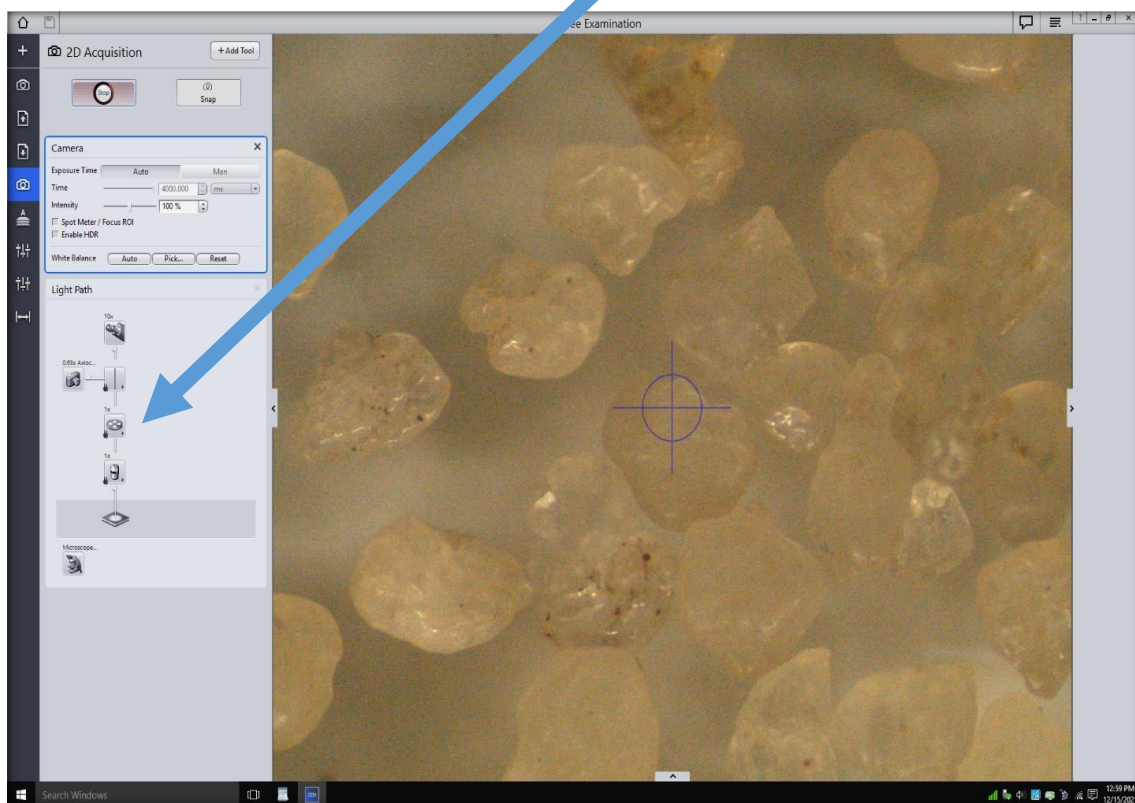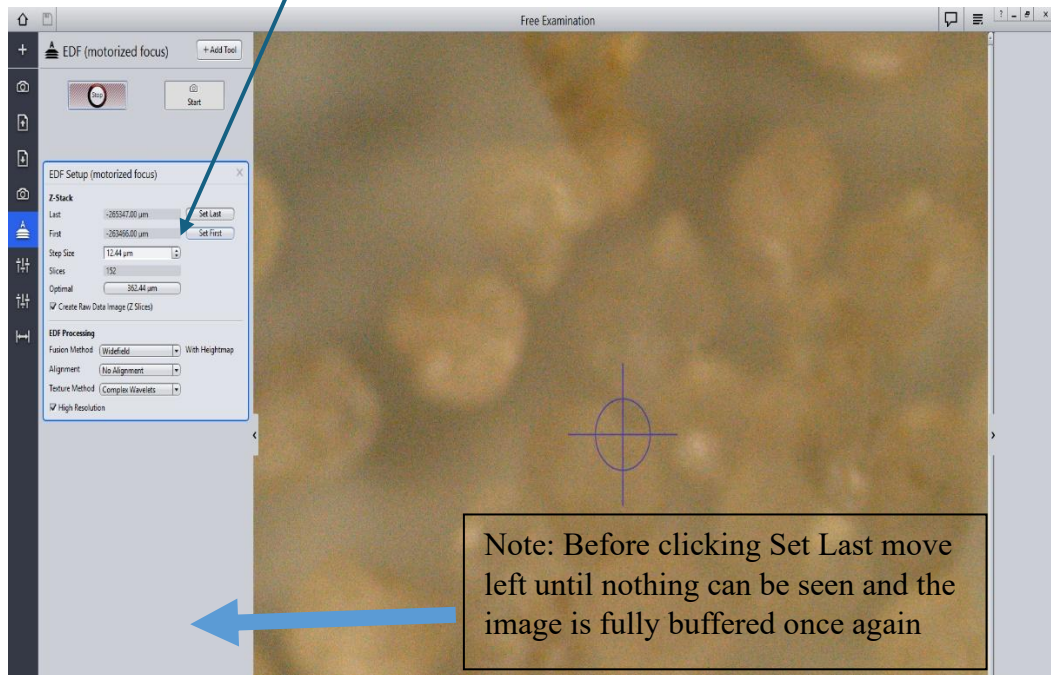
5- Click on the z-stack icon to initiate the z-stack window
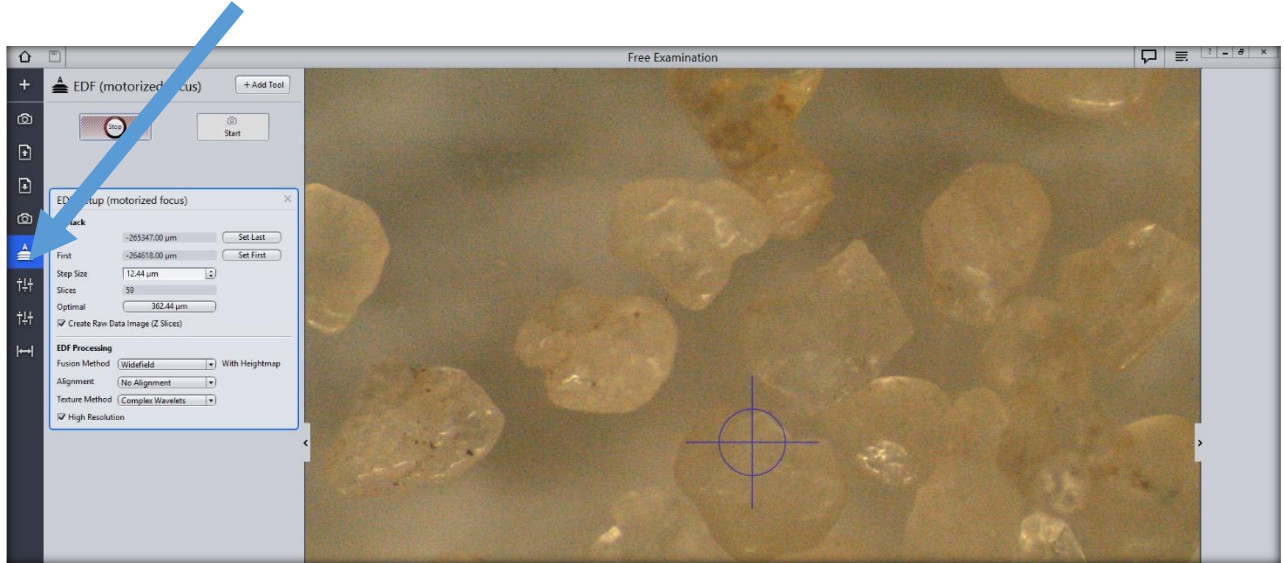
6- The z-stack is a set of images at different z-axis levels. These images should cover all the depth in interest. To select where the z-stack starts, click on Set First after you move the camera level manually till you reach a point above your sample and your sample will be just out of focus.


Note: Before clicking Set First move right until nothing can be seen and the image is fully buffered

7- Then you need to specify the end of the height z when you have covered all the depth of the area of interest. Click on Set Last

Note: Before clicking Set Last move left until nothing can be seen and the image is fully buffered once again

8- Select Step Size; The software will calculate the optimum z-step depth depending on the magnification which is used. by clicking on this depth, you will automatically choose this depth and the software will calculate the number of images required to cover the depth you specified in your selection of the z-stack. You may choose a smaller z-step to obtain the images but note that decreasing the z-step will increase the number of images in your analysis and the time to capture these images and process them. Do Not choose a larger z-step otherwise, the accuracy in the z-direction will be less.
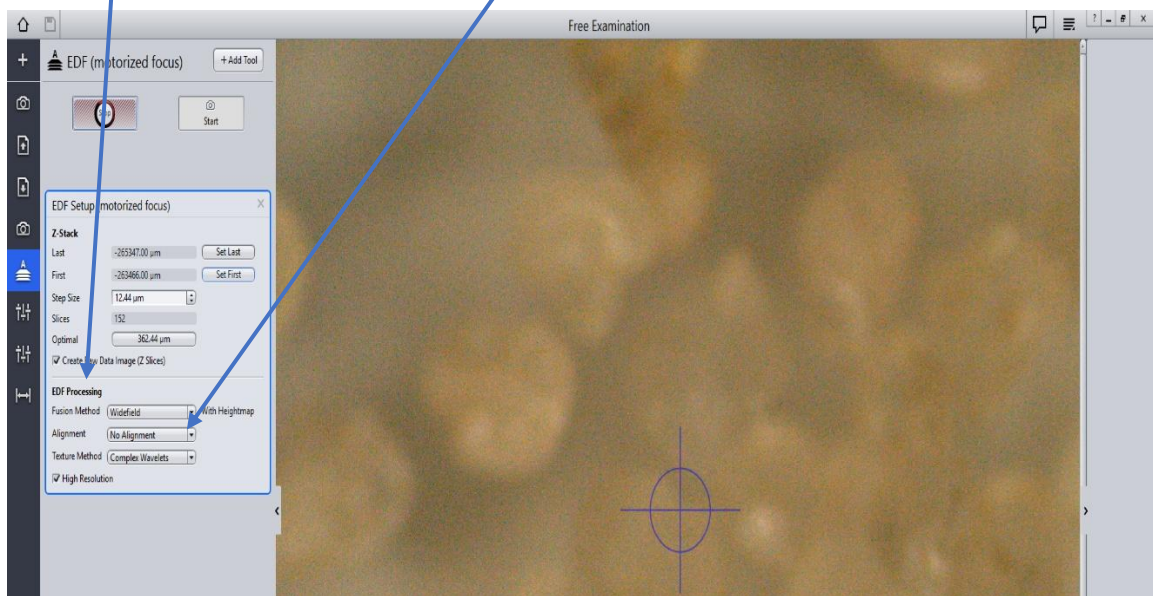
9-Click Start; as soon as the z-stack process is started, a more compacted image is generated
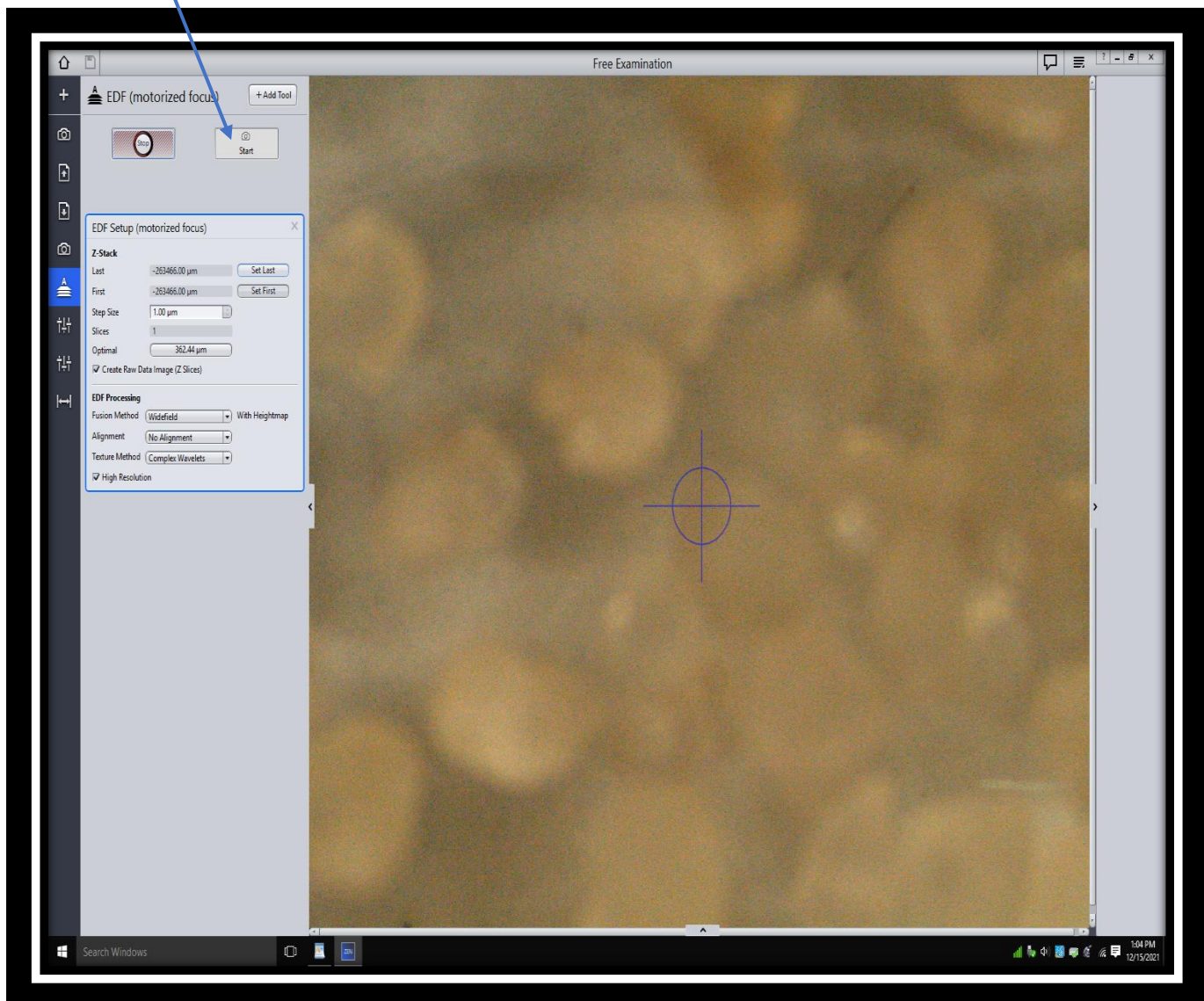
10- Remember always to save your images in the right folder with the extension (czi) otherwise jpeg images will not be suitable for 3D analysis in ConfoMap.